

## Abstract

# Purification, Characterisation and Crystallisation from a Range of Rhodospirillineae Pigment-protein Complexes.

by

Andrew Gall

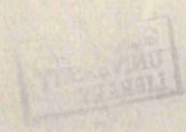
A thesis submitted for the degree of Doctor of Philosophy.

University of Glasgow.

Department of Botany.

May 1994.

0380  
1/1/94



ProQuest Number: 13834026

All rights reserved

INFORMATION TO ALL USERS

The quality of this reproduction is dependent upon the quality of the copy submitted.

In the unlikely event that the author did not send a complete manuscript and there are missing pages, these will be noted. Also, if material had to be removed, a note will indicate the deletion.



ProQuest 13834026

Published by ProQuest LLC (2019). Copyright of the Dissertation is held by the Author.

All rights reserved.

This work is protected against unauthorized copying under Title 17, United States Code  
Microform Edition © ProQuest LLC.

ProQuest LLC.  
789 East Eisenhower Parkway  
P.O. Box 1346  
Ann Arbor, MI 48106 – 1346

## Abstract

A range of photosynthetic integral membrane pigment-protein complexes were purified from several species of purple bacteria. The light-harvesting complexes that were isolated were the RC-LHI conjugate (also called the *core* conjugate) and the B800-850 peripheral light-harvesting complex (LHII). Uniform growth and protein purification protocols were established for each species.

The stability of the RC-LHI conjugates was species dependent. The most stable *cores* were obtained from *Rp. acidophila*, *Rp. cryptolactis* and *Rp. palustris*. The least stable RC-LHI conjugates were from *R. centenum* and *Rb. sphaeroides*.

Biochemical analysis of the RC-LHI conjugate found that all the species investigated had a similar RC:BChl *a* ratio of approximately ~1:30. An experimentally determined extinction coefficient for BChl *a* at 880nm (which is used to calculate the RC:BChl *a* ratios) for each species was obtained and found to lie within the range of 100-120 mM<sup>-1</sup> cm<sup>-1</sup>. When the RC:BChl *a* ratios were recalculated using the experimentally determined extinction coefficients the average RC:BChl *a* ratio increased to ~1:34.

The purified membrane proteins were then screened to see if suitable crystals could be obtained for structural analysis. Two Dimensional and Three Dimensional crystallisation techniques were utilised and the results compared.

2D arrays of the RC-LHI conjugate from *Rp. palustris* and *Rp. acidophila* were obtained. Initial image analysis the *Rp. acidophila* RC-LHI conjugate suggests a hexagonal lattice with a centre-to-centre distance of approximately 115±5Å,  $\gamma=120^\circ$ ) at a resolution of 19Å. Such an hexagonal arrangement of the RC-LHI conjugate further substantiates the hypothesis that the RC is surrounded by six LHI complexes with a theoretical RC:BChl *a* stoichiometry of 1:28. A square 2D array (unit cell of 62.2Å x 62.2Å,  $\gamma=90^\circ$ ) was obtained from *Rp. cryptolactis* B800-850 (LHII) but was too small for detailed image analysis.

Screening the integral membrane pigment-proteins using the more conventional 3D crystallisation methods of vapour diffusion also produced uniform crystal-like structures for the RC-LHI conjugates from *R. rubrum* and *Rp. palustris* but these were too small (<0.2 mm) for x-ray analysis. 3D crystals of LHII were obtained from *Rp. sphaeroides* and *Rp. palustris* (low light form). The 3D LHII crystals from *Rp. palustris* diffracted to between 9-11Å.

It is clear that both crystallisation approaches can produce suitable lattices for 3D structural analysis. The results also indicated that although the method of structural determination may be important it may not be the most significant. Probably the most important factor is the choice of pigment-protein complex, its purity, stability and whether or not it will crystallise.

## Abbreviations

### Acknowledgements

I wish to acknowledge my sincere gratitude to my supervisor Prof. R.J. Cogdell for his guidance and encouragement for the duration of my studies. Many thanks are also due to Dr. P.J. Dominy, (Dept. of Botany, Glasgow University) for his help and specifically his advice on numerical analysis.

My gratitude is extended to Dr W. Kühlbrandt and Dr. D.N. Wang (EMBL, Heidelberg), for their patience in tutoring me the rudiments of Electron Microscopy and Two-dimensional crystallography. An acknowledgement must also be paid to Mr I. Robertson (biological EM Unit, University of Glasgow) for his general advice on EM and to Mr. M. Cryklaff (EMBL, Heidelberg) for his skill at preparing specimens for cryo-EM.

The help from Dr A. Kuppe, Dr R. Nunn (EMBL, Heidelberg), Dr A. Hawthornthwaite (Dept. of Botany, University of Glasgow), and Mr. G. MacDermott, (Dept. of Chemistry, University of Glasgow), was greatly appreciated for their guidance in the Three-dimensional crystallisation screens.

Thanks to Mr T. N. Tait (Dept. of Botany, University of Glasgow), for his photography. Special thanks are due to the technicians Miss E. Halloran and Frau C. Döer, a.k.a. *The Dragon*. My appreciation is also extended to the *Science and Engineering Research Council* for their provision of a scholarship.

Finally a general acknowledgement must be made to the members of the *Arnott* and *Hooker* laboratories for stimulating conversations and friendship.

NIR	near infrared
O.D.	optical density
α-Glc	α-D-glucopyranoside
RC	reaction centre
UAc	uranyl acetate
PC	phosphatidylcholine
PE	phosphatidylethanolamine
PEG	polyethylene glycol
PG	phosphatidylglycerol

## Abbreviations

### Declaration

In this Thesis the S.I. standard is used throughout where possible, other abbreviations used are listed below:-

Ø	bacteriopheophytin
λ	wavelength
Å	angstrom
Abs.	absorption
BChl	bacteriochlorophyll
BPheo	bacteriopheophytin
Chl	chlorophyll
CL	cardiolipin
D <sub>A</sub> D <sub>B</sub>	BChl <i>a</i> special pair
DEAE	diethylethyl-amino ethyl cellulose
ε <sub>λ<sub>nm</sub></sub>	extinction coefficient at λnm
INT	fluorescence intensity
LDAO	N,N-dimethyldodecylamine-N-oxide
LHI	light-harvesting complex I
LHII	light-harvesting complex II
LM	n-dodecyl β-D-maltoside
NIR	near infrared
O.D.	optical density
β-OG	n-ocetyl-β-D-glucopyranoside
RC	reaction centre
UAc	uranyl acetate
PC	phosphatidylcholine
PE	phosphatidylethanolamine
PEG	polyethylene glycol
PG	phosphatidylglycerol

## **Declaration**

This thesis is less than 100,000 words in length, exclusive of tables, maps, bibliographies and appendices. The work reported in this thesis was performed entirely by myself unless otherwise cited or acknowledged. Its contents have not previously been submitted for any other degree. The research for this thesis was performed between October 1990 and October 1993.

signed..!

Andrew Gall

1<sup>st</sup> May 1994

## Index

Abstract	ii
Acknowledgements	iii
Abbreviations	iv
Declaration	v
Table of Contents	vi
Table of Figures	ix
Dedication	xii

## Table of Contents

### **Chapter One: Introduction**

<b>1.1 An Overview of Photosynthesis:</b>	<b>1</b>
<b>1.2 Taxonomy of the Rhodospirillales:</b>	<b>5</b>
<b>1.3 Rhodospirillineae Photosynthetic Systems:</b>	<b>7</b>
1.3.1 Peripheral Light-Harvesting Antenna Complex Variability:	8
1.3.2 The Polypeptides and Bacteriochlorophyll:	9
1.3.2.1 Antenna Polypeptide Sequence Homology:	13
1.3.3 The Carotenoids:	18
1.3.3.1 Photoprotection:	18
1.3.3.2 Accessory Light-Harvesting:	19
<b>1.4 The Structure of the Rhodospirillaceae PSU:</b>	<b>20</b>
1.4.1 The Light-Harvesting Complexes:	20
1.4.2 The Reaction Centre:	24
1.4.2.1 The L and M Polypeptides:	28
1.4.2.2 The H Polypeptide:	28
1.4.3 The Reaction Centre Light-Harvesting Conjugate:	29
<b>1.5 Electron Flow Through the PSU:</b>	<b>34</b>
1.5.1 Electron Flow Through the Reaction Centre:	34
1.5.2 Electron Flow Beyond the Reaction Centre:	37
<b>1.6 Structural Determination of Biological Macromolecules:</b>	<b>39</b>
1.6.1 NMR	39
1.6.2 EM:	42
1.6.2.1 The Advantages of EM:	42
1.6.2.2 Disadvantages of EM:	46
1.6.2.2.1 Exposure to High Vacuum:	46
1.6.3 Negative Staining:	48
1.6.4 Structural Analysis: a Combined Approach:	49

<b>1.7 Thesis Aims:</b>	<b>51</b>
<b>2.1 Cell Culturing:</b>	<b>52</b>
<b>2.2 Cell Harvesting:</b>	<b>53</b>
<b>2.3 Membrane Preparation:</b>	<b>53</b>
<b>2.4 Absorption Spectroscopy:</b>	<b>54</b>
<b>2.5 Fluorescence Spectroscopy:</b>	<b>54</b>
2.5.1 Correction and Normalisation of LS50 Data:	55
2.5.2 Optimising Fluorescence Data Collection:	57
<b>2.6 Isolation of Bacteriochlorophyll Containing Complexes:</b>	<b>58</b>
2.6.1 Membrane Solubilisation:	58
2.6.2 Sucrose Gradient Centrifugation:	58
2.6.3 Anion Exchange:	59
2.6.4 Gel Filtration:	59
2.6.6 Detergent Exchange:	60
2.6.7 Determination of RC: LH Antenna Bacteriochlorophyll Ratio:	62
2.6.7.1 Bacteriochlorophyll Assay:	62
2.6.7.2 Reaction Centre Assay:	62
<b>2.7 Polypeptide Analysis; Concentration and Composition:</b>	<b>63</b>
2.7.1 Protein Concentration:	63
2.7.2 Protein Composition:	65
<b>2.8 3D Crystallography:</b>	<b>65</b>
<b>2.9 2D Crystallography:</b>	<b>66</b>
<b>2.10 Electron Microscopy:</b>	<b>68</b>
2.10.1 Carbon Coated Grids:	68
2.10.2 Negative Staining:	68
<b>2.11 Transmission Electron Microscopy (T.E.M.):</b>	<b>69</b>
<b>2.12 Optical Bench: Integrity of Order.</b>	<b>69</b>
<b>2.13 Image Processing:</b>	<b>69</b>
<b>3.1 Introduction</b>	<b>70</b>
3.2 Growth of Cell Lines	70
3.2.1 <i>R. centenum</i> :	74
3.2.2 <i>R. rubrum</i> S1	78
3.2.3 <i>Rb. sphaeroides</i> GA	82
3.2.4 <i>Rb. sphaeroides</i> M21	86
3.2.5 <i>Rc. gelatinosus</i> DSM149 and DSM151:	90
3.2.7 <i>Rp. acidophila</i> 7750, 10050 and 7050	95
3.2.8 <i>Rp. cryptolactis</i>	99
3.2.9 <i>Rp. palustris</i> 2.6.1.	103
3.3 Isolation of Core Conjugate (RC-LHI)	108

3.3.1 <i>R. centenum</i> :	108
3.3.2 <i>R. rubrum</i> :	134
3.3.3 <i>Rp. acidophila</i> :	137
3.2.4 <i>Rp. palustris</i> strain 2.6.1:	145
3.3.5. <i>Rp. cryptolactis</i> :	149
3.3.6 <i>Rb. sphaeroides</i> strains GA and M21:	152
3.3.7 <i>Rc. gelatinosus DSM149 and DSM151</i>	152
<b>3.4 Isolation of Peripheral Light-Harvesting Antenna Complexes:</b>	<b>156</b>
3.4.1 <i>Rp. acidophila</i> (strains 10050, 7750, 7050):	156
3.4.2 <i>Rb. sphaeroides</i> :	156
3.4.3 <i>Rp. cryptolactis</i> :	156
3.4.4 <i>Rp. palustris</i> 2.6.1. and <i>Rc. gelatinosus</i> DSM149:	156
<b>3.5: Summary of Pigment-Protein Characterisation:</b>	<b>162</b>
<b>4.1 Introduction:</b>	<b>163</b>
4.1.1 2D Crystallographic Concepts for Membrane Proteins:	166
4.1.2 Isolated Reaction Centre - LHI Conjugates:	167
<b>4.2 Microdialysis of RC-LHI:</b>	<b>174</b>
<b>4.3 Affect of pH on RC-LHI 2D Arrays:</b>	<b>181</b>
<b>4.4 Microdialysis of a Range of RC-LHI and LHII Complexes.</b>	<b>182</b>
4.4.1 <i>Rp. cryptolactis</i> :	183
4.4.2 <i>Rp. palustris</i> strain 2.6.1:	187
4.4.3 <i>C. purpuratum</i> , <i>R. rubrum</i> , <i>R. centenum</i> , <i>Rb. sphaeroides</i> , and <i>Rc. gelatinous</i> :	191
4.4.4 <i>Rp. acidophila</i> strains 7750, 10050 and 7050:	192
<b>4.4. Image Processing of the RC-LHI Conjugate:</b>	<b>200</b>
<b>4.6 Structural Significance of RC-LHI 2D Arrays:</b>	<b>203</b>
<b>4.7 Summary of 2D Crystallogenesis Studies.</b>	<b>205</b>
<b>5.1 Introduction:</b>	<b>207</b>
<b>5.2 Range of Photosynthetic Proteins Studied:</b>	<b>216</b>
<b>5.3 Magic 46 Protocol:</b>	<b>219</b>
5.3.1 <i>Rp. palustris</i> strain 2.6.1. :	223
5.3.2 <i>R. centenum</i> :	228
5.4 Summary of <i>Magic 46</i> Incubations:	230
<b>5.5 FASTPEG SCREEN:</b>	<b>231</b>
5.5.1 <i>Rc. gelatinosus</i> strain 149 B800-850:	235
5.5.2 <i>Rb. sphaeroides</i> B800-850:	235
5.5.3 <i>Rp. palustris</i> strain 2.6.1. B800-850:	237
<b>5.6 <i>R. rubrum</i> strain S1:</b>	<b>238</b>
<b>5.7 Summary of Three Dimensional Crystallography.</b>	<b>240</b>
<b>6.1 Discussion:</b>	<b>241</b>

<b>A.1: Bacterial Culture Soln's:</b>	<b>249</b>
<b>A.2: Tannin Assay Solutions:</b>	<b>252</b>
<b>A3: PAGE Stock Solutiuons:</b>	<b>253</b>
<b>A4.1: Magic 46 Stock Solutions:</b>	<b>255</b>
<b>A4.2: FASTPEG Stock Solutions:</b>	<b>256</b>
<b>References:</b>	<b>257</b>

## Table of Figures

Figure 1.1: Classification of the Rhodospirillales including the genera Rhodospirillaceae.	2
Figure 1.2: Types of intra-cytoplasmic membrane.	3
Figure 1.3: Absorption characteristics of the photosynthetic pigments from a member of the Rhodospirillaceae.	6
Figure 1.4: Similarities in the primary amino acid structures for the Rhodospirillineae $\alpha$ -polypeptides.	10
Figure 1.5: Similarities in the primary amino acid structures for the Rhodospirillineae $\beta$ -polypeptides.	11
Figure 1.6: A structural model for the Rhodospirillaceae light-harvesting minimal unit.	12
Figure 1.7: NIR absorption maxima and primary sequence homology for $\alpha$ -polypeptides of <i>Rp. acidophila</i> and <i>Rp. palustris</i> .	14
Figure 1.8: Absorption spectra of different forms of LHII.	16
Figure 1.9: Structural models for the Rhodospirillaceae light-harvesting antenna.	21
Figure 1.10: Patterson projections and resulting structural model for <i>Rp. acidophila</i> B800-850.	22
Figure 1.13: The $\alpha$ -helices of <i>Rb. sphaeroides</i> reaction centre.	27
Figure 1.14: Cross-section of the surface relief map of the photosynthetic core of <i>Ectothiorhodospira halochloris</i> .	30
Figure 1.15: Six-fold symmetry of bacterial core light-harvesting complexes	31
Figure 1.16: Localisation of detergent ( $\beta$ -OG) in the reaction center crystals of <i>Rb. sphaeroides</i> strain Y.	32
Figure 1.17: Cyclic electron transport in the ICM of an Rhodospirillaceae: <i>Rb. sphaeroides</i> .	36
Figure 1.18: Photosynthetic electron transport model for <i>Rb. capsulatus</i> .	38
Figure 1.19: High resolution data obtained using cry-EM.	41
Figure 1.20: Comparison of the negatively stained 3D reconstruction with the atomic resolution x-ray data for F-actin filaments.	50
Figure 2.1: Nominal quantum efficiency response curve for the Hamamatsu R928 photomultiplier tube and its calculated polynomial equation.	56
Figure 2.2: Typical redox difference absorbance assay for RC-LHI conjugate isolated from a member of the Rhodospirillaceae.	61
Figure 2.3: Protein concentration calibration curve based on turbidity measurements.	64
Figure 2.4: Experimental designs for microdialysis.	67
Figure 3.1: A logistic population growth model.	72
Figure 3.2: Growth curve of <i>Rhodospirillum centenum</i> .	75

Figure 3.3: Growth curve of <i>Rodospirillum rubrum</i> strain S1.	79
Figure 3.4: Growth curve of <i>Rodobacter. sphaeroides</i> strain GA.	83
Figure 3.5: Growth curve of <i>Rhodobacter sphaeroides</i> strain M21.	87
Figure 3.6: Growth curve of <i>Rhodocyclus gelatinosus</i> strain DSM149.	91
Figure 3.7: <i>Rc. gelatinosus</i> strain DSM151 cell density vs time.	94
Figure 3.8: Growth curve of <i>Rp. acidophila</i> strain 7750.	96
Figure 3.9: Growth curve of <i>Rp. cryptolactis</i> .	100
Figure 3.10: Growth curve of <i>Rp. palustris</i> strain 2.6.1.	104
Figure 3.11: Pigmented bands resulting from density centrifugation.	107
Figure 3.12: Fractionation of solubilised <i>R. centenum</i> membranes from a DEAE column when a NaCl gradient was applied.	109
Figure 3.13: Fractionation from a second DEAE column.	111
Figure 3.14: Fractionation of <i>R. centeumn core</i> elutant from a S-200 molecular sieve column.	113
Figure 3.15: Spectroscopic analysis of the pigmented bands from a <i>R. centenum</i> sucrose gradient.	115
Figure 3.16: Thin layer chromatography from Bands I and II from <i>R. centenum</i> .	117
Figure 3.17: Characterisation of purified <i>R. centenum</i> RC-LHI conjugate.	119
Figure 3.18: Typical emission spectrum from <i>R. centenum</i> whole cells excited at 520nm.	122
Figure 3.19: Increased <i>R. centenum</i> whole cell fluorecence due to addition of sodium dithionite.	124
Figure 3.20: Emission spectra fro whole cell <i>R. centenum</i> .	125
Figure 3.21: 3D Emission/excitation fluorecence spectra for a batch of <i>R. centenum</i> membranes and isolated RC-LHI originating from bands I and II.	128
Figure 3.22: Averaged excitation spectra for a batch of <i>R. centenum</i> .	130
Figure 3.23: Tabulated data for the %efficiency for carotenoid transfer in <i>R. centenum</i> to LHI.	132
Figure 3.24: Spectroscopic characterisation of purified <i>R. rubrum</i> strain S1 RC-LHI conjugate.	135
Figure 3.25: Optical density measurements from a continous sucrose gradient of <i>Rp. acidophila</i> strain 7750.	138
Figure 3.26: Pigmented bands of a sucrose gradient from directly solubilised membranes of <i>Rp. acidophila</i> strain 7750.	140
Figure 3.27: Spectroscopic characterisation of purified <i>Rp.acidophila</i> strain 7750 pigment-protein complexes.	141
Figure 3.28: Spectroscopic characterisation of purified <i>Rp.palustris</i> strain 2.6.1 pigment-protein complexes.	146
Figure 3.29: Spectroscopic characterisation of purified <i>Rp.cryptolactis</i> pigment-protein complexes.	150
Figure 3.30: RC:BChl <i>a</i> ratios for the RC-LHI conjugates from <i>Rb. sphaeroides</i> and <i>Rc. gelatinosus</i> .	154
Figure 3.31: Distribution of RC:BChl ratios using the experimentally determined coefficient from isolated RC-LHI conjugates.	157
Figure 3.32: Summary of the reaction centre:Bacteriochlorophyll ratios obtained for purified RC-LHI conjugates.	160
Figure 3.33: SDS-PAGE of the Rhodospirilliaceae pigment-protein complexes.	161
Figure 4.1: High resolution data obtained from cryo-EM.	164
Figure 4.2: Formation of 2D crystals of mambrane proteins by dialysis across a semi-permeable membrane.	165
Figure 4.3: Tabulated list of the Rhodospirillaceae photosynthetic proteins that were screened for their potential rôle in forming 2D crystals.	168
Figure 4.4: Isolated RC-LHI conjugates from a range of Rhodospirillaceae.	170

Figure 4.5: Isolated <i>Rp. acidophila</i> strain 7750 RC-LHI conjugate.	172
Figure 4.6: Experimental design of a 2D microdialysis system.	175
Figure 4.7: Spectrasopic evidence of pigment-protein stability in different detergents.	178
Figure 4.8: 2D arrays from <i>Rp. acidophila</i> strain 7750.	179
Figure 4.9: Summary of 2D incubations of <i>Rp. acidophila</i> strain 7750 RC-LHI conjugate after 48 hours.	180
Figure 4.10: Tubular arrays of <i>Rp. cryptolactis</i> B800-850 (LHII).	184
Figure 4.11: Tubular arrays of <i>Rp. cryptolactis</i> B800-850 (LHII).	185
Figure 4.12: Cryo-electron micrograph of the 2D arrays from <i>Rp. cryptolactis</i> B800-850 (LHII).	186
Figure 4.13: Loose association of <i>Rp. palustris</i> strain 2.6.1. LHII (high light form).	189
Figure 4.14: Negatively stained small mosaic 2D arrays of <i>Rp. palustris</i> strain 2.6.1. RC-LHI conjugate.	190
Figure 4.15: Negatively stained <i>Rp. acidophila</i> strain 7050 RC-LHI vesicles.	193
Figure 4.16: 2D arrays of negatively stained <i>Rp. acidophila</i> RC-LHI ( <i>core</i> ) conjugate.	194
Figure 4.17: Fissures in a 2D array of RC-LHI.	197
Figure 4.18: Non hexagonal arrays of <i>Rp. acidophila</i> strain 10050 RC-LHI conjugate.	198
Figure 4.19: F.F.T of a RC-LHI array.	201
Figure 4.20: Refined lattice templet.	202
Figure 4.21: Comparison of the 2D electron density reconstruction maps of the RC-LHI conjugate from <i>Rp. acidophila</i> strains 10050 and 7750 with <i>R. viridis</i> .	204
Figure 5.1: Solubility of a solute.	208
Figure 5.2: Crystallographic apparatus used for vapour diffusion.	210
Figure 5.3: Photograph of the $\beta$ -OG detergent ring surrounding the hydrophobic domain of the bacterial RC.	212
Figure 5.4: 3D crystallisation of pigment-protein micelles: octaion of lipds, detergents and proteins.	213
Figure 5.5: The screened photosynthetic proteins of the Rhodospillaceae.	217
Figure 5.6: The <i>Magic 46</i> screen.	218
Figure 5.7: Initial <i>Magic 46</i> results.	220
Figure 5.8: Reservoir conditions that produced cystals for <i>Rp. palustis</i> 2.6.1. <i>core</i> conjugate.	222
Figure 5.9: 3D crystals of <i>Rp. palustris</i> 2.6.1. RC-LHI <i>core</i> conjugate.	224
Figure 5.10: The second group of crystallographic trials that produced 3D crystals of <i>Rp. palustris</i> strain 2.6.1 <i>core</i> conjugate.	225
Figure 5.11: Phase change in <i>R. centenum</i> RC-LHI microcrystals.	229
Figure 5.12: The <i>FASTPEG</i> screen.	232
Figure 5.13: 3D crystals of <i>Rb. sphaeroïdes</i> B800-850.	234
Figure 5.14: sheet-like structure of <i>Rp. palustris</i> B800-850 (low light form).	236
Figure 5.15: Crystal-like structures of <i>R. rubrum</i> S1 RC-LHI.	239
Figure 6.1 Comparison of the 2D and 2D Structures for bacteriochlorophyll a-containing species.	246
Figure 6.2 Model ofr the Rhodospirillaceae RC-LHI conjugate.	246

Chapter One:

**To my Mum and Dad.**

## 1.1 An Overview of Photosynthesis:

Photosynthesis is the conversion of electromagnetic energy to useful chemical energy by a group of organisms, called phototropha. They utilise the converted energy to grow and reproduce. The energy originates from the sun and is trapped by the photosynthetic apparatus of these organisms. It is then transformed into a utilizable energy source. In the first instance this source of useful energy is ATP, and NADPH<sub>2</sub>. Photosynthesis has historically been divided into two parts; the *light* and *dark reactions* based on the work by Blackman, (1906) as described by Ganong, (1908) and Speoehr, (1926). These two reactions were separated temporally by Emerson and Arnold, (1932) indicating that two separate processes were involved. It is now known that the

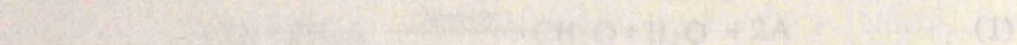
*light reactions* are responsible for the conversion of electromagnetic energy to ATP and NADPH<sub>2</sub> followed by the *dark reactions* which are involved with carbohydrate synthesis. The carbohydrates are used as the building blocks for growth and distribution. The *dark reactions* is outwith the scope of this course but for a general overview Gregory, (1989) can be consulted.

## Chapter One:

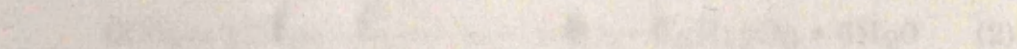
### Introduction

Photosynthesis utilises specific ranges of the electromagnetic spectrum for photosynthesis. These ranges are often called light (i.e. man's terminology) or photoactive radiation a better term is Photosynthetically Active Radiation (PAR).

Blackman (1906) produced a general equation for photosynthesis where the electron donor is H<sub>2</sub>A. This allows all photosynthesis to be described by a single general equation:



where CH<sub>2</sub>O is a solid carbohydrate storage pool. H<sub>2</sub>A is water in plants and cyanobacteria, hydrogen sulphide in sulphur bacteria and organic compounds such as acetate in the purple bacteria. 2A, the oxidised product, is sulphate in plants and cyanobacteria. In sulphur bacteria 2A is sulphur. In the purple bacteria bacteria produce organic compounds such as dimethyl sulphide. The general equation for photochemical reduction has been adapted:

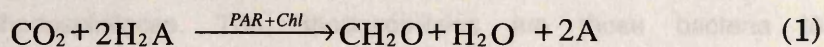


## 1.1 An Overview of Photosynthesis:

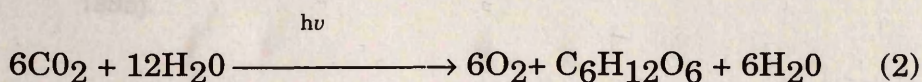
Photosynthesis is the conversion of electromagnetic energy to useful chemical energy by a group of organisms, called phototrophs. They utilise the converted energy to grow and reproduce. The energy originates from the sun and is trapped by the photosynthetic apparatus of these organisms. It is then transformed into a utilizable energy source. In the first instance this source of useful energy is ATP, and NADPH<sub>2</sub>. Photosynthesis has historically been divided into two parts; the *light* and *dark reactions* based on the work by Blackman, (1905) as described by Ganong, (1908) and Spoechr, (1926). These two reactions were separated temporally by Emerson and Arnold, (1932) indicating that two separate processes were involved. It is now known that the *light reactions* are responsible for the conversion of electromagnetic energy to ATP and NADPH<sub>2</sub> followed by the *dark reactions* which are involved with carbohydrate synthesis. The carbohydrates are used as the building blocks for general cell metabolism. The rôle of the *dark reactions* is outwith the scope of this thesis but for a general introductory overview Gregory, (1989) can be consulted.

Phototrophs utilise specific wavelength ranges of the electromagnetic spectrum for photosynthesis. These ranges are often called light (i.e. man's photoreceptive range), however a better term is Photosynthetically Active Radiation (PAR).

C.B. van Neil (1941) produced a general equation for photosynthesis where the electron donor is H<sub>2</sub>A. This allows all photosynthesis to be described by a single general equation;



where CH<sub>2</sub>O is a fixed carbohydrate storage pool. H<sub>2</sub>A is water in plants and cyanobacteria, hydrogen sulphide in sulphur bacteria and organic compounds such as succinate in non-sulphur bacteria. 2A, the oxidised product, is molecular oxygen in plants and cyanobacteria. In sulphur bacteria 2A is sulphur, while the non-sulphur bacteria produce organic compounds such as fumarate. In plants the general equation for photochemical reduction has been adapted to:



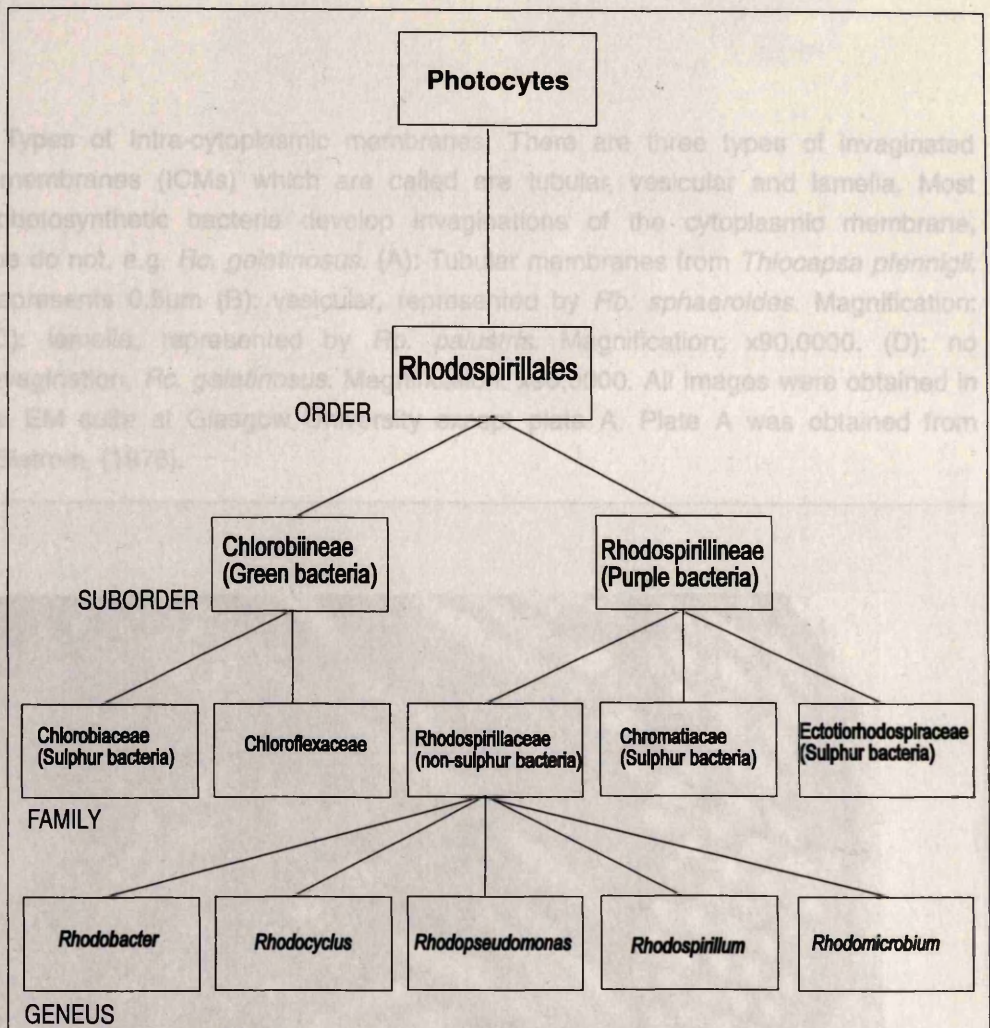
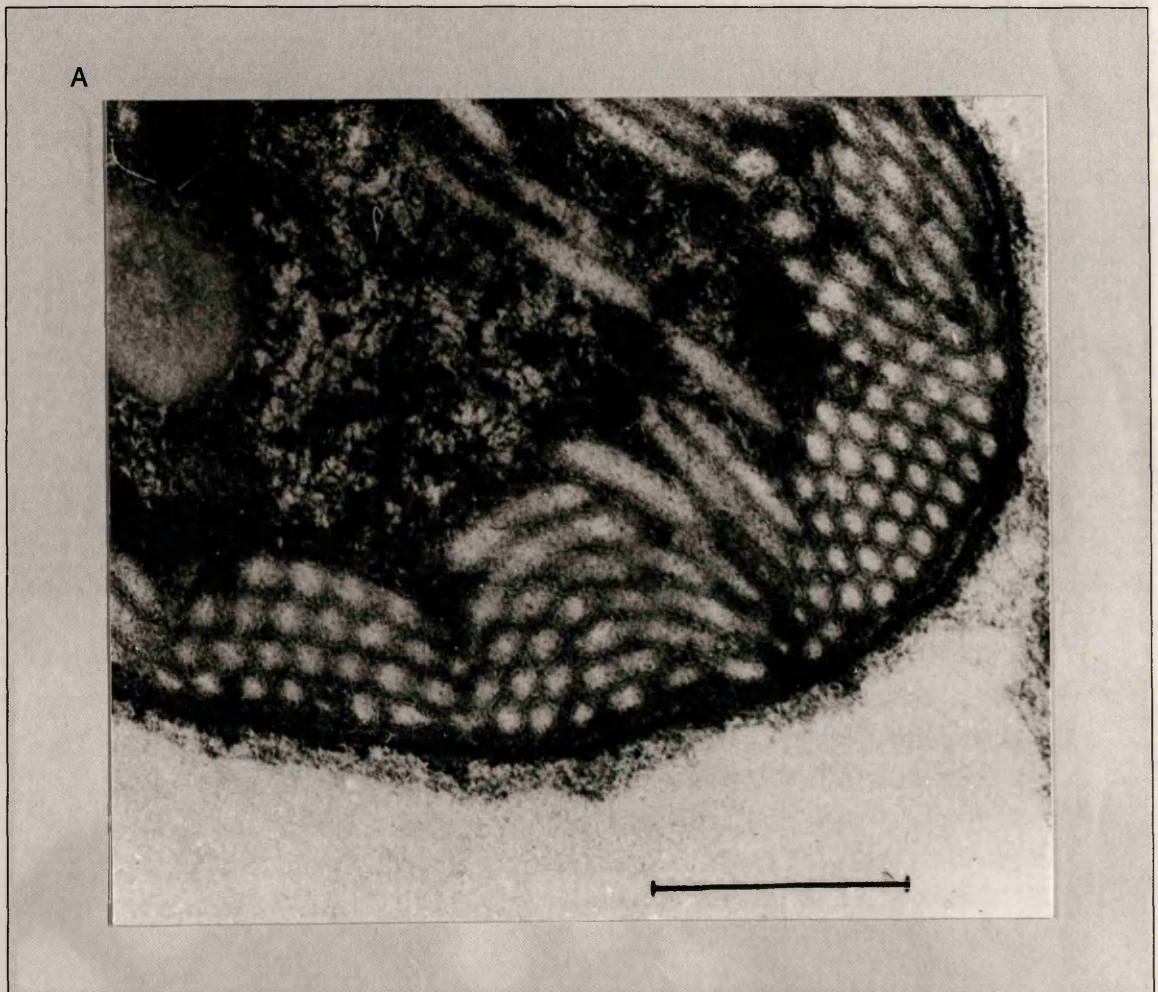
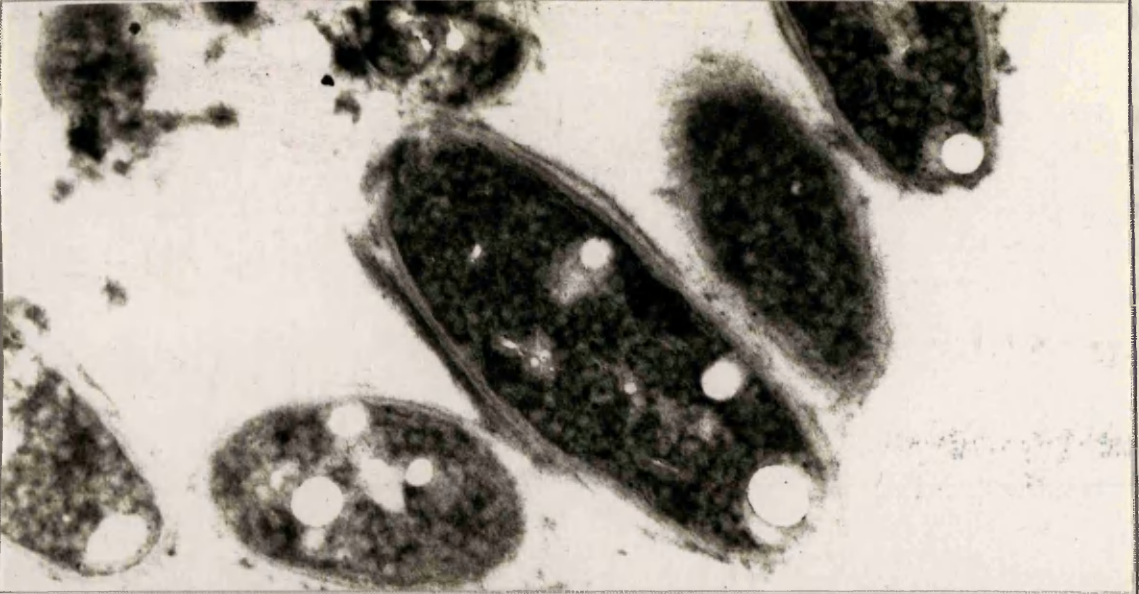


**Figure 1.1:** Classification of the Rhodospirillales including the genera of Rhodospirillaceae. The Rhodospirillales are those bacteria that contain bacteriochlorophyll that are capable of anoxygenic photosynthesis. (Pfennig and Truper, 1979). The order Rhodospirillales splits into two suborders using bacteriochlorophyll composition and ultra-structure as the taxonomic criteria. The suborders are Chlorobiineae (Bacteriochlorophylls *c, d*, or *e* are present in vesicles called chlorosomes located on the innerside of the plasmallema) and Rhodospirillineae (Bacteriochlorophylls *a* or *b* are present in intra-vesicular membranes). Both suborders split into families on the basis of their ability to use sulphur as the electron donor. The non sulphur Rhodospirillineae are the Rhodospirillaceae which are subdivided into the genera as shown above (Imhoff *et al.*, 1984). The origin of photosynthesis is depicted by the photocytes (Lake *et al.*, 1985).

**Figure 1.2:** Types of Intra-cytoplasmic membranes. There are three types of invaginated cytoplasmic membranes (ICMs) which are called are tubular, vesicular and lamella. Most species of photosynthetic bacteria develop invaginations of the cytoplasmic membrane, however some do not, e.g. *Rc. gelatinosus*. (A): Tubular membranes from *Thiocapsa pfennigii*. Scale: Bar represents 0.5 $\mu$ m (B): vesicular, represented by *Rb. sphaeroides*. Magnification: x90,000. (C): lamella, represented by *Rp. palustris*. Magnification: x90,000. (D): no membrane invagination, *Rc. gelatinosus*. Magnification: x90,000. All images were obtained in the Biological EM suite at Glasgow University except plate A. Plate A was obtained from Clayton and Siström, (1978).



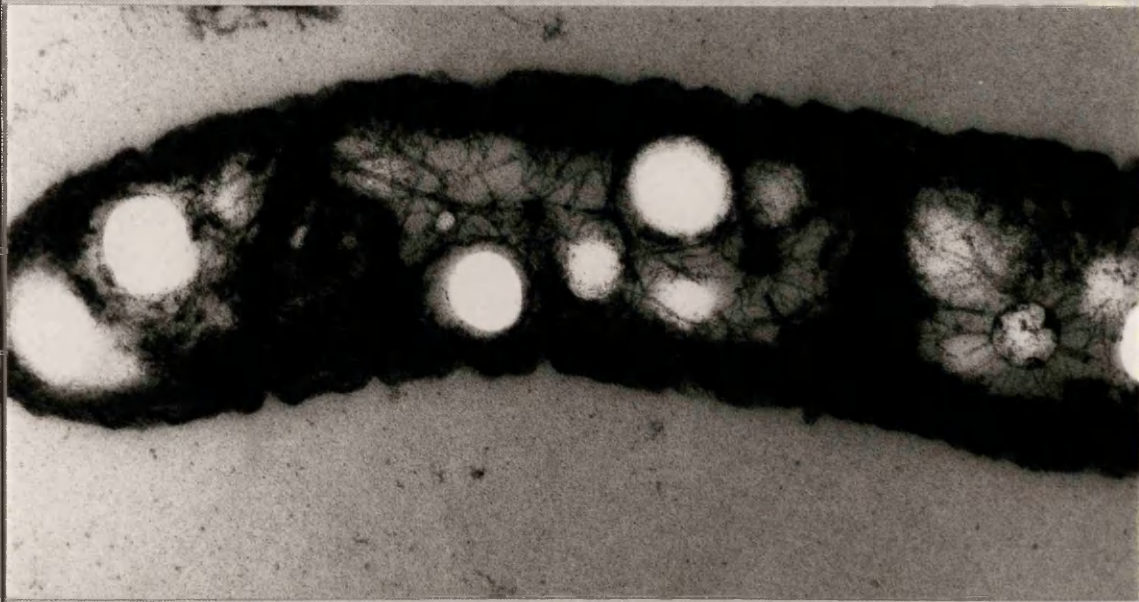
B



C



D



where carbohydrates are formed from carbon dioxide with the oxygen originating from water.

Investigations of photosynthesis at the atomic level require a detailed macromolecular structure which can be used as the basis for understanding function. Such investigations are underway in many laboratories and forms the basis of this thesis.

## 1.2 Taxonomy of the Rhodospirillales:

The order Rhodospirillales, a subset of all phototrophic bacteria, are classified by their ability to undergo anoxygenic photosynthesis using bacteriochlorophylls (Pfennig and Trüper, 1971; Pfennig and Trüper, 1974; Trüper, 1976). The taxonomy within Rhodospirillales is based on morphology, pigment composition and ultra-structure characteristics (Figure 1.1). The order Rhodospirillales splits into the sub-orders Chlorobiineae and Rhodospirillineae, each then splits into families and species.

The Chlorobiineae, or green bacteria, are those species that possess BChl *c, d* or *e* located in organelles called chlorosomes which are not derived from the plasmalemma (Staehelin *et al.*, 1980). The Chlorobiineae are further divided into two families, the Chlorobiaceae and Chloroflexaceae (Trüper and Pfennig, 1978).

The Sub-Order Rhodospirillineae is characterised by having BChl *a* or *b* (Cohen-Bazire and Sistrom, 1966) located in the highly invaginated intracytoplasmic membrane (ICM) which originates from the cytoplasmic membrane (Pfennig, 1967; Pfennig and Trüper, 1973). This extended cell membrane comes in three basic forms: vesicles, lamellae and tubules (Figure 1.2). The Sub-Order Rhodospirillineae is split into three families, the Ectothiorhodospiraceae, Chromatiaceae and Rhodospirillaceae (Imhoff *et al.*, 1984). Both the Ectothiorhodospiraceae and Chromatiaceae utilise sulphur for photosynthesis and are generally strict anaerobes (which implies that they are obligate phototrophs). The Rhodospirillaceae on the other hand generally do not utilise sulphur for photosynthesis. For this reason they are often referred to as the non-sulphur purple bacteria (Pfennig and Trüper, 1973). The Rhodospirillaceae comprise the following genera; *Rhodomicrobium*, *Rhodospirillum* (Molisch, 1907), *Rhodocyclus* (Pfennig, 1978), *Rhodobacter* (Imhoff *et al.*, 1984), and *Rhodopseudomonas* (Molisch, 1907).

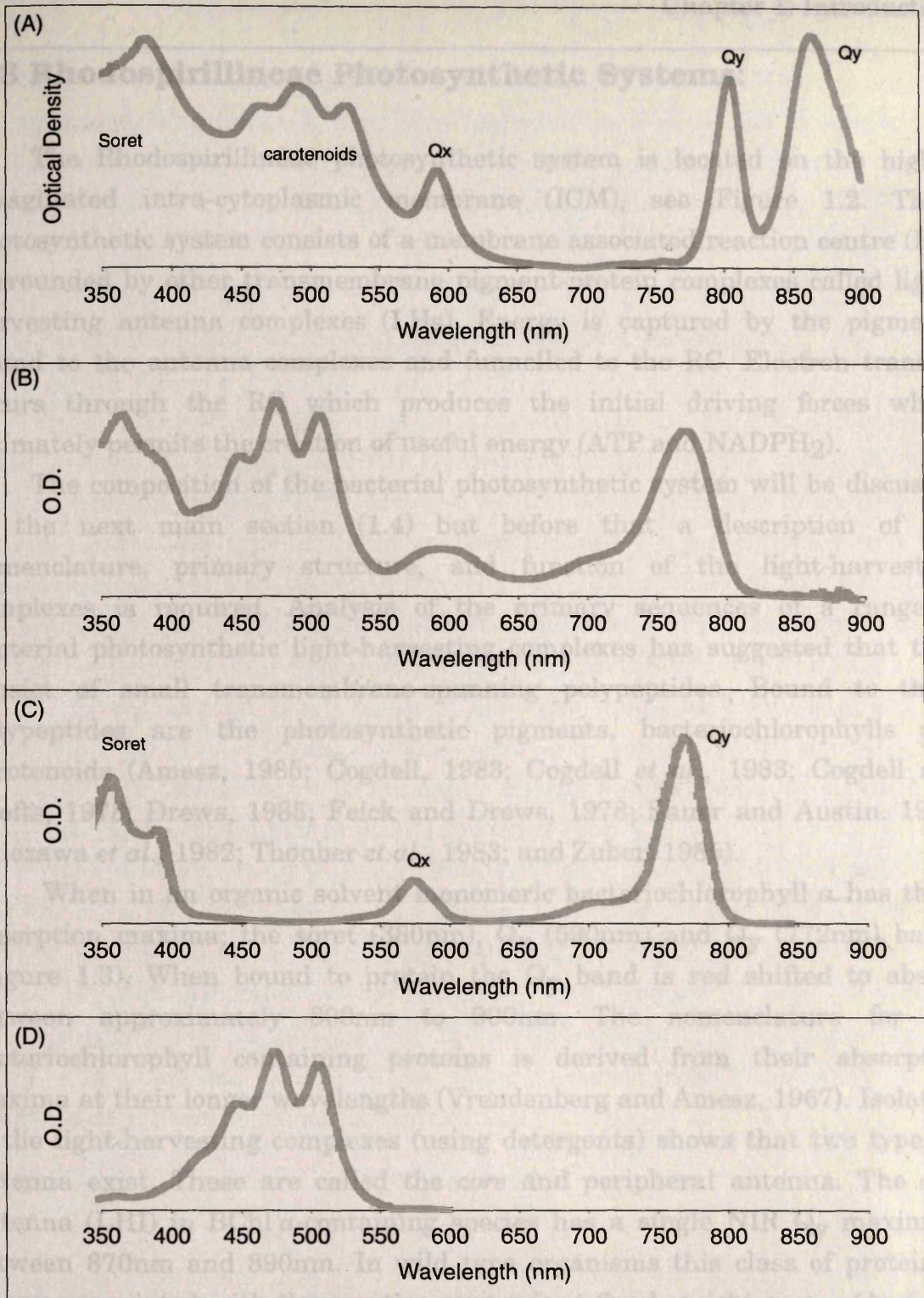


**Figure 1.3:** Absorption characteristics of the photosynthetic pigments from a member of the Rhodospirillaceae. The absorption spectra were collected from *Rhodospseudomonas acidophila* strain 7750. (A): Whole cell absorption spectrum. There are two NIR (Qy) peaks (801nm and 860nm) which represent the absorbance due to bacteriochlorophyll *a* protein interaction. There are also peaks at 590nm (Qx) and 380nm (soret) which are also due to bacteriochlorophyll absorption. Between 380nm and 590nm there are three absorption peaks. These peaks are due to carotenoids. (B): Solvent extracted pigments from (A). The two NIR bacteriochlorophyll *a* peaks are blue shifted to a single peak at 772nm. This blue absorption shift represents the separation of the pigments from the protein. (C): Isolated bacteriochlorophyll *a*, the soret (380nm), Qx (590nm) and Qy (772nm) peaks are marked. (D): Isolated carotenoid (rhodopin). Rhodopin shows the characteristic triplet absorption peaks associated with visible carotenoids.

### 1.3 Rhodospirillineae Photosynthetic Systems:

The Rhodospirillineae photosynthetic system is located on the highly invaginated intra-cytoplasmic membrane (ICM), see Figure 1.2. Their photosynthetic system consists of a membrane associated reaction centre (RC) surrounded by other transmembrane pigment-protein complexes called light-harvesting antenna complexes (LHs). Energy is captured by the pigments bound to the antenna complexes and funnelled to the RC. Electron transfer occurs through the RC which produces the initial driving forces which ultimately permits the creation of useful energy (ATP and NADPH<sub>2</sub>).

The composition of the bacterial photosynthetic system will be discussed in the next main section (1.4) but before that a description of the nomenclature, primary structure, and function of the light-harvesting complexes is required. Analysis of the primary sequences of a range of bacterial photosynthetic light-harvesting complexes has suggested that they consist of small transmembrane-spanning polypeptides. Bound to these polypeptides are the photosynthetic pigments, bacteriochlorophylls and carotenoids (Amesz, 1985; Cogdell, 1983; Cogdell *et al.*, 1983; Cogdell and Crofts, 1978; Drews, 1985; Feick and Drews, 1978; Sauer and Austin, 1978; Shiozawa *et al.*, 1982; Thonber *et al.*, 1983; and Zuber, 1985).

When in an organic solvent monomeric bacteriochlorophyll *a* has three absorption maxima; the *soret* (380nm), Q<sub>x</sub> (590nm) and Q<sub>y</sub> (772nm) bands (Figure 1.3). When bound to protein the Q<sub>y</sub> band is red shifted to absorb between approximately 800nm to 900nm. The nomenclature for the bacteriochlorophyll containing proteins is derived from their absorption maxima at their longer wavelengths (Vrendenberg and Amesz, 1967). Isolation of the light-harvesting complexes (using detergents) shows that two types of antenna exist. These are called the *core* and peripheral antenna. The *core* antenna (LHI) in BChl *a*-containing species has a single NIR Q<sub>y</sub> maximum between 870nm and 890nm. In wild type organisms this class of protein is always associated with the reaction centre in a fixed stoichiometry (Aagaard and Sistrom, 1972). The peripheral antenna, or LHII differ from LHI in that they have two Q<sub>y</sub> bands between 800nm and 860nm and the stoichiometry with the reaction centre is variable. The expression of the different types of peripheral antenna complex and their pigments is dependent on environmental factors such as temperature, light quantity and quality (Clayton and Sistrom, 1978; Cogdell *et al.*, 1983; Heinemeyer and Schmidt, 1983; Robert *et al.*, 1985; Brunisholz *et al.*, 1987; Deinum *et al.*, 1991). All Rhodospirillaceae species produce *core* antenna. Some such as *R. rubrum*, *R.*

*viridis*, *R. centenum* and *R. marina* only produce *core* antenna. Others, such as *Rb. sphaeroides*, produce a peripheral antenna as well as the *core* antenna. Still other species such as *Rp. cryptolactis* (Stadtwald-Demchick *et al.*, 1990), *Rp. acidophila* (Pfennig, 1969) and *Rp. palustris* (Hayashi *et al.*, 1982b) can produce two distinct species of peripheral antenna complexes.

### 1.3.1 Peripheral Light-Harvesting Antenna Complex Variability:

There is variation in the antenna composition in the Rhodospirillaceae. In some species the amount of LHII relative to RC-LHI varies, while in other species multiple types of LHII can also be produced. Examples of species that do not alter their type of LHII composition are *Rb. sphaeroides* and *Rb. capsulatus*. Species such as *Rp. cryptolactis* and *Rp. acidophila* can produce at least two forms of LHII: the B800-820 and B800-850 complexes (Cogdell *et al.*, 1983b; Heinemeyer and Schmidt, 1983; Brunisholz *et al.*, 1987; Bissig *et al.*, 1988;). In *Rp. acidophila* 7750 and 7050 the main environmental stimuli responsible for the switching between B800-850 and B800-820 expression is different. Low temperature is the major environmental factor in strain 7750 while low light is the major stimulus in strain 7050.

The light-harvesting BChls are located within the RC-LHI conjugates and the variable LHII complexes. The bacterial photosynthetic unit (BPSU) is defined as the averaged number of bacteriochlorophylls per reaction centre. Since there is variation in the occurrence and amount of LHII present in growing cells there is variation in the size of the BPSU. Consequently the BPSU size is directly linked to the photosynthetic growth conditions which in turn is dependent on the ambient habitat.

### 1.3.2 The Polypeptides and Bacteriochlorophyll:

The antenna complexes of the Rhodospirillaceae consist of two membrane associated polypeptides called  $\alpha$  and  $\beta$  which form an  $\alpha,\beta$ -heterodimer. The  $\alpha,\beta$ -heterodimer contains bacteriochlorophylls and carotenoids (Amesz, 1985; Cogdell, 1983; Cogdell *et al.*, 1983; Cogdell and Crofts, 1978; Drews, 1985; Feick and Drews, 1978; Sauer and Austin, 1978; Shiozawa *et al.*, 1982; Thonber *et al.*, 1983; and Zuber, 1985). The two polypeptides present,  $\alpha$  and  $\beta$ , are in a molar ratio of 1:1 (Brunisholz *et al.*, 1981a; Brunisholz *et al.*, 1981b; Bissig *et al.*, 1988; Bissig *et al.*, 1990; Cogdell *et al.*, 1983; Cogdell and Thonber 1980; Fuglistaller *et al.*, 1984; Tadros *et al.*, 1983; Tadros *et al.*, 1984; Tadros *et al.*, 1985; Theiler *et al.*, 1984a; Theiler *et al.*, 1984b). In some complexes such as *Rb. capsulatus* B800-850 (LHII)(Shiozawa *et al.*, 1982) and *R. viridis* B1020 (LHI)(Jay *et al.*, 1984) a third colourless polypeptide ( $\gamma$ ) is also present. Again the molar ratio is 1:1:1. This  $\gamma$  polypeptide has been found in all B1020 species of the Ectothiorhodospiraceae which show a characteristic *core* structure determined by electron microscopy (Engelhardt *et al.*, 1983; Stark, 1984; Stark *et al.*, 1986).

The molar ratio of  $\alpha:\beta$  is 1:1, however there are antenna complexes that produce multiple  $\alpha$  and  $\beta$  polypeptides. Examples of multiple  $\alpha$  polypeptide species are found in *Ectothiorhodospira halophila* B890 ( $\alpha_1, \alpha_2$ ) and *Rp. palustris* strain 2.6.1. B800-850 ( $\alpha_1, \alpha_2, \alpha_3$ , and  $\alpha_4$ ). Variation in the  $\beta$  polypeptide also occurs, e.g. the  $\beta_1, \beta_2$  and  $\beta_3$  B800-850 $\beta$  polypeptides in *Rp. palustris* strain 2.6.1. and the  $\beta_1$  and  $\beta_2$  polypeptides in *C. vinosum* B800-820 (Hayashi *et al.*, 1982a; Bissig *et al.*, 1990; Cogdell *et al.*, 1990).

Evans, (1989) has suggested that the B800-850 complex from *Rp. palustris* strain 2.6.1. grown under high light conditions has an  $\alpha_1:\alpha_2:\alpha_3:\alpha_4$  molar ratio of 2:2:2:1 (giving a high 850/800 absorbance ratio) but under low light conditions the molar ratio is 2:6:2:1 (giving a reduced 850/800 absorbance ratio). Adaptation of LHII polypeptide composition can help to maximise the amount of PAR capture in bacterial photosynthesis. This ability, however, appears to be both species and strain specific (Evans, 1989; Gardiner, A.T., personal communication).





## 1.3.2.1 Antenna Polypeptide Sequence Homology:

Examination of the primary structures of the  $\alpha$  and  $\beta$  polypeptides which make up the light-harvesting antenna reveals that there are regions of amino acid sequence homology. The sequences of several integral membrane-spanning hydrophobic  $\alpha$ -helices and  $\beta$ -strands are shown in Figures 1.4 and 1.5 illustrate the amino acid sequences of the  $\alpha$  and  $\beta$  polypeptides which were collated and read by the authors (Zuber and Wagner-Huber, 1984) and have been analysed using the conserved histidine (H or H<sub>9</sub>) as a reference point.

Labelling (Jay *et al.*, 1983), protein synthesis (Brunisholz *et al.*, 1986), UV-CD experiments (Breton and Scheraga, 1984; Cardell and Scheraga, 1985) have indicated that the polypeptides contain a central hydrophobic  $\alpha$ -helix located between the two BChls.

Labelled data for the animal  $\alpha/\beta$  light-harvesting heterodimer of *R. rubrum* B890 to be prepared (Brunisholz *et al.*, 1986), see Figure 1.6. The amino acid sequences of the  $\alpha$  and  $\beta$  N-termini are located on the cytoplasmic side with a single membrane-spanning  $\alpha$ -helix between them. For *R. rubrum* B890 (Figure 1.6) the cytoplasmic N-termini are located on the cytoplasmic side forming a two-turn amphipathic helix (12 residues) and the conserved Proline (see Figure 1.4), located on the periplasmic side. The  $\alpha$ -helix twists into the membrane. A conserved histidine residue is located on the membrane at the periplasmic C-terminus. The amino acid sequences of the  $\alpha$  and  $\beta$  C-termini are long in many species (e.g. *R. gelatinosus* DSM 151) and generally are approximately only 18 amino acids in length. Although Figure 1.6 represents *R. rubrum* B890 it is generally thought to apply equally well to the other light-harvesting antennas.

An examination of Figures 1.4 and 1.5; there are many regions of primary structure homology between the  $\alpha$  and  $\beta$  polypeptides. The amino acid sequences of the  $\alpha$  and  $\beta$  N-termini are located on the cytoplasmic side with a single membrane-spanning  $\alpha$ -helix between them. For *R. rubrum* B890 (Figure 1.6) the cytoplasmic N-termini are located on the cytoplasmic side forming a two-turn amphipathic helix (12 residues) and the conserved Proline (see Figure 1.4), located on the periplasmic side. The  $\alpha$ -helix twists into the membrane. A conserved histidine residue is located on the membrane at the periplasmic C-terminus. The amino acid sequences of the  $\alpha$  and  $\beta$  C-termini are long in many species (e.g. *R. gelatinosus* DSM 151) and generally are approximately only 18 amino acids in length. Although Figure 1.6 represents *R. rubrum* B890 it is generally thought to apply equally well to the other light-harvesting antennas.

**Figure 1.6:** A structural model for the Rhodospirillaceae light-harvesting minimal unit. It is based on one  $\alpha$  and one  $\beta$  apoprotein from *R. rubrum* LHI (B890). In this model two BChls are attached to the grey shaded histidines located on membrane spanning hydrophobic  $\alpha$ -helices, flanked by two polar head groups (Zuber, 1986). Amino acid sequences follow the IUPAC-IUB Joint Commission on Biochemical Nomenclature (1984).

### 1.3.2.1 Antenna Polypeptide Sequence Homology:

Examination of the primary structures of the  $\alpha$  and  $\beta$  polypeptides which make up the light-harvesting complex reveals that there are regions of conserved amino acid sequences. The sequences all show a central membrane-spanning hydrophobic region flanked by polar N- and C- termini. Figures 1.4 and 1.5 illustrate the conserved sequences for the  $\alpha$  and  $\beta$  polypeptides which were collated and redrawn from Zuber and Brunisholz, 1986; Zuber, 1990; and Wagner-Huber *et al.*, 1992; (and references therein). The primary sequences have been analysed using the conserved Histidine (H or His) as a reference point.

Labelling (Jay *et al.*, 1983), protease digestion (Brunisholz *et al.*, 1986), UV-CD and IR spectroscopy (Breton and Nabdryk, 1984; Cogdell and Scheer, 1985) experiments have indicated that the polypeptides contain a central hydrophobic  $\alpha$ -helix located within the membrane (Breton and Nabdryk, 1984). All this biochemical data has enabled a model for the minimal  $\alpha/\beta$  light-harvesting heterodimer of *R. rubrum* B890 (LHI) to be proposed (Brunisholz *et al.*, 1986), see Figure 1.6. The model predicts both the  $\alpha$  and  $\beta$  N-termini are located on the cytoplasmic side while both C-termini are on the periplasmic side with a single membrane-spanning region between them. For *R. rubrum* B890 (Figure 1.6) the cytoplasmic N-terminus of the  $\alpha$  polypeptide forms a two turn amphipathic helix (12-14 amino acids), and the conserved Proline (see Figure 1.4), located at H-19 is where the polypeptide twists into the membrane. A 20-23 amino acid  $\alpha$ -helix results leaving the membrane at the periplasmic C-terminus. The C-terminus can be up to 36 amino acids long in some species (e.g. *Rc. gelatinosus*) but generally is approximately only 18 amino acids in length. Although Figure 1.6 represents *R. rubrum* B890 it is generally thought to apply equally well to the other light-harvesting antennae. On examination of Figures 1.4 and 1.5; there are many regions of primary sequence homology as indicated by the shaded boxed regions. Much of the data derives from Edman protein degradation analysis but sometimes has been determined using DNA sequences. These two independent approaches act as double checks for the true primary structure. Occasionally these checks do result in sequence discrepancies. For example the derived B800-850 $\alpha$  polypeptide in *Rc. gelatinosus* DSM 151 has been sequenced from a genomic DNA library open reading frame corresponding to the  $\alpha$  and  $\beta$  polypeptides. The derived DNA sequence for the  $\alpha$  polypeptide at residues H+1 to H+6 is GLAGK (Simmons, A.E., personal communication) instead of GLLAK as

measured by Edman degradation (Figure 1.4, Brunisholz *et al.*, 1982). However the apparent degree of homology for all the  $\alpha$  and  $\beta$  polypeptides is very high giving similar primary structures and proposed functional properties of the apoproteins. A greater divergence of primary structural sequence would

polypeptide		1	2	3	4	5	6	7	8	9	10	11	12	13	14	15	associated antenna complex (NIR peak)
<i>Rp. palustris</i> strain 2.6.1 B800-850- $\alpha$ 1	H	F	A	V	L	S	N	T	T	W	F	S	K	Y	W	N	B800-850 (high 850nm)
<i>Rp. palustris</i> strain 2.6.1 B800-850- $\alpha$ 3	H	Y	A	V	L	S	N	T	T	W	F	P	K	Y	W	N	B800-850 (high 850nm)
<i>Rp. palustris</i> strain 2.6.1 B800-850- $\alpha$ 4	H	F	A	V	L	S	N	T	T	W	F	P	K	Y	W	N	B800-850 (high 850nm)
<i>Rp. palustris</i> strain 2.6.1 B800-850- $\alpha$ 2	H	F	A	V	L	T	H	T	T	W	V	A	K	F	M	N	LL-B800-850 (high 800nm)
<i>Rp. acidophila</i> strain 7050 B800-820- $\alpha$	H	A	A	V	L	T	H	T	T	W	Y	A	A	F	L	Q	B800-820 (820nm)
<i>Rp. acidophila</i> strain 7750 B800-820- $\alpha$	H	L	A	V	L	T	H	T	T	W	F	P	A	F	T	Q	B800-820 (820nm)
<i>Rp. acidophila</i> strain 7050 B800-850- $\alpha$	H	A	A	V	L	S	H	T	T	W	F	P	A	Y	W	Q	B800-850 (850nm)
<i>Rp. acidophila</i> strain 7750 B800-850- $\alpha$	H	L	A	I	L	S	H	T	T	W	F	P	A	Y	W	Q	B800-850 (850nm)
<i>Rp. acidophila</i> strain 10050 B800-850- $\alpha$	H	L	A	I	L	S	H	T	T	W	F	P	A	Y	W	Q	B800-850 (850nm)
		1	2	3	4	5	6	7	8	9	10	11	12	13	14	15	

proved that single amino acid substitution can cause a blue absorption shift in B800-850 complexes.

**Figure 1.7:** NIR absorption maxima and primary sequence homology for  $\alpha$  polypeptides of *Rp. acidophila* and *Rp. palustris*. The amino acid locations associated with the observed NIR peaks (H+10, H+13, H+14) are shaded light grey as is the conserved histidine. The NIR shifts (850nm  $\rightarrow$  820nm and HL-B800-850  $\rightarrow$  LL-B800-850) are correlated with amino acid changes at H+10 (Y  $\rightarrow$  F) and at H+13,+14 (YW  $\rightarrow$  F#). The # character represents one of three possible amino acid substitutions. The amino acid changes that cause the NIR shifts described in the text are shaded dark grey. Amino acid lettering follows the IUPAC-IUB Joint Commission on Biochemical Nomenclature (1984).

These result from intricate interactions between pigments (bacteriochlorophylls and carotenoids) and their polypeptide backbones. These complex interactions enable heterologous energy transfer to occur from the

measured by Edman degradation (Figure 1.4, Brunisholz *et al.*, 1982). However the apparent degree of homology for all the  $\alpha$  and  $\beta$  polypeptides is very high giving similar primary structures and proposed functional properties of the apoproteins. A greater divergence of primary structural sequence would surely have resulted if the regions of homology do not have very similar rôles in all the light-harvesting antenna of all the Rhodospirillineae.

For both the  $\alpha$  and  $\beta$  polypeptides there is a three amino acid consensus sequence of [Arginine/Lysine]-[Isoleucine/Leucine/Valine]-[Tryptophan] in the vicinity of the conserved Histidine (see Figures 1.4 and 1.5). There is always a large aromatic residue at H+4, and located approximately one helical turn away, a small one at H-4. This suggests a conserved function, possibly pigment-protein interaction in the *in vivo* complexes due to their proximity to the BChl  $a$  binding histidine. Analysis of the peripheral antenna polypeptides provides evidence that a change in residue type produces an absorption shift in the NIR absorption peaks. Figure 1.7 illustrates that highly homologous primary sequences between different strains or different  $\alpha$ -polypeptides within the same strain, differing only at specific aromatic residues (located at H+10,+13 and +14), can cause significant absorption changes at the NIR wavelengths. These specific changes give rise to the absorption characteristics of the B800-850 and B800-820 complexes in *Rp. acidophila* and the absorption shifts observed in *Rp. palustris* 2.6.1. Figure 1.8 shows the blue shift phenomena (850nm  $\rightarrow$  820nm NIR absorbance peak) for two of the examples described above. The above examples only correlate NIR absorption with primary sequence data. This however does suggest that specific amino acid changes in the vicinity of the BChl  $a$  are capable of influencing the  $Q_y$  absorption peak. Indeed Fowler *et al.*, (1992), using directed mutagenesis proved that single amino acid substitution can cause a blue absorption shift in B800-850 complexes.

Bacteriochlorophyll-protein interactions are often discussed in relation to absorption characteristics but carotenoids also play a rôle in the location of the  $Q_y$  maximum. The carotenoidless mutant G9<sup>+</sup> of *R. rubrum* has a  $Q_y$  maximum of 872nm compared to 881nm for the wild type (Parkes-Loach *et al.*, 1988). Both strains of *R. rubrum* have the same amino acid sequences (Brunisholz *et al.*, 1984), consequently the carotenoids account for the red shift in S1. It is clear that the absorption characteristics of the light-harvesting antenna complexes result from intricate interactions between pigments (bacteriochlorophylls and carotenoids) and their polypeptide backbones. These complex interactions enable heterologous energy transfer to occur from the

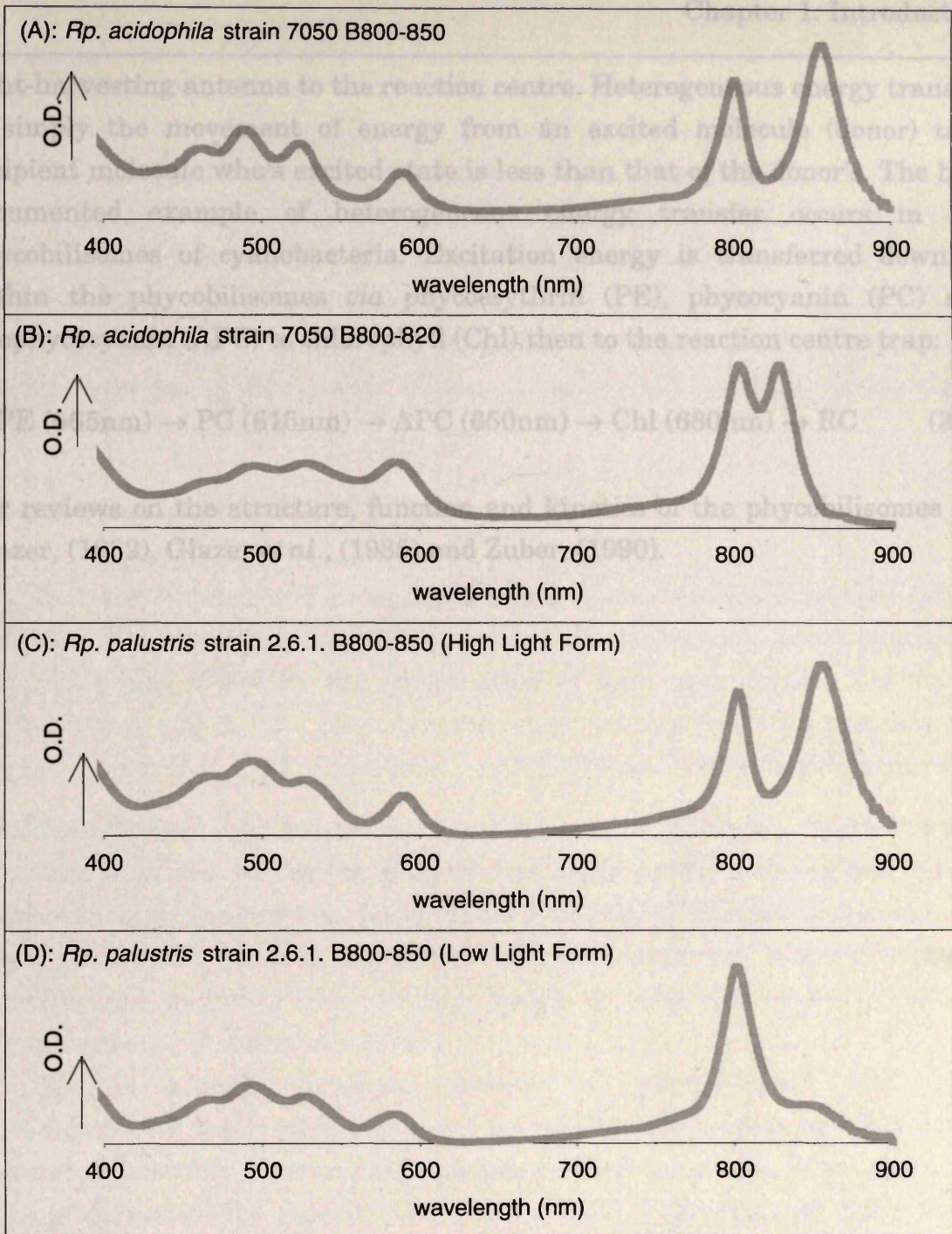
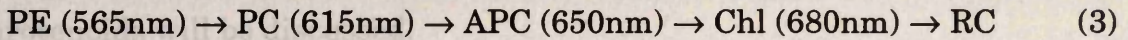


**Figure 1.8:** Absorption spectra of the different forms of LHII. (A): B800-850 complex of *Rp. acidophila* 7050. (B): B800-820 complex of *Rp. acidophila* 7050. The only difference between the two complexes are the amino acid sequences illustrated in Figure 1.7. Therefore the amino acid changes at positions H+13 and +14, from YW to FL, cause the change in the far-red NIR absorption peak from 850nm to 820nm. (C): B800-850 complex from *Rp. palustris* 2.6.1 (high light form). (D): Low light form of the B800-850 complex of *Rp. palustris* 2.6.1. The amino acid changes at the positions described in Figure 1.7 cause the NIR maxima to blue shift from 850nm to 800nm. From these two examples it is evident that minor amino acid changes can cause major bathochromic shifts in the absorption spectrum of a pigment-protein complex.

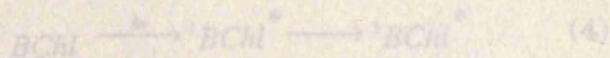
light-harvesting antenna to the reaction centre. Heterogeneous energy transfer is simply the movement of energy from an excited molecule (donor) to a recipient molecule whose excited state is less than that of the donor's. The best documented example of heterogeneous energy transfer occurs in the phycobilisomes of cyanobacteria. Excitation energy is transferred downhill within the phycobilisomes *via* phycoerythrin (PE), phycocyanin (PC) and allophycocyanin (APC) to chlorophyll (Chl) then to the reaction centre trap:



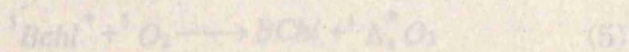
For reviews on the structure, function and kinetics of the phycobilisomes see Glazer, (1982), Glazer *et al.*, (1985) and Zuber, (1990).

In 1956 Siström and co-workers, using a carotenoidless mutant (strain R26) and wild type *Rb. sphaeroides*, showed that the mutant strain, which only had BChl, was killed by the combination of light and oxygen, due to the photodynamic effect. The photodynamic effect results from the production of singlet oxygen ( $^1\Delta_g O_2$ ) (Foote *et al.*, 1970). Singlet oxygen is produced when BChl (or Chl in plants) is irradiated in the presence of oxygen. Singlet oxygen is a very powerful oxidant capable of destroying lipids, proteins and nucleic acids eventually causing cell death (Foote *et al.*, 1970). Singlet oxygen can also result in the formation of the other biological dangerous species; hydrogen peroxide and hydroxyl free radicals, which in turn can cause irreparable cellular damage (Foote *et al.*, 1970).

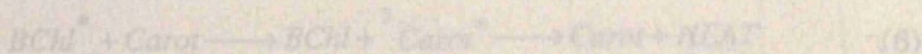
The carotenoids, however, prevent the photodynamic effect. The mechanism that the carotenoids use to prevent the photodynamic effect can be best summarised by a series of simple generalised equations. When irradiated BChl is excited to the singlet state  $BChl(^1BChl^*)$  this then produces triplet BChl ( $^3BChl^*$ ):



The triplet BChl reacts with ground (triplet) state molecular oxygen to form singlet oxygen ( $^1\Delta_g O_2$ ) and ground state BChl:



The carotenoids prevent the photodynamic effect by eliminating the singlet oxygen by two routes. The carotenoid's main route of photoprotection occurs by reacting directly with the triplet bacteriochlorophyll:



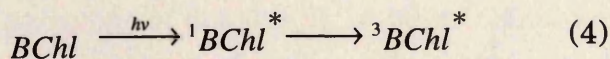
### 1.3.3 The Carotenoids:

The carotenoid pigments are unsaturated hydrocarbons consisting of eight isoprenoid units (Isler *et al.*, 1971; Cogdell and Frank, 1987), and their oxygenated derivatives. The photosynthetically associated carotenoids *in vivo* have two rôles: photoprotection (Sistrom *et al.*, 1956), and accessory light-harvesting (Warburg and Negelein, 1923; Goedheer, 1959). They absorb energy between 450nm and 570nm (Figure 1.3D). Both functions of carotenoids will be discussed.

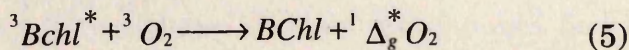
#### 1.3.3.1 Photoprotection:

In 1956 Sistrom and co-workers, using a carotenoidless mutant (strain R26) and wild type *Rb. sphaeroides*, showed that the mutant strain, which only had BChl, was killed by the combination of light and oxygen, due to the photodynamic effect. The photodynamic effect results from the production of singlet oxygen ( $^1\Delta_g^* O_2$ ) (Foote *et al.*, 1970). Singlet oxygen is produced when BChl (or Chl in plants) is irradiated in the presence of oxygen. Singlet oxygen is a very powerful oxidant capable of destroying lipids, proteins and nucleic acids eventually causing cell death (Foote *et al.*, 1970). Singlet oxygen can also result in the formation of the other biological dangerous species; hydrogen peroxide and hydroxyl free radicals, which in turn can cause irreparable cellular damage (Foote *et al.*, 1970).

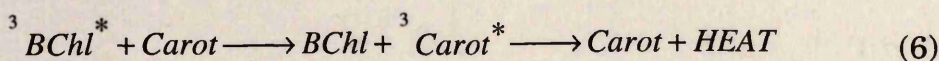
The carotenoids, however, prevent the photodynamic effect. The mechanism that the carotenoids use to prevent the photodynamic effect can be best summarised by a series of simple generalised equations. When irradiated BChl is excited to the singlet state BChl ( $^1BChl^*$ ) this then produces triplet BChl ( $^3BChl^*$ ):



The triplet BChl reacts with ground (triplet) state molecular oxygen to form singlet oxygen ( $^1\Delta_g^* O_2$ ) and ground state BChl:

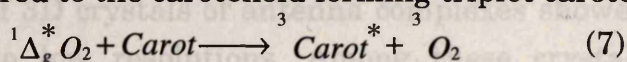


The carotenoids prevent the photodynamic effect by eliminating the singlet oxygen by two routes. The carotenoid's main route of photoprotection occurs by reacting directly with the triplet bacteriochlorophyll.



### 1.4 The Structure of the Rhodospirillaceae PSU:

The second route of photoprotection relies on the triplet carotenoid having a lower or equal energy level compared to singlet oxygen. This is approximately 94.1 KJ mol<sup>-1</sup> (Foote and Denny, 1968). The energy from singlet oxygen is transferred to the carotenoid forming triplet carotenoid :



The result is ground state molecular oxygen and carotenoid triplet which is quickly converted to ground state carotenoid with energy dissipating as heat as described by equation 6. Only Carotenoids with nine or more conjugated carbon-carbon double bonds are capable of removing singlet oxygen from the environment (Cogdell *et al.*, 1992; Crouse, J.B *et al.*, 1963; Foote *et al.*, 1970, and references therein).

#### 1.3.3.2 Accessory Light-Harvesting:

The carotenoids have a second function, they act as accessory light-harvesting pigments (Goedheer, 1959). They absorb in the visible wavelengths of the electromagnetic spectrum, typically between 470-570nm (e.g. rhodopin, Figure 1.3D) giving the bacteria their distinctive red-purple colour. The energy absorbed by the carotenoids is then passed to the bacteriochlorophylls. Since the carotenoids absorb energy in a region the bacteriochlorophyll does not (i.e. 470-570nm), they increase the overall energy capture suitable for photosynthesis.

Crystallographic data for the relative packing of the two  $\alpha$ -helices of the *Rp. acidophila* strain 10050 light-harvesting B800-850 antenna complex. The *Rp. acidophila* B800-850 model is based on Patterson projections. Figure 1.10A is a Patterson projection through the a/b axis of symmetry of the B800-850 crystal. The Patterson projection shown in Figure 1.10A indicates that there are rings of density at 1.05nm, 1.42nm, and 2.40nm. These rings are proposed to represent the distances within and between a trimer of  $\alpha/\beta$  B800-850 tetramers (Figure 1.10C). Figure 1.10B indicates that a single  $\alpha$ -helical domain probably is present by the regular spaced repeating regions of electron density. These dense regions are thought to represent the turns in an  $\alpha$ -helix (Figure 1.10B, see Cogdell and Hawthornthwaite, 1993).

A 3D modelling algorithm for predicting the  $\alpha$ -helical arrangement in transmembrane membrane proteins has been produced by Donnelly *et al.*, (1993). They successfully created 3D models for the transmembrane  $\alpha$ -helical

## 1.4 The Structure of the Rhodospirillaceae PSU:

### 1.4.1 The Light-Harvesting Complexes:

Initially x-ray analysis of 3D crystals of antenna complexes showed that they only diffracted x-rays to low resolutions. Among these crystals are: *Rb. capsulatus* B800-850 (Mäntele *et al.*, 1985; Welte *et al.*, 1985), *Rp. acidophila* B800-820 (Guthrie *et al.*, 1992), *Rb. sphaeroides* strain 2.4.1 B800-850 (Allen *et al.*, 1985a; Allen *et al.*, 1985b), *Rb. sphaeroides* B875 (Nunn *et al.*, 1992), *Rp. acidophila* strain 7750 (Cogdell *et al.*, 1985), *Rp. acidophila* strain 10050 (Papiz *et al.*, 1989), *Rp. palustris* B800-850 (Wacker *et al.*, 1986) and *R. salexigens* B800-850 (Wacker *et al.*, 1988). However high resolution (sub. 3Å) has now been achieved for a number of antenna pigment-proteins. The high resolution data to date are; 2.4Å for *R. molischianum* B800-850 (Michel, 1991), 2.5Å for *Rp. acidophila* B800-850 (Papiz *et al.*, 1989; Cogdell and Hawthornthwaite, 1993) and 2.8Å for *Rb. sphaeroides* B875 (Nunn., R., personal communication).

The lack of a high resolution structure has however not deterred people from creating models. Based on pigment ratios and other biochemical information Kramer *et al.*, (1984), used spectroscopic techniques to study the positions of the photosynthetic pigments in *Rb. sphaeroides* B800-850, thereby producing a model for their orientation within the B800-850 complex (see Figure 1.9). Papiz (see Cogdell and Hawthornthwaite, 1993) has produced a model based on crystallographic data for the relative packing of the two  $\alpha$ -helices of the *Rp. acidophila* strain 10050 light-harvesting B800-850 antenna complex. The *Rp. acidophila* B800-850 model is based on Patterson projections. Figure 1.10A is a Patterson projection through the a/b axis of symmetry of the B800-850 crystal. The Patterson projection shown in Figure 1.10A indicates that there are rings of density at 1.05nm, 1.42nm, and 2.40nm. These rings are proposed to represent the distances within and between a trimer of  $\alpha/\beta$  B800-850 tetramers (Figure 1.10C). Figure 1.10B indicates that a single  $\alpha$ -helical domain probably is present by the regular spaced repeating regions of electron density. These dense regions are thought to represent the turns in an  $\alpha$ -helix (Figure 1.10B, see Cogdell and Hawthornthwaite, 1993).

A 3D modelling algorithm for predicting the  $\alpha$ -helical arrangement in transmembrane membrane proteins has been produced by Donnelly *et al.*, (1993). They successfully created 3D models for the transmembrane  $\alpha$ -helical

the addition of the connections to the model would not particularly alter the helical arrangement of the model. If this is the case (and can be determined once the x-ray structure has been solved) then the algorithms that produced it may prove useful in modeling other transmembrane structures.

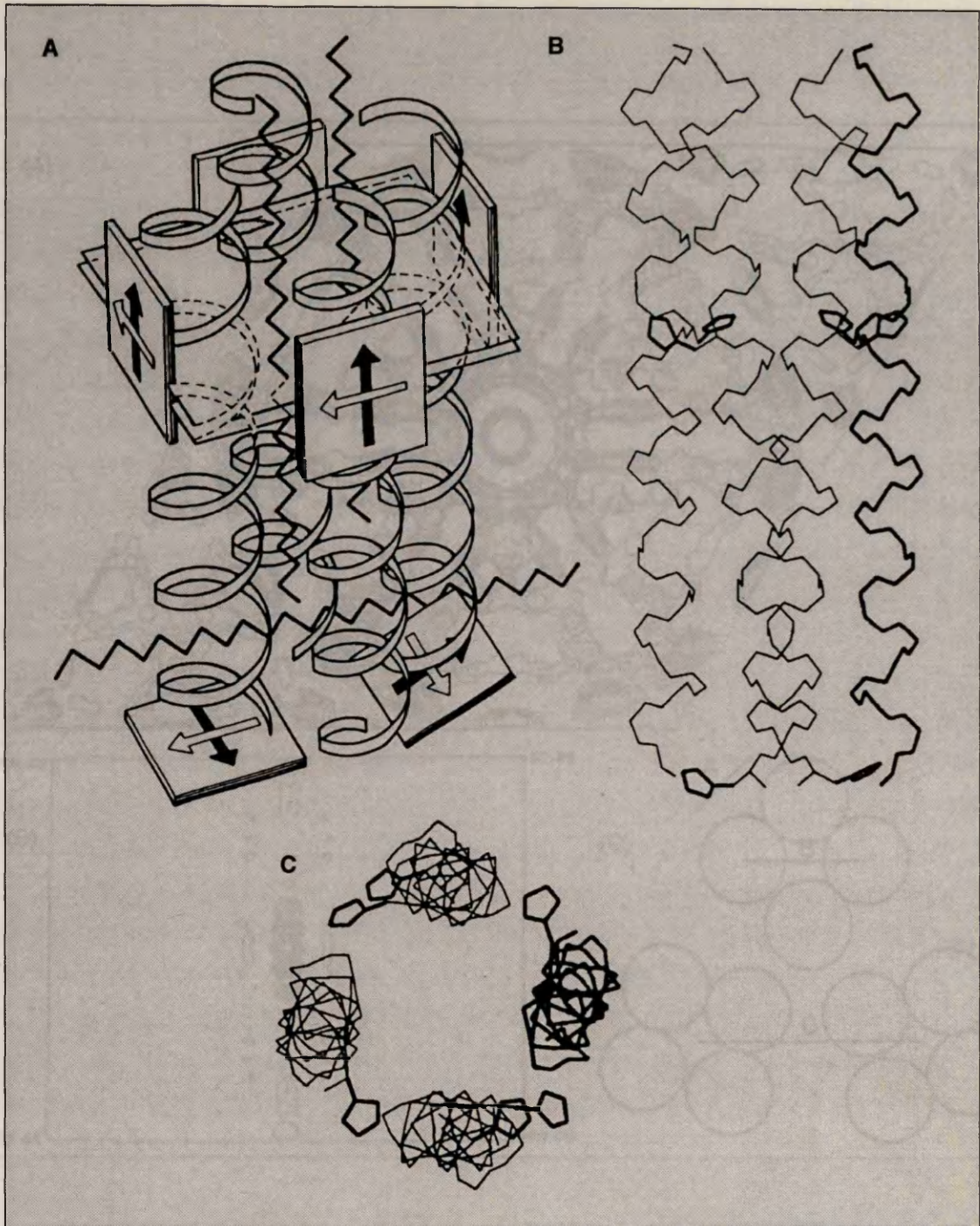


**Figure 1.9:** Structural models for the Rhodospirillaceae B800-850 light harvesting complex (A): Membrane spanning  $\alpha$ -helical model for *Rb. sphaeroides* B800-850 (Kramer, 1984). The squares represent BChl<sub>a</sub>. The Q<sub>y</sub> (open arrows) and Q<sub>x</sub> (filled arrows) transitions are depicted. The four upper Bchl's are 850nm absorbing, the lower two are 800nm absorbing. The spirals are the  $\alpha$ -helices, with the zig zags illustrating the positions of the carotenoids. (B) 3D  $\alpha$ -helical model along the c-axis of symmetry (using Papiz's model; see Codell and Hawthornwhaite, 1993) for *Rp. acidophila* B800-850 light harvesting complex (Donnelly and Cogdell, 1993). As with Kramer's model the B800-850 is a  $\alpha\beta$  tetramer, one  $\alpha$ -helix (one of the  $\alpha$ -B800-850 polypeptides) is shown in bold. The conserved histidines are also depicted in bold. Note that all the conserved histidines in the  $\alpha\beta$  polypeptides are arranged in a ring. The two conserved histidines of the  $\beta$ -B800-850 polypeptides are also located opposite each other. (C): A perpendicular view with respect to the membrane. Again one of the  $\alpha$ -B800-850 polypeptides and all conserved histidines are shown bold. It should be evident from this figure that the conserved histidines are located between the helices. The location of the bacteriochlorophylls and carotenoids cannot however be determined. However using Kramer's model (Kramer, 1984; figure 1.9A) and the model by Donnelly and Cogdell (1993) their general location can be estimated. The authors of the *Rp. acidophila* model assume that the addition of the cofactors to the model will not significantly alter the helical arrangement of the model. If this is the case (and can be determined once the x-ray structure has been solved) then the algorithms that produced it may prove useful in modeling other transmembrane structures.

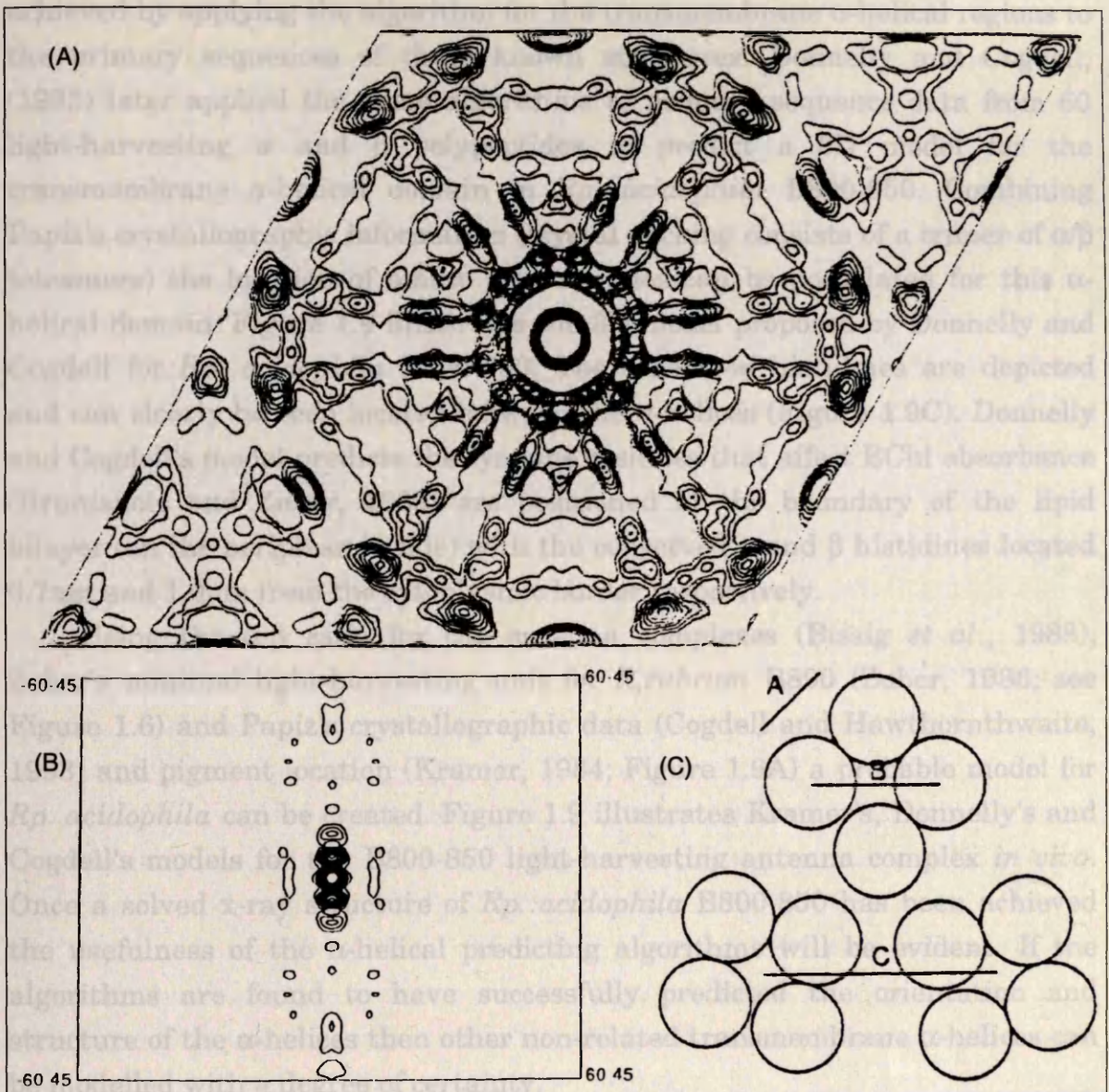


**Figure 1.10 :** Patterson Projections and Resulting Structural Model for *Rp. acidophila* B800-850. (A): Patterson projection in the a/b axis of crystallographic symmetry. There are regions of density at 1.05nm(A), 1.42nm(B) and 2.40nm(C). Since part (A) indicates eighteen fold symmetry (and not the six fold normally associated with space group R32) Papiz has produced a model for the B800-850  $\alpha$ -helical packing: a trimer of tetramers. (B): Patterson projection map on the c-axis of symmetry. (C) Proposed model for the B800-850  $\alpha$ -helix packing in *Rp. acidophila* strain 10050 crystals. The distances marked A,B, and C are 1.05nm,1.42nm and 2.40nm respectively.

domains in bacteriorhodopsin and bacterial reaction centres. This was achieved by applying the algorithm for the transmembrane  $\alpha$ -helical regions to the primary sequences of these known structures. Donnelly and Cogdell, (1993) later applied the same algorithms to primary sequence data from 60 light-harvesting  $\alpha$  and  $\beta$  polypeptides to predict a 3D model for the transmembrane  $\alpha$ -helical domain in *Rp. acidophila* B800-850. Combining Papiz's crystallographic information (crystal packing consists of a trimer of  $\alpha/\beta$  tetramers) the location of amino acid residues can be postulated for this  $\alpha$ -helical domain. Figure 1.9 illustrates the 3D model proposed by Donnelly and Cogdell for *Rp. acidophila* B800-850. The conserved histidines are depicted and can clearly be seen located between the  $\alpha$ -helices (Figure 1.9C). Donnelly and Cogdell's model predicts the tyrosine residues that affect BChl absorbance (Brunisholz and Zuber, 1988) are positioned at the boundary of the lipid bilayer (on the periplasmic side) with the conserved  $\alpha$  and  $\beta$  histidines located 0.7nm and 1.0nm from the cytoplasmic border respectively.

Using the  $\alpha:\beta$  ratio for the antenna complexes (Bissig *et al.*, 1988), Zuber's minimal light-harvesting unit for *R. rubrum* B890 (Zuber, 1986; see Figure 1.6) and Papiz's crystallographic data (Cogdell and Hawthornthwaite, 1993) and pigment location (Kramer, 1984; Figure 1.9A) a probable model for *Rp. acidophila* can be created. Figure 1.9 illustrates Kramer's, Donnelly's and Cogdell's models for the B800-850 light-harvesting antenna complex *in vivo*. Once a solved x-ray structure of *Rp. acidophila* B800-850 has been achieved the usefulness of the  $\alpha$ -helical predicting algorithms will be evident. If the algorithms are found to have successfully predicted the orientation and structure of the  $\alpha$ -helices then other non-related transmembrane  $\alpha$ -helices can be modelled with a degree of certainty.

### 1.4.2 The Reaction Centre:

Deisenhofer, Michel and their co-workers (Michel, 1982; Deisenhofer *et al.*, 1984; Deisenhofer *et al.*, 1985; Deisenhofer and Michel, 1989) first produced three dimensional crystals giving atomic resolution of the reaction centre from *Rhodospseudomonas viridis*. Since Deisenhofer's and Michel's breakthrough, the only other RC's which have had their structure solved are those from *Rb. sphaeroides*: strain R26 (Chang *et al.*, 1986; Allen *et al.*, 1987a; Allen *et al.*, 1987b; Yeates *et al.*, 1987; Chang *et al.*, 1991); strain R2.4.1 (Allen *et al.*, 1988; Yeates *et al.*, 1988) (Figures 1.11, 1.12 and 1.13); and the wild type strain Y (Reiss-Husson *et al.*, 1992). For reviews regarding the structure and function of the reaction centre see Feher *et al.* (1989), Rees *et al.* (1989), Deisenhofer and Michel (1989), Deisenhofer and Michel (1991a), and Deisenhofer and Michel (1991b).

The structure of the reaction centre from *R. viridis* shows the positions of the different cofactors and proteins in the complex. Knowing the location of the cofactors and proteins enables investigations into the specific rôles played by all the constituents (amino acid motifs, polypeptides and co-factors) of the reaction centre to be made.

The *Rb. sphaeroides* bacterial reaction centre consists of three polypeptides Light (L), Medium (M) and Heavy (H) with a molar ratio of 1:1:1 (Clayton and Haselkorn, 1972; Feher and Okamura, 1978; Okamura *et al.*, 1982) but in *R. viridis* a fourth polypeptide is present, the cytochrome *c* (cyt *c*) which is located on the periplasmic side. Again the molar ratio is 1:1:1:1. In both *Rb. sphaeroides* and *R. viridis* the RC contains four bacteriochlorophylls two of which are termed the 'special pair' or D<sub>A</sub>D<sub>B</sub>, two bacteriopheophytins ( $\phi_A$  and  $\phi_B$ ) and one (*R. viridis*) or two (*Rb. sphaeroides*) quinones. The quinones (Q<sub>A</sub> and Q<sub>B</sub>) can be either ubiquinone (e.g. *Rb. sphaeroides*) or menaquinone (e.g. *R. viridis* and *C. vinosum*). In wildtype reaction centres there is one carotenoid molecule (labelled C in Figure 1.11B). Both the Carot<sup>-</sup> and Carot<sup>+</sup> reaction centres contain one non-heme (Fe<sup>2+</sup>) iron (Feher and Okamura, 1978; Pasron, 1978; Cogdell *et al.*, 1976; Jolchine and Reiss-Husson, 1974; Straley *et al.*, 1973).

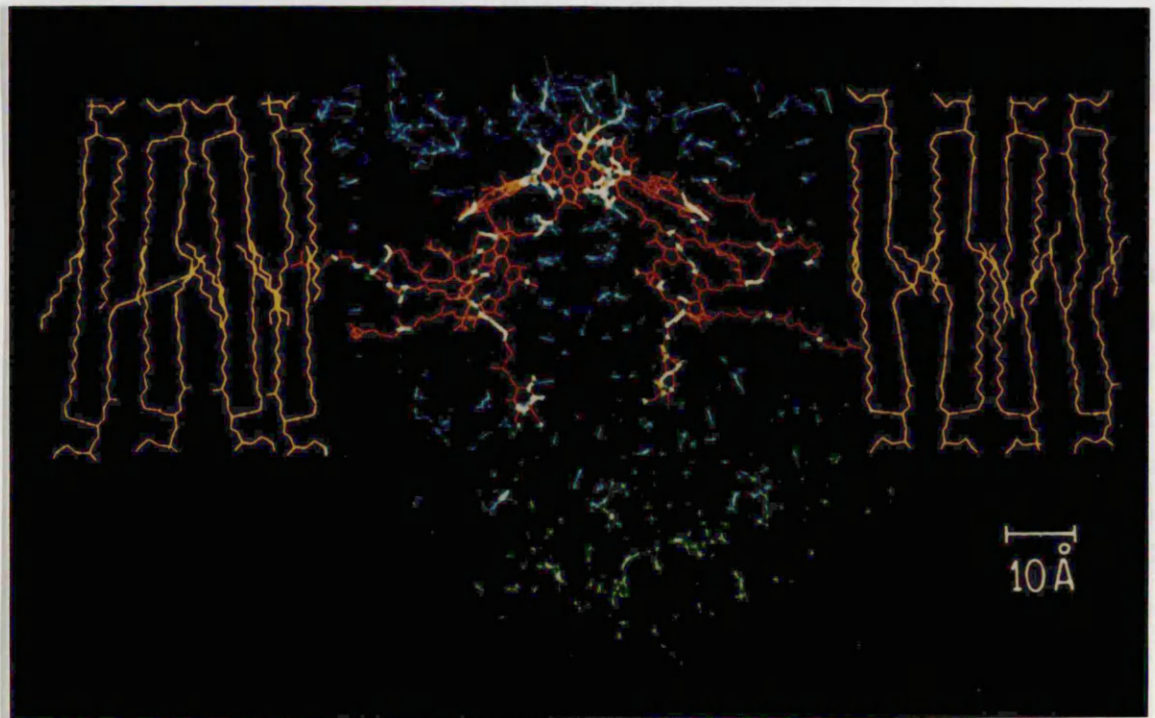
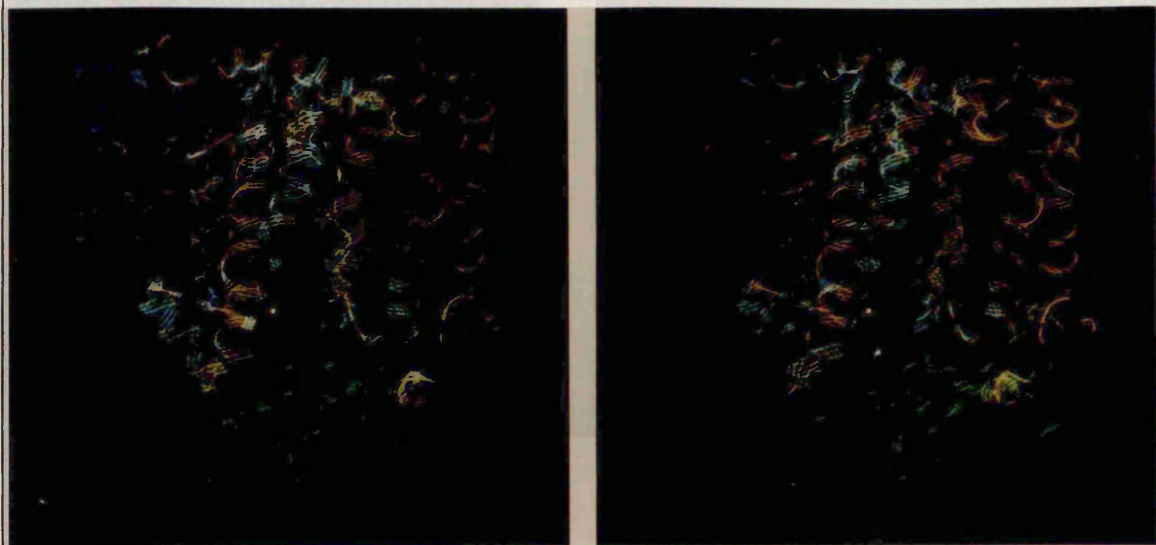


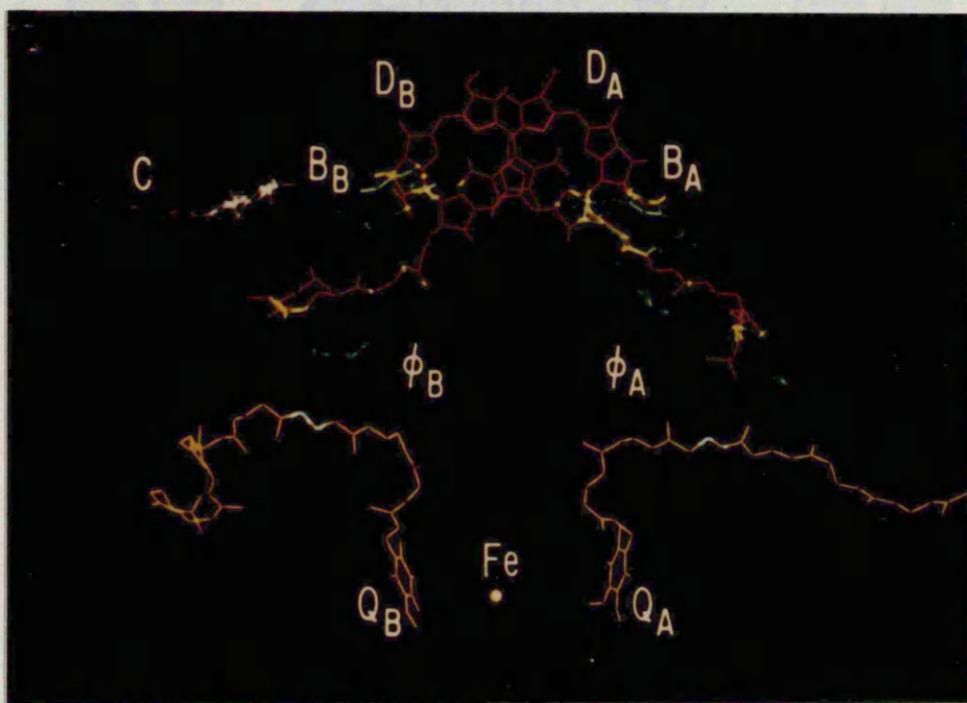
**Figure 1.11:** *Rb. sphaeroides* strain 2.4.1. reaction centre structure. L and M polypeptides (blue), H polypeptide (green) with the cofactors in red. In *Rb. sphaeroides* strain 2.4.1. the associated cytochrome is only loosely associated with the RC but in *R. viridis*, the x-ray structure shows an integrated, four heme cytochrome. In *R. viridis* the above diagram would have the cytochrome  $c_2$  located on the periplasmic (top) side.

**Figure 1.12:** *Rb. sphaeroides* strain 2.4.1 reaction centre axis of symmetry. The axis of symmetry lies vertically in the plane of the page. (A): Stereo view of the LM-complex carbon backbone. The M polypeptide has been rotated by 180° onto the L polypeptide. The white indicates where the carbon backbone of L and M occupy the same space when one is rotated by 180° onto the other. (B): Symmetry of the cofactors. D<sub>A</sub>D<sub>B</sub>: special pair (BChl a dimer, red). B<sub>A</sub>,B<sub>B</sub>: BChl a monomers (green).  $\phi_A, \phi_B$ : bacteriopheophytin (blue). Q<sub>A</sub>: primary acceptor (quinone, yellow). Fe: non-haem Fe<sup>2+</sup> (white). Q<sub>B</sub>: primary acceptor (quinone, yellow). C: carotenoid (purple). (C): Stereo view of the co-factor structure within the bacterial reaction centre.

A



B



C



## 1.3.2.1 The L and M Polypeptides

Each of the L and M polypeptides contains five membrane-spanning helices labelled A to E (Michel, 1982; Deisenhofer et al., 1984; Deisenhofer et al., 1985; Allen et al., 1987; Allen et al., 1988). The association of these helices is presented in Figure 1.13. The D and E helices form a central core (Figure 1.13) with the A, B and C helices forming an outer shell (Figure 1.13A). The two polypeptides are linked together by disulfide bonds (Figure 1.13B).

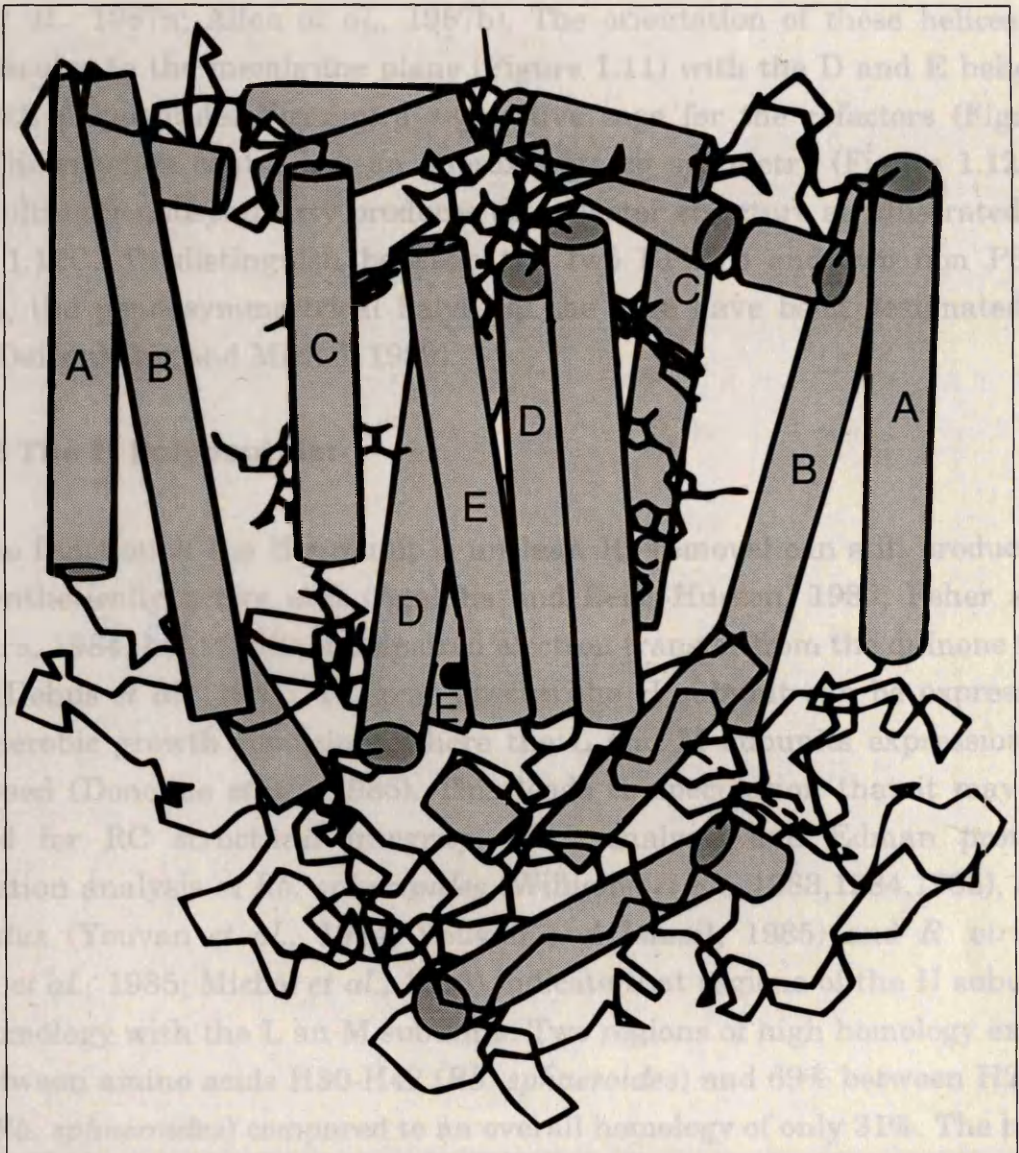


**Figure 1.13:** The  $\alpha$ -helices of *Rb. sphaeroides* reaction centre. The five transmembrane helices of both the L (right) and M (left) polypeptides are labelled A to E. The only unlabelled transmembrane helix belongs to the H polypeptide. The  $\alpha$ -helices are shaded cylinders against a carbon backbone. The black circle depicts the location of the non-haem iron.

concerns the H polypeptide. In contrast with the L and M polypeptides, the H polypeptide has only one membrane protruding  $\alpha$ -helix (Figure 1.13). The majority of H is located at the cytoplasmic surface forming a globular domain. This domain consists of a small  $\alpha$ -helix and two regions of  $\beta$ -sheet. This globular domain is the site where the H polypeptide is bound to the L and M polypeptides. As already stated the role of the H polypeptide is unclear, other than its structural importance to the electron flow by maintaining cofactor tertiary structure by

### 1.4.2.1 The L and M Polypeptides:

Both the L and M polypeptides contain five membrane-spanning helices labelled A to E (Michel, 1982; Deisenhofer *et al.*, 1984; Deisenhofer *et al.*, 1985; Allen *et al.*, 1987a; Allen *et al.*, 1987b). The orientation of these helices is perpendicular to the membrane plane (Figure 1.11) with the D and E helices from both polypeptides forming a supportive cage for the cofactors (Figure 1.13). The reaction centre has an approximate  $c_2$  symmetry (Figure 1.12A). The resulting pseudosymmetry produces the cofactor structure as illustrated in Figure 1.12C. To distinguish between the two BPheos and two non P870 BChl *as*, the pseudosymmetrical halves of the cage have been designated A and B (Deisenhofer and Michel, 1989).

### 1.4.2.2 The H Polypeptide:

The function of the H subunit is unclear. Its removal can still produce a photosynthetically active unit (Agalidis and Reiss-Husson, 1983; Feher and Okamura, 1984) but results in impaired electron transfer from the quinone  $Q_A$  to  $Q_B$  (Debus *et al.*, 1985). In some species the H subunit can be expressed under aerobic growth conditions where the L and M subunits expression is suppressed (Donohue *et al.*, 1986). This leads to speculation that it may be required for RC structural integrity. DNA analysis and Edman protein degradation analysis of *Rb. sphaeroides* (Williams *et al.*, 1983, 1984, 1985), *Rb. capsulatus* (Youvan *et al.*, 1984; Youvan and Ismail, 1985) and *R. viridis* (Michel *et al.*, 1985; Michel *et al.*, 1986) indicate that regions of the H subunit have homology with the L and M subunits. Two regions of high homology exist; 60% between amino acids H30-H42 (*Rb. sphaeroides*) and 69% between H229-H240 (*Rb. sphaeroides*) compared to an overall homology of only 31%. The high homology at these residues is where the H polypeptide is in contact with the conserved regions of the L and M polypeptides. This region of homology may be due to an evolutionary conserved tertiary structure between H, M and L which is conducive to RC structural integrity and functional electron flow through the RC. Unlike the L and M polypeptides, the H polypeptide has only one membrane protruding  $\alpha$ -helix (Figure 1.13). The majority of H is located at the cytoplasmic surface forming a globular domain. This domain consists of a small  $\alpha$ -helix and two regions of  $\beta$ -sheet. This globular domain is the site where the H polypeptide is bound to the L and M polypeptides. As already stated the rôle of the H polypeptide is unclear, other than its structural importance to the electron flow by maintaining cofactor tertiary structure by

creating rigidity in the L and M polypeptides (Debus *et al.*, 1985). Its globular domain may act as a site for antenna attachment or as a site for new photosynthetic unit synthesis (Michel and Deisenhofer, 1986).

### 1.4.3 The Reaction Centre Light-Harvesting Conjugate:

As already stated, it is very difficult to crystallise membrane proteins for conventional x-ray crystallography. It is even more difficult to crystallise a supra-complex such as the reaction centre light-harvesting conjugate (RC-LHI). This is due to the fact that when the *core* (RC-LHI) is isolated it is usually inherently unstable although Wacker *et al.* (1986), Welte *et al.* (1986) and Mäntele *et al.*, (1988), have succeeded in producing small crystals of RC-LHI, or *core*, from *Rp. palustris*. The crystals are however not suitable for detailed x-ray analysis.

Using detergents, intact *cores* can be isolated and studied using electron microscopy (E.M.). 2D crystallography (which uses E.M.) has permitted the molecular shell of the RC to be determined. The *core* of *R. viridis* was studied by comparing EM studies of the reaction centre with the solved 3D x-ray structure (Miller, 1979; Miller, 1982; Miller and Jacob, 1983; Engelhardt *et al.*, 1983; Jay *et al.*, 1984, Stark *et al.*, 1984; Deisenhofer *et al.*, 1984; Deisenhofer *et al.*, 1985). The data suggests that the reaction centre is surrounded by LHI having six-fold symmetry. Cross section analysis of 2D (Miller and Jacobs, 1983) and 3D crystals (Deisenhofer *et al.*, 1984) for *R. viridis* reaction centre indicates that it cannot have a symmetry greater than two-fold (Stark *et al.*, 1984). Using STEM-mass mapping and TEM for *E. halochloris* a model for the structure for the BPSU has been proposed (Figure 1.14, Engelhardt *et al.*, 1986). The presence of the colourless  $\gamma$ -polypeptide in the Ectotiorhodospiraceae has led to the hypothesis that this polypeptide has a unique rôle in forming the *core* structure as determined by electron microscopy. For reviews on STEM see Engel, (1982) and Wall and Hainfeld, (1986). The hexagonal array observed in the *E. halochloris* BPSU (Engelhardt *et al.*, 1986) has a symmetrical RC. The six-fold symmetry for the *core* is however an artefact due to data averaging. The data processing relied on an averaged data set obtained from a lipid bilayer containing an array. This however does not mean that the antenna complexes are not arranged with six-fold symmetry. The light-harvesting polypeptides may be arranged with six-fold symmetry, but the RC could be oriented in any direction normal to the plane of the membrane axis resulting in the rotationally averaged RC

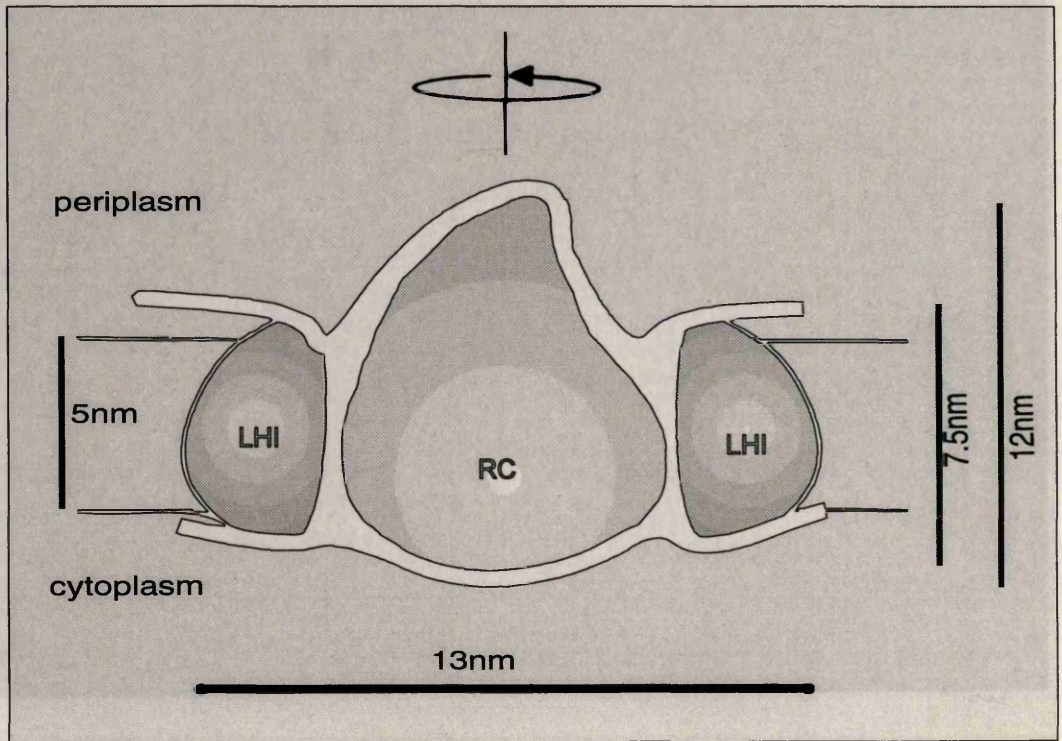


**Figure 1.14:** Cross-section of the surface relief map of the photosynthetic core of *Ectothiorhodospira halochloris*. These data were collected using TEM and STEM electron micrographs from both stained and unstained specimens. The micrographs illustrate that the reaction centre can be in various orientations within the plane of the membrane. The *core* complex protrudes from both sides of the lipid bilayer forming elliptical structures. (Engelhardt *et al*, 1986).

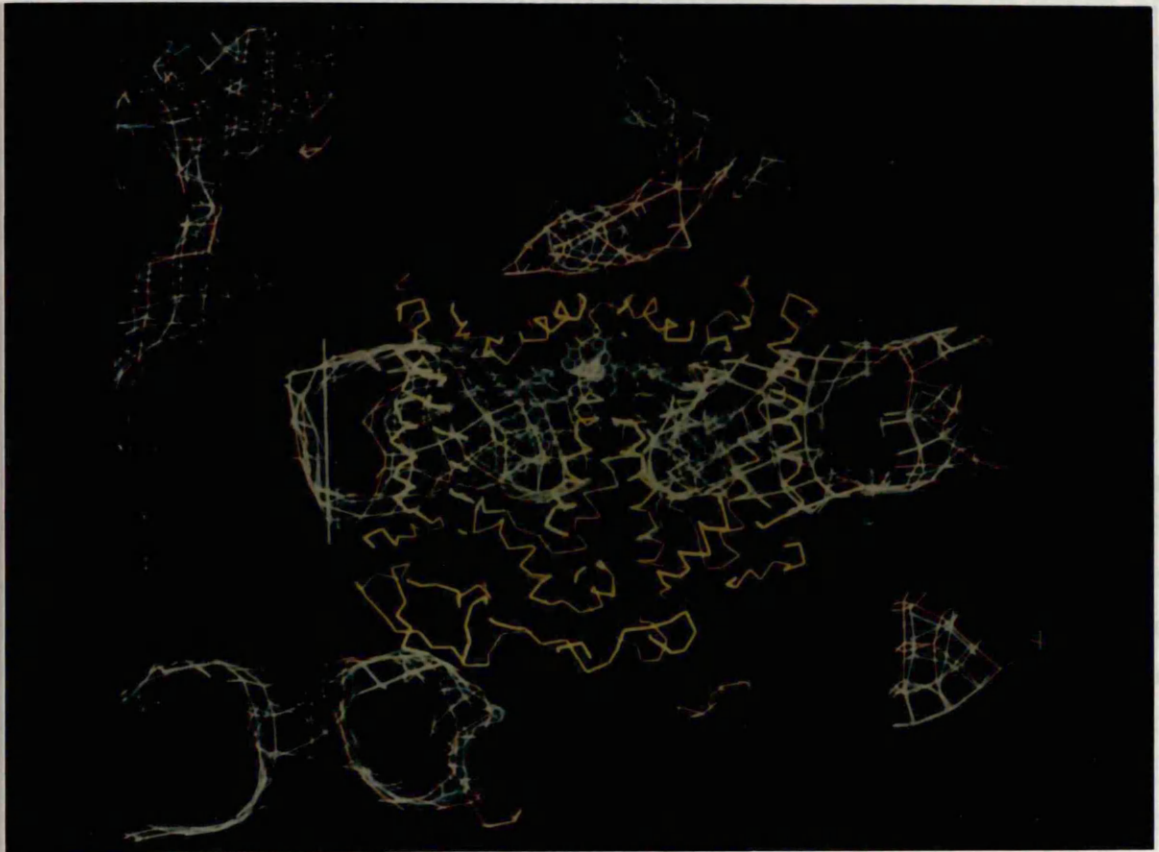
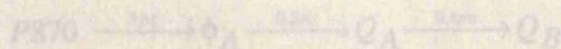


**Figure 1.16:** Localisation of detergent ( $\beta$ -OG) in the reaction centre crystals of *Rb. sphaeroides* strain Y. The reaction centre polypeptides (yellow) enclose the cofactors (blue). There are two contour levels of detergent rings surrounding the RC (violet colours). The two contours depict the extremes of the detergent reconstruction and are very similar to each other. The LHI (B1020) model from Stark *et al.*, (1984) has been added (green) to the model and indicates that the detergent rings (violet) probably replace the membrane lipids *in vivo*. Redrawn from Roth *et al.*, (1991).

structure (Figure 1.15A). Indeed, conformation that isolated LHI (lacking RC) has a six-fold symmetry (Figure 1.15C) has come from *R. marina* (Meckenstock *et al.*, 1992; Meckenstock *et al.*, 1993), *R. rubrum* B890 (Ghosh *et al.*, 1993) and *Rb. sphaeroides* B875 (Boonstra *et al.*, 1993), all of which are BChl<sub>a</sub>-containing species. The resolution of these structures is such that it is unclear where the rotational position of the asymmetrical RC within the RC-LHI conjugate lies *in vivo*.

Studies of 3D, detergent rich, reaction centre crystals have provided useful information on the packing of detergent molecules surrounding the protein which may act as substitute for LHI complexes *in vivo*. In 1989 Roth *et al.*, used neutron diffraction techniques to show that deuterium labelled LDAO is positioned in rings surrounding the RC transmembrane  $\alpha$ -helices for a LDAO-RC crystal of *R. viridis*. They later showed using the same technique, with  $\beta$ -OG-RC crystals of *Rb. sphaeroides* (Roth *et al.*, 1991), the main protein  $\beta$ -OG interactions are also hydrophobic. Superimposing the bacterial LHI model proposed by Stark *et al.*, (1984) onto the  $\beta$ -OG detergent ring, the authors suggest that there are no significant gaps in the long RC diameter (Figure 1.16). This suggests that the detergents are occupying the space where the light-harvesting complexes would be *in vivo*. In the short diameter axis Roth *et al.*, (1991) suggest that the observed gaps between the RC and LHI model are presumably where phospholipids are located within this membrane conjugate. The work by Roth *et al.*, (1991) has illustrated that protein-detergent interactions in ordered crystals may indeed act as suitable surrogates for protein-membrane or protein-protein interactions *in vivo*.



The x-ray structure indicates that pseudosymmetry occurs in the cofactor structure of the reaction centre. As stated above, absorption spectroscopy indicates that electron transfer via the  $Q_A$  is the preferred route. The asymmetry in electron pathway may have arisen from a number of factors. Three possible factors creating asymmetry are:

- (i) the special pair is not a completely symmetrical structure,
- (ii) one of the tetrapyrroles is folded in one axis.

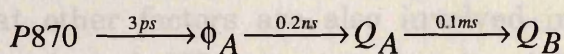
## 1.5 Electron Flow Through the PSU:

### 1.5.1 Electron Flow Through the Reaction Centre:

The unidirectional electron transfer through the reaction centre was postulated over 30 years ago (Clayton, 1962). *In vivo* excitation energy enters the reaction centre from the light-harvesting complexes at the two excitation coupled BChls which are termed the 'special pair', P870 or  $D_A D_B$  (Feher *et al.*, 1989). Electrons then pass through the reaction centre to the cytoplasmic side of the membrane causing a  $\Delta p$  to be formed which ultimately forms the cellular currency, ATP and  $NADH_2$ .

If oxygen is present then the photodynamic effect is possible (see section 1.3.3.1.). However if a carotenoid is located within the RC, triplet BChl is quickly converted to ground state BChl thus preventing photooxidative damage (Cogdell *et al.*, 1975; Cogdell, 1978). The x-ray structure locates the carotenoid beside the 'B' branch of the RC (Figure 1.12B).

The 'A' branch has been shown to be the major path for electron flow through the reaction centre. When using low temperature absorption spectroscopy the  $\phi_A$  (bacteriopheophytin<sub>A</sub>) absorption peak splits up into two peaks (at approximately 530nm and 545nm). When electron transfer occurs only the long wavelength absorbing band of  $\phi_A$  alters, and with the aid of linear dichroism studies on RC crystals it has been shown that the electron path throughout the RC occurs mainly *via* the 'A' path (for a review see DiMugno and Norris, 1993). Studies have shown that electron transfer is at least 20 fold greater *via* the 'A' path than the 'B' path (Michel-Beyerle *et al.*, 1988). Electron flow via the 'A' chain of cofactors results in the kinetics summarised by Kirmairer and Holten in 1987;



The x-ray structure indicates that pseudosymmetry occurs in the cofactor structure of the reaction centre. As stated above, absorption spectroscopy indicates that electron transfer *via* the  $\phi_A$  is the preferred route. The asymmetry in electron pathway may have arisen from a number of factors. These possible factors creating asymmetry are;

- (i) the special pair is not a completely symmetrical structure, one of the tetrapyrroles is folded to one side.

- (ii) the overlap between  $B_A$  and P870 is greater than  $B_B$  and P870. This enables a greater overlap of electron orbits, favouring electron transfer.
- (iii) The  $\Phi_{AB_A}$  distance is 0.15nm shorter than  $\Phi_{BB_B}$ , again favouring electron transfer.
- (iv) The cofactors bind differently on sides A and B, that, plus the distribution of charged residues, result in electrostatic interactions and micro-environments preferentially favouring the 'A' path. One result is that the  $Fe^{2+}$  is closer to  $Q_A$  than  $Q_B$  by approximately 0.2nm (*Rb. sphaeroides*).

It is not known which, if any, of the above factors produces the observed differences in electron transfer between the 'A' and 'B' pathways in the RC. The non  $D_A D_B$  BChl $_A$  molecule itself may also act as a transitional electron acceptor (Zinth *et al.*, 1983; Zinth *et al.*, 1985; Dressler *et al.*, 1991 Shreve *et al.*, 1992;) aiding electron transfer by producing a transient charge separation between  $D_A D_B$  and  $\phi_B$  (Parson and Holten, 1986). In the solved structures for *Rb. sphaeroides* and *R. viridis* quinones are present. Studies of isolated RCs from *R. viridis* where only  $Q_A$  is present (and not  $Q_B$ ) are still capable of being photoactivated (Deisenhofer *et al.*, 1984). This is further evidence that the primary acceptor is functional (menaquinone in *R. viridis* and ubiquinone in *Rb. sphaeroides*) and is indeed  $Q_A$ .

The reaction centre has an approximate  $C_2$  symmetry (see Figure 1.12A) with a hydrogen bond connected to  $\phi_A$  located on the A chain that is not present on the B chain (*R. viridis*). When the hydrogen bond is removed by mutagenesis the  $Q_x$  absorption band of  $\phi_A$  alters to approximately 535nm (Bylina *et al.*, 1988). However the electrons still mainly migrate along the A branch suggesting that other factors are also involved in the preferential electron flow along the A branch. When  $\phi_A$  is reduced and  $D_A D_B$  is excited to its singlet state, it causes triplet BChl to be formed. Consequently the preference for the A branch is not solely dependent on the different Redox potentials between the pairs of cofactors in the two branches, but, is the result of a much more, and as yet unknown, complex interaction within the whole reaction centre.

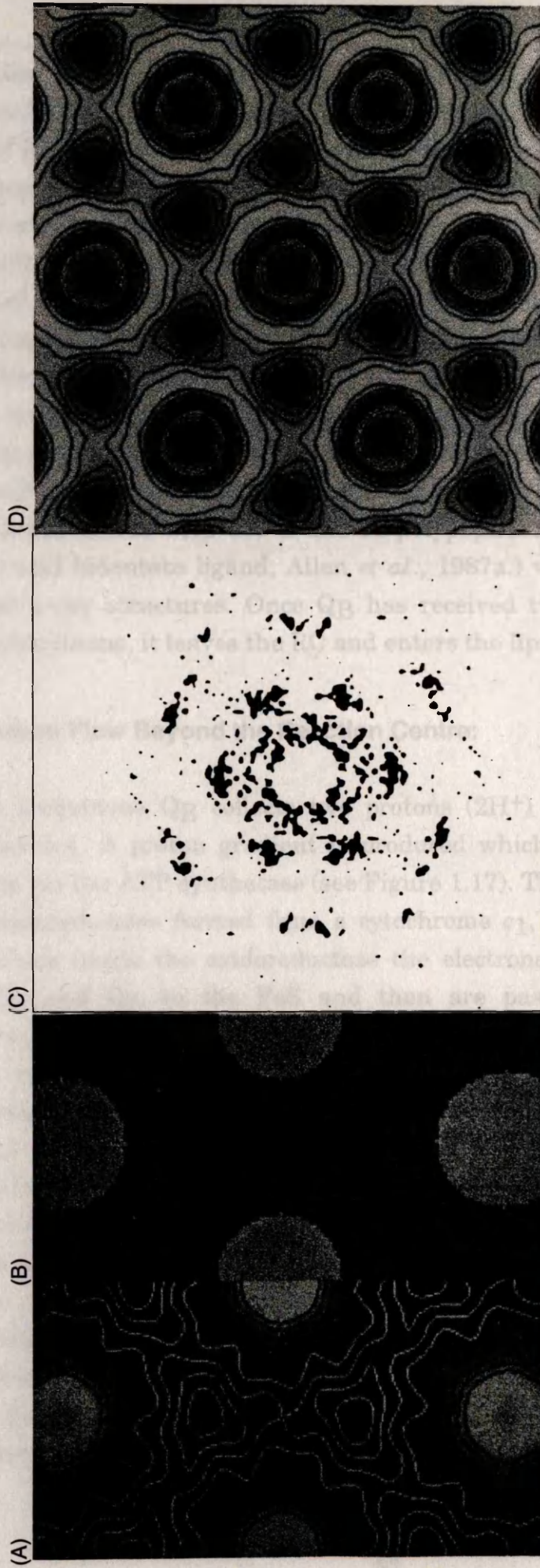


**Figure 1.15:** Six-fold symmetry of bacterial core light-harvesting complexes. (a): Image analysis of 2D arrays of *E. halochloris* core (Engelhardt *et al.*, 1986.). The *E. halochloris* core with a rotationally averaged reaction centre appears to have six-fold symmetry for the core light-harvesting complexes. (b): STEM mass determination of the *E. halochloris* core. Most of the mass is associated with the reaction centre. (c): Diffraction pattern of a 2D array of *R. rubrum* B873 indicating a hexagonal structure (Redrawn from Ghosh *et al.*, 1993). (d): Image processing of (c) reveals a hexagonal unit cell of 12.3nm with a central hole of 5nm surrounded by a 10nm ring of protein. Similar results have been obtained for *R. marina* but with smaller unit cell dimensions (Meckenstock *et al.*, 1992). The hole is thought to be the location of the reaction centre *in vivo*.

Studies into the rôle of whole regions of the RC protein cage with respect to electron flow are now under way. N.Woodbury and co-workers are producing a series of RC mutants in *Rb. capsulatus* by replacing amino acid motifs of the M polypeptide with L polypeptide residues (Woodbury, N., personal communication). The creation of a series of localised symmetrical reaction centres will aid in determining the major influences that cause the functional asymmetry observed in electron flow through the wild type RC. The first of these symmetrical mutants is *sym1* (Taguchi *et al.*, 1992; Stocker *et al.*, 1992).

Electrons then pass from  $Q_A$  to  $Q_B$  and may be facilitated by  $Fe^{2+}$ . However removal of this non-haem iron does not result in any significant loss of electron flow from  $Q_A$  to  $Q_B$ . Its rôle is unclear and may be similar to the rôle of the H polypeptide, that of maintaining reaction centre stability. It forms six co-ordinate bonds with the L and M polypeptides (four histidines and a Glutamic acid bidentate ligand; Allen *et al.*, 1987a.) which are conserved for the solved x-ray structures. Once  $Q_B$  has received two electrons forming a reduced ubiquinone, it leaves the RC and enters the lipid bilayer.

### 1.5.2 Electron Flow Beyond the Reaction Centre:

The ubiquinone  $Q_B$  collects two protons ( $2H^+$ ) and transfers them to cytochrome  $bc_1$ . A proton gradient is produced which is then used for ATP production *via* the ATP synthetase (see Figure 1.17). The electrons are utilised by the oxidoreductase formed from a cytochrome  $c_1$ , cytochrome  $b$  and FeS protein. Once inside the oxidoreductase the electrons flow through the two haems,  $Q_c$  and  $Q_z$ , to the FeS and then are passed to cytochrome  $c_2$ . Cytochrome  $c_2$  is then able to migrate to the oxidised reaction centre, donating electrons back to  $D_A D_B$ . The reaction centre is now reduced and ready to be photoactivated again. In *Rb. sphaeroides* the cytochrome  $c_2$  is closely associated with the cytochrome  $bc_1$  (Hall *et al.*, 1989). A model has been proposed for the existence of supra-complex between the reaction centre and the cytochromes (Joliot *et al.*, 1989). For recent reviews on quinones see Konstantinov, (1990); Rich, (1983); Robertson and Dutton, (1988); and Semenov, (1993). The main pathway involving type  $c$  cytochromes during photosynthesis is cytochrome  $c_2$ -RC, but it has been shown that other routes are possible. Using complementation analysis Jenney and Daldal (1993) have recently shown that a membrane-associated cytochrome ( $c_y$ ) can also mediate in photosynthetic growth in *Rb. capsulatus* (Figure 1.18).



The cyclic electron transport chain (Figure 1.17) in conjunction with a residual respiratory chain are ultimately responsible for the reduction of  $\text{NAD}^+$  to NADH and the formation of ATP, (Mitchell, 1961; Nicolle, 1982).

## 1.6 Structural Determination of Biological Macromolecules:

The atomic structures of hundreds of soluble proteins have been solved using conventional x-ray crystallography. For recently solved structures see Henderson and Wüthrich, (1991, 1992, 1993). However only a handful of atomic structures have been obtained for membrane proteins. Since the formation of 3D crystals from proteins is often difficult, other approaches to structural determination must be considered. The classic examples of atomic resolution data from membrane proteins are the bacterial reaction centre (Michel, 1982; Daisenhofer and Michel, 1989) and cytochrome  $c_2$  (Weiss et al., 1981). Recently the non-membrane associated protein cytochrome  $c_1$  (Story et al., 1992a) has also been solved using conventional x-ray crystallography (Story et al., 1992a) but its structure is of the biologically inactive storage form (Story et al., 1992b). As a result the solved structure of Rec A (Henderson et al., 1990) in its active form, may not be able to predict the structure of other proteins *in vivo*. It has taken years of painstaking methodical crystallographic trials to achieve the prominent atomic structures named above. Advances in technology, suitable for studying biological material, now

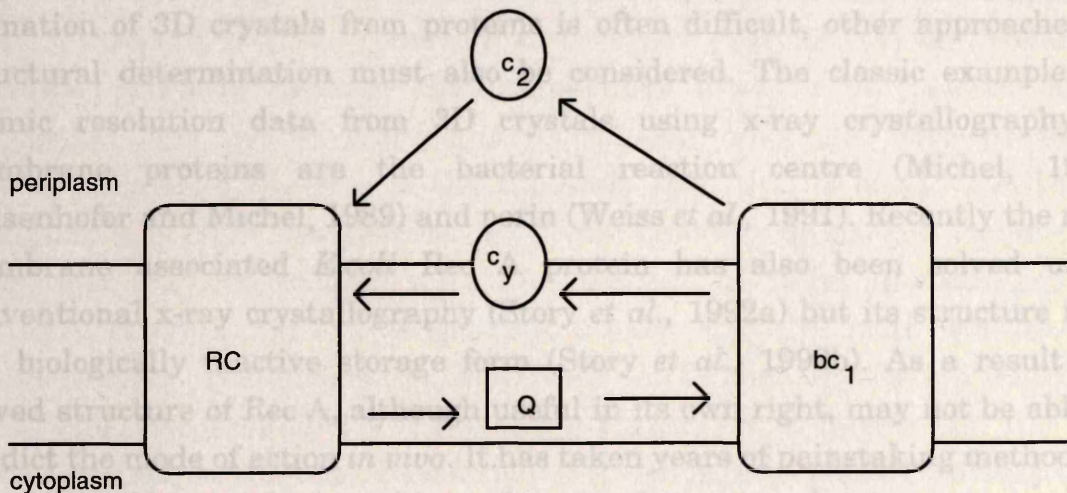


**Figure 1.18:** Photosynthetic electron transport model for *Rb. capsulatus*. The classical model with a soluble carrier (cytochrome,  $c_2$ ) is supplemented with a membrane associated carrier ( $c_y$ ). Q:quinone. RC:reaction centre.  $bc_1$ : cytochrome  $bc_1$ . Redrawn from Jenney and Daldal, (1993).

### 1.6.1 NMR

The use of NMR has increased with the advent of commercially available spectrometers up to 750 MHz (e.g. Bruker AX series), and improving 2D, 3D and 4D NMR algorithms for data conversion. Protein structures in solution have been solved by this approach but only up to a maximum size of approximately 150 amino acid residues. Using this method soluble proteins up to ~25-50kDa can be studied to atomic resolution [for reviews see Clore and Gronenborn, (1991); and Wagner et al., (1992)].

The major benefit in using NMR over conventional x-ray crystallography (and EM crystallography) is that no artefacts from crystal packing will arise.

The cyclic electron transport chain (Figure 1.17) in conjunction with a residual respiratory chain are ultimately responsible for the reduction of  $\text{NAD}^+$  to  $\text{NADH}$  and the formation of ATP, (Mitchell, 1961; Nicolls, 1982).

## 1.6 Structural Determination of Biological Macromolecules:

The atomic structures of hundreds of soluble proteins have been solved using conventional x-ray crystallography. For recently solved structures see Henderson and Wüthrich, (1991, 1992, 1993). However only a handful of atomic structures have been obtained for membrane proteins. Since the formation of 3D crystals from proteins is often difficult, other approaches to structural determination must also be considered. The classic examples of atomic resolution data from 3D crystals using x-ray crystallography of membrane proteins are the bacterial reaction centre (Michel, 1982; Deisenhofer and Michel, 1989) and porin (Weiss *et al.*, 1991). Recently the non-membrane associated *E.coli* Rec A protein has also been solved using conventional x-ray crystallography (Story *et al.*, 1992a) but its structure is of the biologically inactive storage form (Story *et al.*, 1992b). As a result the solved structure of Rec A, although useful in its own right, may not be able to predict the mode of action *in vivo*. It has taken years of painstaking methodical crystallographic trials to achieve the prominent atomic structures named above. Advances in technology, suitable for studying biological material, now also enable the use of nuclear magnetic resonance (NMR), and electron microscopy (EM) to provide similar near-atomic resolution data. This opens up more avenues of research to the ultimate goal; a solved high resolution structure of a membrane protein.

### 1.6.1 NMR

The use of NMR has increased with the advent of commercially available spectrometers up to 750 MHz (e.g. Bruker AX series), and improving 2D, 3D and 4D NMR algorithms for data conversion. Protein structures in solution have been solved by this approach but only up to a maximum size of approximately 150 amino acid residues. Using this method soluble proteins up to ~25-50kDa can be studied to atomic resolution [for reviews see Clore and Gronenborn, (1991); and Wagner *et al.*, (1992)].

The major benefit in using NMR over conventional x-ray crystallography (and EM crystallography) is that no artefacts from crystal packing will arise.

When crystallised, a protein's surface may distort due to crystal packing. If crystal distortion occurs, it will alter the surface topology of the protein where ligands bind and general protein-environment interactions occur. These interactions, being of great biological significance, could be misinterpreted or ignored in a conventional crystallographic structure. NMR is also able to observe the motions of proteins, enabling the study of protein-ligand conformations which enable the kinetics of ligand binding to be investigated for which 3D crystals may be unsuitable (Wager *et al.*, 1992; and references therein). Examples of these are the elastase inhibitor elgin *c* (Wager *et al.*, 1992) and protein-nucleic acid interactions (Kaptein, 1993).

The major problem with NMR structural analysis is that small proteins must be used. It is thus, generally, of no direct practical use to membrane associated proteins because the polypeptides have to be isolated using detergents. The use of detergents (permitting functional proteins to be isolated) increases the size of the specimen such that it often exceeds the maximum size NMR can process. NMR can, however, be used in conjunction with other methods to help solve the structure of larger systems. If the original macromolecule can be split into smaller domains, some of which will become suitably sized fragments, then NMR can be used to provide useful data of the type discussed above. Combining structural data from x-ray, EM and NMR can lead to the characterisation of a biologically significant structure. One such example of combining all three types of data collection is that of dihydrolipoly transacetylase (DeRosier, 1992).

		0.8nm
	27kDa	0.83nm
	17.5kDa	1.0nm

Figure 1.16: High resolution data obtained using cryo-EM. The column size does not report the resolution of the micrographs but indicates the resolution for the individual protein domains. The boxed resolutions are for 2D reconstructions, and 3D reconstructions (boxed). The 0.34nm 3D reconstruction for LHCB5 is submitted for publication (Kühnbrandt, W., personal communication). Adapted from Steiner *et al.* (1992).

SPECIMEN	SIZE	RESOLUTION
<b>Purple membrane (bacteriodopsin)</b>	27kDa	0.28nm (0.35nm)
<b>LHCII a/b</b>	25kDa	0.34nm (0.6nm,0.34m)
<b>PhoE porin</b>	37kDa	0.35nm (0.6nm)
<b>OmpF porin</b>	37kDa	0.35nm
<b>Crotoxin</b>	10kDa and 14kDa	0.35nm
<b><math>\alpha</math>-helical coiled protein from praying mantis</b>		0.4nm
<b>CaATPase</b>	109kDa	0.6nm
<b>Cytochrome oxidase</b>	4.5-45kDa	0.7nm
<b>bacterial S-layer</b>	91kDa	0.8nm
<b>T4 DNA helix destabilizing protein gp 32<sup>I</sup></b>	27kDa	0.85nm
<b>T.M.V.</b>	17.5kDa	1.0nm

**Figure 1.19:** High resolution data obtained using cryo-EM. The subunit size does not depict the total size of the macromolecule but illustrates the resolution for the individual protein domains. The depicted resolutions are for 2D reconstructions, and 3D reconstructions (bracketed). The 0.34nm 3D reconstruction for LHCIIa/b is submitted for publication (Kühlbrandt, W., personal communication). Adapted from Bremer *et al.*, (1992).

## 1.6.2 EM: Data for Both Amplitudes and Phases are Collected.

Electron Microscopy (EM) is the main competitor to x-ray crystallography for the structural determination of biological macromolecules. It is now possible to attain resolutions higher than 1nm as Figure 1.19 indicates. Figure 1.19 illustrates a list of published 2D and 3D reconstructions. There are both advantages and disadvantages in using electron microscopy compared to the conventional x-ray crystallographic approach, and these will be discussed below.

### 1.6.2.1 The Advantages of EM:

#### 1.6.2.1.1 Less Protein is per Trial:

Often protein concentrations in the range of 5-10mg ml<sup>-1</sup> are required for the formation of 3D crystals. The formation of 2D crystals from membrane proteins can be obtained from protein concentrations as low as 1mg ml<sup>-1</sup> (Dorset *et al.*, 1983; Hovmoller *et al.*, 1983; and Miller and Jacob, 1983). Since a lower protein concentration often forms 2D crystals, then for any given quantity of protein it is theoretically possible to screen a wider range of experimental conditions when compared to 3D x-ray crystallography. For the isolation of rare, and difficult, proteins this approach may well provide a significant advantage over conventional 3D x-ray crystallography.

#### 1.6.2.1.2 Purity of Sample May Not be a Critical Importance.

The formation of 2D crystals is facilitated by the macromolecule having a degree of internal symmetry (Jap *et al.*, 1992; Kühlbrandt, 1992). In some cases this property enables the use of a less-than-pure specimen compared to traditional 3D crystallographic methods (Phipps *et al.*, 1991). Any contamination can be seen directly under the electron microscope and ignored. However, it should also be stated that for the highest resolution data (obtained by cryo-EM) specimen purity is of critical importance. The highest resolution of published EM data to date for a biological macromolecule is the 0.28nm resolution map for the porin of purple membrane which was prepared from a very pure sample (Baldwin *et al.*, 1988).

### 1.6.2.1.3 Data for Both Amplitudes and Phases are Collected.

The main historic difficulty with x-ray crystallography is the lack of phase information from diffraction maps originating from x-ray sources. The amplitudes are made up of a series of sinusoidal waves, their intensities indicating the relative electron densities within the structure. In diffraction maps the positional information is given by the phases. Unfortunately for x-ray crystallography, the phase information is not directly obtained. The phase information, however, can be obtained from isomorphous replacement, molecular replacement, non-crystallographic symmetry averaging, multiple wavelength anomalous dispersion and anomalous scattering techniques. These methods of data acquisition and manipulation produce electron density maps and eventually a 3D structure. For introductions to x-ray crystallography and macromolecular modelling see Blundell, (1976) and Rhodes, (1993).

If on processing the x-ray crystallographic space groups of native and manipulated data sets (e.g. isomorphous replacement) have similar unit cell dimensions (<0.5%), then a direct comparison can be made between the two Patterson projections. This emphasises the high densities resulting from the electrons associated with the heavy atoms and by careful analysis the phases can be obtained. However not all heavy atoms are suitable; some alter the space group and are useless while others cause general crystal degradation. There is also the possibility that the biological macromolecule does not have any accessible binding sites. If no apparent binding sites are present then molecular biologists can use biochemical and primary structure information to create mutants capable of accepting heavy atoms (for an example see Fowler *et al.*, 1992). Once the hurdle of obtaining phase information has been passed, a solved structure is possible. The phase errors using x-ray derived data can be as high as 60°, but calculated EM phase errors on average are about 25°, which often results in a much stronger specimen signal-to-noise ratio (Kühlbrandt, 1992).

Data from electron microscopy (unlike x-ray data collection) does produce both amplitude (relative densities) and phase (positional) information. The captured image, taken at optimal defocus, is the result of a single point source passing through the specimen, causing a diffraction pattern whose origin is the specimen's point of contact with the incident electron beam. It is usually refocussed within the microscope and captured by a recording device, either a film negative or a CCD camera attached to a computer. The diffraction pattern can also be directly captured by recording methods on an EM. When an electron micrograph negative from an optimally defocussed image is placed on

an optical bench (a coherent narrow beam of laser electromagnetic radiation), it forms a diffraction pattern which can be analysed. The diffraction image contains phase information in reciprocal space which provides a workable source of information for structural analysis.

Reciprocal space (which is the Fourier transform of real space) is often used to calculate structural maps of 2D arrays. This is because the amount of data that needs to be manipulated in order to produce a map is much less than if the full real space data set was to be used. X-ray crystallography also uses reciprocal space to calculate 3D structures. Optimum defocussed images are usually processed by forward Fourier transformation (FFT). The FFT procedure calculates reciprocal space data from a real space data set (or *visa versa*). Diffraction patterns directly captured by EM require very large, ordered and hydrated specimens examined under liquid nitrogen or helium temperatures (Kühlbrandt, 1992). Unfortunately for all but the highest quality 2D arrays, examination by cryo-E.M. is an impractical approach. The diffraction patterns (either the FFTs or a direct diffraction pattern) then undergo image analysis to form either 2D or 3D structural (electron density) maps.

#### **1.6.2.1.4 It is Considered a Natural State for Membrane Proteins.**

True membrane proteins are located within a lipid bilayer, allowing them to move freely within the plane of the membrane (Singer and Nicolson, 1972). As a result, protein-protein, protein-cofactor, and protein-lipid interactions create biological activity.

The hydrophobic effect, as described by Sharp (1991), accounts for the formation of 2D crystals by providing a net gain in entropy. This interaction results in an array of proteins within the lipid bilayer. The protein's hydrophobic domain(s) is/are located within the membrane, as *in vivo*, and the hydrophilic domain(s), as *in vivo*, is/are located extrinsically to the membrane. On forming 2D crystals the proteins can be inserted either bidirectionally or unidirectionally. If they are inserted unidirectionally, they appear to have the same gross characteristics of natural membranes. This leads to the postulation that 2D crystals may be in a less stressed environment compared to detergent enriched 3D crystals that are grown for x-ray crystallography. Detergents are known to be capable of denaturing proteins and the mechanism of 2D crystal formation, by definition, removes them from a detergent enriched environment and data collection results from a near *in vivo* structure. Atomic force microscopy has indicated that lipids are also removed during detergent

removal when forming 2D arrays (for an example see Lyon *et al.*, 1993). Although not *in vivo*, artificial lipid bilayers may accommodate membrane proteins better than detergent shells. As already stated above 2D crystals, in some cases, can be produced by detergent removal from unpure preparations (Engel *et al.*, 1992). The crudeness of sample permits a greater number of the natural lipids that are associated with the protein to be isolated with it. In the natural membrane specific lipid species, not all of which are ubiquitous, have been shown to be very important in forming 2D arrays (Sternberg *et al.*, 1992). Therefore the ability of a crude specimen to crystallise may indeed provide a better model of the *in vivo* structure than a completely pure (and thus lipid stripped) protein if the lipids play a major rôle in the *in vivo* structure and function of the biological macromolecule under investigation.

#### 1.6.2.1.5 Very Large Biological Systems can be Studied.

The near-atomic 3D structure of proteins that have been solved can be measured in the kDa size range. There are however many important biological systems that are in the kDa-MDa range. These include RNA polymerase I, and the Adenovirus capsid. For these biological macromolecules conventional x-ray crystallography of the full structure is near impossible due to their size and fragile nature. X-ray crystallography can however study the macromolecule's subunit structure to atomic resolution. These very large macromolecules can however be studied by single particle analysis or by studying 2D crystals. In the case of single particle analysis numerous electron micrographs, or CCD images, can be examined and classified into different orientations. These sets of images can then be processed to form a set of averaged orientations. The averaged orientations can in turn be manipulated to produce a 3D reconstruction of the original specimen. For proteins in the kDa-MDa range, relatively low resolution data ( $\geq 2\text{nm}$ ) obtained from negatively stained images can provide very useful topographical information using the above method. This is especially true if primary sequence data is known as in the case of RNA polymerase I. A negatively stained 3D reconstruction of the ~650kDa RNA polymerase I complex at 3nm resolution has been produced (Schultz *et al.*, 1993). Schultz *et al.*, isolated a putative DNA binding site and catalytic centre for this important biological protein using regions of conserved residues from various polymerase sequences (Delarue *et al.*, 1990) including primary sequence homology from *Halobacterium halobium*, *Methanobacterium thermoautotrophicum*, *Sulfolobus acidocaldarius*, *Saccharomyces cerevisiae* and *Drosophila melanogaster*.

Adenovirus (Rowe *et al.*, 1953) is a large virus (140nm in diameter) that causes enteric dysentery and conjunctivitis in man. The virus consists of at least eleven proteins; the major one called hexon (or polypeptide II) has been solved to a resolution of 0.29nm by x-ray crystallography (Roberts *et al.*, 1986). There are 240 hexons on the surface of Adenovirus. The whole capsid structure has been solved to a resolution of 3.5nm by using single particle cryo-EM analysis (Stewart *et al.*, 1991). The Adenovirus capsid surface is made up of a series of a 'group of nine hexons'. In 1989 Furcinitti *et al.*, investigated the structure of isolated 'group of nine hexons' using STEM and managed to distinguish a minor protein (polypeptide IX). This was achieved by creating a difference map between the STEM data and a projected x-ray image of nine hexons. Recently Stewart *et al.*, (1993) have applied this technique to the reconstructed 3D EM structure and created a three dimensional difference map by subtracting the 240 hexons (from Roberts *et al.*, 1986) from the 3D EM image. This has resulted in (i) the assignment of the binding sites of other proteins to hexon, (ii) the density of six minor capsid proteins to be calculated, and (iii) initiated a reappraisal of the biochemical data on Adenovirus capsid formation.

These examples demonstrate that low resolution EM alone (RNA polymerase I [Schultz *et al.*, 1993]) can provide useful structural and functional information. Comparison of low resolution EM data with high resolution x-ray data (Adenovirus [Stewart *et al.*, 1993], RC-LHI [Roth *et al.*, 1989, 1991]) can also provide valuable information on individual components within a large biological macromolecule.

### 1.6.2.2 Disadvantages of EM:

#### 1.6.2.2.1 Exposure to High Vacuum:

In order for an EM to produce a diffraction pattern the electron beam must be under high vacuum ( $<10^{-5}$  MPa). Biological material is not designed to be structurally intact or operational under such extreme conditions. The specimen must therefore be protected from excess dehydration whilst being examined under vacuum. See sections 1.6.2.2.3 and 1.6.3 for a description of countermeasures.

If you ignore the source of the x-ray beam the whole process of x-ray crystallography of proteins is less severe compared to electron microscopy. 3D crystals are grown in a mother liquor and transferred into either a glass or quartz capillary, still in the mother liquor. If a crystal specimen is susceptible

to small temperature changes, the temperature of the crystal can be maintained by passing a stream of air (at the desired temperature) over the capillary tube containing the mounted crystal during data collection. This temperature control is not possible with EM. In x-ray analysis the specimen is in its original mother liquor, at constant atmospheric pressure and temperature from initial seeding to data collection. Both x-ray and EM analysis produce radiation damage to biological specimens. The only significant specimen damage using x-rays will occur as a result of radiation damage whereas in E.M. it may also be due to temperature differences and dehydration.

#### 1.6.2.2.2 The Missing Cone:

A series of tilted EM specimens are required to produce a 3D model of the original macromolecule. The data (usually collected on micrographs) is digitised and then Fourier transformed. This provides regions of high signal to noise ratios along the reciprocal lattice axes. These data points of high signal to noise ratios can then be monitored and combined to predict a 3D model for the specimen. Although phase and amplitudes are collected there is a constraint on the amplitudes for extreme tilted specimens. The specimen holders and specimen grids within the electron microscope only permit data to be recorded up to a tilting angle of approximately  $\pm 60^\circ$ . In some cases however the tilt angle can be as high as  $85^\circ$  by manually bending the specimen grid. A Tilt of  $90^\circ$  is impossible because the electron beam would be stopped by the specimen grid supporting the specimen. If a tilt series collects data up to  $\pm 60^\circ$  from the normal then 87% of the total reciprocal space will be collected (Amos *et al.*, 1982). This mechanical constraint results in a loss of data in the 0,0 lattice line. Any reconstruction to 3D would result in missing data points predicting zero mass. To combat this missing information, specimens normal to the plane of the membrane are often analysed, providing information for that lattice line. Combining the two sets of data enable the missing cone to be filled. The lack of such additional structural information perpendicular to the plane of the membrane does not prevent 3D models from being predicted.

### 1.6.2.2.3 Radiation Damage and Low Contrast Levels in Biological Specimens:

Specimens exposed to EM are under high vacuum and are thus subject to extreme water loss. To reduce specimen damage the sample's hydration shell must be protected. If unprotected the loss of the hydration shell leads to specimen denaturation and stickiness (Kistler and Kelleberger, 1977). Hydration shells are maintained by using cryogens. This involves embedding specimens in a cryogen such as vitrified water (Dubochet *et al.*, 1988), glucose (Henderson *et al.*, 1990) or trehalose (Jap *et al.*, 1990) by rapidly plunging the specimen into liquid ethane. Cryo-EM however produces low levels of contrast between specimen ( $\rho_{\text{PROTEIN}}=1.35\text{g/ml}$ ) and embedding medium (vitrified water,  $\rho_{\text{H}_2\text{O}}=1.0$ ; sugar,  $\rho_{\text{SUGAR}} \approx \rho_{\text{PROTEIN}}$ ). Often the 2D lattice of a cryo-EM specimen cannot be directly visualised using either the phosphorous screen or CCD cameras (Kühlbrandt, W, personal communication). Embedding does retain structural integrity, with no hydration loss occurring in specimens prepared by water vitrification. These embedding methods however have one major disadvantage. The specimen is so sensitive to radiation damage it often vaporises on contact with the electron beam when data collection occurs. This means that you often cannot examine the specimen directly under the EM to judge its suitability for structural analysis. Scanning the specimen while in the TEM must therefore be done using very low dose methods resulting in time consuming data collection. The specimen can generally only then be studied by image processing the data at a later date. There is a short cut: negative staining.

### 1.6.3 Negative Staining:

Negative staining produces a degree of radiation protection with high contrast between specimen and supportive medium. The high contrast levels result from using heavy atoms in the stain. The electron dense heavy atoms (e.g. uranium; used in the stain uranyl acetate) produce strong diffraction patterns which can be easily detected and analysed. The down side of negative staining is that it produces low resolution information. The resolution is typically in the range 1.5nm to 3.0nm but under specific conditions can produce reflections down to 1nm (Fujiyoshi, J., personal communication). This method of data collection is only capable of providing structural information relating to the specimen's molecular envelope where the stain can penetrate. If higher resolution data is required then cryo-EM must be undertaken.

### 1.6.4 Structural Analysis: a Combined Approach:

Combining information from biochemical analysis with either EM (Sass *et al.*, 1989; Unwin and Henderson, 1975; Henderson *et al.*, 1990; Jap *et al.*, 1992; Kühlbrandt and Wang, 1991) or x-ray crystallography (Deisenhofer and Michel, 1986; Weiss *et al.*, 1991) can result in solved structures at high resolution. Both crystallographic methods require high quality crystals to obtain the highest resolutions, but x-ray crystallography lacks phase information. The phase information from 2D arrays results from correlative data with respect to a reference area. 2D correlation peaks can be obtained for data within a unit cell (Engel *et al.*, 1992) which in theory can be compared to x-ray data sets. As a result negatively stained 2D arrays with low resolution (>1.5nm), high signal-to-noise ratio, can potentially have the ability to produce the phase information necessary for solving high resolving x-ray data sets.

The most common use of combining EM and x-ray data is to combine high resolution information (x-ray) with lower resolution (EM) information allowing biological functions to be postulated. Examples of this actin filaments (Figure 1.20, Bremer *et al.*, 1992), and Adenovirus (2D: Stewart *et al.*, 1993; 3D: Roberts *et al.*, 1986). Combining x-ray and E.M. data does sometimes lead to structural discrepancies as in the case of actin filaments. Figure 1.20 illustrates that the discrepancy occurs at the DNase-I binding loop and may be due to the differing conformations *in vivo*. The difference in structure between the two models is probably due to a differing conformation in f-actin filaments when associated with DNase I complex.

The solved x-ray structure of a protein, although at the atomic level, may be in the wrong state for direct functional analysis. For example, the recently announced *E. coli* Rec A protein (Clark and Margulies, 1965) x-ray structure (Story *et al.*, 1992a; Story *et al.*, 1992b) is the storage form and not the biochemically active ternary complex. EM is currently being used to study the differences between the x-ray structure with the *in vivo* DNA-protein filaments (Egelman, 1993). Just as in the case of the actin filaments discussed by Bremer *et al.*, (1992), this will hopefully lead to a greater understanding of this *E.coli* protein.

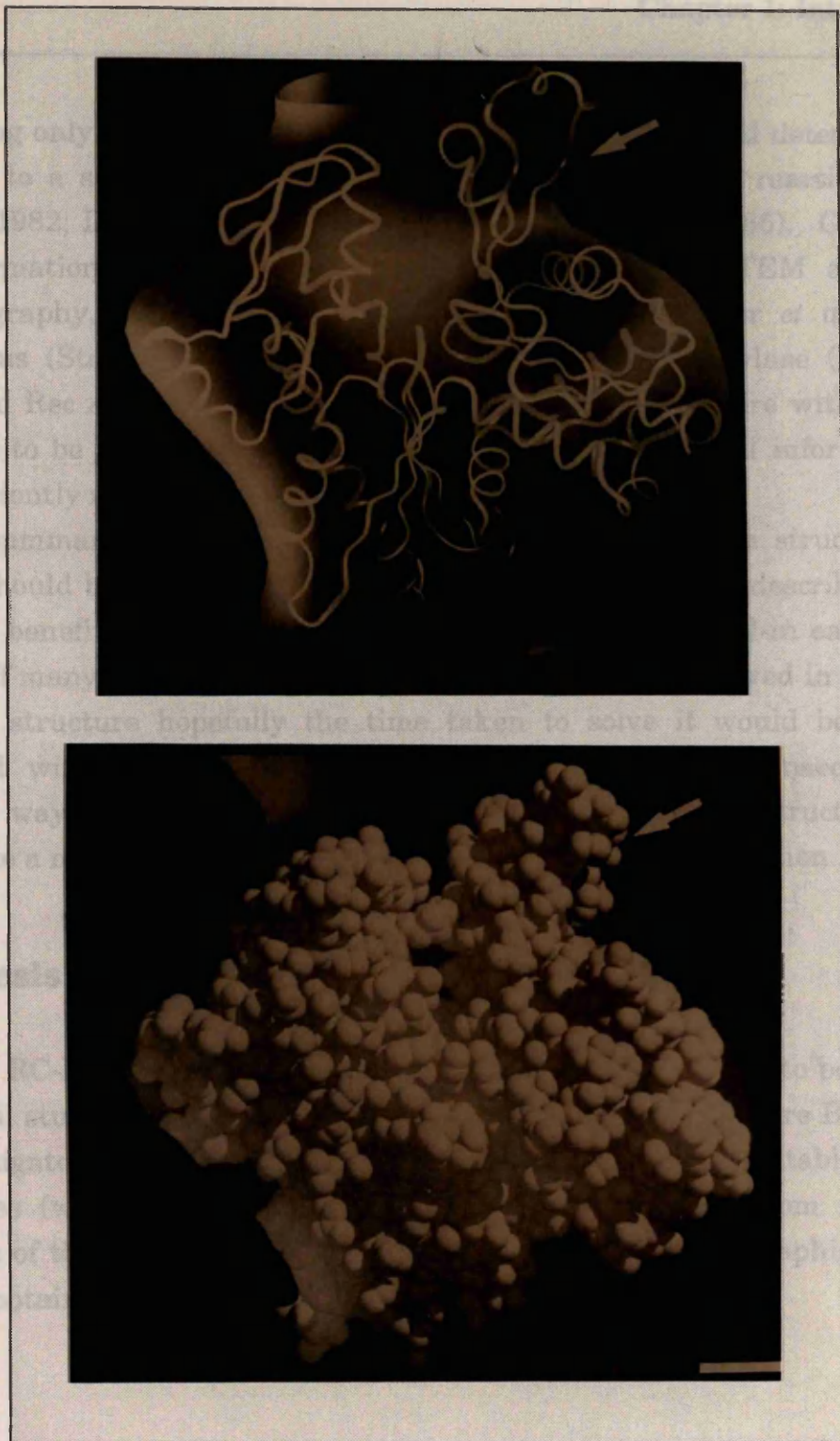


**Figure 1.20:** Comparison of the negatively stained 3D reconstruction with the atomic resolution x-ray data for F-actin filaments. Note the arrows depicting the location of the differing structure between the proposed negative stained and x-ray structures. This discrepancy occurs at the proposed DNA-I binding loop. The x-ray model is superimposed onto the EM model. Two representations of atomic structure are depicted; ribbon (top) and space filling van der Waals sphere (bottom) models. The difference in structure is probably due to a differing conformation in f-actin filaments when associated with DNase I complex. Redrawn from Bremer *et al.*, (1992). Bar 0.5nm.

Using only biochemical data and one method of structural determination can lead to a solved structure. An example is the bacterial reaction centre (Michel, 1982; Deisenhofer *et al.*, 1984; Deisenhofer *et al.*, 1985). Combining the information from Biochemical analysis, NMR, EM, STEM and x-ray crystallography, as in the cases of actin filaments (Bremer *et al.*, 1992), Adenovirus (Sterwart *et al.*, 1993), dihydrolipoly transacetylase (DeRosier, 1992) and Rec A (Egelman, 1993) permits a coherent structure with reliable functions to be postulated where a single source of structural information is not sufficiently reliable.

In summary a multi-disciplinary approach to obtain the structure of a system should be undertaken because each of the disciplines described above has both benefits and disadvantages. In combination they fill-in each others pitfalls. If many avenues of structural determination are involved in obtaining a solved structure hopefully the time taken to solve it would be reduced compared with using only traditional x-ray techniques. Consequently a practical way to obtain a functional model for a unknown structure is to undertake a multi-disciplinary approach to structural determination.

## Materials and Methods

### 1.7 Thesis Aims:

The RC-LHI supra-complex of the Rhodospirillaceae needs to be solved if functional studies into energy capture and flow through the entire BPSU is to be investigated. The aims of this thesis is simply, (i) to purify stable RC-LHI conjugates (which are inherently unstable when *in vitro*) from numerous members of the Rhodospirillaceae and, (ii) to set up crystallographic trials in order to obtain suitable crystals for structural analysis.

## 2.1 Cell Culturing:

Bacterial cell lines were stored as glycerol stocks, by mixing 1ml aliquots of viable cell cultures with sterile glycerol in a 3:1 ratio and storing them at  $-70^{\circ}\text{C}$ , thus ensuring a constant supply of uncontaminated cell lines. When needed stab cultures were prepared from the frozen stocks. These cultures consisted of 25ml McCartney bottles half filled with 1.5% Agar and the appropriate media (THERMED for *Rp. cryptolactis*, CENMED for *R. centenum*, Pfennig's media for *Rp. acidophila*, Salt enriched Pfennig's media for *R. marina*, and c-succinate for *Rp. polustris*, *Rb. sphaeroides* and *R. rubrum*), see appendices 1.1-1.4.

Stabs were inoculated and sealed air tight, then grown photoheterotrophically under high illumination ( $300 \mu\text{moles cm}^{-2} \text{s}^{-1}$ ). The source of irradiation came from banks of 150W incandescent bulbs situated in a growth chamber maintained at a constant temperature of  $28^{\circ}\text{C} \pm 2^{\circ}\text{C}$ , except for *Rp. cryptolactis* ( $37^{\circ}\text{C} \pm 1^{\circ}\text{C}$ ) and *R. centenum* ( $42^{\circ}\text{C} \pm 1^{\circ}\text{C}$ ). Once grown in agar supplemented with the appropriate medium (usually within a few days) the stabs were flooded with the same type of liquid medium, resealed and allowed to grow anaerobically. After one days growth the liquid culture was removed from the 25ml McCartney bottle and used to inoculate either a 115ml or 500ml flat sided glass medical bottle. These cultures were allowed to grow and in turn were used as inocula for either 10l glass pyrex bottles or a series of 200ml bottles. Flat sided bottles were used because this ensured a high surface to volume ratio allowing the maximum practical levels of irradiation to penetrate into the centre of the bottles. The 10l bottles, however, produced low levels of irradiation in the centre of even partially grown cultures. The increasing cell count created shadowing and hence lower energy penetration to the centre of the bottle. To combat this a large magnetic flea was placed in the 10l bottles allowing the cultures to be circulated while growing. This measure, although not producing the same irradiation levels as in the centre of the 200ml bottles, did result in 'high light' cell cultures if harvested at the appropriate time especially if only core producing species were used.

Single colonies were isolated regularly to check for cross contamination. This was achieved by inoculating air dried agar plates, supplemented with the appropriate medium (see above), from serially diluted cultures. The plates were placed in GasPak<sup>®</sup> (BHI Microbiology Systems) containers providing an anoxygenic environment. This allowed the plated cultures to pigment up when

## 2.1 Cell Culturing:

Bacterial cell lines were stored as glycerol stocks, by mixing 1ml aliquots of viable cell cultures with sterile glycerol in a 3:1 ratio and storing them at  $-70^{\circ}\text{C}$ , thus ensuring a constant supply of uncontaminated cell lines. When needed stab cultures were prepared from the frozen stocks. These cultures consisted of 25ml McCartney bottles half filled with 1.5% Agar and the appropriate media (THERMED for *Rp. cryptolactis*, CENMED for *R. centenum*, Pfennig's media for *Rp. acidophila*, Salt enriched Pfennig's media for *R. marina*, and c-succinate for *Rp. palustris*, *Rb. sphaeroides* and *R. rubrum*), see appendices 1.1-1.4.

Stabs were inoculated and sealed air tight, then grown photoheterotrophically under high illumination ( $300 \mu\text{moles cm}^{-2} \text{s}^{-1}$ ). The source of irradiation came from banks of 150W incandescent bulbs situated in a growth chamber maintained at a constant temperature of  $28^{\circ}\text{C} \pm 2^{\circ}\text{C}$ , except for *Rp. cryptolactis* ( $37^{\circ}\text{C} \pm 1^{\circ}\text{C}$ ) and *R. centenum* ( $42^{\circ}\text{C} \pm 1^{\circ}\text{C}$ ). Once grown in agar supplemented with the appropriate medium (usually within a few days) the stabs were flooded with the same type of liquid medium, resealed and allowed to grow anaerobically in the light. After about one days growth the liquid culture was removed from the 25ml McCartney bottle and used to inoculate either a 115ml or 500ml flat sided glass medical bottle. These cultures were allowed to grow and in turn were used as inocula for either 10l glass pyrex bottles or a series of 500ml bottles. Flat sided bottles were used because this ensured a high surface to volume ratio allowing the maximum practical levels of irradiation to penetrate into the centre of the bottles. The 10l bottles, however, produced low levels of irradiation in the centre of even partially grown cultures. The increasing cell count created shadowing and hence lower energy penetration to the centre of the bottle. To combat this a large magnetic flea was placed in the 10l bottles allowing the cultures to be circulated while growing. This measure, although not producing the same irradiation levels as in the centre of the 500ml bottles, did result in 'high light' cell cultures if harvested at the appropriate time especially if only core producing species were used.

Single colonies were isolated regularly to check for cross contamination. This was achieved by inoculating air dried agar plates, supplemented with the appropriate medium (see above), from serially diluted cultures. The plates were placed in GasPaK<sup>®</sup> (BBL Microbiology Systems) containers providing an anoxygenic environment. This allowed the plated cultures to *pigment up* when

irradiated. Single colonies were isolated and grown up as described above. All transfers were carried out under aseptic conditions in a laminar air flowhood using sterile media and materials.

## 2.2 Cell Harvesting:

Cultures were harvested in 5L aliquots in a MSE coolspin centrifuge at 2.5K xg, 4°C for 30 minutes. The supernatant was discarded and the pellets resuspended in MES buffer (20mM MES, 100mM KCl, pH6.8) to wash them. After a short centrifugation (12K xg, 4°C for 10 mins in a Sigma K20), the cells were either resuspended in a minimal amount of MES (pH 6.8) buffer and stored at - 20°C for future use or used to immediately prepare membranes.

## 2.3 Membrane Preparation:

### VICM Producing Species:

Vesicular ICM species (e.g. *Rb. sphaeroides*) produce small inverted vesicles when *French Pressed*. These inverted vesicles are called chromatophores. Other species produce membranes (lamellae or tubules) when *French Pressed* and chromatophores. Examples of lamellae-producing species (non-VICM) species are *Rp. acidophila*, *Rp. cryptolactis* and *Rp. palustris*.

Following harvesting the cells were homogenised in MES buffer (20mM MES, 100mM KCl, pH6.8) containing a few grains of DNase (bovine Pancreas Deoxyribonuclease 1, Sigma Chemical Company) and magnesium chloride (Sigma Chemical Company). The magnesium ions acted as cofactors to the DNase. The sample was pressed twice through a pre-cooled "French" pressure cell at 10 ton.inch<sup>-2</sup>. The result was a mixture of broken and unbroken cells. In the vesicular ICM producing species, unbroken cells were removed by centrifugation (12K xg, 4°C for 10 mins in a Sigma K20 centrifuge). The resulting supernatant was then spun to pellet the chromatophores (243K xg, 4°C for 60 mins in a Sorval ultracentrifuge). The resulting pellet was resuspended in a minimal volume of 20mM TRIS.HCl, pH8.0 and either frozen or used immediately. The chromatophores were then diluted with 20mM TRIS.HCl, pH8.0 to an optical density (O.D.) of 50cm<sup>-1</sup> at the NIR peak (between 800nm and 880nm) measured by a Shimadzu 160A scanning spectrophotometer. The chromatophores were then solubilised using the appropriate detergent and detergent concentration.

### Non-VICM Producing Species:

Non-chromatophore producing species were treated similarly to VICM species except no low speed spin was performed.

## 2.4 Absorption Spectroscopy:

Two UV-VIS spectrophotometers were routinely used. The first was a Shimadzu 160A scanning absorption spectrophotometer which required a large sample volume for accurate measurements (3ml cuvette with a path length of 1cm). If a lower sample volume needed to be analysed a Shimadzu UV-PC2101 scanning absorption spectrophotometer was used.

Accurate whole cell absorption readings were obtained using the UV-PC2101 with the integrating sphere peripheral attached. This attachment reduces the net effect of light scattering caused by particulate material thereby increasing the transmission levels detected by the phototube. Data was collected on the UV-PC2101 using Windows<sup>®</sup>-based software. The specifications of the integrating sphere allowed reliable data to be collected from 350nm to 800nm, however data collection needed to be enhanced further into the NIR where the bacterial photosynthetic protein-pigment complexes absorb. This was achieved by replacing the standard photomultiplier with a Hamamatsu R928 photomultiplier. This permitted a strong signal to noise ratio between 800nm and 900nm if the hardware was set to the manufacture's specifications and software set to a *very slow* (50nm min<sup>-1</sup>) scan speed.

## 2.5 Fluorescence Spectroscopy:

Fluorescence spectroscopy was carried out using the commercially available Perkin Elmer LS50 Fluorescence Spectrometer. The LS50 fluorescence spectra were detected using a Hamamatsu R928 Photomultiplier tube (Hamamatsu Photonics UK Ltd.) and recorded at a rate of 100nm min<sup>-1</sup>. The R928 gives extended sensitivity in the NIR wavelengths compared to the standard photomultiplier supplied with the machine. Data collection was enhanced by altering the operating PMT voltage of the detector from its default value to the maximum the LS50 permits (900V). The data was further improved by correcting for the R928 Quantum Efficiency (QE) at each recorded wavelength. The emission data was corrected using a polynomial equation derived from a scanned and digitised data sheet provided by Hamamatsu Photonics UK Ltd.

The LS50 uses diffraction gratings to obtain monochromatic excitation wavelengths. To prevent higher orders of *light* being detected by the R928 phototube, transmission filters (cut-off at 700nm) were located between the sample and R928 detector.

### 2.5.1 Correction and Normalisation of LS50 Data:

The quantum efficiency (QE) of the R928 photomultiplier decreases as wavelength increases thereby reducing the signal-to-noise ratio as the wavelength increases. The decreasing QE is very significant when collecting data at the near infra red wavelengths: for example, at 900nm the efficiency is less than 0.1% that at 450nm (see Figure 2.1). To account for the quantum efficiency at each recorded wavelength ( $\lambda$ ) the nominal spectral response curve (data sheet T-1000, Hamamatsu Photonics UK Ltd) was scanned, digitised and analysed using a Personal Computer running Windows<sup>®</sup> software. The scanned spectral response data for the R928 photomultiplier was used to create a polynomial equation that corrected for the QE in fluorescence data at each recorded wavelength. The spectral response curve was scanned at 400dpi using a Logitech 256 greyscale Scanman<sup>®</sup> in combination with PhotoTouch<sup>™</sup> version 2.1 software (logitech, Inc, Fremont. A94555, USA). The image was saved in Windows<sup>®</sup> bitmap format (bmp) and loaded into Digitize<sup>™</sup> version 0.98 (Y. Danon, Troy, NY12180, U.S.A) and digitised. The output file from Digitize<sup>™</sup> was then loaded into the spreadsheet package Excel v4.0<sup>™</sup> and a regression equation calculated. The regression analysis was undertaken by Dr P.J.Dominy, Department of Botany, University of Glasgow. The regression analysis produced a seventh order polynomial equation, shown below:

$$\text{Log}_{10}(\text{QE}) = a + (b \times x) + (c \times x^2) + (d \times x^3) + (e \times x^4) + (f \times x^5) + (g \times x^6) + (h \times x^7) \quad (7)$$

where  $\chi$  is the recorded wavelength and the constants a,b,c,d,e,f,g and h are -2.1924, 3.3769x10<sup>-01</sup>, -1.9926x10<sup>-03</sup>, 6.2044x10<sup>-06</sup>, -1.0971x10<sup>-08</sup>, 1.0912x10<sup>-11</sup>, -5.5635x10<sup>-15</sup>, and 1.0845x10<sup>-18</sup> respectively. Figure 2.1 illustrates the nominal quantum efficiency of the R928 photomultiplier tube and its regression equation with associated errors.

## 2.5.2 Optimising Fluorescence Data Collection:

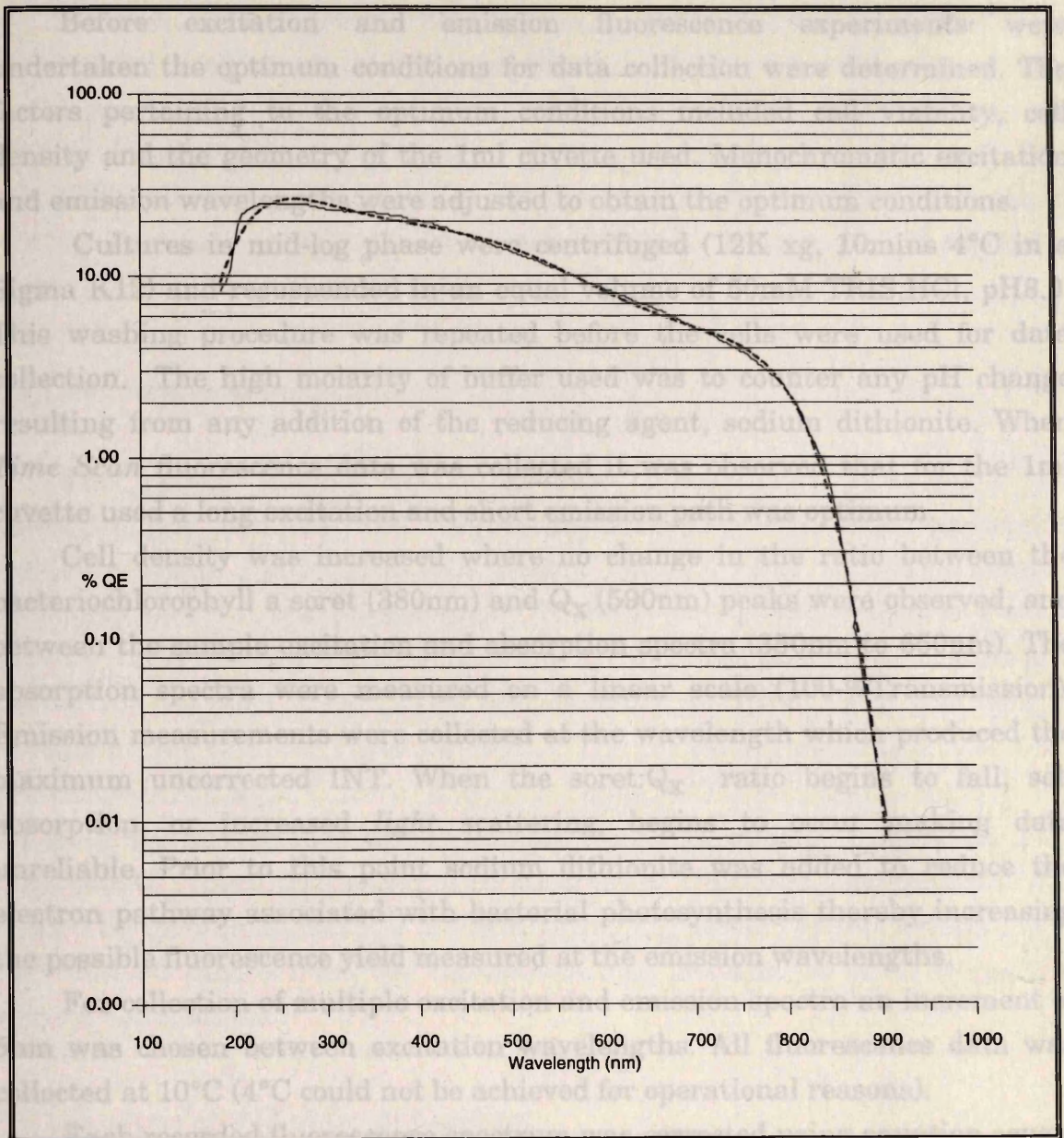


**Figure 2.1:** Nominal Quantum Efficiency (QE) response curve for the Hamamatsu R928 Photomultiplier tube (solid line) and its calculated polynomial equation (dotted line). Note that the 7<sup>th</sup> order polynomial equation (see text) is for logQE and that the y-axis is a logarithmic scale. The graph shows that regression equation fits well for the experimental operating wavelengths between 350nm and 900nm. The polynomial equation was calculated by Dr. P.J. Dominy, Department of Botany, University of Glasgow. The standard error for the y estimate is 0.033. Regression analysis by a least squares method indicates that  $R^2 = 0.998$ .  $F = 26632.614$ . Degrees of freedom = 393. Residual sum of squares = 201.890. Residual sum of squares = 0.426.

## 2.5.2 Optimising Fluorescence Data Collection:

Before excitation and emission fluorescence experiments were undertaken the optimum conditions for data collection were determined. The factors pertaining to the optimum conditions included cell viability, cell density and the geometry of the 1ml cuvette used. Monochromatic excitation and emission wavelengths were adjusted to obtain the optimum conditions.

Cultures in mid-log phase were centrifuged (12K xg, 10mins 4°C in a Sigma K12) and resuspended in an equal volume of 50mM TRIS.HCl, pH8.0. This washing procedure was repeated before the cells were used for data collection. The high molarity of buffer used was to counter any pH change resulting from any addition of the reducing agent, sodium dithionite. When *Time Scan* fluorescence data was collected it was observed that for the 1ml cuvette used a long excitation and short emission path was optimum.

Cell density was increased where no change in the ratio between the bacteriochlorophyll a solet (380nm) and  $Q_x$  (590nm) peaks were observed, and between the sample excitation and absorption spectra (350nm to 650nm). The absorption spectra were measured on a linear scale (100-%Transmission). Emission measurements were collected at the wavelength which produced the maximum uncorrected INT. When the solet: $Q_x$  ratio begins to fall, self absorption, or increased *light* scattering, begins to occur making data unreliable. Prior to this point sodium dithionite was added to reduce the electron pathway associated with bacterial photosynthesis thereby increasing the possible fluorescence yield measured at the emission wavelengths.

For collection of multiple excitation and emission spectra an increment of 5nm was chosen between excitation wavelengths. All fluorescence data was collected at 10°C (4°C could not be achieved for operational reasons).

Each recorded fluorescence spectrum was corrected using equation seven. To obtain an absolute level of fluorescence intensity (INT) is impractical because although the maximum QE of the R928 is 28% (data sheet T-1000, Hamamatsu Photonics UK Ltd) the maximum efficiency of the LS50-R928 hardware optical system is unknown. The %T and INT data were normalised at 590nm and compared. The maximum detectable INT was given the arbitrary value of 100 (A.U.). All other data points were normalised against this peak value.

## 2.6 Isolation of Bacteriochlorophyll Containing Complexes:

Methods used to isolate RC-LHI conjugates and LHII complexes were based on Cogdell *et al.*, (1983) and Dawkins (1988). Isolating the various complexes involved a series of procedures: (i) solubilisation, (ii) sucrose gradient centrifugation, (iii) anion exchange and (iv) gel filtration. The differences between protein isolation and purification for the individual species will be discussed in the results section (Chapter Three), but the general purification steps are outlined below.

### 2.6.1 Membrane Solubilisation:

The optical density (O.D.) of the photosynthetic membrane (or chromatophore sample) was diluted to  $50\text{cm}^{-1}$  at the NIR absorption maximum using 20mM TRIS.HCl, pH8.0. The O.D. was measured using a Shimadzu UV160A spectrophotometer. N,N-dimethyl-N-dodecylamine-N-oxide (LDAO) *purum* (Fluka Biochemicals) was added to the membrane sample and stirred for 15 mins at 4°C. The concentration of LDAO used was species dependent, see Chapter Three for details. The solubilised membrane was then centrifuged (12K xg, 4°C for 10 mins in a Sigma K20 centrifuge) to remove any unsolubilised material. The supernatant was immediately diluted at least three-fold to reduce the detergent concentration. The solubilised material was diluted because constant high levels of LDAO ( $>0.25\%_{w/v}$ ) causes separation of the reaction centre from the light-harvesting antenna as well as general protein degradation.

### 2.6.2 Sucrose Gradient Centrifugation:

Solubilised membrane sample was loaded onto either a continuous or discontinuous sucrose gradient. The gradient ranged from 0.2M to 1.2M sucrose in a buffer of LDAO '*purum*' (Fluka Biochemicals), 10mM TRIS.HCl, pH8.0. The concentration of LDAO used in the gradients was species dependant; usually 0.1% or 0.2% ( $w/v$ ). After centrifugation (197K xg, 4°C for up to 16 hours using precooled T865 rotors in Sorval ultracentrifuges; models 55B, 65B and Combi) discrete pigmented bands were formed. These bands were then isolated and the pigment-proteins purified. The sucrose gradient protocol was based on the method by Firsow and Drews, (1977).

### 2.6.3 Anion Exchange:

Using diethylethly-aminoethylcellulose (DEAE) (DE52, Whatman; or Fractogel 650(s), Merck) protein species were isolated by anion exchange. Columns were prepared, and equilibrated to a pH of 8.0 using 10mM TRIS.HCl,pH8.0. Once equilibrated, detergent containing buffer (0.1% w/v LDAO, 10mM TRIS.HCl,pH8.0) was added to provide a homogenous environment for the solubilised membranes. To this was added the solubilised material which originated from either directly solubilised membranes or the pigmented bands from sucrose gradients. Once loaded, spectra from column eluate were periodically taken to ensure that all unbound protein (measured by the absorbance at 275nm) had passed through the DEAE column. When no detectable peak at 275nm was present a salt gradient was applied from 10mM NaCl to 150mM NaCl (in 0.1% w/v LDAO, 10mM TRIS.HCl,pH8.0). Eluted fractions were collected and analysed by absorption spectroscopy. The spectroscopically pure fractions were then pooled for future use. If peripheral antennae were also to be collected, the salt gradient was increased to 350mM NaCl. If required, the pooled fractions were dialysed against, or diluted with, 0.1%LDAO, 10mM TRIS.CL,pH8.0 and subjected to another DEAE column, with the spectroscopically pure aliquots again being pooled. This resulted in a dilute, but relatively pure, preparation suitable for further purification by gel filtration.

Gel filtration only allows small volumes of sample to be fractionated at any one time. To speed up the purification process, the spectroscopically pure fractions were first concentrated by a small Fractogel 650(s) column then subjected to gel filtration. The Fractogel 650(s) column was eluted with either 200mM NaCl (*core* fractions) or 350mM NaCl (peripheral antenna fractions) as described above. The spectroscopically pure aliquots were then passed down a gel filtration column.

### 2.6.4 Gel Filtration:

Gel filtration was used to further purify the samples. Sephacryl S-200 (Pharmacia) was used buffered in 0.1%LDAO(w/v), 10mM TRIS.HCl,pH8.0 in 1m glass columns (Pharmacia KX type, 26mm internal diameter). Approximately 500ml of buffer was used to equilibrate the column after any previous run. Up to 5ml of purified fraction was loaded onto the columns and the elutant collected in 0.5ml aliquots using a BioRad Econo fraction collector.

### 2.6.6 Detergent Exchange:

The spectroscopically pure aliquots from section 2.6.4 were pooled and subjected to anion exchange as in section 2.6.3 and the sample was eluted with buffer containing salt and the new detergent. Before eluting the purified complex, the loaded column was allowed to equilibrate with the new detergent, i.e. buffer containing LDAO was replaced with buffer and containing the new detergent. The spectroscopically pure aliquots were pooled and the salt removed by either dialysis or by filtration (using centricons<sup>®</sup> or filtricons<sup>®</sup>). The latter approach of salt removal was preferred as it also has the ability to concentrate the sample. The use of filtration devices reduced salt levels by up to 99% (centricons<sup>®</sup> and filtricons<sup>®</sup> data sheets).

Figure 2.2: Typical Redox difference absorbance assay for RC-LHI conjugate isolated from a member of the Rhodospirillaceae. An equal volume of purified RC-LHI, with an NIR maximum O.D. of approximately  $1.0 \text{ cm}^{-1}$ , was placed in the sample and reference cuvettes and a spectrum recorded (baseline spectrum). The reference cuvette was completely reduced by addition of sodium ascorbate. Potassium ferricyanide was added to the sample cuvette until complete oxidised sample observed (reduced/oxidised spectrum). Some sodium ascorbate was then added to the sample cuvette to ensure that irreversible oxidation had not occurred in the RC-LHI system. The difference in absorption at 600nm was measured (dotted line) and the RC concentration calculated using the extinction coefficient of  $\epsilon_{600\text{nm}} = 133 \text{ nM}^{-1} \text{ cm}^{-1}$  (Clayton et al., 1972). Irreversible oxidation of the RC-LHI would occur if the difference spectrum at 600nm did not revert to the original baseline spectrum upon addition of sodium ascorbate. In the example above the RC-LHI has not undergone irreversible BChl *a* oxidation. Redox assays were carried out in 3ml cuvettes (path length of 1cm) using a Shimadzu UV-2101PG scanning absorption spectrophotometer. The Redox assay above is from purified *Rp. cryptolactis* RC-LHI.

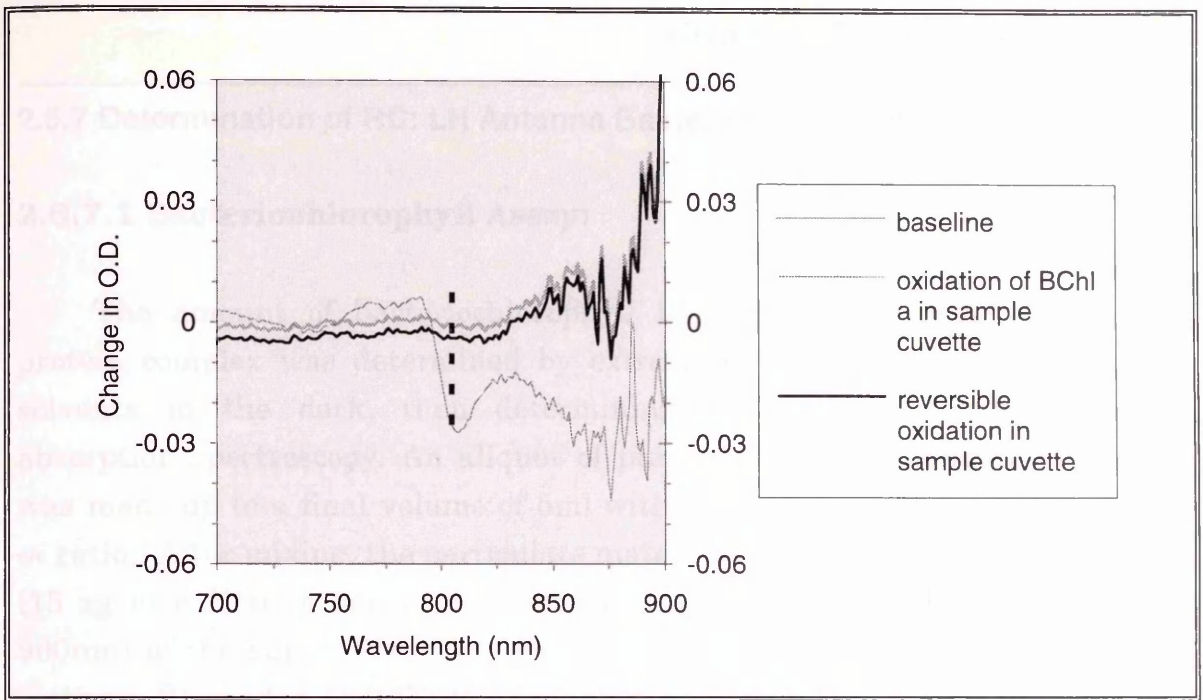


**Figure 2.2:** Typical Redox difference absorbance assay for RC-LHI conjugate isolated from a member of the Rhodospirillaceae. An equal volume of purified RC-LHI, with an NIR maximum O.D. of approximately  $1.0 \text{ cm}^{-1}$ , was placed in the sample and reference cuvettes and a spectrum recorded (baseline spectrum). The reference cuvette was completely reduced by addition of sodium ascorbate. Potassium ferricyanide was added to the sample cuvette until complete oxidised sample occurred (reduced/oxidised spectrum). Some sodium ascorbate was then added to the sample cuvette to ensure that irreversible oxidation had not occurred in the RC-LHI system. The difference in absorption at 800nm was measured (dotted line) and the RC concentration calculated using the Extinction coefficient of  $\epsilon_{\Delta 800\text{nm}} = 133 \text{ mM}^{-1} \text{ cm}^{-1}$  (Clayton *et al.*, 1972). Irreversible oxidation of the BChl *a* would occur if the difference spectrum at  $\sim 870\text{nm}$  did not revert to the original baseline spectrum upon addition of sodium ascorbate. In the example above the RC-LHI has not undergone complete irrecoverable BChl *a* oxidation. Redox assays were carried out in 3ml cuvettes (path length of 1cm) using a Shimadzu UV-2101PC scanning absorption spectrophotometer. The Redox assay above is from purified *Rp. cryptolactis* RC-LHI.

## 2.6.7 Determination of RC: LH Antenna Bacteriochlorophyll Ratio:

### 2.6.7.1 Bacteriochlorophyll Assay:

The amount of bacteriochlorophyll in a sample of purified pigment-protein complex was determined by extracting the pigments, using organic solvents in the dark, then determining the pigment concentration by absorption spectroscopy. An aliquot of purified RC-LHI conjugate (15-200 $\mu$ l) was made up to a final volume of 5ml with an acetone:methanol mixture (7:2 v/v ratio). After mixing, the particulate material was removed by centrifugation (15 xg in a Hettich bench top centrifuge) and an absorption spectrum (700-900nm) of the supernatant was recorded against an acetone:methanol blank (using a Shimadzu UVPC-2101 scanning spectrophotometer). The extinction coefficient at 772nm for bacteriochlorophyll in the organic solvent is 76 mM<sup>-1</sup>cm<sup>-1</sup>. (Cohen-Bazire *et al.*, 1957; Clayton, 1966). The concentration of BChl a in the undiluted sample was then calculated using the extinction coefficient and absorbance data.

### 2.6.7.2 Reaction Centre Assay:

This assay is based on the reversible blue shift in absorption at approximately 800nm, resulting from the oxidation of the reaction centre. An aliquot of RC-LHI was diluted with the appropriate detergent containing buffer to produce a maximum NIR O.D. of approximately 1.0cm<sup>-1</sup>. 3ml cuvettes were used in a Shimadzu UVPC-2101 scanning spectrophotometer and a baseline recorded with both sample and reference cuvettes containing the diluted *core* conjugate. Redox absorption differences were recorded at 800nm. To ensure complete reduction of the sample in the reference cuvette a small quantity of sodium ascorbate was added. The Redox associated difference spectrum was recorded from 900nm to 700nm upon addition of potassium ferricyanide to the sample cuvette. Potassium ferricyanide was added until the blue shift at 800nm had reached completion. Figure 2.2 is an example of a Redox assay from a batch of purified RC-LHI conjugate. To ensure that irreversible bleaching of light-harvesting BChl a had not occurred, sodium ascorbate was added to the sample cuvette. Reversibility in difference absorption spectrum should occur. Irreversible oxidation of BChl a can be seen spectroscopically by bleaching of the NIR 870/883nm absorption band.

The reaction centre concentration was calculated using the absorption extinction coefficient for the change in absorbance at the ~800nm,

$\epsilon_{\Delta 800\text{nm}} = 133\text{mM}^{-1}\text{cm}^{-1}$  (Clayton *et al.*, 1972). Total BChl *a* was determined using the 880nm absorption for the diluted *core* sample. The extinction coefficient for total BChl *a* at 880nm is  $\epsilon_{880\text{nm}} = 120\text{mM}^{-1}\text{cm}^{-1}$  (Clayton, 1971).

The RC:LH BChl *a* ratio was then determined. The extinction coefficient 880nm for total BChl *a* content was also experimentally determined using the results from bacteriochlorophyll assays (section 2.6.7.1.). The experimentally determined BChl *a* extinction coefficient was then also used to calculate RC:BChl *a* ratios.

## 2.7 Polypeptide Analysis; Concentration and Composition:

### 2.7.1 Protein Concentration:

Protein concentrations were determined using the Tannin Assay (Mejbaum-Katenellenbogen and Dobryszczyka, 1959), see appendix 2. This relied on turbidity measurements as an indicator of protein concentration. An aliquot of purified pigment-protein was made up to 1ml with distilled water and left to equilibrate at 30°C for 5mins. To this was added 1ml of freshly filtered Tannin Reagent, also equilibrated to 30°C, and the reaction left to incubate for 10mins at 30°C. The reaction was fixed by addition of 1ml of 0.2% (w/v) Acacia solution. Protein standards (10-80 $\mu\text{g ml}^{-1}$ ) were also prepared as described above from standard Bovine Serum Albumin fraction V (B.S.A., fraction V, SIGMA Chemical Company). After fixation optical density measurements were taken at 500nm for both the standard and sample proteins and a calibration curve produced using the B.S.A data (for an example of a calibration curve see Figure 2.3). The B.S.A. calibration curve was then used to calculate the concentration of the sample proteins.

Figure 2.3: Protein concentration calibration curve based on turbidity measurements. The protein standard Bovine Serum Albumin fraction IV (B.S.A.) was used to create calibration curves based on the protocol by Mejbaum-Katenellenbogen and Dobryszczyka, (1959). Protein preparations were then quantified using the B.S.A. calibration curve.

## 2.7.2 Protein Composition:

Polyacrylamide gel electrophoresis (PAGE) was used to determine the protein composition of isolated complexes based on Laemmli, (1970) as adapted by Schagger and von Jagow, (1987).

A 15mm plastic spacer was wedged between two clean glass plates and the resulting sandwich clamped into a gel pourer. The solution was then poured into the gel apparatus. A layer of 50% (w/v) methanol:water was poured on top of the resolving gel, resulting in a smooth gel surface (sans meniscus) and a non-oxidized gel. Once the gel had set (after about 40min), the methanol:water was removed and a stacking gel was poured onto the resolving gel and a plastic comb inserted. Once the stacking gel had set the gel sandwich was removed from the gel pourer and inserted into the Studier-type gel apparatus. Buffers (Appendix 3.1) were added to the two reservoirs and the plastic comb removed.

Protein samples (50µg) were prepared by adding an equal volume of Gel Sample Buffer (Appendix 3.2). The mixture was then either boiled for 2mins at 100°C or incubated at 70°C for 30mins. The gels were run for approximately 16 hours (overnight) at 15mA and switched off when the blue dye front had just reached the bottom of the gel. Once electrophoresis was complete the gel was removed from the glass plates and placed in Stainer (Appendix 3.3) for a few hours, then placed in Destainer (Appendix 3.4). Several washes in Destainer were performed before the protein bands could be observed.

## 2.8 3D Crystallography:

Vapour diffusion was the most common method for setting up 3D trials as described by Michel and Oesterhelt, 1989. Two types of chamber were used, large scale vapour diffusion chambers and Crocker plates. The latter were more convenient owing to their smaller size.

A range of conditions in the same run was used to screen for crystals and were prepared by the method of Wilson and Wilson, 1987. The major 46 (U.C.L.A., USA) set of solutions was tried and used as a basis for a semi-factorial screening system. The results of crystallographic trials from Dewkins, (1988) were also used as a starting point for 3D crystallography.

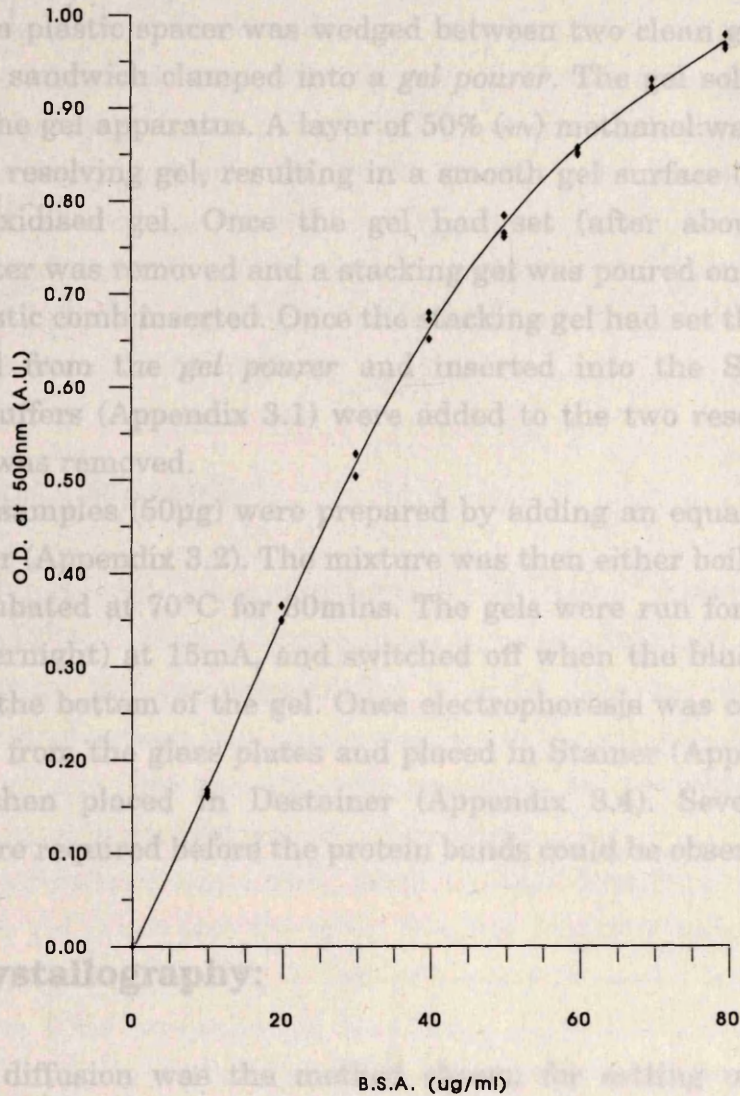


**Figure 2.3:** Protein concentration calibration curve based on turbidity measurements. The protein standard Bovine Serum Albumin fraction IV (B.S.A.) was used to create calibration curves based on the protocol by Meijbaum-Katenellenbogen and Dobryszczyka, (1959). Protein preparations were then quantified using the B.S.A. calibration curve.

### 2.7.2 Protein Composition:

Polyacrylamide gel electrophoresis (PAGE) was used to determine the protein composition of isolated complexes based on Laemmli, (1970) as adapted by Schägger and von Jagow, (1987).

A 1.5mm plastic spacer was wedged between two clean glass plates and the resulting sandwich clamped into a *gel pourer*. The gel solution was then poured into the gel apparatus. A layer of 50% (v/v) methanol:water was poured on top of the resolving gel, resulting in a smooth gel surface (*sans meniscus*) and a non-oxidised gel. Once the gel had set (after about 40min), the methanol:water was removed and a stacking gel was poured onto the resolving gel and a plastic comb inserted. Once the stacking gel had set the gel sandwich was removed from the *gel pourer* and inserted into the Studier-type gel apparatus. Buffers (Appendix 3.1) were added to the two reservoirs and the plastic comb was removed.

Protein samples (50 $\mu$ g) were prepared by adding an equal volume of Gel Sample Buffer (Appendix 3.2). The mixture was then either boiled for 2mins at 100°C or incubated at 70°C for 30mins. The gels were run for approximately 16 hours (overnight) at 15mA, and switched off when the blue dye front had just reached the bottom of the gel. Once electrophoresis was complete the gel was removed from the glass plates and placed in Stainer (Appendix 3.3) for a few hours, then placed in Destainer (Appendix 3.4). Several washes in Destainer were required before the protein bands could be observed.

### 2.8 3D Crystallography:

Vapour diffusion was the method chosen for setting up 3D trials as described by Michel and Oesterhelt, 1980. Two types of chamber were used; large scale vapour diffusion chambers and Crychem<sup>®</sup> plates. The latter were more convenient owing to their smaller size and the ability to directly compare a range of conditions in the same tray. The Crychem<sup>®</sup> plates were also more practical because they allowed smaller incubations to be set up. If a crystal chamber was to be used again it was cleaned and checked for any scratches to reduce the number of possible nucleation sites. Reduced nucleation sites help to produce large crystals (McPherson, 1982). The *magic 46* (U.C.L.A., U.S.A) set of solutions was tried and used as a basis for a semi-factorial screening system. The results of crystallographic trials from Dawkins, (1988) were also used as a starting point for 3D crystallography.

Purified protein was mixed with the mother liquor (crystallographic incubation solution) in a 1:1 ratio and centrifuged for 10 mins (3k xg at 20°C) to precipitate any unsolubilised material. The supernatant was pipetted into a well surrounded by a reservoir of mother liquor and the chamber sealed. The Crychem<sup>®</sup> plates were sealed with either siliconised glass cover slips and vacuum grease or clear plastic adhesive tape (p/n TA-2, JBL Scientific Ltd). Standard electrical tape was used to seal the large scale vapour diffusion plates. The temperature was maintained by using incubation cabinets. After observing the crystallographic trials for two-to-three weeks the conditions were slightly altered by independently varying the constituent factors affecting crystal growth. These factors included; detergent type, protein concentration, temperature, pH, ionic strength, precipitant concentration and type, salt type and concentration.

## 2.9 2D Crystallography:

Two dimensional crystallisation trials were prepared based on Kühlbrandt, (1992). The sample conditions initially contained detergent levels above the critical micelle concentration (C.M.C). Dialysis was then used to reduce the detergent (and lipid) concentration in the samples below the C.M.C value causing the detergent-protein micelles to aggregate. If suitable conditions were present, 2D crystals were formed

The experimental apparatus used is that described by Kühlbrandt, (1992). Figure 2.4 illustrates the main features of this system. To maintain a constant temperature,  $\pm 0.2^\circ\text{C}$ , a Techne (tempette model) circulating water bath was used. This was achieved by placing the beakers (Figure 2.4B) on a platform within the waterbath and filling the bath with water such that the crystal chambers were covered to at least the depth of the dialysate (reservoir) solution. Aliquots of sample were removed at intervals using glass capillaries and routinely examined by negative staining Transmission Electron Microscopy (T.E.M.).

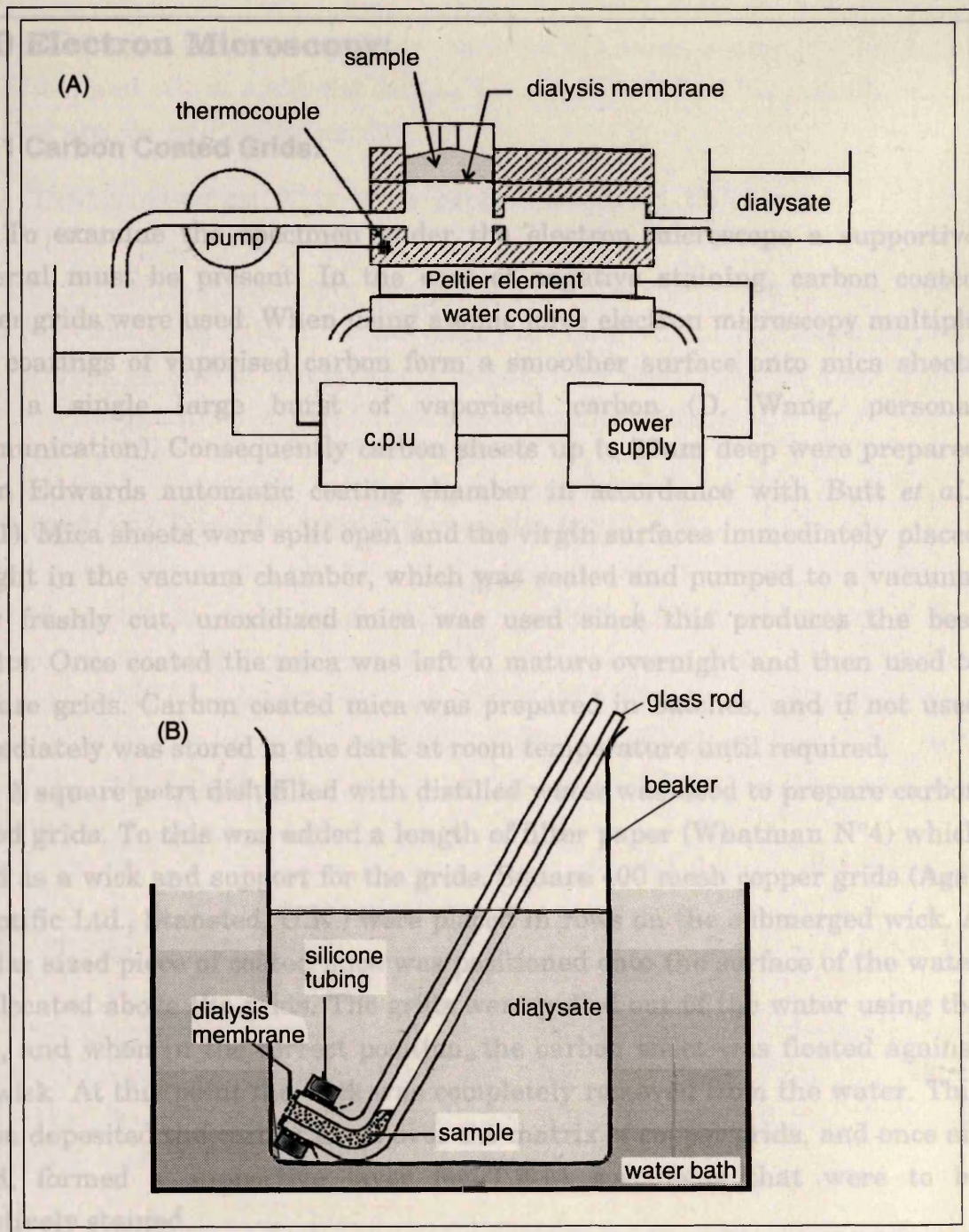


**Figure 2.4:** Experimental designs for microdialysis. The rationale behind microdialysis is the net removal of small molecules from a sample by diffusion across a membrane into the dialysate under controlled conditions. This can be achieved by a computer (cpu) controlled temperature sensitive apparatus (top) or by a simpler system (bottom). An example of computer controlled apparatus is that of Paul *et al.*, (1992). In the top diagram temperature is maintained by a heating block attached to a thermocouple while in (B) it is supplied by a large reservoir of water, i.e. a water bath. In (A) the prewarmed dialysate is constantly replaced while in (B) it is replaced by a batch method after equilibrating to the correct temperature. The apparatus used for 2D crystallographic trials was the simpler design as described by Kühlbrandt, (1992).

## 2.10 Electron Microscopy:

### 2.10.1 Carbon Coated Grids:

To examine the specimen under the electron microscope a supportive material must be present. In the case of negative staining, carbon coated copper grids were used. When using atomic force electron microscopy multiple thin coatings of vaporised carbon form a smoother surface onto mica sheets than a single large burst of vaporised carbon (D. Wang, personal communication). Consequently carbon sheets up to 20nm deep were prepared in an Edwards automatic coating chamber in accordance with Butt *et al.*, (1991). Mica sheets were split open and the virgin surfaces immediately placed upright in the vacuum chamber, which was sealed and pumped to a vacuum. Only freshly cut, unoxidized mica was used since this produces the best results. Once coated the mica was left to mature overnight and then used to prepare grids. Carbon coated mica was prepared in batches, and if not used immediately was stored in the dark at room temperature until required.

A square petri dish filled with distilled water was used to prepare carbon coated grids. To this was added a length of filter paper (Whatman N°4) which acted as a wick and support for the grids. Square 400 mesh copper grids (Agar Scientific Ltd., Stansted, U.K.) were placed in rows on the submerged wick. A similar sized piece of coated mica was positioned onto the surface of the water and located above the grids. The grids were pulled out of the water using the wick, and when in the correct position, the carbon sheet was floated against the wick. At this point the wick was completely removed from the water. This action deposited the carbon sheet over the matrix of copper grids, and once air dried, formed a supportive layer for T.E.M specimens that were to be negatively stained.

### 2.10.2 Negative Staining:

2% (w/v) uranyl acetate (U.A.) in filtered Analar® water was used to stain specimens. Approximately 2µl of specimen was dropped onto a coated grid clamped in a pair of anti-capillary forceps (Duemont, Switzerland), and left for 30s to bind to the grid. The majority of the specimen was removed by blotting, using the hairs from a piece of ripped N°4 Whatman filter paper. The fine hairs produced by ripping the filter paper provide a better blotting system than uncut paper or paper cut by scissors (W. Kühlbrandt, personal

communication). Complete solvent removal did not occur. A drop of 2%U.A.(w/v) was added and left to stain the sample for a further 30s. This procedure was repeated and the grid left to air dry.

### **2.11 Transmission Electron Microscopy (T.E.M.):**

The following microscopes were used to examine specimens; Jeol 100-C, Ziess 902 (Biological E.M. suite University of Glasgow, U.K.), Philips 301 and Jeol 2000-EX (E.M.B.L, Heidelberg, Germany). Of these the Jeol 100-C, Ziess 902 and Philips 301 were used for routine screening of samples.

### **2.12 Optical Bench: Integrity of Order.**

Coherent laser beams were used to produce diffraction images of E.M negatives to establish the degree of order of a specimen. Two optical benches were used. The first was located at EMBL, Heidelberg, and has been well documented (Erickson *et al.*, 1978) while the second (Biological E.M. suite University of Glasgow) consisted of a simple straight path (resulting in a very small diffraction pattern) arrangement.

### **2.13 Image Processing:**

EM negatives were scanned and digitised using a Perkin Elmer micodensitometer (model 1010-GM) and then processed using the *MRC, Cambridge Image Processing System* (discussed by Amos *et al.*, 1982; and Henderson *et al.*, 1990) on a VAX mini computer.

### 3.1 Introduction

If a structure of a biological macromolecule is required, the first step is to ensure the constant quality of starting material. The pigment-protein complexes under investigation were isolated using the techniques described in the previous Chapter. In the introductory Chapter it was noted that the production of the different LHs was environmentally dependent (for a review see Zuber, 1986). There are also reports of lipid variation in the pigment-protein complexes due to environmental and isolation techniques (Pucheu *et al.*, 1974; Russell and Harwood, 1979; Donohue *et al.*, 1982a/b; Kaufmann *et al.*, 1982; Imhoff *et al.*, 1982). A uniform supply of protein was required from a range of species, and for this reason a series of growth curves were determined which allowed standardised harvesting conditions to be established (section 3.2).

cells were then isolated and purified (Section 3.3). Species dependent purification of these photosynthetic proteins were based on Firsov and Drews, (1977); Cogdell *et al.*, (1983); and Dawkins, (1988).

## Chapter Three:

### 3.2 Growth of Cell Lines

## Cell Culture and Protein Purification

Bacterial cell lines from a range of species were stored as either glycerol stocks (section 2.1), agar slabs or liquid cultures until required for 3D and 2D crystallographic trials. Actively growing photoheterotrophic cells (mid-log

The batches of cells were harvested as described in Chapter Two. Both 10l and flat sided 500ml glass bottles were used to grow the purple bacteria. When core complex was required the bacteria were cultured in the flat sided 500ml glass bottles. 10l pyrex<sup>®</sup> bottles were only used for low-light cultures, when specific isolation of LHII was desired. The bulk of the cells were grown in 500ml bottles. The absorbance at 650nm is directly proportional to the number of cells present (Gardiner, 1993; Simmons, A.E., personal communication). By observing the optical density at 650nm the lag, logarithmic and stationary phases of growth were determined for each species, when grown in the 500ml bottles. This established an optimum harvesting time (with respect to late-log phase) for each cell line investigated.

When a batch of protein was needed, an appropriate actively growing cell line was subcultured every 12 hours for 36 hours, then used as the inoculum (~2% v/v). The inoculum for the growth curves was also subcultured in the same manner. Generally, six bottles were used for a growth curve data set.

### 3.1 Introduction

If a structure of a biological macromolecule is required, the first step is to ensure the constant quality of starting material. The pigment-protein complexes under investigation were isolated using the techniques described in the previous Chapter. In the introductory Chapter it was noted that the production of the different LHs was environmentally dependent (for a review see Zuber, 1986). There are also reports of lipid variation in the pigment-protein complexes due to environmental and isolation techniques (Pucheu *et al.*, 1974; Russell and Harwood, 1979; Donohue *et al.*, 1982a/b; Kaufmann *et al.*, 1982; Imhoff *et al.*, 1982). A uniform supply of protein was required from a range of species, and for this reason a series of growth curves were determined which allowed standardised harvesting conditions to be established (section 3.2). The pigment-protein complexes from the uniformly grown and harvested cells were then isolated and purified (Section 3.3). Species dependent purification of these photosynthetic proteins were based on Firsow and Drews, (1977); Cogdell *et al.*, (1983); and Dawkins, (1988).

### 3.2 Growth of Cell Lines

Bacterial cell lines from a range of species were stored as either glycerol stocks (section 2.1), agar stabs or liquid cultures until required for 3D and 2D crystallographic trials. Actively growing photoheterotrophic cells (mid-log phase) were used as 2% inocula for large scale culturing by a batch method. The batches of cells were harvested as described in Chapter Two. Both 10l and flat sided 500ml glass bottles were used to grow the purple bacteria. When core complex was required the bacteria were cultured in the flat sided 500ml glass bottles. 10l pyrex<sup>®</sup> bottles were only used for low-light cultures, when specific isolation of LHIII was desired. The bulk of the cells were grown in 500ml bottles. The absorbance at 650nm is directly proportional to the number of cells present (Gardiner, 1993; Simmons, A.E., personal communication). By observing the optical density at 650nm the lag, logarithmic and stationary phases of growth were determined for each species, when grown in the 500ml bottles. This established an optimum harvesting time (with respect to late-log phase) for each cell line investigated.

When a batch of protein was needed, an appropriate actively growing cell line was subcultured every 12 hours for 36 hours, then used as the inoculum (~ 2% v/v). The inoculum for the growth curves was also subcultured in the same manner. Generally, six bottles were used for a growth curve data set.

Five of these were used to obtain data on the growth of the culture while the sixth was used as a control.

The synthesis of the pigment-proteins involved in photosynthesis are known to be regulated by molecular oxygen (Kiley and Kaplan, 1987; Kiley and Kaplan, 1988; Lee *et al.*, 1989), its presence reducing the levels of photosynthetic complexes present (i.e. the pigment-protein complexes RC-LHI and LHII). Any unintentional addition of oxygen into the growing culture (by repeated sample removal) could alter the growth conditions of the culture, when directly compared to a control culture that has not had repeated sample removal. Control bottles were used to reduce the possibility of producing erroneous growth curve data sets. Data was not collected from these bottles until the culture was in mid-late log phase (as predetermined from initial observations).

In order to obtain data, while causing as little disturbance to the growing culture, rubber gas seals were used instead of the normal screw caps. This enabled the sterile needle of a hypodermic syringe to penetrate the contents of the bottle whereupon a small volume was removed from the culture. Approximately 1000 $\mu$ l was removed at each time point. When a sample was removed, an equal volume of inert nitrogen gas was injected. to ensure a positive pressure in the bottle, relative to the growth chamber. Sterile needles and syringes were used, and prior to injection the rubber seals were wiped with absolute ethanol to sterilise the outer surface of the seal. Absorbance spectra were taken from 350nm to 900nm (using a Shimadzu UV2101-PC with integrating sphere attached, slit width 5nm, sampling interval 1nm, and a software regulated scan rate of *very slow*) and the spectra analysed.

The absorption spectra from the control and sample bottles were compared using analysis of variance. If found to be similar, the data sets were then combined and used to find optimal harvesting times. Since invaginated membrane (ICM or VICM) production would be lower in an oxygenated sample it is also possible that the NIR peaks (800-890nm) would have different heights, shapes and/or ratios when comparing control with sample replicate bottles. It is generally understood that RC-LHI conjugate is synthesised first, followed by LHII (for a discussion on early works see Neiderman and Gibson, 1978). Consequently any reduction in photosynthetic growth may result in an RC-LHI enriched absorbance spectrum. The reduced 650nm absorbance and difference in NIR ratios acted as a guide for the deleterious affects of oxygen.

At least two independent growth curves were obtained for each strain that was investigated. Once they were shown not to be significantly different

(using analysis of variance to a confidence limit of 95%, or  $P=0.05$ ), the combined data sets were used to estimate an optimum harvesting time. This was achieved by applying the simple Verhulst-Pearl growth, or logistic model for population growth (Pearl, 1927). This model relies on the following assumptions;

- (i) All organisms (photosynthetic bacteria) have an equal fitness and are identical at any given time.
- (ii) All organisms have the same ability to reproduce and die.
- (iii) The rate of population increase depends upon the number (N) of organisms present at any given time, with the rate of population increase proportional to the degree of habitat (growth medium) saturation. All environmental factors are constant.

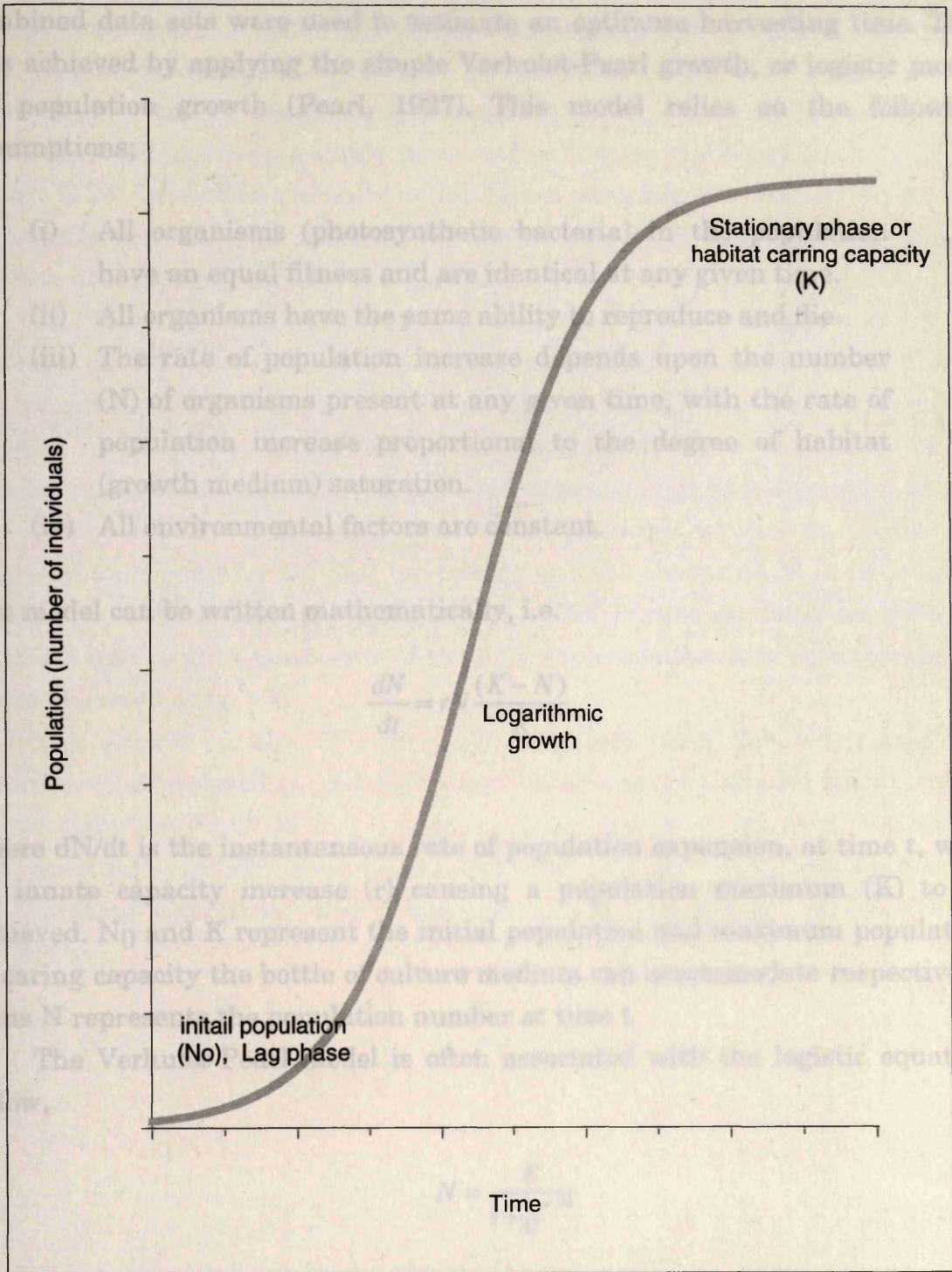


**Figure 3.1:** A logistic population growth curve. The simple logistic Verhulst-Pearl model above was used to predict the optimum harvesting times for the bacterial stains under investigation. The model relies on all environmental factors being constant.

against time, see Figure 3.1. The logistic model was applied to quantify the fitness of the calculated curves using the probability (p) value as a guide.

The following pages illustrate the results of the growth curves for the individual cell lines. Generally the lag-log phase occurs about 24-36 hours after inoculation. The individual species will be discussed separately.

(using analysis of variance to a confidence limit of 95%, or  $P=0.05$ ), the combined data sets were used to estimate an optimum harvesting time. This was achieved by applying the simple Verhulst-Pearl growth, or logistic model for population growth (Pearl, 1927). This model relies on the following assumptions;

- (i) All organisms (photosynthetic bacteria) in the population have an equal fitness and are identical at any given time.
- (ii) All organisms have the same ability to reproduce and die.
- (iii) The rate of population increase depends upon the number ( $N$ ) of organisms present at any given time, with the rate of population increase proportional to the degree of habitat (growth medium) saturation.
- (iv) All environmental factors are constant.

The model can be written mathematically, i.e.

$$\frac{dN}{dt} = rN \frac{(K - N)}{K}$$

where  $dN/dt$  is the instantaneous rate of population expansion, at time  $t$ , with an innate capacity increase ( $r$ ) causing a population maximum ( $K$ ) to be achieved.  $N_0$  and  $K$  represent the initial population and maximum population or carrying capacity the bottle of culture medium can accommodate respectively. Thus  $N$  represents the population number at time  $t$ .

The Verhulst-Pearl model is often associated with the logistic equation below,

$$N = \frac{K}{1 + e^{a-bt}}$$

where  $a$  and  $b$  represent constants associated with the gradient and height of the curve. The model produces a sigmoidal curve when population number is plotted against time, see Figure 3.1. The  $\chi^2$  test was then applied to quantify the fitness of the calculated curves using the probability ( $p$ ) value as a guide.

The following pages illustrate the results of the growth curves for the individual cell lines. Generally the late-log phase occurs about 24-36 hours after inoculation. The individual species will be discussed separately.

### 3.2.1 *R. centenum*:

*R. centenum* is a "core only" producing species. This bacterium was grown at a raised temperature compared to the other species investigated. Its optimum growth rate occurs at approximately 42°C. No significant differences were observed between sample and control bottles (collected at 24hrs). As Figure 3.2A illustrates virtually no lag phase occurs in this bacterium for the time scale studied. Both the RC-LHI (absorbance at 874nm) and cell density (650nm absorbance) increase to a plateau.

The raised 874nm absorbance between 28-36 hours occurred in all ten replicate growth curves, thus it is probably not an artefact. This is similar to the growth pattern found in *R. rubrum* (Figure 3.3A). The stationary phase appears to occur between 32-36hrs after inoculation. The overall curve of cell density (measured at 650nm) versus time appears to have a sigmoidal shape. The Verhulst-Pearl population growth model was applied to locate the optimum time point for RC-LHI harvesting and the constants  $N_0$ ,  $r$ ,  $K$ ,  $a$  and  $b$  ultimately derived (see previous section). The statistical function  $\chi^2$  (Chi squared) was used as a measure of the fit of the modelled data when compared to the observed data.

The growth model (Figure 3.2B) suggests that the Verhulst-Pearl equation (the probability,  $p=0.999$  when using the  $\chi^2$  test) for an averaged initial inoculum  $N_0=0.06$ ,  $t=0$  (i.e. 2% v/v initial inoculum, see section 3.2) has the constants  $r=0.06$ ,  $K=0.66$ ,  $a=4.53$  and  $b=0.27$ . This resulted in a standardised harvesting of *R. centenum* in late-log phase  $22\pm 2$ hrs after inoculation.

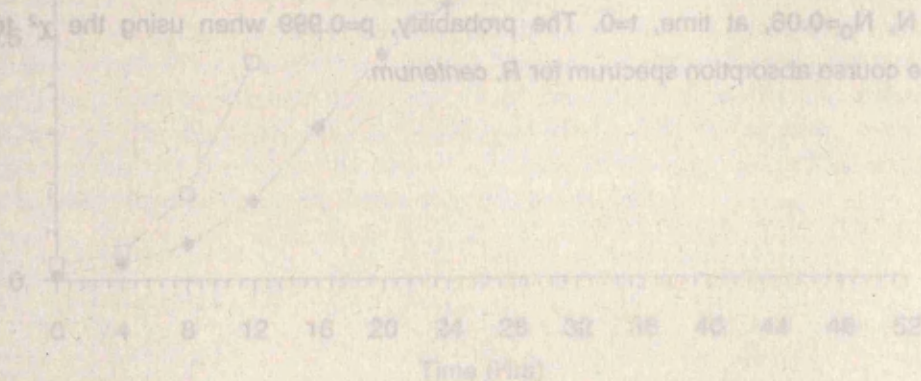


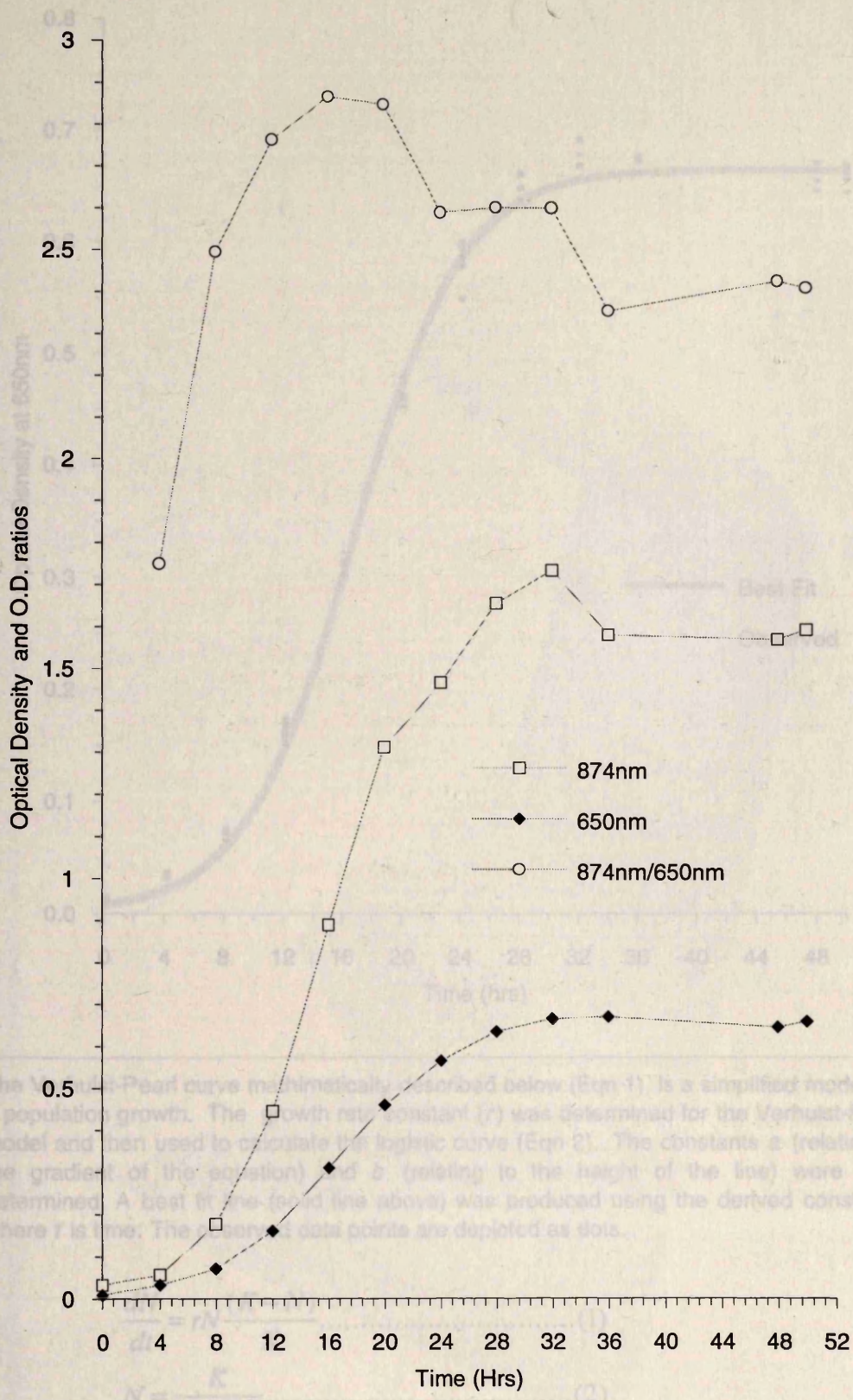
**Figure 3.2:** Growth curve of *Rhodospirillum centenum*. Two independent growth curves were monitored. Samples from control bottles were obtained at 24 hours to investigate the presence of any oxygen trigger due to repeated sample removal. The variances ( $s^2$ ) from each data set were compared to each other and also to their controls. The  $s^2$  between data sets and their controls and between datasets (measured at the cell density, 650nm) are less than 0.001. The data for the growth curves were similar, thus were combined to produce averaged graphs for significant wavelengths. (A): Optical density-time course plot for RC-LHI (874nm) and cell density (650nm). The ratio of RC-LHI:cell density (874nm/650nm) is also shown. The data indicates that cell density reach a plateau within 32-36 hours. The RC-LHI:cell density ratio, as with other species, reaches a maximum value during log phase then drops when the absorbance at 650nm reaches a stationary value. (B): Analysis for cell density (650nm) using the Verhulst-Pearl (logistic) population growth model. The model suggests that for the growth conditions used

$$\frac{dN}{dt} = 0.06N \frac{(0.66 - N)}{0.66}$$

$$N = \frac{K}{1 + e^{4.53 - 0.27t}}$$

where initial  $N$ ,  $N_0=0.06$ , at time,  $t=0$ . The probability,  $p=0.999$  when using the  $\chi^2$  test. (C): Averaged time course absorption spectrum for *R. centenum*.

(A): Optical Density-Time Course Plot for RC-LHI (874nm) and Cell Density (650nm).



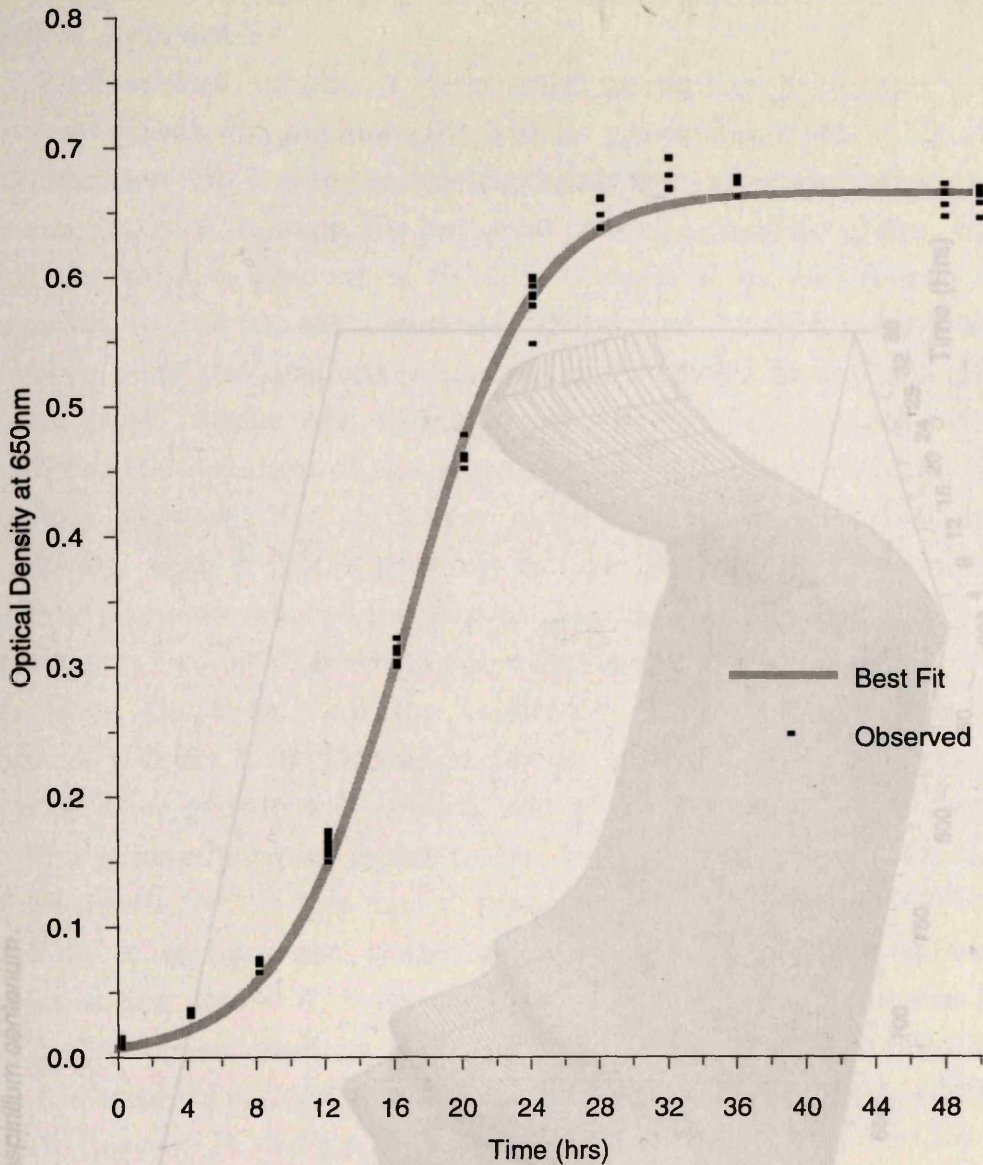
The Verhulst-Pearl curve mathematically described below (Eqn-1) is a simplified model for a population growth. The growth rate constant ( $r$ ) was determined for the Verhulst-Pearl model and then used to calculate the logistic curve (Eqn-2). The constants  $a$  (relating to the gradient of the equation) and  $b$  (relating to the height of the line) were then determined. A best fit curve (solid line above) was produced using the derived constants where  $t$  is time. The observed data points are depicted as dots.

$$N = \frac{K}{1 + e^{-rt}} \quad (1)$$

$$N = \frac{K}{1 + e^{-a(t-b)}} \quad (2)$$

The constants were calculated to be  $N_0 = 0.07$   
 $r = 0.07$   
 $K = 0.66$   
 $a = 4.53$   
 $b = 0.27$

(B): Analysis of Cell Density: Verhulst-Pearl Curve.



The Verhulst-Pearl curve mathematically described below (Eqn 1) is a simplified model for a population growth. The growth rate constant ( $r$ ) was determined for the Verhulst-Pearl model and then used to calculate the logistic curve (Eqn 2). The constants  $a$  (relating to the gradient of the equation) and  $b$  (relating to the height of the line) were then determined. A best fit line (solid line above) was produced using the derived constants where  $t$  is time. The observed data points are depicted as dots.

$$\frac{dN}{dt} = rN \frac{(K - N)}{K} \dots\dots\dots(1)$$

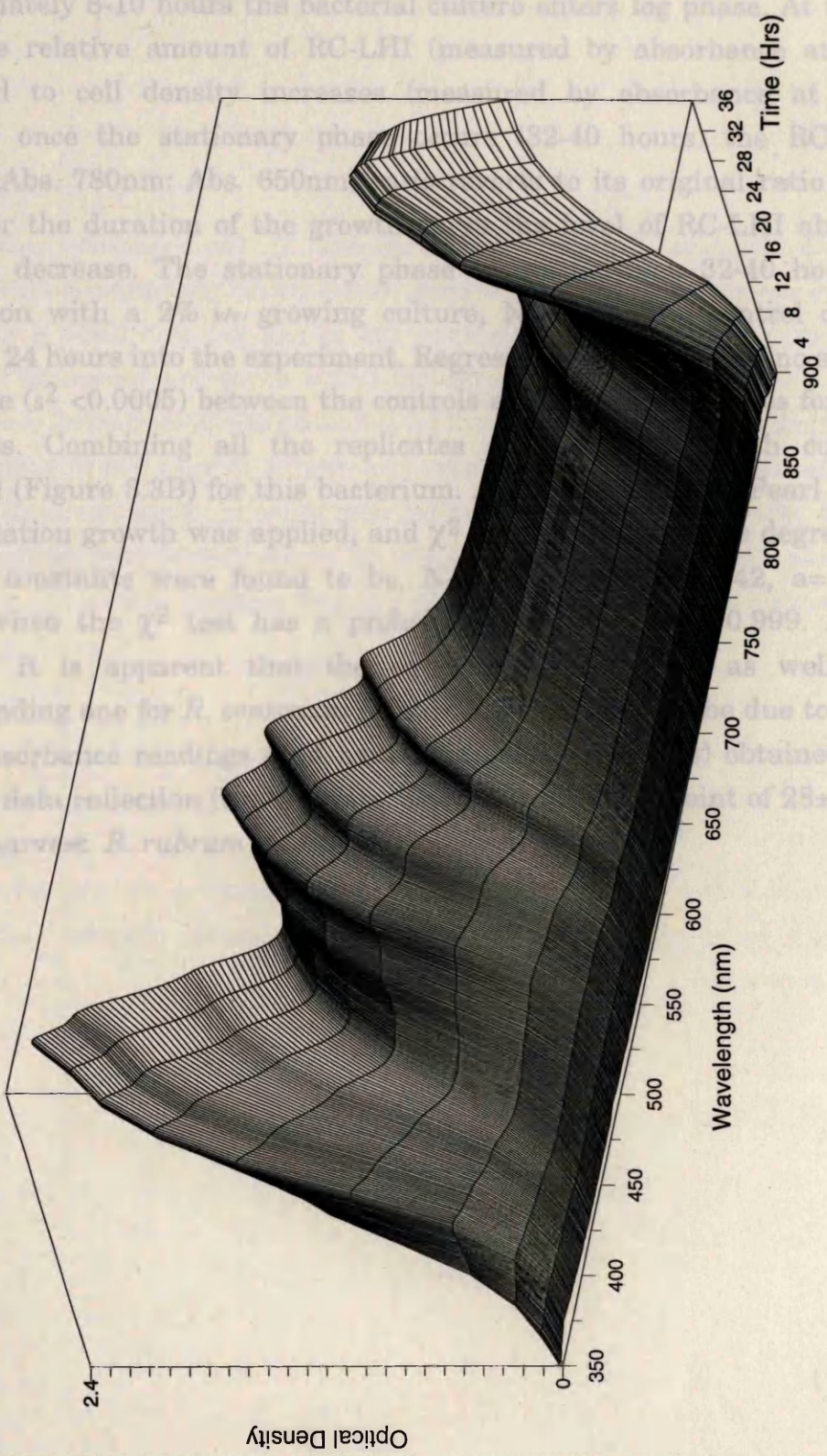
$$N = \frac{K}{1 + e^{-at}} \dots\dots\dots(2)$$

The constants were calculated to be  
 $N_0 = 0.07$   
 $r = 0.07$   
 $K = 0.66$   
 $a = 4.53$   
 $b = 0.27$

3.2.2 *R. rubrum* S1

This species is also a "novel" producing bacterium. Unlike the previous species, *R. centronum*, this species grows vigorously at 28±2°C. Figure 3A suggests that (using the combined data only) after and initial lag phase of approximately 8-10 hours the bacterial culture enters log phase. At this time point the relative amount of RC-LHI (measured by absorbance at 880nm) compared to cell density increases (measured by absorbance at 650nm) however once the stationary phase is reached (32-40 hours) RC-LHI/cell density (Abs: 780nm: Abs: 650nm) returns to its original ratio of about 0.5:1. For the duration of the growth phase the ratio of RC-LHI/absorbance does not decrease. The stationary phase was reached 32 hours after inoculation with a 7% w/v growing culture, and the data was collected 24 hours into the experiment. Regression analysis showed no difference ( $s^2 < 0.0005$ ) between the controls and the experimental data sets. Combining all the replicates and a linear regression was induced (Figure 3B) for this bacterium. The population growth was applied, and  $\chi^2$  analysis was used. The constants were found to be,  $a = 0.0001$  and  $b = 0.24$  where the  $\chi^2$  test has a probability of 0.999. Although the  $\chi^2$  test has a probability of 0.999, it is apparent that the data is not following the model for *R. rubrum* as well as the data obtained for the other species. The lag phase of 28±1 hr was observed for the growth of *R. rubrum*.

(C): Averaged Time Course Absorption Spectrum for *Rhodospirillum centronum*.



### 3.2.2 *R. rubrum* S1

This species is also a "core only" producing bacterium. Unlike the previous species, *R. centenum*, this species grows vigorously at  $28 \pm 2^\circ\text{C}$ . Figure 3.3A suggests that (using the combined data sets) after an initial lag phase of approximately 8-10 hours the bacterial culture enters log phase. At this time point the relative amount of RC-LHI (measured by absorbance at 880nm) compared to cell density increases (measured by absorbance at 650nm). However once the stationary phase occurs (32-40 hours) the RC-LHI:cell density (Abs. 780nm: Abs. 650nm) ratio reverts to its original ratio of about 1.5:1. For the duration of the growth curve the level of RC-LHI absorbance does not decrease. The stationary phase occurs between 32-40 hours after inoculation with a 2% v/v growing culture,  $N_0=0.03$ . The control data was collected 24 hours into the experiment. Regression analysis found no statistical difference ( $s^2 < 0.0005$ ) between the controls and replicate samples for the two data sets. Combining all the replicates an averaged growth curve was produced (Figure 3.3B) for this bacterium. Again the Verhulst-Pearl equation for population growth was applied, and  $\chi^2$  used to measure the degree of best fit. The constants were found to be,  $N_0=0.03$ ,  $r=0.06$ ,  $k=0.42$ ,  $a=4.96$  and  $b=0.23$  when the  $\chi^2$  test has a probability value,  $p$ , of  $p=0.999$ . Although  $p=0.999$ , it is apparent that the equation does not fit as well as the corresponding one for *R. centenum* (Figure 3.2B). This may be due to the very small absorbance readings (and hence inaccurate readings) obtained for the first few data collection (time) points. The arbitrary time point of  $28 \pm 1$  hr was used to harvest *R. rubrum* strain S1.

This species is also a "core only" producing bacterium. Unlike the previous species, *R. centenum*, this species grows vigorously at 28±2°C. Figure 3.3A suggests that (using the combined data sets) after an initial lag phase of approximately 8-10 hours the bacterial culture enters log phase. At this time point the relative amount of RC-LHI (measured by absorbance at 880nm) compared to cell density increases (measured by absorbance at 650nm). However once the stationary phase occurs (32-40 hours) the RC-LHI:cell density (Abs. 780nm: Abs. 650nm) ratio reverts to its original ratio of about 1.5:1. For the duration of the growth curve the level of RC-LHI absorbance

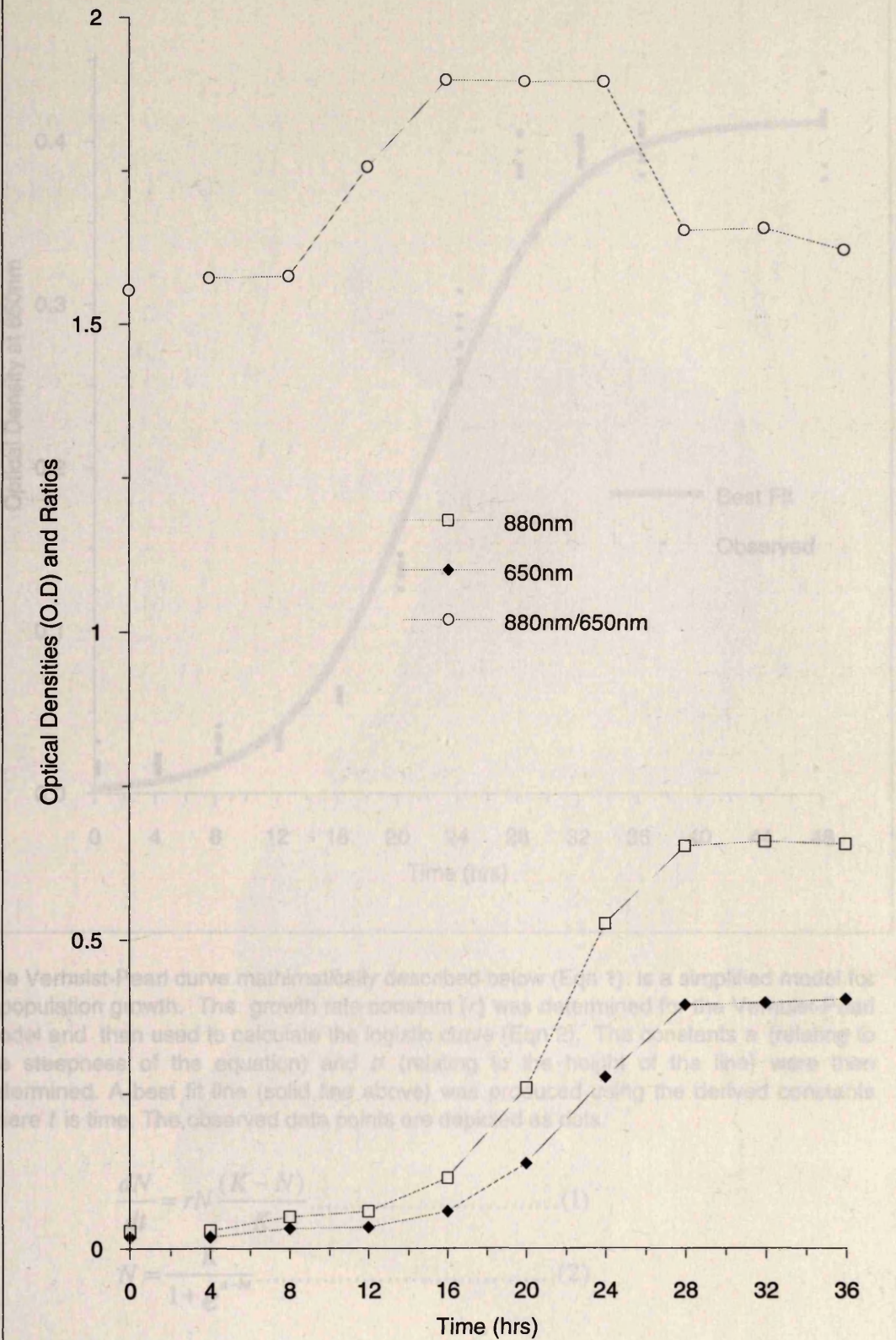
**Figure 3.3:** Growth curve of *Rhodospirillum rubrum* strain S1. Two independent growth curves, each with five replicate bottles and a control bottle, were monitored when grown anaerobically in the light at 28±2°C. Analysis of variance indicates that  $s^2$  was less than 0.004 at 650nm and absorbance differences were not significant. (A): Optical density-time course plot for RC-LHI (874nm) and cell density (650nm). The ratio of RC-LHI:cell density (874nm/650nm) is also shown. The data indicates that cell density reaches a plateau within 32-40 hours. The RC-LHI:cell density ratio, as with other species, reaches a maximum value during log phase then drops when cell density reaches a stationary value. (B): Analysis for cell density (650nm) using the Verhulst-Pearl (logistic) population growth model indicates that for the growth conditions used

$$\frac{dN}{dt} = 0.03N \frac{(0.42 - N)}{0.42}$$

$$N = \frac{K}{1 + e^{4.96 - 0.22t}}$$

where initial  $N$ ,  $N_0=0.06$ , at time,  $t=0$ . The probability of the observed vs. the expected values was  $p=0.999$  when the  $\chi^2$  was applied. (C): Averaged time course absorption spectrum for *Rhodospirillum rubrum*.

(A): Optical Density-Time Course Plot for RC-LHI (880nm) and Cell Density (650nm).

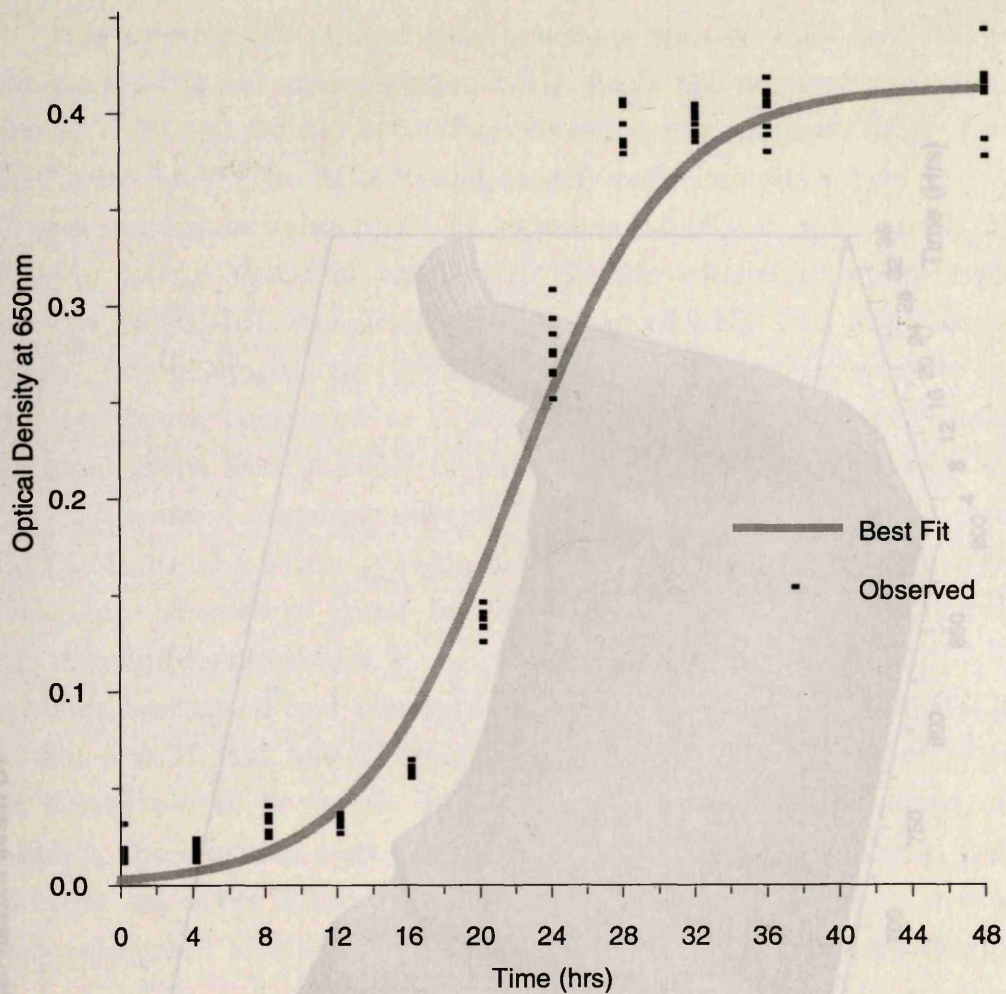


The Verhulst-like curve mathematically described below (Eqn 1) is a simplified model for a population growth. The growth rate constant ( $r$ ) was determined from the observed data and then used to calculate the logistic curve (Eqn 2). The constants  $a$  (relating to the steepness of the equation) and  $K$  (relating to the height of the line) were then determined. A best fit line (solid line above) was produced using the derived constants where  $t$  is time. The observed data points are depicted as dots.

$$\frac{dN}{dt} = rN \left( \frac{K-N}{K} \right) \quad (1)$$

The constants were calculated to be Nos: 0.03  
 $r = 0.06$   
 $K = 0.42$   
 $a = 4.96$   
 $b = 0.23$

(B): Analysis of Cell Density: Verhulst-Pearl Curve.



The Verhulst-Pearl curve mathematically described below (Eqn 1) is a simplified model for a population growth. The growth rate constant ( $r$ ) was determined for the Verhulst-Pearl model and then used to calculate the logistic curve (Eqn 2). The constants  $a$  (relating to the steepness of the equation) and  $b$  (relating to the height of the line) were then determined. A best fit line (solid line above) was produced using the derived constants where  $t$  is time. The observed data points are depicted as dots.

$$\frac{dN}{dt} = rN \frac{(K-N)}{K} \dots\dots\dots(1)$$

$$N = \frac{K}{1 + e^{a-bt}} \dots\dots\dots(2)$$

The constants were calculated to be  $N_0 = 0.03$

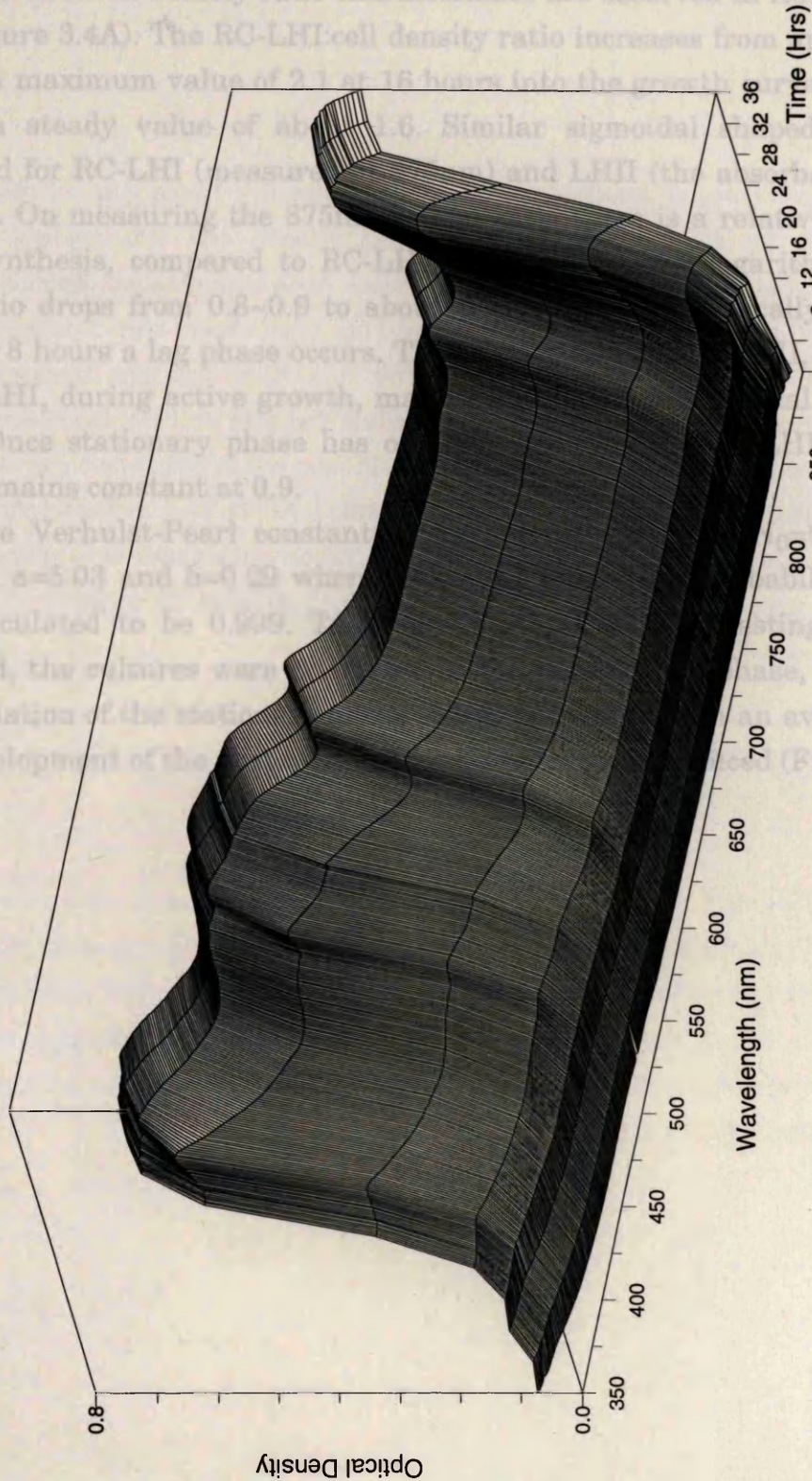
- $r = 0.06$
- $K = 0.42$
- $a = 4.96$
- $b = 0.23$

3.2.3 *Rb. sphaeroides* GA

This strain of *Rb. sphaeroides* produces both RC-LHI and the peripheral light-harvesting antenna complex, LHII. As in the previous two examples the same RC-LHI:cell density ratio characteristics are observed in *Rb. sphaeroides* GA (Figure 3.4A). The RC-LHI:cell density ratio increases from approximately 1.0, to a maximum value of 2.1 at 16 hours into the growth cycle, then levels off to a steady value of about 1.6. Similar sigmoidal plots were observed for RC-LHI (measured at 875 nm) and LHII (the absorbance peak at 699 nm). On measuring the 875 nm absorbance, the ratio increases from 0.8-0.9 to about 1.6. The ratio drops from 0.8-0.9 to about 0.4. Prior to 8 hours a lag phase occurs. The RC-LHI, during active growth, increases. LHII. Once stationary phase has been reached, the ratio remains constant at 0.9.

The Verhulst-Pearl constant  $K$  is calculated to be 0.02,  $r=0.99$ ,  $a=5.03$  and  $b=0.29$  which are calculated to be 0.029. The sigmoidal curves were observed, the squares were plotted against the logarithm of the time of development of the RC-LHI (Figure 3.4C).

(C): Averaged Time Course Absorption Spectrum for *Rhodospirillum rubrum* strain S1



### 3.2.3 *Rb. sphaeroides* GA

This strain of *Rb. sphaeroides* produces both RC-LHI and the peripheral light-harvesting antenna complex, LHII. As in the previous two examples the same RC-LHI:cell density ratio characteristics are observed in *Rb. sphaeroides* GA (Figure 3.4A). The RC-LHI:cell density ratio increases from approximately 1.0, to a maximum value of 2.1 at 16 hours into the growth curve, then levels off to a steady value of about 1.6. Similar sigmoidal shaped plots were observed for RC-LHI (measured at 875nm) and LHII (the absorbance peak at 849nm). On measuring the 875nm/849nm ratio there is a relative increase of LHII synthesis, compared to RC-LHI synthesis, during logarithmic growth. The ratio drops from 0.8-0.9 to about 0.7, which is statistically significant. Prior to 8 hours a lag phase occurs. The relative increase of LHII, with respect to RC-LHI, during active growth, may be due to the preferential synthesis of LHII. Once stationary phase has occurred however the RC-LHI:cell density ratio remains constant at 0.9.

The Verhulst-Pearl constants were determined to be  $N_0=0.02$ ,  $r=0.05$ ,  $K=0.34$ ,  $a=5.03$  and  $b=0.29$  where Using the  $\chi^2$  test the probability value,  $p$ , was calculated to be 0.999. To ensure the optimum harvesting of RC-LHI occurred, the cultures were harvested at the mid-late log phase, just prior to the initiation of the stationary phase ( $24\pm 2$ hrs). Once again an average plot of the development of the absorption characteristics was produced (Figure 3.4C).

This strain of *Rb. sphaeroides* produces both RC-LHI and the peripheral light-harvesting antenna complex, LHII. As in the previous two examples the same RC-LHI:cell density ratio characteristics are observed in *Rb. sphaeroides* GA (Figure 3.4A). The RC-LHI:cell density ratio increases from approximately 1.0, to a maximum value of 2.1 at 16 hours into the growth curve, then levels off to a steady value of about 1.0. Similar sigmoidal shaped plots were

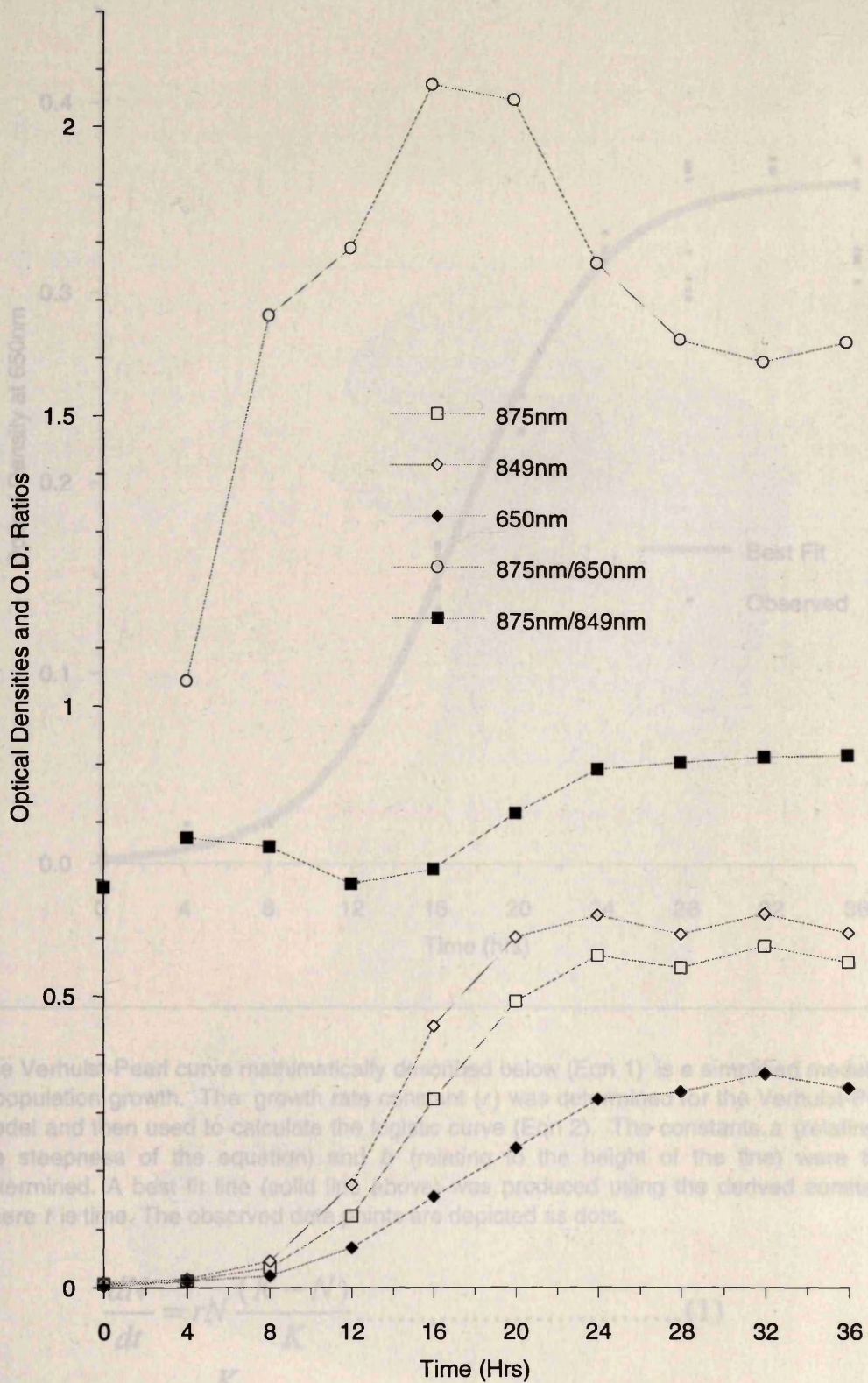
**Figure 3.4:** Growth curve of *Rhodobacter sphaeroides* strain GA. Figure 3.4A indicates similar sigmoidal curves for cell density (650nm), RC-LHI (875nm) and LHII (849nm) temporal absorbencies after being checked for any oxygen triggers. None were detected. It also shows that an increase in RC-LHI:cell density ratio occurs (12-20 hrs, open circles) after a decrease in RC-LHI:LHII ratio (875nm:849nm, solid black squares). The RC-LHI:LHII ratio then increases from 0.7 to the constant value of 0.9. These spectra may indicate that after an initial lag phase of about  $6 \pm 1$  hrs RC-LHI is preferentially produced (RC-LHI:LHII ratio = 0.9) but as soon as the culture density increases beyond the initial level ( $N_0=0.022$ ) LHII is then preferentially reduced (RC-LHI:LHII ratio  $\geq 0.7 \leq 0.9$ ). Eventually the relative production and turnover of RC-LHI compared to LHII reaches a steady value. Applying the Verhulst-Pearl equation the constants below were determined (Figure 3.4B),

$$\frac{dN}{dt} = 0.05N \frac{(0.34 - N)}{0.34}$$

$$N = \frac{K}{1 + e^{5.02 - 0.29t}}$$

where initial  $N$ ,  $N_0=0.022$ , at time,  $t=0$ . Using the  $\chi^2$  test the probability value was calculated to be,  $p=0.999$ . From the results obtain for the growth curves standardised harvesting of *Rb. sphaeroides* strain GA occurred 24 hrs after inoculation. (C): Averaged time course absorption spectrum for *Rb. sphaeroides* strain GA. As before and averaged time course absorption spectrum was produced. Absorption blips occur at approximately 530nm and 360nm, these were caused by hard/software errors in the Shimadzu spectrophotometer.

(A): Optical Density-Time Course plot for RC-LHI (875nm) and Cell Density (650nm).

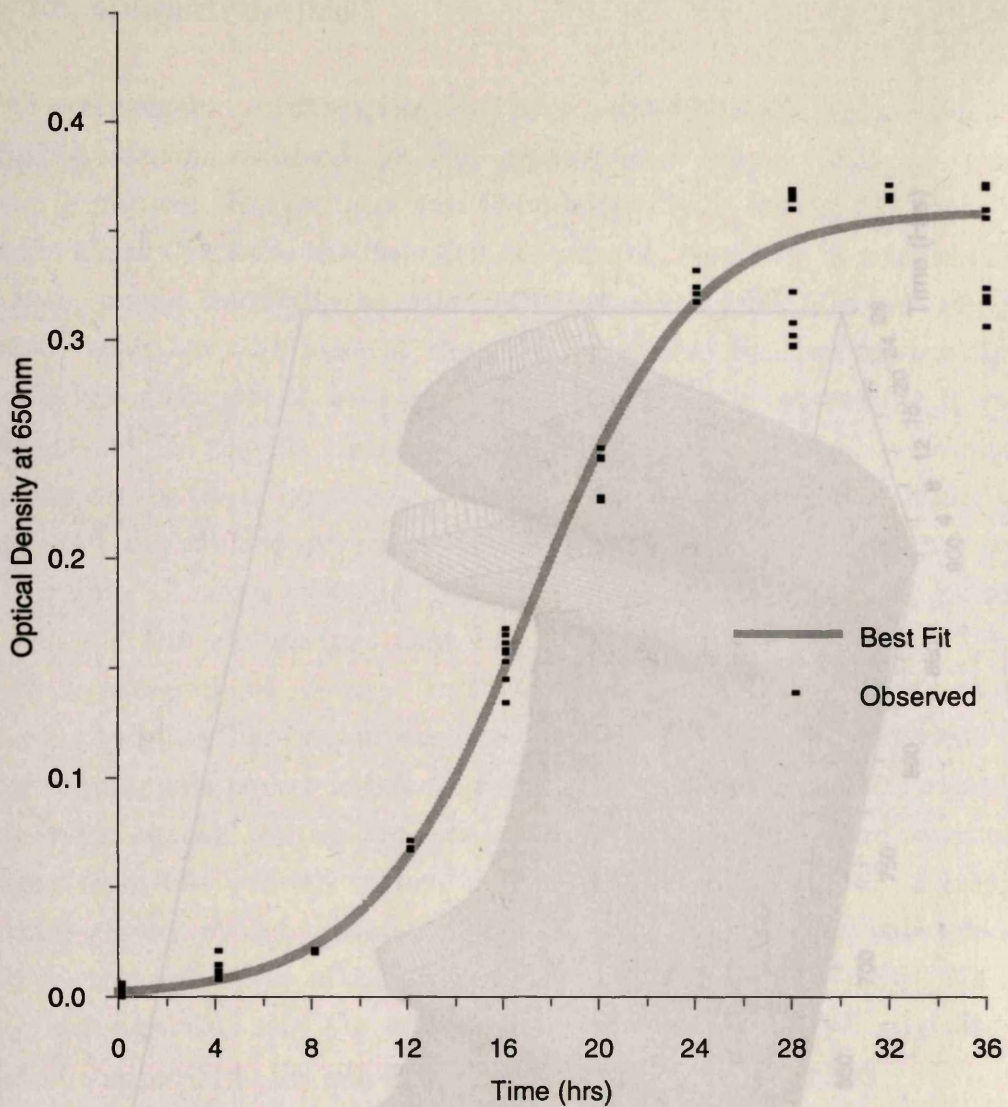


The Verhulst-Pearl curve mathematically described below (Eqn 1) is a sigmoidal model for population growth. The growth rate parameter ( $\gamma$ ) was determined for the Verhulst-Pearl model and then used to calculate the logistic curve (Eqn 2). The constants  $a$  (relating to the steepness of the equation) and  $b$  (relating to the height of the first wave that determined a best fit line (solid line) above) was produced using the derived constants where  $t$  is time. The observed data points are depicted as dots.

$$N = \frac{K}{1 + e^{-a(t-b)}} \quad (1)$$

The constants were calculated to be  $N_0 = 0.05$   
 $a = 0.09$   
 $K = 0.34$   
 $b = 5.03$   
 $\gamma = 0.25$

(B): Analysis of Cell Density: Verhulst-Pearl Curve.



The Verhulst-Pearl curve mathematically described below (Eqn 1) is a simplified model for a population growth. The growth rate constant ( $r$ ) was determined for the Verhulst-Pearl model and then used to calculate the logistic curve (Eqn 2). The constants  $a$  (relating to the steepness of the equation) and  $b$  (relating to the height of the line) were then determined. A best fit line (solid line above) was produced using the derived constants where  $t$  is time. The observed data points are depicted as dots.

$$\frac{dN}{dt} = rN \frac{(K - N)}{K} \dots\dots\dots(1)$$

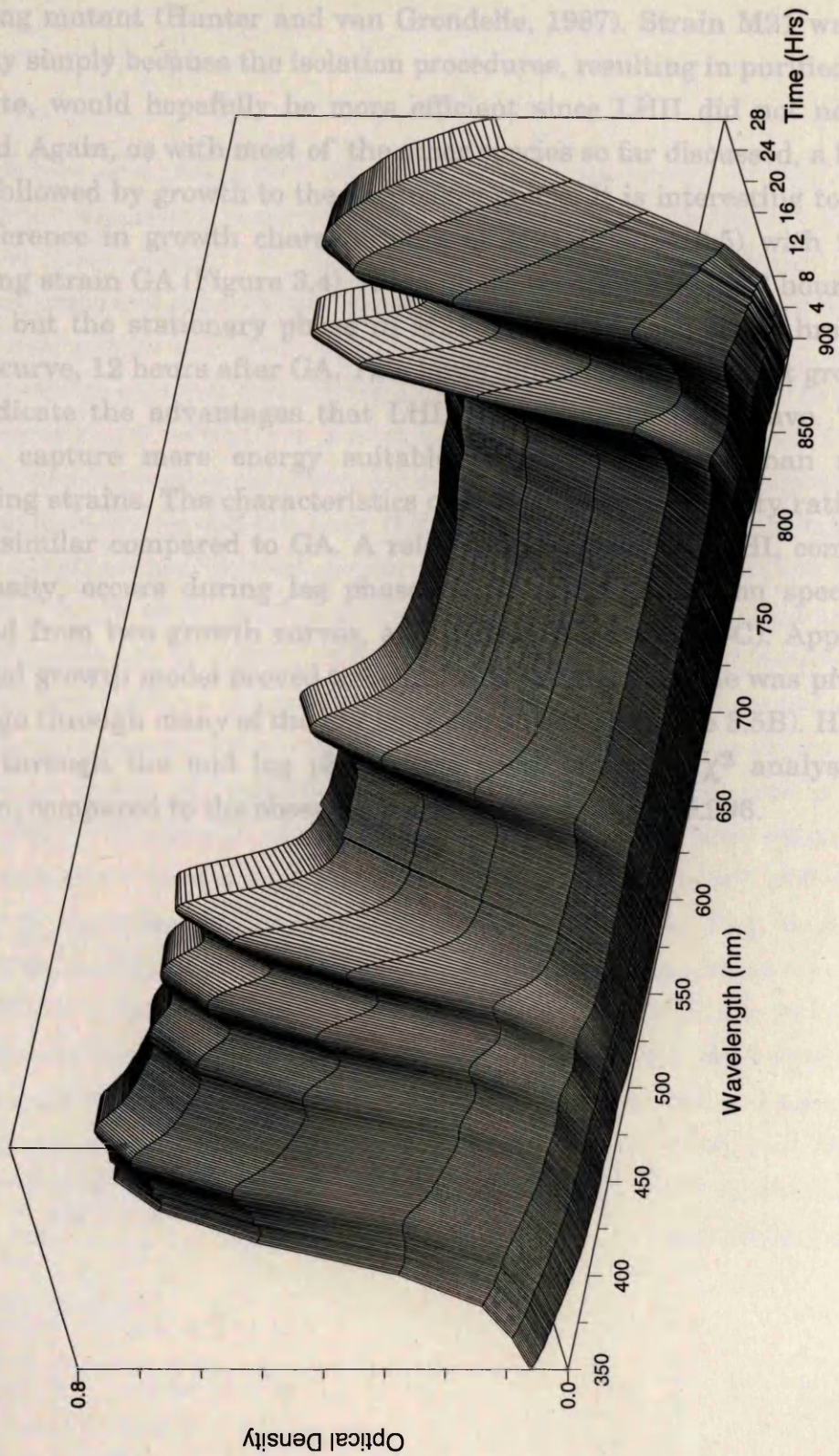
$$N = \frac{K}{1 + e^{a-bt}} \dots\dots\dots(2)$$

The constants were calculated to be  
 $N_0 = 0.02$   
 $r = 0.05$   
 $K = 0.34$   
 $a = 5.03$   
 $b = 0.29$

3.4 *Rh. sphaeroides* M21

The mutagen *n*-nitrosoguanidine was applied to *Rh. sphaeroides* strain CIB8253 which resulted in *Rh. sphaeroides* strain M21, a non-LHI reducing mutant (Hunter and van Grondelle, 1987). Strain M21 was chosen for study simply because the isolation procedure, resulting in purified RC-LHI conjugate, would hopefully be more efficient since LHI did not need to be removed. Again, as with most of the studies so far discussed, a lag phase occurs followed by growth to the stationary phase. It is interesting to compare the difference in growth characteristics between the LHI producing strain GA (Figure 3.4) and the non-LHI producing strain M21. The growth curves for both strains are shown in Figure 3.4. The growth curve for strain M21 is very similar to that of strain GA, but the stationary phase is reached at a lower growth rate, 12 hours after GA. The growth curves indicate the advantages that LHI provides to the cells. They are able to capture more energy suitable for growth than non-LHI producing strains. The characteristics of the growth curves are very similar compared to GA. A reduction in growth rate, or density, occurs during lag phase. This is evident from the growth curves. The growth curves for strain M21 go through many of the same phases as strain GA. The lag phase is followed by a rapid increase in growth rate, reaching the stationary phase, compared to the non-LHI producing strain.

(c): Averaged Time Course Absorption Spectrum of *Rhodobacter sphaeroides* strain GA.



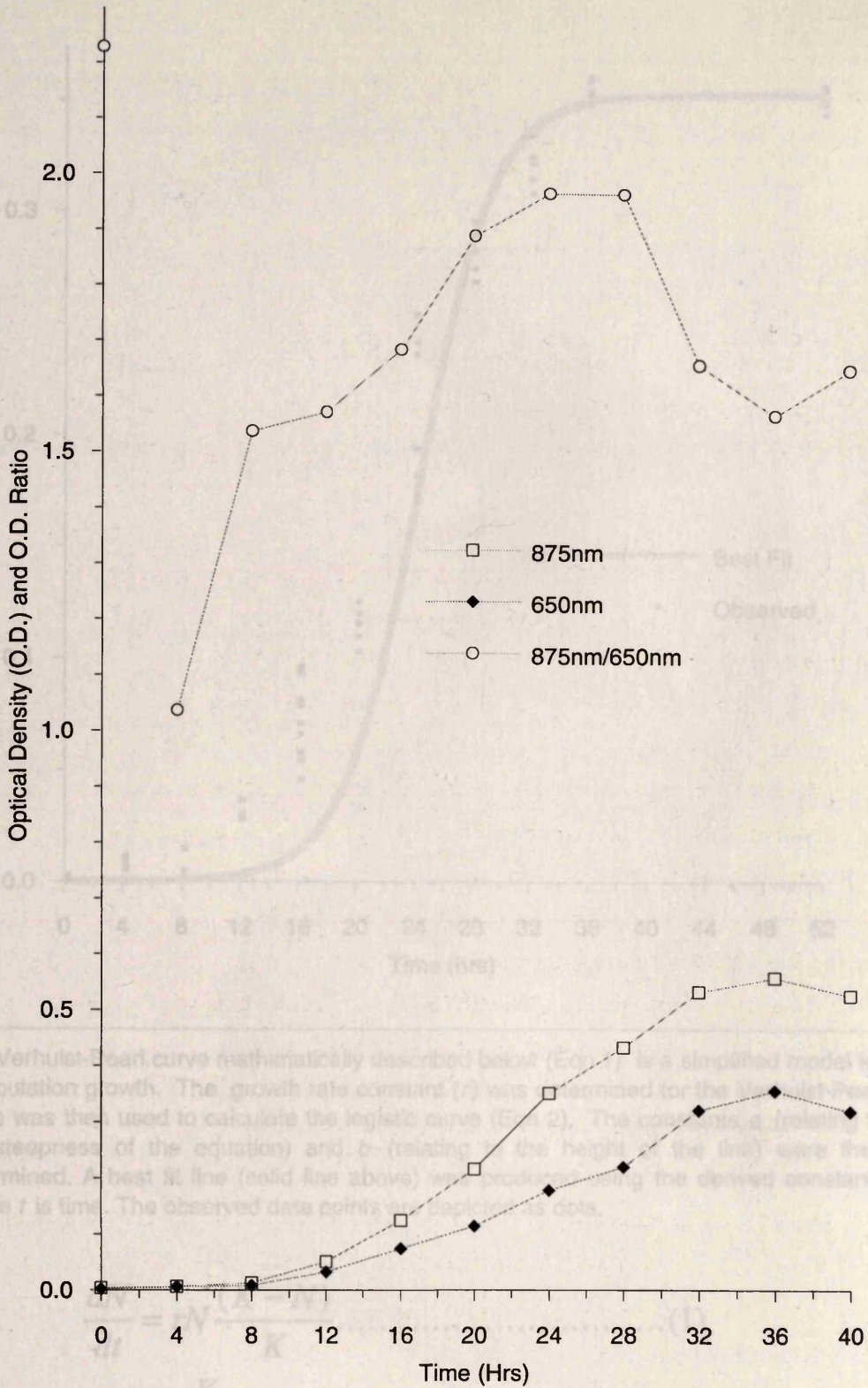
### 3.2.4 *Rb. sphaeroides* M21

The mutagen n-nitrosoguanidine was applied to *Rb. sphaeroides* strain NCIB8253 which resulted in *Rb. sphaeroides* strain M21, a non-LHII producing mutant (Hunter and van Grondelle, 1987). Strain M21 was chosen for study simply because the isolation procedures, resulting in purified RC-LHI conjugate, would hopefully be more efficient since LHII did not need to be removed. Again, as with most of the other species so far discussed, a lag phase occurs followed by growth to the stationary phase. It is interesting to compare the difference in growth characteristics of M21 (Figure 3.5) with the LHII producing strain GA (Figure 3.4). A lag phase occurs for about 8 hours in both strains, but the stationary phase in M21 occurs between 32-63 hrs into the growth curve, 12 hours after GA. This large difference in apparent growth rate may indicate the advantages that LHII containing bacteria have. They are able to capture more energy suitable for photosynthesis than non-LHII containing strains. The characteristics of the RC-LHI:cell density ratio in M21 is very similar compared to GA. A relative increase in RC-LHI, compared to cell density, occurs during log phase. Once again absorption spectra were averaged from two growth curves, and plotted (Figure 3.5A-C). Applying the sigmoidal growth model proved to be difficult. Although a line was produced it did not go through many of the low time point values (Figure 3.5B). However it passed through the mid log phase time point onwards.  $\chi^2$  analysis of the equation, compared to the observed data indicated that  $p=0.996$ .

The mutagen *n*-nitrosoguanidine was applied to *Rb. sphaeroides* strain NCIB8253 which resulted in *Rb. sphaeroides* strain M21, a non-LHI producing mutant (Hunter and van Grondelle, 1987). Strain M21 was chosen for study simply because the isolation procedure, resulting in purified RC-LHI conjugate, would hopefully be more efficient since LHI did not need to be removed. As with most of the other species we have discussed, a lag phase

**Figure 3.5:** Growth of *Rhodobacter sphaeroides* strain M21. Two growth curves were determined independently, each with controls. The control bottles were monitored at 28hrs after inoculation and compared to the data collected at 28 hours from the growth curve replicates. 28hrs was chosen because initial trials indicated that mid-late log phase was reached at this time point. The controls were used to indicate the presence of any oxygen trigger mechanism resulting from repeated sample removal from the replicate bottles. As in the previous growth curves the variance from each data set was compared to the variances from their controls, and found not to be dissimilar. The  $s^2$  between controls and data sets measured at the cell density measurement (650nm) is less than 0.0004, while  $s^2$  between data sets is less than 0.0001. Since both data sets are statistically similar at 28hrs (the time point at late log phase), the raw data was combined and used to plot averaged graphs for significant wavelengths. (A): Optical Density-Time course plot for RC-LHI (875nm) and cell density (650nm). The ratio of RC-LHI:cell density (875nm/650nm) is also plotted. The graph indicates that both the RC-LHI abundance and cell density levels out. The RC-LHI:cell density ratio although not smooth increases then also levels out. This indicates that there is a carrying capacity, with respect to membrane abundance, for RC-LHI in this bacterium. (B): Analysis for cell density (650nm), using the Verhulst-Pearl model produced the constants of;  $N_0=0.002$ ,  $r=0.054$ ,  $K=0.359$ ,  $a=9.40$  and  $b=0.38$ . The  $\chi^2$  was used and the probability value,  $p$ , found to be  $p=0.996$ . However it is clear from figure 3.5B the equation does not go throughout the data points at  $t \leq 20$  hrs. Consequently the equation must be wrong. This implies that the simple sigmoidal model must be in error. However the equation was used to determine where the optimum harvesting of RC-LHI would occur. Since the line does pass through the data points from mid-log phase onwards for this region the equation holds true. The harvesting of *Rb. sphaeroides* M21 was standardised at  $28 \pm 2$ hrs after inoculation. An averaged absorption spectrum was plotted (figure 3.5C) as before. Absorption blips occur at approximately 530nm and 360nm, these were caused by hard/software errors in the Shimadzu spectrophotometer.

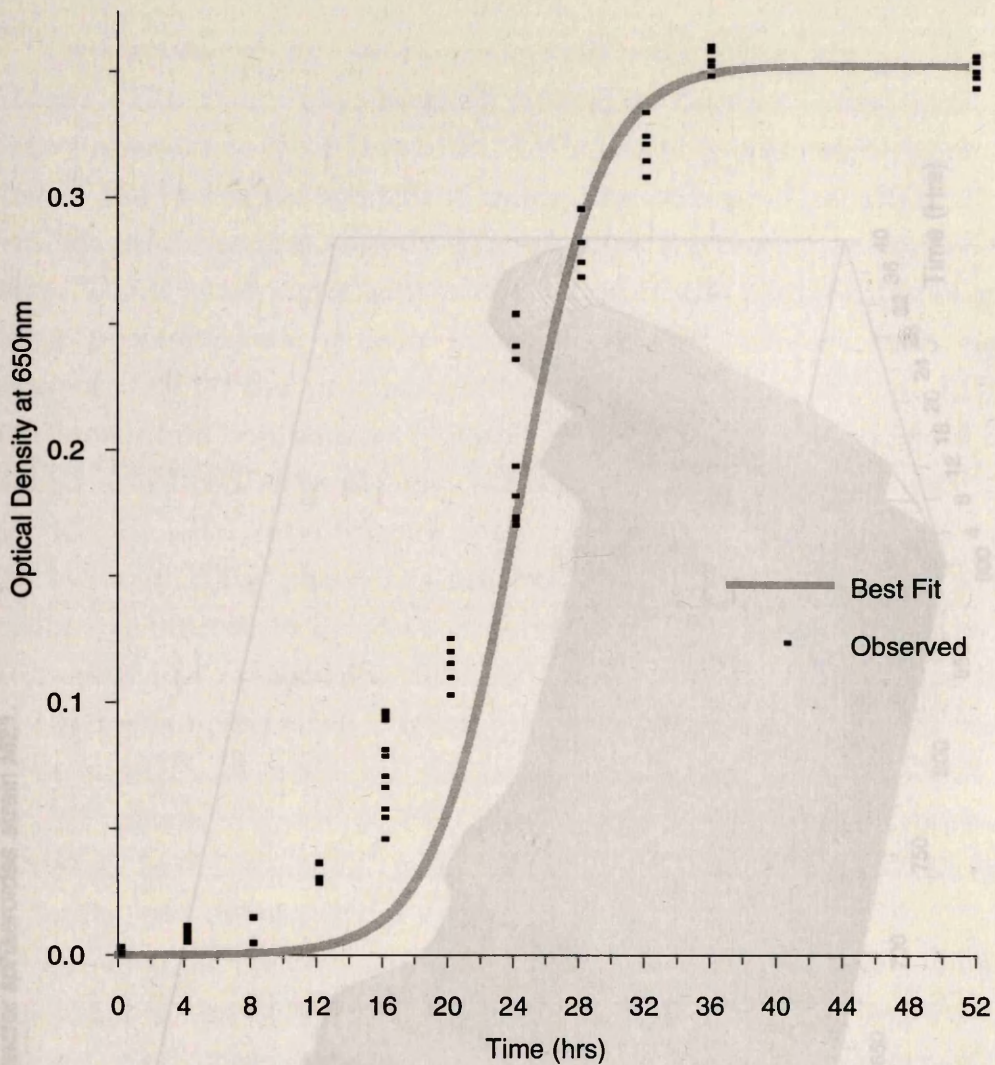
(A): Optical Density-Time course plot for RC-LHI (875nm) and Cell Density (650nm).



$$N = \frac{K}{1 + e^{-at}} \quad (2)$$

The constants were calculated to be  $N_0 = 0.00$   
 $r = 0.05$   
 $K = 0.56$   
 $a = 2.40$   
 $b = 0.39$

(B): Analysis of Cell Density: Verhulst-Pearl Curve.



The Verhulst-Pearl curve mathematically described below (Eqn 1) is a simplified model for a population growth. The growth rate constant ( $r$ ) was determined for the Verhulst-Pearl curve was then used to calculate the logistic curve (Eqn 2). The constants  $a$  (relating to the steepness of the equation) and  $b$  (relating to the height of the line) were then determined. A best fit line (solid line above) was produced using the derived constants where  $t$  is time. The observed data points are depicted as dots.

$$\frac{dN}{dt} = rN \frac{(K - N)}{K} \dots\dots\dots (1)$$

$$N = \frac{K}{1 + e^{a-bt}} \dots\dots\dots (2)$$

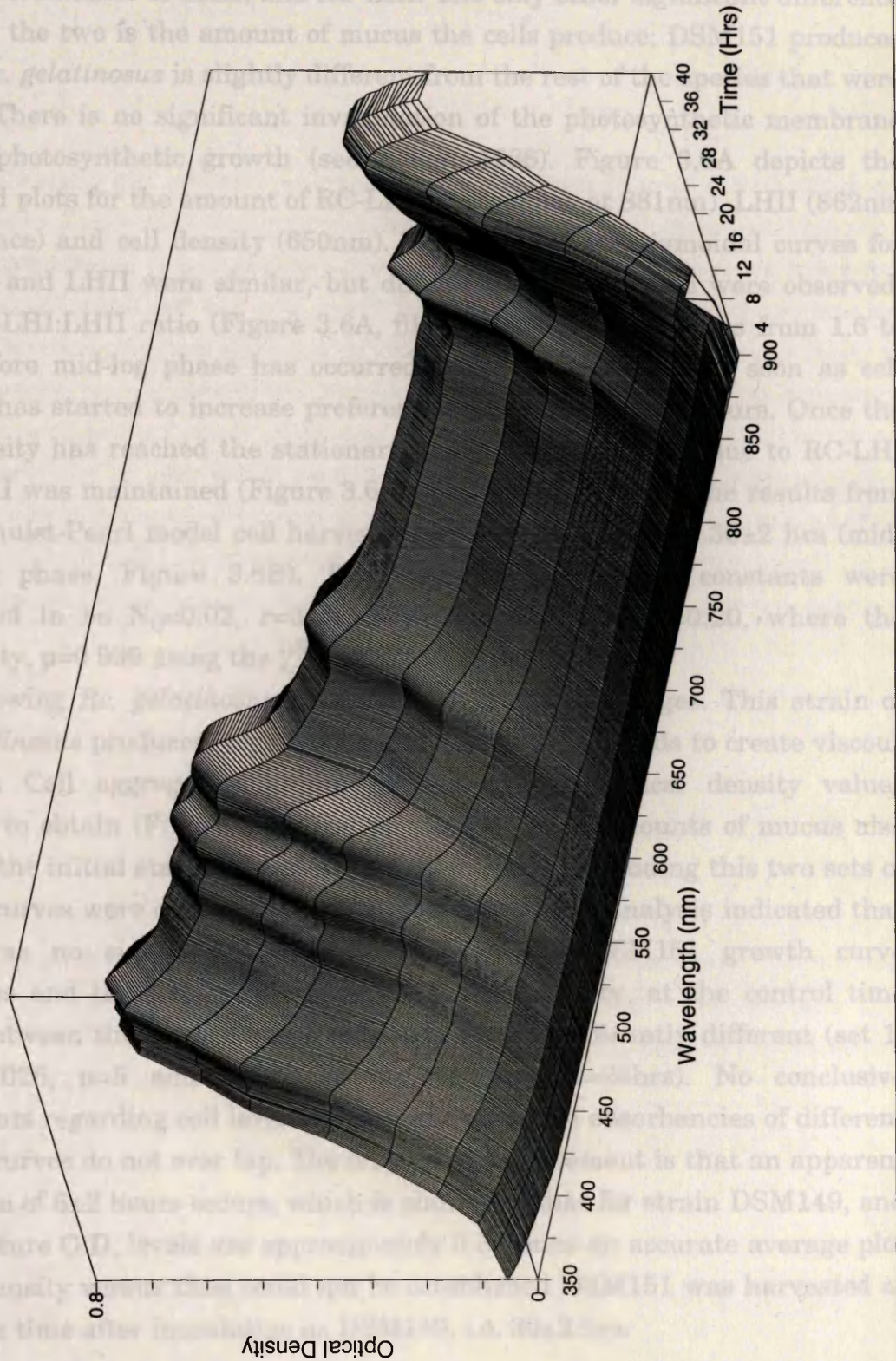
The constants were calculated to be  
 $N_0 = 0.00$   
 $r = 0.05$   
 $K = 0.36$   
 $a = 9.40$   
 $b = 0.39$

3.2.5 *Re. gelatinosus* DSM149 and DSM151:

Two strains of *Re. gelatinosus* were chosen for study, DSM149 and DSM151. The main physiological difference between these strains is the relative abundance of LHII, and RC-LHI. The only other significant difference between the two is the amount of mucus the cells produce: DSM151 produces more. *Re. gelatinosus* is a highly anaerobic bacterium that grows in the dark. There is no significant investment in the photosynthetic apparatus during photosynthetic growth (see Figure 3.5B). Figure 3.6C depicts the averaged plots for the amount of RC-LHI (862nm absorbance) and cell density (650nm).

RC-LHI and LHII were similar, but cell density was lower. The RC-LHI:LHII ratio (Figure 3.6A, Figure 3.6B) was 1.6 before mid-log phase has occurred. Once cell density has started to increase preferentially, RC-LHI was maintained (Figure 3.6C). The results from the Michaelis-Menten model cell harvest constants were calculated to be  $N_p=0.02$ ,  $r=0.99$ , where the probability,  $p=0.99$  using the  $\chi^2$  test. Growing *Re. gelatinosus* produces a viscous mucus that creates a high density value. The amount of mucus this strain produces is indicated that the growth curve is different (set 1) than the control time. No conclusive differences of different frequencies of different growth curves do not overlap. The apparent is that an apparent phase of 5.2 hours occurs, which is similar to the strain DSM149, and culture CO<sub>2</sub> levels are approximately 0.1. An accurate average plot of cell density after incubation of DSM149, LA, Wis2000

(C): Averaged Time Course Absorption Spectrum for *Rhodobacter sphaeroides* strain M21.



### 3.2.5 *Rc. gelatinosus* DSM149 and DSM151:

Two stains of *Rc. gelatinosus* were chosen for study, DSM149 and DSM151. The main physiological difference between these strains is the relative abundance of LHII, and RC-LHI. The only other significant difference between the two is the amount of mucus the cells produce; DSM151 produces more. *Rc. gelatinosus* is slightly different from the rest of the species that were grown. There is no significant invagination of the photosynthetic membrane during photosynthetic growth (see Zuber, 1986). Figure 3.6A depicts the averaged plots for the amount of RC-LHI (absorbance at 881nm), LHII (862nm absorbance) and cell density (650nm). The shape of the sigmoidal curves for RC-LHI and LHII were similar, but differences in the shape were observed. The RC-LHI:LHII ratio (Figure 3.6A, filled circles) rapidly drops from 1.6 to 0.95 before mid-log phase has occurred. This suggests that as soon as cell density has started to increase preferential LHII production occurs. Once the cell density has reached the stationary phase the absorbance due to RC-LHI and LHII was maintained (Figure 3.6A, open squares). Using the results from the Verhulst-Pearl model cell harvesting was standardised to  $30 \pm 2$  hrs (mid-late log phase, Figure 3.6B). The Verhulst-Pearl model constants were calculated to be  $N_0=0.02$ ,  $r=0.03$ ,  $K=0.39$ ,  $a=4.84$  and  $b=0.20$ , where the probability,  $p=0.999$  using the  $\chi^2$  test.

Growing *Rc. gelatinosus* DSM151 had its disadvantages. This strain of *Rc. gelatinosus* produces large amounts of mucus which tends to create viscous cultures. Cell aggregation occurs making reliable optical density values difficult to obtain (Figure 3.7). The presence of large amounts of mucus also hinders the initial stages of protein isolation. Notwithstanding this two sets of growth curves were collected and analysed. Regression analysis indicated that there was no significant variation between the DSM151 growth curve replicates and their controls. However the cell density, at the control time point, between the growth curve data sets were significantly different (set 1:  $0.218 \pm 0.026$ ,  $n=5$  and set 2:  $0.160 \pm 0.021$ ,  $n=5$ ,  $t=24$ hrs). No conclusive statements regarding cell level can be made since the absorbancies of different growth curves do not overlap. The only reliable statement is that an apparent log phase of  $6 \pm 2$  hours occurs, which is similar to that for strain DSM149, and final culture O.D. levels are approximately 0.3. Since an accurate average plot of cell density versus time could not be established DSM151 was harvested at the same time after inoculation as DSM149, i.e.  $30 \pm 2$  hrs.

3.2.5 *Rc. gelatinosus* DSM149 and DSM151

Two strains of *Rc. gelatinosus* were chosen for study, DSM149 and DSM151. The main physiological difference between these strains is the relative abundance of LHII and RC-LHI. The only other significant difference between the two is the amount of mucus the cells produce; DSM151 produces more *Rc. gelatinosus* is slightly different from the rest of the species that were grown. There is no significant investigation of the photosynthetic membrane during photosynthetic growth (see Table 1988, Figure 3.6A depicts the

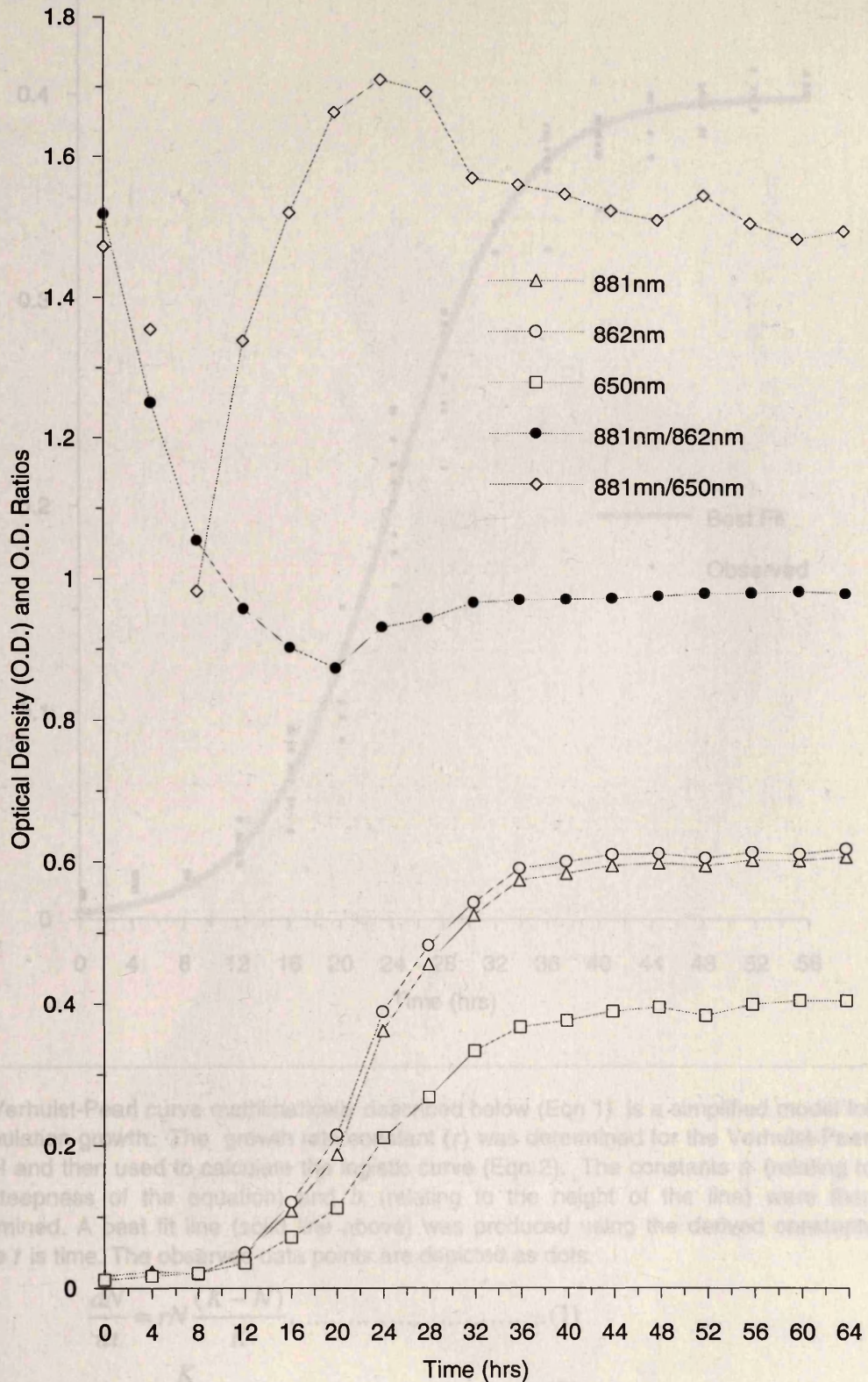
**Figure 3.6:** Growth curve of *Rhodocyclus gelatinosus* strain DSM149. Two independent growth curves were determined. Samples from control bottles were obtained at 24 hours to investigate the presence of any oxygen trigger due to repeated sample removal. The  $s^2$  between data sets and their controls and between data set, measured at 650nm, were less than 0.001. The data for the two growth curves were similar and thus were combined to produce averaged graphs for significant wavelengths. (A): Optical density-time course plot for RC-LHI (881nm) and cell density (650nm). The ratio of RC-LHI:cell density (874nm/650nm) is also shown. The data indicates that cell density reaches a plateau within 36-40 hours. The RC-LHI:cell density ratio, as with other species, reaches a maximum value during log phase then drops when cell density levels reach a stationary value. The relative ratio, with respect to LHII levels, of core complex (RC-LHI) reduces as time progresses reaching a steady state of approximately 0.95. (B): Analysis for cell density using the Verhulst-Pearl and logistic population growth models as templates., i.e.

$$\frac{dN}{dt} = 0.03N \frac{(0.39 - N)}{0.39}$$

$$N = \frac{K}{1 + e^{4.84 - 0.20t}}$$

where initial  $N$ ,  $N_0 = 0.027$ , at time,  $t = 0$ , where the probability,  $p = 0.999$  when using the  $\chi^2$  test. (C): Averaged time course absorption spectrum for *Rc. gelatinosus* strain DSM149. Absorption blips occur at approximately 530nm and 360nm, these were caused by hard/software errors in the Shimadzu spectrophotometer.

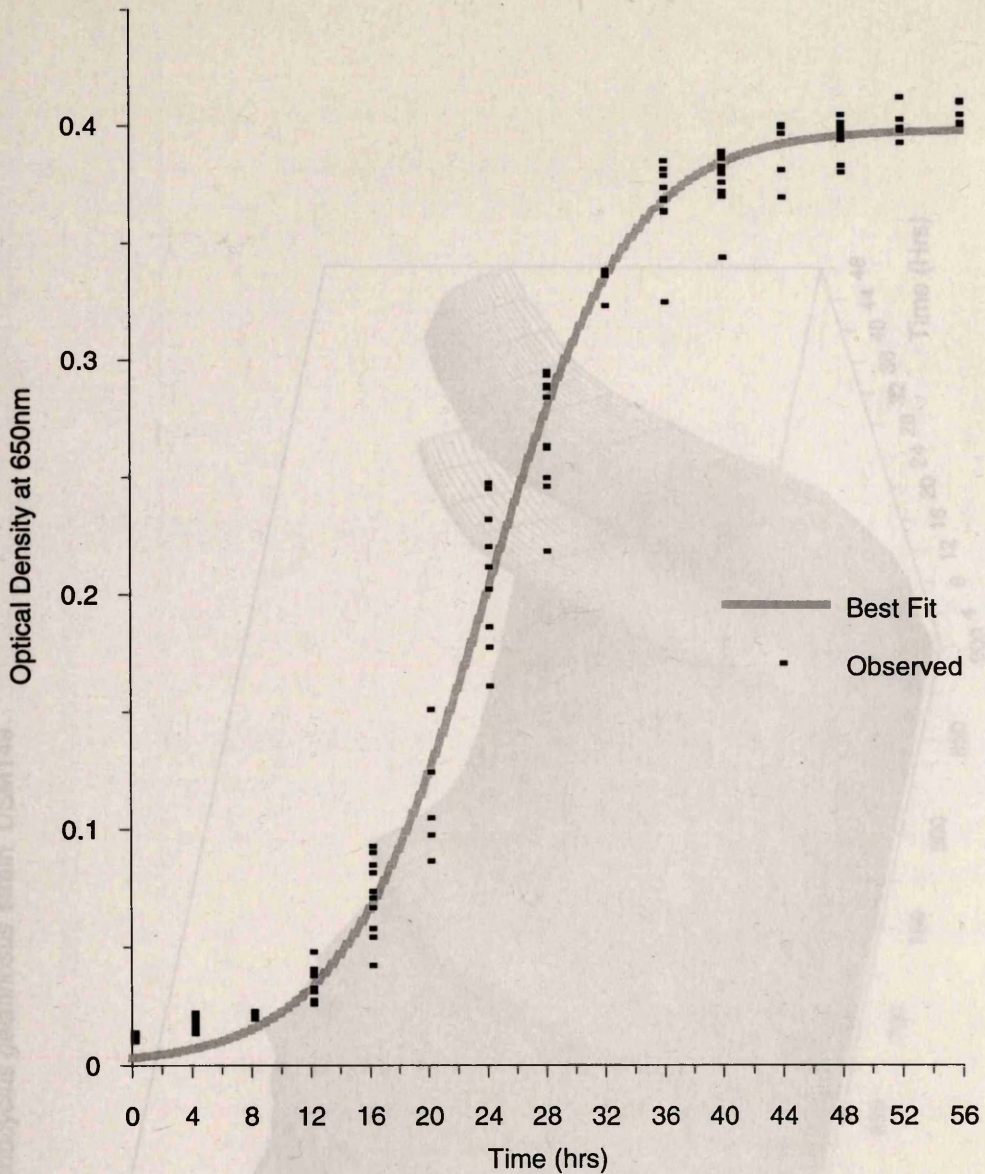
(A): Optical Density-Time Course Plot of RC-LHI (881nm), LHII (862nm) and Cell Density (650nm)



$$N = \frac{K}{1 + e^{-a(t-b)}} \quad (2)$$

The constants were calculated to be  $N_{\infty} = 0.03$   
 $r = 0.03$   
 $K = 0.20$   
 $a = 4.94$   
 $b = 0.20$

(B): Analysis of Cell density: Verhulst-Pearl Curve.



The Verhulst-Pearl curve mathematically described below (Eqn 1) is a simplified model for a population growth. The growth rate constant ( $r$ ) was determined for the Verhulst-Pearl model and then used to calculate the logistic curve (Eqn 2). The constants  $a$  (relating to the steepness of the equation) and  $b$  (relating to the height of the line) were then determined. A best fit line (solid line above) was produced using the derived constants where  $t$  is time. The observed data points are depicted as dots.

$$\frac{dN}{dt} = rN \frac{(K-N)}{K} \dots\dots\dots(1)$$

$$N = \frac{K}{1 + e^{-at}} \dots\dots\dots(2)$$

The constants were calculated to be  
 $N_0 = 0.03$   
 $r = 0.03$   
 $K = 0.39$   
 $a = 4.84$   
 $b = 0.20$



3.1.7 *Rp. acidophila* 7750, 10050 and 7050

Growth curves of *Rp. acidophila* strains 7750, 10050 and 7050 were obtained. For each strain two independent growth curves were produced. Samples from control bottles were obtained at 24 hours. The  $s^2$  within data sets and their controls and between data sets (measured at 650nm) were less than 0.001 and not significantly different.

*Rp. acidophila* 7750:

Figure 3.5 depicts the results for strain 7750 (A): Optical density-time curve for RC-LHI (890nm) and cell density (650nm). The ratio of RC-LHI to cell density (890nm/650nm) is also shown. The data indicates that cell density levels reach a plateau within 32-40 hours (Figure 3.8B). The RC-LHI to cell density ratio, as with other species, reaches a maximum value during lag phase then drops when cell density levels reach a stationary value. The relative ratio, with respect to LHI levels, of core complex (RC-LHI) reduces as time progresses reaching a steady state of approximately 0.80. (B): Analysis for cell density using the Verhulst-Pearl population growth model the initial population density  $N_0$  is 0.01, at time,  $t=0$ , where the probability,  $p=0.99$  using the  $\chi^2$  test. (C): Averaged time course absorption spectrum for *Rp. acidophila* strain 7750.

*Rp. acidophila* 10050 and 7050:

These two strains produced similar results to strain 7750. Consequently all *Rp. acidophila* strains were harvested  $26 \pm 2$  hrs after inoculation.

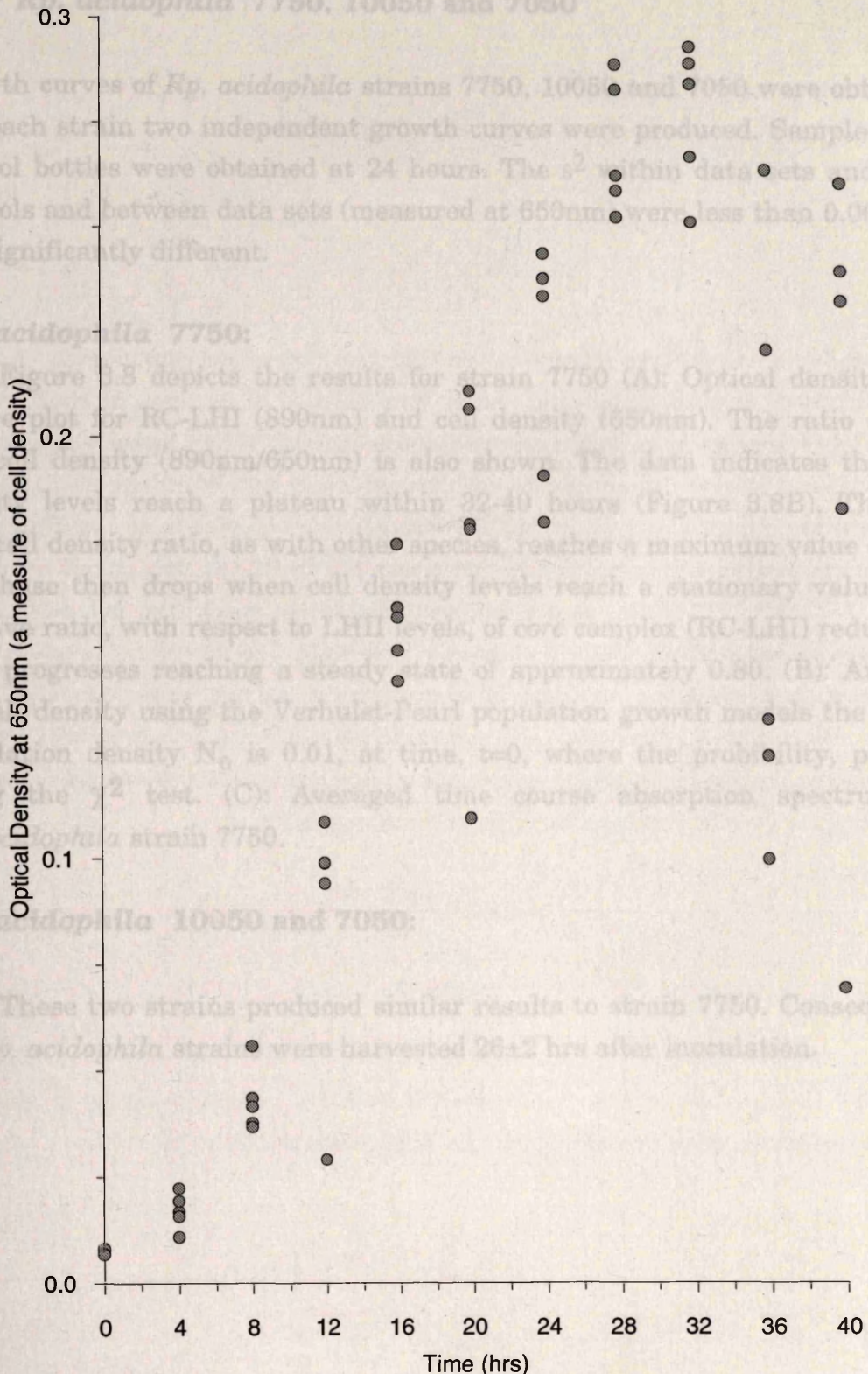


**Figure 3.7:** *Rp. gelatinosus* DSM151 cell density vs. Time. The relatively high level of mucus production by DSM151 causes large variations in optical density (O.D.) measurements, recorded at 650nm (a measure of cell density), making reliable analysis difficult. As a result an averaged growth curve for strain DSM151 could not be produced. The above plot represents the data from one growth curve with each symbol representing a single absorbance measurement.

### 3.2.7 *Rp. acidophila* 7750, 10050 and 7050

Growth curves of *Rp. acidophila* strains 7750, 10050 and 7050 were obtained. For each strain two independent growth curves were produced. Samples from control bottles were obtained at 24 hours. The  $s^2$  within data sets and their controls and between data sets (measured at 650nm) were less than 0.001 and not significantly different.

#### *Rp. acidophila* 7750:

Figure 3.8 depicts the results for strain 7750 (A): Optical density-time course plot for RC-LHI (890nm) and cell density (650nm). The ratio of RC-LHI:cell density (890nm/650nm) is also shown. The data indicates that cell density levels reach a plateau within 32-40 hours (Figure 3.8B). The RC-LHI:cell density ratio, as with other species, reaches a maximum value during log phase then drops when cell density levels reach a stationary value. The relative ratio, with respect to LHII levels, of core complex (RC-LHI) reduces as time progresses reaching a steady state of approximately 0.80. (B): Analysis for cell density using the Verhulst-Pearl population growth models the initial population density  $N_0$  is 0.01, at time,  $t=0$ , where the probability,  $p=0.999$  using the  $\chi^2$  test. (C): Averaged time course absorption spectrum for *Rp. acidophila* strain 7750.

#### *Rp. acidophila* 10050 and 7050:

These two strains produced similar results to strain 7750. Consequently all *Rp. acidophila* strains were harvested  $26 \pm 2$  hrs after inoculation.

Growth curves of *Rp. acidophila* strains 7750, 10050 and 7050 were obtained. For each strain two independent growth curves were produced. Samples from control bottles were obtained at 24 hours. The  $s^2$  within data sets and their controls and between data sets (measured at 650nm) were less than 0.001 and not significantly different.

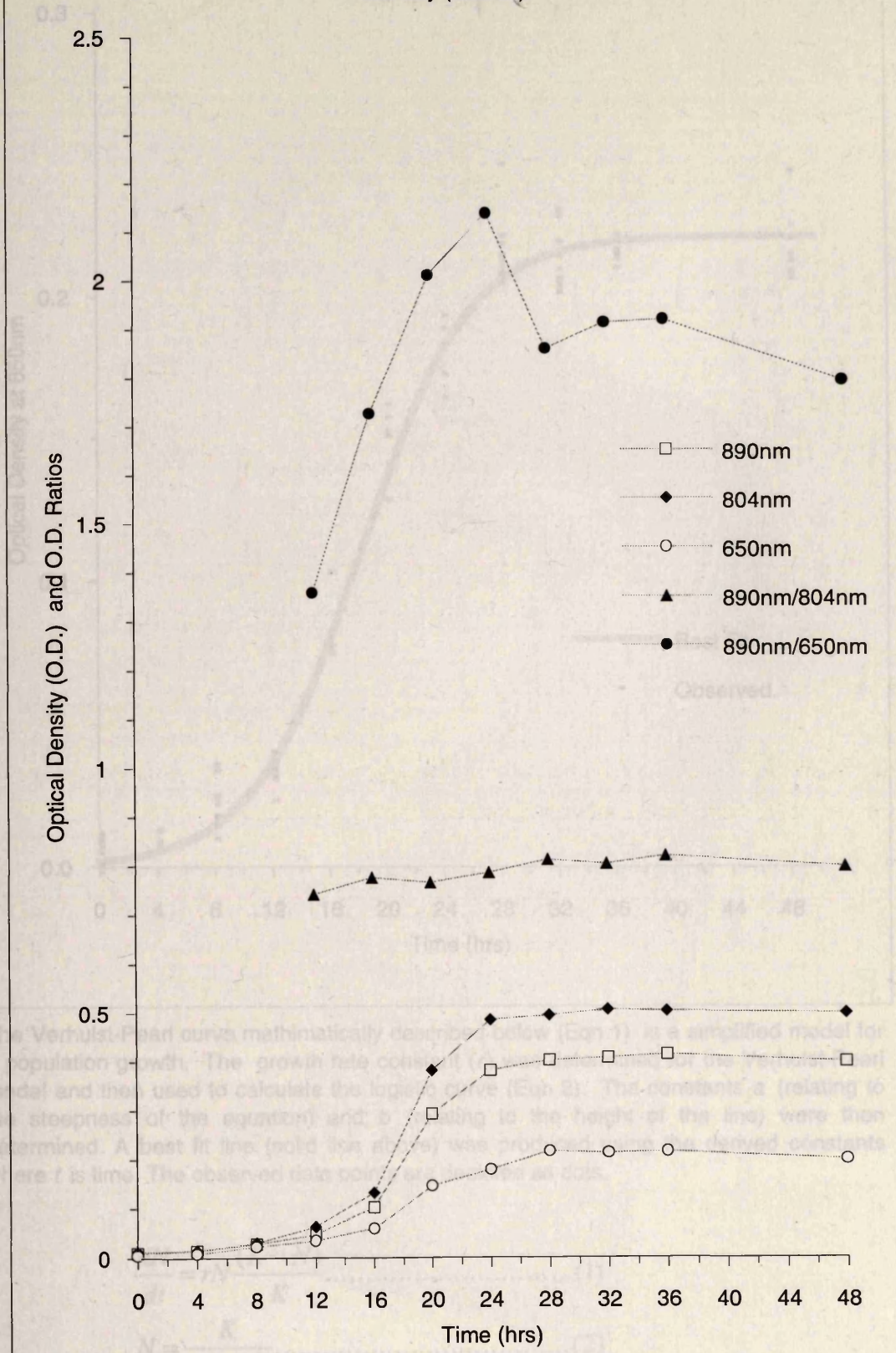
**Figure 3.8:** Growth curve of *Rp. acidophila* strain 7750. Two independent growth curves (A and B) were determined. Samples from control bottles were obtained at 24 hours to investigate the presence of any oxygen trigger due to repeated sample removal. The  $s^2$  between data sets and their controls and between data set (measured at the cell density, 650nm) are less than 0.001. The data for the two growth curves are similar and were combined to produce averaged graphs for significant wavelengths. (A): Optical density-time course plot for RC-LHI (890nm) and cell density (650nm). The ratio of RC-LHI:cell density (890nm/650nm) is also shown. The data indicates that cell density reaches a plateau within 32-40 hours (Figure 3.8B). The RC-LHI:cell density ratio, as with other species, reaches a maximum value during log phase then drops when cell density reaches a stationary value. The relative ratio, with respect to LHII levels, of core complex (RC-LHI) reduces as time progresses reaching a steady state of approximately 0.80. (B): Analysis for culture density using the Verhulst-Pearl population growth model suggests that

$$\frac{dN}{dt} = 0.05N \frac{(0.22 - N)}{0.22}$$

$$N = \frac{K}{1 + e^{4.75 - 0.26t}}$$

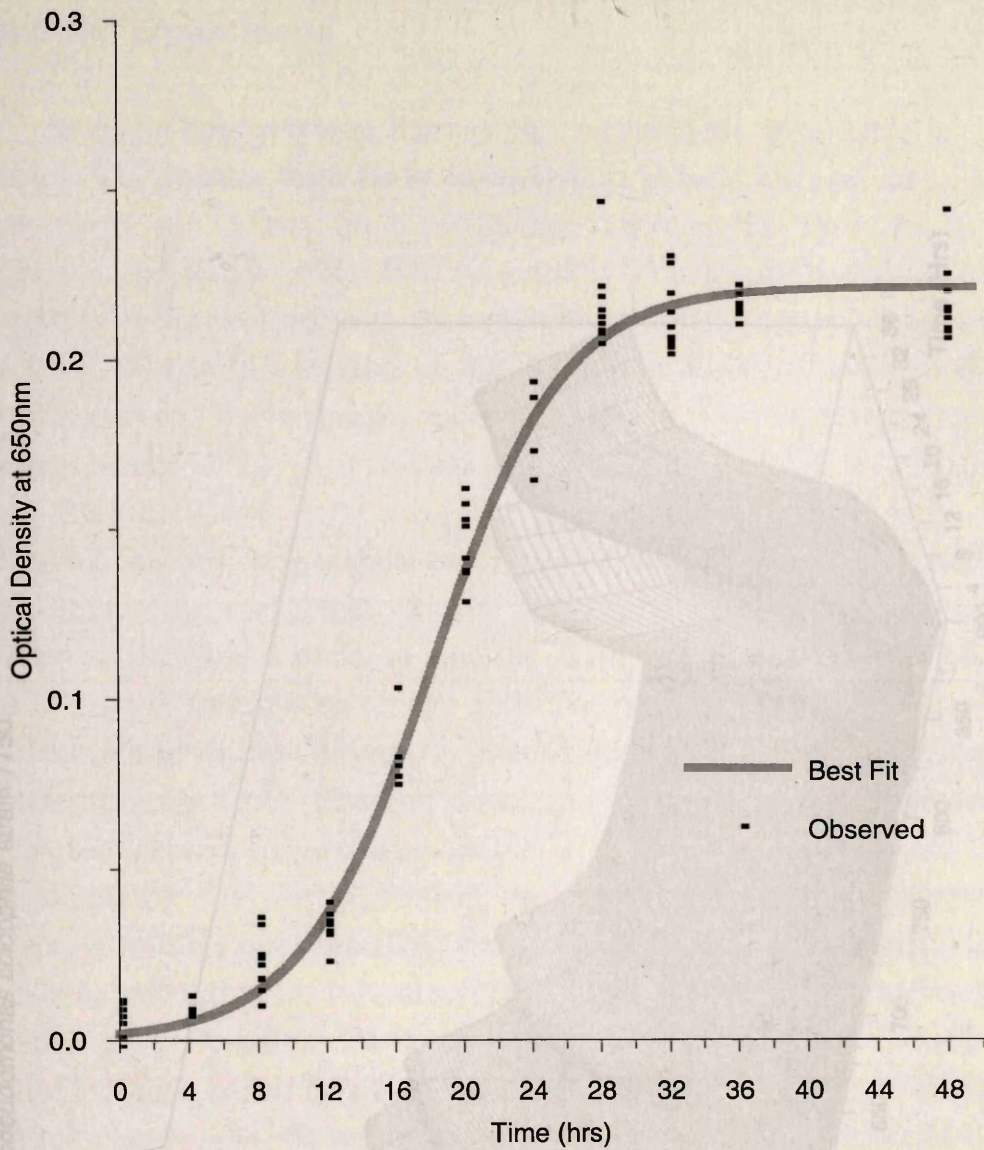
where initial  $N$ ,  $N_0=0.010$ , at time,  $t=0$ , where the probability,  $p=0.999$  using the  $\chi^2$  test. (C): Averaged time course absorption spectrum for *Rp. acidophila* strain 7750.

(A): Optical Density-Time Course Plot for RC-LHI (890nm), LHII (804nm) and Cell Density (650nm).



The constants were calculated to be  $N_0 = 0.01$   
 $r = 0.05$   
 $K = 6.22$   
 $A = 4.75$   
 $B = 0.25$

(B): Analysis of Cell Density: Verhulst-Pearl Curve.



The Verhulst-Pearl curve mathematically described below (Eqn 1) is a simplified model for a population growth. The growth rate constant ( $r$ ) was determined for the Verhulst-Pearl model and then used to calculate the logistic curve (Eqn 2). The constants  $a$  (relating to the steepness of the equation) and  $b$  (relating to the height of the line) were then determined. A best fit line (solid line above) was produced using the derived constants where  $t$  is time. The observed data points are depicted as dots.

$$\frac{dN}{dt} = rN \frac{(K - N)}{K} \dots\dots\dots(1)$$

$$N = \frac{K}{1 + e^{a-bt}} \dots\dots\dots(2)$$

The constants were calculated to be  $N_0 = 0.01$

$r = 0.06$

$K = 0.22$

$a = 4.75$

$b = 0.26$



### 3.2.8 *Rp. cryptolactis*

As with the previous species *Rp. cryptolactis* is a lamellae producing species. The results from three independent growth curves, using the control time point at 72 hrs (post inoculum), allowed the data to be averaged (Figure 3.9). Analysing the data recorded at 72 hrs indicated that there was no statistical difference between the replicates and their control bottles for each of the three growth curves. Also no difference was observed between the separate growth curves. The average optical density  $\pm$  S.D. at 650nm for the three growth curves at 72 hrs were; set 1:  $0.3112 \pm 0.0027$ , set 2:  $0.3185 \pm 0.0033$ , and set 3:  $0.3163 \pm 0.0065$ .

This species can produce two types of LHII, the B800-850 and B800-822 light-harvesting complexes. It was noticed that by the time the stationary phase was reached a residual amount of B800-822 complex was present. This can be seen in figure 3.29A (page 150). The ratio of LHI (absorbance at 880nm) to LHII (absorbance at 862nm) remained approximately constant during active growth (Figure 3.9A). The cell density:RC-LHI ratio also remained constant during the growth curve (Figure 3.9A).

Applying the Verhulst-Pearl equation to all the data points failed to provide a reliable outcome. This was probably due to the exceptionally long lag phase associated (approximately 24-28 hrs) with this bacterium. For this reason it is possible that the medium *THERMED* chosen to grow *Rp. cryptolactis* is not an optimum one. If only the data points associated with mid log phase onwards were applied to the model a *best fit* could be achieved where the probability,  $p=0.999$  using the  $\chi^2$  test and where  $N_0=0.04$ ,  $r=0.01$ ,  $K=0.40$ ,  $a=7.20$ ,  $b=0.12$ . (Figure 3.9B).

3.2.8 *Rp. cryptolactis*

As with the previous species *Rp. cryptolactis* is a lamellae producing species. The results from three independent growth curves using the control time point at 72 hrs (post inoculum), allowed the data to be averaged (Figure 3.9). Analysing the data recorded at 72 hrs indicated that there was no statistical difference between the replicates and their control bottles for each of the three growth curves. Also no difference was observed between the separate growth curves. The average optical density  $\pm$  S.D. at 650nm for the three growth curves at 72 hrs were; set 1:  $0.3112 \pm 0.0027$ , set 2:  $0.3185 \pm 0.0033$ , and set 3:  $0.3163 \pm 0.0066$ .

This species can produce two types of LHI, the B800-820 and B800-822 light-harvesting complexes. It was noticed that by the time the stationary phase was reached a residual amount of B800-822 complex was present. This can be seen in figure 3.28A (page 150). The ratio of LHI (absorbance at 680nm)

**Figure 3.9:** Growth curve of *Rp. cryptolactis*. (A): Optical density time course plot for RC-LHI (open squares), LHII (open triangles) and cell density (open circles). The O.D. values and the absorbance ratios of RC-LH:LHII (filled triangles), RC-LHI:cell density (filled circles). (B): Analysis of cell density vs. time. The application of the Verhulst-Pearl model to the data points from 56 hrs onwards produced a best fit line where the probability,  $p=0.999$  using the  $\chi^2$  test. (C): Averaged time course absorption spectrum.

phase associated (approximately 24-28 hrs) with this bacterium. The reason it is possible that the medium THYMED chosen to grow *Rp. cryptolactis* is not an optimum one. If only the data points associated with mid log phase onwards were applied to the model a best fit could be achieved where the probability,  $p=0.999$  using the  $\chi^2$  test and where  $N=0.04$ ,  $r=0.01$ ,  $K=0.40$ ,  $a=7.30$ ,  $b=0.12$  (Figure 3.9B).

(A): Optical Density-Time Course Plot for RC-LHI (880nm), LHII (862nm) and Cell Density (650nm).

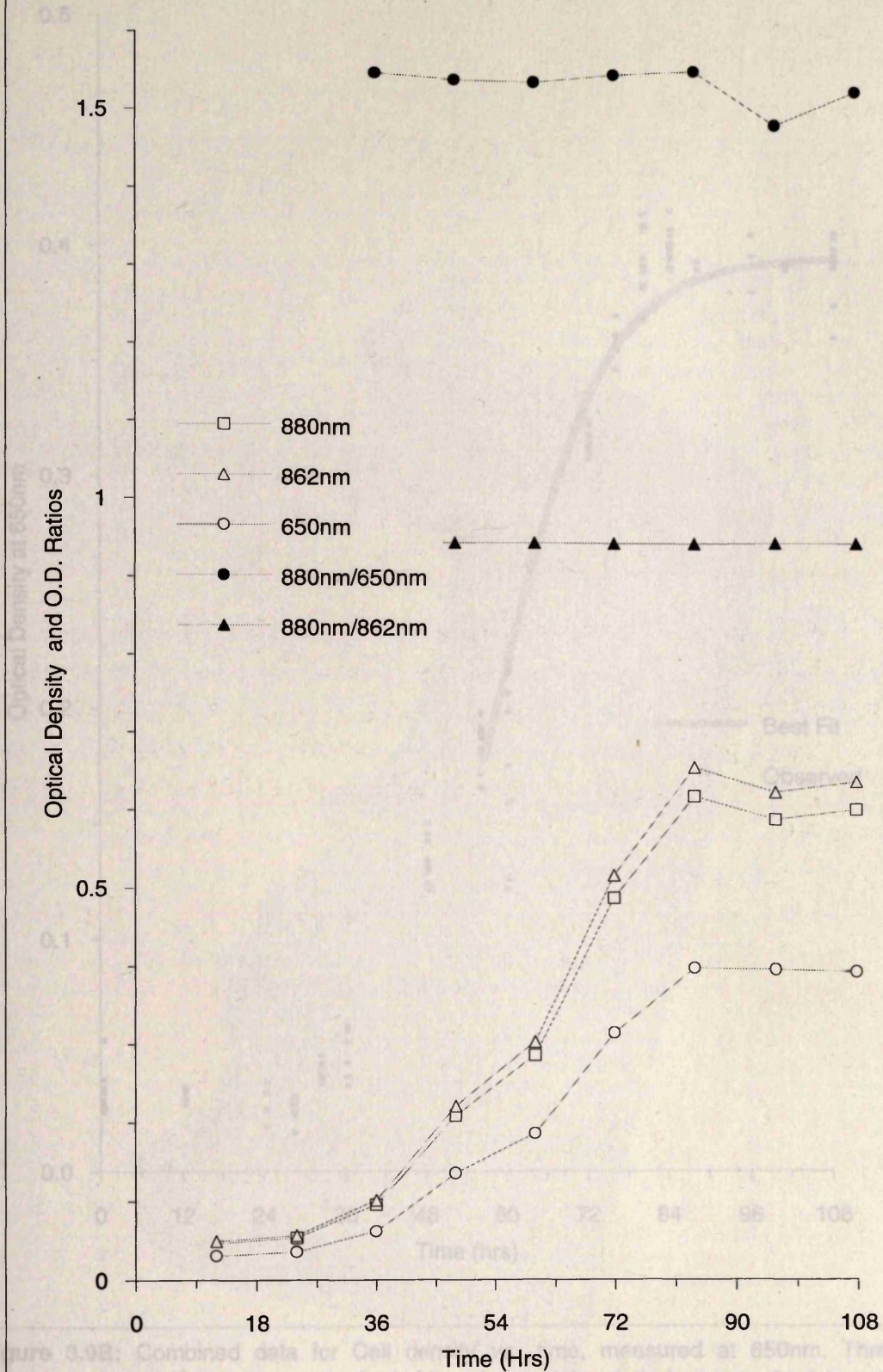
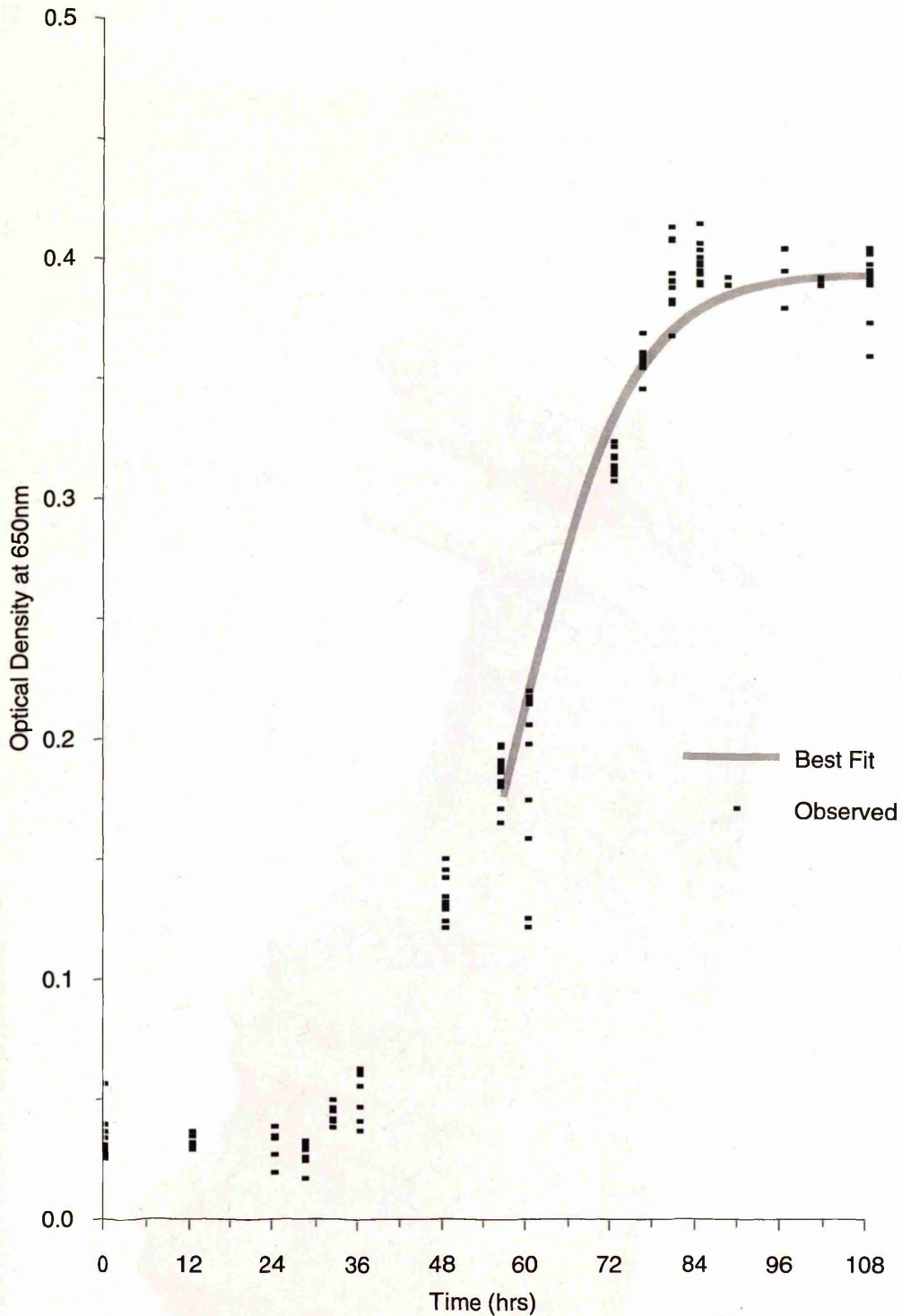


Figure 3.9B: Combined data for Cell density (650nm), measured at 850nm. Three independent growth curves were obtained and the data plotted above. Applying the Verhulst-Pearl model to all the data points failed to provide a suitable answer. Consequently this model was applied to the data points (best fit line) that were in mid-log phase and beyond.

This resulted in  $N_0=0.04$ ,  $r=0.01$ ,  $K=0.40$ ,  $b=7.2$ ,  $d=0.12$ . From the calculated curve the standardized harvesting time for *Rp. cryptovictis* was  $72 \pm 2$  hrs.

(B): Analysis of Cell Density:



**Figure 3.9B:** Combined data for Cell density vs. time, measured at 650nm. Three independent growth curves were obtained and the data plotted above. Applying the Verhulst-Pearl model to all the data points failed to provide a suitable answer. Consequently the model was applied to the data points (best fit line) that were in mid-log phase and beyond.

This resulted in  $N_0=0.04$ ,  $r=0.01$ ,  $K=0.40$ ,  $a=7.2$ ,  $b=0.12$  From the calculated curve the standardized harvesting time for *Rp. cryptolactis* was  $72\pm 2$ hrs.



### 3.2.9 *Rp. palustris* 2.6.1.

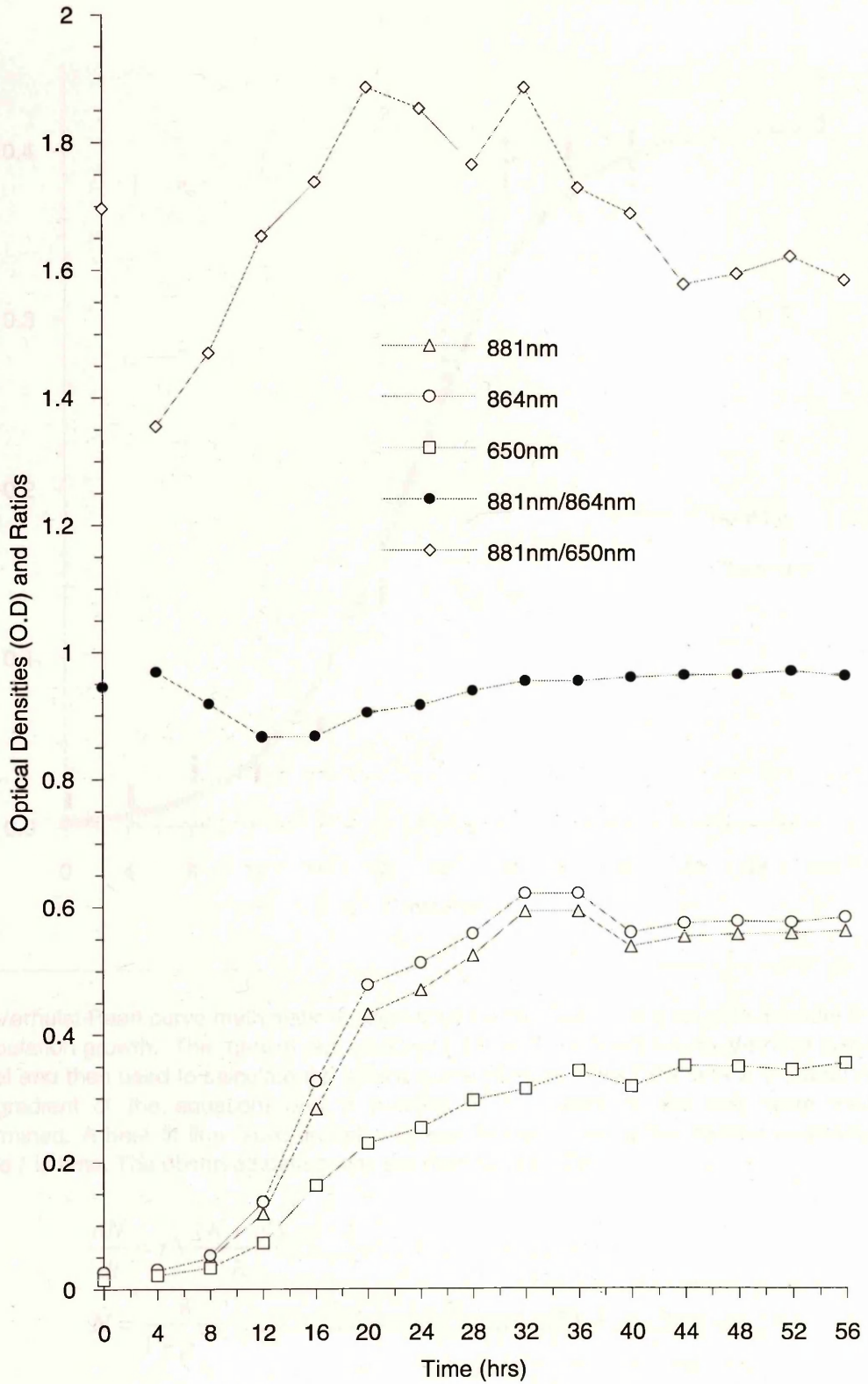
As with the previous two species *Rp. palustris* is a lamellae producing species. This bacterium has the ability to out compete other strains in a mixed culture. When growing 2.6.1 it was noted that a very small difference in inocula between bottles (i.e. total number of viable cells added) caused noticeable differences in growth, as measured by the turbidity of the cultures. For this reason extras care was taken when subculturing this species. The results from independent growth curves, using the control time point of 24 hrs, allowed the data to be averaged (Figure 3.10). The results suggest that as with the other species investigated the relative ratio of RC-LHI:LHII quickly drops once the culture is in log phase, but then rises to a steady value of 0.95 (Figure 3.10A, black circles). The data also indicates that a peak in the RC-LHI:cell density ratio occurs during logarithmic growth (Figure 3.10A, open diamonds). Again the RC-LHI (Figure 3.10A, open triangles) and LHII (Figure 3.10A, open circles) plots mimic the sigmoidal curve produced for the cell density (Figure 3.10A, open squares).

Applying the Verhulst-Pearl model to the culture data set proved to be difficult. The Verhulst-Pearl constants were calculated to be;  $N_0=0.03$ ,  $r=0.06$ ,  $K=0.42$ ,  $a=4.96$  and  $b=0.22$ , where the probability,  $p=0.999$  when the  $\chi^2$  test was applied.

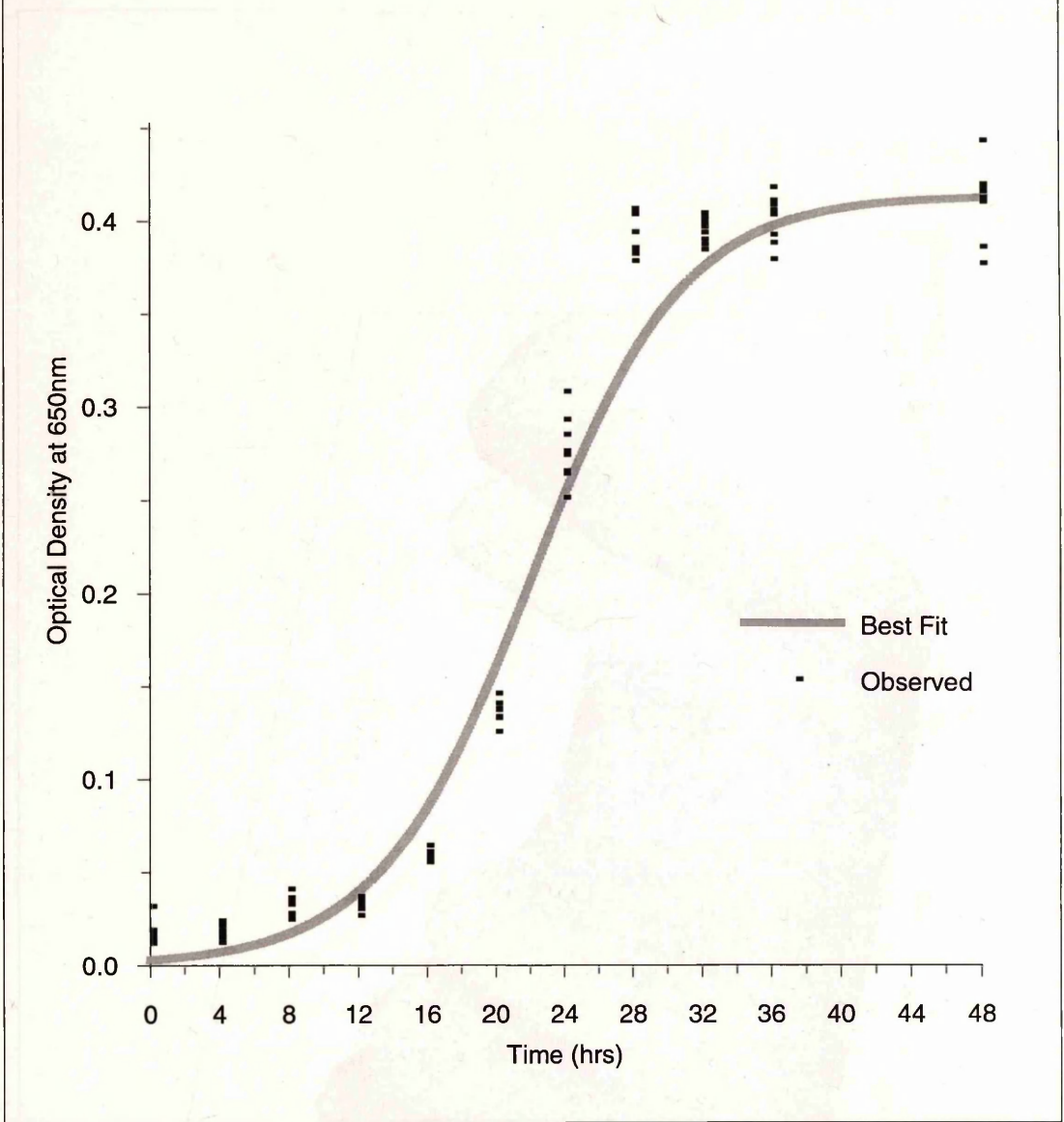
Comparing the modelled curve for *R. centenum* (Figure 3.2B), which also has  $p=0.999$ , indicates that the modelled curve for *Rp. palustris* 2.6.1. is not a perfect fit for the data set. However using the data *Rp. palustris* strain 2.6.1. was harvested  $26\pm 2$ hrs after a 2% (v/v) inoculation.

**Figure 3.10:** Growth of *Rhodospseudomonas palustris* strain 2.6.1. Two growth curves (A and B) were determined independently, each with controls. Data from the control bottles were collected 24hrs after inoculation and compared to the data collected from the growth curve replicates. 24hrs was chosen because initial trials indicated that mid-late log phase was reached at this time point. The controls were used to indicate the presence of any oxygen trigger mechanism resulting from repeated sample removal from the replicate bottles. As in the previous growth curves the variance from each data set were compared to the variances from their controls, and found not to be dissimilar. The  $s^2$  between controls and data sets measured at the cell density measurement (650nm) is less than 0.0005, while  $s^2$  between data sets is less than 0.0001. Since both data sets are similar at 24hrs (the time point at late log phase) the raw data was combined and used to plot averaged graphs for significant wavelengths. (A): Optical Density-Time course plot for RC-LHI (881nm) and cell density (650nm). The ratio of RC-LHI:cell density (881nm/650nm) is also plotted. The graph indicates that both the RC-LHI and cell density then plateau's out. The RC-LHI:cell density ratio although not smooth increases then also levels out. This indicates that there is a carrying capacity, with respect to membrane abundance, for RC-LHI in this bacterium. (B): Regression analysis for cell density (650nm) and the use of the Verhulst-Pearl model produced the constants of;  $N_0=0.030$ ,  $r=0.06$ ,  $K=0.42$ ,  $a=4.96$  and  $b=0.32$ , where the probability,  $p=0.999$  when using the  $\chi^2$  test. However it is clear from figure 3.11B the equation does not go throughout the initial data points. Consequently the equation must be in error. This suggests that the simple Verhulst-Pearl sigmoidal model must be in error. However the equation was used to determine where the optimum harvesting of RC-LHI would occur. Since the line does pass through the data points from mid-log phase onwards (excluding the  $t=28$ hrs data) for this region the equation holds true. The harvesting of *Rp. palustris* 2.6.1 was standardised at  $26\pm 2$ hrs after inoculation. An averaged temporal absorption spectrum was plotted (Figure 3.11C) as before. Absorption blips occur at approximately 530nm and 360nm, these were caused by hard/software errors in the Shimadzu spectrophotometer.

(A): Optical Density-Time Course Plot of RC-LHI (881nm), LHII (864nm) and Cell Density (650nm).



(B): Analysis of Cell Density: Verhulst-Pearl Curve.



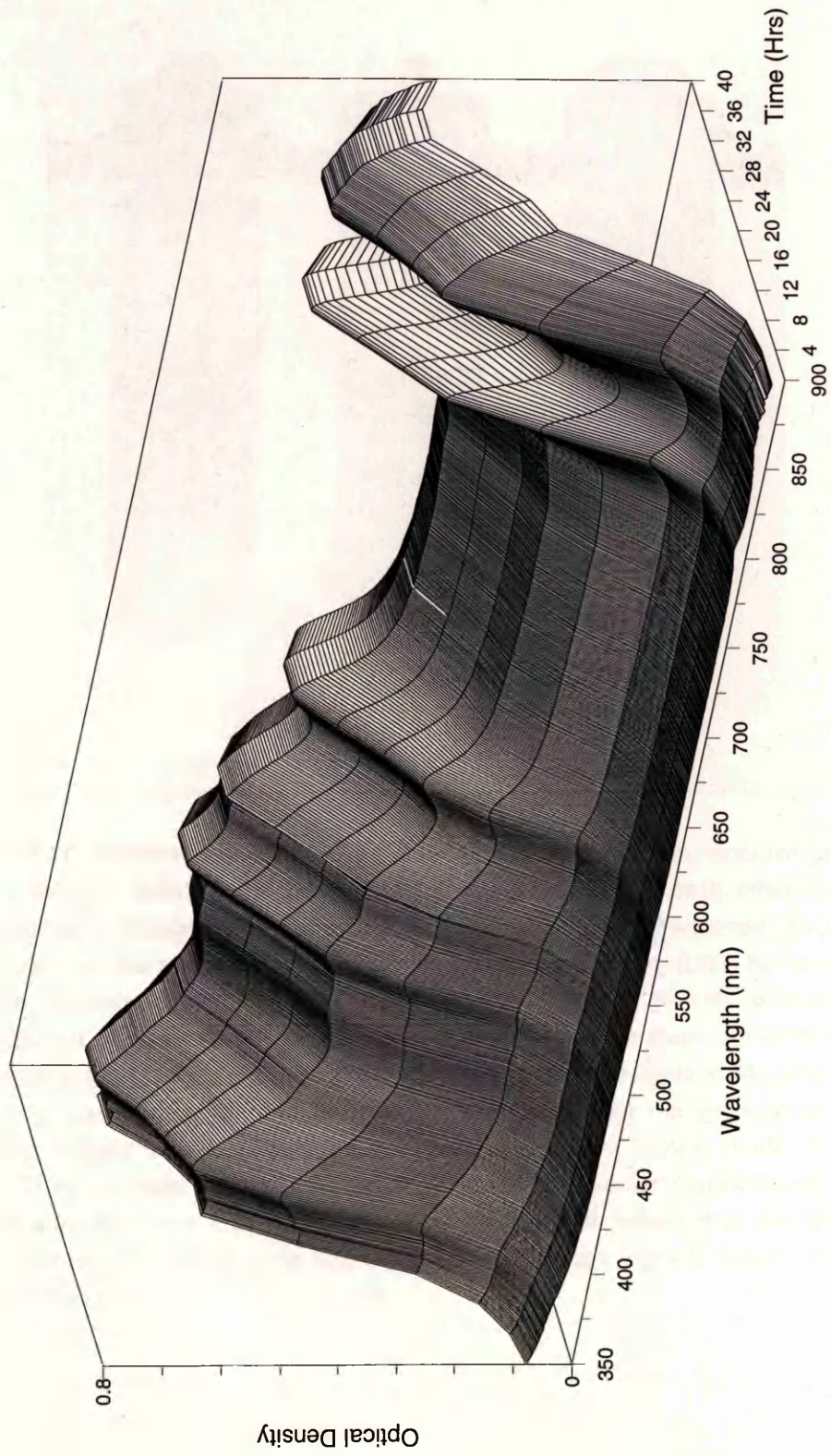
The Verhulst-Pearl curve mathematically described below (Eqn 1) is a simplified model for a population growth. The growth rate constant ( $r$ ) was determined for the Verhulst-Pearl model and then used to calculate the logistic curve (Eqn 2). The constants  $a$  (relating to the gradient of the equation) and  $b$  (relating to the height of the line) were then determined. A best fit line (solid line above) was produced using the derived constants where  $t$  is time. The observed data points are depicted as dots.

$$\frac{dN}{dt} = rN \frac{(K - N)}{K} \dots\dots\dots(1)$$

$$N = \frac{K}{1 + e^{a-bt}} \dots\dots\dots(2)$$

The constants were calculated to be  $N_0 = 0.03$   
 $r = 0.06$   
 $K = 0.42$   
 $a = 4.96$   
 $b = 0.23$

(C) Time Course Spectrum for *Rp. palustris* strain 2.6.1.





### 3.3 Isolation of Core Conjugate (RC-LHI)

The isolation of RC-LHI *core* conjugate is described in Chapter Two. Sucrose gradients were employed in many of the strains under investigation to separate the RC-LHI from LHII (Firsow and Drews, 1977). Figure 3.11 illustrates the two typical bands present when this method was used. Note that in Figure 3.11 only one band is present in the LHII- *Rb. sphaeroides* M21 mutant. Sucrose gradients were also used to separate the two forms of LHII (i.e. B800-850 from B800-820) in mixed populations of LHII.

Once RC-LHI was purified it was characterised as described in Chapter Two (see sections 2.6 and 2.7). The isolation procedures and RC-LHI characterisation for each cell line that was investigated is outlined separately below.

#### 3.3.1 *R. centenum*:

*R. centenum* is a little studied, "core only" producing species. It is very similar in physiological properties to the commonly used bacterium *R. rubrum*. (Yildiz *et al.*, 1991) Cultures in mid-late log phase ( $22 \pm 2$  hrs from a 2% *v/v* inoculum, see section 3.2.1) were harvested and *French Pressed* as described in Chapter Two. *R. centenum* cells were found to be easily disrupted by *French Pressing*. The optimum condition for membrane solubilisation was found to be a sample optical density of  $25 \text{ cm}^{-1}$  at 871nm which was then solubilised for 15 min. at room temperature using 0.7% (*w/v*) LDAO purum (Fluka Biochemicals). This bacterial species produces high levels of RC-LHI, and when combined with the characteristics of easy cell disruption and solubilisation should, in theory, provide a good source of protein for structural studies. As with the other species that were studied, high levels of LDAO were reduced quickly to minimise protein degradation. Solubilised preparations were centrifuged to pellet any unsolubilised material, and the supernatant LDAO concentration was immediately reduced to 0.1% (*w/v*) by dilution with 20mM TRIS.HCl, pH8.0. Other species could cope with higher LDAO levels ( $\sim 0.2\text{-}0.3\%$  *w/v*, e.g. *Rp. palustris*), for the few hours an anion exchange column would take, but this was found not to be the case for this species. Unfortunately the fact that the membranes are so easily solubilised is probably a contributing factor to the final unsuitability of *R. centenum core* for structural studies (see Chapters Four and Five). Basically the isolation of *R. centenum core* conjugate relied on the quickest turn around possible from membrane to purified complex in  $\beta$ -OG or LM *via* the stages of solubilisation, anion exchange, sucrose gradients, gel filtration and finally detergent exchange. The best way to obtain high quality *core* from *R. centenum* would be

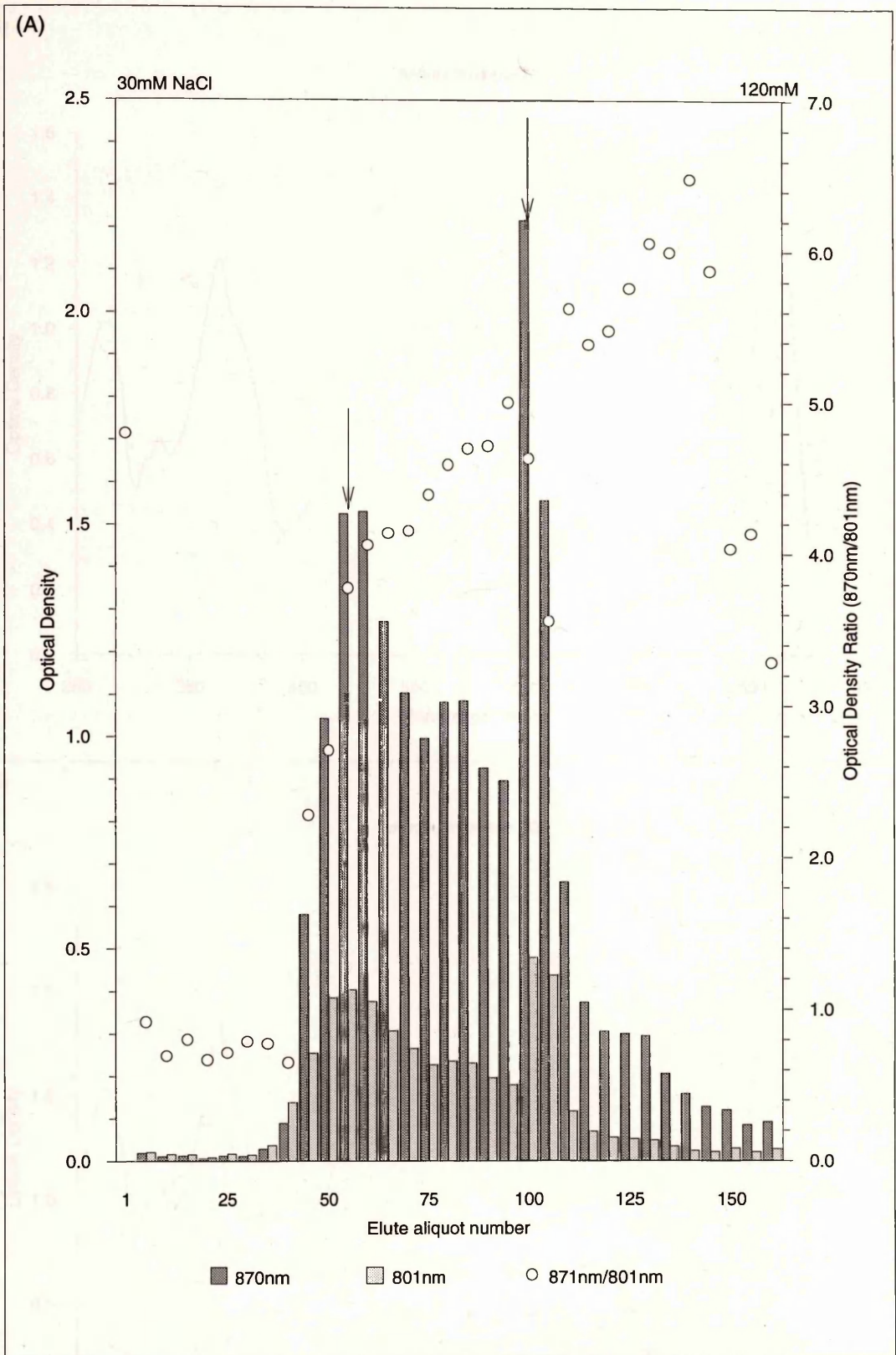
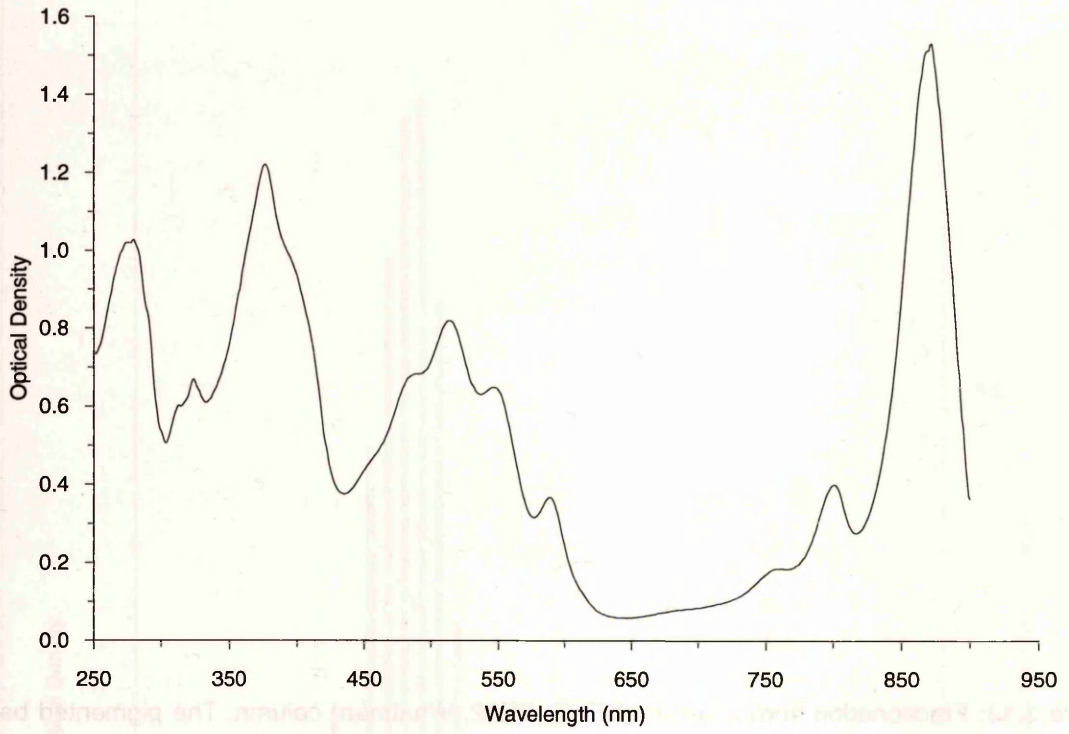


**Figure 3.12:** Fractionation of solubilised *R.centenum* membranes from a DEAE column when a NaCl gradient was applied. (A): Elute obtained from a DEAE column. The linear salt (NaCl) gradient applied was from 30mM to 120mM. The 870nm/801nm absorption represents an approximation the LHI:RC ratio. The two aliquotes that are marked with arrows were then examined in more detail. (B): Absorption spectrum of aliquot number 55. (C): Absorption spectrum of aliquot number 100.

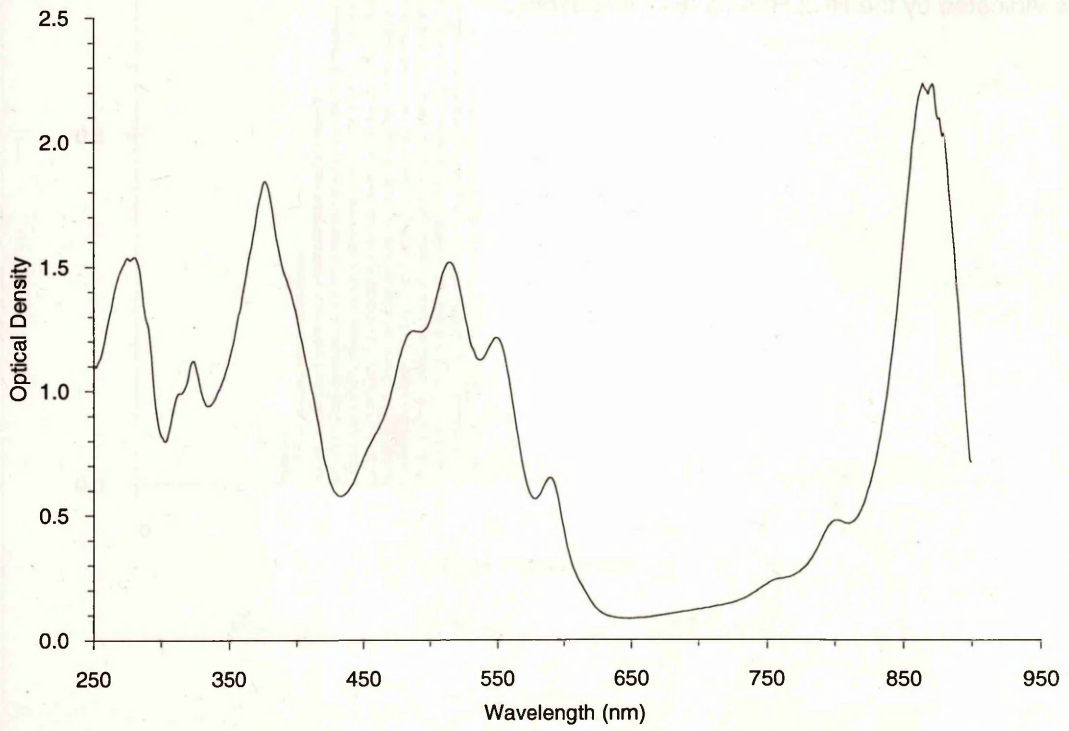
(B)

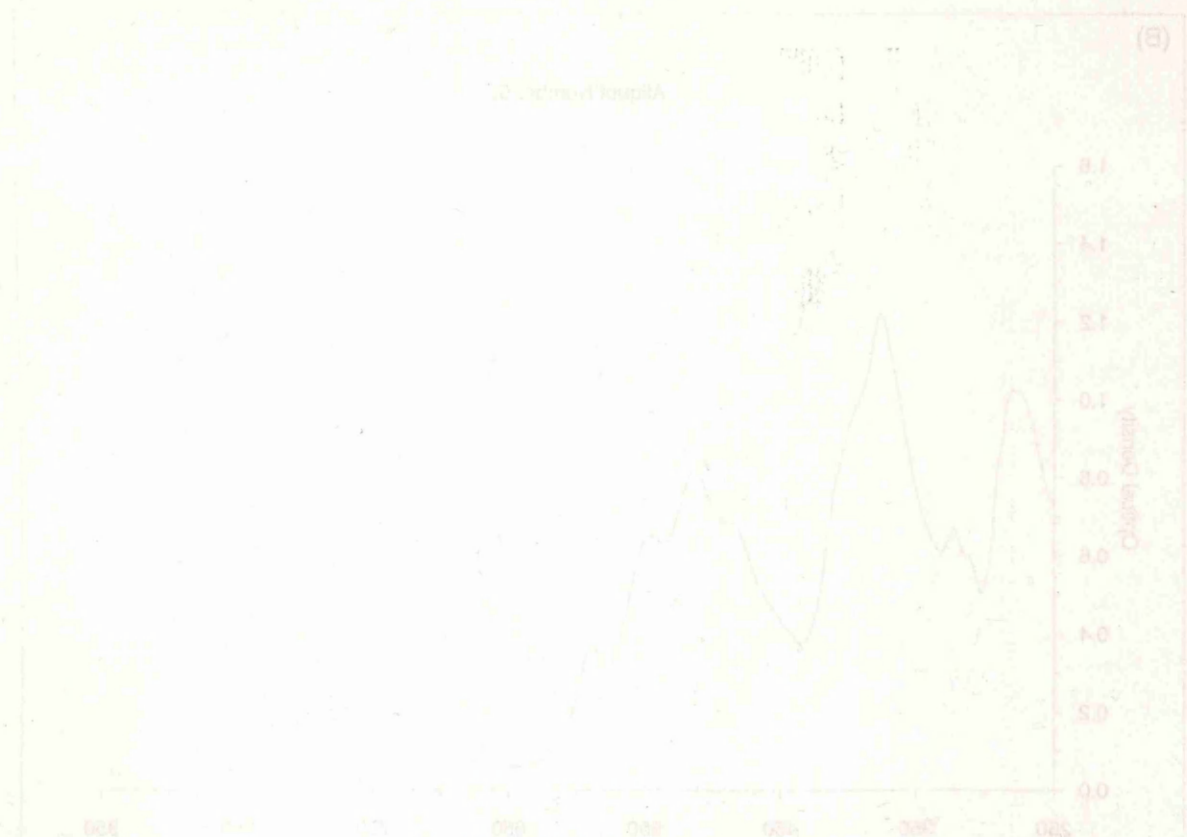
Aliquot Number 55



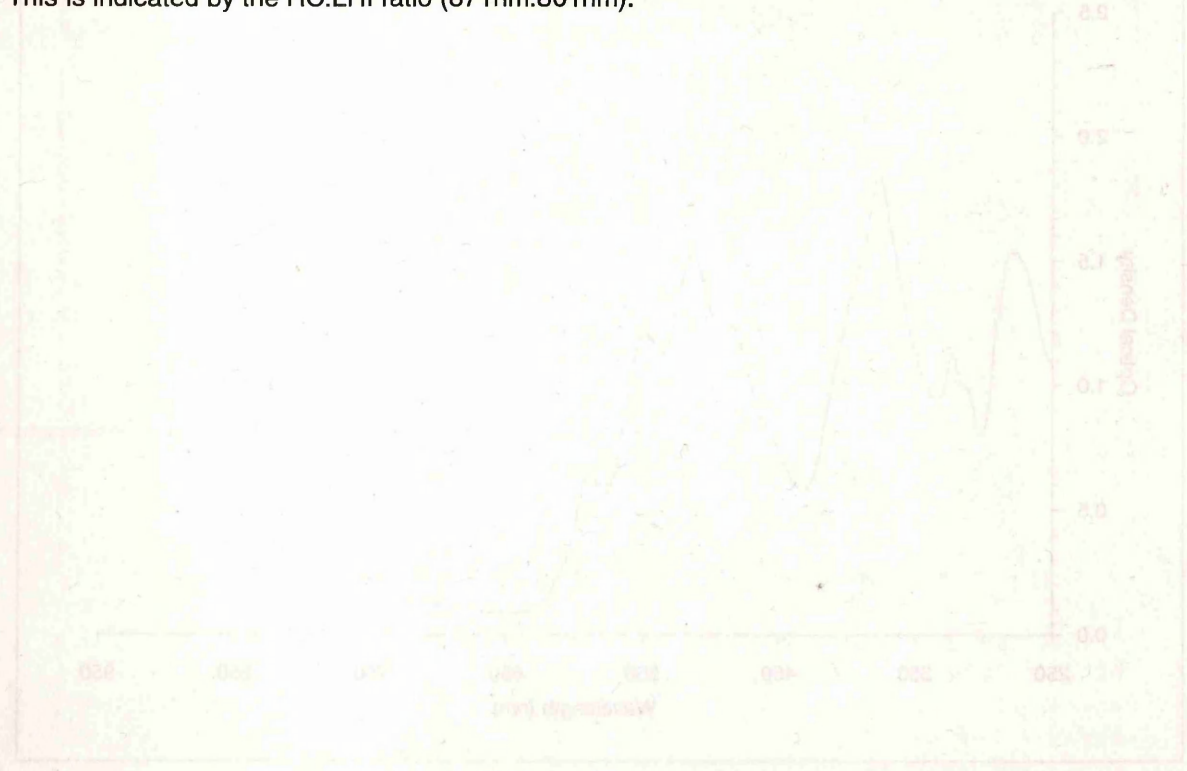
(C)

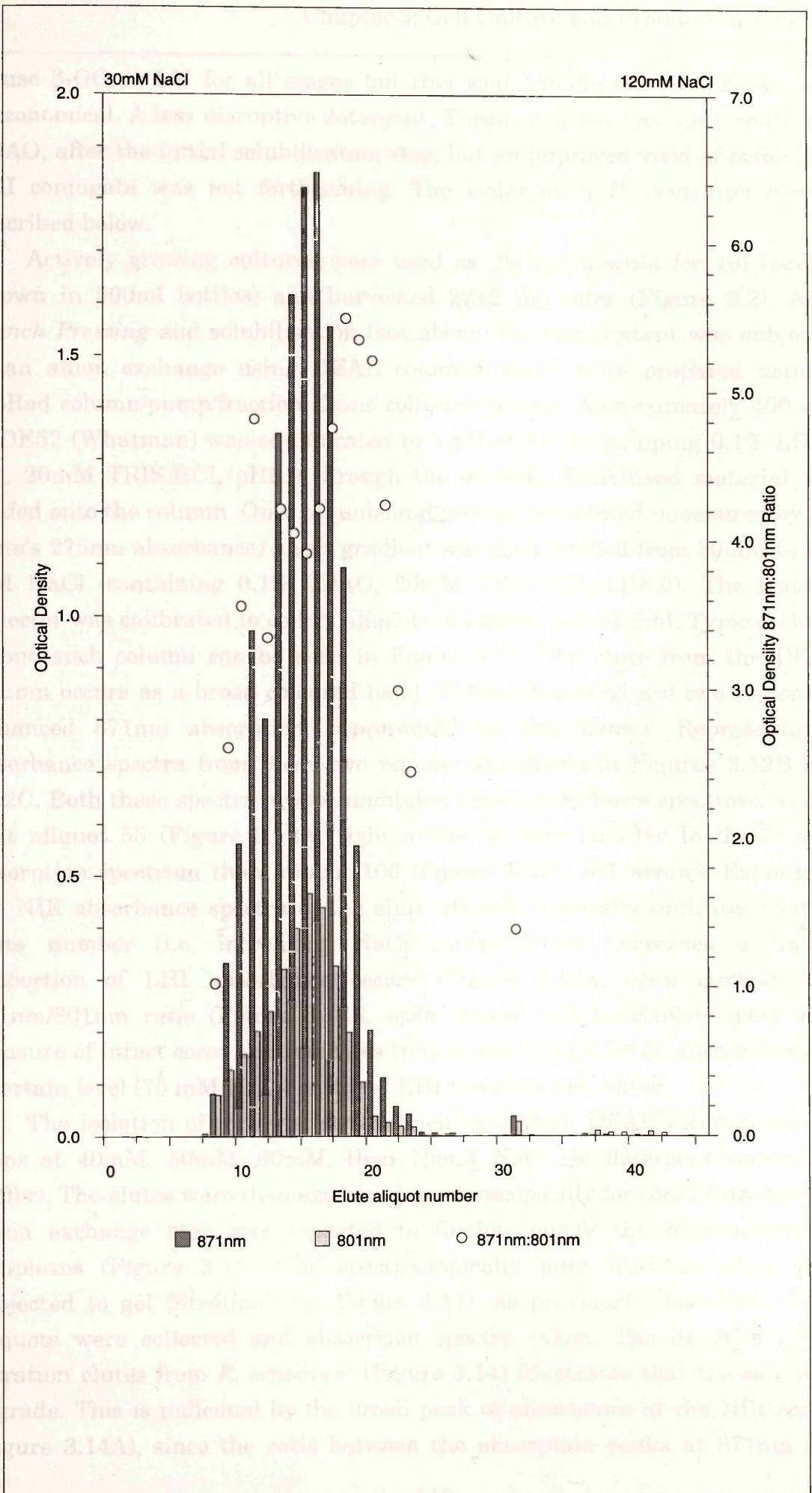
Aliquot Number 100





**Figure 3.13:** Fractionation from a second DEAE (DE52, Whatman) column. The pigmented band, unlike that from the elute from an initial DEAE column (e.g. figure 3.14A), produces one NIR peak. As in the elute from an initial DE52 column fractionation resulted from a salt gradient (30mM-120mM NaCl), which produced enriched LHI fractions that were eluted after intact *core* fractions. This is indicated by the RC:LHI ratio (871nm:801nm).





to use  $\beta$ -OG or LM for all stages but this would make the purification cost astronomical. A less disruptive detergent, Thesit, was used as a alternative to LDAO, after the initial solubilisation step, but an improved yield of stable RC-LHI conjugate was not forthcoming. The isolation of *R. centenum* core is described below.

Actively growing cultures were used as 2% (v/v) inocula for 10l batches (grown in 500ml bottles) and harvested  $22 \pm 2$  hrs later (Figure 3.2). After *French Pressing* and solubilisation (see above) the supernatant was subjected to an anion exchange using DEAE columns which were prepared using a BioRad column/pump/fraction Econo collector system. Approximately  $400 \text{ cm}^3$  of DE52 (Whatman) was equilibrated to a pH of 8.0 by pumping 0.1% LDAO (v/v), 20mM TRIS.HCl, pH8.0 through the column. Solubilised material was loaded onto the column. Once all unbound protein was eluted (measured by the elute's 275nm absorbance) a salt gradient was then applied from 30mM to 120 mM NaCl (containing 0.1% LDAO, 20mM TRIS.HCl, pH8.0). The fraction collector was calibrated to collect aliquots of approximately 5ml. Typical elutes of one such column can be seen in Figure 3.12. The elute from the DEAE column occurs as a broad coloured band. Within this band are two regions of enhanced 871nm absorption, represented by the arrows. Representative absorbance spectra from these two regions are shown in Figures 3.12B and 3.12C. Both these spectra are for undiluted elutes and shows spectroscopically that aliquot 55 (Figure 3.12A, right arrow) is more similar to the *in vivo* absorption spectrum than aliquot 100 (Figure 3.12A, left arrow). Examining the NIR absorbance spectra of the elute aliquots generally indicates that as elute number (i.e. increasing NaCl concentration) increases a higher proportion of LHI absorbance occurs (Figure 3.12A, open circles). The 871nm/801nm ratio (Figure 3.12A, open circles) can be crudely used as a measure of intact *cores* and indicates that as salt (NaCl) levels increase above a certain level (75 mM NaCl) enriched LHI fractions are eluted.

The isolation of *core* was streamlined by eluting DEAE columns in salt steps at 40mM, 50mM, 60mM, then 75mM NaCl (in detergent containing buffer). The elutes were then examined spectroscopically for *core* integrity. The anion exchange step was repeated to further purify the pigment-protein complexes (Figure 3.13). The spectroscopically pure fractions were then subjected to gel filtration (e.g. Figure 3.14), as previously described. 500 $\mu$ l aliquots were collected and absorption spectra taken. The example of gel filtration elutes from *R. centenum* (Figure 3.14) illustrates that the *core* does degrade. This is indicated by the broad peak of absorbance at the NIR region (Figure 3.14A), since the ratio between the absorption peaks at 871nm (i.e.

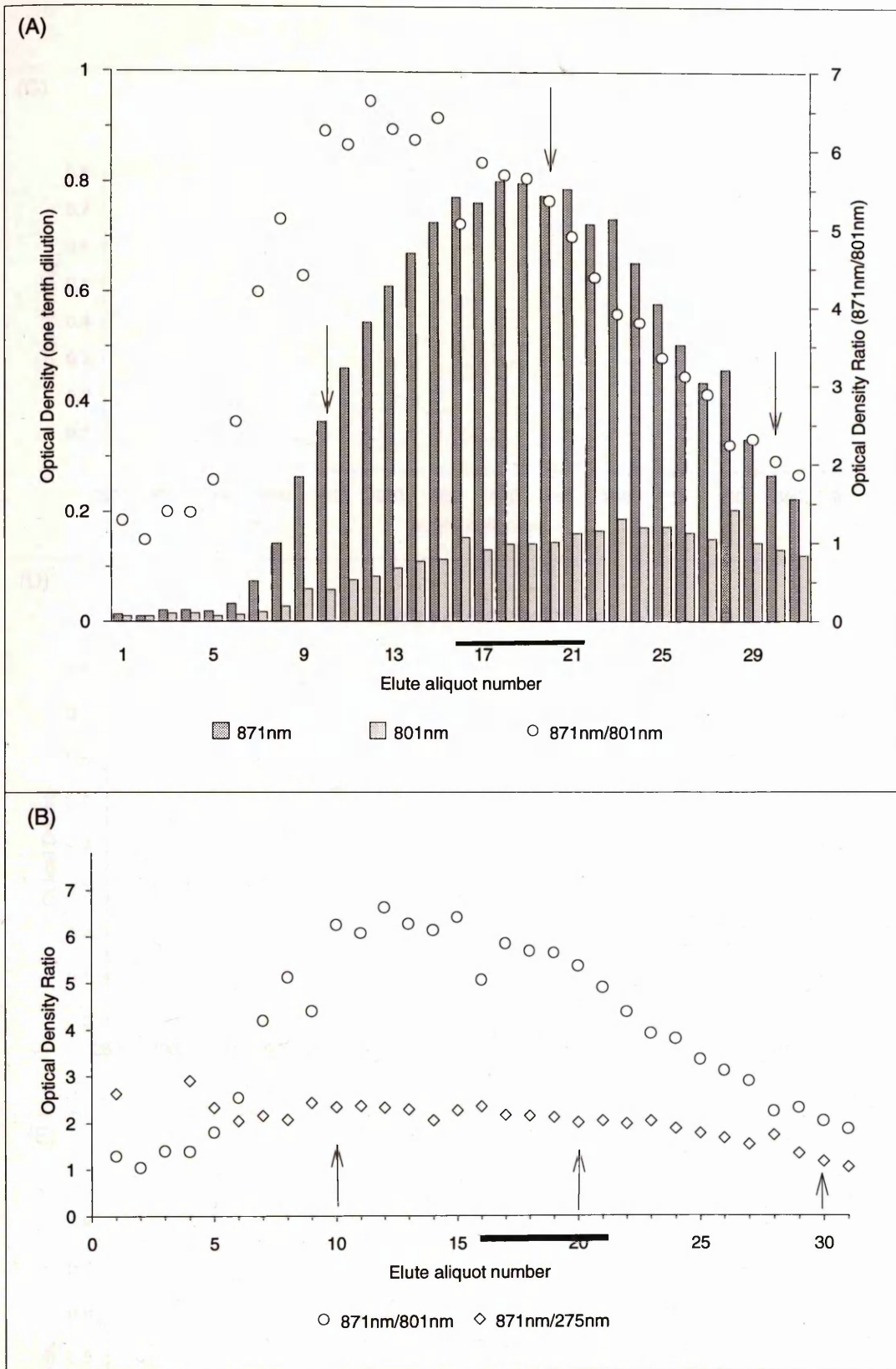
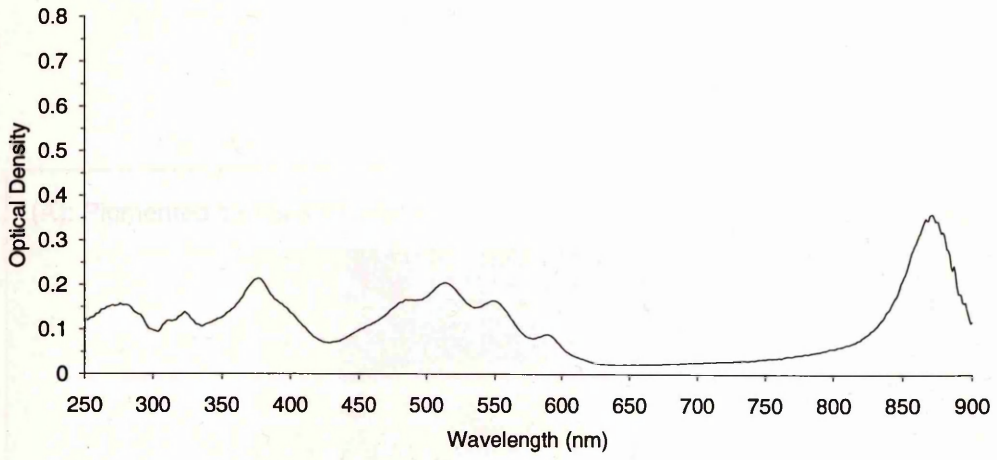


**Figure 3.14:** Fractionation of *R. centenum core* elutant from a S-200 molecular sieve column. (A): Absorption data (1/10th dilution) for 0.5ml Elute aliquots obtained from a 1m molecular sieve column. The relative ratio of LHI:RC is depicted. (B): The LHI:RC ratio and core:protein (871nm/275nm) varies with aliquot. As in part (A) aliquots 10, 20 and 30 have been highlighted by arrows (C): Absorption spectrum of aliquot number 10. (D): Absorption spectrum of aliquot number 20. (E): Absorption spectrum of aliquot number 30. From the absorption spectra it is clear that the aliquots are not homogenous; first LHI enriched fractions appear followed by the *core* fractions followed by RC enriched fractions.

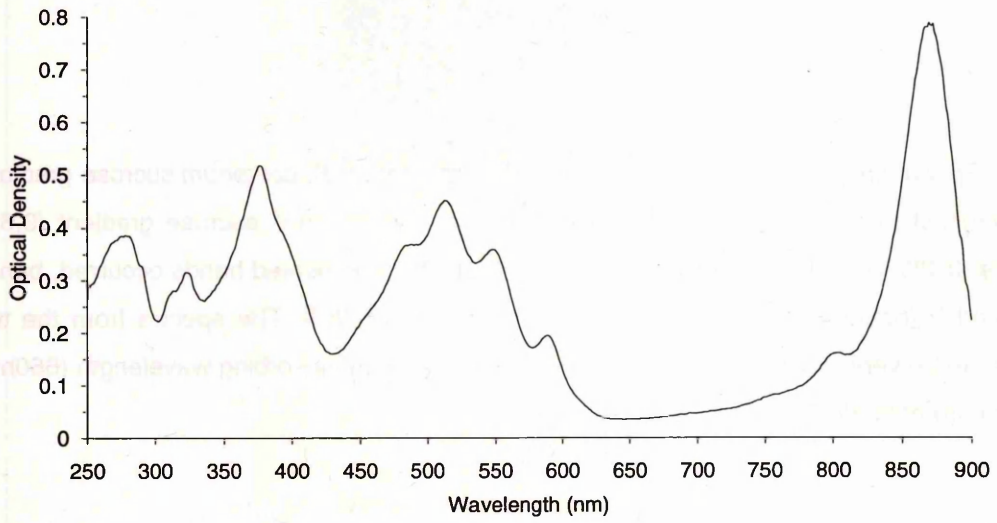
(C)

Aliquot Number 10



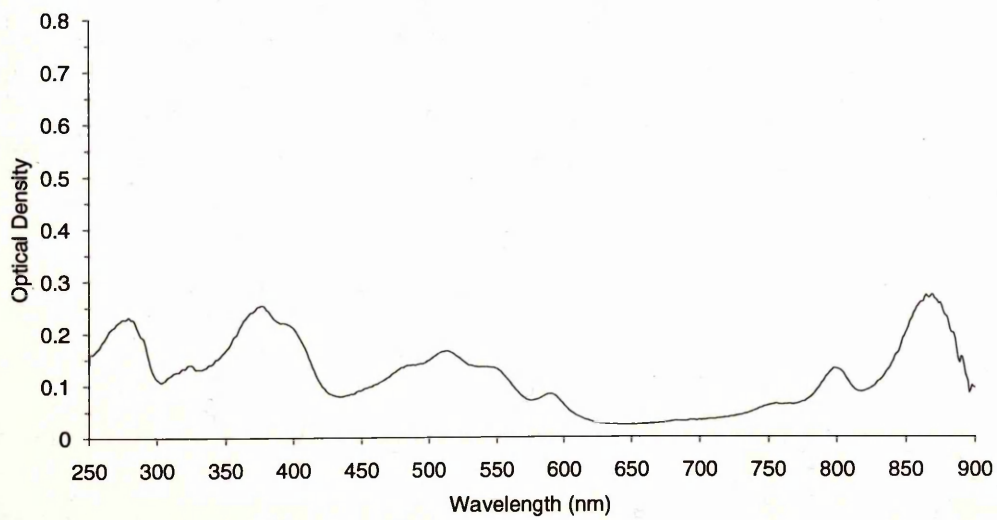
(D)

Aliquot Number 20



(E)

Aliquot Number 30



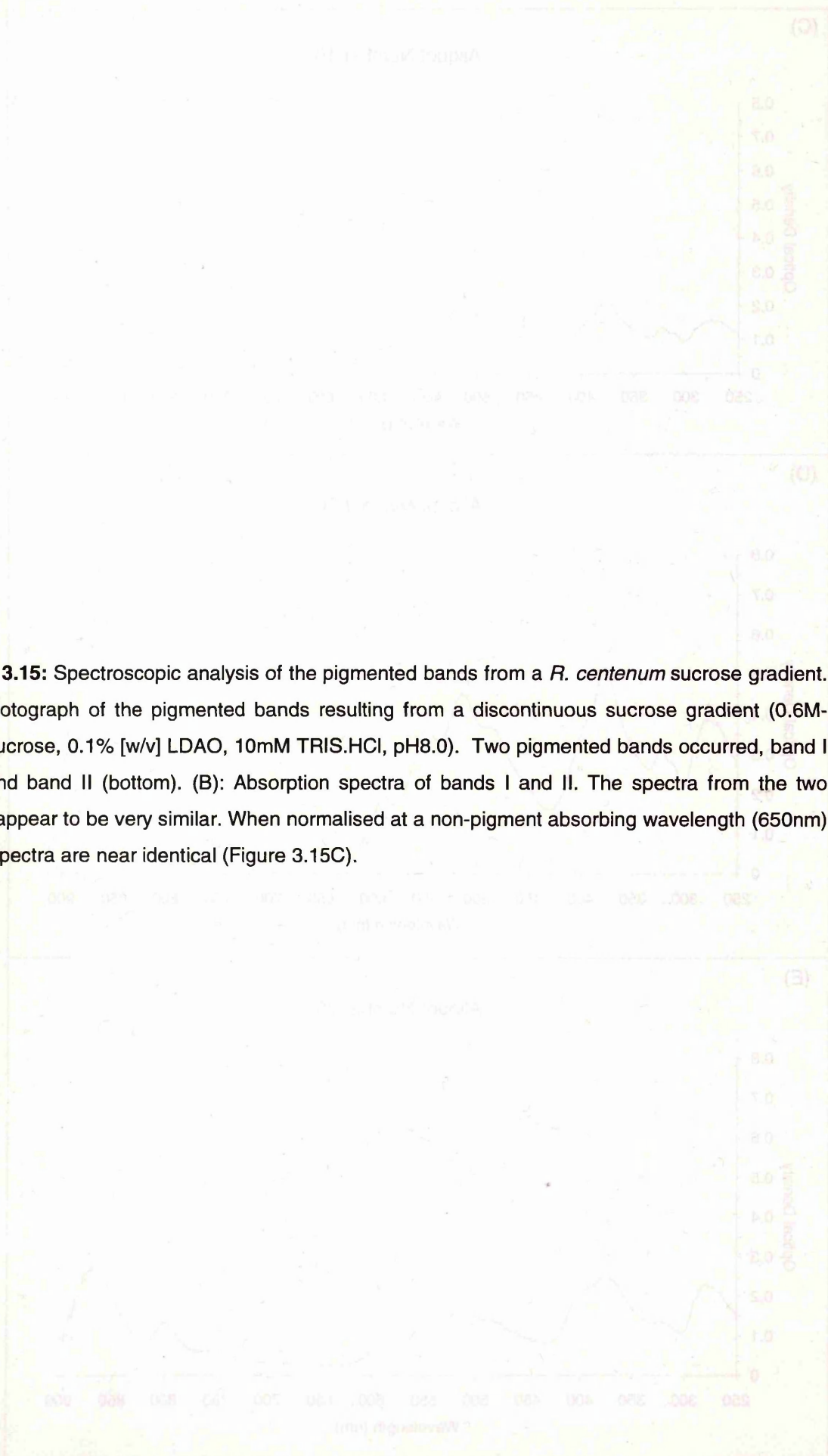
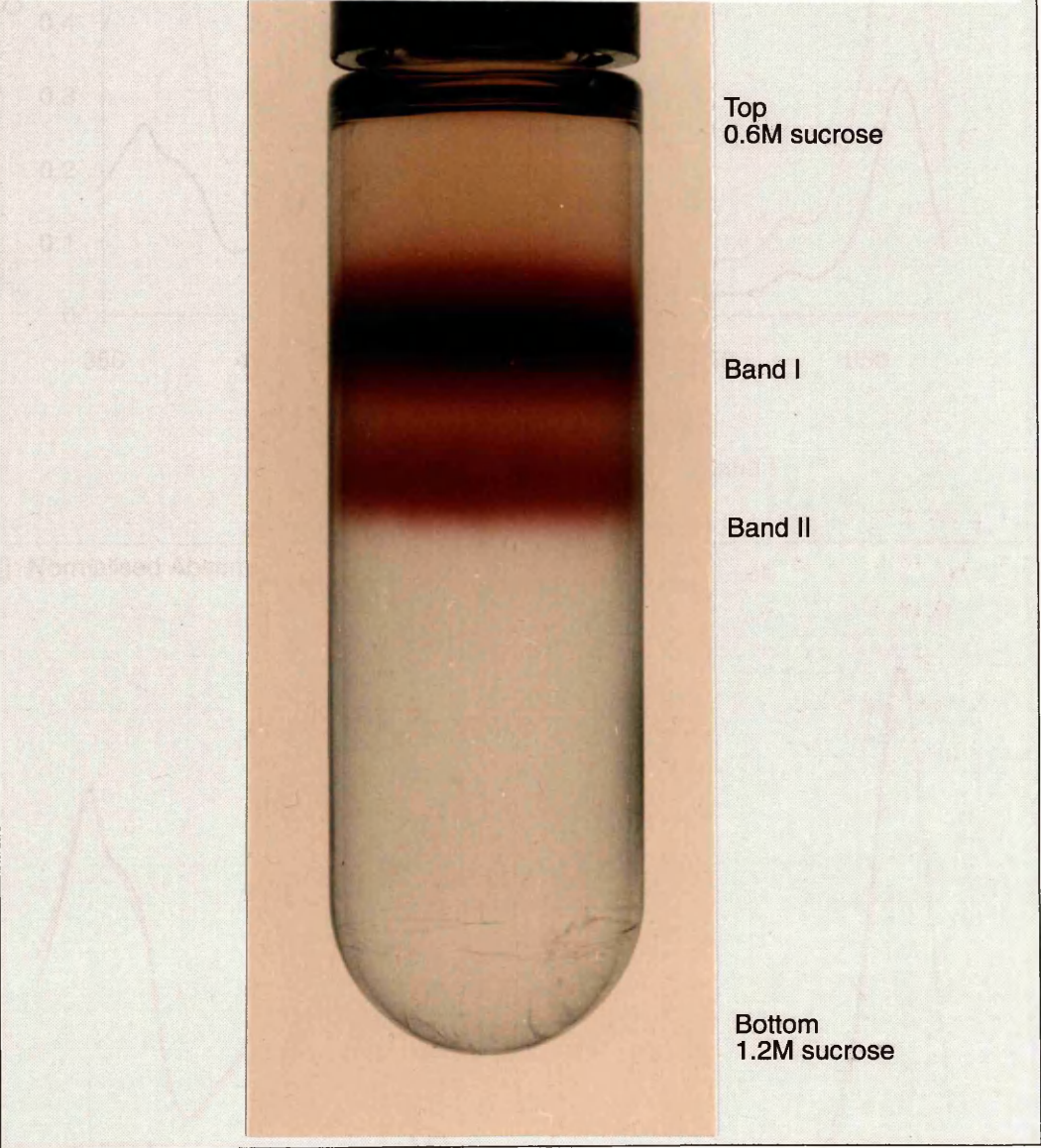


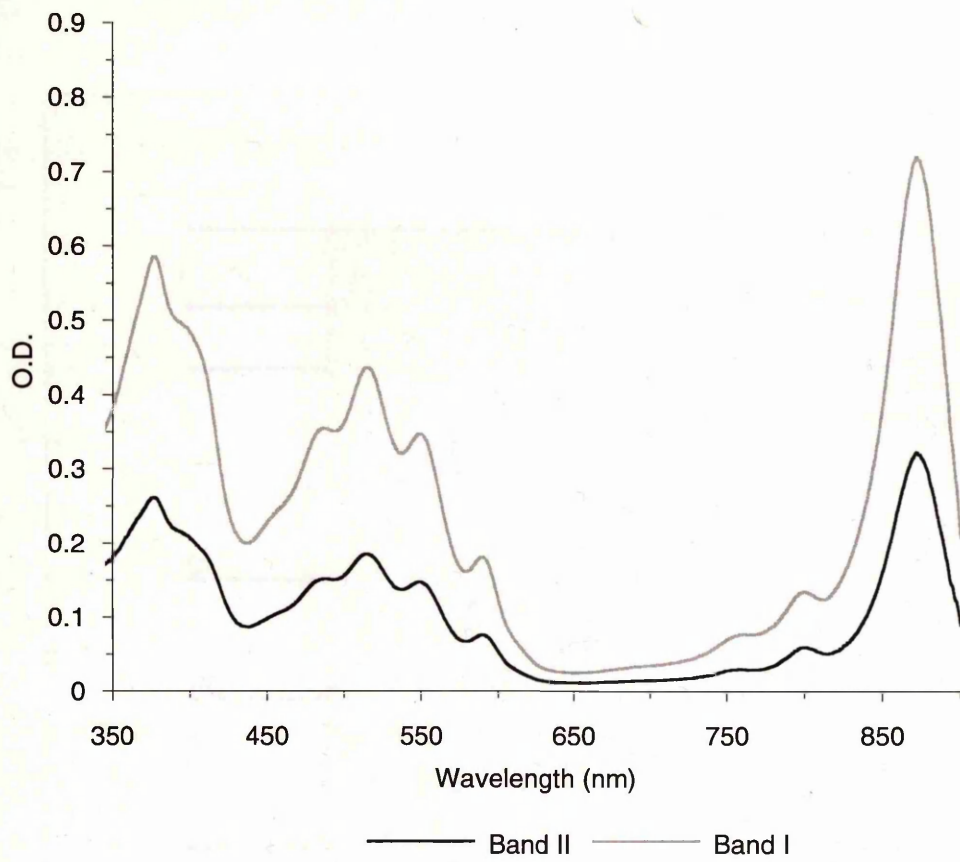
**Figure 3.15:** Spectroscopic analysis of the pigmented bands from a *R. centenum* sucrose gradient. (A): Photograph of the pigmented bands resulting from a discontinuous sucrose gradient (0.6M-1.2M sucrose, 0.1% [w/v] LDAO, 10mM TRIS.HCl, pH8.0). Two pigmented bands occurred, band I (top) and band II (bottom). (B): Absorption spectra of bands I and II. The spectra from the two bands appear to be very similar. When normalised at a non-pigment absorbing wavelength (650nm) these spectra are near identical (Figure 3.15C).

(B) Absorption Spectra of *R. centenum*

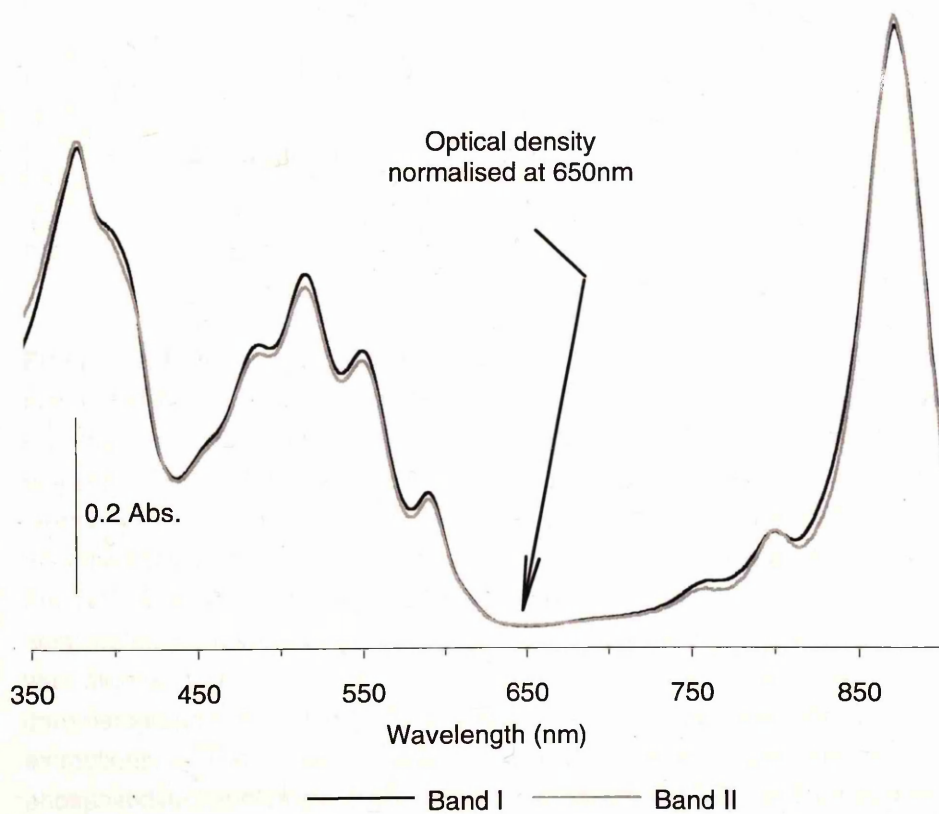
(A): Pigmented bands of *R. centenum* resulting from a discontinuous sucrose gradient



(B): Absorption Spectra of Bands I and II.



(C): Normalised Absorption Spectra of Bands I and II



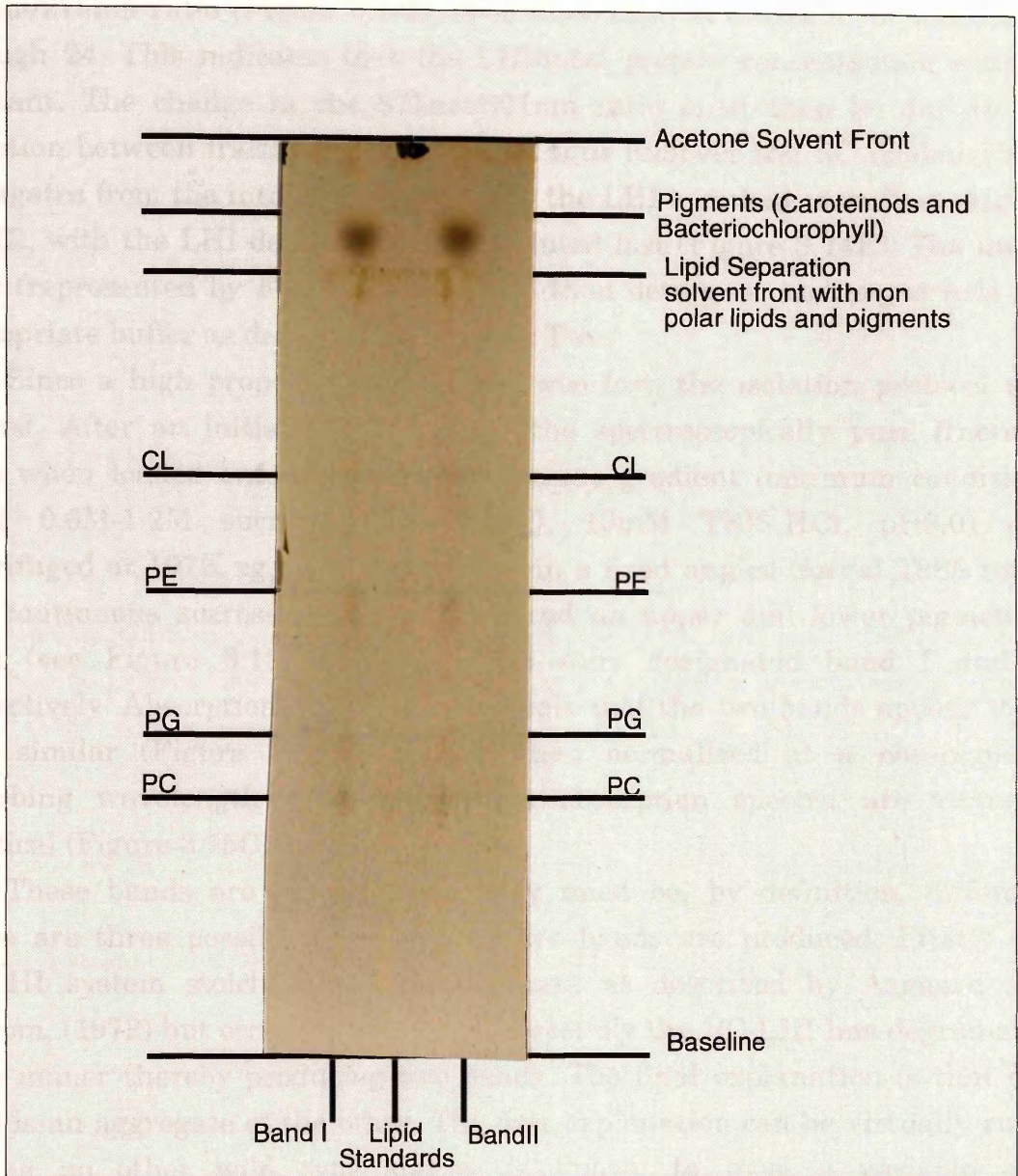


**Figure 3.16:** Thin layer chromatography from Bands I and II of *R. centenum*. The pigmented bands resulting from the sucrose gradients described in the body of the text had their lipids extracted using the method by Russell and Hardwood, (1979). The lipid extraction was loaded onto a TLC plate (Alugram® SILG, Macherey-Nagel, Düren, Germany) and pre-run in 100% Acetone to separate the pigments from the lipids. The acetone solvent front is marked above, as are the resultant pigment spots. Once air dried the TLC plate was then placed in the lipid extraction system (chloroform: methanol: acetic acid: water, 85:15:10:3.5) described by Russell and Hardwood, (1979). The solvent front was allowed to migrate to a point just below the pigment spot formed by the previous chromatographic run. Lipid standards were loaded between the two *R. centenum* extractions. The polar lipid standards were: phosphatidylcholine (PC), phosphatidylethanolamine (PE), phosphatidylglycerol (PG), and cardiolipin (CL). The above TLC plate was developed using molybdate spray to detect the phospholipids, then by iodine vapour for general lipid detection (see Imhoff *et al.*, 1982).

LHI) and 801nm (i.e. RC) change with fraction number. The overall 871nm/275nm ratio (Figure 3.14B, open diamonds) is constant for aliquots 6 through 24. This indicates that the LHI/total protein concentration ratio is constant. The change in the 871nm/801nm ratio must then be due to RC variation between fractions. Gel filtration thus removes the RC depleted *core* conjugates from the intact ones by eluting the LHI enriched *cores* first (Figure 3.14C), with the LHI depleted fractions eluted last (Figure 3.14E). The intact *cores* (represented by Figure 3.14D) were then detergent exchanged into the appropriate buffer as described in Chapter Two.

Since a high proportion of RC-LHI was lost, the isolation protocol was altered. After an initial DE52 column, the spectroscopically pure fractions were when loaded onto a continuous sucrose gradient (optimum conditions being 0.6M-1.2M sucrose, 0.1% LDAO, 10mM TRIS.HCl, pH8.0) and centrifuged at 197K xg, 4°C for 16 hours in a fixed angled Sorval T865 rotor. The continuous sucrose gradients produced an upper and lower pigmented band (see Figure 3.15A). These bands were designated band I and II respectively. Absorption spectroscopy reveals that the two bands appear to be very similar (Figure 3.15B). Indeed when normalised at a non-pigment absorbing wavelength (i.e. 650nm) the absorption spectra are virtually identical (Figure 3.15C).

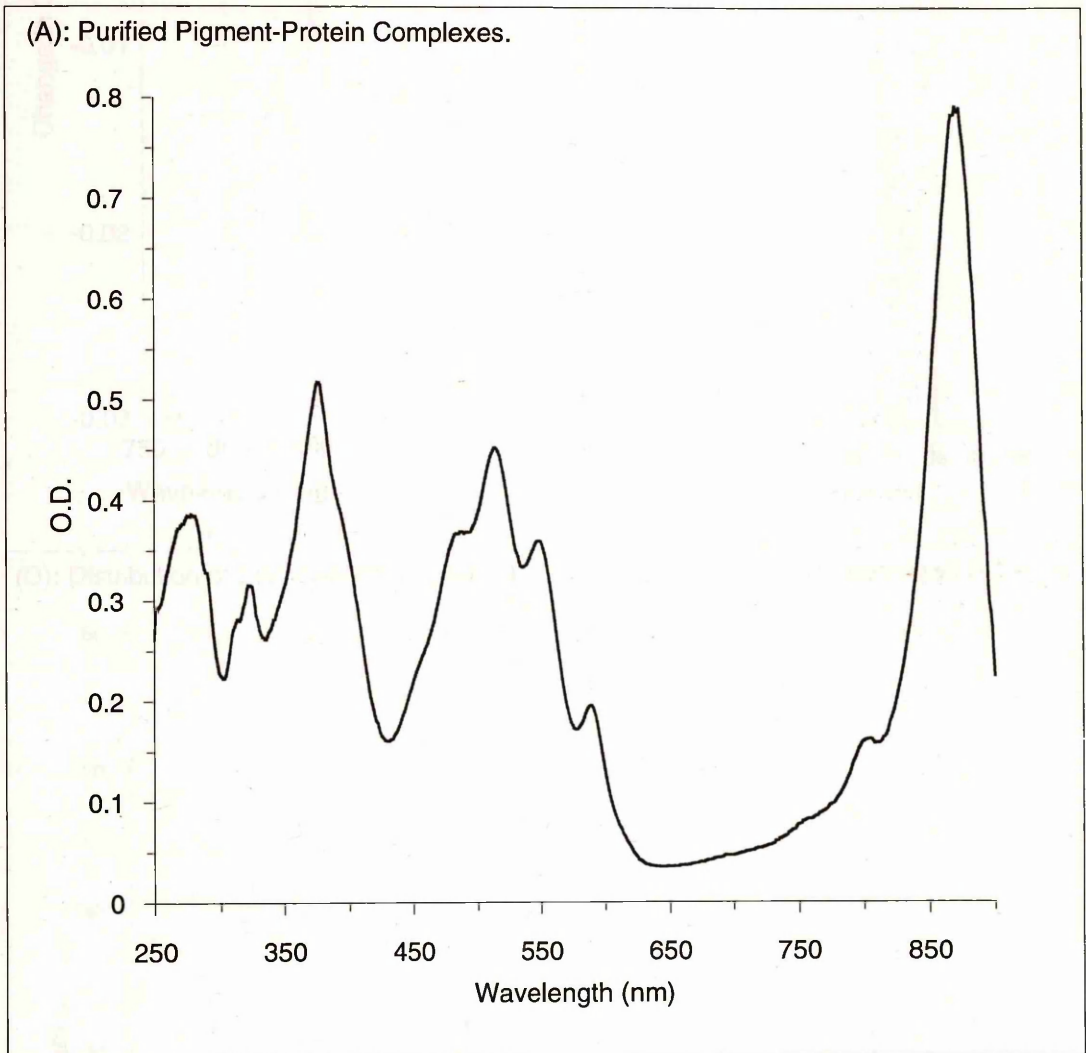
These bands are discrete thus they must be, by definition, different. There are three possible reasons why two bands are produced. Firstly the RC-LHI system stoichiometry is not fixed, as described by Aagaard and Siström, (1972) but occurs in two forms. Secondly the RC-LHI has degraded in some manner thereby producing two bands. The final explanation is that one band is an aggregate of the other. The first explanation can be virtually ruled out as no other wild type species is known to have a variable *core* stoichiometry (Aagaard and Siström, 1972). The degradation of one band to the other, or protein aggregation, are the more plausible alternatives.

During isolation, different amounts of lipid may be removed from each *core* resulting in RC-LHI conjugates of different densities. Using thin layer chromatography, no detectable difference occurred between bands I and II (Figure 3.16). Since no lipid differences could be established, the difference in density of the two bands must be due to another factor. Non-specific protein degradation may occur resulting in more than one band. The RC-LHI conjugate is made up of a number of polypeptides ( $\alpha$ ,  $\beta$ , L, H, and M), pigments (bacteriochlorophylls, bacteriopheophytins, and carotenoids), and lipids. If any of the above components were to randomly disassociate from the *core* then a smeared band would result. There is not much degraded protein at the top of

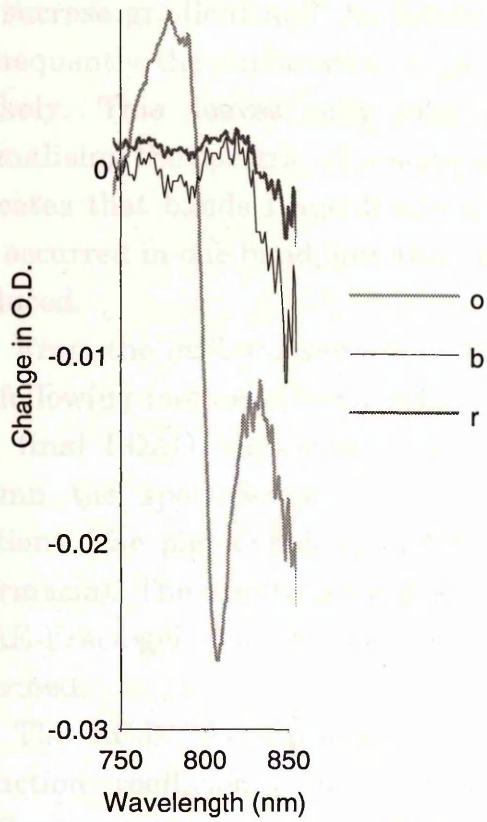


(B): Example of the  
Rafix Assay

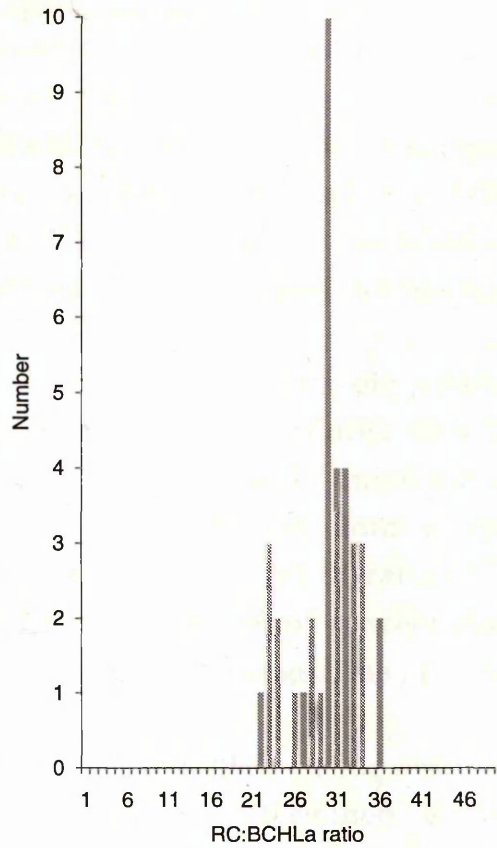
(A): Purified Pigment-Protein Complexes.



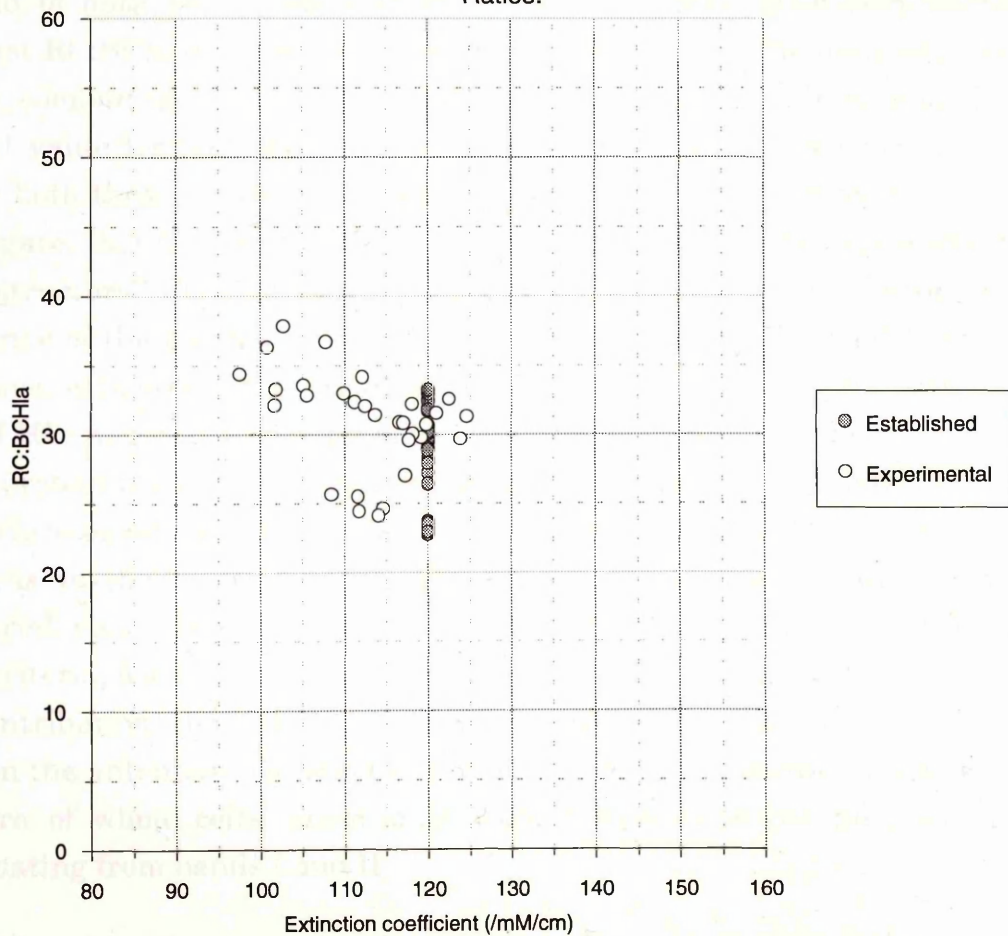
(B): Example of the  $\Delta$  Abs. at  $\sim 800\text{nm}$  for a Redox Assay.



(C): Distribution of RC:BChl Ratios



(D): Distribution of Established Calculated Extinction Coefficients and Associated RC:BChl Ratios.



the sucrose gradient and the bands appear not to be diffuse (Figure 3.17A). Consequently the explanation of general pigment-protein degradation is also unlikely. This leaves only one explanation, that of *core* aggregation. Normalising the spectra, at a non-pigment absorbing wavelength (i.e. 650nm), indicates that bands I and II are similar. This suggests that no relative RC loss occurred in one band, and that protein aggregation causes two bands to be produced.

From the initial observations the RC-LHI was then routinely purified by the following method. Firstly solubilised membranes were diluted with buffer to a final LDAO concentration of 0.1% (w/v). After a single anion exchange column the spectroscopically pure fractions were loaded onto a sucrose gradient. The pigmented band(s) was then subjected to gel filtration (S-200, Pharmacia). The spectroscopically pure fractions were then concentrated on DEAE-Fractogel 650(s) (Merck) and detergent exchanged as previously described.

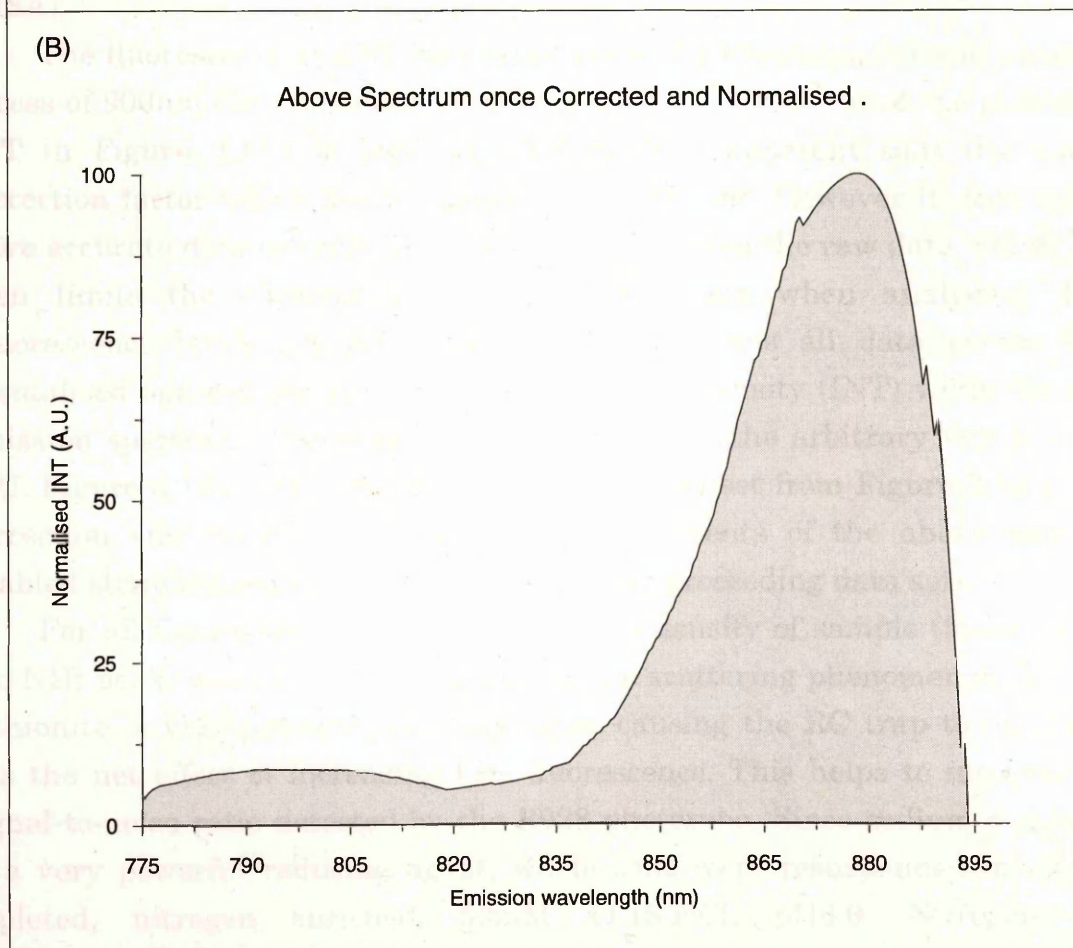
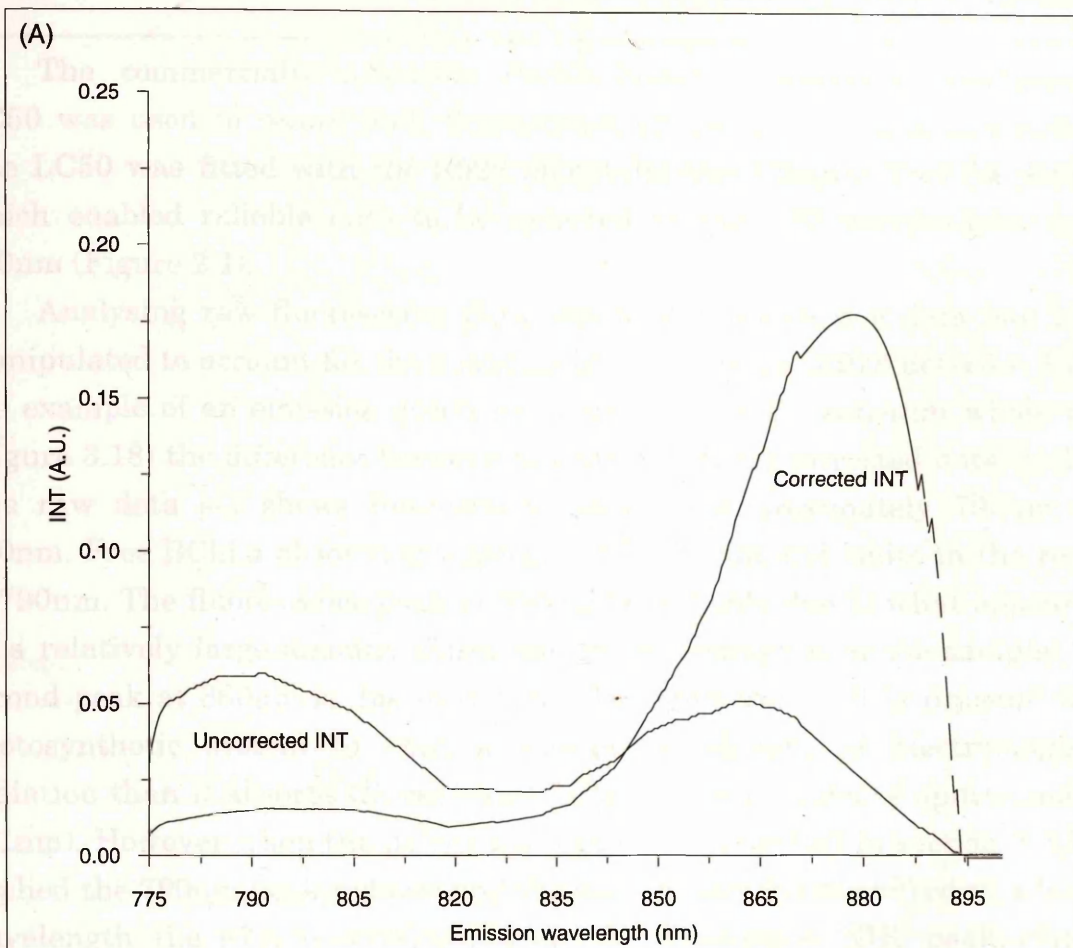
The RC:BChl  $a$  ratio was determined to be  $1:29 \pm 3$  (using established extinction coefficients) or  $1:31 \pm 3$ ,  $n=31$  (using a determined extinction coefficient at 880nm of  $113 \pm 7 \text{ mM}^{-1}\text{cm}^{-1}$ ,  $n=31$ ). The modal value for the RC:BChl  $a$  ratios were 30 and 32 respectively (Figures 3.17C and 3.32). The spread of data points, when plotting the determined extinction coefficients against RC:BChl  $a$  ratios, may suggest a slight slope to the data set. However when comparing the spread of data points (using correlation analysis) the modal value for both axes showed that no correlation was evident,  $r=-0.34$ . Since both these bands, once processed for protein purification, yield RC-LHI conjugate, this leaves us with the question as to which one represents the *in vivo* structure? Fluorescence spectroscopy was the tool used to establish *core* integrity of the purified RC-LHI from these two bands. For wild type *cores* it has been established that there is probably a fixed stoichiometry between RCs and LHI (Aagaard and Sistrom, 1972), therefore any differences may arise from protein-protein, protein-pigment, and pigment-pigment contacts.

Carotenoids are known to be able to transfer the energy from incident photons to the reaction centre thereby increasing the overall efficiency of bacterial photosynthesis (Goedheer, 1959; Frank and Cogdell, 1987). Using this criteria, a simple way to establish *core* integrity is to determine the degree of contribution that directly excited carotenoids make to energy transfer within the antennae. To establish a reference level the excitation and emission spectra of whole cells, membranes were compared to the purified proteins originating from bands I and II.

(A) Typical fluorescence emission spectrum from *R. centenum* whole cells excited at 520nm (maximum carotenoid absorbance wavelength). Actual data from the LC50-R928 with transmission filters in situ produce very low levels of fluorescence intensity (INT). This is due to large amounts of light scattering by the sample which results in poor detection of INT by the phototube. Accounting for phototube QE greatly enhances levels of fluorescence as you approach 900nm. In the uncorrected spectrum at 780 nm there is the maximum INT for the spectrum but once the QE correction equation has been applied (see text) this peak is greatly reduced and no longer is the maximum INT value. Although the maximum INT should be in excess of 900nm (see text) the limitations of the hardware and the scattering affect produce the artifact of a maximum peak at approximately 881nm. (B): Corrected and normalised emission spectrum. The corrected emission spectrum in (A) was normalised. This was achieved by giving the maximum corrected fluorescence data point the arbitrary INT value of 100 A.U. All other data points were then referenced to that maximum value. The decreasing INT for wavelengths greater than 880nm indicates that the correcting factor for the extreme wavelengths is insufficient, and also accounts for the jagged corrected INT readings.

**Figure 3.18:** (A) Typical fluorescence emission spectrum from *R. centenum* whole cells excited at 520nm (maximum carotenoid absorbance wavelength). Actual data from the LC50-R928 with transmission filters in situ produce very low levels of fluorescence intensity (INT). This is due to large amounts of light scattering by the sample which results in poor detection of INT by the phototube. Accounting for phototube QE greatly enhances levels of fluorescence as you approach 900nm. In the uncorrected spectrum at 780 nm there is the maximum INT for the spectrum but once the QE correction equation has been applied (see text) this peak is greatly reduced and no longer is the maximum INT value. Although the maximum INT should be in excess of 900nm (see text) the limitations of the hardware and the scattering affect produce the artifact of a maximum peak at approximately 881nm. (B): Corrected and normalised emission spectrum. The corrected emission spectrum in (A) was normalised. This was achieved by giving the maximum corrected fluorescence data point the arbitrary INT value of 100 A.U. All other data points were then referenced to that maximum value. The decreasing INT for wavelengths greater than 880nm indicates that the correcting factor for the extreme wavelengths is insufficient, and also accounts for the jagged corrected INT readings.

Carotenoids are known to be able to transfer the energy from incident photons to the reaction centre thereby increasing the overall efficiency of bacterial photosynthesis (Goodbeer, 1989; Frank and Cogdell, 1987). Using this criteria, a simple way to establish core integrity is to determine the degree of contribution that directly excited carotenoids make to energy transfer within the antennae. To establish a reference level the excitation and emission spectra of whole cells, membranes were compared to the purified proteins originating from bands I and II.



The commercially available Perkin-Elmer fluorescence spectrometer LC50 was used to record both fluorescence emission and excitation spectra. The LC50 was fitted with the R928 phototube (see Chapter Two for details) which enabled reliable data to be collected in the NIR wavelengths up to 900nm (Figure 2.1).

Analysing raw fluorescence data was inappropriate, the data had to be manipulated to account for the quantum efficiency of the R928 detector. Using the example of an emission spectrum obtained from *R. centenum* whole cells (Figure 3.18) the difference between raw and QE-R928 corrected data is clear. The raw data set shows fluorescence peaks at approximately 790nm and 860nm. Free BChl *a* absorbs at approximately 772nm and emits in the region of 790nm. The fluorescence peak at 790nm is probably due to what appears to be a relatively large amount of free bacteriochlorophyll *a* in the sample. The second peak at 860nm is due to the RC-LHI fluorescence. It is unusual for a photosynthetic system to emit a shorter wavelength of electromagnetic radiation than it absorbs (*R. centenum* NIR absorption peak is approximately 871nm). However when the polynomial equation (described in section 2.5.1) is applied the 790nm peak reduces and the second peak is red shifted to a longer wavelength (i.e. 871nm → 881nm) than the absorption NIR peak (Figure 3.18A).

The fluorescence of LHI from members of the Rhodospirillaceae occurs in excess of 900nm (for an example see Deinum *et al.*, 1991). Since the maximum INT in Figure 3.18A is less than 900nm it is apparent that the simple correction factor which has been applied is insufficient. However it does enable more accurate data collection and interpretation than the raw data alone. This then limits the observations that can be made when analysing data. Fluorescence levels are arbitrary units (A.U.), thus all data points were normalised against the maximum fluorescence intensity (INT) value for each emission spectrum. The maximum INT was given the arbitrary value of 100 A.U. Figure 3.18B illustrates the normalised data set from Figure 3.18A. The correction and normalisation of INT measurements of the above example enabled standardised data manipulation for all proceeding data sets.

For all fluorescence studies an optimum density of sample (measured at the NIR peak) was established to counter the scattering phenomenon. Sodium dithionite (a very powerful reducing agent causing the RC trap to be closed) has the net effect of increasing LHI fluorescence. This helps to increase the signal-to-noise ratio detected by the R928 phototube. Since sodium dithionite is a very powerful reducing agent, whole cells were resuspended in oxygen depleted, nitrogen enriched, 50mM TRIS.HCl, pH8.0. Nitrogen was

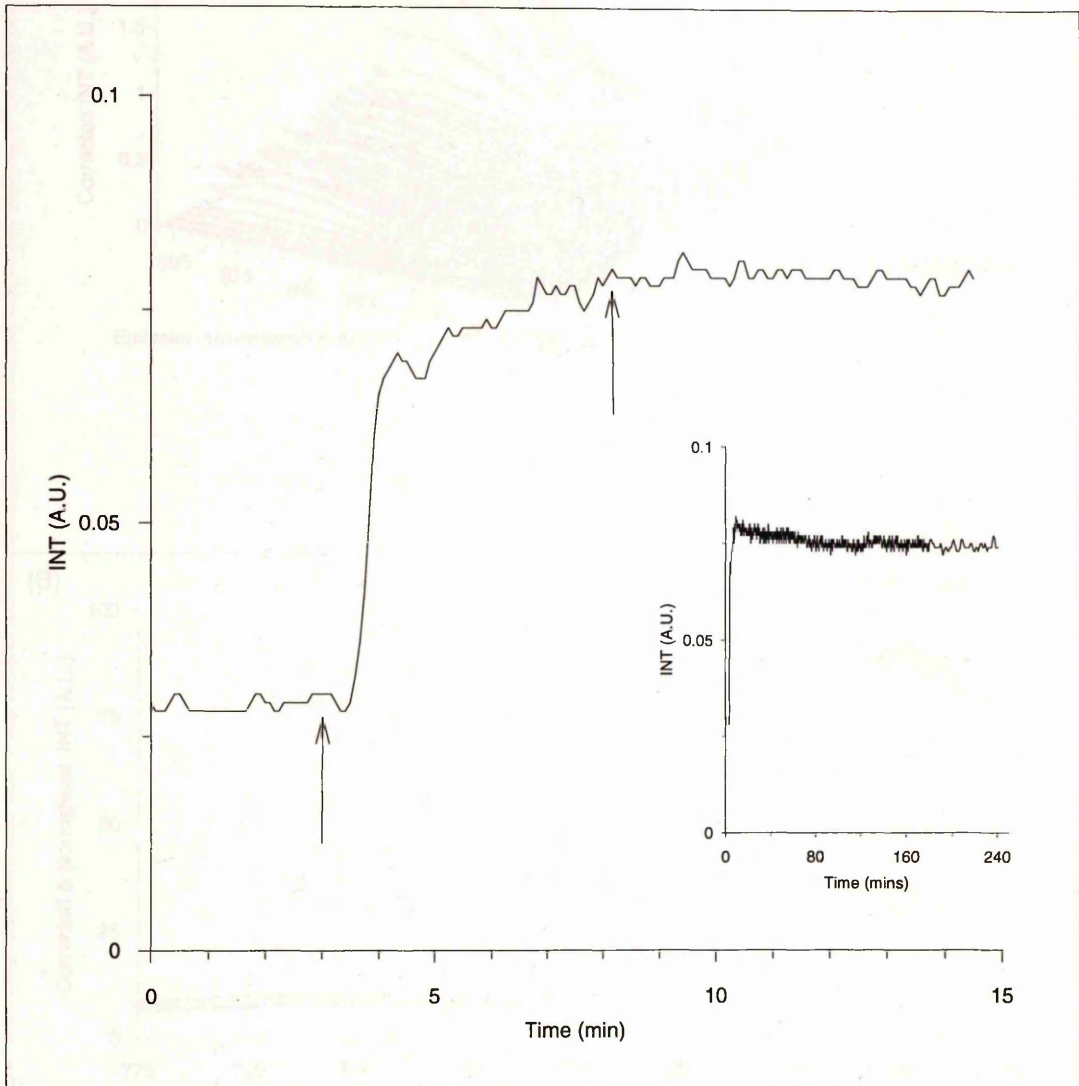


**Figure 3.19:** Increased *R. centenum* whole cell fluorescence due to addition of sodium dithionite. Addition of  $6\mu\text{M}$  sodium dithionite causes the maximum increase in uncorrected fluorescence detectable by the LC50-R928 hardware. On addition of dithionite (right arrow) a lag of 5 mins occurs until a raised level of INT is achieved (left arrow). The raised fluorescence is maintained for at least 4 hours (insert).

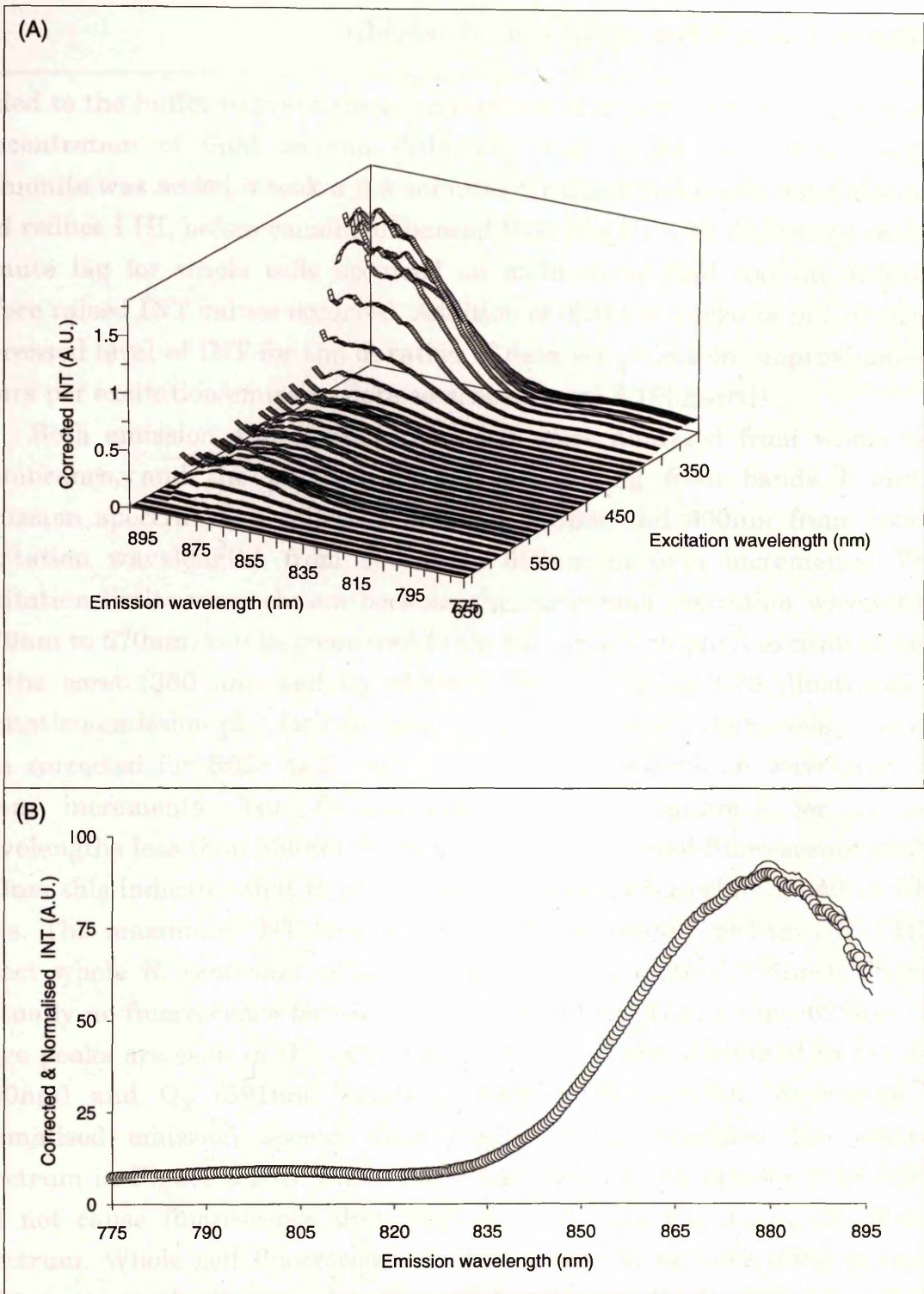


**Figure 3.20:** Emission spectra for whole cell *R. centenum*. (A): Corrected 3D emission spectrum for *R. centenum* whole cells. Spectra were collected every 10nm in this example and corrected for R928 quantum efficiency. Note that the fluorescence for wavelengths greater than 630nm are negligible consequently when averaging the normalised spectra only excitation wavelengths between 350nm and 630nm were used. All the spectra indicate a reduced signal-to-noise ratio for wavelengths in excess of 895nm. This is due to a combination of poor whole cell fluorescence and limitations of the hardware used. (B): Averaged, corrected and normalised emission spectra for *R.centenum* whole cells (350nm 630nm excitation wavelengths). The average value (open circles) is flanked by the standard errors (solid lines),  $n=29$ . Both spectra (A and B) but especially figure A indicated fluorescence of free bacteriochlorophyll *a* by raised fluorescence observed at approximately 790nm. This indicates that not all the incident radiation is being passed to LHI.

added to the buffer to lower the concentration of oxygen present. An optimum concentration of  $6\mu\text{M}$  sodium dithionite was established. When sodium dithionite was added it took a few minutes for the dithionite to enter the cells, and reduce LHI, before causing enhanced INT. Figure 3.19 illustrates that a 5 minute lag for whole cells occurred on addition of  $6\mu\text{M}$  sodium dithionite before raised INT values occurred. Addition of dithionite results in a continual increased level of INT for the duration of data set collection (approximately 4 hours per excitation/emission data sets, see Figure 3.19[insert]).

Both emission and excitation spectra were analysed from whole cells, membranes, and the purified RC-LHI originating from bands I and II. Emission spectra were collected between 775nm and 900nm from incident excitation wavelengths from 350nm to 650nm in 5nm increments. These excitation limits were chosen because the carotenoid excitation wavelengths (470nm to 570nm) can be compared to the bacteriochlorophyll excitation peaks at the *soret* (380 nm) and  $Q_x$  (590nm) bands. Figure 3.20 illustrates the excitation/emission plot for one data set of *R. centenum* whole cells. The data was corrected for R928 Q.E. and plotted against excitation wavelengths at 10nm increments. The fluorescence levels are minimal for emission wavelengths less than 830nm. Since there is only a small fluorescence peak at 790nm this indicates that there is very little free bacteriochlorophyll in whole cells. The maximum INT level occurs at approximately 881nm (RC-LHI in intact whole *R. centenum* cells absorbs at approximately 874nm). There is virtually no fluorescence for excitation wavelengths greater than 625nm. Two large peaks are seen in the excitation spectra and are attributed to the *soret* (380nm) and  $Q_x$  (591nm) bands of bacteriochlorophyll *a*. Averaging the normalised emission spectra from Figure 3.20A produces the emission spectrum in Figure 3.20B. Since excitation wavelengths greater than 620nm did not cause fluorescence they were omitted from the averaged emission spectrum. Whole cell fluorescence studies proved to be very difficult due to light scattering by the samples. Corrected and normalised excitation/emission spectra were then obtained for membranes and purified proteins originating from bands I and II, see Figure 3.21.

To collect data sets with a higher signal-to-noise ratio, a different approach was used. Multiple scans were collected for a single emission wavelength. The emission wavelength chosen was 860nm (the maximum fluorescence from uncorrected emission spectra). For each data set the sampling rate was reduced from 100 to 50nm  $\text{min}^{-1}$ . Each data set comprised of 10 emission spectra. The multiple emission spectra were averaged and then normalised as before. One data set is shown in Figure 3.22. The absorption

added to the buffer to lower the concentration of oxygen present. An optimum concentration of 0.1M sodium dithionite was established. When sodium dithionite was added it took a few minutes for the dithionite to enter the cells, and reduce LIII, before causing enhanced INT. Figure 3.19 illustrates that a 5 minute lag for whole cells occurred in addition to 0.1M sodium dithionite before raised INT values occurred. Addition of 0.1M sodium dithionite to a continuous increased level of INT for the duration of data set collection was approximately 4 hours per excitation/emission data set, see Figure 3.19 (b).

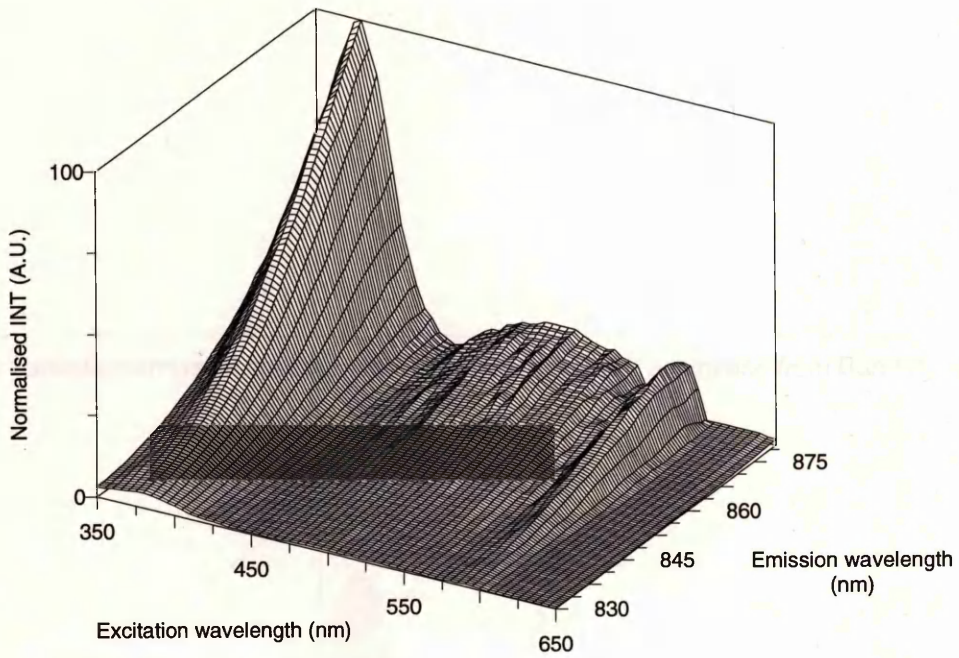
Both emission and excitation spectra were measured for membranes, membranes and the purified RC-LHI originating from bands I and II. Emission spectra were collected between 700nm and 900nm, excitation excitation wavelengths from 350nm to 650nm in 20nm increments. These excitation limits were chosen because the maximum excitation wavelengths (470nm to 670nm) can be compared to the bacteriochlorophyll excitation peaks

**Figure 3.21:** 3D Emission/excitation spectra for a batch of *R. centenum* membranes and isolated RC-LHI originating from bands I and II. The fluorescence data was corrected and normalised as described in section 2.5.1. (A): 3D emission/excitation spectrum for membranes. Two distinct peaks occurred at approximately 380nm (~100 A.U.) and 590nm (~25 A.U.) which are due to the  $Soret$  and  $Q_x$  bands of bacteriochlorophylla respectively. Between these two peaks lies a region of raised fluorescence with a maximum fluorescence value of approximately 20 A.U. (B): 3D Emission/excitation spectrum for purified RC-LHI originating from band I of a sucrose gradient (see section 2.6.2). (C): 3D Emission/excitation spectrum for purified RC-LHI originating from band II of a sucrose gradient. For both emission/excitation spectra for purified RC-LHI the signal to noise ratio is less when compared to that for the membrane spectrum. This was considered to be due to the presence of detergent in the sample.

normalised emission spectra from Figure 3.20A produce the emission spectrum in Figure 3.20B. Since excitation wavelengths greater than 620nm did not cause fluorescence they were omitted from the averaged emission spectrum. Whole cell fluorescence studies proved to be very difficult due to light scattering by the samples. Corrected and normalised excitation/emission spectra were then obtained for membranes and purified RC-LHI originating from bands I and II, see Figure 3.21.

To collect data sets with a higher signal-to-noise ratio, a different approach was used. Multiple scans were collected for a single emission wavelength. The emission wavelength chosen was 800nm (the maximum fluorescence from uncorrected emission spectra). For each data set the sampling rate was reduced from 100 to 50nm  $min^{-1}$ . Each data set comprised of 10 emission spectra. The multiple emission spectra were averaged and then normalised as before. One data set is shown in Figure 3.22. The absorption

(A): Excitation/emission spectrum for *R.centenum* membranes.



(B): Excitation/emission spectrum for *R.centenum* RC-LHI originating from Band I.

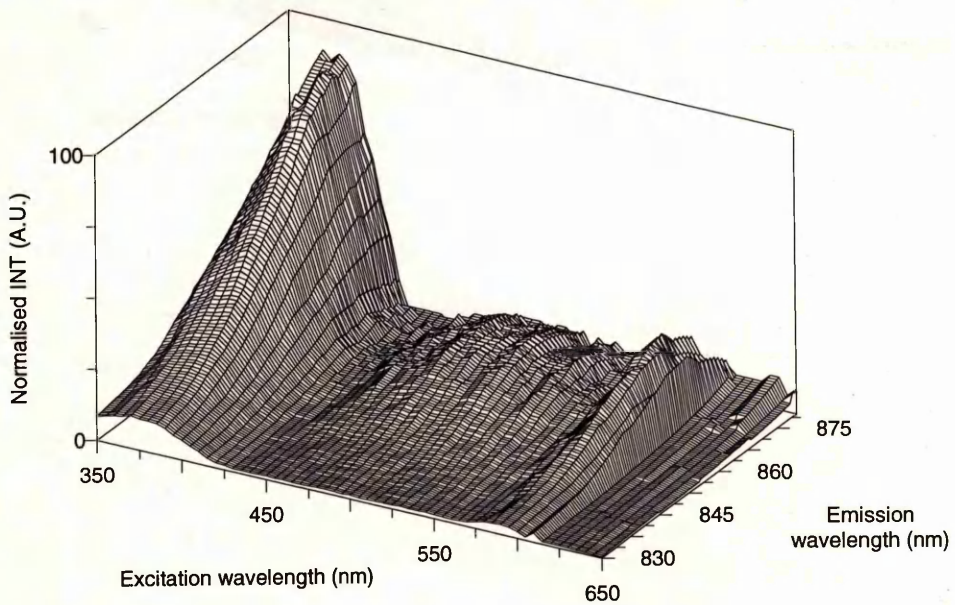
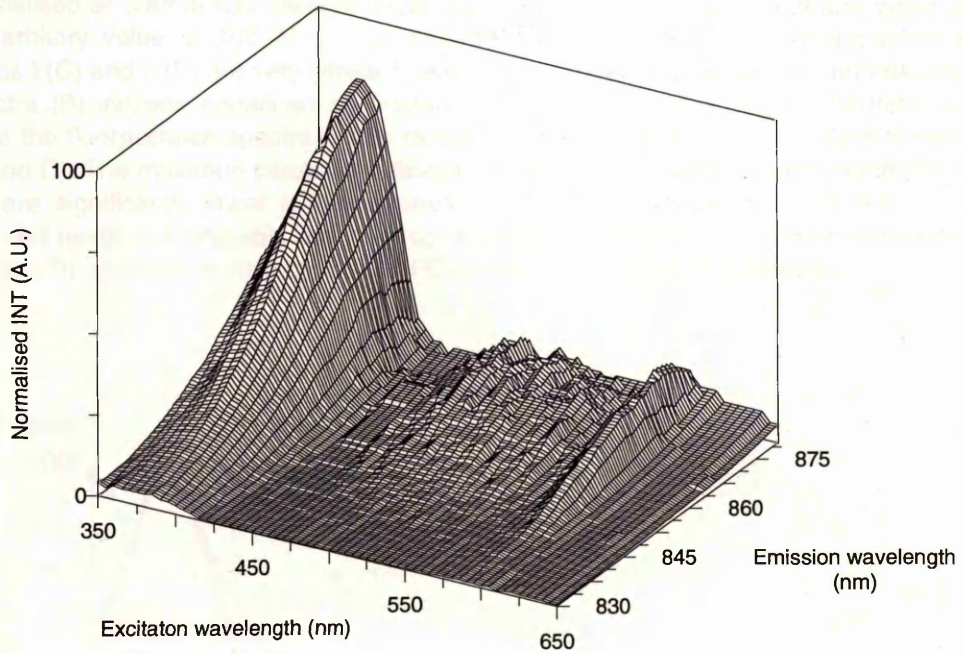
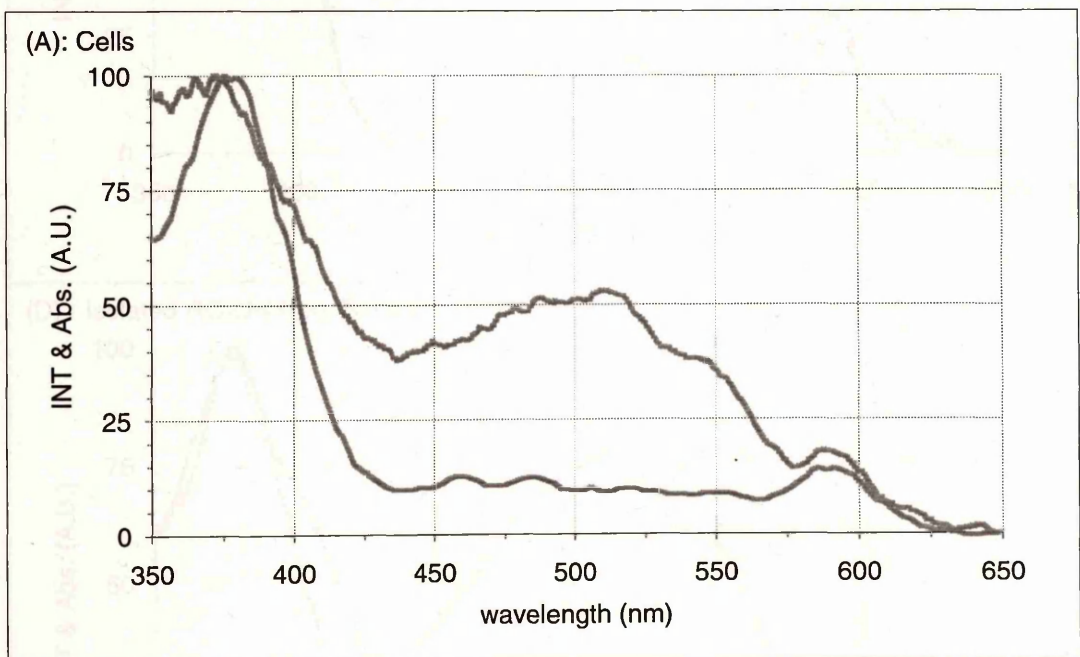


Figure 3.22: Average excitation/emission spectra for *R. centenum* RC-LHI originating from Band II.

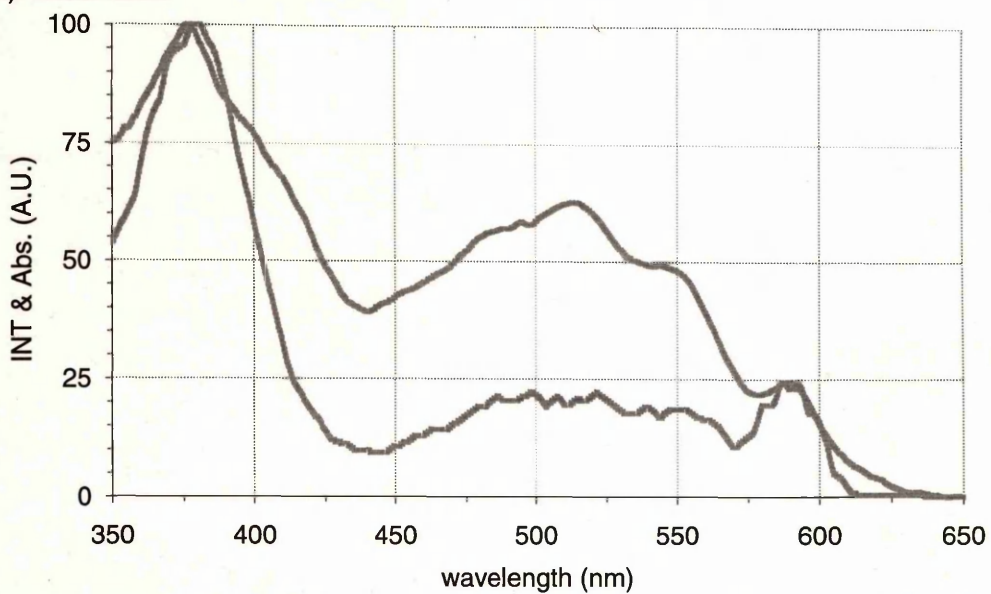
(C): Excitation/emission spectrum for *R. centenum* RC-LHI originating from Band II.



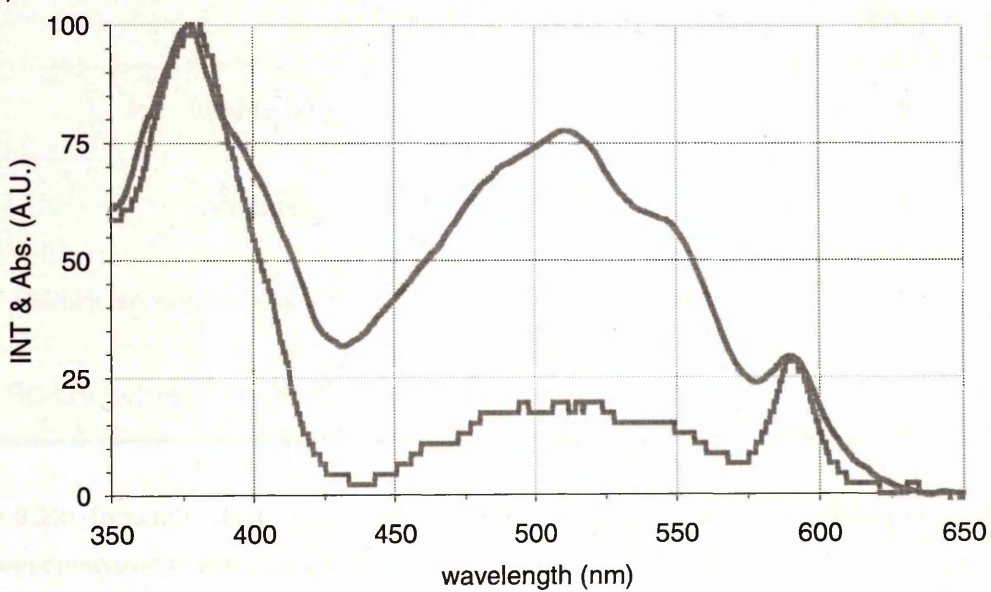
**Figure 3.22:** Averaged excitation spectra for a batch of *R. centenum*. The spectra are from whole cells (A), membranes (B) and purified *core* conjugate originating from bands I (C) and II (D). All spectra are corrected and normalised as described in the text. The excitation spectra illustrate that the *soret:Qx* fluorescence ratio is generally constant however for the whole cell excitation spectra is somewhat higher. This difference may be due to self absorption, or scattering; see text. All spectra (absorption and excitation) are normalised at 590nm (*Qx* band of bacteriochlorophyll *a*) with the maximum value given the arbitrary value of 100 A.U. The absorption and excitation spectra originating from bands I (C) and II (D) are very similar to each other. Both the whole cell (A) and membrane spectra (B) indicate enhanced absorption in the near U.V.-*soret* region (350nm-380nm) while the fluorescence spectra in this range are very similar to that of purified complexes (C and D). The maximum carotenoid absorption peaks for C and D are the same (78 A.U.) but are significantly lower in membranes (63 A.U.) and whole cells (53 A.U.). These reduced levels are probably due to a combination of the very low sample concentration (<0.1 O.D) and poor detection by the UV-PC2101 UV-VIS spectrophotometer.



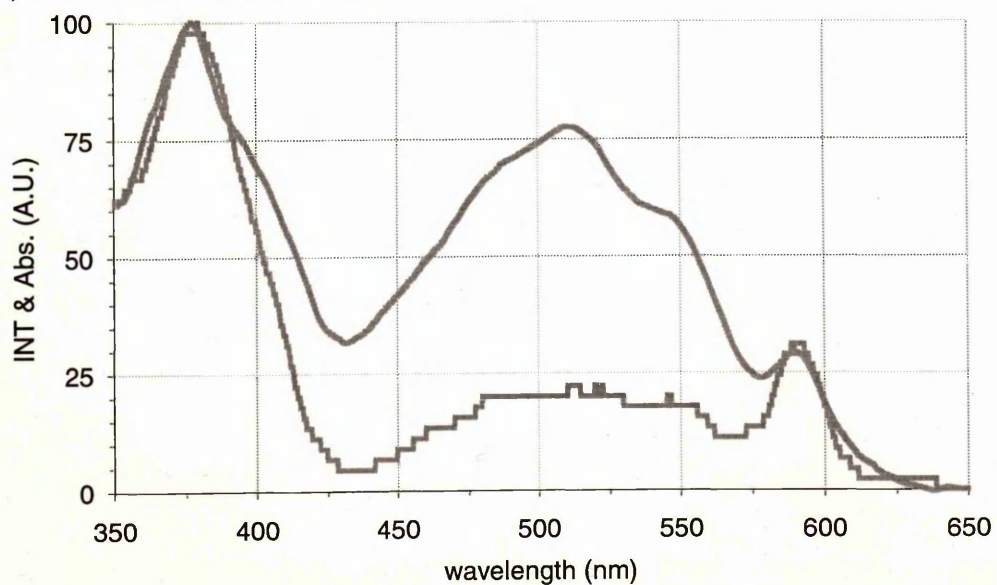
(B): Membranes



(C): Isolated RC-LHI from Band I



(D) : Isolated RC-LHI from Band II



	%Eff.at 530nm±S.D.	%Eff. at Max. Car. Abs.±S.D.	number of replicates
whole cells	24±1.5	29±3.9	3
membranes	31±3.5	33±2.3	2
RC-LHI isolated from band I	31±5.9	30±6.6	2
RC-LHI isolated from band II	25±2.4	26±3.3	4

**Figure 3.23:** Tabulated data for the %efficiency (%Eff.) for carotenoid transfer in *R. centenum* to LHI when compared to absorbance.

excitation spectra are of different scales and units, but they are both linear units. Consequently the data was normalised at the  $Q_x$  bacteriochlorophyll band (590nm) with the maximum normalised data point given the arbitrary value of 100 A.U. In Figure 3.22 the absorbance and fluorescence spectra are similar for the BChl *a* bands, consequently significant specimen self absorption has not occurred. Direct comparisons were then made pertaining to the rôle of carotenoids in the isolated RC-LHI, based on the protocol by van Grondelle *et al.*, (1982).

Carotenoids have a triple absorption spectra. Since no comparable peaks occurred in the excitation spectra (Figure 3.22) the averaged carotenoid efficiencies were calculated by comparing the absorption and excitation values at 530nm and at the wavelengths that produced the highest absorbance levels in the carotenoid visible absorbing range (450nm-570nm).

In *R. centenum* the efficiency of energy transfer to LHI is approximately 30% when the carotenoids are directly excited (Figure 3.23). There is no statistical difference in carotenoid activity between any of the states of protein purification. It is not surprising that the carotenoid efficiency in *R. centenum* is similar to the comparable value for *R. rubrum* (Goedheer, 1959) since both have similar carotenoids.

In summary the purified RC-LHI from *R. centenum*, originating from Bands I and II, is spectroscopically identical with no differences observed by SDS-PAGE (Figure 3.33).

### 3.3.2 *R. rubrum*:

The isolation of pigment-protein complex from this strain of *R. rubrum* was based on Dawkins, (1988). Membranes were prepared (see section 2.3) and diluted to an optical density of  $50 \text{ cm}^{-1}$ . They were then solubilised with 1.0% (w/v) LDAO as described in section 2.6.1 and loaded on to DE52 (Whatman) anion exchange columns (see section 2.6.3). Two DE52 columns were used to purify the RC-LHI; the spectroscopically pure elute fractions from the first were loaded on to the second. The spectroscopically pure elute fractions from the second column were concentrated by another DE52 column (section 2.6.3) and then passed through a gel filtration column (S-200 sephacryl, Pharmacia; section 2.6.4). This produced purified RC-LHI which was then detergent exchanged, concentrated, and de-salted as described in Chapter Two. An absorption spectrum of purified RC-LHI (salt free) is shown in Figure 3.24A. The RC-LHI was then characterised by the protocol described in section 2.6.7. Figure 3.24C suggests that for purified RC-LHI the RC:BChl *a* ratio is  $1:30 \pm 4$ ,  $n=74$  using the established coefficients for both the bacteriochlorophyll and RC-Redox assays. When using the experimentally determined extinction coefficients the RC:LHI ratios alter slightly to  $1:33 \pm 5$ . The relationship between RC:BChl *a* ratio and determined extinction coefficients (Figure 3.24D) suggests that the standard deviation (S.D.) for the determined extinction coefficient at 880nm is spread evenly from the mean,  $116 \pm 6 \text{ mM}^{-1} \text{ cm}^{-1}$ ,  $n=74$ .

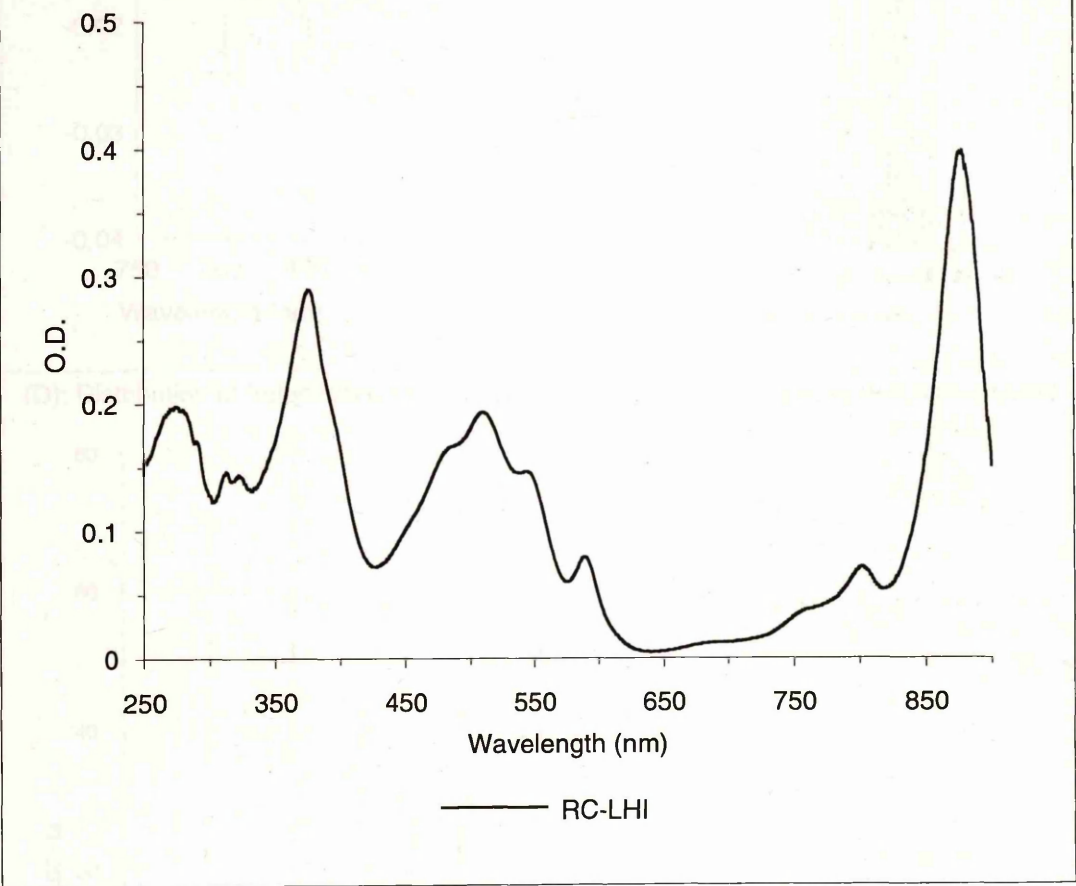
The isolation of pigment-protein conjugates from the strain of *R. rubrum* was based on Dawkins (1988). Membranes were prepared (see section 2.3) and diluted to an optical density of 50  $\text{cm}^{-1}$ . They were then solubilised with 1.0% ( $w/v$ ) IDAO as described in section 2.6.1 and loaded on to DEAE (Whatman) anion exchange columns (see section 2.6.3). Two DEAE columns were used to purify the RC-LHI; the spectroscopically pure eluate fractions from the first were loaded on to the second. The spectroscopically pure eluate fractions from the second column were concentrated by another DEAE column (section 2.6.3) and then passed through a gel filtration column (S-200 Sepharose, Pharmacia; section 2.6.4). This produced purified RC-LHI which was then detergent exchanged, concentrated, and de-salted as described in chapter Two. An absorption spectrum of purified RC-LHI (see text) is shown in Figure 3.24A. The RC-LHI was then characterised by the protocol described in section 2.6.7.

**Figure 3.24:** Spectroscopic characterisation of purified *R. rubrum* strain S1 RC-LHI conjugate. (A): Absorption spectrum of purified *R. rubrum* RC-LHI. (B): An example of the change in absorbance detected at  $\sim 800\text{nm}$  during a Redox assay (see section 2.6.7). (C): Distribution of RC:BChl *a* ratios determined using the established extinction coefficients (see section 2.6.7). The spread of RC:BChl *a* appears to be gaussian-like with a mean ratio of  $1:30 \pm 4$ ,  $n=74$ . The modal value is 1:32. (D): Distribution of the established and experimentally determined extinction coefficients and their associated RC:BChl *a* ratios. The experimentally determined coefficient for BChl *a* at  $880\text{nm}$  was determined to be  $111 \pm 6 \text{ mM}^{-1} \text{ cm}^{-1}$ ,  $n=74$ . The mean RC:BChl *a* ratio using these values is  $1:33 \pm 5$  with an associated modal value of 1:33. All errors are standard deviations (S.D.).

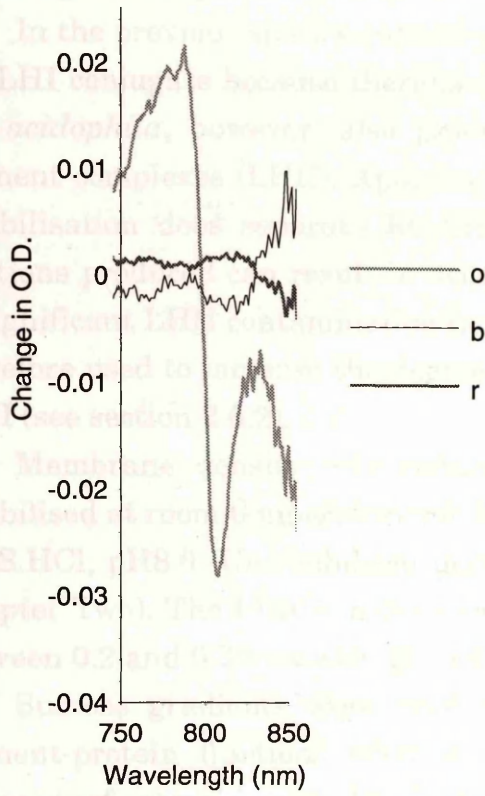
(B): Example of the J Abs. of RC-LHI in a Purified Lysate.



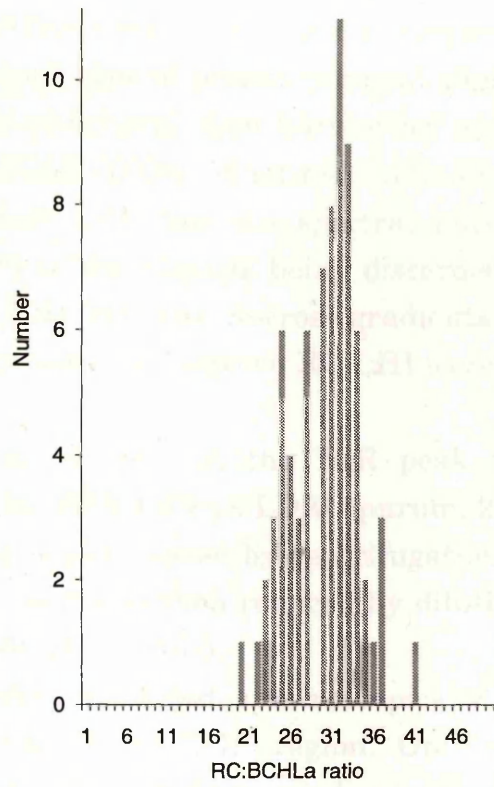
(A): Absorption Spectrum of Purified RC-LHI



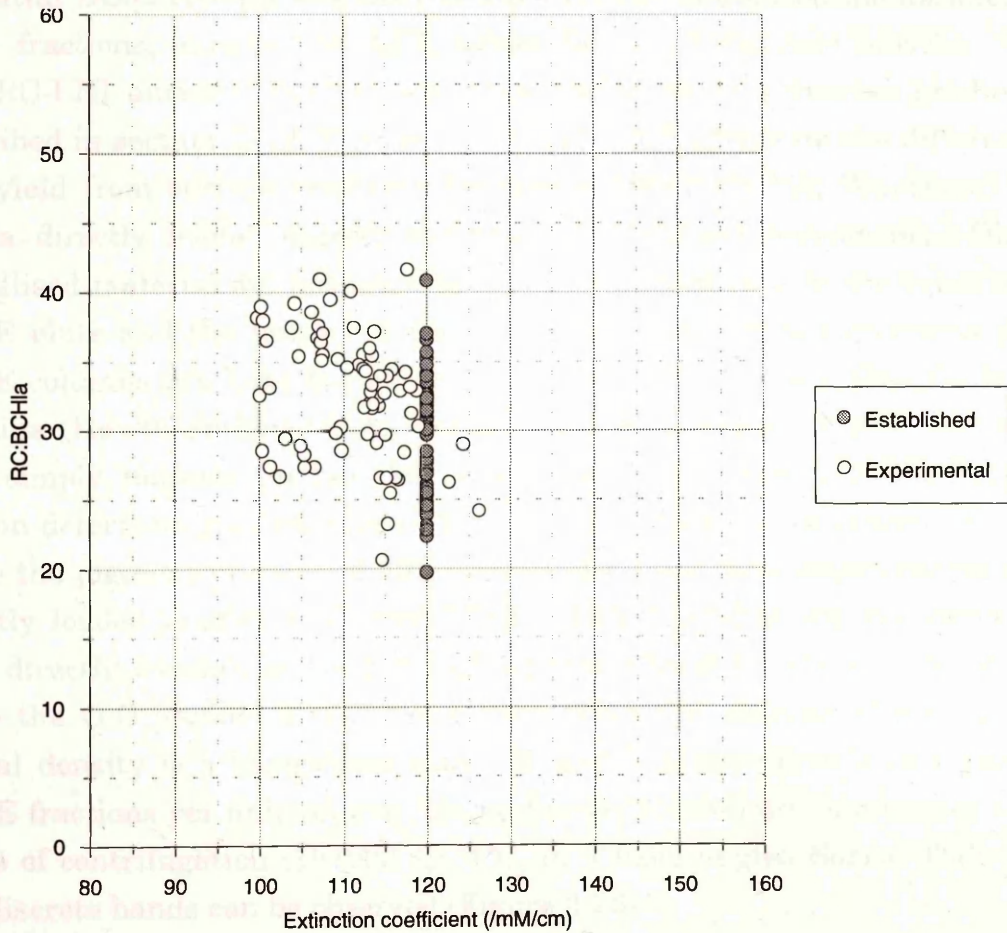
(B): Example of the  $\Delta$  Abs. at  $\sim 800\text{nm}$  from a Redox Assay.



(C): Distribution of RC:BChl Ratios.



(D): Distribution of Established and Calculated Extinction coefficients and Associated RC:BChl ratios.



### 3.3.3 *Rp. acidophila*:

In the previous species sucrose gradients were not required to prepare the RC-LHI conjugate because there is only one type of protein-pigment complex. *Rp. acidophila*, however, also produces peripheral light-harvesting protein-pigment complexes (LHII). Applying a DEAE (DE52, Whatman) column after solubilisation does separate RC-LHI from LHII but the spectral purity of fractions produced can result in over 70% of the aliquots being discarded due to significant LHII contamination in RC-LHI fractions. Sucrose gradients were therefore used to increase the degree of separation between RC-LHI (*core*) and LHII (see section 2.6.2).

Membrane density was reduced to  $50 \text{ cm}^{-1}$  at the NIR peak when solubilised at room temperature for 15 min. with 1.0% *w/v* LDAO purum, 20mM TRIS.HCl, pH8.0. Unsolubilised material was removed by centrifugation (see Chapter Two). The LDAO in the supernatant was then reduced by dilution to between 0.2 and 0.3% *w/v* with 20 mM TRIS.HCl, pH8.0.

Sucrose gradients were used as they produced spectroscopically pure pigment-protein fractions when examined in the NIR region. Only small volumes of sample may be loaded on to a sucrose gradient otherwise overloading results causing the pigmented bands to overlap. To overcome this an initial DE52 column was used to separate the solubilised membranes into three fractions, enriched RC-LHI, mixed RC-LHI-LHII, and enriched LHII. The RC-LHI enriched fraction was then loaded on to a sucrose gradient as described in section 2.6.2. Figures 3.25A and 3.25B illustrate the difference in *core* yield from sucrose gradients between a DEAE (DE52, Whatman) elute and a directly loaded sucrose gradient of solubilized membranes. Directly solubilised material did not migrate to the same positions in the tubes as the DEAE elute and the latter did not appear to have any proteinaceous pellet. DEAE columns can have the ability to separate loosely associated lipids from proteins (Hawthornthwaite, A., personal communication). The DEAE elutes may simply migrate further due to reduced lipid content in the pigment-protein-detergent-lipid micelles (Figure 3.25B). If lipids were removed it would make the pigment-proteins of different density than their counterparts in the directly loaded gradients (Figure 3.25A). Both diagrams are the same scale thus directly comparing their RC-LHI peaks (Band II) shows that at least twice the O.D. (which means more than twice the amount of protein since optical density is a logarithmic scale) of *core* is produced in a *core* enriched DEAE fractions per unit volume. Using directly solubilised membranes after 5 hours of centrifugation (197000 xg, 4°C, in a fixed angled Sorval T865 rotor) two discrete bands can be observed (Figure 3.26).

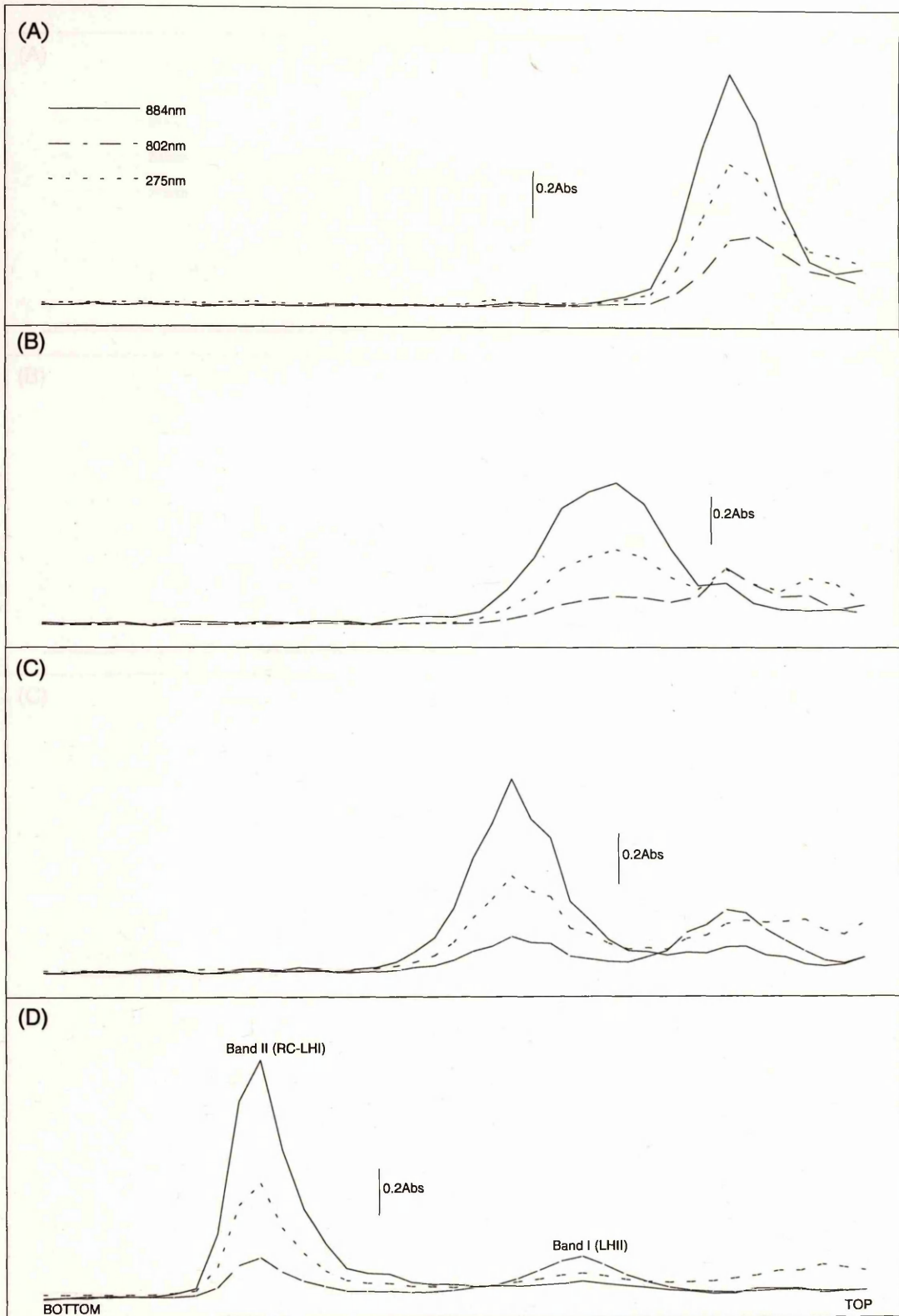


**Figure 3.25A:** Optical Density measurements from a continuous sucrose gradient (0.3M-1.2M, 0.2% LDAO, 10mM Tris.HCl, pH8.0) of *Rp. acidophila* strain 7750. The sample has been enriched with *core* conjugate. Absorbance measurements were taken after 1 (A), 3 (B), 5 (C) and 16 hours (D). Centrifugation occurred at 197000 xg, 4°C in a Sorval T865 rotor. Measurements at 884nm illustrate the amount of LHI (RC-LHI conjugate), while 802nm depicts the amount of antenna pigment-protein present and 275nm indicates general protein (aromatic amino acid residues) levels. After five hours two discrete bands can be detected and isolated.

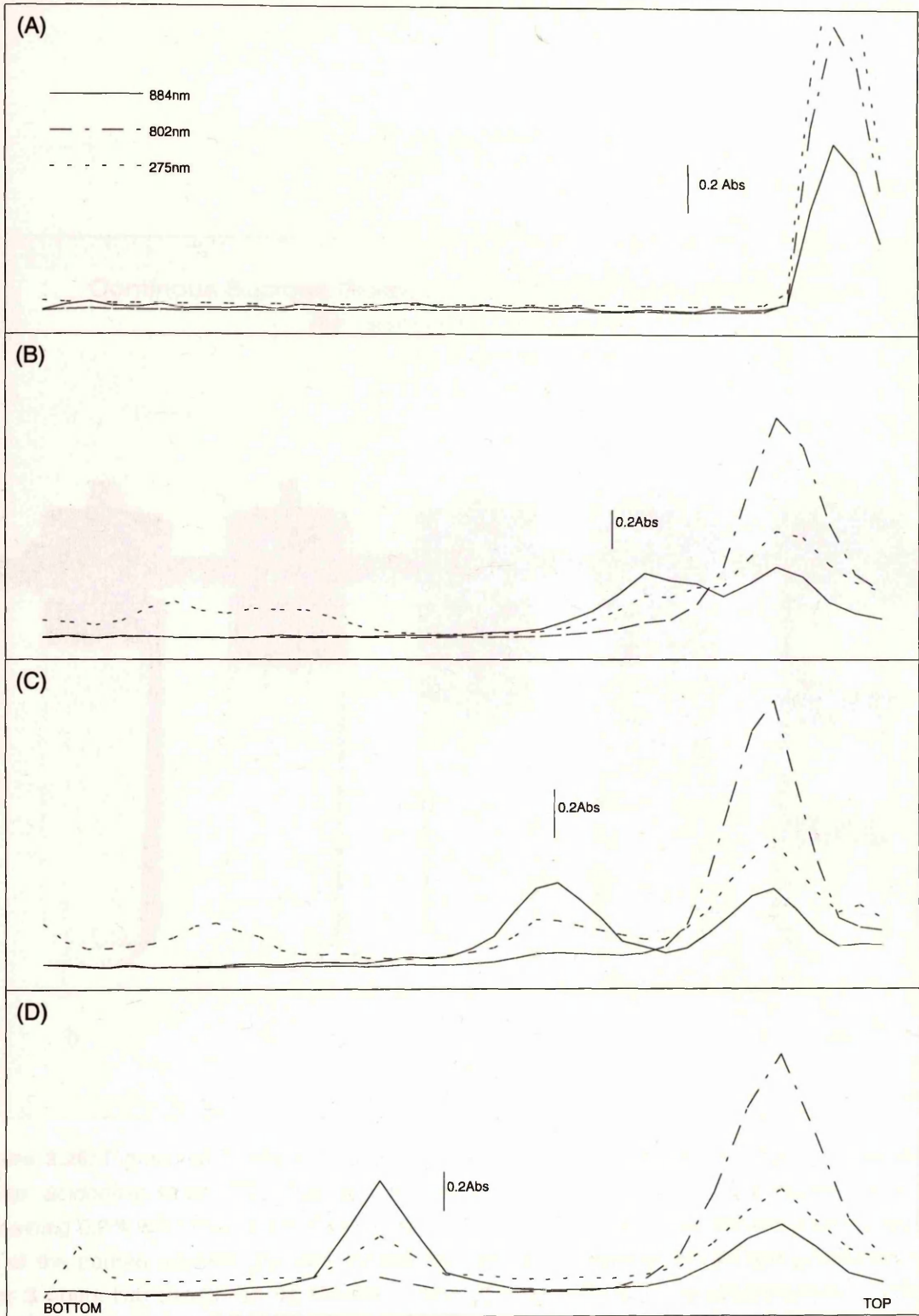


**Figure 3.25B:** Optical Density measurements from a continuous sucrose gradient (0.3M-1.2M, 0.2% LDAO, 10mM Tris.HCl, pH8.0) for solubilised *Rp. acidophila* strain 7750 membranes. The spectra were obtained after (A) 0 (control), 3 (B), 5 (C) and 16 hours (D). samples were centrifuged at 197000 xg, 4°C in a Sorval T865 rotor. The measurements at 884nm illustrate the amount of LHI (RC-LHI conjugate), 802nm depicts the amount of antenna pigment-protein present, while 275nm indicates general protein (aromatic amino acid residues) levels. After five hours or more two discrete bands can be detected.

Continuous Sucrose Gradients from Solubilised Membranes of  
*Rp. acidophila* strain 7750.

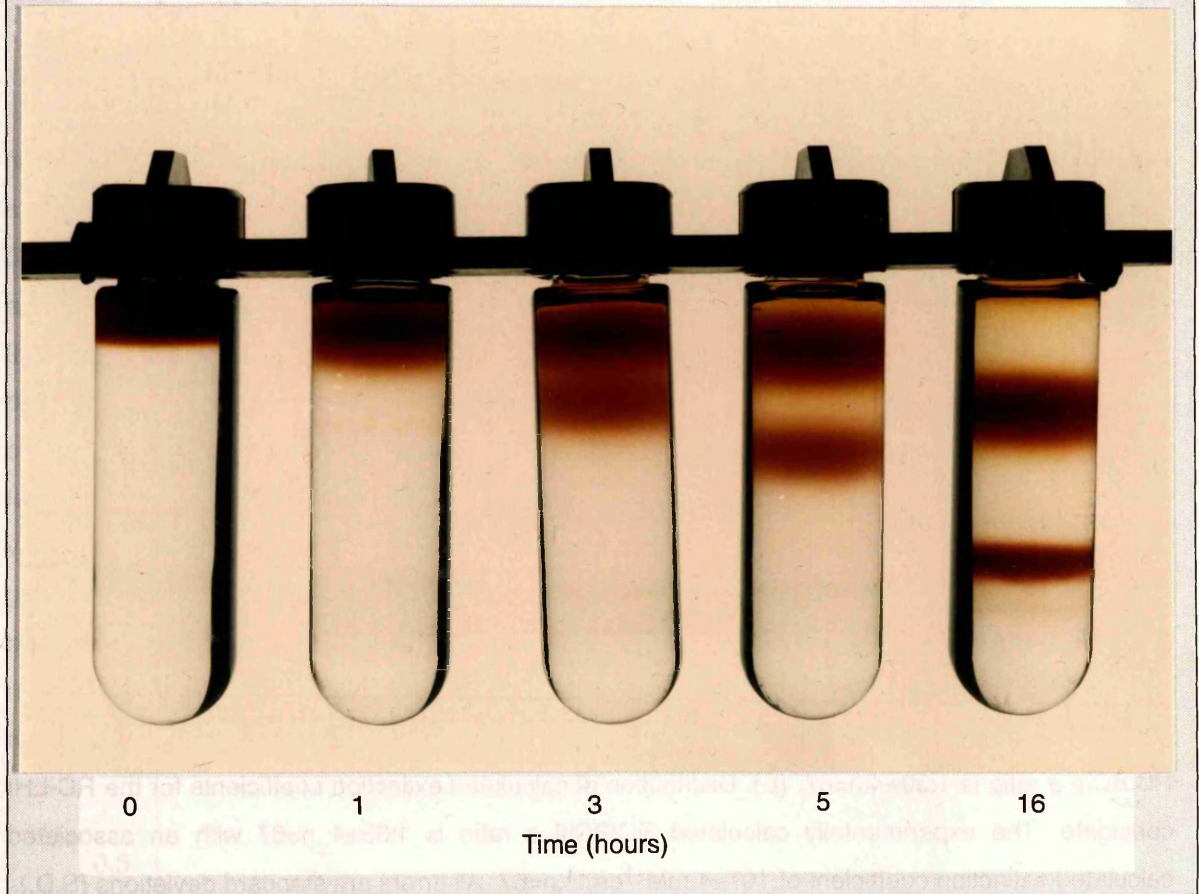
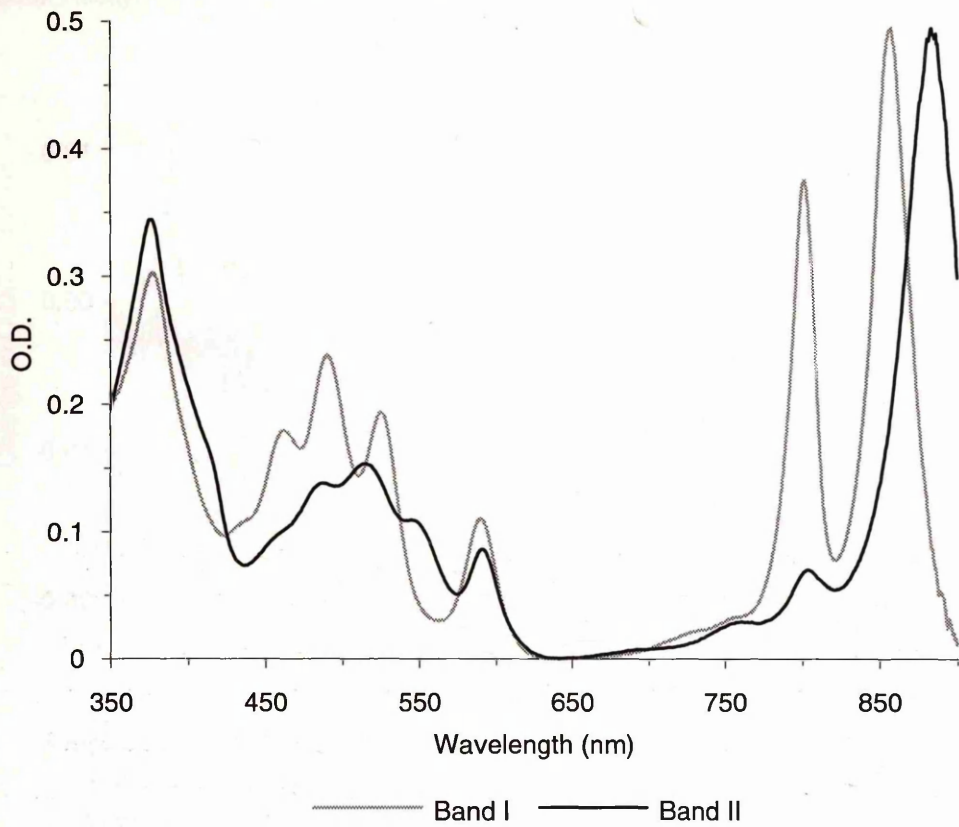


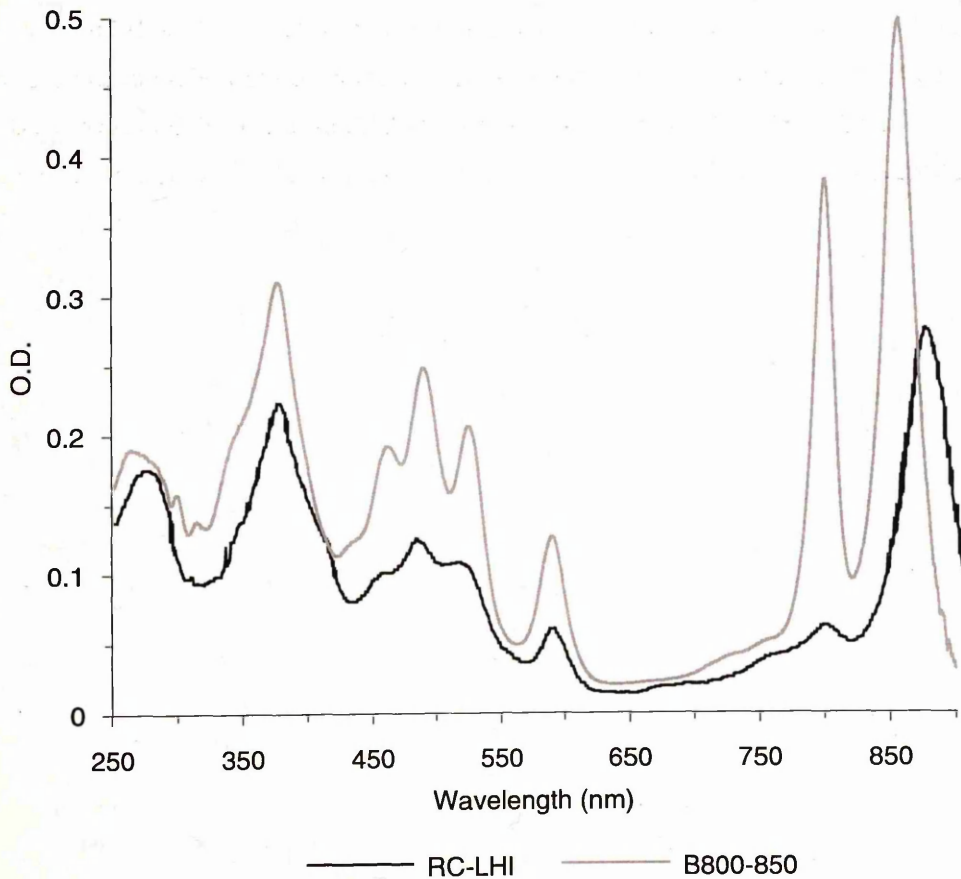
**Figure 3.26:** Pigmented bands of a continuous sucrose gradient from directly solubilised membranes of *Rp. acidophila* strain 7750. The sucrose gradient was from 0.3M to 1.2M sucrose in a buffer containing 0.2% w/v LDAO and 10mM TRIS.HCl, pH 8.0. The solubilised sample was loaded at the top of the poured gradient (i.e. zero hours) then allowed to separate into its two pigmented bands. After 3 hours two bands can be observed. After approximately 5 hours centrifugation (197000 xg, 4°C, in a T865 rotor) two discrete bands can be isolated. The pigmented bands reach their final positions between 12 and 16 hours at 197000 xg.

**Figure 3.27:** Spectroscopic Characterisation of *Rp. acidophila* strain 7750 Pigment-Protein Complexes. (A): Absorption Spectra of pigmented bands (bands I and II) resulting from a discontinuous sucrose gradient (1.2M, 0.6M, 0.3M sucrose in 0.15% LDAO w/v, 20mM TRIS.HCl, pH8.0). (B): Absorption Spectra of the purified pigment-protein complexes resulting from the protocols in the body of the text. (C) Example of a Redox assay on the isolated and purified RC-LHI conjugate (*core*). The optical density of the sample was adjusted to approximately 1.0 A.U. and reduction-oxidation spectra obtained by continually adding sodium ascorbate and ferric cyanide to the reference and sample cuvettes respectively. This was done until no absorbance change at approximately 800nm was observed. The absorbance change at approximately 800nm is ultimately used to calculate the RC:BChl a ratio. To ensure that irreversible bleaching of the light-harvesting bacteriochlorophyll had not occurred the oxidised cuvette was reduced (by adding ascorbate) and the blue shift eliminated. Key: b:- baseline, rd:- blue shift at 800nm, or:- oxidation reversibility in sample (D): Distribution of RC:BChl a ratios using the established extinction coefficients. The mean RC:BChl a ratio is  $1:30 \pm 4, n=67$ . (E): Distribution of calculated extinction coefficients for the RC-LHI conjugate. The experimentally calculated RC:BChl a ratio is  $1:33 \pm 4, n=67$  with an associated calculated extinction coefficient of  $107 \pm 4 \text{ mM}^{-1}\text{cm}^{-1}, n=67$ . All errors are standard deviations (S.D.).

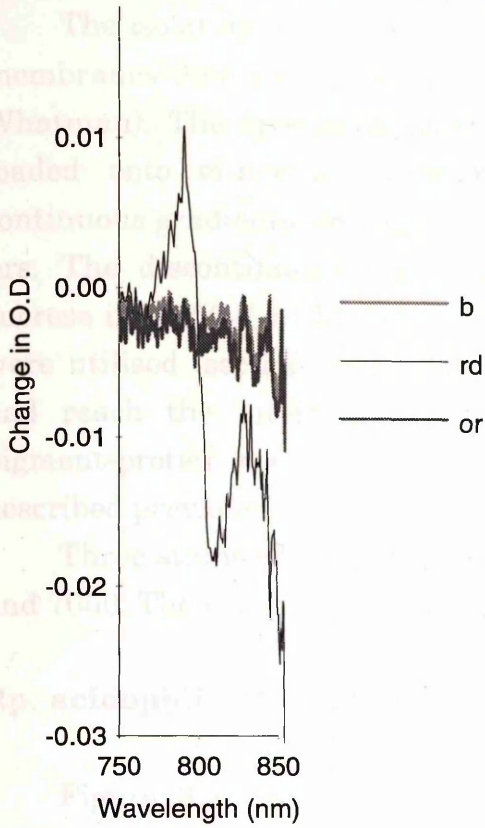
(A): Absorption Spectra of Bands I and II.



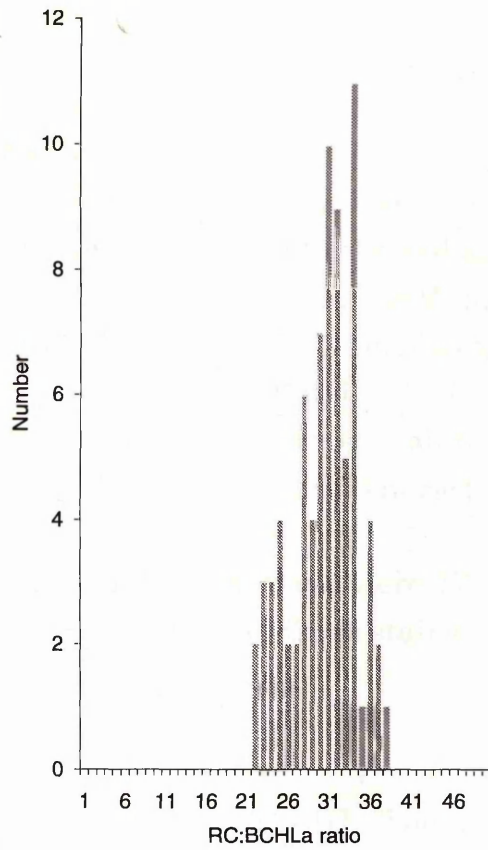
(B): Purified Pigment-Protein Complexes.



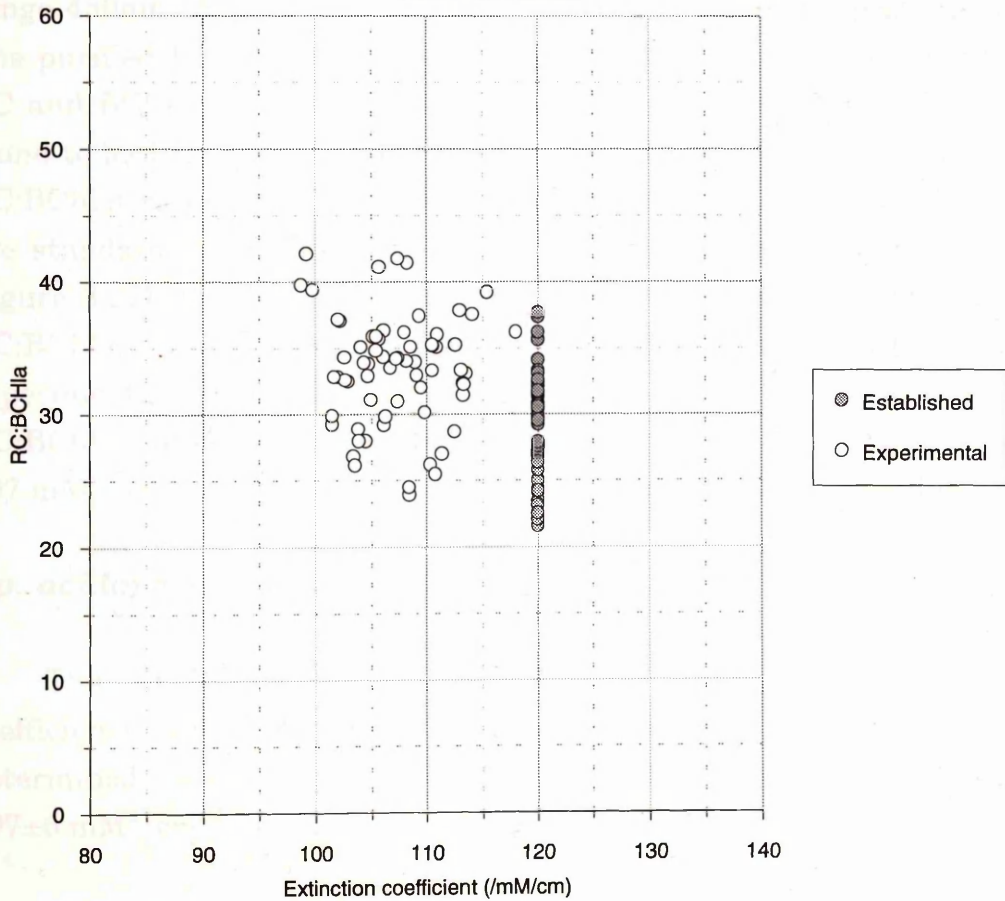
(C): Example of the  $\Delta$  Abs. at  $\sim 800\text{nm}$  for a Redox Assay.



(D): Distribution of RC:BChI Ratios



(E): Distribution of Established and Calculated Extinction Coefficients and Associated RC:BChI Ratios.



The isolation of *Rp. acidophila* was standardised by first solubilising the membranes then subjecting them to a DEAE anion exchange column (DE52, Whatman). The spectroscopically pure elutes (RC-LHI enriched) were then loaded onto either a continuous or discontinuous sucrose gradient. If continuous gradients were used the pigmented bands were collected after  $12 \pm 2$  hrs. The discontinuous gradients had three steps, 1.2M, 0.6M and 0.3M sucrose in 0.15% (w/v) LDAO, 20mM TRIS.HCl. When discontinuous gradients were utilised (section 2.6.2) they were collected when Band II (bottom band) had reach the interface between the two denser sucrose solutions. The pigment-protein complexes were then further purified and characterised as described previously.

Three stains of *Rp. acidophila* were investigated, these were 7750, 10050 and 7050. The isolation procedures were identical for all three stains.

### ***Rp. acidophila* strain 7750**

Figure 3.27 outlines the characterisation of RC-LHI. The pigmented bands (Figure 3.27A) represent crudely purified B800-850 (Band I) and RC-LHI (Band II). Notice that the carotenoid composition is different (absorption range 450nm - 570nm) in the peripheral and *core* pigment-protein complexes. The purified RC-LHI conjugates (Figure 3.27B) were then analysed for their RC and BChl *a* content. The determined extinction coefficient at 880nm was found to be  $107 \pm 4, n=67$ . Using the established and determined coefficients the RC:BChl *a* ratios are  $1:30 \pm 4, n=67$  and  $1:33 \pm 4, n=67$  respectively. All errors are standard deviations (S.D.) where n represents the number of samples. Figure 3.27D shows clearly that there is an approximate gaussian spread of RC:BChl *a* ratios between the values of 1:21 and 1:40. Plotting the experimentally determined BChl *a* coefficient at 880nm against the calculated RC:BChl *a* ratios illustrates that the experimentally determined coefficient is  $107 \text{ mM}^{-1}\text{cm}^{-1}, n=67$  with an even spread of data points around it.

### ***Rp. acidophila* strain 10050**

The RC:BChl *a* ratios were  $1:35 \pm 3, n=82$  (established extinction coefficient) and  $1:39 \pm 4, n=82$  (determined extinction coefficient). The determined extinction coefficient at 880nm was calculated to be  $107 \pm 6 \text{ mM}^{-1}\text{cm}^{-1}, n=82$ .

***Rp. acidophila* strain 7050**

The RC:BChl *a* ratios were 1:31±3, n=25 (established extinction coefficient) and 1:35±4, n=25 (determined extinction coefficient). The determined extinction coefficient at 880nm was calculated to be 108±4 mM<sup>-1</sup>cm<sup>-1</sup>, n=25.

### 3.2.4 *Rp. palustris* strain 2.6.1:

The optical density of the *Rp. palustris* membranes, measured at the NIR peak (875nm, high *light* grown cultures; 800nm, low *light* grown cultures), was reduced to 50 cm<sup>-1</sup> with 20mM TRIS.HCl, pH8.0. The membranes were then solubilised at room temperature for 15 min. with 1.0% w/v LDAO purum (Fluka Biochemicals). Once solubilised the sample was centrifuged as described in section 2.6.1 and the pellet discarded. The concentration of LDAO was then reduced to between 0.2% and 0.3% (w/v) LDAO. This species does not stick well to a DEAE column directly after detergent solubilisation. As a result sucrose gradients were employed to separate LHII from the RC-LHI conjugate. Sucrose gradients (0.3M to 1.2M sucrose, 0.15% (w/v) LDAO, 10mM TRIS.HCl, pH8.0) were prepared as described in section 2.6.2. Figure 3.28A shows typical *Rp. palustris* strain 2.6.1. absorption spectra of the pigmented bands from sucrose gradients. In "low *light*" grown cells the abundance of band I is greatly enhanced relative to band II. As a consequence of this *Rp. palustris* was usually grown under "high *light*" conditions when RC-LHI isolation was required.

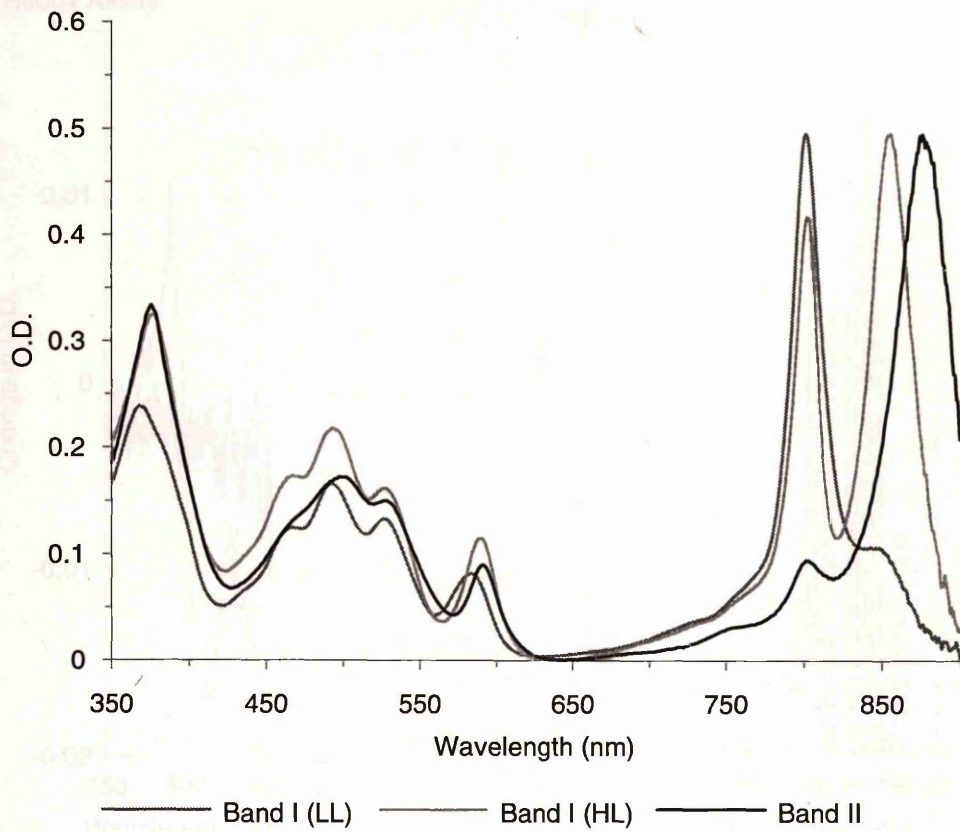
The pigmented bands were dialysed against, or diluted with 0.1% (w/v) LDAO, 20mM TRIS.HCl, pH 8.0 to remove the sucrose (sucrose reduces the binding of these proteins to DEAE). An anion exchange step (see section 2.6.3) was carried out to further remove any peripheral antennae and other general protein contamination. A second DE52 column was only occasionally required to further fractionate the two bands. The spectroscopically pure fractions were collected and the samples were dialysed against 0.1% w/v LDAO, 10mM TRIS.HCl, pH 8.0 to remove the salt. The dialysed samples were then concentrated (section 2.6.3) and loaded onto gel filtration columns (section 2.6.4), then detergent exchanged and desalted (section 2.6.6). Figure 3.28B shows absorption spectra of the purified and de-salted *Rp. palustris* pigment-protein complexes.

3.2.4 *Rp. palustris* strain 2.6.1:

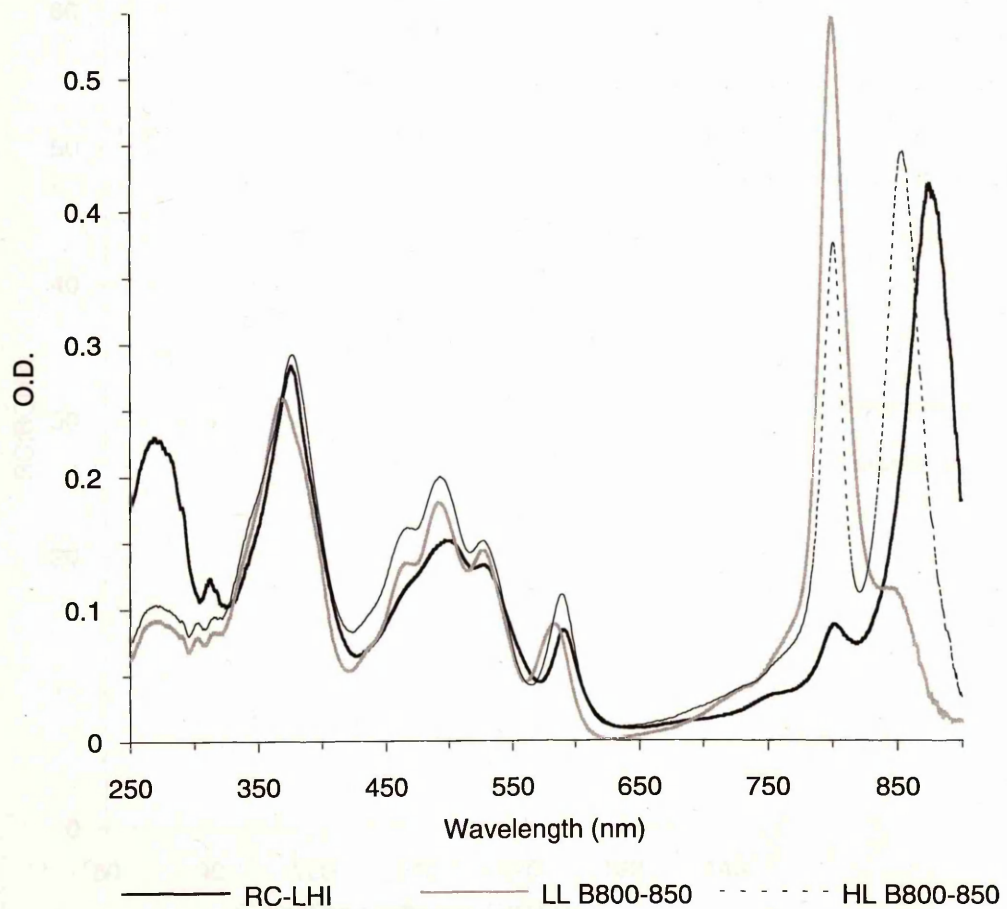
The optical density of the *Rp. palustris* membranes, measured at the NIR peak (876nm, high light grown cultures; 800nm, low light grown cultures), was reduced to  $80 \text{ cm}^{-1}$  with  $20 \text{ mM TRIS.HCl}$ , pH 8.0. The membranes were then solubilised at room temperature for 15 min. with 1.0% w/v LDAO (Sigma) (Lukas Biochemicals). Once solubilised the sample was centrifuged as described in section 2.6.1 and the pellet discarded. The concentration of LDAO was then reduced to between 0.2% and 0.3% w/v LDAO. This species does not stick well to a DEAE column directly after detergent solubilisation. A 20% w/v sucrose gradient was employed to separate LHII from the RC:BChl complexes. Sucrose gradients (0.3M to 1.2M sucrose, 0.15% w/v LDAO, 10mM TRIS.HCl, pH 8.0) were prepared as described in section 2.6.2. Figure 3.28A shows typical *Rp. palustris* strain 2.6.1 absorption spectra of the pigmented bands from sucrose gradients. In "low light" grown cells the absorption of band I is greater

**Figure 3.28:** Spectroscopic characterisation of *Rp. palustris* strain 2.6.1. pigment-protein complexes. (A): Absorption spectra of the pigmented bands (bands I and II) from a discontinuous sucrose gradient (1.2M, 0.6M and 0.3M sucrose in 0.2%w/v LDAO, 20mMTRIS.HCl, pH 8.0). (B): Absorption spectra of the purified protein complexes. (C) Example of the change in absorbance at 800nm for a Redox assay. Key:-B, baseline; rd, blue shift at 800nm; or, oxidation reversibility. (D): Distribution of the RC:BChl *a* ratios using the established extinction coefficients against. Mean RC:BChl *a* ratio is  $1:25 \pm 4$ ,  $n=42$ . (E): Distribution of the established and calculated extinction coefficients against RC:BChl ratios. Mean RC:BChl ratio is  $1:29 \pm 7$ ,  $n=42$ . The mean calculated extinction coefficient at 880nm was  $105 \pm 11$ ,  $n=42$ . On examination of the spread of data suggests a correlation between the RC:BChl ratio and calculated extinction coefficient. However, correlation analysis shows no significant relationship ( $r=-.68$ ,  $n=42$ ).

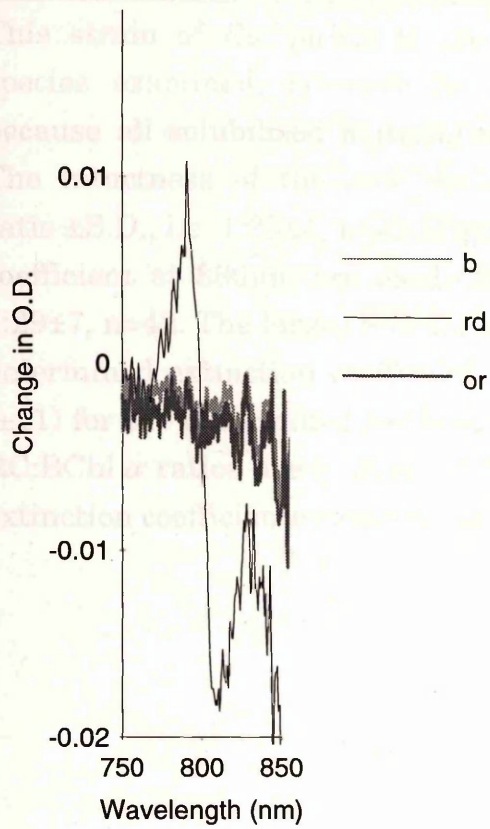
(A): Absorption Spectra of Bands I and II.



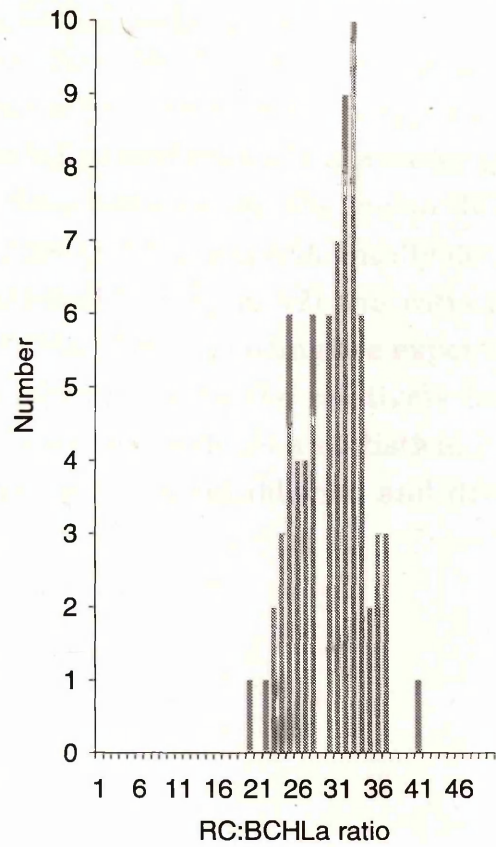
(B): Purified Pigment-Protein Complexes.



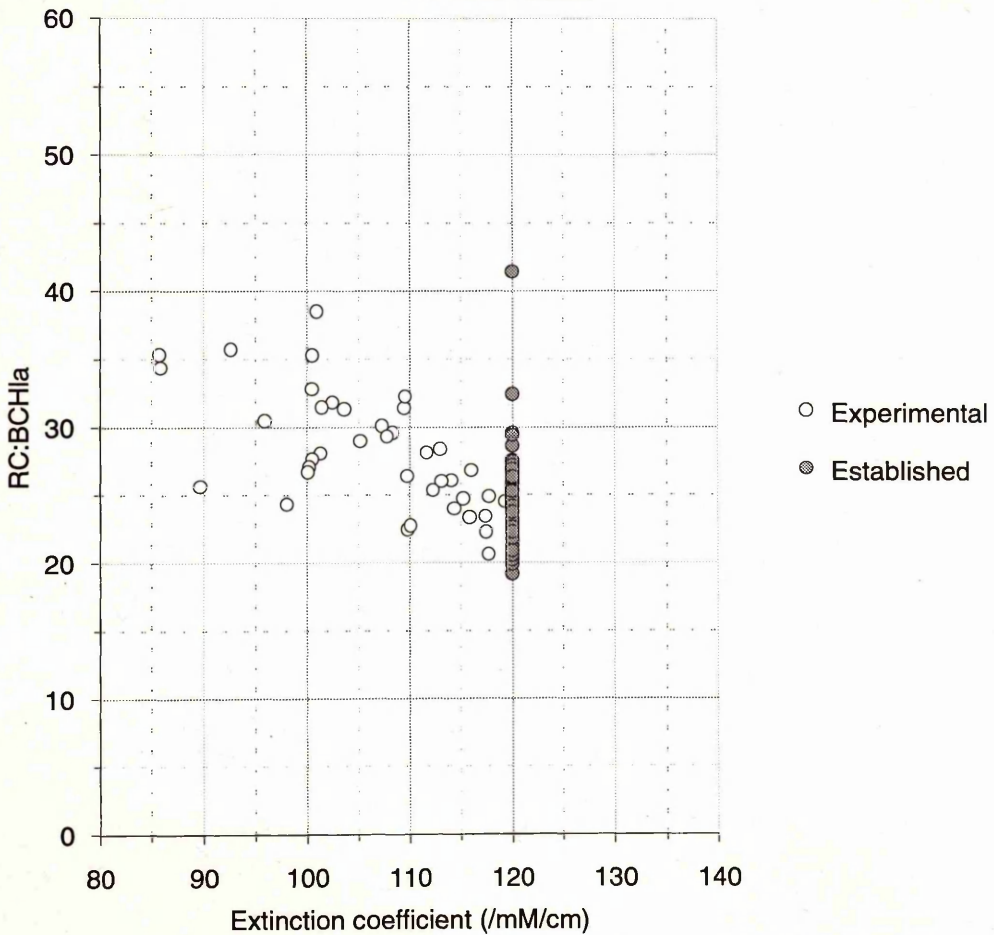
(C): Example of the  $\Delta$  Abs. at  $\sim 800\text{nm}$  for a Redox Assay.



(D): Distribution of RC:BChI Ratios



(E): Distribution of Established and Calculated Extinction Coefficients and their Associated RC:BChI Ratios.



This strain of *Rp. palustris* produces very stable cores compared to other species examined, however its purification steps are among the longest because all solubilised material must be passed through a sucrose gradient. The intactness of the core can be demonstrated by the mean RC:BChl *a* ratio  $\pm$ S.D., i.e.  $1:25 \pm 4$ ,  $n=42$  (Figure 3.28D). When experimentally determined coefficient at 880nm are used ( $105 \pm 11 \text{ mM}^{-1} \text{ cm}^{-1}$ ,  $n=42$ ) the ratio alters to  $1:29 \pm 7$ ,  $n=42$ . The larger S.D. for the RC:BChl *a* ratio using the experimentally determined extinction coefficient is probably due to the relatively large S.D. ( $\pm 11$ ) for the determined coefficient. Using the mode as a statistical guide the RC:BChl *a* ratios are 1:33 and 1:25-28 using the established and determined extinction coefficients respectively.

### 3.3.5. *Rp. cryptolactis*:

The isolation procedures for the RC-LHI from this bacterium were similar to *Rp. acidophila*. The spectroscopically pure fractions from a DE52 (Whatman) column were layered onto a sucrose gradient and the pigmented bands isolated. *Rp. cryptolactis* can produce two types of LHII, these are the B800-850 and B800-820 complexes. Separation for B800-820 from B800-850 was found to be easiest using sucrose density centrifugation. The optimum conditions to separate the two LHII forms into two pigmented bands was 12 hours at 197K xg (4°C in a T865 rotor) in a continuous gradient of 0.3M to 0.6M sucrose, 0.15% LDAO (w/v), 20mM TRIS.HCl, pH 8.0. Figure 3.29A demonstrates that even under "high light" growth conditions B800-820 can be produced. In the absorption spectrum of band I (LHII) in Figure 3.29A there is a shoulder at 822nm which is indicative of the presence of B800-820 complex within the native membrane (Stadtwald *et al.*, 1990).

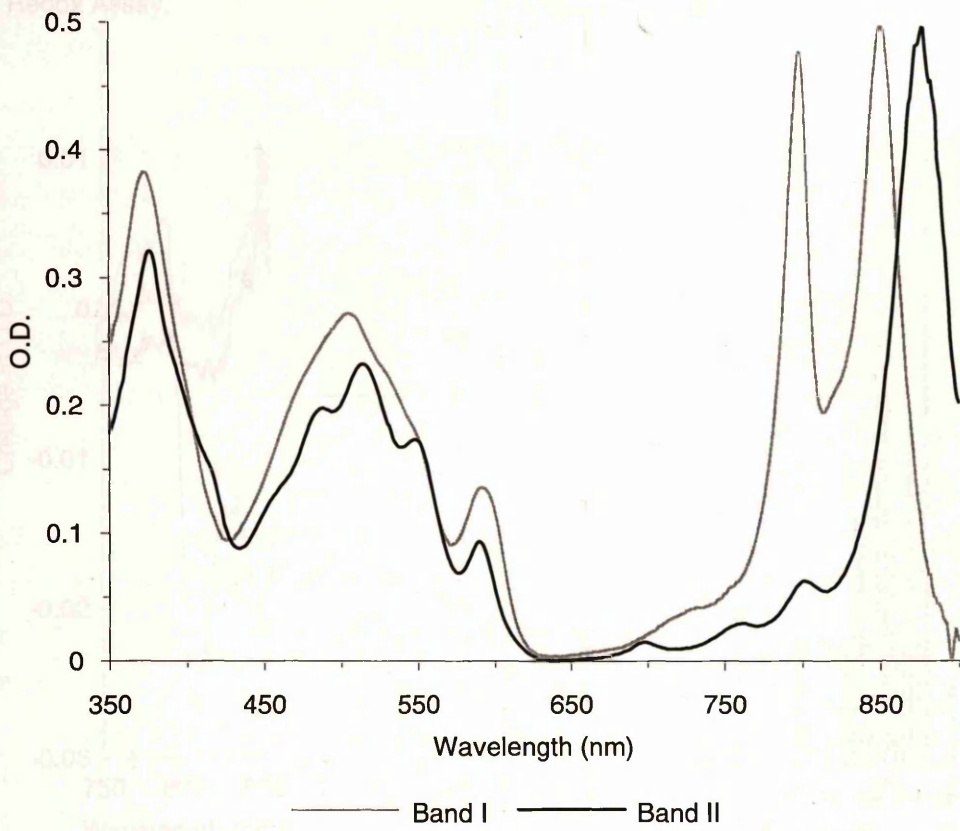
The RC-LHI was then purified as previously described. Redox Assays in combination with bacteriochlorophyll assays suggest that the RC:LHI ratio is  $1:33 \pm 5$ ,  $n=26$  (or 1:36 modal) using the established coefficients or  $1:32 \pm 5$ ,  $n=26$  (or 1:37 modal) using the calculated coefficient at 880nm of  $117 \pm 7 \text{ mM}^{-1}\text{cm}^{-1}$ ,  $n=26$  (Figure 3.29). Unlike the previous examples the modal and mean values are less similar. This means that either one value is wrong or that the optimum method of RC-LHI isolation was never truly obtained. Although 26 individual Redox assays were carried out the spread of RC:BChl *a* ratios (Figure 3.29D) suggests that the true value does lie somewhere between the mean and modal values.

Only further assays will establish the true RC:BChl *a* ratio. The experimentally determined coefficient for bacteriochlorophyll at 880nm was very similar to that obtained for *R. rubrum* ( $\epsilon_{880\text{nm}} = 120 \text{ mM}^{-1}\text{cm}^{-1}$ , Clayton *et al.*, 1972).

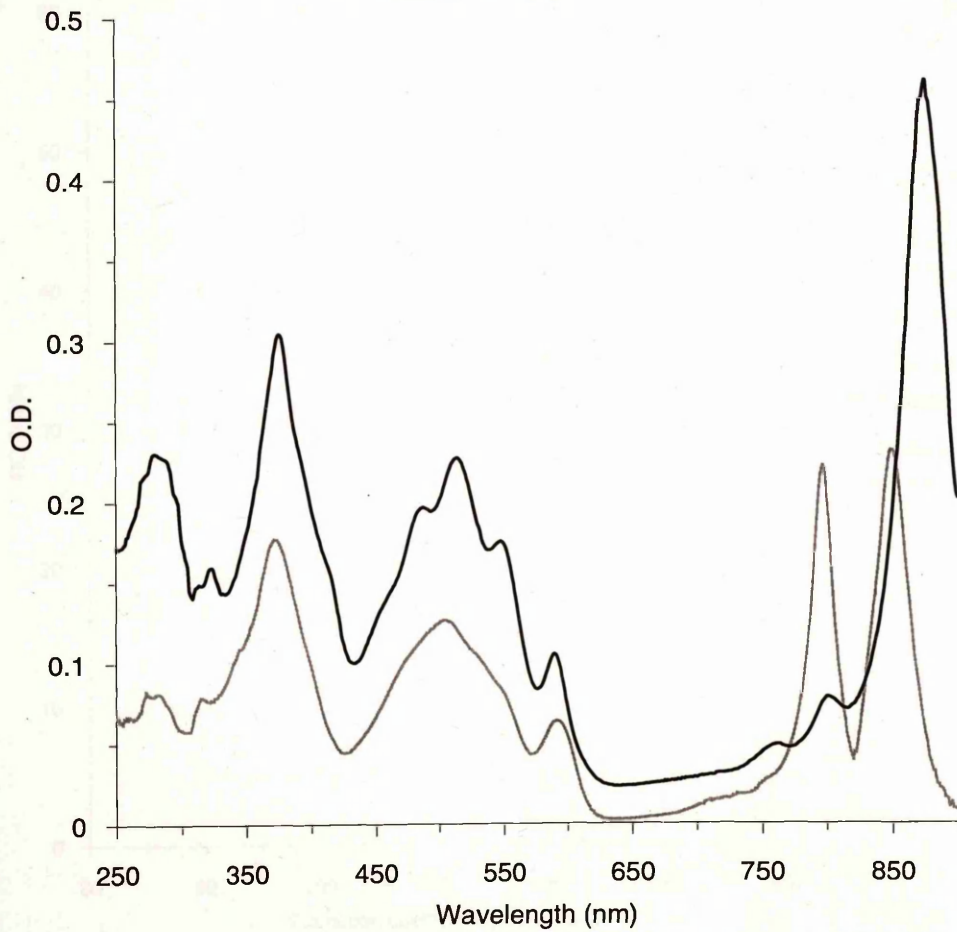
The isolation procedures for the RC-LHI from this bacterium were similar to *Rp. acidiphila*. The spectroscopically pure fractions from a DEAE (Whatman) column were layered onto a sucrose gradient and the pigmented bands isolated. *Rp. cryptolactis* can produce two types of LHI, these are the B800-850 and B800-820 complexes. Separation for B800-820 from B800-850 was found to be easiest using density centrifugation. The optimum conditions to separate the two LHII forms into two pigmented bands was 18 hours at 197K xg (4°C to a T865 rotor) in a continuous gradient of 0.3M to 0.6M sucrose, 0.15% LDAO (w/v), 20mM TRIS.HCl, pH 8.0 (figure 3.29A). demonstrates that even under "high light" growth conditions B800-820 can be produced in the absorption spectrum of band I (LHI) in *Rp. cryptolactis* (figure 3.29B).

**Figure 3.29:** Spectroscopic analysis of *Rp. cryptolactis* pigment-protein complexes. (A): Absorption spectra of the pigmented bands (bands I and II, upper and lower respectively) resulting from a discontinuous sucrose gradient (1.2M, 0.6M and 0.3M sucrose in 0.2% (w/v) LDAO purum, 20mM TRIS.HCl, pH8.0). There is a shoulder at approximately 822nm in the band I absorption spectrum. This is due a residual amount of the B800-820 peripheral complex present in the B800-850 band. The B800-820 can be easily separated from the B800-850, by either DEAE columns or further sucrose gradients followed by gel filtration. (B): Absorption spectra of the purified pigment-protein complexes (RC-LHI and B800-850) resulting from the protocols described in the body of the text. (C): An example of the reversible absorbance shift at 800nm associated with the RC-Redox assay. key:- b; baseline, or; RC associated Redox absorption shift, rd; RC oxidation/reduction reversibility. (D): Distribution of the RC:BChl ratio using the established extinction coefficients. The mean value is  $1:31 \pm 5$ ,  $n=26$  (modal value is 36). (E): Distribution of the established and experimentally determined extinction coefficients at 880nm against RC:BChl ratio. The experimentally determined extinction coefficient was calculate to be  $117 \pm 7$ ,  $n=26$ . All errors are standard deviations (S.D.).

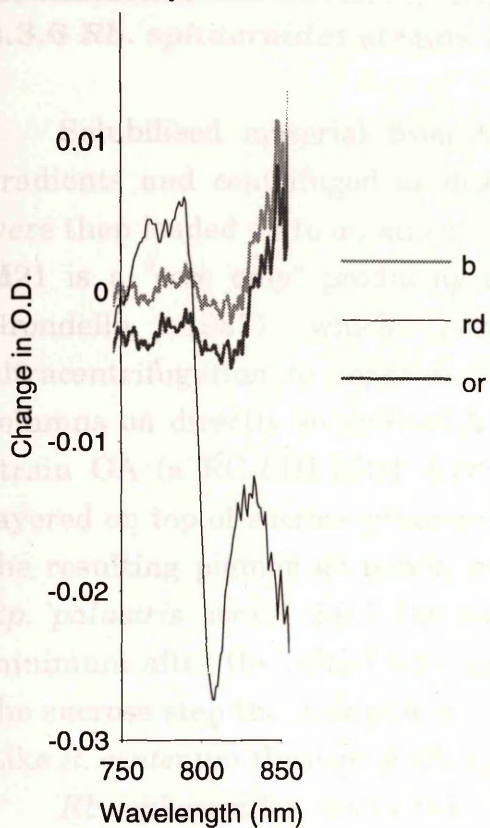
(A): Absorption Spectra of Bands I and II.



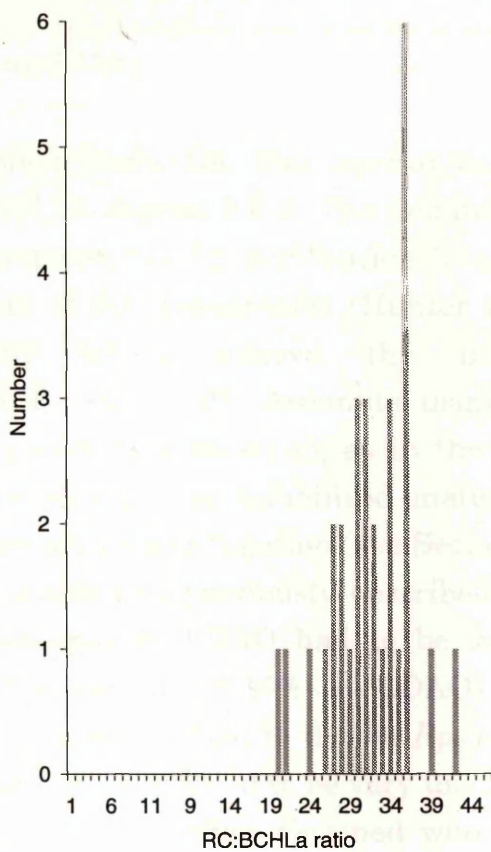
(B): Absorption of Purified Pigment-Protein Complexes.



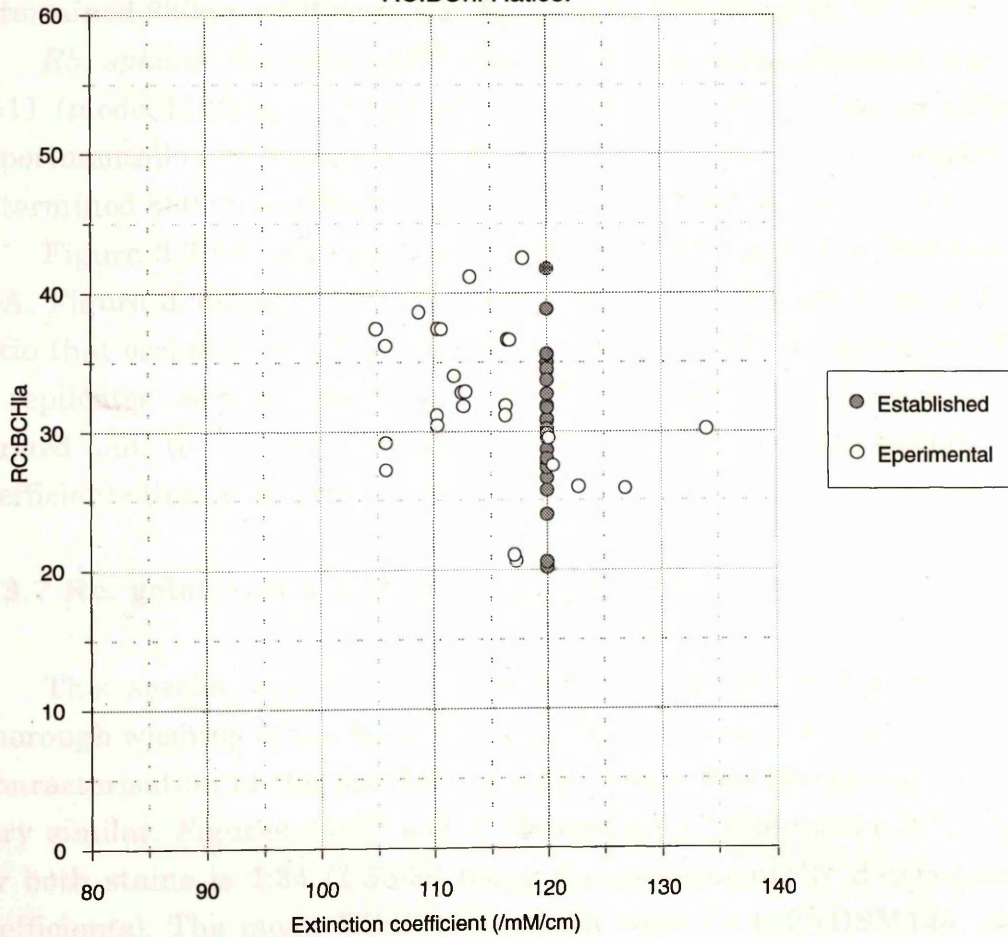
(C): Example of the  $\Delta$  Abs. at  $\sim 800\text{nm}$  for a Redox Assay.



(D): Distribution of RC:BChI Ratios



(E): Distribution of Established and Calculated Extinction Coefficients and Associated RC:BChIa Ratios.



### 3.3.6 *Rb. sphaeroides* strains GA and M21:

Solubilised material from *Rb. sphaeroides* GA was layered to sucrose gradients and centrifuged as described in section 2.6.2. The isolated bands were then loaded on to an anion exchange column for purification. The mutant M21 is a "core only" producing strain of *Rb. sphaeroides* (Hunter and van Grondelle, 1987) which hopefully would remove the need for ultracentrifugation to separate RC-LHI from LHII. Attempts using DEAE columns on directly solubilised M21 membranes failed so, as in the case for strain GA (a RC-LHI-LHII producing strain), the solubilised material was layered on top of sucrose gradients and after centrifugation (see Section 2.6.2) the resulting pigmented bands were isolated as previously described. Unlike *Rp. palustris* strain 2.6.1 the concentration of LDAO had to be kept to a minimum after the initial solubilisation step (~0.1-0.15% (w/v) LDAO). Beyond the sucrose step the isolation of RC-LHI was identical to that of *Rp. palustris*. Like *R. centenum* the core of *Rb. sphaeroides* was found to be very unstable.

*Rb. sphaeroides* strain GA; the RC:BChl *a* ratios obtained were 1:29±2, n=9 (mode 1:28) and 1:34±4, n=9 (mode 1:35) for the established and experimentally determined 880nm coefficients. The experimentally determined 880nm coefficient was found to be 105±10, n=9.

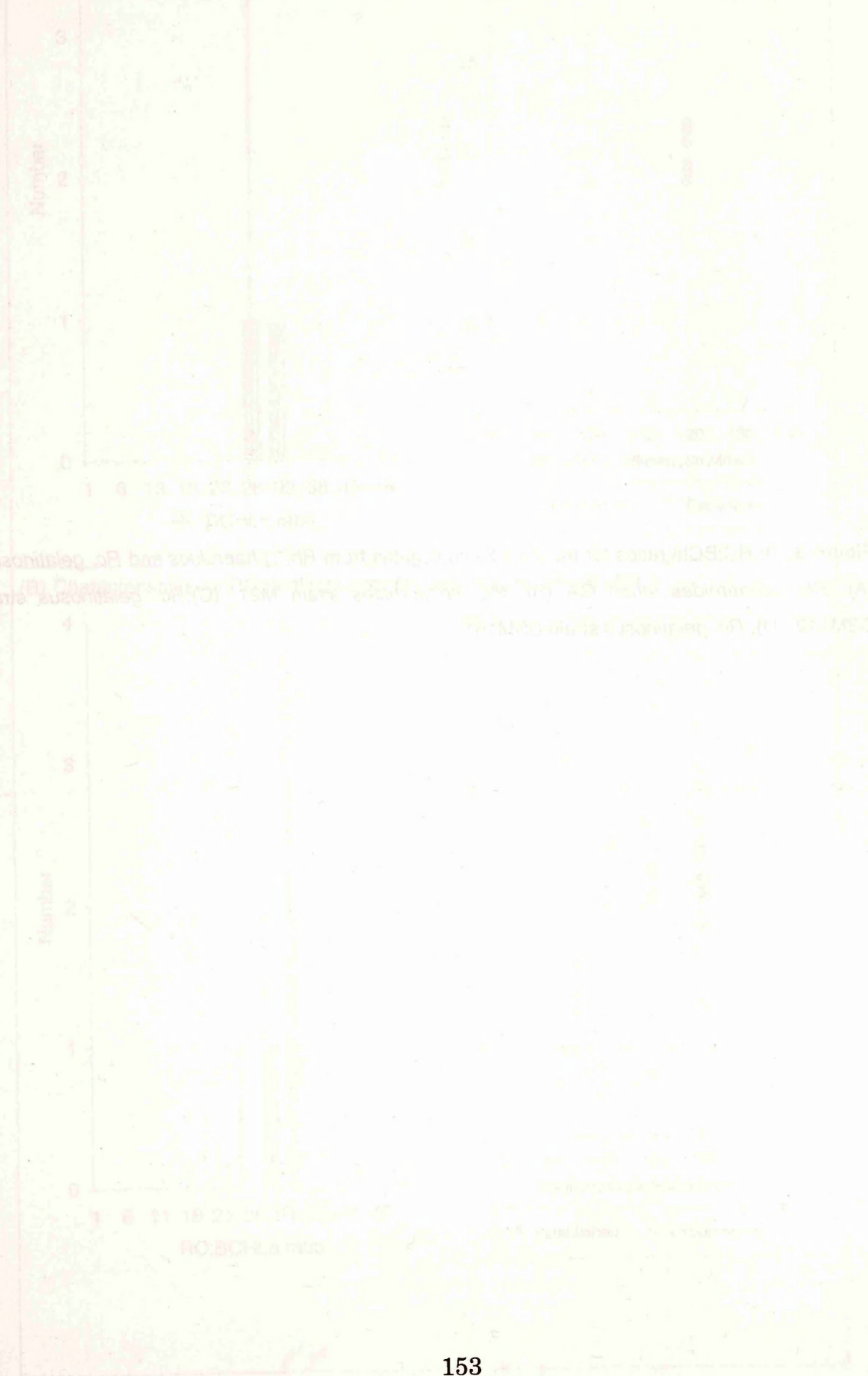
*Rb. sphaeroides* strain M21; the RC:BChl *a* ratios obtained were 1:30±3, n=11 (mode 1:32) and 1:37±5, n=11 (mode 1:29-35) for the established and experimentally determined 880nm coefficients. The experimentally determined 880nm coefficient was found to be 100±7, n=11.

Figure 3.30 illustrates the spread of RC:BChl *a* ratios. For both strains (GA, Figure 3.30A and M21, Figure 3.30B) there appears to be a RC:BChl *a* ratio that occurs more often than the other ratios. Since only a small number of replicates were analysed (M21, n=11; GA, n=9) further work needs to be carried out to further substantiate the RC:BChl *a* ratios and extinction coefficients that were determined.

### 3.3.7 *Rc. gelatinosus* DSM149 and DSM151

This species was isolated in a similar manner to *Rp. palustris* 2.6.1. Thorough washing of the harvested cells was ensured prior to *French pressing*. Characterisation of the purified RC-LHI from these two strains proved to be very similar. Figures 3.30C and D illustrate that the modal RC:BChl *a* ratio for both stains is 1:34 (1:35-36 using the experimentally determined 880nm coefficients). The mean RC:BChl *a* values were 1:34±2 (DSM149, n=23) and

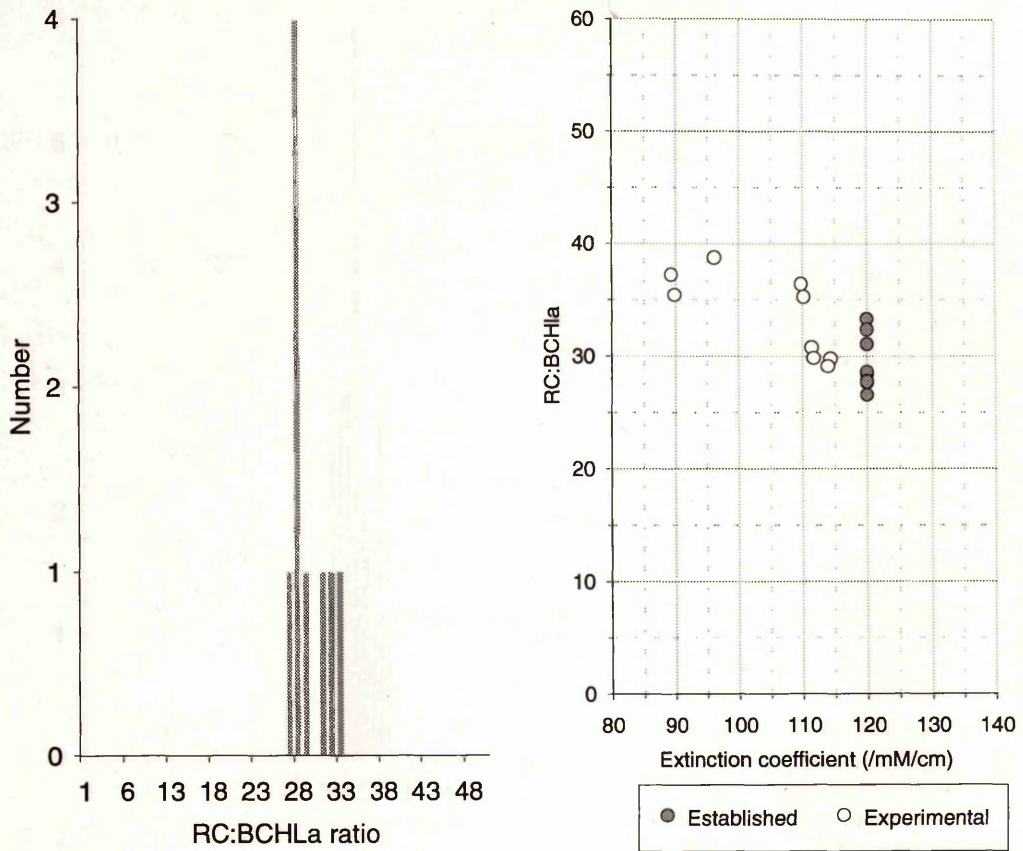
1:34±3 (DSM151, n=19). Using the experimentally determined coefficients for BChl *a* at 880nm ( $116\pm5 \text{ mM}^{-1}\text{cm}^{-1}$ , n=23 for DSM149;  $116\pm2 \text{ mM}^{-1}\text{cm}^{-1}$ , n=19 for DSM151) were  $1:35\pm2$  (DSM149, n=23) and  $1:36\pm3$  (DSM151, n=19).



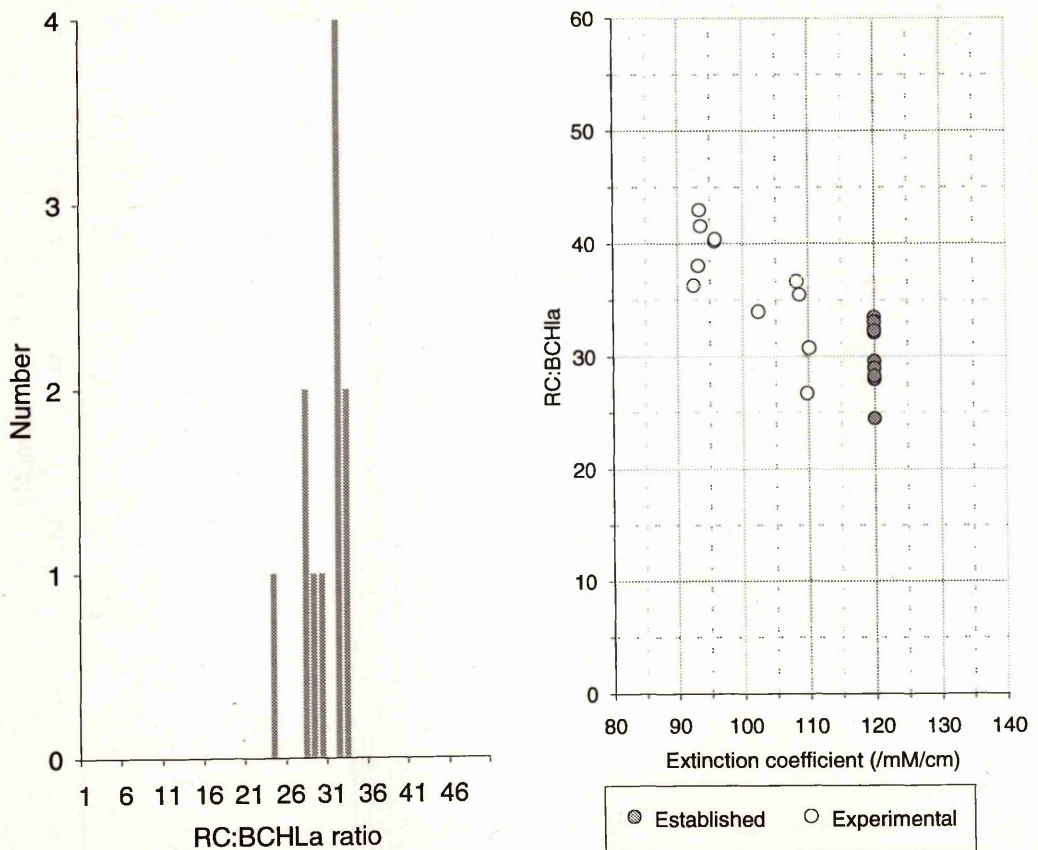
1:34±3 (DSM151, n=19). Using the experimentally determined coefficients for Bchl  $a$  at 880nm ( $116±5 \text{ m}^{-1} \text{M}^{-1}$ , n=23) for DSM149,  $115±2 \text{ m}^{-1} \text{M}^{-1}$ , n=19 for DSM151) were 1:35±2 (DSM149, n=23) and 1:36±3 (DSM151, n=19).

**Figure 3.30:** RC:BChl ratios for the RC-LHI conjugates from *Rb. sphaeroides* and *Rc. gelatinosus*. (A): *Rb. sphaeroides* strain GA (B): *Rb. sphaeroides* strain M21. (C):*Rc. gelatinosus* strain DSM149. (D): *Rc. gelatinosus* strain DSM151.

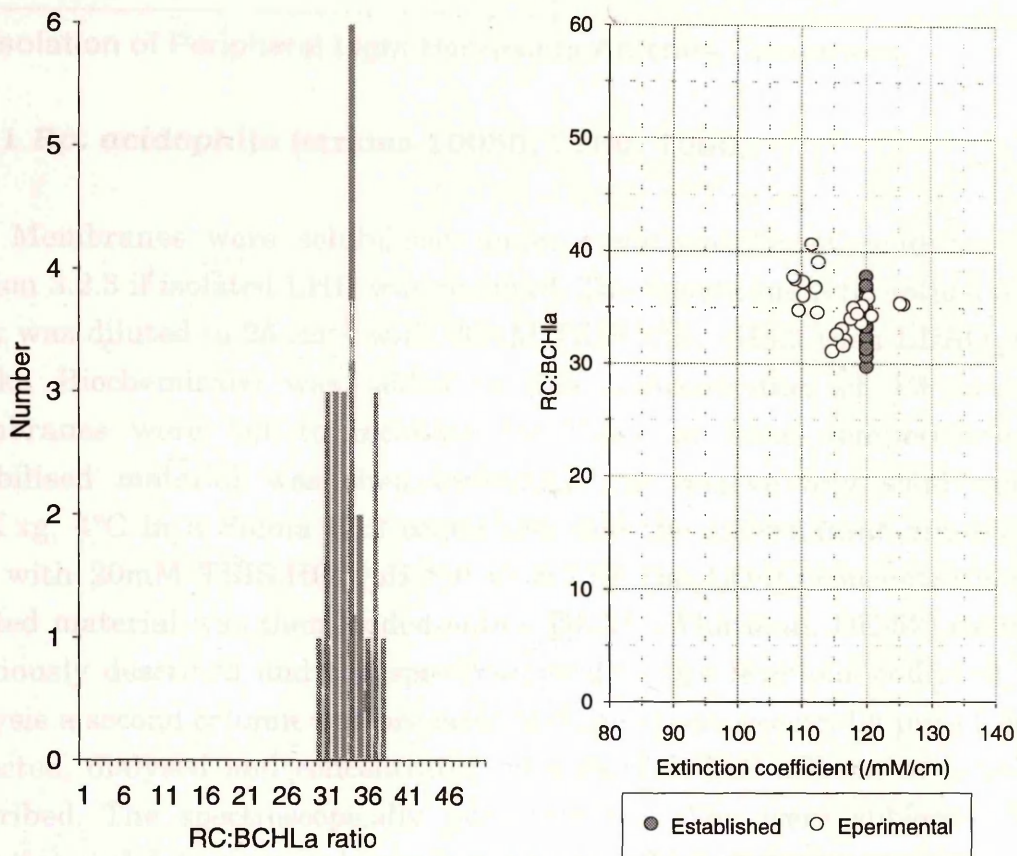
(A) Characterisation of RC:Bchl ratios for *Rb. sphaeroides* strain GA.



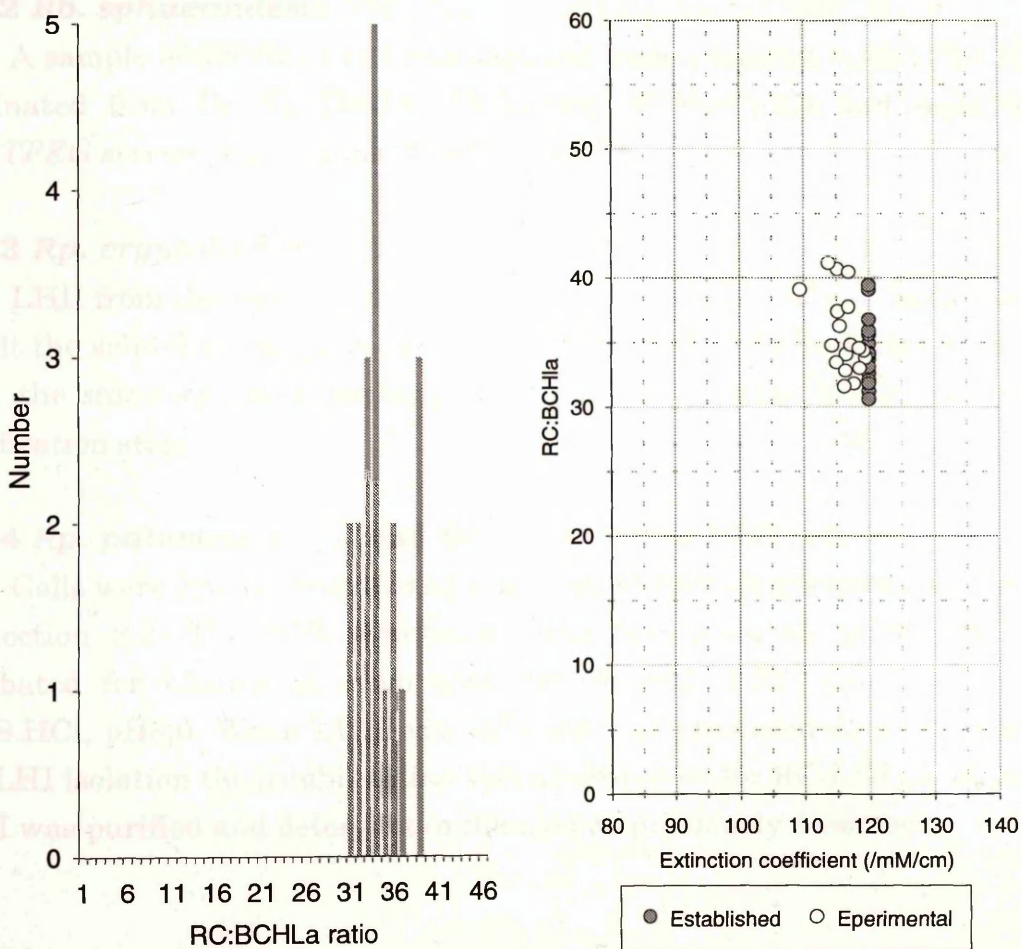
(B) Characterisation of RC:Bchl ratios for *Rb. sphaeroides* strain M21.



(C) Characterisation of RC:Bchl ratios for *Rc. gelatinosus* strain DSM149.



(D) Characterisation of RC:Bchl ratios for *Rc. gelatinosus* strain DSM151.



### 3.4 Isolation of Peripheral Light-Harvesting Antenna Complexes:

#### 3.4.1 *Rp. acidophila* (strains 10050, 7750, 7050):

Membranes were solubilised under slightly different conditions than section 3.2.3 if isolated LHII was required. The membrane NIR optical density peak was diluted to  $25\text{ cm}^{-1}$  with 20mM TRIS.HCl, pH8.0 then LDAO *purum* (Fluka Biochemicals) was added to final concentration of 1% (w/v). The membranes were left to incubate for 1hour at room temperature. The solubilised material was then centrifuged to remove any solid material (10K xg, 4°C in a Sigma K12 centrifuge) and the supernatant diluted three fold with 20mM TRIS.HCl, pH 8.0 to reduce the LDAO concentration. The diluted material was then loaded onto a DEAE (Whatman, DE-52) column as previously described and the spectroscopically pure fractions collected. After dialysis a second column was prepared and the spectroscopically pure fractions collected, dialysed and concentrated on a third DEAE column as previously described. The spectroscopically pure fractions then were subjected to gel filtration and detergent exchange (see section 2.6).

#### 3.4.2 *Rb. sphaeroides*:

A sample of purified LHII was acquired from a mutant strain (the sample originated from Dr. G. Fowler, University of Sheffield) and used in the FASTPEG screen (see Chapter 4, section 4.5.2).

#### 3.4.3 *Rp. cryptolactis*:

LHII from this species was collected as a by-product of *core* isolation. As a result the solubilisation procedure is that described of the isolation of the *core*, with the *standard* anion exchange/gel filtration columns being used for the purification steps.

#### 3.4.4 *Rp. palustris* 2.6.1. and *Rc. gelatinosus* DSM149:

Cells were *French Pressed* and subjected to sucrose gradients as described in section 3.2. The NIR membrane peak was reduced to  $50\text{ cm}^{-1}$  then incubated for 45mins at room temperature with 1.0% (w/v) LDAO, 20mM TRIS.HCl, pH8.0. When LHII was collected and processed as a by-product of RC-LHI isolation the solubilisation was as described for RC-LHI isolation. The LHII was purified and detergent exchanged as previously described.

## 3.4 Isolation of Peripheral Light-Harvesting Antenna Complexes

3.4.1 *Rp. acidophila* (strains 10050, 7750, 7050)

Membranes were solubilised under slightly different conditions than section 3.2.3 if isolated LHI was required. The membrane NIR optical density peak was diluted to  $25 \text{ cm}^{-1}$  with 20mM TRIS-HCl, pH 8.0 then LDAO perum (Fluka Biochemicals) was added to final concentration of 1% (w/v). The membranes were left to incubate for 1 hour at room temperature. The solubilised material was then centrifuged to remove any solid material (10K xg, 4°C in a Sigma K12 centrifuge) and the supernatant diluted three fold with 20mM TRIS-HCl, pH 8.0 to reduce the LDAO concentration. The diluted material was then loaded onto a DEAE (Waters, DE-52) column as

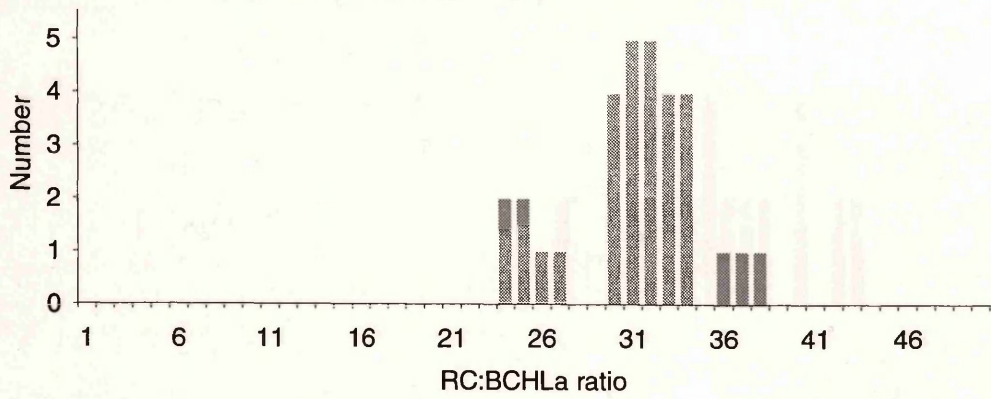
**Figure 3.31:** Distribution of RC:BChl ratios using the experimentally determined extinction coefficient from isolated RC-LHI core conjugates. In samples where fewer data points were collected the RC:BChl ratio distribution becomes less defined. The Histograms are for the isolated RC-LHI conjugates from (A): *R. centenum*, (B): *R. rubrum* S1, (C): *Rp. cryptolactis*, (D): *Rp. palustris* 2.6.1., (E): *Rb. sphaeroides* M21, (F): *Rb. sphaeroides* GA, (G): *Rc. gelatinosus* DSM149, (H): *Rc. gelatinosus* DSM151, (I): *Rp. acidophila* 7750, (J): *Rp. acidophila* 10050, and (K): *Rp. acidophila* 7050.

LHI from this species was collected as a by-product of core isolation. As a result the solubilisation procedure is that described of the isolation of the core, with the standard anion exchange filtration column being used for the purification steps.

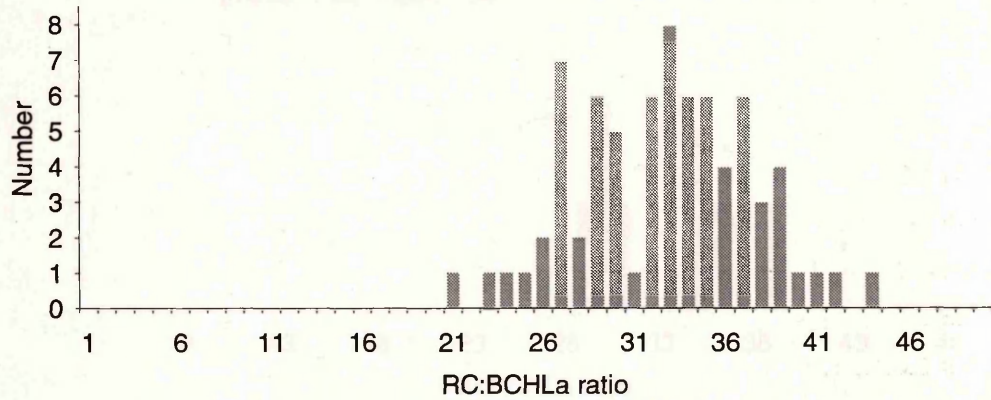
3.4.4 *Rp. palustris* 2.6.1. and *Rc. gelatinosus* DSM149

Cells were French Pressed and subjected to sucrose gradients as described in section 3.2. The NIR membrane peak was reduced to  $50 \text{ cm}^{-1}$  then TRIS-HCl, pH 8.0. When LHI was collected and processed as a by-product of RC-LHI isolation the solubilisation was as described for RC-LHI isolation. The LHI was purified and detergent exchanged as previously described.

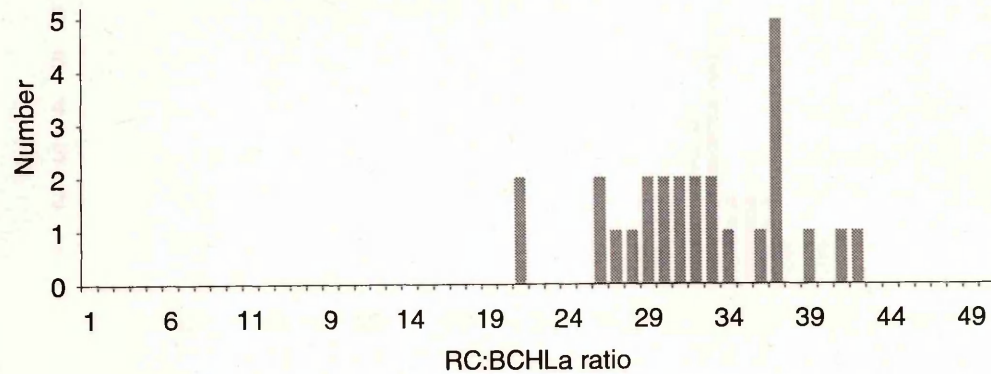
(A): Distribution of RC:BChla ratios for *R. centenum* (mode: 1:32, mean 1:31)



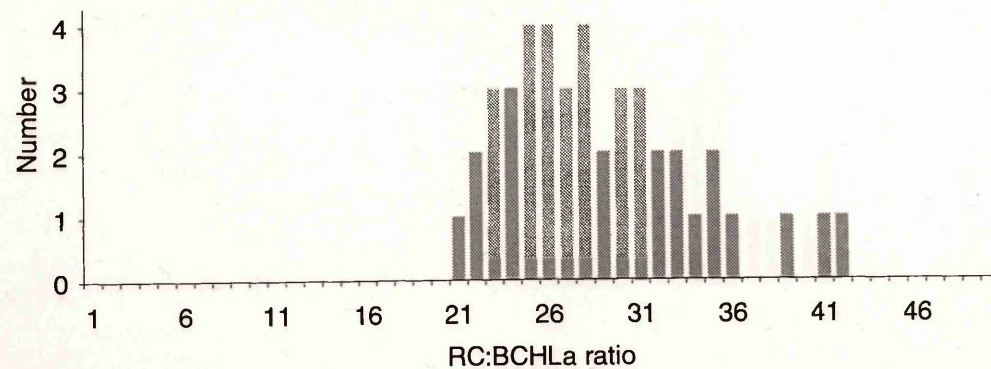
(B): Distribution of RC:BChla ratios for *R. rubrum* S1 (mode: 1:33, mean 1:34)



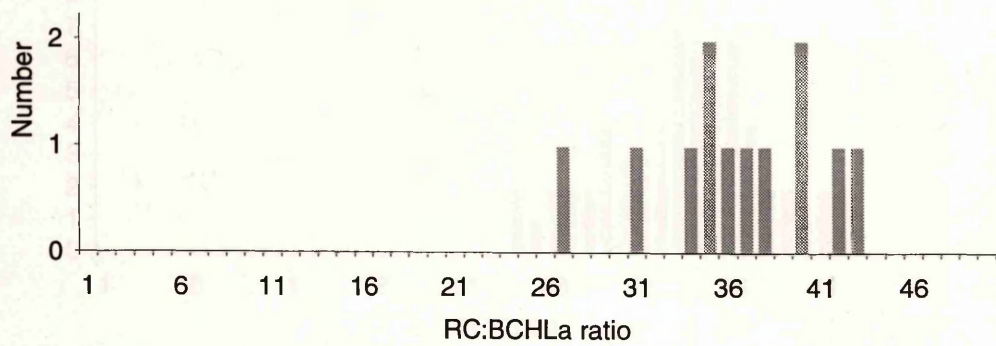
(C): Distribution of RC:BChla ratios for *Rp. cryptolactis* (mode: 1:37, mean 1:32)



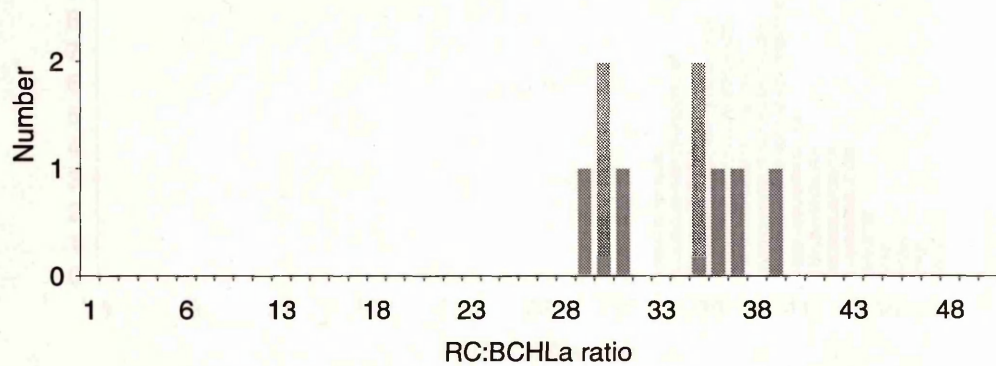
(D): Distribution of RC:BChla ratios for *Rp. palustris* 2.6.1 (mode: 1:25-28, mean 1:29)



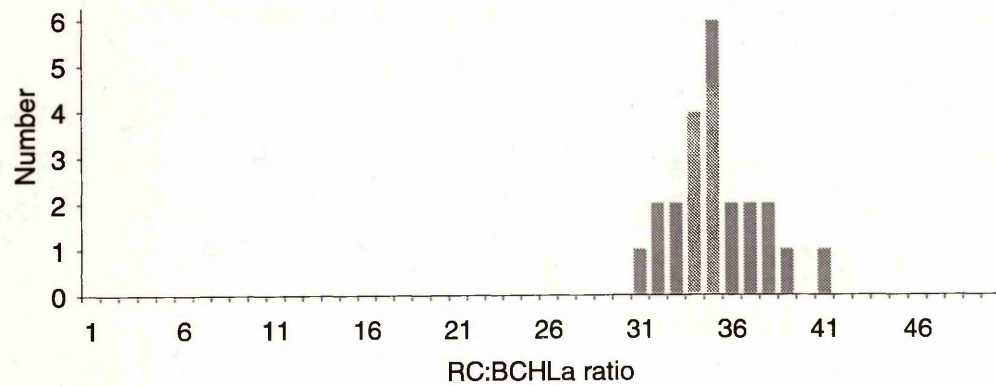
(E): Distribution of RC:BChla ratios for *Rb. sphaeroides* M21  
(mode: 1:35-40, mean 1:37)



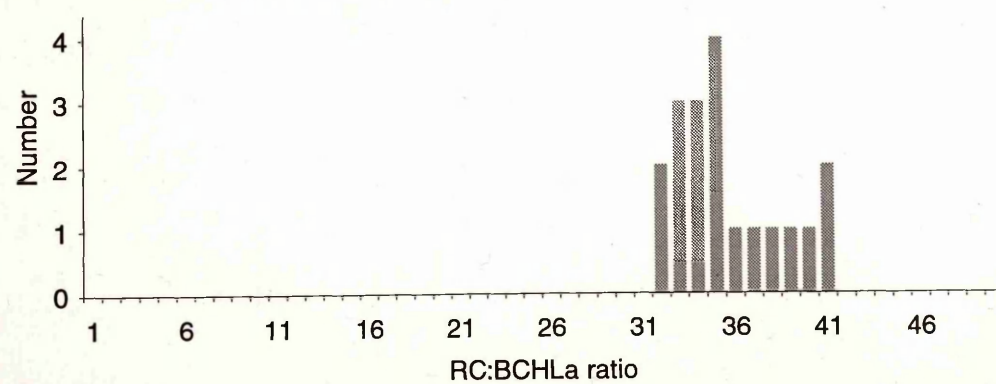
(F): Distribution of RC:BChla ratios for *Rb. sphaeroides* GA  
(mode: 1:35, mean 1:34)



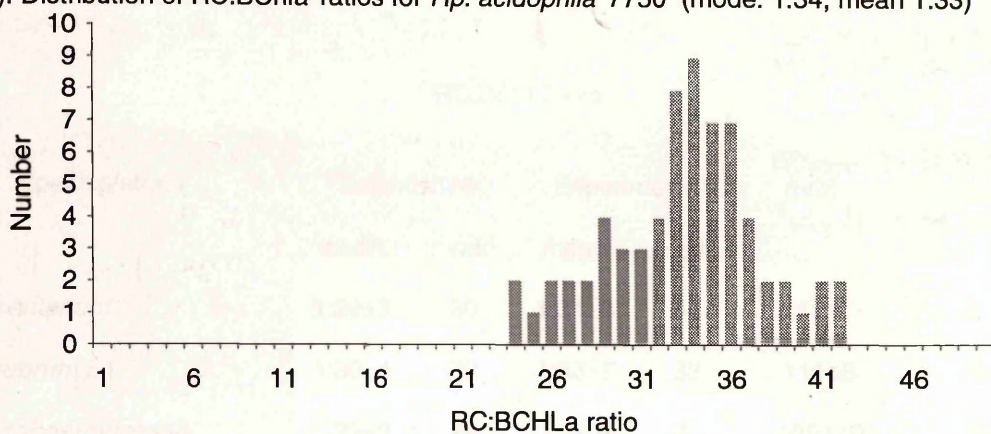
(G): Distribution of RC:BChla ratios for *Fc. gelatinosus* DSM149  
(mode: 1:35, mean 1:35)



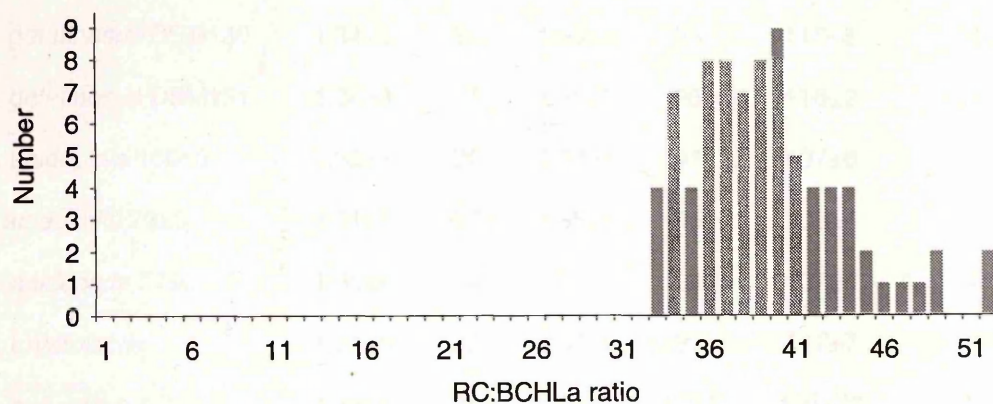
(H): Distribution of RC:BChla ratios for *Fc. gelatinosus* DSM151  
(mode: 1:35, mean 1:36)



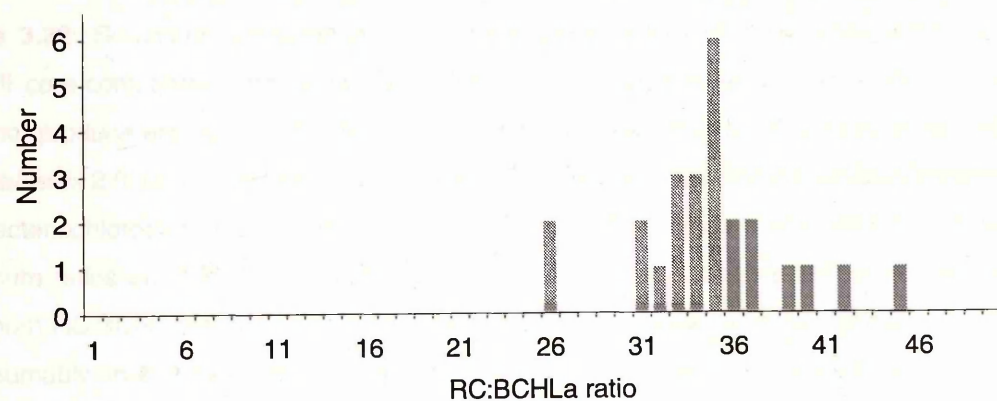
(I): Distribution of RC:BChla ratios for *Rp. acidophila* 7750 (mode: 1:34, mean 1:33)



(J): Distribution of RC:BChla ratios for *Rp. acidophila* 10050 (mode: 1:41, mean 1:39)



(K): Distribution of RC:BChla ratios for *Rp. acidophila* 7050 (mode: 1:35, mean 1:35)



Species/strain	RC:BChl Ratio				Experimentally derived extinction coefficient at 880nm	
	Established		Experimental		$\epsilon_{880\text{nm}}$ ( $\text{mM}^{-1}\text{cm}^{-1}$ )	Number of replicats
	mean	mode	mean	mode		
<i>R. centenum</i>	1:29±3	30	1:31±3	32	113±7	31
<i>R. rubrum</i> S1	1:30±4	32	1:33±5	33	111±6	74
<i>Rb. sphaeroides</i> GA	1:29±2	28	1:34:4	35	105±10	9
<i>Rb. sphaeroides</i> M21	1:30±3	32	1:37±5	29/35	100±7	11
<i>Rc. gelatinosus</i> DSM149	1:34±2	34	1:35±2	35	116±5	23
<i>Rc. gelatinosus</i> DSM151	1:34±3	34	1:36±3	35	116±2	19
<i>Rp. acidophila</i> 10050	1:35±3	34	1:39±4	41	107±6	82
<i>Rp. acidophila</i> 7050	1:31±3	28/34	1:35±4	35	108±4	25
<i>Rp. acidophila</i> 7750	1:30±4	34	1:33±4	34	107±4	67
<i>Rp. cryptolactis</i>	1:31±5	36	1:32±5	37	117±7	26
<i>Rp. palustris</i> 2.6.1.	1:25±4	33	1:29±7	25/28	105±11	42

**Figure 3.32:** Summary of the Reaction Centre:Bacteriochlorophyll ratios obtained from purified RC-LHI core conjugates. The overall RC:BChl ratios are very similar. Indeed analysis of variance does not produce any significant difference between species. The RC:BChl ratio ranges from 1:22 (*Rp. palustris* 2.6.1.) to 1:38 (*Rp. acidophila* 10050) using the established coefficients for RC-redox and bacteriochlorophyll assays. Using the experimentally determined coefficients the minimum and maximum ratios are 1:22 (*Rp. palustris* 2.6.1.) and 1:52 (*Rp. acidophila* 10050) respectively. The maximum RC:BChl ratio of 1:52 is out with the rest of the data set from *Rp. acidophila* 10050 thus is presumably an erroneous result. If this data point is ignored then the maximum ratio is 1:49. The average RC:BChl ratio although useful does not in its self indicate the distribution of RC:BChl ratios. Using the mode statistic (most abundant measurement) indicates that the RC:BChl ratios varies between 1:28-36 (established) and 1:29-41 (experimentally determined coefficients). From the modal figures above and the previous histograms the spread of RC:BChl is generally gaussian. Comparing ratios and extinction coefficients between strains suggests that their is little difference between them with respect to core integrity.

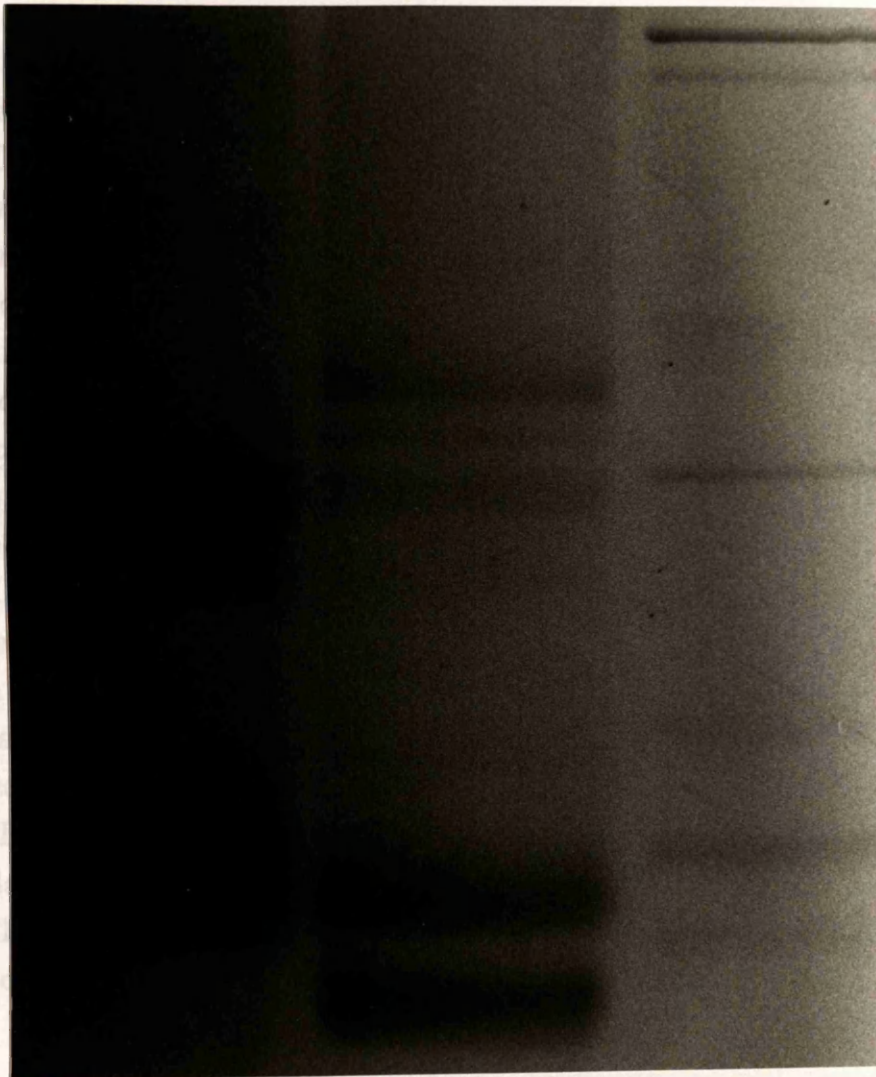
**Figure 3.33:** SDS-PAGE of the Rhodospirillaceae pigment-protein complexes. Examples of purified RC-LHI conjugate from *Rp. palustris* strain 2.6.1, *Rp. acidophila* strain 7750 and *R. centenum* are depicted. As with previous reports the purified complexes produce three reaction centre bands corresponding to the H, M and L polypeptides and two low molecular weight bands which represent the light-harvesting alpha and beta polypeptides. Protein molecular weight standards were used to identify the molecular weights of the Coomassie blue stained bands. The protein standards used were: Aprotinin (6.5 KDa), Lysozyme (14.4 KDa), Trypsin inhibitor (21.5 KDa), Carbonic anhydrase (31.0 KDa), Ovalbumin (45.0 KDa), Serum albumin (66.2 KDa) and Phosphorylase b (97.4 KDa). (A): PAGE Gel of purified *Rp. palustris* strain 2.6.1 and *Rp. acidophila* strain 7750 RC-LHI conjugates. *Rp. palustris* strain 2.6.1; the calculated molecular weights for the H, M and L polypeptides were 32 KDa, 29 KDa and 26 KDa respectively. Note that the H and M bands are not easily distinguished. The alpha and beta polypeptides virtually ran together on the gel and were calculated to be 10 KDa and 9 KDa respectively. Similar bands were obtained for *Rp. acidophila*, but the bands were easier to distinguish. The molecular weights of the H, M, L,  $\alpha$  and  $\beta$  bands were 38 KDa, 34 KDa, 31 KDa, 11 KDa and 6 KDa respectively. (B): Purified RC-LHI from *R. centenum* originating from the pigmented bands (bands I and II) formed by sucrose gradient centrifugation. Both lanes produce identical bands on the gel with the molecular weights of the H, M, L,  $\alpha/\beta$  bands calculated to be 35 KDa, 29 KDa, 21.4 KDa and 10 KDa respectively.

(A)

*Rp. palustris*  
2.6.1

*Rp. acidophila*  
7750

Protein  
Standards

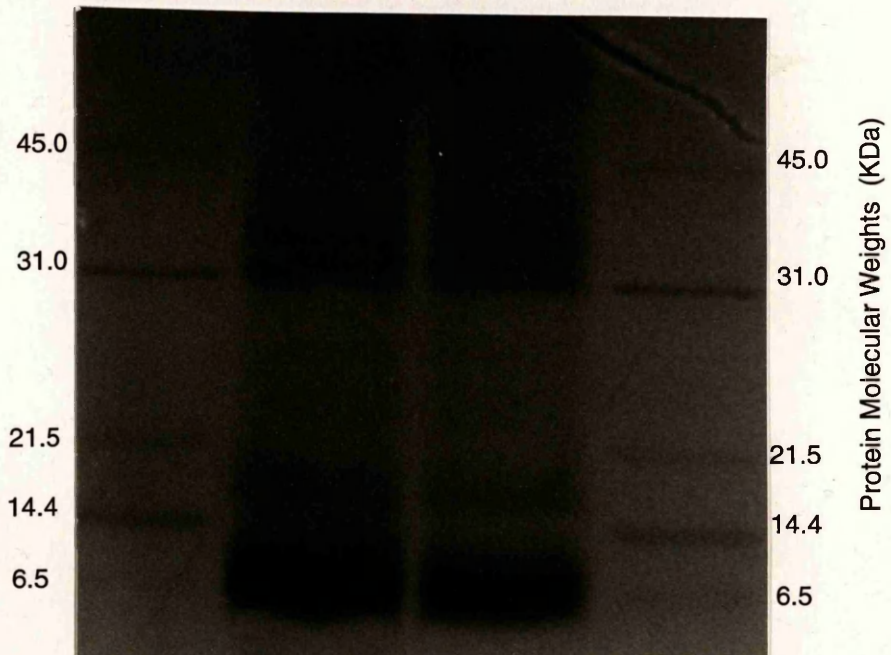


(B)

Protein  
Standards

*R. centenum*  
BAND I    BAND II

Protein  
Standards



### 3.5: Summary of Pigment-Protein Characterisation:

The isolation and purification of RC-LHI from a range of species has shown that some isolated *cores* are more stable than others. Amongst the more stable RC-LHI conjugates *in vitro* were those from *Rp. acidophila*, *Rp. cryptolactis* and *Rp. palustris*, with the least stable *cores* being from *Rb. sphaeroides* and *R. centenum*. The isolation of LHII for all species, on the other hand, was straight forward.

Using the experimentally determined coefficient, at 880nm, for the RC-LHI conjugates ( $\sim 100\text{-}120 \text{ mM}^{-1}\text{cm}^{-1}$ ) the histograms of number vs. RC:BChl *a* ratio (Figure 3.31) are similar to the histograms on the previous pages (i.e. 1:25-35). When comparing RC-LHI stoichiometry, all the strains appear to produce similar mean and modal values for the RC:BChl *a* ratio (Figure 3.32). Consequently the RC-LHI stoichiometry appears to be similar for all species investigated. The variation in the mean, modal and calculated extinction coefficients is thought to be due to the variation in *core* stability when isolated from the *in vivo* system. Further analysis however may still be required to reduce the variation in the species specific extinction coefficients at 880nm. SDS-PAGE was used to confirm that pure pigment-protein complexes were isolated (Figure 3.33). It appears that all the members of the Rhodospirillaceae, including the recently isolated species *Rp. cryptolactis* (Stadtward *et al.*, 1990), possess a similar RC-LHI conjugate.



## 4.1 Introduction:

The x-ray analysis of the reaction centres from *Rp. viridis* and *Rb. sphaeroides* have provided valuable structural information on the heart of bacterial photosynthesis. However no structure is as yet forthcoming for either the entire core conjugate (RC-LHI) or light-harvesting complexes (LHI and LHII) using conventional x-ray crystallography. It is therefore useful to investigate other avenues of structural determination such as electron microscopy (E.M.) and image analysis of 2D crystals, or arrays. If an E.M. structure can be produced from a 2D array of either RC-LHI or LHII, even at a low resolution, useful structural information could be obtained as in the case for RNA polymerase I (see Chapter One; Schultz *et al.*, 1993). In theory, the phase information from the lattice co-ordinates from an E.M. structure could also be used as a starting point for high resolution x-ray data analysis (Engel *et al.*, 1992).

Naturally occurring 2D arrays are found but are few in number (see Chapter One). Sometimes crude protein preparations can produce 2D arrays (e.g. connexins 46 and 50; Lampe *et al.*, 1991), however, many examples of 2D arrays have been produced from purified proteins. Examples of high resolution data obtained from some purified proteins can be seen in Figure 4.1. There are even cases where over expression of a protein (by genetic manipulation of the host organism) causes the packing of the over expressed membrane protein such that pseudo-natural arrays are formed in the host membrane. Examples are fumarate reductase (Cole *et al.*, 1985) and glycerol-3-phosphate acyl transferase (Wilkinson *et al.*, 1986). However these induced *natural* arrays are not the norm. Usually over-expressed membrane protein ends up denatured in inclusion bodies (e.g. psaC from PSI; Golbeck, J., personal communication).

Under suitable conditions rapid freezing of trans-membrane protein 2D arrays can lead to the elucidation of temporal structural changes within membrane associated proteins. Such rapid freezing of membranes has produced direct evidence for the structural changes in the proteins involved in the photocycle of bacteriorhodopsin (Subramaiam *et al.*, 1993).

SPECIMEN	SIZE	RESOLUTION
Purple membrane (bacteriodopsin)	27kDa	0.28nm (0.35nm)
LHCII a/b	25kDa	0.34nm (0.6nm,0.34m)
PhoE porin	37kDa	0.35nm (0.6nm)
OmpF porin	37kDa	0.35nm
Crotoxin	10kDa and 14kDa	0.35nm
$\alpha$ -helical coiled protein from praying mantis		0.4nm
CaATPase	109kDa	0.6nm
Cytochrome oxidase	4.5-45kDa	0.7nm
bacterial S-layer	91kDa	0.8nm
T4 DNA helix destabilizing protein gp 32 <sup>†</sup>	27kDa	0.85nm
T.M.V.	17.5kDa	1.0nm

**Figure 4.1:** High resolution data obtained using cryo-EM. Adapted from Bremer *et al.*, (1992). The subunit size does not depict the total size of the macromolecule but illustrates the resolution for the individual protein domains. The depicted resolutions are for 2D reconstructions, and 3D reconstructions (bracketed). The 0.34nm 3D reconstruction for LHCIIa/b is submitted for publication (Kühlbrandt, W., personal communication; Kühlbrandt *et al.*, 1994).

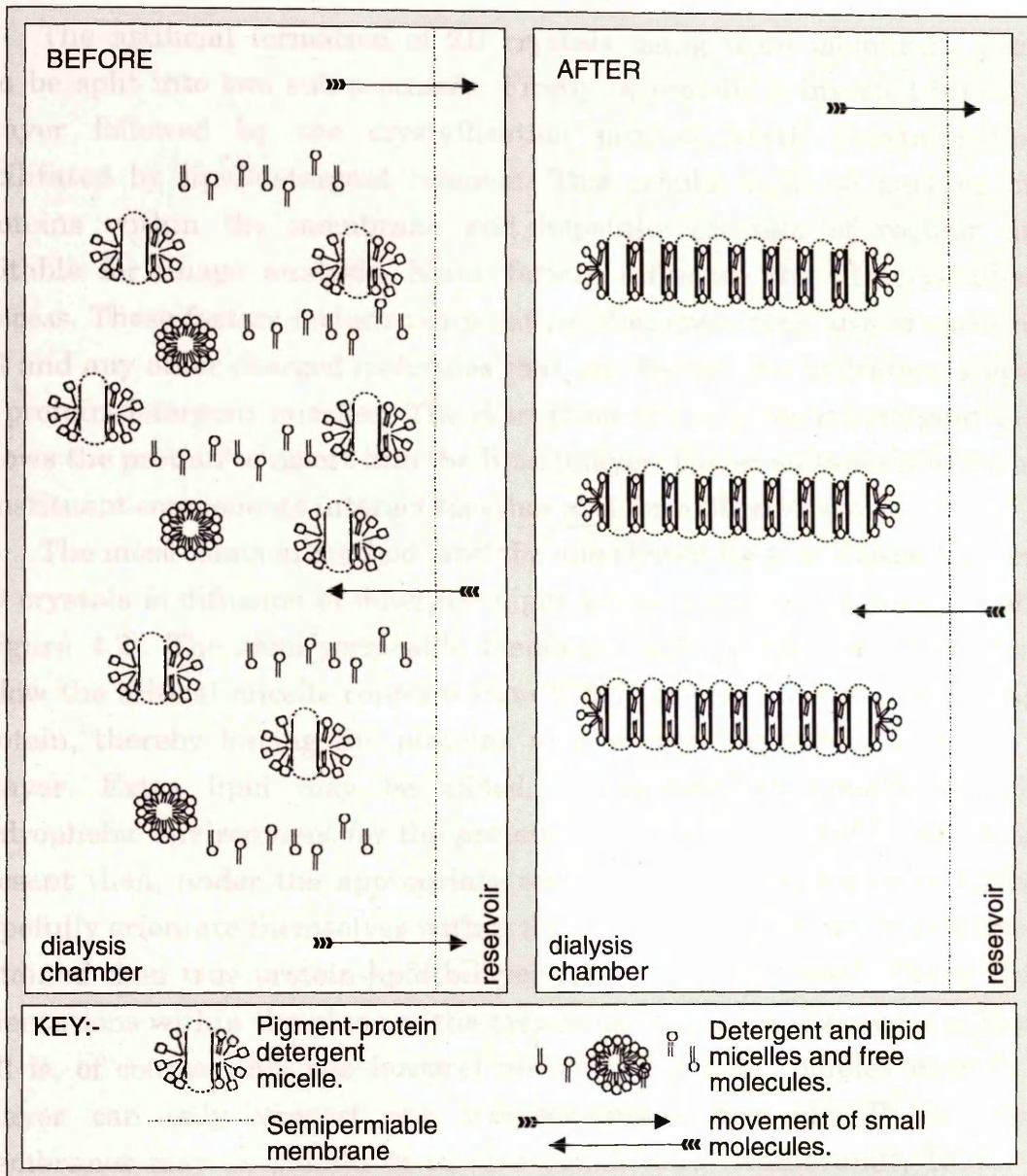


**Figure 4.2:** Formation of 2D crystals of membrane proteins by dialysis across a semi-permeable membrane. Protein-detergent micelles are mixed with excess lipids and detergent. The initial detergent concentration is above its CMC level in the dialysis chamber. Eventually net removal of detergent across the membrane (dotted line) causes the formation of 2D arrays. Proteins insert into the lipid bilayers then form crystallographic contacts when excess detergent and lipids are removed.

### 4.1.1 2D Crystallographic Concepts for Membrane Proteins:

The artificial formation of 2D crystals using trans-membrane proteins can be split into two sub-processes. Firstly, a protein is inserted into a lipid bilayer followed by the crystallisation process itself. Crystallisation is facilitated by lipid/detergent removal. This results in close packing of the proteins within the membrane and hopefully creation of regular arrays suitable for image analysis. Many factors influence the 2D crystallisation process. These factors include temperature, detergent type, use of extra lipids, pH and any other charged molecules that can disrupt the hydration properties of protein-detergent micelles. The disruption of the protein-detergent micelle allows the protein to insert into the lipid bilayer. Under suitable conditions the constituent components interact together and form 2D crystals.

The most common method (and the one chosen for this thesis) for forming 2D crystals is diffusion of detergent/lipid across a semi-permeable membrane (Figure 4.2). The semi-permeable membrane allows detergent levels to fall below the critical micelle concentration (CMC) in the chamber containing the protein, thereby forcing the proteins to associate themselves with the lipid bilayer. Extra lipid may be added, if required, to provide a suitable hydrophobic environment for the proteins. If suitable and sufficient lipids are present then, under the appropriate conditions, the membrane proteins will hopefully orientate themselves within the membrane. If optimal conditions are obtained then true protein-lipid bilayer sheets can be formed. These uniform orientations within the plane of the membrane sheet are 2D crystals. The unit cell is, of course, only one integral membrane protein complex deep (a lipid bilayer can only support one transmembrane domain). These artificial membranes may be similar to *in vivo* membranes (Kühlbrandt, 1992). They allow the integral membrane proteins to diffuse and hopefully orientate themselves into positions that make them stable within the lipid environment. This is considered to increase stability at the boundary between the aqueous and non-aqueous environments. *In vivo* membrane proteins themselves are located in just a lipid-rich environment. Therefore 2D crystals of membrane proteins can presumably be regarded as closer to their *in vivo* state when compared to detergent rich 3D protein-detergent micelle crystals (Kühlbrandt, 1992).

As stated above removal of detergent and integration into a lipid layer may cause 2D crystal formation. For integral membrane proteins a lipid bilayer is used. Monolayers of lipid can also be used to create 2D crystals. This is where only a single hydrophobic domain from a membrane associated

protein protrudes into the membrane, permitting crystal contacts to occur. For reviews on monolayer 2D crystallography see Newman, (1991) and Kornberg and Darst, (1991).

#### 4.1.2 Isolated Reaction Centre - LHI Conjugates:

Previous reports using transmission electron microscopy (T.E.M.) of isolated photochemically active particles from *Rb. sphaeroides* (Garcia *et al.*, 1968; Reed *et al.*, 1972), *R. viridis* (Stark, 1984), *E. halochloris* (Engelhardt *et al.*, 1986) and *C. vinosum* (Garcia *et al.*, 1966; Halsey and Byers, 1975) indicate that uniformly sized particles can be obtained. The uniform size of these solubilised particles and the biochemical evidence from Dawkins, (1988) has suggested that isolated RC-LHI conjugates consist of uniform disc-like structures with a fixed RC:LHI stoichiometry. It has been reported that the disc-like photosynthetic particles of *R. viridis* (Stark, 1984) and *E. halochloris* (Engelhardt *et al.*, 1986) produce regular arrays *in vivo*. Isolated LHI (i.e. RC-LHI lacking the RC) from *R. marina*, which also produces *in vivo* sheets, forms small sheet-like aggregates (Meckenstock, R., personal communication). During the isolation of the photosynthetic particles from *C. vinosum* (Halsey and Byers, 1975) it was noted that small square shaped sheet-like aggregates occurred which contained between 9 and 16 of these particles. Therefore the question arose whether this was an artefact resulting from the purification process or a resemblance of arrangement within the *in vivo* ICM. Halsey and Byers, (1975) concluded that the observed square-like aggregates probably resulted from "parallel packing of linear polymers" however single polymer chains were never detected by them.

From the work on *Rb. sphaeroides*, *Rp. viridis*, *E. halochloris*, and *C. vinosum* it may indeed be possible to form regular 2D arrays of these purified photosynthetic particles from a number of species. By doing so it would establish that it is potentially possible for all Rhodospirillineae RC-LHI conjugates to associate themselves. If such arrays could be established a structure for a suitable RC-LHI supra-complex (e.g. *Rb. sphaeroides* or *Rp. acidophila*) could also be elucidated.

The results of T.E.M studies from a range of pigment-protein complexes (see Figure 4.3) is discussed below, and is split into two sections. The first deals with isolated pigment-protein complexes, while the second discusses the crystallographic aspects.

Species	strain	RC-LHI	HLII
<i>Cr. purpuratum</i>	type	1	n/i
<i>R. centenum</i>	type	3	n/a
<i>R. rubrum</i>	S1	5	n/a
<i>Rb. sphaeroides</i>	GA	3	3
	M21	3	n/a
<i>Rc. gelatinosus</i>	DSM 149	5	3
	DSM 151	3	n/i
<i>Rp. acidophila</i>	10050	15	4
	7750	12	3
	7050	7	n/i
<i>Rp. cryptolactis</i>	type	6	6
<i>Rp. palustris</i>	2.6.1. (HL)	5	2
	(LL)	3	3

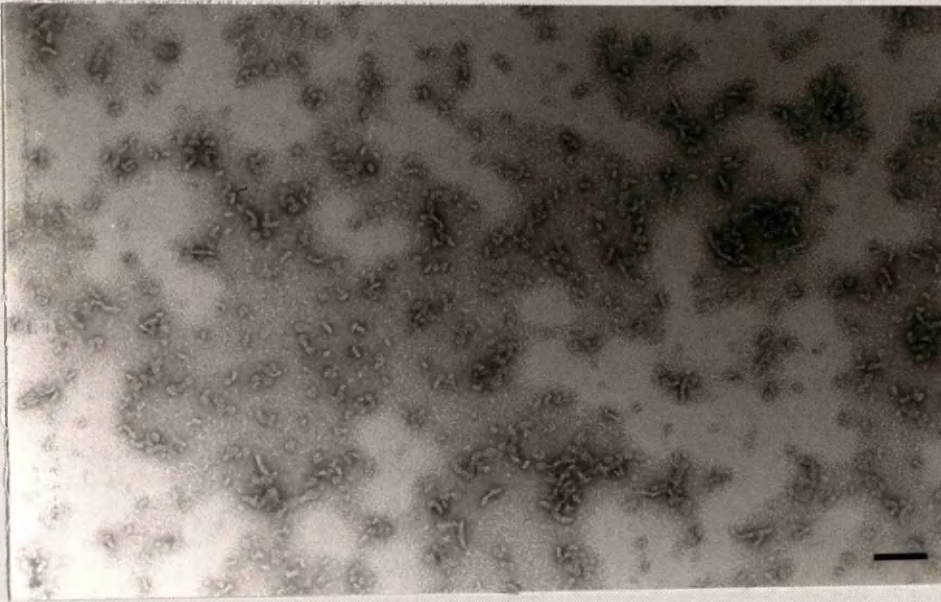
**Figure 4.3:** Tabulated list of the Rhodospirillineae photosynthetic proteins that were screened for their potential rôle in forming 2D crystals. The numbers refer to the isolation and screening of individual pigment-protein batches. n/a:- not applicable, this strain does not produce this type of pigment-protein complex. n/i:- pigment-protein complex not investigated.

Purified RC-LHI from a range of species was examined by transmission electron microscopy (T.E.M.) using negative stains. Figure 4.3 shows a list of RC-LHI and LHII complexes that were studied for their possible ability to form 2D arrays. Examination of the isolated pigment-protein complexes under T.E.M. was done before 2D crystallisation trials were attempted to ensure that homogenous photosynthetic complexes were present and that no contamination was apparent. The protocol used to stain and examine the specimens is described in section 3.3. Figure 4.4 illustrates some examples of the purified *core* conjugate from a number of species. It should be noted that the electron micrographs of different strains within a species show no apparent differences, consequently only one strain of each is depicted for those species where more than one strain was investigated. The electron micrographs show that the *core* from these species produce monomeric disc like structures. The diameter of these objects is between 10nm and 13nm with an apparent depth of less than 7nm. The use of single particle analysis was ruled out because of their relatively small size and their potential for producing 2D arrays. The depth of these photosynthetic particles was derived from stained objects which appeared to lie on their sides. All of the specimens in Figure 4.4 (and also those strains not depicted) indicate that the purified RC-LHI conjugates prepared in Chapter Three are of uniformly sized photosynthetic particles. When fully solvated (i.e. in a detergent rich environment) these isolated particles exist as single entities.

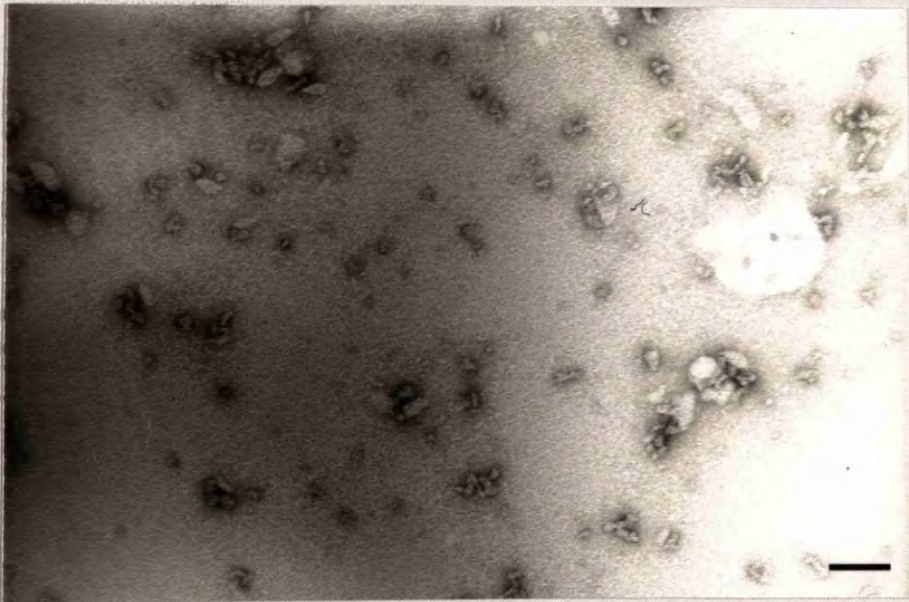
Figure 4.4 illustrates an electron micrograph of *Rc. gelatinosus* strain 149. This strain of *Rc. gelatinosus* appears to aggregate very easily, forming an amorphous precipitate. The isolation protocol for *Rc. gelatinosus* RC-LHI (see sections 3.3.4. and 3.3.7.) is similar to that of *Rp. palustris* 2.6.1. (Figure 4.4), but the T.E.M. images are very dissimilar. The reason for this is unclear but may be due to some unknown unique properties of the *Rc. gelatinosus* proteins. The reason could be due to the staining protocols or detergents used. The majority of the other species and strains, however, produce more uniformly sized photosynthetic particles with little aggregation or amorphous precipitate.

**Figure 4.4:** Isolated RC-LHI conjugates from a range of Rhodospirillaceae. (A): *R. rubrum*. (B): *Rb. sphaeroides* strain M21. (C): *Rc. gelatinosus* strain DSM149. (D): *Rp. cryptolactis*. (E): *Rp. palustris* strain 2.6.1. Bar:100nm

A



B



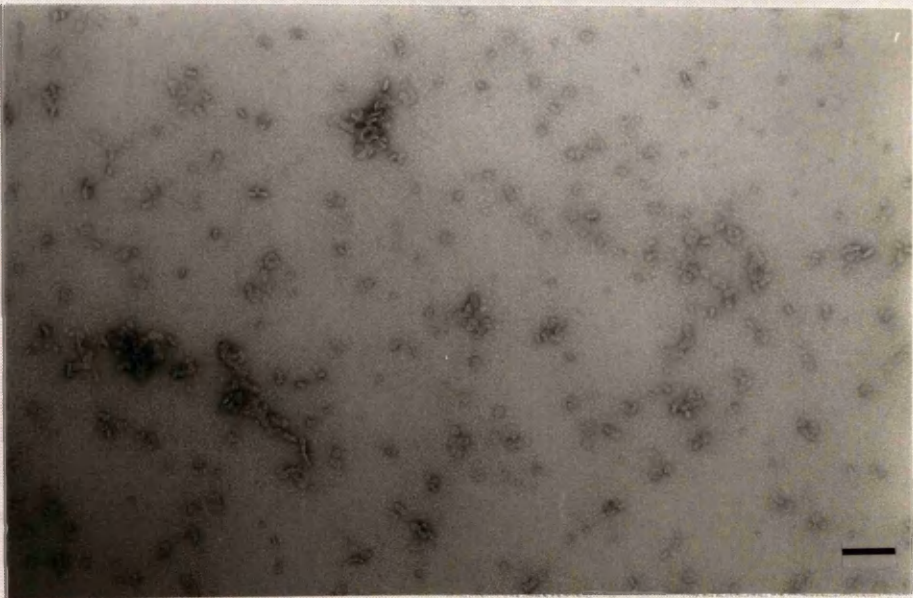
C



D



E



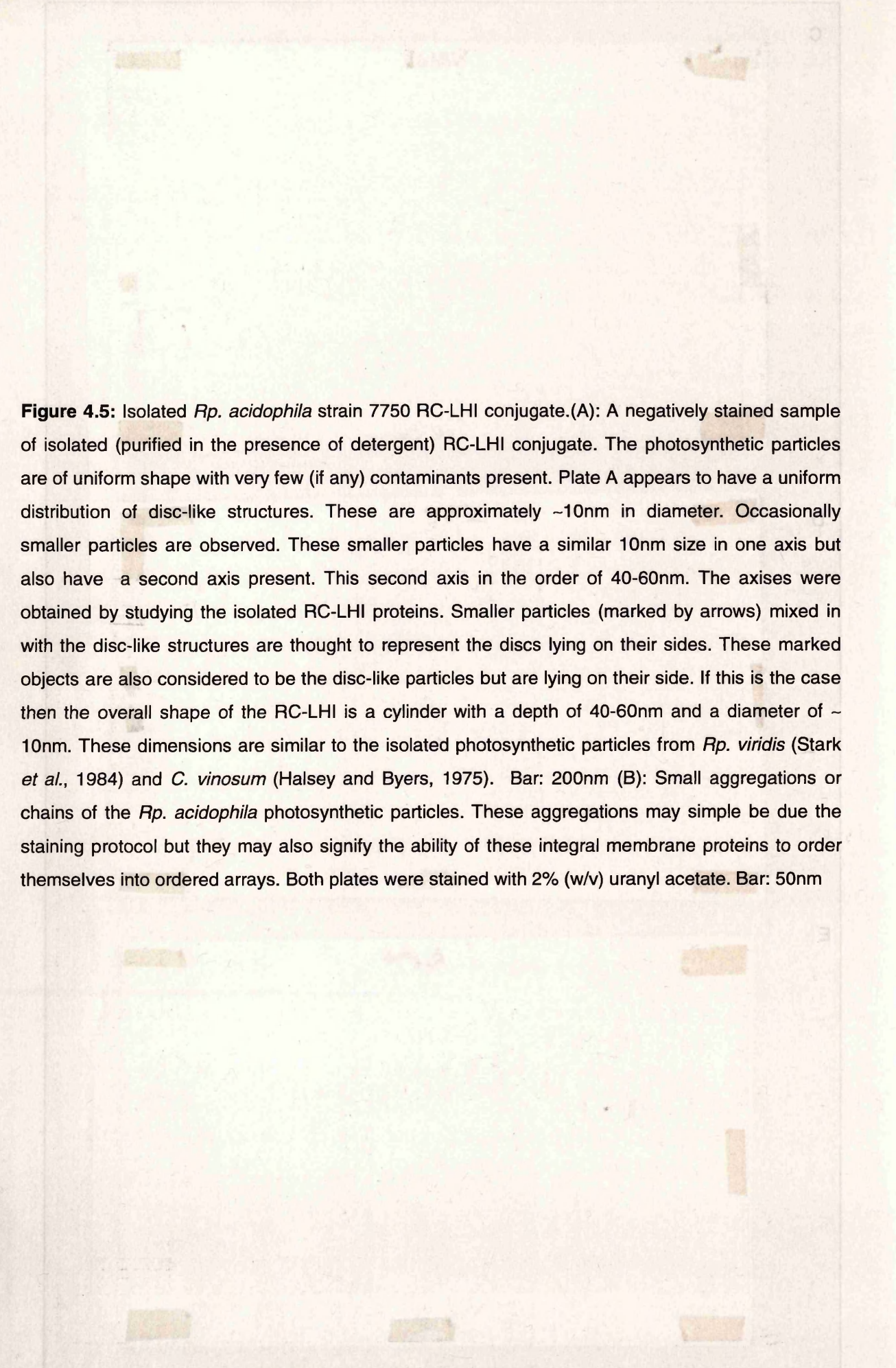
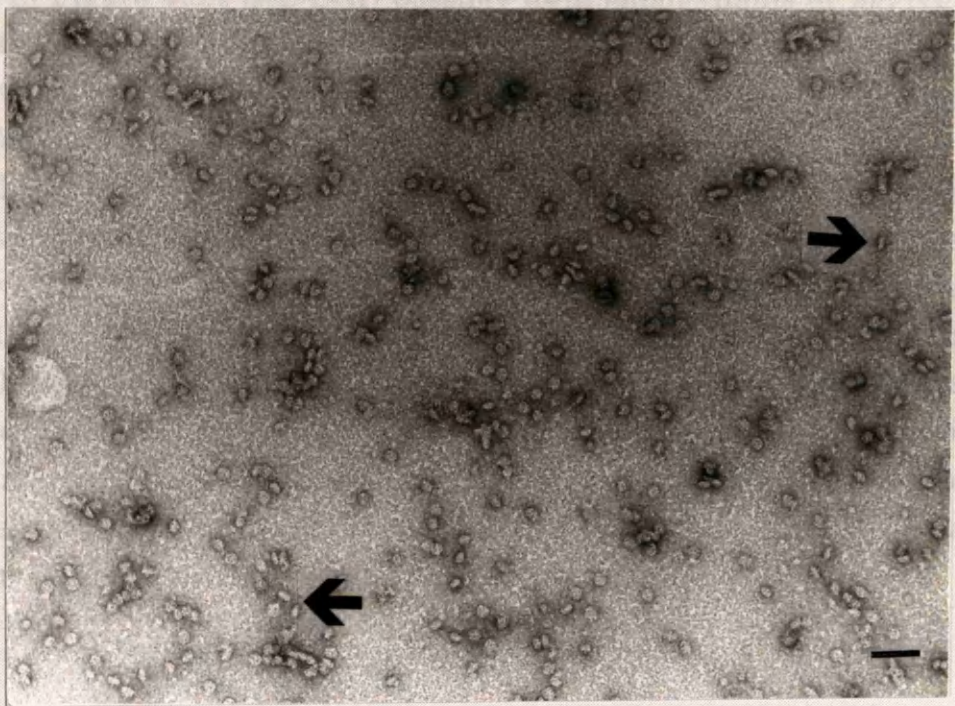
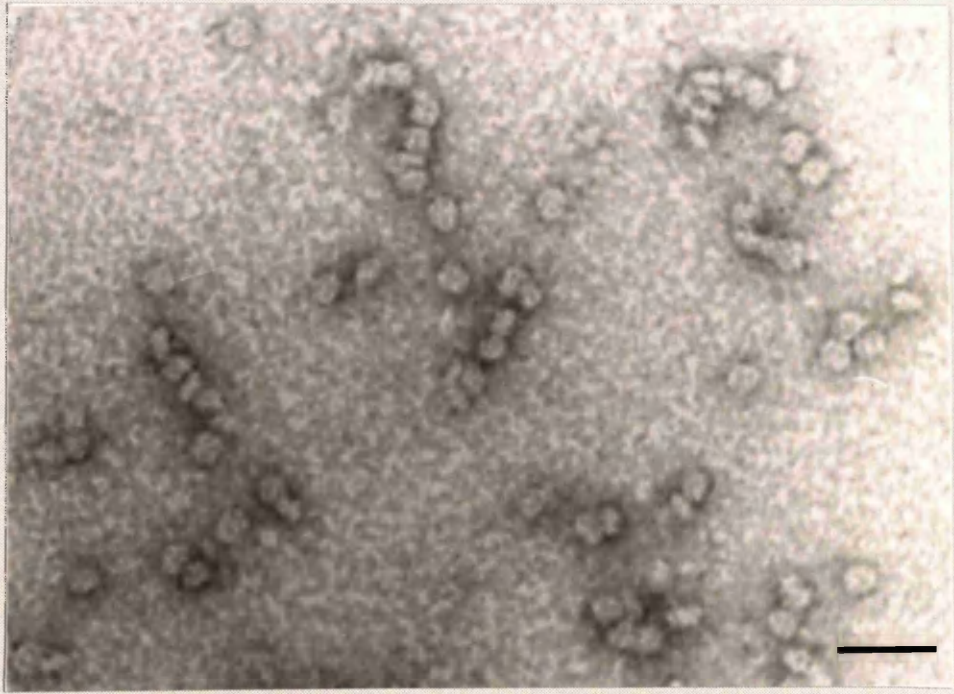


**Figure 4.5:** Isolated *Rp. acidophila* strain 7750 RC-LHI conjugate. (A): A negatively stained sample of isolated (purified in the presence of detergent) RC-LHI conjugate. The photosynthetic particles are of uniform shape with very few (if any) contaminants present. Plate A appears to have a uniform distribution of disc-like structures. These are approximately ~10nm in diameter. Occasionally smaller particles are observed. These smaller particles have a similar 10nm size in one axis but also have a second axis present. This second axis is in the order of 40-60nm. The axes were obtained by studying the isolated RC-LHI proteins. Smaller particles (marked by arrows) mixed in with the disc-like structures are thought to represent the discs lying on their sides. These marked objects are also considered to be the disc-like particles but are lying on their side. If this is the case then the overall shape of the RC-LHI is a cylinder with a depth of 40-60nm and a diameter of ~10nm. These dimensions are similar to the isolated photosynthetic particles from *Rp. viridis* (Stark *et al.*, 1984) and *C. vinosum* (Halsey and Byers, 1975). Bar: 200nm (B): Small aggregations or chains of the *Rp. acidophila* photosynthetic particles. These aggregations may simply be due to the staining protocol but they may also signify the ability of these integral membrane proteins to order themselves into ordered arrays. Both plates were stained with 2% (w/v) uranyl acetate. Bar: 50nm

(A)



(B)



4.2 *Rp. acidophila*, like the majority of other species investigated, can be easily isolated and purified as discrete disc-like particles (Figure 4.5). On close examination these electron micrographs indicate that the photosynthetic particles in Figure 4.5A (RC-LHI) possibly form small chains or aggregations (Figure 4.5B). Whether the presence of these chains in Figure 4.5B is a true representation of the *in vivo* membrane, or detergent-protein micelle, or simply an artefact of staining is unknown and an answer to this is virtually impossible. From general observations however, it appears that most, if not all species, show some degree of protein association while solubilised in detergent just above the CMC value (e.g. 0.1%<sub>(w/v)</sub> LDAO and 0.8%<sub>(w/v)</sub>  $\beta$ -OG). It can also be postulated that the close association of these photosynthetic particles (RC-LHI), as shown in Figure 4.5B, may enable these supra-complexes to aggregate into small chains of linear polymers. The use of detergents however leaves a major question. If the aggregation is not a staining artefact then are the aggregations caused by the presence of detergent, or by the natural ability of the particles to associate themselves with each other?

The conditions for producing good 2D crystals of *R. rubrum* RC-LHI (Dawkins, 1988) were initially used with the RC-LHI after the detergent was removed. This was achieved by taking a small volume (100  $\mu$ l) in the bottom of a boiling dialysis bag and dialysing it into a 20 mM TRIS-HCl, pH 8.0 dialysis buffer. A sample (approximately 10  $\mu$ l) was removed at 15 min and dialysed into a 20 mM TRIS-HCl, pH 8.0 dialysis buffer. The buffer contained 20 mM TRIS-HCl, pH 8.0, 0.1 M NaCl, 0.1 M Na<sub>2</sub>S<sub>2</sub>O<sub>4</sub>, 0.1 M Na<sub>2</sub>SO<sub>4</sub>, 0.1 M Na<sub>2</sub>HPO<sub>4</sub>. Attempts were made to produce 2D crystals from the RC-LHI precipitate and generally failed. It was thought that the RC-LHI particles, during the incubation, the procedure outlined above, had some of the RC-LHI particles.

The addition of PEGs in the dialysis buffer was attempted to prevent amorphous precipitation. Therefore the PEG was removed from the dialysis sample and an entirely new experimental design was then employed in conjunction with completely new initial incubation conditions. The incubation contained 3 mM sodium azide, and for the  $\beta$ -OG samples 1%  $\beta$ -OG, 0.1 M TRIS-HCl, pH 8.0. The order of pipetting was such that all components of the membrane protein solution (detergent, RC-LHI, and higher than the CMC value (i.e. 1%  $\beta$ -OG) if salts were added) to the protein mixture were also prepared as stock solutions at 100  $\times$  concentration. The addition of sodium azide to the RC-LHI solution was to prevent possible bacterial growth.

The conditions for producing good 2D crystals of *R. rubrum* RC-LHI (Dawkins, 1988) were initially used with the RC-LHI after the detergent was removed. This was achieved by taking a small volume (100  $\mu$ l) in the bottom of a boiling dialysis bag and dialysing it into a 20 mM TRIS-HCl, pH 8.0 dialysis buffer. A sample (approximately 10  $\mu$ l) was removed at 15 min and dialysed into a 20 mM TRIS-HCl, pH 8.0 dialysis buffer. The buffer contained 20 mM TRIS-HCl, pH 8.0, 0.1 M NaCl, 0.1 M Na<sub>2</sub>S<sub>2</sub>O<sub>4</sub>, 0.1 M Na<sub>2</sub>SO<sub>4</sub>, 0.1 M Na<sub>2</sub>HPO<sub>4</sub>. Attempts were made to produce 2D crystals from the RC-LHI precipitate and generally failed. It was thought that the RC-LHI particles, during the incubation, the procedure outlined above, had some of the RC-LHI particles.

## 4.2 Microdialysis of RC-LHI:

Aliquots of detergent-purified protein were mixed with other extra lipids, salts, and buffer then subjected to microdialysis to remove excess detergent and lipid. These membrane proteins must be in buffers containing detergent above the detergent's CMC value until microdialysis was initiated. The preparation for microdialysis was as follows. Protein concentration was determined (see section 2.7.1) and the correct volume of protein pipetted into an 1.5ml eppendorf tube. If excess lipid was to be added it was pipetted into the protein mixture. Lipid stock solutions were prepared at concentrations of  $10\text{mg ml}^{-1}$  in the same buffered solution as the pigment-protein complexes. The correct volume of buffer was then added to a pigment-protein sample to reduce the protein concentration to the desired level. This was achieved by adding a mixture of buffer (e.g. 10mM TRIS.HCl, pH8.0), sodium azide (300mM unbuffered stock solution in Analar<sup>®</sup> water) and detergent (e.g. 10%  $\beta$ -OG, 10mM TRIS.HCl, pH8.0) such that the final sample preparation contained 3mM sodium azide, and for the  $\beta$ -OG samples, 1%  $\beta$ -OG in 10mM TRIS.HCl, pH8.0. The order of pipetting was such that at no time were the membrane proteins subjected to detergent levels much higher than the CMC value (i.e. 1% (w/v) for  $\beta$ -OG). If salts were added to the protein mixture these were also prepared as stock solutions in buffer containing detergent. The addition of sodium azide in both the dialysis chamber and the outer reservoir was to prevent possible bacterial growth.

The conditions for producing small 3D crystals of *R. rubrum* RC-LHI (Dawkins, 1988) were initially used with the aim of producing 2D arrays by detergent removal. This was achieved by boring a small hole (1mm diameter) in the bottom of a button dialysis apparatus. Once prepared (Sambrook *et al.*, 1989) dialysis tubing was attached, and the button was floated onto 50ml of dialysis buffer. A sample preparation of *R. rubrum* core was pipetted into the button and dialysed at 4°C against 50ml of buffer. The buffer consisted of 20mM TRIS.HCl, pH8.0 and various salt (NaCl) concentrations. Numerous attempts were unsuccessful in producing 2D arrays. Only amorphous precipitate and occasionally small 3D microcrystals were formed. Increasing the incubating temperature enhanced only the rate of protein degradation.

The addition of PEG in the dialysis chamber was the probable cause of amorphous precipitation. Therefore the PEG was removed from the protein sample and an entirely new experimental design was then employed in conjunction with completely new initial incubation conditions. Consequently

the conditions that produce 3D crystals are not necessarily suitable for crystallographic studies. New 2D trials were not used or used only on previously formed 3D crystals and the experimental apparatus was that described by Kuhlbrandt, (1997).

This new approach made use of a different dialysis chamber (Figure 4.6). Approximately 10cm long, L-shaped, glass tubes being approximately 10mm long with an internal diameter of 3-4 mm were used to hold the protein solution in the dialysis chamber (Figure 4.6). The L-shaped end was held in place by a ring of silicon tubing (Sambrook et al., 1989, Spectralab) which is held in place by a ring of silicon tubing (Sambrook et al., 1989, Spectralab) against non-detergent dialysis buffer.

Initially three proteins were dialysed in this apparatus, *R. ruber* (strain 51, Dr. Peter Drenth), *R. ruber* (strain 57) and *R. ruber* (strain 58). These proteins were dialysed in this apparatus when purified. Protein solutions were prepared in the presence of the detergent (Sambrook et al., 1989, Spectralab) (Kuhlbrandt, 1997). The dialysis buffer was prepared in the presence of the detergent (Sambrook et al., 1989, Spectralab) (Kuhlbrandt, 1997). The dialysis buffer was prepared in the presence of the detergent (Sambrook et al., 1989, Spectralab) (Kuhlbrandt, 1997).

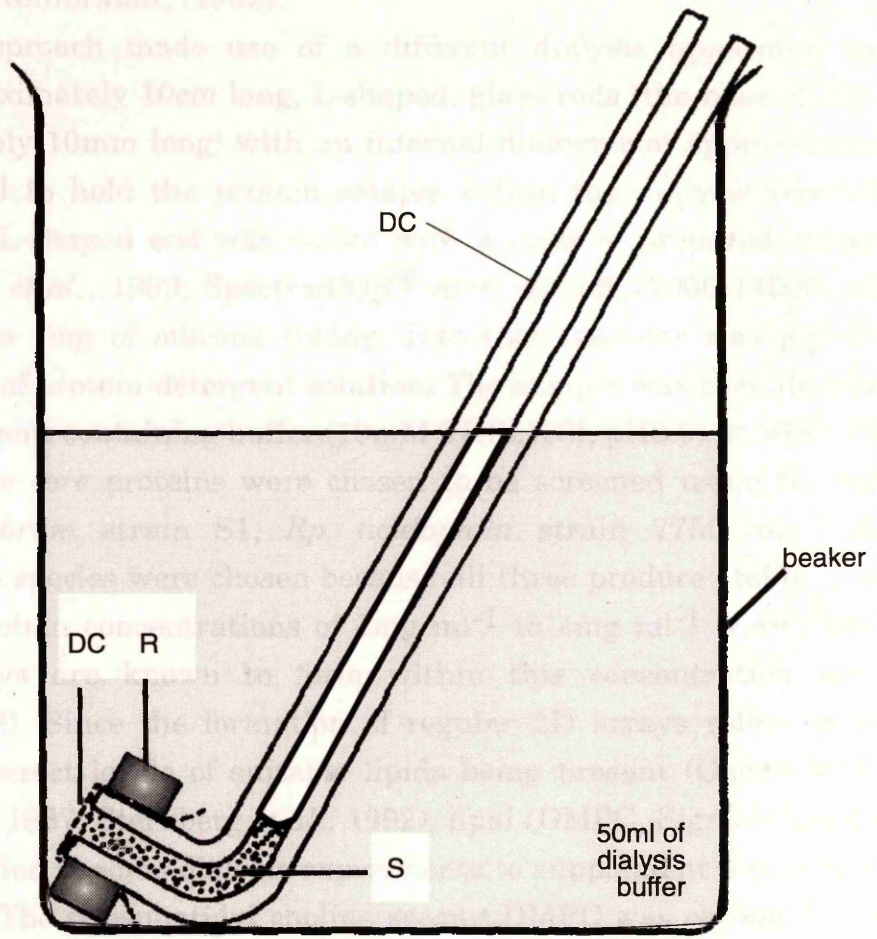


**Figure 4.6:** Experimental design of a 2D microdialysis dialysis system. A beaker is filled with 50ml of dialysis buffer and placed in a water bath to maintain a constant temperature. Into the dialysis buffer is placed a prepared microdialysis dialysis chamber. The dialysis chamber (DR) is prepared by sealing a piece of dialysis tubing (DT) which is held in place by a ring of silicon tubing (R). Once sealed and checked for leaks the microdialysis chamber is loaded with sample (S) such that no air bubbles occur at the dialysis tubing surface. Air bubbles at the DT surface inhibit the diffusion of molecules across the membrane. Once loaded the system is sealed with Nescofilm ® to prevent dialysis buffer evaporation.

There are several reasons why this system is preferred over other systems. Firstly, the transition temperature is relatively low (25°C) and the head group is not too large. This is important for the integral membrane protein. Secondly, the lipid bilayer is not too thick and the degradation is not too fast. This is important for the stability of the system. Thirdly, the system is generally simple to use and does not require special equipment. This is important for the accessibility of the system.

the conditions that produce 3D crystals are not necessarily very useful for 2D crystallographic studies. New 2D trials were not based on incubations that previously formed 3D crystals and the experimental apparatus was altered to that described by Kühlbrandt, (1992).

This new approach made use of a different dialysis apparatus (see Figure 4.6). Approximately 10cm long, L-shaped, glass rods (the base of the L being approximately 10mm long) with an internal diameter of approximately 3-4 mm were used to hold the protein sample within the dialysis reservoir (Figure 4.6). The L-shaped end was sealed with a piece of prepared dialysis tubing (Sambrook *et al.*, 1989; Spectra/POR<sup>®</sup> m.w. cut off 12000-14000) and held in place by a ring of silicone tubing. Into this chamber was pipetted between 50-100µl of protein-detergent solution. The sample was then dialysed against non-detergent containing buffer (10mM TRIS.HCl, pH8.0) at 26±0.2°C.

Initially three *core* proteins were chosen to be screened using the new apparatus; *R. rubrum* strain S1, *Rp. acidophila* strain 7750 and *Rp. cryptolactis*. These species were chosen because all three produce stable *cores* when purified. Protein concentrations of 1mg ml<sup>-1</sup> to 4mg ml<sup>-1</sup> were chosen because 2D arrays are known to form within this concentration range (Kühlbrandt, 1992). Since the formation of regular 2D arrays relies on the presence of the correct levels of suitable lipids being present (Cherry *et al.*, 1978; Popot *et al.*, 1987; Sternberg *et al.*, 1992), lipid (DMPC, Sigma Chemical Company) was added to some dialysis experiments to supplement any possible lipid deficiencies. The phosphatidyl choline species DMPC was chosen for two reasons. Firstly its transition temperature is relatively low (23°C), secondly the head group is small with a short (14-carbon) and straight backbone. The net effect being that the DMPC *in vitro* membrane can probably cope with any integral membrane protein system that one may wish to imbed within the lipid bilayer at a temperature which hopefully does not cause protein degradation. As previously stated the formation of 2D arrays by this method generally results by the net removal of detergent (and lipid) from the system.

There are two schools of thought as to which type of detergent the protein should be in prior to dialysis, "high CMC" detergents (e.g. β-OG) or "low CMC" detergents such as LM and LDAO (Kühlbrandt, 1992; Jap *et al.*, 1992). The problem with using "low CMC" detergents is often extensive periods are required for complete detergent dialysis to occur. This could be measured in weeks as in the case for the erythrocyte BandIII proteins (Wang, D.N., personal communication). The major problems with the isolated RC-LHI are two-fold. Firstly the proteins are stable in only a few detergents some of which are "low CMC" types (e.g. LM) while others are "high CMC" types (e.g. β-OG).

The second problem is long term stability with respect to temperature. The RC-LHI system when isolated is considered to be unstable under prolonged incubations at room temperature, as measured by absorption spectroscopy. Thus using "low CMC" detergents could subject the proteins to high detergent levels for long incubation periods causing *core* instability. The combination of long term detergent dialysis with "low CMC" detergents could itself be the cause of any failed crystallographic trials. Consequently  $\beta$ -OG (a "high CMC" detergent) was used as the first choice for crystallographic trials although trials were also attempted using LDAO and LM (two "low CMC" detergents).

Experiments were undertaken with *R. rubrum* strain S1, *Rp. acidophila* strain 7750 and *Rp. cryptolactis*, each in the three detergent types. Protein concentrations ( $1\text{-}4\text{mg ml}^{-1}$ ) and salt gradients were varied (0,50,100,200 and 400mM NaCl or  $\text{MgCl}_2$  in 10mM TRIS.HCl, pH8.0, 3mM sodium azide) as were the protein:DMPC ratios (1:1, 2:1, 3:1, 5:1, 10:1, 100:1, no added lipid). The reservoir buffer in the dialysis chamber was 10mM TRIS.HCl, pH 8.0. (i.e. the same buffer and pH the *cores* were isolated in). The dialysis buffer was replaced every 12 hours with fresh buffer pre-incubated at  $26^\circ\text{C}$ . General observations were noted when aliquots of the crystallographic trials were examined under E.M. using negative staining at various time points. From these experiments it was apparent that only  $\beta$ -OG containing samples were suitable for future analysis. Figure 4.7 illustrates the differences between the detergent types for one crystallisation experiment - only the  $\beta$ -OG sample is spectroscopically intact. Indeed protein samples that initially contained the detergent LDAO generally denatured as indicated by sample colour change from red to green. The green colour is associated with free pigments which have been lost from the pigment-protein complexes. The results also indicated that the *Rp. acidophila* strain 7750  $\beta$ -OG-RC-LHI was capable of producing probable regular structures within lipid bilayers. Regular membrane structures (Figure 4.8) occurred when the protein concentration was between 1 and  $2\text{ mg ml}^{-1}$ . These structures were optimum when a slight salt (50-100mM sodium chloride) gradient was applied with a moderately high initial phosphatidylcholine content ( $0.5\text{mg ml}^{-1}$ ). Vesicles containing probable 2D arrays of RC-LHI were sometimes located next to regular shaped sheet-like structures. Figure 4.9 summarises the differences associated with a 100mM sodium chloride gradient when compared to a non-salt dialysis system. When magnesium chloride ( $\text{MgCl}_2$ ) was used it was noted that large vesicles containing protein arrays were obtained however no sheets were produced. Also the use of magnesium chloride appeared to cause increased aggregation of the vesicle structures. The use of divalent ions has lead others to postulate

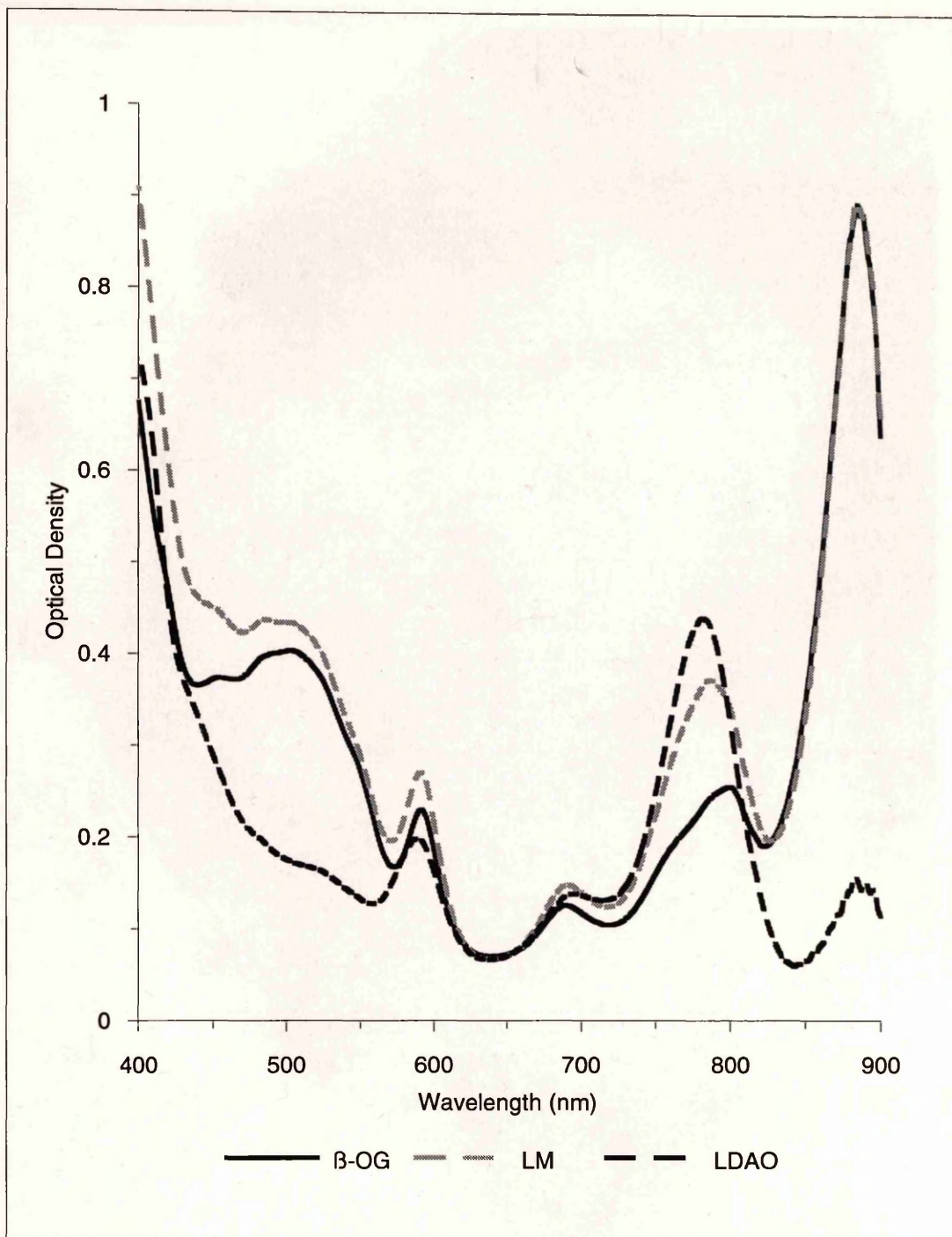


**Figure 4.7:** Absorption Spectra of RC-LHI conjugates after 48 hours of dialysis. Purified pigment-protein complexes from *Rp. acidophila* strain 7750 solubilised in three different detergents ( $\beta$ -OG, LM and LDAO) were dialyzed against 100mM NaCl, 3mM sodium azide, 10mM TRIS.HCL, pH8.0 at 26°C and the absorption spectra recorded after 48 hours incubation, then normalized at 650nm. Comparing the normalized absorption spectra to that of purified RC-LHI from *Rp. acidophila* strain 7750 (Figure 3.27) the extent of denaturation caused by prolonged incubation in the different detergents were established. The  $\beta$ -OG solubilised RC-LHI had some oxidized BChl *a* (absorption shoulder at ~780nm). The LM sample had more oxidized BChl *a* than the  $\beta$ -OG sample. Stable RC-LHI from *Rp. acidophila* strain 7750 can be obtained using both  $\beta$ -OG and LM. However LM has a much lower CMC than  $\beta$ -OG. The third sample, LDAO, caused greater pigment-protein denaturation. There is a large relative reduction in LHI absorbance (890nm absorption peak) with an associated increase in oxidized BChl *a* (~780nm). The visible carotenoid absorption range (470nm-540nm) also showed signs of denaturation in the LDAO sample. The reduced carotenoid absorbance may be due to either oxidation of the carotenoids and/or by their removal from the pigment-protein complexes by dialysis.



**Figure 4.8:** 2D arrays of RC-LHI from *Rp. acidophila* strain 7750. Vesicles containing 2D arrays of pigment-protein complexes. Magnification: x 75K.

RC-LHI: DPMC ratio (mg ml <sup>-1</sup> :mg ml <sup>-1</sup> )	no added lipid	1:1	2:1	3:1	5:1	10:1	100:1
No added NaCl	Amorphous precipitate	Many vesicles are formed with some amorphous precipitate present with occasional areas of 2D arrays	Small but numerous membrane sheets of RC-LHI with vesicles present	Mainly amorphous precipitate but some small vesicles present	Mainly precipitate with few vesicles	Mainly precipitate with very few vesicles	Mainly precipitate
100mM NaCl	Amorphous precipitate	Precipitate and aggregations of vesicles. Some of the aggregated vesicles show 2D arrays.	Many small lattice sheets of RC-LHI present	Few vesicles formed but mainly amorphous precipitate	Mainly precipitate with very few vesicles	Mainly precipitate with very few vesicles	Mainly precipitate

**Figure 4.9:** Summary of 2D incubations of *Rp. acidophila* strain 7750 RC-LHI conjugate after 48Hours. The reservoir solutions contained either no added salt (top row) or 100mM NaCl (bottom row) and 3mM sodium azide, 10mM TRIS.HCl, pH8.0. Addition of the azide was required to prevent any potential bacterial growth. Varying amounts of lipid (DMPC) were added to the protein solutions (1mg ml<sup>-1</sup> RC-LHI, 1% w/v β-OG, 3mM sodium azide, 10mM Tris.HCl, pH8.0). The reservoir buffers were changed every 12 hours. The table suggests that the protein:DMPC ratios of 1:1 and 2:1 produce 2D arrays with the 2:1 ratio producing more 2D sheet like structures. Of the two salt levels 100mM produced slightly more protein containing membrane sheets that produced 2D arrays.

that the divalent ions cause stacking in 2D arrays (Kühlbrandt, W.K, personal communication). Multiple layers of 2D arrays are inconvenient for image analysis since the stacked arrays are not always aligned, and alignment is preferred, when image analysis is undertaken. As a result divalent ions should generally not be used as the initial choice of salt.

Since the initial experiments using the three sources of *cores* (RC-LHI) only produced regular membrane structures in the  $\beta$ -OG prepared RC-LHI from *Rp. acidophila* strain 7750 the experimental parameters were varied for this dialysis system.

### 4.3 Affect of pH on RC-LHI 2D Arrays:

2D arrays were produced from *Rp. acidophila* strain 7750 RC-LHI when incubated at pH 8.0. When isolated in detergent the detergent-protein micelle from this species is most stable around pH 8.0. However it does not necessarily apply that the optimum pH for *cores* in a membrane system is the same. Using protein concentrations of 1 and 2 mg ml<sup>-1</sup> with zero, 0.5 and 1.0 mg ml<sup>-1</sup> DMPC added, the pH of the incubations was altered and observations recorded. This was achieved by two separate methods.

Firstly the 2D arrays produced in section 4.2 were formed. The dialysis buffer was then changed to another pH and left for 48 hrs then examined by T.E.M. The pH range was initially between 6.0 and 9.5 in 0.5 increments. The 10mM TRIS buffer was replaced with MES (pH 6.0, 6.5), HEPES (pH 7.0, 7.5) and CHAPS (pH 9.0, 9.5). The second method was to dialyse the protein for 24 hrs at 4°C in the new pH then set up 2D trials as described in section 4.2.

Any improvement in the diffraction patterns (as seen by an optical bench) would establish that an optimum incubation pH was obtained. The results however indicated that any alteration from the initial incubation pH of 8.0 caused 2D array breakdown.

None of the arrays using the first method produced coherent spots on an optical bench, and no arrays were produced by the second method. The lack of arrays using the second protocol could possibly be attributed to the incubation period. Between 36-48 hours are required for complete dialysis to occur. Since the isolated proteins are not stable in pHs other than about 8.0 then the relatively long period before complete detergent removal occurred could be sufficient for significant protein degeneration to take place.

The first approach, that of altering the pH of existing arrays, seemed to be the best way to alter the pH. But again results indicated that any alteration

to the pH resulted in degradation. Basically the arrays broke up, the 2D arrays were dramatically reduced in size while diffraction patterns were generally not observed for pHs other than 8.0.

From these observations it appears that the optimum pH conditions for 2D dialysis experiments is to dialyse the pigment-protein complexes in the same buffer and pH in which they were isolated. Any variation causes instability in these proteins and loss of array formation. The information obtained from the 2D trials using different detergents and pHs for *Rp. acidophila* RC-LHI were used as the basis of screening protocols for a range of other purified pigment-protein complexes.

#### 4.4 Microdialysis of a Range of RC-LHI and LHII Complexes.

A number of *cores* (RC-LHI) and peripheral light-harvesting antennae complexes (LHII) from a range of different strains and species were also screened for their potential ability to produce 2D arrays by microdialysis. The pigment-protein complexes investigated are shown in Figure 4.3.

A short explanation why these species and strains were investigated will be given. As previously stated the isolation and purification of the RC-LHI conjugate is optimal when achieved quickly. The purification of the RC-LHI depends on separating the LHI and LHII from the RC-LHI. This can be achieved by sucrose gradients or multiple anion exchanges followed by gel filtration. However if there is no peripheral antenna (LHII) present then the purification steps become easier. The coloured elutes from the purification steps only need to be separated into two fractions, intact and degraded *cores*, which are then further purified. For this reason the RC-LHI was purified from a range of "core only" strains. These "core only" strains were *R. centenum*, *R. rubrum* and *Rb. sphaeroides* strain M21. All but M21 are wildtype strains. The *Rb. sphaeroides* strain is a non-LHII expressing mutant (Hunter and van Grondelle, 1987). The x-ray structure for *Rb. sphaeroides* reaction centre has been solved. For a review on the x-ray structure see Feher *et al.*, (1989). Consequently a solved *Rb. sphaeroides* RC-LHI structure would be useful.

The remaining strains studied all contained peripheral antenna complexes. Investigations into the x-ray structure of LHII from different *Rp. acidophila* strains is being undertaken (Cogdell, R.J., private communication). X-ray diffraction analysis of *Rp. acidophila* LHII crystals suggests that the resolution is more consistent in some strains than others. Attempts were made to see if 2D array formation was strain specific. Different

strains of *Rp. acidophila* were investigated to attempt to improve on the initial microdialysis observations from strain 7750. Two other *Rp. acidophila* strains were chosen, these were 10050 and 7050. All three *Rp. acidophila* strains produce similar *cores* but it is possible that different factors (e.g. lipids) may be associated with the *cores* which may affect 2D array formation. The remaining species (*C. purpuratum*, *Rc. gelatinosus*, *Rp. cryptolactis* and *Rp. palustris*) were also chosen as possible sources for 2D pigment-protein arrays and are discussed separately.

#### 4.4.1 *Rp. cryptolactis*:

The RC-LHI conjugate from *Rp. cryptolactis* (Stadtwald *et al.*, 1990) did not produce 2D arrays although the native colour of these pigment-protein complexes was maintained throughout the duration of the dialysis experiments when using  $\beta$ -OG at pH8.0-8.2. This species of Rhodospirillaceae produces two types of peripheral light-harvesting antennae (LHII). They are the B800-850 and B800-820 light-harvesting antennae complexes. The B800-850 form was investigated and found to produce small protein arrays within tubular shaped vesicles (Figure 4.10). The optimum concentration of protein in the dialysis chamber was found to be 2mg ml<sup>-1</sup> with between 0.125-0.25mg ml<sup>-1</sup> of added DMPC. The incubations were dialysed against 50-100mM NaCl in 10mM TRIS.HCl, pH8.0-8.1 at 26°C. Occasionally small sheet-like structures were observed on the E.M. grids (Figure 4.10; centre). However it is unclear whether these resulted from broken vesicles, or represented true *in vitro* sheets. On closer examination of the tubular vesicles the protein arrays appear to have a square packing, since optical bench image manipulation produces a square shaped series of reflections, with a centre to centre distance of 62.2Å, at a resolution of 4.0nm. Figure 4.11 is an enhanced magnification of the B800-850 arrays from *Rp. cryptolactis*. In Figure 4.11 the individual structural units can be seen. They appear to be circular in shape with a hole in the centre. The resolution of these arrays was generally poor ( $\approx$ 2.6-4.0nm), however where regions of flattened vesicles were evident (as in the sheet-like structure in Figure 4.10) the resolution was increased to between 2.5-2.0nm. It should be noted that the typical resolutions obtained were greater than 2.5nm. Owing to the small size of the arrays and the poor crystal packing image analysis was not undertaken. Uranyl acetate (2%<sub>w/v</sub>) was used to stain the arrays and its typical maximum resolution is about 2nm.



**Figure 4.10:** Tubular arrays of *Rp. cryptolactis* B800-850 (LHII). Negatively stained (2% w/v uranyl acetate) tubular 2D arrays of *Rp. cryptolactis* B800-850. Occasionally membrane-protein sheets are observed, centre and bottom centre. It is unclear whether these sheets are artifacts of the staining procedure or represent a true structure. The protein-containing vesicles eventually from elongated closed vesicles or tubules. The surface of these membrane structures have square arrays. Magnification: x80k.

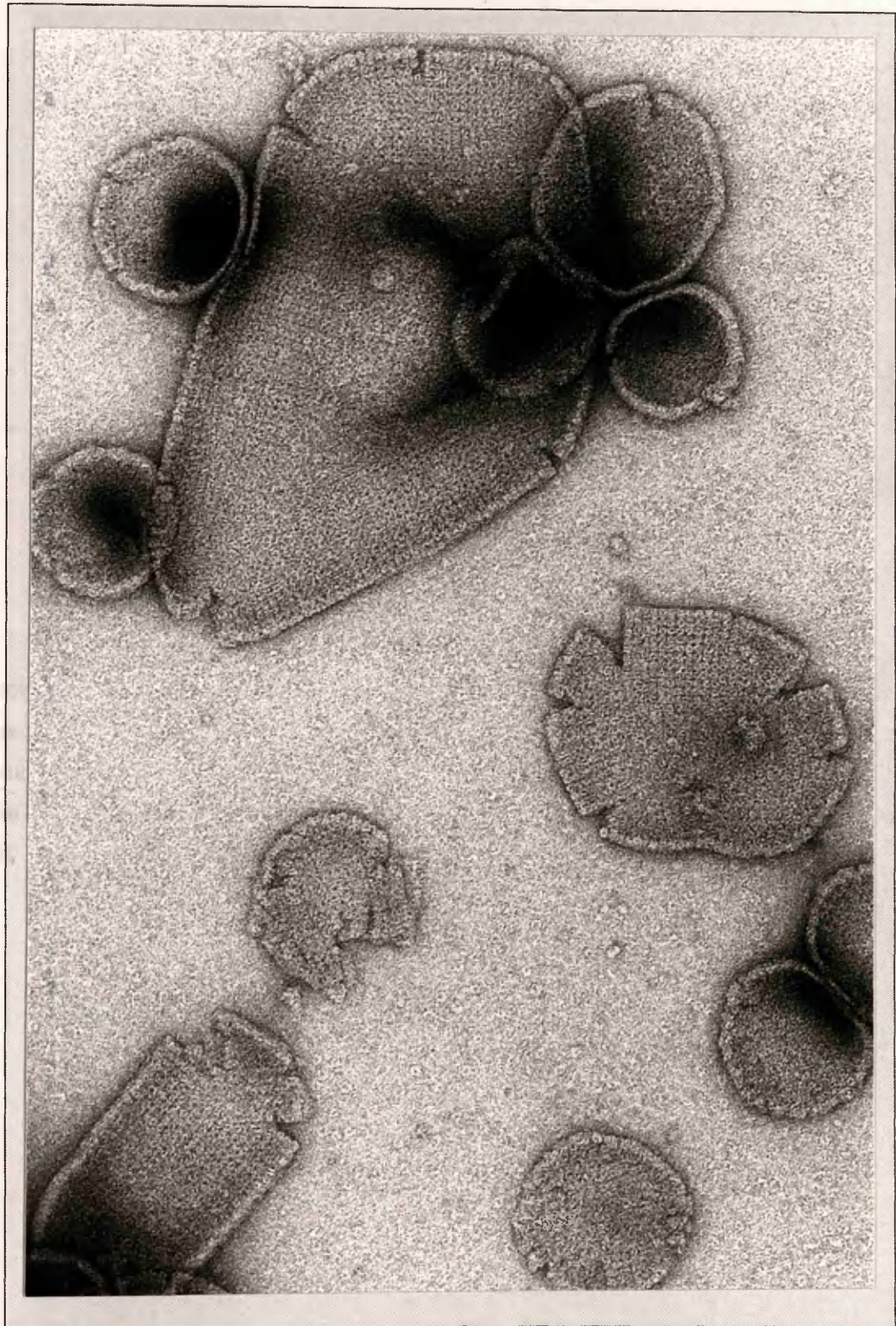


**Figure 4.11:** Tubular arrays of *Rp. cryptolactis* B800-850 (LHII). Higher magnification than Figure 4.10 of negatively stained (2% w/v uranyl acetate) of 2D arrays from *Rp. cryptolactis* B800-850 complex. The ring-like structures of the probable individual B800-850 complexes can be seen. Notice that there is a stain penetrating hole in the centre of the B800-850 ring structures and the rings form arrays that appear to have square symmetry (in the plane of the membrane). Magnification: x200K.

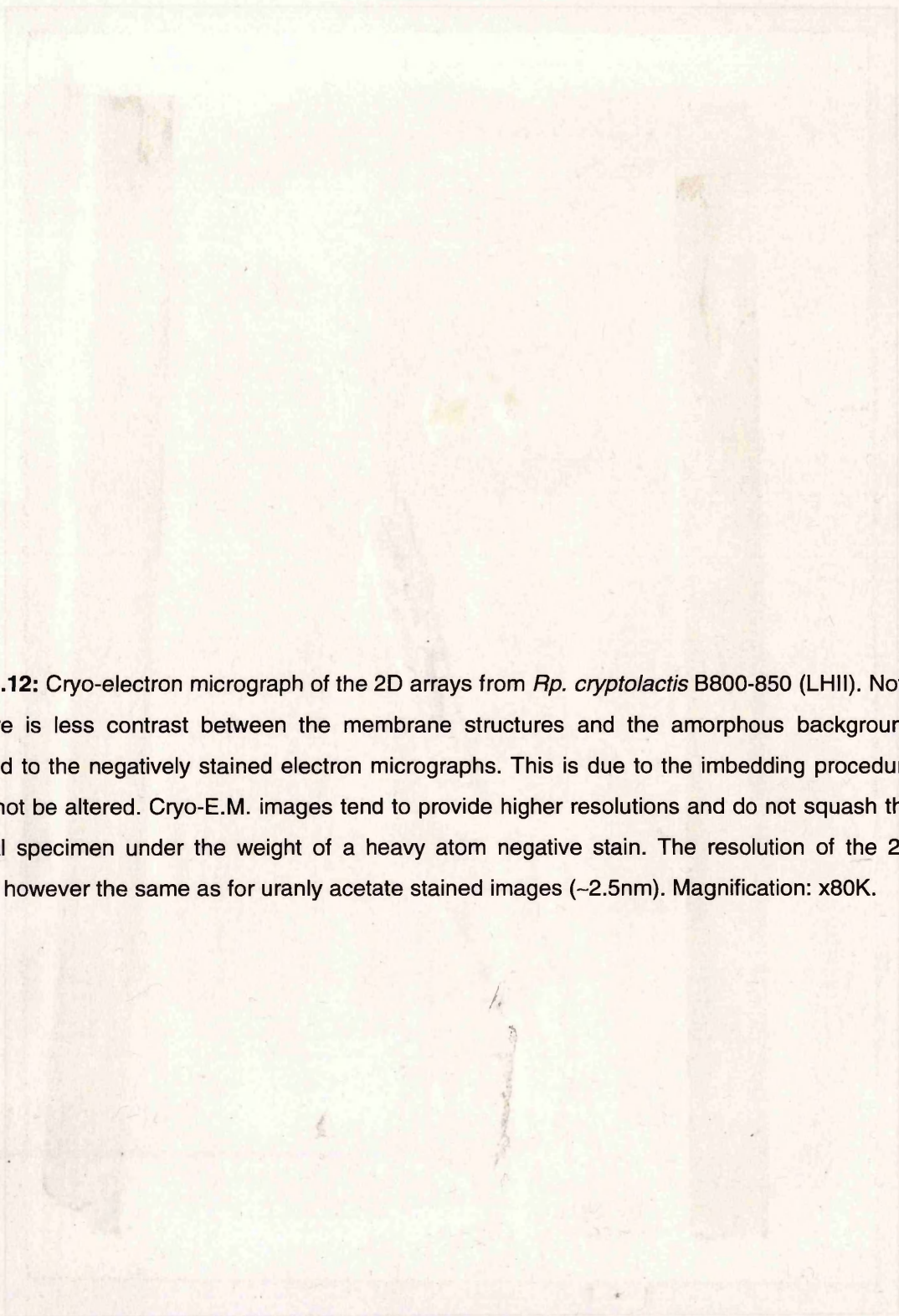


**Figure 4.12:** Cryo-electron micrograph of the 2D arrays from *Rp. cryptolactis* B800-850 (LHII). Note that there is less contrast between the membrane structures and the amorphous background compared to the negatively stained electron micrographs. This is due to the imbedding procedure and cannot be altered. Cryo-E.M. images tend to provide higher resolutions and do not squash the biological specimen under the weight of a heavy atom negative stain. The resolution of the 2D arrays is however the same as for uranyl acetate stained images (~2.5nm). Magnification: x80K.

Figure 4.11: Tubular arrays of *Rp. cryptolactis* B800-850 (LHII). Higher magnification than Figure 4.10 of negatively stained (2% w/v uranyl acetate) of 2D arrays from *Rp. cryptolactis* B800-850 complex. The ring-like structure of the protolactin individual B800-850 complexes can be seen. Notice that there is a stain penetrating hole in the centre of the B800-850 ring structures and the rings form arrays that appear to have square symmetry (in the plane of the membrane). Magnification: x200K.



Cryo-EM was used to see if greater resolutions could be obtained. Whole carbon grids were prepared and used as the supportive structure for B800-850 complexes in amorphous frozen water. Cryo-EM grids were prepared as described by Fukami and Adachi, (1965). On plunging the specimen (B800-850) into liquid ethane, specimens were prepared against an amorphous background. Image capture of LHII occurred where the specimens were embedded in the holes of the supportive material. Figure 4.12 is an example of a cryo-EM electron micrograph. Two holes in the supportive material can be seen. These are located top right and bottom of the plate. The vesicles containing the pigment-protein complexes can be seen. Some of these lie in the holes and were examined using an optical bench. It was hoped that regions of enhanced resolution would be obtained, however the highest resolution was the same as for negative staining.

The overall contrast in the cryo-EM images is poorer than the negatively stained specimens. Striations could be detected in the vesicles. In the lower centre of Figure 4.12 small patches of cubic ice can be seen. From the cryo-EM electron micrographs the 2D arrays of LHII grow as long tubes.

The primary sequence of the polypeptides from *Rp. cryptolactis* B800-850 has not been established. Its ability to form 2D arrays may result from a unique primary structure. Until other biochemical information is available it is impossible to speculate if this pigment-protein complex has any special properties.

#### 4.4.2 *Rp. palustris* strain 2.6.1:

Both the RC-LHI and LHII pigment-protein complexes were investigated. There are two structural types of LHII produced by this species. The two absorption spectra have similar NIR peak wavelengths but the "low light" form the LHII structure is altered causing the relative height of the 800nm peak to be greatly enhanced (Hayashi *et al.*, 1982b; Robert *et al.*, 1985). See Figure 1.7 for the differences in relative absorption from the high (HL) and low light (LL) forms of *Rp. palustris* LHII. Neither the HL nor the LL form produced any type of regular array but loose associations occurred as visualised by T.E.M. An example of the loose association of the B00-850 from *Rp. palustris* strain 2.6.1. can be seen in Figure 4.13. In Figure 4.13A two regions of LHII associations can be detected, these are in the centre and top right of the plate.

It is unclear whether the loose association results from the staining and drying procedures or is a true facsimile of the protein's characteristics. It

generally takes up to one week for complete detergent ( $\beta$ -OG) removal to occur. However after three weeks incubation the homogeneous background of small protein aggregations are still apparent even when an amorphous aggregation is observed. These small aggregations may actually represent very small crystallographic contacts between individual polypeptides or complexes.

An explanation for the failure to create 2D arrays could be that the amount of lipid present may be too great to allow 2D arrays to form. However long incubation periods (which should remove excess lipid) failed to produce 2D arrays. Also the addition of phospholipase A<sub>2</sub>, which should remove all excess lipid, followed by dialysis did not produce close packing of the LHII complexes. Therefore there must be another explanation other than general protein degradation.

One possible explanation for the homogeneous protein background with regions of loose protein association is the polypeptide composition of the B800-850. Evans, (1989) and Cogdell *et al.*, (1990) postulated that the overall  $\alpha_1:\alpha_2:\alpha_3:\alpha_4$  molar ratios can alter from 2:2:2:1 to 2:6:2:1. If a heterogeneous B800-850 is produced from HL grown cells then the formation of true crystallographic contacts could be every difficult. However the B800-850 could still have enough structural integrity to allow general association resulting in the observed packing as illustrated in Figure 4.13.

The RC-LHI of *Rp. palustris* strain 2.6.1. was also investigated by microdialysis to see if 2D arrays could be established. 3D crystals have been reported (Wacker *et al.*, 1986; Welte *et al.*, 1986) as well as the 3D crystals in Chapter Five with the aim of using conventional x-ray analysis techniques. Both 2D and 3D crystals rely on protein-protein contacts to form regular arrays, and it is therefore likely that successful 2D arrays would be obtained. Since crystallographic contacts have been observed in three dimensions (Wacker *et al.*, 1986; Chapter Five) then 2D arrays are potentially possible. After numerous attempts only one batch of protein managed to produce 2D arrays which resulted from a low light (LL) grown culture. The 3D crystals in Chapter Five were also from low light grown cells. It would be convenient to state that only LL cells produced suitable pigment-protein complexes whereby the apparent ability to form either 2D or 3D crystals was due to a factor associated with the LL form. The obvious answer would be to state that the differences could be due to different lipid levels or types associated with RC-LHI under high and low light environmental regimes. The LL form being the only one suitable for crystal growth. However only one batch formed arrays, and it could simply be coincidence that the 3D crystals in chapter Five are also from LL grown cells.

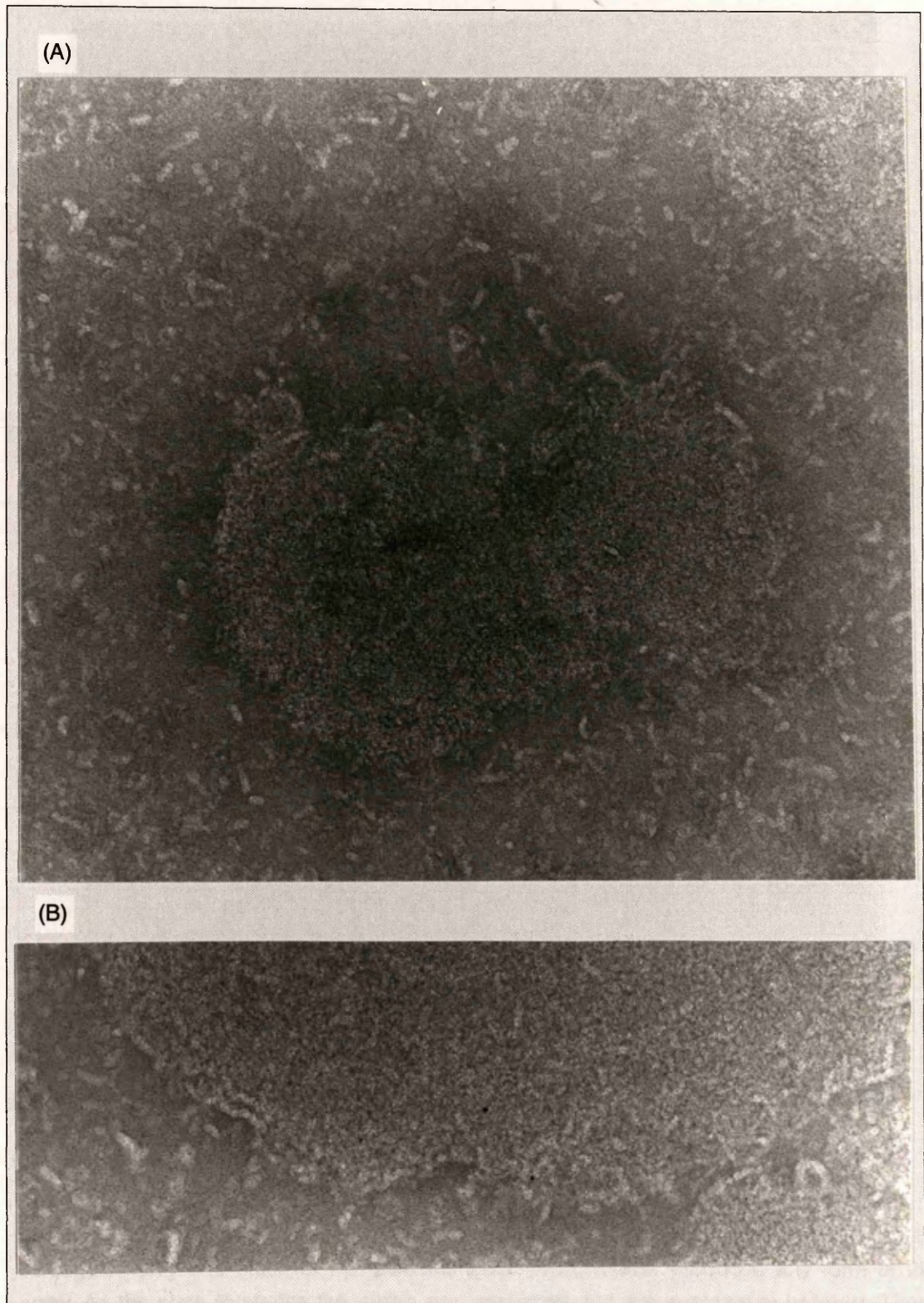


**Figure 4.13:** Loose association of *Rp. palustris* strain 2.6.1. LHII (high light form). (A): In a sea of isolated LHII (B800-850) complexes aggregates begin to form. Two regions can be observed, centre and top right. (B): A high magnification of an edge of an aggregation. No regular arrays were detected in either the LL or HL forms of *Rp. palustris* 2.6.1 LHII. Both plates were negatively stained with 2% (w/v) uranyl acetate. Magnification, A: x90K, B: x182K.



**Figure 4.14:** Negatively stained small mosaic 2D arrays of *Rp. palustris* 2.6.1. RC-LHI conjugate. Only one batch of *Rp. palustris* 2.6.1. RC-LHI ever produced any form of 2D array. As the plate illustrates the arrays are very small and are very poorly ordered. There are no apparent regions on the electron micrograph that indicate uniform packing of the proteins in the plane of the membrane (x and y planes). If the packing was ordered then there would be detectable rows of proteins regularly lined up in both the x and y planes. Using an optical bench no region gave a sufficiently ordered region that was suitable to calculate a rough centre to centre distance between cores. Note however that all the edges and rips in the sheet have angles of  $120^\circ$ , indicating that the packing material is hexameric in structure. Similar angled breaks in core lattice can be observed in *Rp. acidophila* RC-LHI conjugate. Negative stain: 2% (w/v) uranyl acetate. Magnification: x80K.

Figure 4.14 illustrates the result from the only batch of RC-LHI from *Rp. palustris* strain 2.6.1. that formed 2D arrays. Very small sheets were formed but protein packing was highly mosaic. This resulted in a virtually useless diffraction pattern (only first order spots could be seen). Attempts to increase resolution by gently raising the incubation temperature to 30°C then lowering it to its original temperature were unsuccessful. The increase of incubation temperature was achieved by changing the thermostat temperature setting from 26°C to 30°C. Once the raised temperature was achieved the samples were left incubating for 1 hour then the water bath thermostat was reset back to 26°C. Once the temperature in the dialysis chambers cooled to 26°C samples were taken for T.E.M.

#### 4.4.3 *C. purpuratum*, *R. rubrum*, *R. centenum*, *Rb. sphaeroides*, and *Rc. gelatinous*:

The RC-LHI conjugates from *C. purpuratum*, *Rc. gelatinous* (strains DSM149 and DSM151), *Rb. sphaeroides* (strains M21 and GA), *R. rubrum* strain S1 and *R. centenum* were subjected to 2D crystallisation trials. All produced general protein aggregation and denaturation. It should be noted that only one batch of *C. purpuratum* was isolated and purified for 2D crystallographic trials. The RC-LHI from this species was considered too unstable to attempt any large scale isolation, purification and crystallographic trials. It is not surprising that both *Rb. sphaeroides* and *R. centenum* cores did not produce any suitable results since the purified cores from these species were amongst the most unstable that were isolated. The lack of arrays in any of the above strains is probably due to their inability to survive prolonged periods in a detergent enriched environment.

Of the strains named above only *C. purpuratum*, *Rb. sphaeroides* strain GA, *Rc. gelatinous* strains DSM149 and DSM151 are capable of producing LHII. The LHII from *Rc. gelatinosus* strain DSM149 and *Rb. sphaeroides* strain GA were screened. Like the RC-LHI from these strains no 2D arrays were detected.

#### 4.4.4 *Rp. acidophila* strains 7750, 10050 and 7050:

The RC-LHI conjugates from these strains of *Rp. acidophila* were amongst the most stable, only the RC-LHI from *Rp. palustris* and possibly *Rp. cryptolactis* were considered to be more stable. The RC-LHI from all three stains were subjected to crystallographic trials.

All the above *Rp. acidophila* strains produce LHII. As in the previous examples of *Rp. cryptolactis* and *Rp. palustris* there are two forms of LHII in strains 7750 and 7050 (Cogdell *et al.*, 1983b; Heinemeyer and Schmidt, 1983). These are characterised by their NIR absorption maxima; and are the B800-820 and B800-850 complexes (see Figure 1.7). Only the B800-850 form from strains 7750 and 10050 were isolated and 2D crystallisation trials attempted. None of the LHII (B800-850) light-harvesting antennae complexes formed 2D arrays.

The RC-LHI conjugates from *Rp. acidophila* however did produce 2D arrays. Figure 4.9 illustrates the trends associated with array formation. At least  $1\text{mg ml}^{-1}$  of purified protein was required for formation of 2D arrays. As Figure 4.3 indicates there were over thirty separate batches of purified protein screened by microdialysis. The 2D crystallographic trials indicated that possible lipid variation occurred in RC-LHI preparations. This was indicated by variations in the amount of extra lipid (DMPC) required to form 2D arrays. At first it was thought that this was simply due to slightly different isolation procedures from differently grown cultures. However cells were grown and harvested and protein purified in a uniform manner as described in Chapter Three. When different batches of cells were isolated simultaneously, variation also occurred in purified RC-LHI, with respect to extra lipid requirement for 2D array formation. The isolation processes involved protocols that were considered to be very good at removing excess free lipids from detergent-solubilised membrane proteins; i.e. anion exchange (DE52, Whatman) and gel filtration (Sephacryl S-200, Pharmacia) (Hawthornthwaite, A., personal communication). However between  $0.12\text{mg ml}^{-1}$  and  $1.00\text{mg ml}^{-1}$  of extra lipid (DMPC) was required before arrays could be formed. Generally only between  $0.12\text{mg ml}^{-1}$  and  $0.50\text{mg ml}^{-1}$  of DMPC was required to allow array formation. The change from sheet to vesicular structures usually occurred as more lipid was added, until an optimum was reached.

*Rp. acidophila* strain 7050 RC-LHI conjugates never produced any evidence of 2D arrays (see Figure 4.15) even although seven batches of protein were isolated and screened. The RC-LHI conjugates from *Rp. acidophila* strains 10050 and 7750 however did form 2D arrays (Figure 4.16).

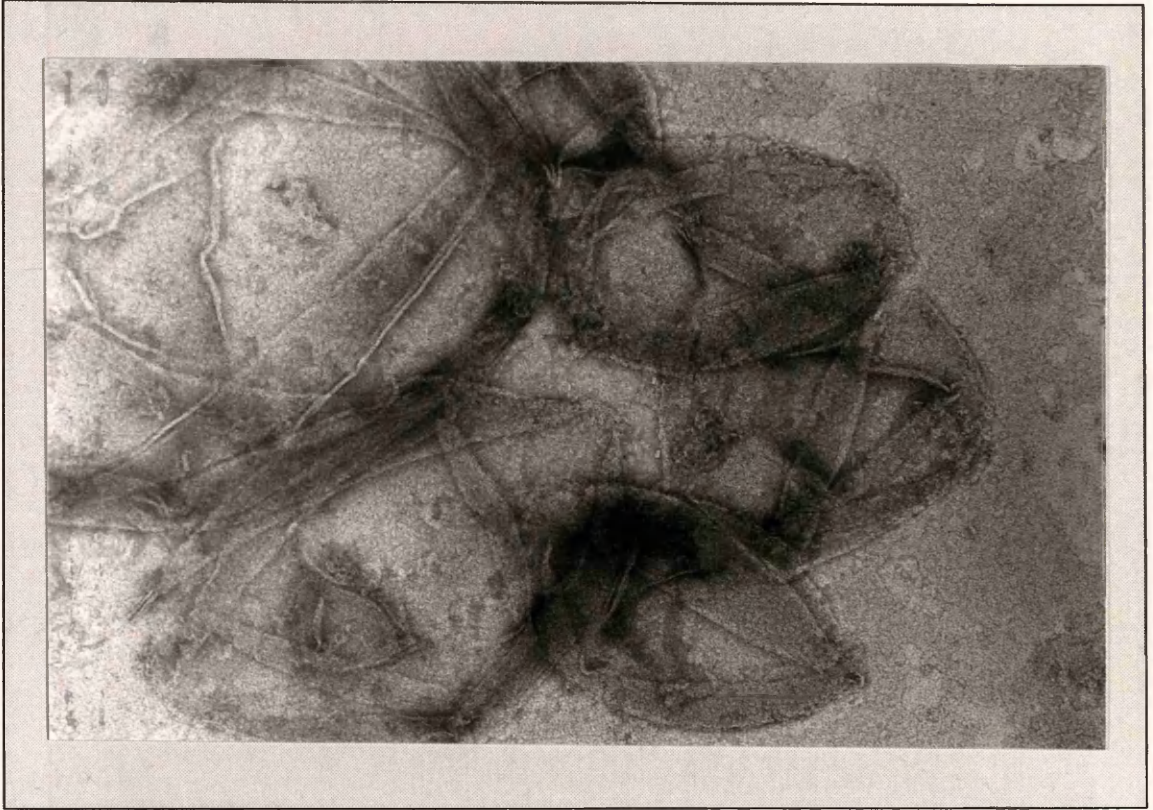


**Figure 4.15:** Negative stain of *Rp. acidophila* strain 7050 RC-LHI vesicles. Unlike strains 10050 and 7750 this strain of *Rp. acidophila* never produced regular arrays of RC-LHI. The plate illustrates the lipid-protein vesicles formed from one dialysis experiment. Negative stain 2%(w/v) uranyl acetate. Magnification: x68K.

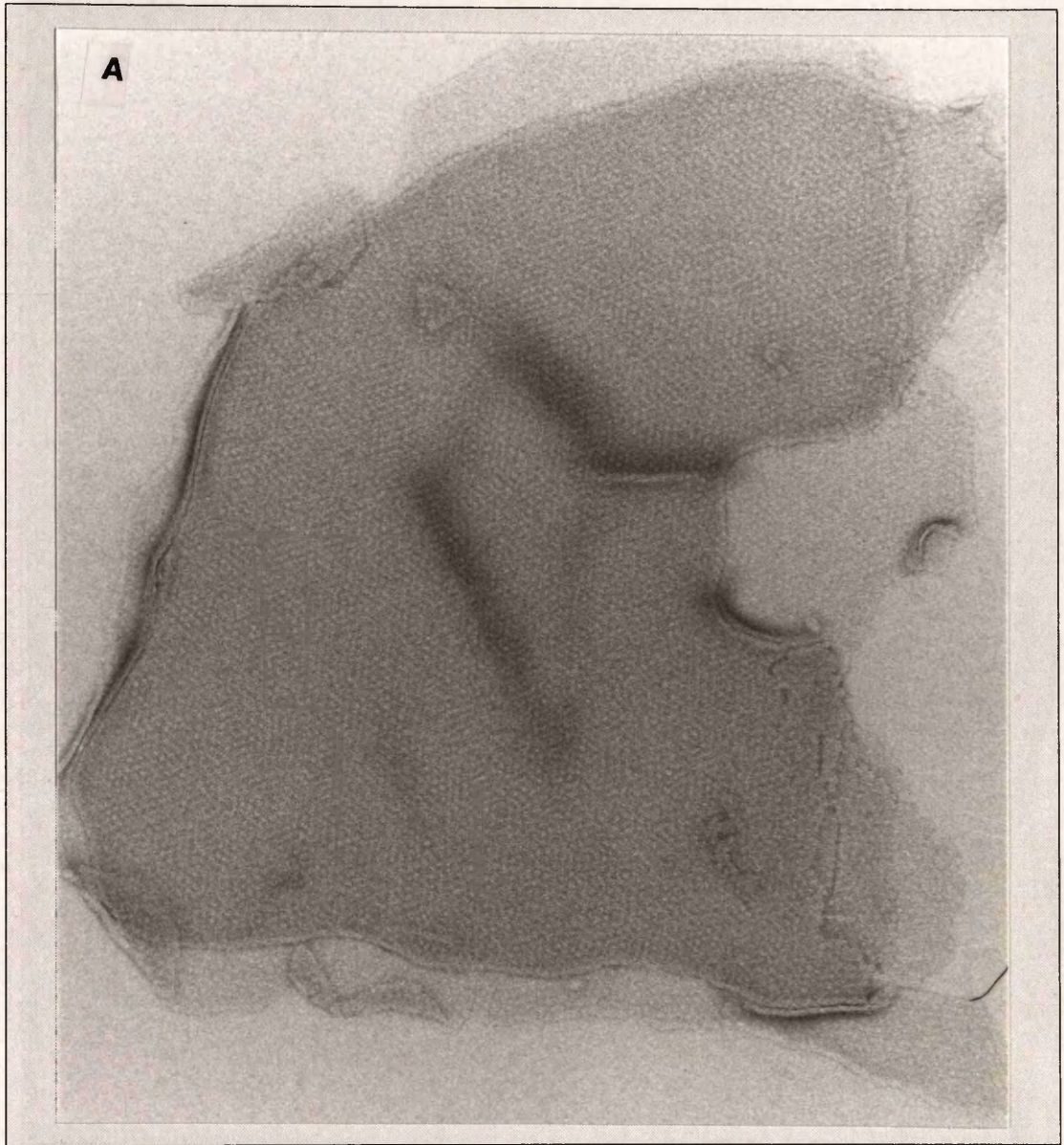


**Figure 4.16:** 2D arrays of negatively stained *Rp. acidophila* RC-LHI (core) conjugate. (A) 2D array from strain 10050. (B): 2D array from strain 7750. A regular array of core conjugate can be seen in these electron micrograph plates. On close examination of the surface of the 2D sheet, parallel to the plane of the page (x and y planes), rows of protein can be seen. These are small light grey circular objects within the membrane sheet. Rotating the plate by  $120^\circ$  also produces a regular protein matrix and upon a further  $120^\circ$  rotation yet another plane axis of symmetry is present. Using optical diffraction techniques the lattice is hexameric with a resolution of approximately 2.0-2.5nm. Negative stain: 2% (w/v) uranyl acetate. Magnification: x80K.

**B**



Figure 4.16 illustrates the 2D arrays from RC-LHI conjugates of 7750 and 10050. Both Figures show that the apparent packing of the pigment-protein complexes has a hexameric structure. This is evident if you rotate the electron micrographs along the plane of the page.

The diffraction patterns produced on an optical bench suggest that the 2D arrays of RC-LHI from *Rp. acidophila* are hexameric in shape. The six-fold symmetry of the 2D crystal therefore most likely has a p6 type symmetry. In p6 symmetry each RC-LHI (monomeric unit) has the same orientation as that of its immediate neighbours within the plane of the membrane. However, since the RC does not have six-fold symmetry (Deisenhofer *et al.*, 1984) the RC-LHI conjugate cannot have true six-fold symmetry. The surrounding LHI may, however, provide a pseudo six-fold structure at the boundary of this protein conjugate. Figure 4.17 illustrates what appear to be cracks in the 2D array radiating from the centre. These fissures are uniformly jagged and the edges have 120° angles. This suggests that the rips in the 2D arrays occur between the monomeric units and that the RC-LHI 2D crystal structure has, at least, a pseudo six-fold symmetry. If a non-six-fold symmetry was present then the radial fissures may not be present. Assuming the same gross structural features with the *core* from *Rp. viridis* (Stark *et al.*, 1984) then there is a 5° slope (normal to the perpendicular plane of the membrane) between the EP and ES sides of the RC-LHI. These angled sides would cause the membrane structure to have a slight arch. Sample preparation for T.E.M. could cause the arched 2D sheets to rip when dried and flattened against the copper grid. Crystalline sheets were never found to be greater than 1.5 µm in diameter. The fact that there was a limit to the size of 2D sheet formation also lends weight to a p6, or pseudo p6, symmetry because it is probable that the 2D array would collapse due to structural stress caused by the growing arched 2D array. Heavy metal shadowing of RC-LHI 2D arrays will establish whether unidirectional or bi-directional protein insertion into the lipid bilayer is present, and hence, whether or not an arched array is actually produced.

*Rp. acidophila* strain 10050, like 7750, produced six-fold symmetry for the RC-LHI conjugate. However two batches of isolated RC-LHI from 10050 did not produce six-fold symmetry but a square lattice. Figure 4.18 shows the square arrays of RC-LHI from this strain of *Rp. acidophila*. The 2D crystal packing was highly mosaic and as Figure 4.18 depicts no large square arrays were detected. Optical bench diffraction patterns from the square arrays indicated poor crystal packing. Plate B in Figure 4.18 illustrates the squareness of the arrays. Notice the holes between the *cores* (circular objects).

Figure 4.16 illustrates the 2D arrays from RC-LHI conjugates of 7750 and 10050. Both Figures show that the apparent packing of the pigment-protein complexes has a hexameric structure. This is evident if you rotate the electron micrographs along the plane of the page.

The diffraction patterns produced on an optical bench suggest that the 2D arrays of RC-LHI from *Rps. acidophila* are hexameric in shape. The six-fold symmetry of the 2D crystal therefore most likely has a  $pg$  type symmetry. In  $pg$  symmetry each RC-LHI (monomeric unit) has the same orientation as that of its immediate neighbours within the plane of the membrane. However, since the RC does not have six-fold symmetry (Deisenhofer et al., 1984) the

**Figure 4.17:** Fissures in a 2D array of RC-LHI. Diffraction patterns on an optical bench suggest that the 2D arrays of RC-LHI from *Rps. acidophila* are hexameric in shape. The six-fold symmetry thus has at least a pseudo  $p6$  symmetry. In  $p6$  symmetry each RC-LHI (monomeric unit) is in the same orientation as all its immediate neighbours. The above micrograph illustrates radial cracks in the 2D array. These fissures are jagged and the edges have  $120^\circ$  angles. This implies that the tears are between the monomeric units and the structure has a pseudo  $p6$  symmetry. Crystalline sheets were never found to be greater than  $1.5 \mu\text{m}$ . Assuming the same gross structural features with the core from *Rp. viridis* (Stark et al., 1984) then there is a  $5^\circ$  slope (normal to the perpendicular plane of the membrane) in the membrane spanning regions of the RC-LHI. These angled sides, if  $p6$ , or pseudo  $p6$ , crystallographic contacts are present, would cause the membrane structure to have a slight arc. E.M. sample preparation would cause the arced 2D sheets to rip when dried and flattened against the copper grid under the weight of negative stain. Magnification:  $\times 120\text{K}$ .

Copper grid. Crystalline sheets were never found to be greater than  $1.5 \mu\text{m}$  in diameter. The fact that there was a limit to the size of 2D sheet formation also lends weight to a  $pg$ , or pseudo  $pg$ , symmetry because it is probable that the 2D array would collapse due to structural stress caused by the growing arched 2D array. Heavy metal shadowing of RC-LHI 2D arrays will establish whether unidirectional or bi-directional protein insertion into the lipid bilayer is present, and hence, whether or not an arched array is actually produced.

*Rps. acidophila* strain 10050, like 7750, produced six-fold symmetry for the RC-LHI conjugate. However two patches of isolated RC-LHI from 10050 did not produce six-fold symmetry but a square lattice. Figure 4.18 shows the square arrays of RC-LHI from this strain of *Rps. acidophila*. The 2D crystal packing was highly mosaic and as Figure 4.18 depicts no large square arrays were detected. Optical bench diffraction patterns from the square arrays indicated poor crystal packing. Plate B in Figure 4.18 illustrates the squareness of the arrays. Notice the holes between the cores (circular objects).



many fine cracks and indentations. The cracks are of various lengths and directions, and some are quite deep. The surface is dark and appears to be composed of many small, interconnected parts, with some larger, more prominent cracks and indentations. The overall appearance is rough and uneven.

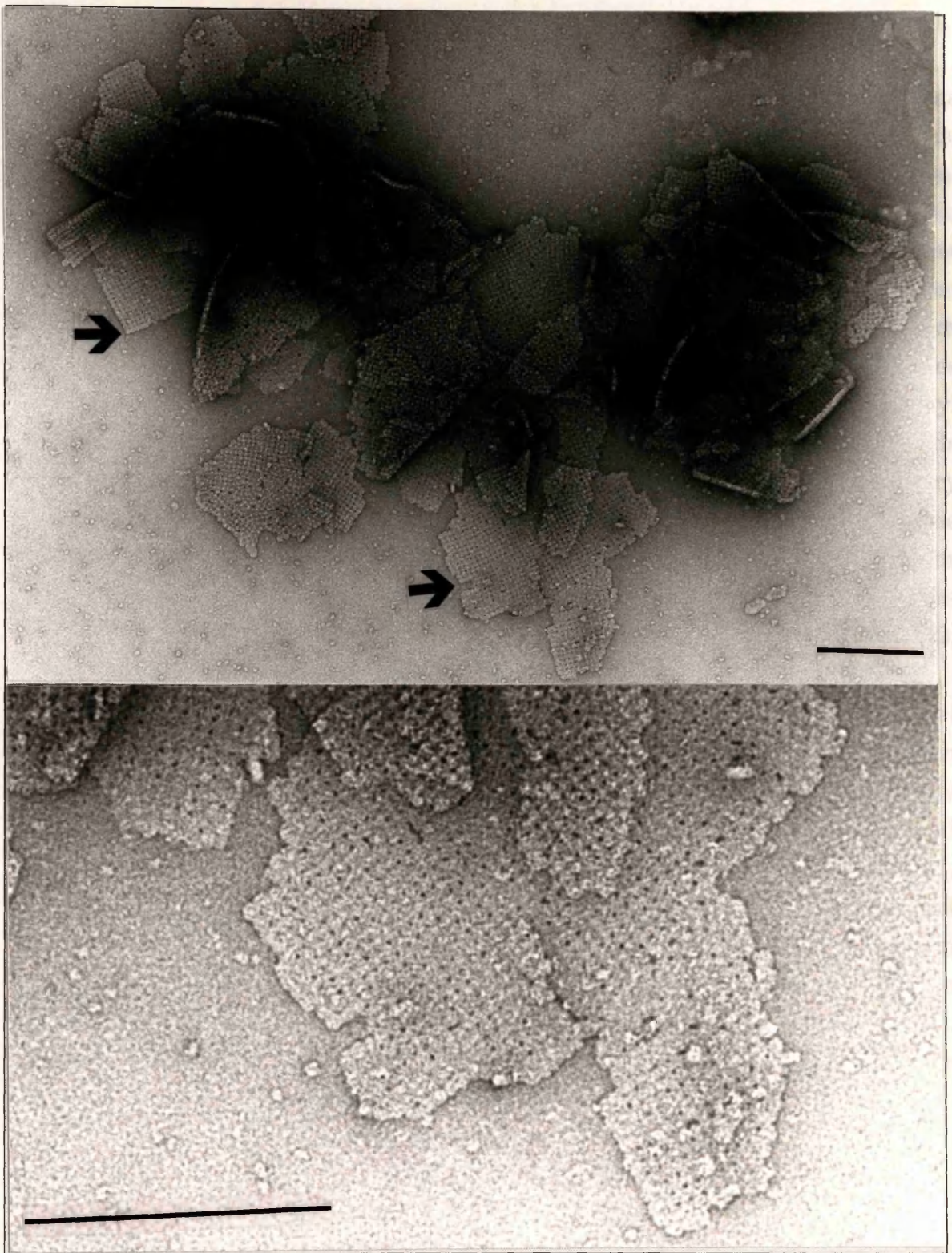


**Figure 4.18:** Non hexagonal arrays of *Rp. acidophila* strain 10050 RC-LHI conjugate. Negative stained (2% uranyl acetate) reveals that for at least one batch of RC-LHI conjugate the protein packing was square and not the normal hexagonal arrangement. The arrays formed were small compared to the hexagonal lattices. Plate A shows such small RC-LHI arrays. The presence of many free RC-LHI photosynthetic particles can also be seen in the electron micrograph. The free RC-LHI's are the small circular objects spread evenly over the micrograph. By looking at the edges of the arrays the square packing of these photosynthetic particles can be seen. Two typical examples are indicated by the black arrows on Plate A. On increasing the magnification holes can be observed between the RC-LHI conjugates. Plate B represents a magnified area of plate A. Notice that in both plates the packing of RC-LHI conjugate produces small mosaic patches of lattice. There is no large region of uniform membrane protein packing. Bar: 200nm

There are two possibilities why a different RC-LHI lattice structure was present; these are lipid variation and also possibly differing RC Redox states. A change in Redox state may cause a conformational change in the protein. Any such conformational change could possibly affect the crystallographic contacts in an array, and thus, ultimately change crystal packing. The importance of sample Redox state has been reported as for cytochrome oxidase (Wakabayashi *et al.*, 1972), but the more likely cause in structural differences is lipid variation. The Rhodospirillaceae have as their major lipid classes phosphatidyl choline (PC), phosphatidyl ethanolamine (PE), phosphatidyl glycerol (PG), and diphosphatidyl glycerol (DPG). The major fatty acids (generally saturated 16 and 18 carbons chains) distribution can vary (Kaufmann *et al.*, 1982) but are generally similar (Knacker *et al.*, 1985). The significant lipids in the Rhodospirillaceae membrane may not be the major lipid species but rather the more rarer and unusual lipids such as N-acylphosphatidylserine (Russell and Harwood, 1979; Imhoff *et al.*, 1982; Donohue *et al.*, 1982).

Slight differences in growth conditions may dramatically affect the final lipid composition when RC-LHI conjugates are isolated and purified. Such differences in overall lipid content, due to growth conditions, have already been shown in *Rp. viridis* (Pucheu *et al.*, 1974). Pucheu *et al.*, (1974) showed that addition of yeast extract causes lipid proportions to vary. Kaufmann *et al.*, (1982) have established that different distributions of both fatty acid and lipid class occurred between different membrane protein fractions. Such variation may occur in the yet unnamed and minor lipids of the Rhodospirillaceae (Russell and Harwood, 1979; Imhoff *et al.*, 1982; Donohue *et al.*, 1982). Therefore any slight differences in cell culturing may result in dramatic differences in lipid composition in isolated *cores*.

The rôle of hopanoids as membrane stabilisers (Ourisson *et al.*, 1987) in 2D crystallisation and general protein-membrane interactions is generally ignored. It is possible that the *in vivo* 2D arrays could be as much to do with the presence of these prokaryote triterpenoids as well as the major lipid classes named above. Recent evidence suggests that these amphiphilic lipids can have either potential negative or positive charges (Llopiz *et al.*, 1992). In protein-membrane interaction they may be of major or negligible physiological and/or structural importance. If they are significant then their presence in isolated pigment-protein complexes may be a requirement for high resolving 2D array formation.

Ignoring hopanoids the presence of specific lipids can aid both 3D and 2D crystal formation as exemplified by LHCII a/b (Wang, D.N, personal

communication) and the 2D arrays in bacteriorhodopsin (Sternberg *et al.*, 1992). Both the square and hexagonal 2D arrays from *Rp. acidophila* originated from RC-LHI conjugates with similar absorption spectra and protein composition. Therefore the appearance of a square lattice (Figure 4.18), compared to the usual hexagonal lattice (Figure 4.16), presumably is due to lipid variation.

#### 4.4. Image Processing of the RC-LHI Conjugate:

Electron micrographs with RC-LHI 2D arrays from *Rp. acidophila* 10050 and 7750 were digitised using a Perkin-Elmer microdensitometer (model 1010-GM). Regions of 2D arrays (20mm x 20mm) were scanned in 20  $\mu\text{m}$  steps at a resolution of 0.5nm (attainable final resolution of 1.5nm) using a square aperture. The digitised optical density data was converted to a suitable format for image analysis. The Image Processing software, created by the M.R.C., Cambridge, was used to produce 2D reconstructions of the RC-LHI from *Rp. acidophila*.

The digitised and converted data was Fourier transformed (FFT) (FFTRANS.EXE) to produce Miller reflections ( $k,h$ ) with Cartesian co-ordinates ( $x,y$ ). Figure 4.19 is an example of one FFTRANS output from a RC-LHI *Rp. acidophila* 10050 2D crystal. The FFT of the 2D array produces Friedel symmetry thus only half the image is required to illustrate the features present. The Miller reflections were reliable to 4,-2.

Background scattering from the carbon support and dirt particles was reduced by manipulating the FFT output. This was achieved by removing the extreme high (>200) and low (<130) optical densities, and permitting the diffraction spots to stand out against the background noise. Typical diffraction spots from RC-LHI can be seen in Figure 4.19 and are circled to allow easier recognition against the filtered background. The origin of the Fourier transform, or diffraction pattern, is given the Miller reflection of 0,0. All other Miller reflections are located by  $x$  and  $y$  Cartesian co-ordinates.

The co-ordinates ( $k,h;x,y$ ) of the FFTRANS output are then image manipulated by the processing software described below. A rough lattice was produced by the programme EMBOX.EXE (a similar programme to the standard NNBOX.EXE) and used as the input to MMBOX.EXE, which produced a refined lattice containing amplitudes and phases. The output from this was then subjected to further lattice refinement by MMLATREF.EXE.

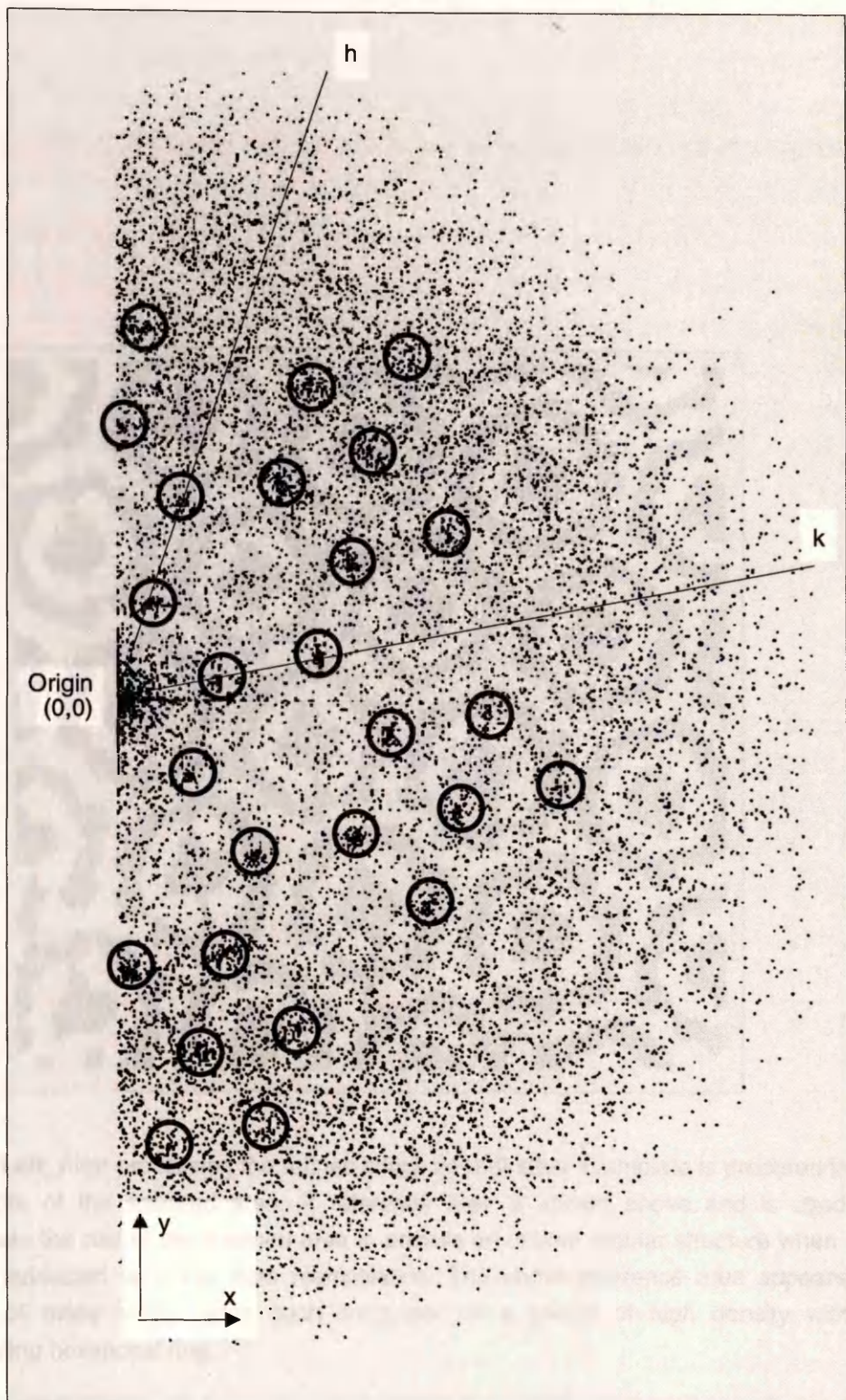


**Figure 4.19:** Fast Fourier Transform (F.F.T.) of a RC-HLI Array. A digitised area was subjected to a F.F.T. resulting in the image above. The image has been cropped such that only the area containing the diffraction spots is depicted. Note that the extreme density values have been filtered out (<130 and >200 A.U.) thus making it possible for the diffraction spots to be seen. To aid detection these reflections have been circled. The F.F.T origin is given Miller indices  $(h,k)$  lattice co-ordinates of 0,0. The  $h$  and  $k$  lattice axis are indicated by the lines. The  $x, y$  axes are also shown. Due to Friedel symmetry only one half of the image is plotted.

This programme utilises the image operations from IBM's X-PIX. Further improvement occurred by applying the IBM's PLOT EXE - run by JOBA.COM. The programme JOBA.COM was written in a series of individual programmes within the MRC software which ultimately produced optimised lattice parameters including measurements of lattice distortions. JOBA.COM first creates a mask (MASKTRAN EXE) of the Fourier transform data to attempt to increase the signal to noise ratio by further refining the lattice parameters.



used as a reference image are used as a region of interest central of that there final procedure up to now indeed six three fold the three coordinates.

scanned area is the assumed of a scanned area to have a indicates propagate. The processing lattice has also have to correlate a lattice coordinates. iron density shows the 7750 and to have a

**Figure 4.20:** After processing the refined lattice co-ordinates a template is prepared from the centre of the scanned area. A reference area is shown above and is used to manipulate the rest of the scanned area to provide an unbent regular structure when the data is subjected to further data manipulation. The above reference area appears to consist of many similar units each comprised of a centre of high density with a surrounding hexagonal ring.

RC. Each unit is composed of a central dark spot surrounded by a lighter ring. Figure 4.21 is a 3D reconstruction of the structure. The THRESHOLD was set at 0.5. The structure was obtained after four iterations. The structure is shown in the 3D array. From previous reports other have shown the structure of the Rhodospirillum rubrum at least pseudo-reconstructed by Cheng et al., 1984; Deisenhofer et al., 1985; Cheng et al., 1986. By comparing the 3D reconstructions of *Rp. rubrum* with *Rp. rubrum* (LMI - Figure 4.21C);

This programme optimises the lattice co-ordinates from MMBOX.EXE. Further improvement occurred by applying the MMLATREF.EXE output to JOBA.COM. The programme JOBA.COM was actually a series of individual programmes within the MRC software which ultimately produced optimised lattice parameters including measurements of lattice distortion. JOBA.COM first creates a mask (MASKTRAN.EXE) of the Fourier transform data to attempt to increase the signal to noise ratio by further refining the lattice parameters using the above programmes. Once achieved a small boxed area is used as a template (BOXIM.EXE) to which all other regions of the scanned image are compared to. Figure 4.20 illustrates the boxed image of a scanned region of 10050 lattice. Note that the repeating objects appear to have a central object surrounded by a hexagonal ring. The processed data indicates that there may indeed be six-fold symmetry in the RC-LHI conjugate. The final process is to pictorially display a 2D reconstruction. The image processing up to now has assumed that the image had  $p1$  symmetry. If the lattice has indeed sixfold symmetry (Figure 4.20) then it must, by definition, also have three fold symmetry. The programme THREEFOLD.EXE was used to correlate the three axes, by comparing the amplitudes and phases of the lattice co-ordinates of paired Millar indices from the final processed co-ordinates.

The final result of the image processing was averaged electron density maps that were assumed to have six-fold symmetry. Figure 4.21 shows the final 2D reconstructions of *Rp. acidophila* RC-LHI from strains 7750 and 10050. Both 10050 (Figure 4.21A) and 7750 (Figure 4.21B) appear to have a central region surrounded by a hexameric ring structure.

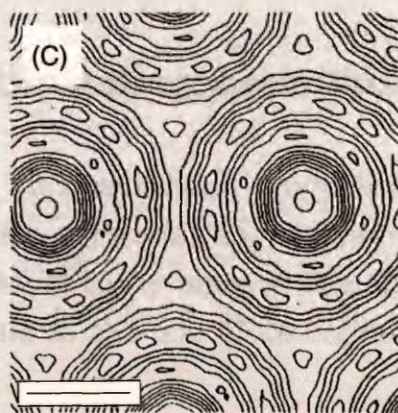
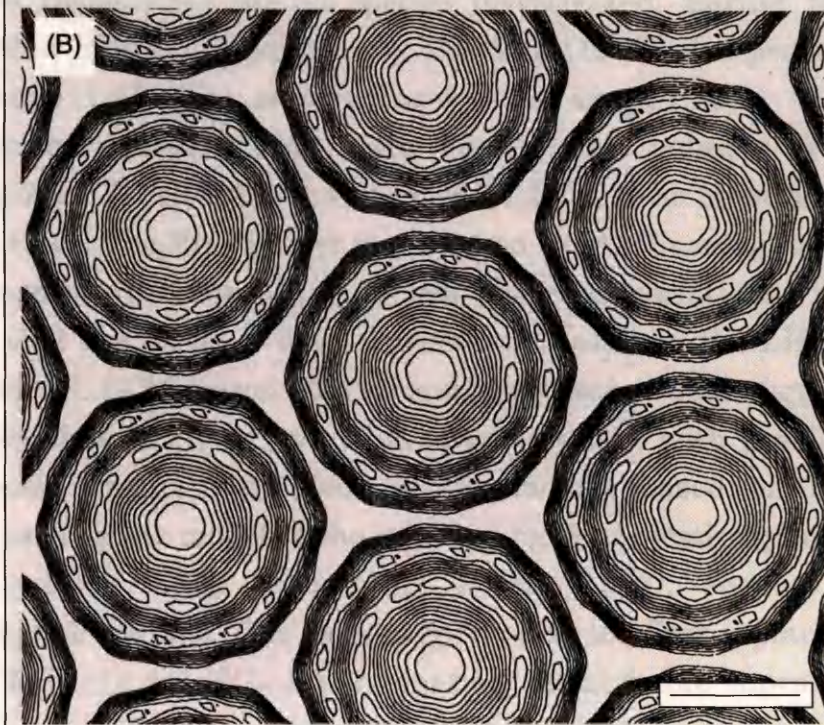
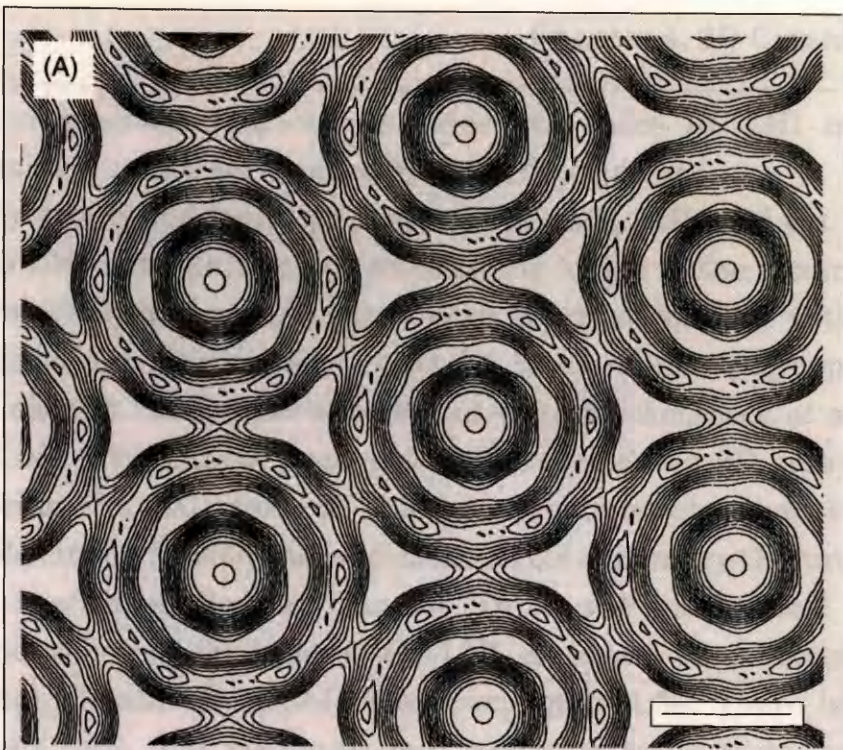
#### 4.6 Structural Significance of RC-LHI 2D Arrays:

It is proposed that the ring structure in Figure 4.21 for *Rp. acidophila* RC-LHI comprises of the six LHI (B875) light-harvesting antennae complexes. Each LHI comprises of two  $\alpha$  and two  $\beta$  polypeptides, four bacteriochlorophylls and two carotenoids (for a review see Zuber, 1986). The central region in Figure 4.21 is symmetrical due to the rotational symmetry imposed by the THREEFOLD programme. No direct structural information can thus be obtained other than the existence of the reaction centre (RC) in the 2D array. From previous reports others have shown that the RC from other species of the Rhodospirillinaea have at best pseudo two-fold symmetry (Stark *et al.*, 1984; Deisenhofer *et al.*, 1985; Chang *et al.*, 1986). By comparing the 2D reconstructions of *Rp. acidophila* with *Rp. viridis* RC-LHI (Figure 4.21C;

**Figure 4.21:** Comparison of the 2D electron density reconstruction maps of the RC-LHI conjugate from *Rp. acidophila* strains 10050 and 7750 with *Rp. viridis*. Negatively stained arrays (2%w/v U.A.) from *Rp. acidophila* RC-LHI were digitised and processed using the MRC Image Processing Software on a VAX minicomputer to produce 2D reconstructions. (A): 2D reconstruction of *Rp. acidophila* strain 10050 RC-LHI at 1.9nm resolution. Bar: 5nm (B): 2D reconstruction of *Rp. acidophila* strain 7750 RC-LHI at 1.9nm resolution. Bar: 5nm. (C): 2D reconstruction of *Rp. viridis* RC-LHI at 1.8nm resolution, redrawn from Stark, (1984) Bar: 5nm. The reconstruction from *Rp. acidophila* strain 10050 is from one array while that of 7750 is an averaged plot from two processed arrays. Comparing the overall shape and dimensions of the two *Rp. acidophila* reconstructions with each other and with that derived for the RC-LHI of *Rp. viridis* by Stark, (1984) indicate that all are very similar. Image (C) has near perfect sixfold symmetry while both plates (A) and (B) have decreasing symmetry. The apparent degree of symmetry is dependent on the number of data points which most likely accounts for the increased averaged symmetry from plate (A) to (C). The relative positions of the peaks and the centre to centre distances are also very similar. All appear to have six-fold symmetry at this resolution with centre to centre distances of 12.0nm (*Rp. viridis*) and 11.5nm (*Rp. acidophila*). The proposed reaction centre diameter for all three reconstructions is approximately 4.5nm.

#### 4.6 Structural Significance of RC-LHI 2D Arrays

It is proposed that the ring structure in Figure 4.21 for *Rp. acidophila* RC-LHI comprises of the six LHI (B875) light-harvesting antennae complexes. Each LHI comprises of two  $\alpha$  and two  $\beta$  polypeptides, four bacteriochlorophylls and two carotenoids (for a review see Zuber, 1986). The central region in Figure 4.21 is symmetrical due to the rotational symmetry imposed by the THREEFOLD programme. No direct structural information can thus be obtained other than the existence of the reaction centre (RC) in the 2D array. From previous reports others have shown that the RC from other species of the Rhodospirillinae have at best pseudo two-fold symmetry (Stark et al., 1984; Deisenhofer et al., 1985; Chay et al., 1986). By comparing the 2D reconstructions of *Rp. acidophila* with *Rp. viridis* RC-LHI (Figure 4.21C)



Stark, 1984) a generalisation can be made. All three RC-LHI conjugates consist of a reaction centre surrounded by six LHI complexes.

There are two  $\alpha$  and two  $\beta$  polypeptides in each LHI, and six LHIs per RC, with each LHI antenna complex constituting a side of the hexameric RC-LHI structure. This then assumes that each RC is associated with 24 *core* antenna polypeptides. The principle that 24 *core* antenna polypeptides are present with each RC is further substantiated by Meckenstock *et al.*, (1993) and Ghosh *et al.*, (1993). Both these groups have produced 2D arrays of LHI (RC-LHI lacking the RC) from *R. marina* (Meckenstock *et al.*, 1993) and *R. rubrum* (Ghosh *et al.*, 1993) that indicate six-fold symmetry (Figure 1.14).

For all species studied in Chapter Three the biochemical evidence appears to indicate that for isolated RC-LHI conjugate the reaction centre: bacteriochlorophyll ratio (RC:BChl) is approximately 1:30. There is however variation in the ratio. The maximum and minimum ratios were found to be 1:43 and 1:20 respectively for all species investigated. Earlier biochemical work on isolated RC-LHI conjugates by Dawkins, (1988) also produced ratios within this range (1:41 - 1:21, mean value was also about 1:30).

If it can be assumed that there are 24 *core* antenna polypeptides associated with the RC then the variation of RC:BChl ratio must be due to one of two possibilities. The first is that the isolated RC-LHI conjugate is possibly inherently unstable thus resulting in the observed variations. The second possibility is that the levels of bacteriochlorophyll alter in the LHI antennae, causing altered RC:BChl ratios. The second hypothesis would suggest that for each  $\alpha/\beta$  heterodimer at least two BChls are present, with possibly a third present in some apoproteins. None of the models based on biochemical information, such as the model of the minimal light-harvesting photosynthetic unit of *R. rubrum* B890 (Brunisholz *et al.*, 1986), suggest a varied bacteriochlorophyll content. This then suggests that the first explanation holds true for the RC-LHI; the RC-LHI is generally an unstable supra-complex *in vitro*.

#### 4.7 Summary of 2D Crystallogenesi Studies.

It appears that photosynthetic membrane proteins of the Rhodospirillaceae are capable of forming 2D arrays *in vitro*. Only the RC-LHI conjugates that are considered to be more stable than the majority produce arrays. This is probably due to the use of detergents as they are thought to

cause significant protein degradation when left in contact with the RC-LHI for prolonged periods.

Since 2D arrays can be formed for both the RC-LHI and LHII, further work using 2D crystallographic techniques could lead to low resolution 3D reconstructions of these pigment-protein complexes. This would, at the very least, allow the orientation of these proteins within the *in vivo* membrane to be established. The fact that 2D crystalline arrays were obtained for *Rp. acidophila* RC-LHI, where none have been reported using 3D crystallography, indicates that E.M. methods are very useful alternatives to the conventional x-ray structural determination methods.

Chapter Five

Three Dimensional Crystallography

## 5.1 Introduction:

Determination of an atomic structure of a biological macromolecule to date still generally relies on x-ray crystallography. In order for a x-ray structure of a protein to be elucidated crystals must be produced with all dimensions being at least 0.1-0.25mm. The crystals must be larger than the width of the x-ray beam for a diffraction pattern to be accurately detected. There is a general relationship which states that the intensity of the diffraction pattern is proportional to the crystal volume and inversely proportional to the unit cell volume (for a review see Drenth and Johnson, 1976). For a given x-ray source the dose of the beam increases as the cross-sectional area decreases causing loss of intensity and a resulting diffraction pattern. This implies that the beam must have a very small cross-sectional area

device. An equally important criteria is the level of beam coherence. The creation of very powerful synchrotron radiation sources along with increased sensitivity of the detectors, will help to reduce the need for large crystals. The SRSI at Grenoble, France will have a small spot size capability for using much smaller crystals than currently possible. Besides the special cases of very small crystals the collection of data for structural determination requires large well ordered crystals with small unit cells.

## Chapter Five: Three Dimensional Crystallography

The formation of protein crystals, as with any molecule, involves the formation of a supersaturated solution followed by a phase change. The molecule, in our case the membrane protein or culture, eventually changes state to a solid. This solid state is called a crystal if the change occurs in a uniform way. The state change from solution to a solid crystal is a complex process. The formation of a crystal is a slow process because a protein, or any other macromolecule, requires a high activation potential energy. The formation of a crystal is usually achieved by increasing the protein's concentration to a state of supersaturation. Supersaturation is that point where the protein concentration is higher than the solubility of that protein. The supersaturated solution will eventually form a crystal nucleus (nucleation) which is followed by the growth of the crystal. A phase change occurs and a new solid state is formed by a crystal nucleus having a low potential energy. This nucleus will grow into a large crystal. Crystals will not grow in a non-supersaturated or an equilibrium solution. A supersaturated solution can be split into two regions of liquid and a solid, see Figure 5.1. The latter is unable to spontaneously reform a solid in the liquid region.

## 5.1 Introduction:

Determination of an atomic structure of a biological macromolecule to date still generally relies on x-ray crystallography. In order for a x-ray structure of a protein to be elucidated crystals must be produced with all dimensions being at least 0.15-0.25mm. The crystals must be larger than the width of the x-ray beam for a diffraction pattern to be accurately detected. There is a general relationship which states that the intensity of the diffraction pattern is proportional to the crystal volume and inversely proportional to the unit cell volume (for a review see Blundell and Johnson, 1976). For a given x-ray source the dose of the beam reduces as the cross-sectional area decreases causing loss of intensity in the resulting diffraction pattern. This implies that the beam must have a sufficient cross-sectional area with large ordered crystals in its path to provide intense spots on the recording device. An equally important criteria is the level of beam coherence. The creation of very powerful synchrotron radiation sources (SRSs), with increased sensitivity of the detectors, will help to reduce the necessity for large crystals. The SRS at Grenoble, France, when completed will have the capability for using much smaller crystals than currently possible. Excluding the special cases of very powerful SRSs the collection of reliable data sets for structural determination requires large well ordered crystals with small unit cells.

The formation of protein crystals, as with any molecule, involves the formation of a supersaturated solution followed by a phase change. The molecule, in our case the membrane protein or solute, eventually changes state to a solid. This solid state is called a crystal if the change occurs in a uniform way. The state change from soluble protein to solid crystal is a complex process. The formation of a crystal is not energetically spontaneous because a protein, or any other molecule, in solution (fully solvated) is at a low potential energy. The forcing of a phase change occurs by gradually increasing the protein's concentration to a state of supersaturation. Supersaturation is that point where the protein's concentration in solution is greater than the solubility of that protein (in its solvent environment) will allow. If a crystal nucleus (nucleation site) is formed in the supersaturated solution a phase change occurs and a regular solid structure is produced which has a lower potential energy. This solid with a lower potential energy is a crystal. Crystal growth may occur provided the solution is supersaturated. Crystals will not form in a non-supersaturated or an equilibrated system. The supersaturated solution can be split into two regions (i) labile and (ii) metastable, see Figure 5.1. The latter is unable to spontaneously form crystals while the labile region

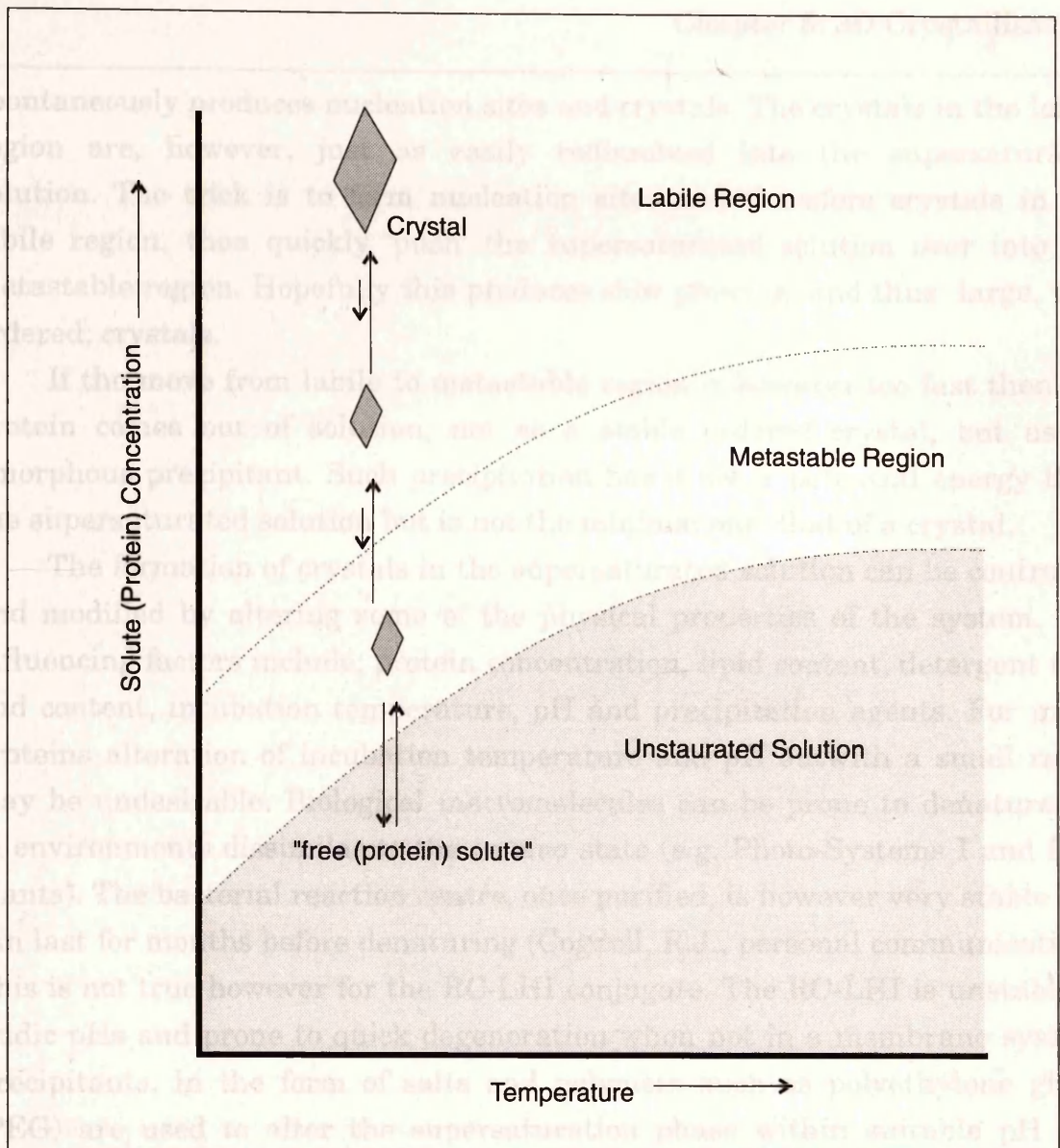


**Figure 5.1:** Solubility of a solute. Three regions are apparent for any given solute-solvent system. These regions are the unsaturated solution and the metastable and labile regions of the supersaturated solution. The diagram illustrates that, for a factor (e.g. temperature), a phase change can occur when the solute concentration in the unsaturated solution is altered. In this example the factor is temperature. For any given temperature as solute concentration is increased a phase change occurs. This occurs at the boundary layer between the unsaturated solution and the metastable region of the supersaturated solution. This increase in solute concentration can occur by solvent removal (e.g. vapour diffusion). Crystals begin to spontaneously form in this region but are just as easily dissolved again. Further increasing of solute (protein) concentration causes the crystal formation into the labile region. Of the two saturated states the labile is the most stable allowing gradual crystal growth to occur. However crystals cannot be initiated in the labile region. Crystals must first occur in the metastable region first, then incubation conditions altered to such that the labile state is produced.

The advantages of using PEG as the precipitant are that low crystallisation conditions have been found a low PEG concentration (0.5-2-3%) can be used that still produces optimal crystals (McPherson, 1991).

spontaneously produces nucleation sites and crystals. The crystals in the labile region are, however, just as easily redissolved into the supersaturated solution. The trick is to form nucleation sites and therefore crystals in the labile region, then quickly 'push' the supersaturated solution over into the metastable region. Hopefully this produces slow growing, and thus large, well ordered, crystals.

If the move from labile to metastable region is however too fast then the protein comes out of solution, not as a stable ordered crystal, but as an amorphous precipitant. Such precipitation has a lower potential energy than the supersaturated solution but is not the minimal one, that of a crystal.

The formation of crystals in the supersaturated solution can be controlled and modified by altering some of the physical properties of the system. The influencing factors include; protein concentration, lipid content, detergent type and content, incubation temperature, pH and precipitation agents. For many proteins alteration of incubation temperature and pH outwith a small range may be undesirable. Biological macromolecules can be prone to denaturation in environments dissimilar to the *in vivo* state (e.g. Photo-Systems I and II in plants). The bacterial reaction centre, once purified, is however very stable and can last for months before denaturing (Cogdell, R.J., personal communication). This is not true however for the RC-LHI conjugate. The RC-LHI is unstable in acidic pHs and prone to quick degeneration when not in a membrane system. Precipitants, in the form of salts and polymers such as polyethylene glycol (PEG) are used to alter the supersaturation phase within suitable pH and temperature regimes. When the supply of solvent becomes the limiting factor salts are preferentially solvated than proteins (Green *et al.*, 1954). This leads to the protein solution becoming supersaturated and suitable for crystal formation. Synthetic polymers such as polyethylene glycol (PEG) alter the solvent's (water) activity thereby producing a supersaturated protein solution. The complex structure, formed by the PEG and solvent, excludes protein association with the solvent, forcing a phase change, and eventual protein precipitation, or crystal formation (Herman, 1982; Lee and Lee, 1981). The degree of competition between salt and protein for water is based on ionic competition with the surface of the polyionic protein playing a major rôle. For proteins to remain in solution they must be hydrated but when water is unavailable they maintain their electrostatic requirements by binding to each other, thus forming precipitation or crystals.

The advantages of using PEG as the precipitant are that once crystallisation conditions have been found a broad PEG concentration (within 2-3%) can be used that still produces optimal crystals (McPherson, 1991).

Often PEG-initiated crystals are produced rather than those precipitated caused by salts (e.g. ammonium sulphate) or organic solvents such as 2-methyl-2,4-pentanediol (McPherson, 1991).

The formation of the super-saturated state relies on the use of layers of water (solvent) available to the protein (solute). The most widely used method, and the one used here, is that of vapour diffusion. For a summary of other possible methods see Millington (1999). This method relies on a protein

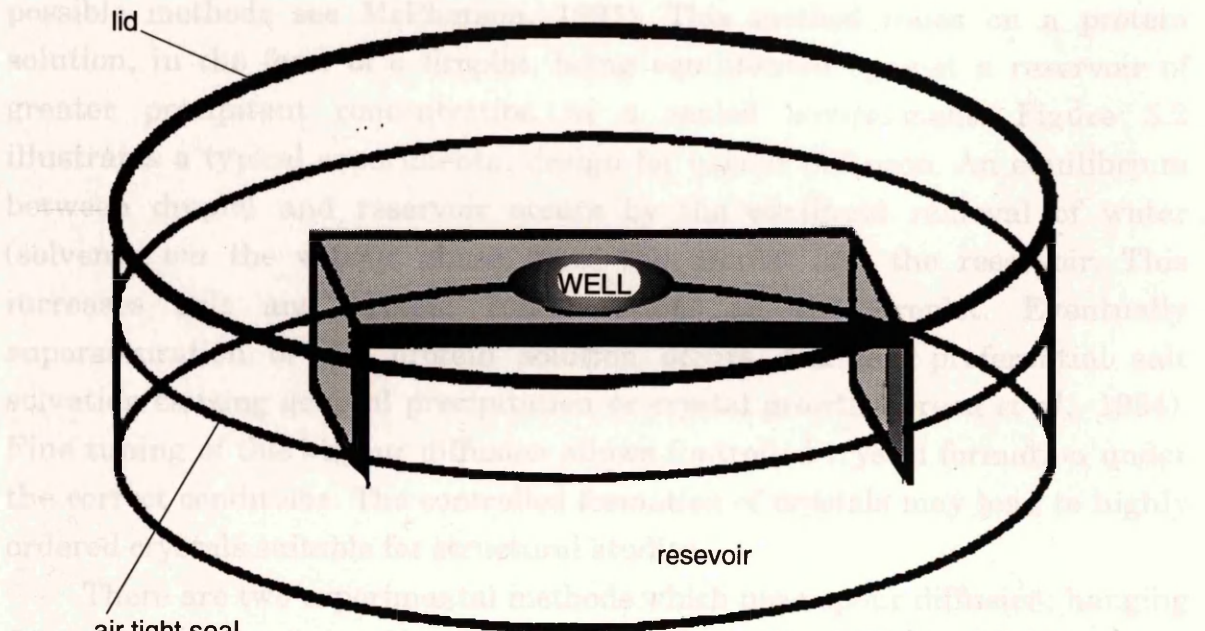


**Figure 5.2.** Crystallographic apparatus used for vapour diffusion. A clear plastic dish has an air-tight seal. The interior of the dish contains a raised platform. In the centre of the platform is small depression, or well. This houses the protein-detergent solution and its mother liquor. Surrounding the platform is a much larger reservoir of precipitating agent. The protein sample concentration increases as vapour is lost from the mother liquor to the reservoir. When the protein levels reach supersaturation crystal formation may occur in the wells. The above sketch is for the large scale vapour diffusion plates. Crychem plates (J.B.L.Scientific Ltd) were also used for crystallographic trials. The basic design of the Crychem plates is similar to the above except they are much smaller and the lid consists of either a glass coverslip or clear tape.

over hanging droplets form. The droplets are formed by the evaporation of the starting conditions. The process is similar to the one used in the vapour diffusion method. The droplets are formed by the evaporation of the same vapour diffusion method.

CrySTALLIZATION OF AN IDEAL CRYSTAL. The first step is to create a protein solution. The proteins themselves. Numerous papers have been published on water (the solvent used in crystallization) is highly sensitive to changes in pH and ionic strength. This is particularly true for the use of ammonium sulphate. McPherson

Often PEG-initiated crystals are produced quicker than those precipitated caused by salts (e.g. ammonium sulphate) or organic solvents such as 2-methyl-2,4-pentanediol (McPherson, 1991).

The formation of the supersaturated state relies on the net removal of water (solvent) available to the protein (solute). The most widely used method, and the one used here, is that of vapour diffusion (for a summary of other possible methods see McPherson, 1991). This method relies on a protein solution, in the form of a droplet, being equilibrated against a reservoir of greater precipitant concentration in a sealed environment. Figure 5.2 illustrates a typical experimental design for vapour diffusion. An equilibrium between droplet and reservoir occurs by the continual removal of water (solvent), *via* the vapour phase, from the droplet into the reservoir. This increases salt and protein concentrations in the droplet. Eventually supersaturation of the protein solution occurs due to preferential salt solvation causing general precipitation or crystal growth (Green *et al.*, 1954). Fine tuning of this vapour diffusion allows controlled crystal formation under the correct conditions. The controlled formation of crystals may lead to highly ordered crystals suitable for structural studies.

There are two experimental methods which use vapour diffusion; hanging drops and sitting drops. The former consists of a droplet of protein-detergent mixture (or protein solution if a water soluble protein is used) suspended over a reservoir solution containing a higher precipitant concentration. The droplet is adhered to the surface of a siliconised glass microscope coverslip by surface tension. The drawback to this approach is that only small protein droplets can be used. If they become too large the surface tension is unable to support them and they fall off into the reservoir below. Approximately 10 $\mu$ l can be used safely by this method. The advantage of this system is that a large range of crystal trials can be undertaken if there is a limited amount of suitable protein available.

The second design, the sitting droplet, has a droplet of protein solution situated in a well surrounded by a reservoir. The advantage of this method over hanging drops is larger protein samples can be used. Using the same starting conditions the formation of crystals by both the hanging and sitting drop methods may lead to crystal formation although not necessarily by the same vapour diffusion route (McPherson, 1991).

Crystallisation of membrane proteins has one major drawback - the proteins themselves. Membrane proteins are not soluble in water (the solvent used in crystallisation is usually water) and on contact with it form non-specific aggregations. This is overcome by the use of detergents. Membrane



**Figure 5.3:** Photograph of the  $\beta$ -OG detergent ring surrounding the hydrophobic domain of the *Rb. sphaeroides* reaction centre. The detergent ring is located where the *in vivo* membrane is located (Roth *et al.*, 1991)

Figure five: 3D structure of the reaction center of *Rb. sphaeroides* and proteins from *Rhodospirillum rubrum* (R1) and *Rhodospirillum rubrum* (R2) protein-detergent complex. The structure is shown as a dotted surface with the detergent ring (beta-OG) shown as a solid surface. The hydrophobic domain is shown as a solid surface. The detergent ring is shown as a solid surface. The structure is shown as a dotted surface with the detergent ring (beta-OG) shown as a solid surface. The hydrophobic domain is shown as a solid surface. The detergent ring is shown as a solid surface. Bottom: Crystals are formed by the reaction center of *Rb. sphaeroides*. Redrawn from Michel, (1991).

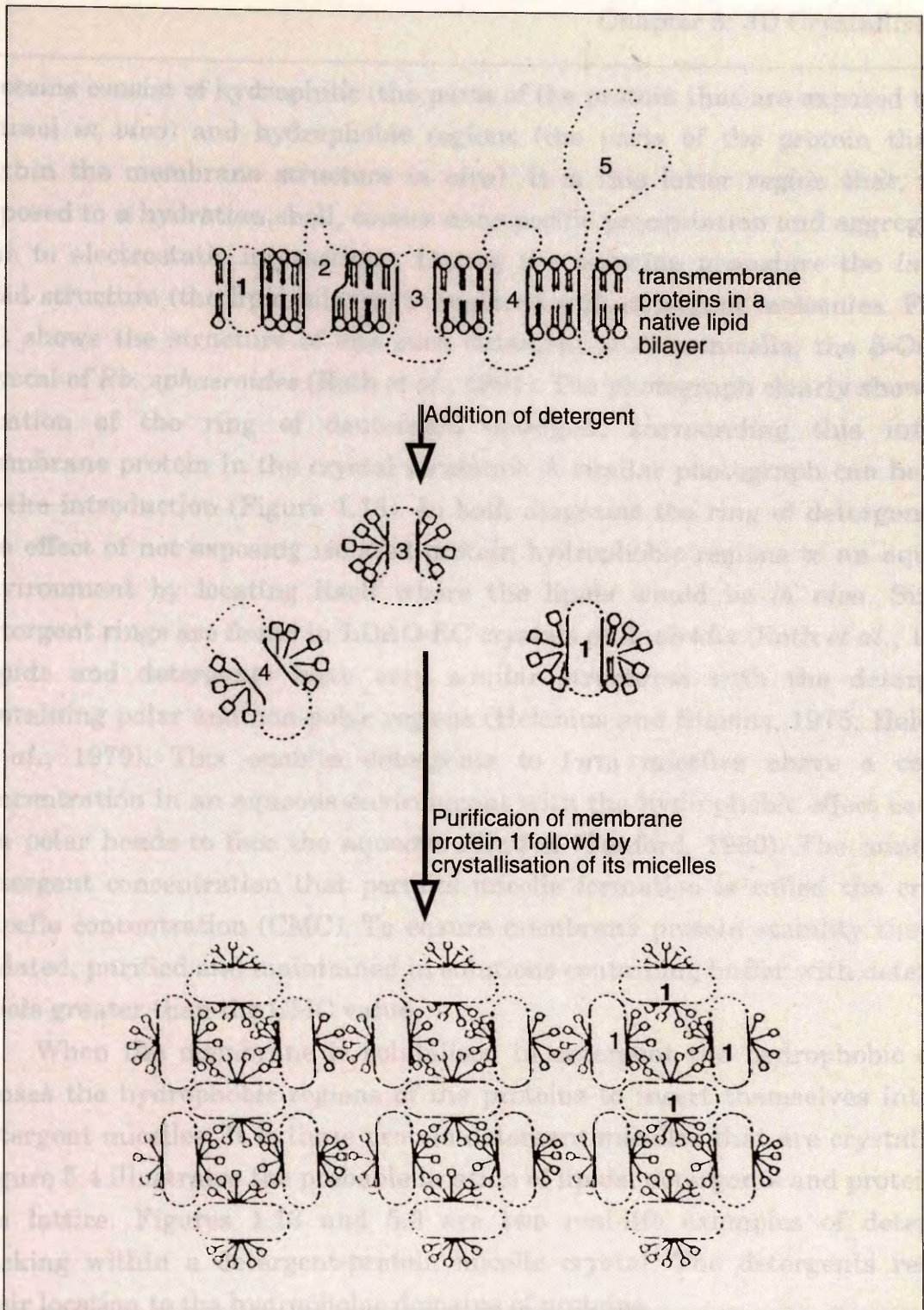


**Figure 5.4:** 3D crystallisation of protein-detergent micelles: location of lipids, detergents and proteins. Membrane proteins 1,2,3,4 and 5 (top) are solubilised in detergent and form protein-detergent micelles (middle). The hydrophilic regions of the proteins are shown by dotted surfaces while the hydrophobic domains have solid surfaces. The detergents protect the hydrophobic regions from the solvent. Some specific lipids are associated with each protein. The lipids are depicted by circles with two tails while the detergents are squares with single tails. Lipids can be seen in association with protein 1 micelles. Bottom: Crystals are formed from purified protein 1 by net removal of available solvent. Redrawn from Michel, (1983).

proteins consist of hydrophilic (the parts of the protein that are exposed to the cytosol *in vivo*) and hydrophobic regions (the parts of the protein that lie within the membrane structure *in vivo*). It is this latter region that, when exposed to a hydration shell, causes non-specific precipitation and aggregation due to electrostatic interactions. During the isolation procedure the *in vivo* lipid structure (the lipid bilayer) is replaced with detergent molecules. Figure 5.3 shows the structure of one such detergent-protein micelle; the  $\beta$ -OG-RC crystal of *Rb. sphaeroides* (Roth *et al.*, 1991). The photograph clearly shows the location of the ring of deuterated detergent surrounding this integral membrane protein in the crystal structure. A similar photograph can be seen in the introduction (Figure 1.13). In both diagrams the ring of detergent has the effect of not exposing isolated protein hydrophobic regions to an aqueous environment by locating itself where the lipids would be *in vivo*. Similar detergent rings are found in LDAO-RC crystals of *R. viridis* (Roth *et al.*, 1989). Lipids and detergents have very similar structures with the detergents containing polar and non-polar regions (Helenius and Simons, 1975; Helenius *et al.*, 1979). This enables detergents to form micelles above a certain concentration in an aqueous environment with the hydrophobic effect causing the polar heads to face the aqueous solution (Tanford, 1980). The minimum detergent concentration that permits micelle formation is called the critical micelle concentration (CMC). To ensure membrane protein stability they are isolated, purified and maintained in solutions containing buffer with detergent levels greater than the CMC value.

When the membrane is solubilised in detergent the hydrophobic effect causes the hydrophobic regions of the proteins to insert themselves into the detergent micelles. It is these protein-detergent micelles that are crystallised. Figure 5.4 illustrates the probable location of lipids, detergents and proteins in the lattice. Figures 1.13 and 5.3 are two real-life examples of detergent packing within a detergent-protein micelle crystal. The detergents restrict their location to the hydrophobic domains of proteins.

The addition of detergents into the crystallisation solution is often a major problem. Phase separation occurs under high precipitant conditions; the detergent-micelles are precipitated out of solution. This phase difference between a detergent rich and detergent poor (aqueous) region causes the membrane proteins to migrate to the detergent rich phase causing general denaturation of proteins. To combat this, small molecules called amphiphiles, are sometimes added to prevent phase separation (Michel, 1983). This is achieved because amphiphiles permit increased salt concentrations to occur

before phase separation occurs. Examples of widely used amphiphiles are heptane-triol and benzamidine hydrochloride.

Amphiphiles also enhance structural integrity of crystals by inserting themselves in the micelle and replacing detergents at vital locations thereby aiding the formation of regular arrays of protein-detergent complexes (Michel, 1983). They achieve this by reducing the radius of the micelle allowing greater protein-protein, protein-detergent and other interactions to occur. Structural stress to the protein can be reduced by these small molecules since they can fill in the gaps between detergents and proteins. This has the effect of reducing the threat of water invading the hydrophobic region and thus limiting any stress from the aqueous solvent used in the crystallographic trial. It should be noted at this point that the size of detergent molecule used is also very important. A large detergent even with an amphiphile added may not form highly ordered crystals (assuming crystals form at all) because the polar heads of the detergent can mask the polar regions of the protein. Consequently the interactions which occur in detergent-protein micelle crystals are reduced or do not form. This, of course, results in either poor or even no crystal growth. There are therefore advantages in using amphiphiles, detergents, proteins and precipitation agents in the correct combination in 3D crystallographic trials because highly ordered crystals can result. However the optimum combination cannot be derived by any other means other than by many experimental crystallographic trials and as a result the formation of well ordered 3D crystals suitable for structural analysis can take a long time.

## 5.2 Range of Photosynthetic Proteins Studied:

Purified reaction centre light-harvesting conjugates (RC-LHI or *cores*) and peripheral light-harvesting complexes (LHII) from a range of Rhodospirillaceae species were screened to observe which ones produced suitable conditions for 3D crystal growth. Figure 5.5 illustrates the range of photosynthetic proteins that were investigated.

During the purification steps it was clear that stable *core* conjugates were easier to obtain from some strains than others. The isolation of stable *cores* from *Rb. sphaeroides* strain GA and strain M21 were amongst the most difficult. Both *R. centenum* and *R. rubrum* produced stable *cores* but were denatured if left for long periods of time in the purification detergent LDAO. The most stable *core* conjugates were from *Rp. acidophila* strains 10050, 7750, *Rp. cryptolactis* and *Rp. palustris* strain 2.6.1. For these reasons studies were concentrated on the last three species. Of the three *Rp. acidophila* strains 10050 was chosen because high resolution data has been collected for its peripheral light-harvesting complex (Cogdell, R.J., private communication). Figure 5.5 also shows which of the species studied contains LHII and whether or not 3D trials were setup. LHII from *Rp. palustris* strain 2.6.1 was investigated in its two forms; the low light (LL) and high light (HL) forms (Zuber and Brunisholz, 1986; Zuber, 1990). It is possible that only one form of LHII will produce crystals. Refer to section 1.3. and Figures 1.7 and 1.8 for an explanation of the differences between HL and LL *Rp. palustris* 2.6.1 B800-850.



Figure 5.5: This Schematic photographic system of the 3D crystallisation. The structural analysis are marked by a '+' and the unsuccessful ones by a '-'. The species names are in bold. The two different LHII complexes produced by *Rp. palustris* strain 2.6.1 are marked with 'LL' and 'HL' for low and high light conditions respectively. The environmental conditions and how different cell cultures behave are also shown. (Zuber, 1990).

Species	strain	RC-LHI	HLII
<i>R.centenum</i>	type	+	n/a
<i>R.rubrum</i>	S1	+	n/a
<i>Rb. sphaeroides</i>	GA	+	-
	M21	+	n/a
<i>Rc. gelatinosus</i>	DSM 149	+	-
	DSM 151	+	-
<i>Rp. acidophila</i>	10050	+	-
	7750	+	-
	7050	+	-
<i>Rp. cryptolactis</i>	type	+	-
<i>Rp. palustris</i>	2.6.1.	+	+

**Figure 5.5:** The Screened photosynthetic proteins of the Rhodospirillaceae. The screened proteins are marked by a '+' and the unscreend ones by a '-'. It should be noted that *in Rp. palustris* there are two distinct LHII complexes produced. These two LHII's are produced under different environmental conditions and have different NIR absorption maxima and polypeptide ratios (Zuber, 1990).

	SALT	BUFFER	PRECIPITANT*
1	0.2M Ca chloride	0.1M Na acetate	30% MPD
2			0.4M KNa tartrate
3			0.4M NH <sub>4</sub> <sup>+</sup> phosphate
4		0.1M TRIS	2.0M NH <sub>4</sub> <sup>+</sup> sulphate
5	0.2M Na citrate	0.1M HEPES	40% MPD
6	0.2M Mg chloride	0.1M TRIS	30% PEG 4000
7		0.1M Na cacodylate	1.4M Na acetate
8	0.2M Na citrate	0.1M Na cacodylate	30% propan-2-ol
9	0.2M NH <sub>4</sub> <sup>+</sup> acetate	0.1M Na citrate	30% PEG 4000
10	0.2M NH <sub>4</sub> <sup>+</sup> acetate	0.1M Na acetate	30% PEG 4000
11		0.1M Na citrate	1.0M NH <sub>4</sub> <sup>+</sup> phosphate
12	0.2M Mg chloride	0.1M HEPES	30% propan-2-ol
13	0.2M Na citrate	0.1M TRIS	30% PEG 400
14	0.2M Ca chloride	0.1M HEPES	28% PEG 400
15	0.2M NH <sub>4</sub> <sup>+</sup> sulphate	0.1M Na cacodylate	30% PEG 8000
16		0.1M HEPES	1.5M Li sulphate
17	0.2M li sulphate	0.1M TRIS	30% PEG 4000
18	0.2M Mg acetate	0.1M Na cacodylate	20% PEG 8000
19	0.2M NH <sub>4</sub> <sup>+</sup> acetate	0.1M TRIS	30% propan-2-ol
20	0.2M NH <sub>4</sub> <sup>+</sup> sulphate	1.0M Na acetate	25% PEG 4000
21	0.2M Mg acetate	0.1m Na cacodylate	30% MPD
22	0.2M Na acetate	0.1M TRIS	30% PEG 4000
23	0.2M Mg chloride	0.1M HEPES	30% PEG 400
24	0.2M Ca chloride	0.1M Na acetate	20% propan-2-ol
25		0.1M Imidazole	1.0M Na acetate
26	0.2M NH <sub>4</sub> <sup>+</sup> acetate	0.1M Na acetate	30% MPD
27	0.2M Na citrate	0.1M HEPES	20% propan-2-ol
28	0.2M Na acetate	0.1M Na cacodylate	30% PEG 8000
29		0.1M HEPES	0.8M K calcium tartrate
30	0.2M NH <sub>4</sub> <sup>+</sup> sulphate		30% PEG 8000
31	0.2M NH <sub>4</sub> <sup>+</sup> sulphate		30% PEG 4000
32			2.0M NH <sub>4</sub> <sup>+</sup> sulphate
33			4.0M Na formate
34		0.1M Na acetate	2.0M Na formate
35		0.1M HEPES	1.8M K phosphate
36		0.1M TRIS	8% PEG 8000
37		0.1M Na acetate	8% PEG 4000
38		0.1M HEPES	1.4M Na citrate
39		0.1M HEPES	2% PEG 400, 2.0M NH <sub>4</sub> <sup>+</sup> sulphate
40		0.1M Na citrate	20% propan-2-ol, 20% PEG 4000
41		0.1M HEPES	10% propan-2-ol, 20% PEG 4000
42	0.05M K phosphate		20% PEG 8000
43			30% PEG 2000
44			0.2M Na formate
45	0.2M Zn acetate	0.1M Na cacodylate	18% PEG 8000
46	0.2M Ca acetate	0.1M Na cocodylate	18% PEG 8000

**Figure 5.6:** The *Magic 46* screen. A series of stock solutions (see appendix 4.1) were used to create the above solutions. When the above solutions (salts, buffers and precipitants) were combined they produced the *Magic 46* crystallographic screen. The pHs of the buffers are described in appendix 4.1. The '\*' depicts w/v or v/v at room temperature.

### 5.3 Magic 46 Protocol:

A screening protocol was established in the early 1990s by the University of California, Berkeley, U.S.A called the *Magic 46* which was used as a starting point for many 3D crystallographic trials.

Hanging drops (5 $\mu$ l) were prepared and placed over 500 $\mu$ l reservoirs in Corning tissue culture plates. The driving force for crystallisation was created by the difference in precipitant concentrations between the hanging drop and the reservoir. 700 $\mu$ l of each screening solution (e.g. number 20 from Figure 5.6) was placed in an eppendorf and centrifuged at 10K xg for 20min to pellet any potential debris that may act as a nucleation site. 2.5 $\mu$ l was placed onto a siliconised virgin glass cover slip. 500 $\mu$ l of the screening solution was placed into the reservoir. Immediately an equal volume of protein solution (2.5 $\mu$ l) was pipetted onto the coverslip and into the screening solution. This has the effect of reducing the droplet precipitant and/or salt concentration relative to the reservoir. Once all the constituents were added, the protein droplets contained a final detergent concentration of 1.0% w/v of  $\beta$ -OG and 3mM sodium azide. The drops were pipetted onto virgin siliconised glass cover slips. The cover slips were sealed onto the tops of the reservoir wells by silicone grease and incubated in the dark, initially at 4°C and 20°C. From the first attempt using *Rp. acidophila* strain 10050 two observations were noticed. Firstly all the wells precipitated within 2 days with many of the trials having complete protein degeneration as indicated by colour changes, and secondly all the 20°C trials were denatured. It was considered that the ionic strength was too great using full-strength *Magic 46* solutions. As a result the trials were repeated using half-strength *Magic 46* solutions in the reservoirs with each trial (mother liquor) containing quarter strength *Magic 46* combinations in the hanging drops. Figure 5.7 illustrates some of the results obtained using half strength *Magic 46* trials. The results from this were much more promising, fewer complete denatured trials occurred and many of the trials that previously lost their native colour maintained their original colour (e.g. Figure 5.7C). The 4°C trials were promising but the 20°C were again all degenerated. Consequently all other trials were then started using initially half strength *Magic 46* solutions and at 4°C.

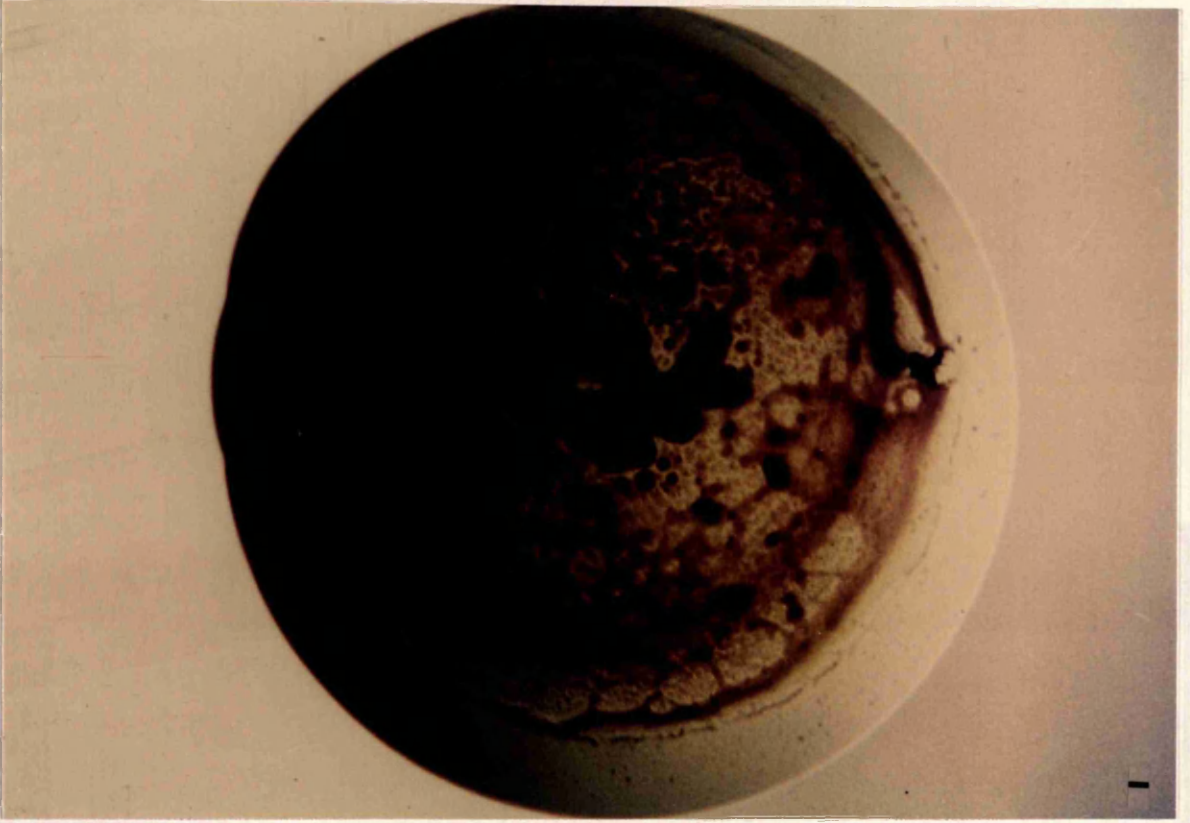
*Rc gelatinosus*, *Rp. sphaeroides*, *Rp. acidophila* strains 7750 and 7050, never produced any crystals. However promising indicators were found with *R. rubrum*, *R. centenum*, *Rp. acidophila* strain 10050 and *Rp. palustris* strain 2.6.1 cores.

**Figure 5.7:** Initial Magic 46 Results. (A): Free bacteriochlorophyll production from a 3D crystallographic trial. The trial (based on Magic #19 trial) had TRIS.HCl to control the pH. The pH of this trial was similar to the pH this pigment-protein complex (*Rp. acidophila* stain 7750 RC-LHI) is most stable in. However the organic solvent propan-2-ol was used as the precipitant. The solvent freed pigments from their apoproteins thereby giving the observed green colour. (B): Phase separation of a crystallographic trial. *Rp. acidophila* stain 7750 RC-LHI core conjugate migrated into the detergent rich micelles. The protein quickly denatures in the high detergent levels. (C): General amorphous precipitation. Oily drops occurred in some trials where the protein-detergent micelles were retained in solution. Some trials further developed by forming amorphous precipitate. The native red colour is maintained in this example from *Rp. palustris* RC-LHI. The trial was based on TRIS.HCl (pH8.0) and a very low PEG level (2% PEG 2000). Other trials that had either general precipitation or oily drops also had colour changes which were associated with protein denaturation. Bar 0.1mm.

(A)



(B)



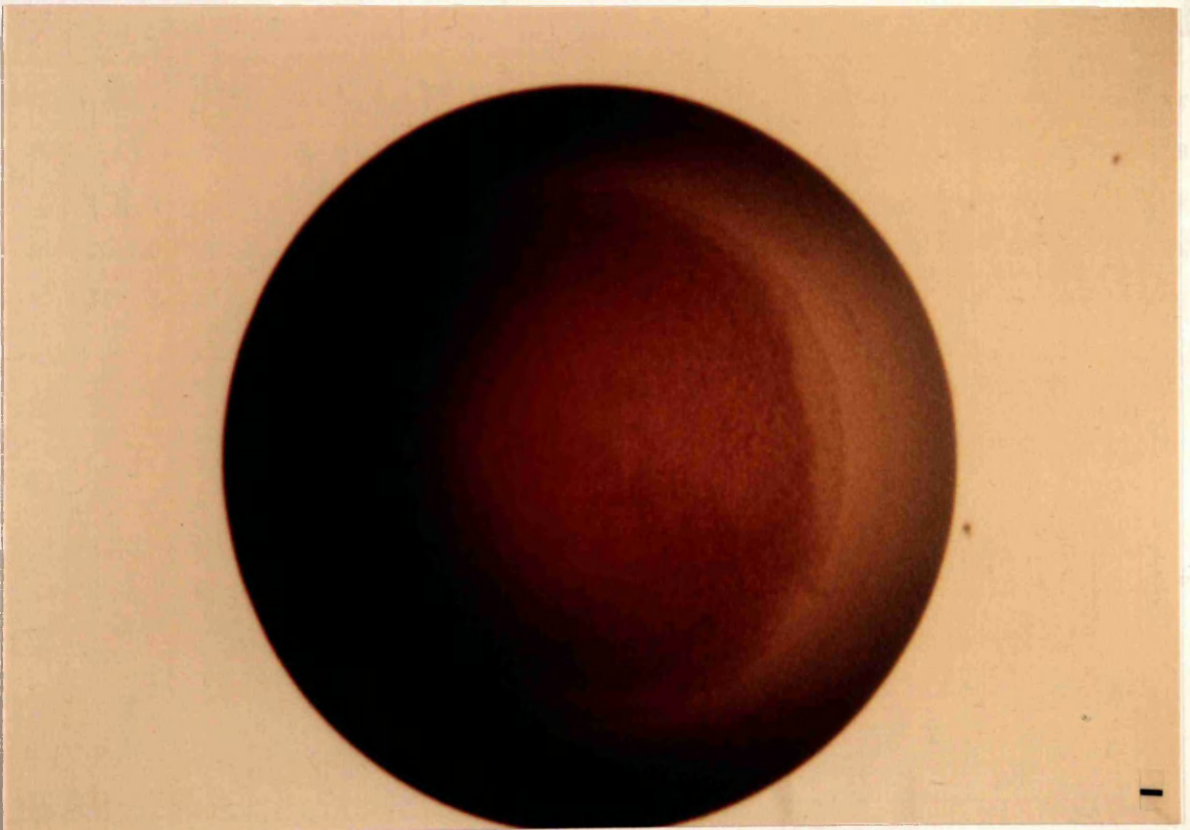
1.35 (1)

0.1M Zn acetate

0.05M Cacodylate (pH 5.50)

5% w/v PEG 1000

(C)



1.35 (1)

0.1M Cu acetate

0.05M Cacodylate (pH 5.50)

5% w/v PEG 1000

### 5.3.1 *Rp. palustris* strain 2.6.1

Half strength Magic 46 screens were used to produce crystals for strains 14, 23, 45, and 46. The first crystals formed when the droplets were left for up to 10 more days to form crystals. These did take the conditions used in the reservoir solutions for the above four trials. The crystal formation conditions will be discussed in decreasing numerical order.

First are trials 45 and 46. These formed crystals that appear to be very unlikely candidates for the protein studied because of the acidic pH of the crystals. These proteins are generally unstable in an acidic pH but the cocodolate buffer was not in pH 5.32 (see appendix A) and from numerous studies the use of this buffer has not helped crystal growth in these membrane proteins (G. McDerwott, personal communication). Yet crystals did form. The most likely explanation is that the protein was in a state of partial denaturation.

Magic 46 Number:	SALT	BUFFER	PRECIPITANT
14	0.1M Ca chloride	0.05M HEPES (pH 7.50)	14% (v/v) PEG 400
23	0.1M Mg chloride	0.05M HEPES (pH7.50)	15% (v/v) PEG 400
45	0.1M Zn acetate	0.05M Cacodylate (pH 5.32)	9% (w/v) PEG 8000
46	0.1M Ca acetate	0.05M Cacodylate(pH 5.32)	9% (w/v) PEG 8000

**Figure 5.8:** Reservoir conditions in half strength *Magic 46* screens that produced crystals for *Rp. palustris* strain 2.6.1 core conjugate. Note that the reservoirs also contained 3mM sodium azide to prevent any bacterial growth in the screening solutions. The protein droplets contained half the concentrations stated in the table. The protein concentration in the droplet was  $5\text{mg}\cdot\text{ml}^{-1}$  with final concentrations of 1% (w/v)  $\beta$ -OG and 3mM sodium azide also present.

### 5.3.1 *Rp. palustris* strain 2.6.1. :

Half-strength *Magic 46* solutions produced crystals in screens 14,23,45, and 46. The first crystals formed within four days with screen #14 taking up to 10 more days to form crystals. Figure 5.8 lists the conditions used in the reservoir solutions for the above four trials. The crystal forming screens will be discussed in decreasing numerical order.

First are trials #46 and #45. These formed crystals in what appears to be very unlikely conditions suitable for the proteins studied because of the acidic pH of the trial buffer. These proteins are generally unstable in an acidic pH but the cacodylate buffer was set to pH 5.23 (see appendix 5.1) and from numerous studies the use of zinc tends not to favour crystal growth in these membrane proteins (G. McDermott, personal communication). Yet crystals did form. They were long, needle shaped but slightly discoloured. Of the two trials #46 yielded the larger *better* looking crystals in that they were more uniform and of a more natural colour. Figure 5.9A is a picture of trial #46 and Figure 5.9B for trial #45. Since the shape and colour was not desirable these conditions were not further investigated.

Within 4 days of setting up the half strength *Magic 46* trials crystals formed in trial #23. These, unlike trials #45 and #46 were not discoloured. The crystals formed were of regular hexagonal shapes. Although small, approximately 20-50µm in diameter, they are all uniform. Figure 5.10A is a photograph of *Rp. palustris* 2.6.1 half-strength *Magic 46* screen #23. As the Figure shows the crystals are of uniform shape and size. There is no discolouring in the well thus general protein denaturation has not occurred. However there is still some redness in the solution which indicates that not all the protein has been utilised for crystal growth.

Approximately 7-10 days into the incubation crystals appeared in screen #14. These crystals also were of regular hexagonal shapes and similar to the crystals in screen #23. The crystals in screen #23 were fewer in number but approximately twice as large. This screening condition was further investigated by varying the PEG concentrations in the reservoir from 15%-8%. Although crystals did appear similar to the ones in Figure 5.10A no increase in size was forthcoming. The crystals were too small for x-ray analysis. The constituents of half-strength #14 droplet, including the contents of the protein solution itself was;

Half-strength Magic 46 solutions produced crystals in screens 14, 23, 45, and 46. The first crystals formed within four days with screen #14 taking up to 10 more days to form crystals. Figure 5.8 lists the conditions used in the reservoir solutions for the above four trials. The crystal forming screens will be discussed in decreasing numerical order.

First are trials #46 and #45. These formed crystals in what appears to be very unlikely conditions suitable for the proteins studied because of the acidic pH of the trial buffer. These proteins are generally unstable in an acidic pH but the cacodylate buffer was set to pH 5.23 (see appendix 5.1) and from numerous studies the use of zinc tends not to favour crystal growth in these membrane proteins (G. McDermott, personal communication). Yet crystals did

**Figure 5.9:** 3D crystals of *Rp. palustris* 2.6.1 RC-LHI core conjugate. Four trials that were based on the *Magic 46* screen produced probable crystals. The four trials could be separated into two groups based on their incubation conditions. The first group produced needle shaped growths. The incubations were based on cacodylate and PEG 8000 as the buffer and precipitant respectively. The salts used were zinc acetate (plate A) and calcium acetate (plate B). More structures formed in the trial that contained zinc (plate A) however the screen that contained the calcium salt (plate B) produced slightly larger needle shaped structures. The structures associated with the calcium also appeared to be more uniform in character. Both trials had relatively large levels of precipitation present and the colour indicated that probable denaturation had occurred. The other two trials are shown in Figure 4.10. bar 0.1mm.

the protein has been utilized for crystal growth. However there is still some redness in the solution which indicates that not all discoloring in the well thus general protein denaturation has not occurred. Figure shows the crystals are of uniform shape and size. There is no photograph of *Rp. palustris* 2.6.1 half-strength Magic 46 crystals. There is no #14. These crystals also were of regular hexagonal shape and similar to the crystals in screen #23. The crystals in screen #28 were fewer in number but approximately twice as large. This screening condition was further investigated by varying the PEG concentrations in the reservoir from 15%–8%. Although crystals did appear similar to the ones in Figure 5.10A no increase in size was forthcoming. The crystals were too small for x-ray analysis. The constituents of half-strength #14 droplet, including the contents of the protein solution itself was;

(A) Figure 5.10: The upper part of a *Polioptila* bird that produced 30 crystals of *P. palustris*

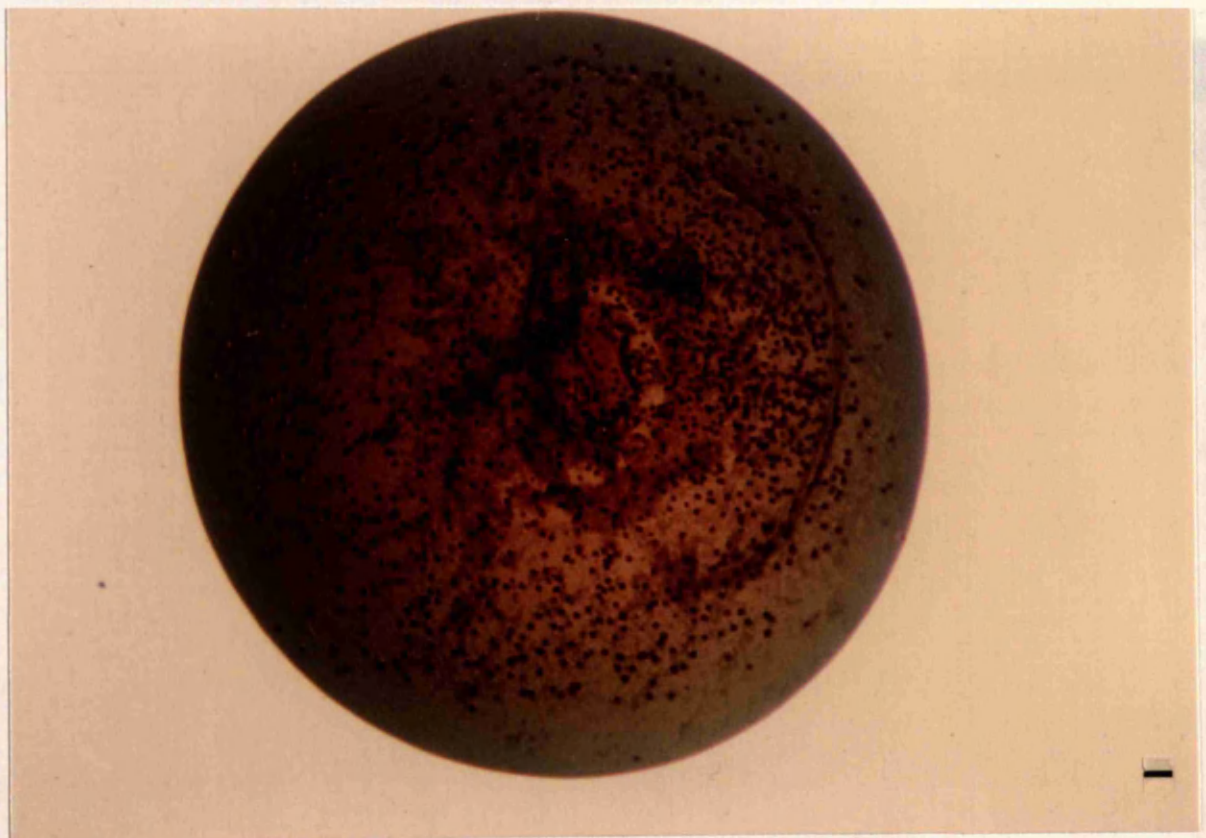


(B)



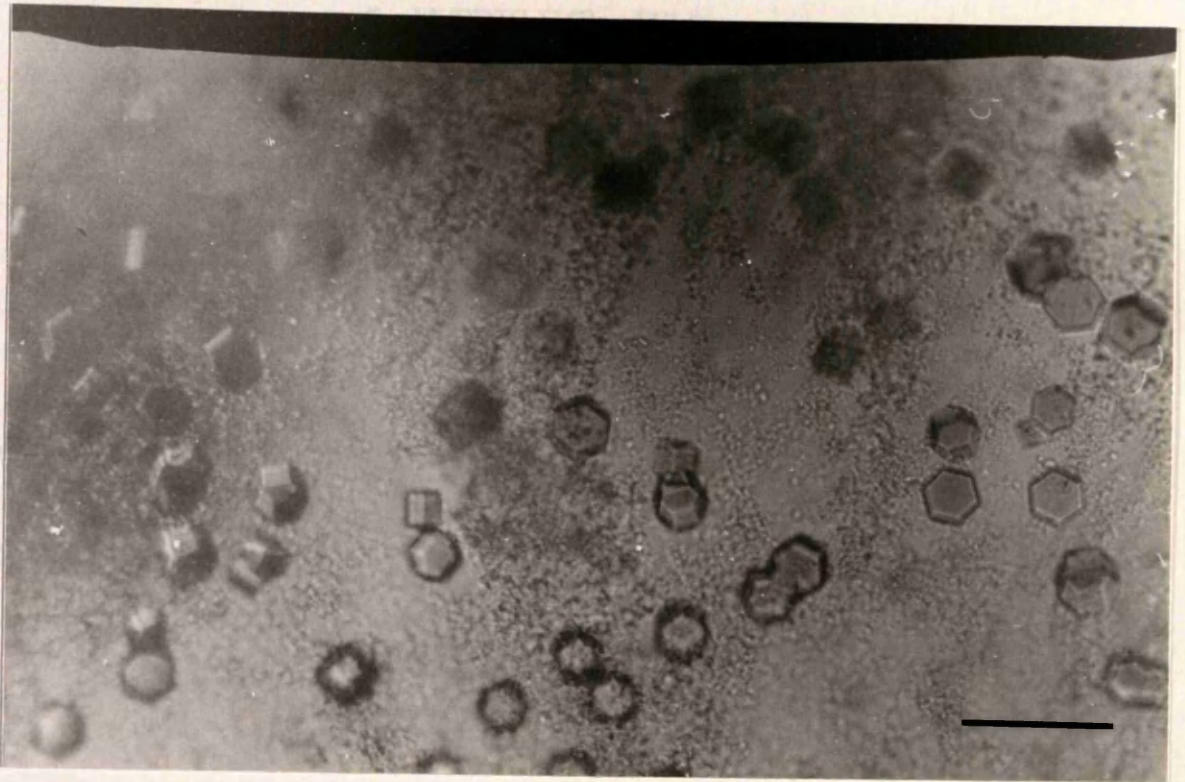
**Figure 5.10:** The second group of crystallisation trials that produced 3D crystals of *Rp. palustris* 2.6.1 RC-LHI core conjugate. Both these trials produced hexagonal shaped pigmented structures. Trial incubations by vapour diffusion occurred by the hanging drop method. (A): Photograph of the hanging drop from an incubation based on *Magic 46* #14. Many regular shaped pigments objects can be seen with some general precipitation evident. There is still a slight red colour present in the mother liquor suggesting that crystallisation was not yet completed. (B) Magnified portion of above plate. This plate illustrates that the objects are of uniform shape; they are very small hexagonal columns. They are too small (25-50 $\mu$ m) however to undergo any x-ray analysis. The central red object clearly shows the hexagonal cross sectional area of the crystals. (C) Magnified portion from the second incubation (based on *Magic 46* #23) that produced hexagonal columns. The pigments structures in this trial although larger (50-75 $\mu$ m) than the trial based on *Magic 46* #14 were still too small to be analysed. General observations suggested that the crystals based on *Magic 46* #23 were larger and fewer in number. Bar 0.1mm.

(A)



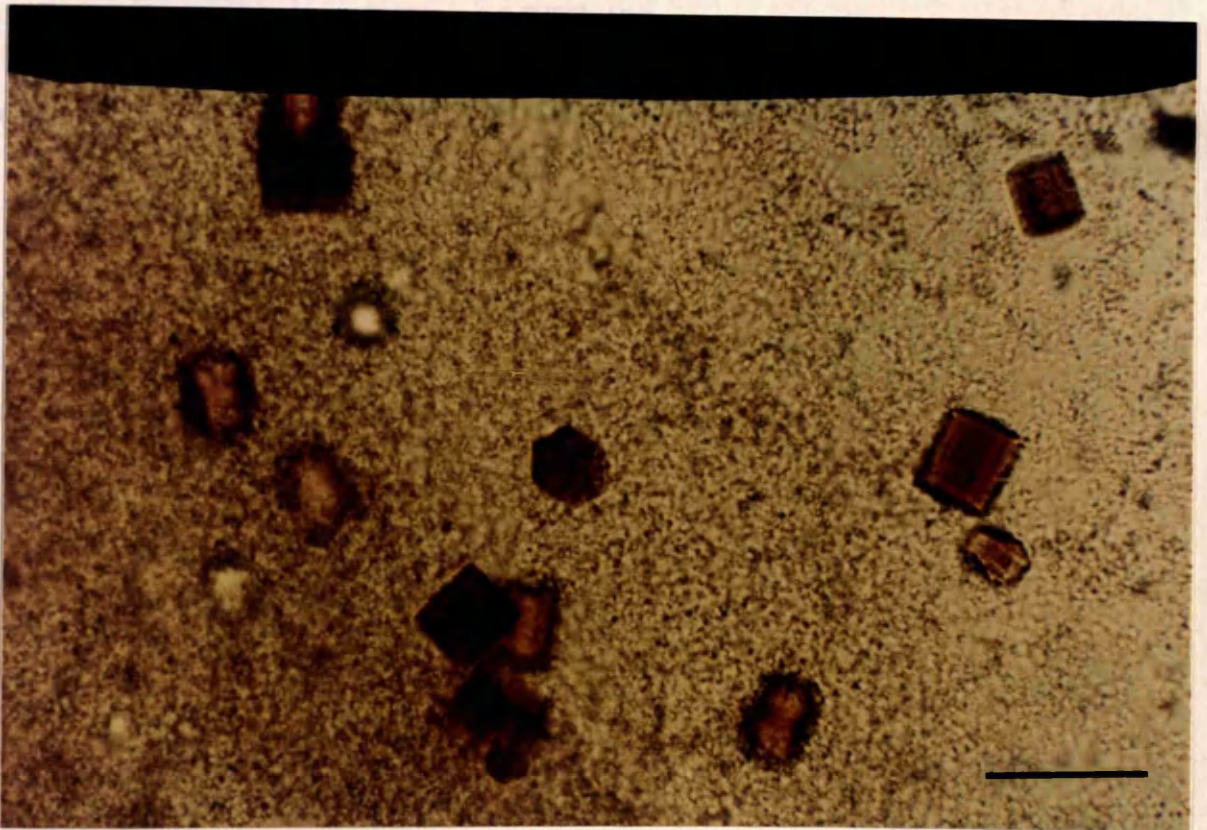
(B)

Droplet constitution: 0.05mg of Rp. palustris 2.6 L. water (5mg.ml<sup>-1</sup>)



Droplet constitution: 300mM magnesium chloride  
200mM HEPES (pH 7.5)  
1.0mM p-DC

(C)



**Droplet constitution:** 0.05mg of *Rp. palustris* 2.6.1. core (5mg.ml<sup>-1</sup>)  
 5mM TRIS.HCl, pH8.0  
 1.25mM sodium chloride (approximate value, based on centricon data sheets; see chapter 3 for details)  
 3mM sodium azide  
 50mM calcium chloride  
 25mM HEPES (pH 7.5)  
 1.0%  $\beta$ -OG  
 7% (v/v) PEG 400

**Reservoir constitution:** 3mM sodium azide  
 100mM calcium chloride  
 50mM HEPES (pH 7.5)  
 14% (v/v) PEG 400

The contents of half-strength trial #23 was very similar to half-strength #14, the differences being :

**Droplet constitution:** 50mM magnesium chloride  
 25mM HEPES (pH 7.5)  
 1.0%  $\beta$ -OG  
 7.5% (v/v) PEG 400

**Reservoir constitution:** 100M magnesium chloride  
 50mM HEPES (pH 7.5)  
 15% (v/v) PEG 400

No amphiphiles were added to the above screens thus the addition of amphiphiles are not a prerequisite for crystal growth in these membrane proteins. The use of amphiphiles may however be required for sufficiently ordered crystals suitable for x-ray analysis.

### 5.3.2 *R. centenum*:

Using colour changes as an indicator this bacterium did not have as much general protein denaturation compared to the majority of initial screens that were set up. However, no single trial produced noticeable crystals. There was one trial system that did produce what appeared to be the beginnings of crystal formation. Small micro-crystals began to form in half strength #26. Figure 5.11 illustrates that as microcrystal formation occurs phase separation is also present. The apparent phase separation is the probable explanation why the micro-crystals are pear shaped. It should be noted that the colour of the sample, even after one month, was similar to freshly purified *core* conjugate. The most puzzling consequence of this screen is the pH of the buffer and precipitant used. The precipitant was 2-methyl-2,4-pentandiol (MPD) with a buffered pH of 5.28. Consequently this could be a starting point for future investigations. However the *core* conjugate from *R. centenum* was difficult to isolate and it was considered that the little protein that was produced should be used for 2D crystallographic trials. This was because less protein is generally needed per 2D crystallographic trial when compared to 3D crystallography. It was hoped that once in a membrane environment *R. centenum core* conjugate would be more stable and thus produce useful structural data. This however was not found to be the case (Chapter Four, section 4.4.3).

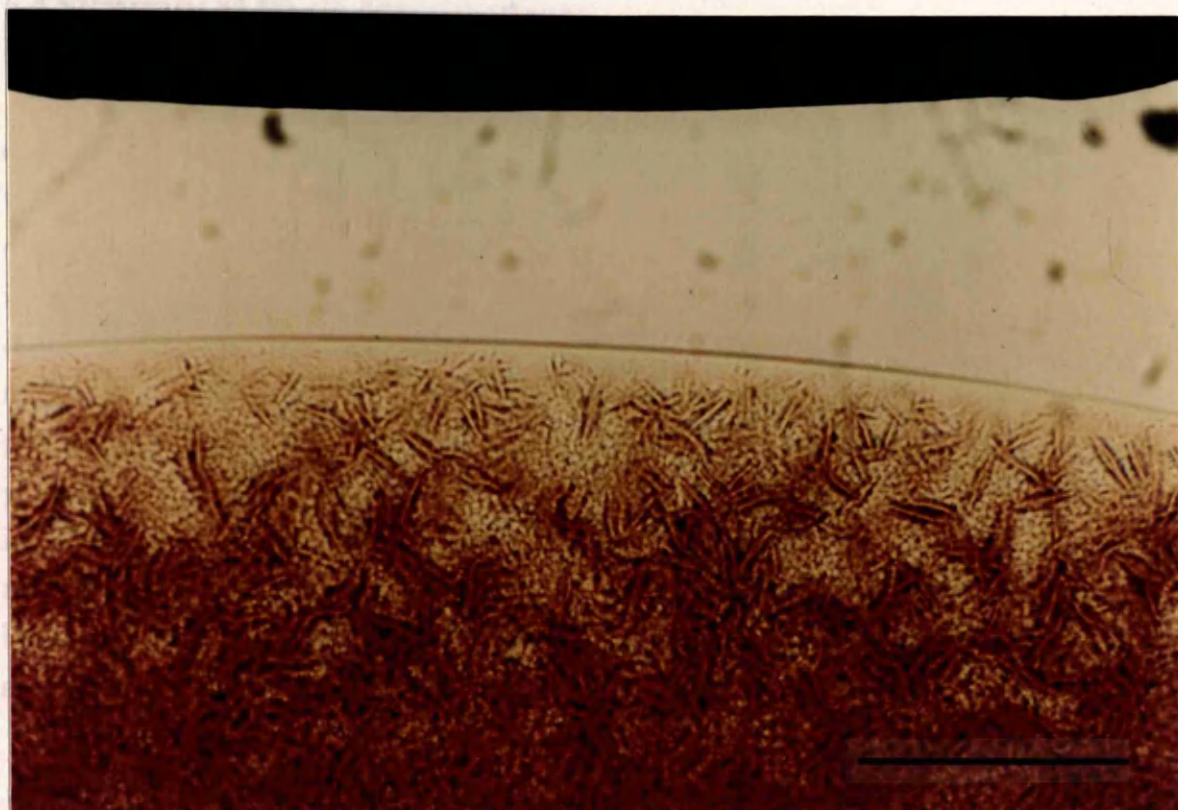


**Figure 5.11:** Phase change in *R. centenum* RC-LHI microcrystals. One range of crystallisation trials (adapted from Magic 46 #26) using this pigment-protein complex formed what appeared to be numerous microcrystals after a few days incubation at 4°C. On further incubation these microcrystals developed into pear shaped structures. A phase change was considered to be responsible for the shape of the growth of these structures. The native colour was maintained throughout the trial indicating that the proteins themselves were probably structurally sound. The isolation of *R. centenum* RC-LHI was found to denature very easily (see chapter three) thus the retention of the red colour was considered a good sign. However the formation of microcrystals does indicate that the optimum conditions have not been found. Bar 0.1mm.



## 5.5 FASTPEG SCREEN:

The most stable incubations from the *Magic 46* trials consisted of polyethylene glycol (PEG) as the precipitant and an alkaline pH. A semi-factorial protocol approach was established by randomly assigning a precipitant, buffer and salt combination until phase separation did not occur in the screening mixture. The formation of the *FASTPEG* screen was based on papers by McPherson, (1976); and Carter and Carter, (1979). These PEG/salt based screens were then used to stimulate crystal growth.

The chosen salts were:

ammonium acetate  
potassium phosphate  
sodium acetate  
magnesium chloride  
zinc acetate.

ammonium sulphate  
sodium citrate  
magnesium acetate  
zinc chloride

with buffered solutions of:

pH6.0 (MES, free salt form)  
pH7.0 (HEPES, free salt form)  
pH8.0 (TRIS.HCl, Trizma base™)  
pH9.0 (CHES)

pH6.5 (MES, free salt form)  
pH7.5 (HEPES, free salt form)  
pH8.5 (TRIS.HCl, Trizma base™)  
pH9.5(CHES).

The precipitant chosen was polyethylene glycol (PEG). A random driving force for precipitation was desired for the screen, consequently a range of PEG molecular weights and concentrations was chosen. The molecular weights of PEG chosen were 200, 300, 400, 600, 1000, 2000, 4000, 6000 and 8000. The final concentrations of PEG in the individual *FASTPEG* screens were either 5, 10, 15, 20, 25, 30, 40, and 50% (v/v) or (w/v) at room temperature. Figure 5.12 illustrates the combinations of precipitants, buffers and salts making up the *FASTPEG* screen. The pH ranges of the trials involved were generally acidic. Buffers at pH 6.0-6.5 were included because some of the acidic screens in the *Magic 46* did not appear to be denatured with respect to colour changes. It was quickly established that low concentrations of the high molecular weight PEGs must be used otherwise phase separation quickly occurs. Forty eight different screens were created to ensure as large a range of screening conditions as

5.5 FASTPEG SCREEN:

The most stable incubations from the *Magic 46* trials consisted of polyethylene glycol (PEG) as the precipitant and an alkaline pH. A semi-factorial protocol approach was established by randomly assigning a precipitant, buffer and salt combination until phase separation did not occur in the screening mixture. The formation of the FASTPEG screen was based on papers by McPherson, (1976) and Carter and Carter, (1979). These PEG-based screens were then used to stimulate crystal growth.

The chosen salts were:

ammonium acetate	potassium phosphate
sodium citrate	sodium acetate
magnesium acetate	magnesium chloride
zinc chloride	zinc acetate

with buffered solutions of

**Figure 5.12:** The FASTPEG screen. A series of stock solutions (see appendix 4.2) were used to create the above solutions. When the salts, buffers and precipitants were combined they produced the FASTPEG screen. This three-dimensional crystallographic screen was derived from observations from *Magic 46* trials. The asterisk "\*" depicts w/v or v/v at room temperature, see appendix 4.2. It is based on salts and PEG as the precipitants.

The precipitant chosen was polyethylene glycol (PEG). A random driving force for precipitation was desired for the screen, consequently a range of PEG molecular weights and concentrations was chosen. The molecular weights of PEG chosen were 200, 300, 400, 600, 1000, 2000, 4000, 6000 and 8000. The final concentrations of PEG in the individual FASTPEG screens were either 5, 10, 15, 20, 25, 30, 40, and 50% (w/v) or (v/v) at room temperature. Figure 5.12 illustrates the combinations of precipitants, buffers and salts making up the FASTPEG screen. The pH ranges of the trials involved were generally acidic. Buffers at pH 6.0-6.5 were included because some of the acidic screens in the *Magic 46* did not appear to be denatured with respect to colour change. It was quickly established that low concentrations of the high molecular weight PEGs must be used otherwise phase separation quickly occurs. Forty eight different screens were created to ensure a large range of screening conditions as

practically possible. This is usually achieved by low dilution culture or Cryobots  
 10 plates per screening trial.

FASTPEG NUMBER	SALT	BUFFER	PRECIPITANT*
1	0.2M NH <sub>4</sub> <sup>+</sup> acetate	0.1M MES pH6.0	10% PEG 8000
2	0.2M K phosphate	0.1M TRIS pH8.5	50% PEG 300
3	0.2M Na citrate	0.1M CHES pH9.5	20% PEG 6000
4	0.2M Zn acetate	0.1M TRIS pH8.5	5% PEG 1000
5	0.2M Na acetate	0.1M MES pH6.5	25% PEG 1000
6	0.2M Zn chloride	0.1M MES pH6.0	20% PEG 600
7	0.2M Mg acetate	0.1M MES pH6.0	5% PEG 6000
8	0.2M Na citrate	0.1M HEPES pH7.5	20% PEG 6000
9	0.2M Mg chloride	0.1M CHES pH9.0	30% PEG 400
10	0.2M NH <sub>4</sub> <sup>+</sup> sulphate	0.1M CHES pH9.5	5% PEG 6000
11	0.2M Ca chloride	0.1M TRIS pH8.0	30% PEG 300
12	0.2M NH <sub>4</sub> <sup>+</sup> sulphate	0.1M MES pH6.5	10% PEG 600
13	0.2M Na acetate	0.1M HEPES pH7.5	20% PEG 400
14	0.2M NH <sub>4</sub> <sup>+</sup> sulphate	0.1M TRIS pH8.0	15% PEG 4000
15	0.2M li sulphate	0.1M TRIS pH8.5	20% PEG 400
16	0.2M Mg chloride	0.1M MES pH6.0	30% PEG 400
17	0.2M Na acetate	0.1M CHES pH9.5	20% PEG 400
18	0.2M K phosphate	0.1M MES pH6.0	10% PEG 200
19	0.2M Ca acetate	0.1M HEPES pH7.5	5% PEG 4000
20	0.2M Ca acetate	0.1M TRIS pH8.5	50% PEG 600
21	0.2M Ca acetate	0.1M CHES pH9.5	25% PEG 8000
22	0.2M Mg acetate	0.1M TRIS pH8.0	5% PEG 2000
23	0.2M Na citrate	0.1M MES pH6.5	25% PEG 6000
24	0.2M Na acetate	0.1M MES pH6.0	10% PEG 1000
25	0.2M Zn chloride	0.1M MES pH6.0	30% PEG 300
26	0.2M Na citrate	0.1M HEPES pH7.0	20% PEG 1000
27	0.2M Zn chloride	0.1M TRIS pH8.5	25% PEG 4000
28	0.2M Na citrate	0.1M HEPES pH7.5	25% PEG 6000
29	0.2M li sulphate	0.1M TRIS pH8.0	50% PEG 300
30	0.2M NH <sub>4</sub> <sup>+</sup> sulphate	0.1M HEPES pH7.0	15% PEG 4000
31	0.2M Ca chloride	0.1M CHES pH9.0	30% PEG 200
32	0.2M NH <sub>4</sub> <sup>+</sup> acetate	0.1M CHES pH9.5	40% PEG 600
33	0.2M Ca acetate	0.1M MES pH6.0	20% PEG 1000
34	0.2M K phosphate	0.1M HEPES pH7.0	40% PEG 200
35	0.2M Mg acetate	0.1M TRIS pH8.5	30% PEG200
36	0.2M NH <sub>4</sub> <sup>+</sup> acetate	0.1M TRIS pH8.0	10% PEG 2000
37	0.2M Mg acetate	0.1M MES pH6.5	40% PEG 6000
38	0.2M Mg chloride	0.1M CHES pH9.0	5% PEG 2000
39	0.2M Zn acetate	0.1M HEPES pH7.0	5% PEG 8000
40	0.2M Ca chloride	0.1M HEPES pH7.5	20% PEG2000
41	0.2M Ca acetate	0.1M HEPES pH7.0	10% PEG 8000
42	0.2M li sulphate	0.1M MES pH6.5	50% PEG 200
43	0.2M Ca chloride	0.1M TRIS pH8.0	20% PEG 8000
44	0.2M NH <sub>4</sub> <sup>+</sup> acetate	0.1M CHES pH9.0	5% PEG 400
45	0.2M Mg chloride	0.1M CHES pH9.0	25% PEG 1000
46	0.2M K phosphate	0.1M CHES pH9.5	30% PEG 200
47	0.2M li sulphate	0.1M MES pH6.0	30% PEG 300
48	0.2M Zn acetate	0.1M HEPES pH7.0	10% PEG 2000

practically possible. This in reality consisted of two tissue culture or Crychem<sup>®</sup> plates per screening trial.

The *FASTPEG* trails were made up by adding one part protein solution to one part *FASTPEG* solution in the well with the driving force being derived from the concentration gradient formed between the well and outer reservoir allowing vapour diffusion to occur. The outer reservoir contained 1x *FASTPEG* solution compared to a 0.5x *FASTPEG* well solution. The *FASTPEG* screens were made up, from a series of stock solutions (see appendix 5.2), to a volume of 1500µl in eppendorf tubes. These were then centrifuged at 3K xg, at room temperature in a bench top centrifuge (Sigma K12) for 20 mins. This was done to remove any precipitant that might be present. For each trial well an appropriate amount of protein was added to another eppendorf containing any extra substances not in the *FASTPEG* screen. To this was added the constituent components from the *FASTPEG* stock solutions making their final concentrations half that of the reservoir. After a quick centrifugation (2mins at 10K xg, R.T.) to remove any precipitant the protein-precipitant solutions were added to their wells, sealed with either tape or glass microscope cover slips, and incubated in the dark at either 17°C, 10°C or 4°C.

Two types of screening plates were used. The first type was Corning tissue culture plates. The wells consisted of hanging drops suspended on siliconised coverslips. Up to 10µl of material was used for each drop - too much material and the drop will fall into the 500 µl reservoir below. The second type of screening apparatus used was Crychem<sup>®</sup> plates (J.B.L. Scientific Ltd.). Up to 20µl could be pipetted into each well in this type of plate. The crychem<sup>®</sup> plates were initially sealed with siliconised glass cover slips. A clear tape (p/n AT-2, JBL Scientific Ltd.) was then found that did not produce vapour droplets on the surface when PEG was used so this tape was then used to seal the crystallographic trials. Crychem<sup>®</sup> plates were easier to set up, compared to hanging drops, since the sitting drop method did not require siliconised coverslips and larger volumes could be used. The larger volumes also meant that any pipetting errors would be less using the sitting drop method compared to hanging drops.

The LHII proteins were investigated (see Figure 5.5) using the *FASTPEG* protocol. The majority of the bacterial photosynthetic harvesting complexes (LHI and LHII) are various shades of red thus any colour change is usually easily detectable. The colour changes are due to separation of the pigments from their apoproteins. Denatured protein tends to have a brown colour with shades of green present.

5.5.1 *Rb. gelatinosus* strain 149 B800-854

It was difficult to tell if *Rb. gelatinosus* 149 had maintained its natural colour. No crystals from *Rb. gelatinosus* strain 149 B800-854 were produced from either full- or half-strength FA TYPE2 medium.

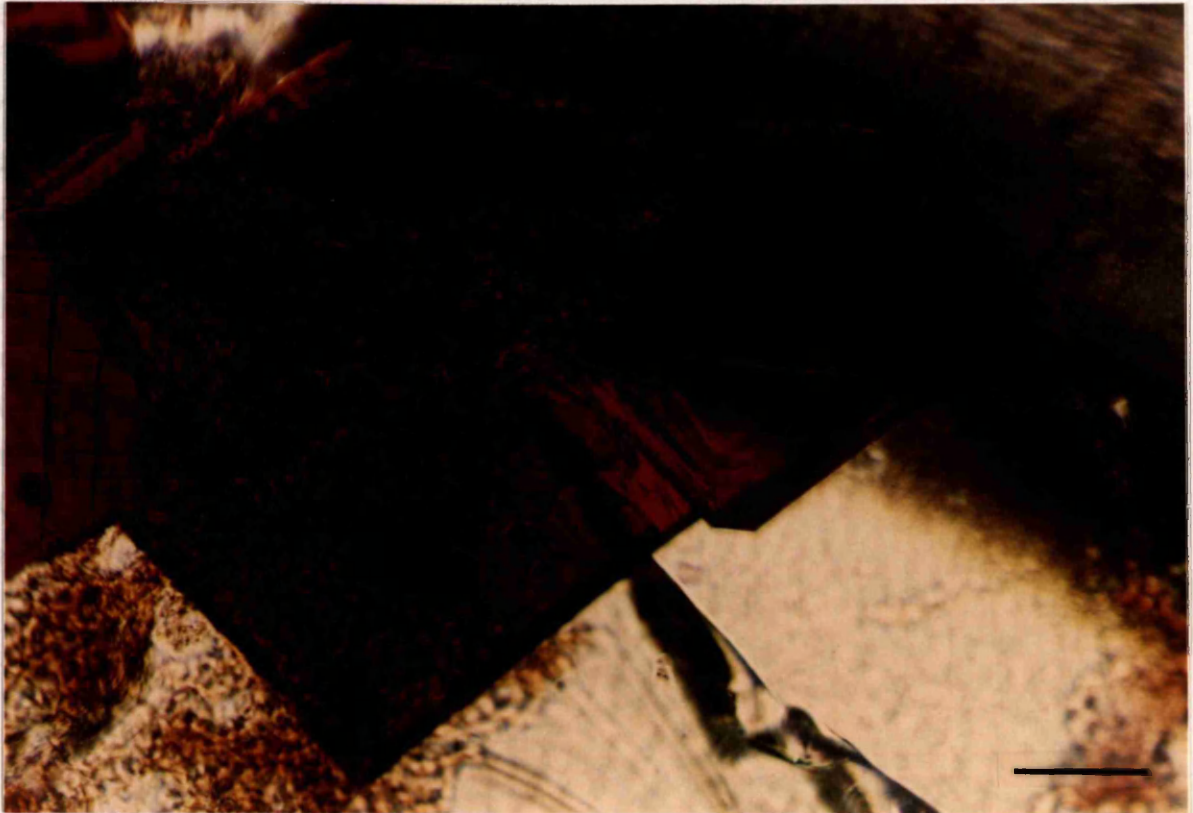


**Figure 5.13:** 3D crystal of *Rb. sphaeroides* B800-850. The protein was supplied by Dr. G. Fowler, University of Sheffield. The pigment-protein complex is from a genetically altered strain of *Rb. sphaeroides*. The crystallisation trial depicted above produced crystals that were of uniform shape. Orthorhombic sheets were obtained. The example above shows crystals growing out from the side of a Crychem® plate. Bar 0.5mm.

### 5.5.1 *Rc. gelatinosus* strain 149 B800-850:

It was difficult to tell if *Rc. gelatinosus* LHII had denatured due its natural colour. No crystals from *Rc. gelatinosus* strain 149 B800-850 were produced from either full- or half-strength *FASTPEG* screens.

### 5.5.2 *Rb. sphaeroides* B800-850:

The B800-850 light-harvesting complex from *Rb. sphaeroides* was obtained from Dr. G. Folwer, University of Sheffield, and was screened using the *FASTPEG* protocol. Half-strength *FASTPEG* trials were set up in Crychem® plates. A few produced small crystals. Of all the wells that produced crystal-like structures (*FASTPEG* #13, #18, #20, #34, and #20) #20 produced relatively large sheets (1.0mm x 1.0mm x 0.1mm). Figure 5.13 illustrates some of the sheets obtained by half-strength *FASTPEG* #20. The photograph shows three sheets; a large one and two small ones attached to the side of the well. Owing to the small amount of protein available no further trials were attempted.

Figure 5.13 illustrates some of the sheets obtained by half-strength *FASTPEG* #20. The photograph shows three sheets; a large one and two small ones attached to the side of the well.



### 5.5.3 *Rp. palustris* strain 2.6.1. B800-850:

Figure 1.7 and sections 1.3 and 1.4 describe how *Rp. palustris* strain 2.6.1. B800-850 has two forms which are produced under different illumination conditions. *Rp. palustris* strain 2.6.1. B800-850 High Light (HL) complex did not produce any crystals however the Low Light (LL) complex did. The FASTPEG screen did produce small crystal-like structures when incubated at 14°C. The screen that produced the best looking crystals was half-strength #20;

Droplet constitution:	<i>Rp. palustris</i> strain 2.6.1. B800-850 LL (5mg.ml <sup>-1</sup> ) 5mM TRIS.HCl, pH8.0 1.25mM sodium chloride (approximate value, based on centricon data sheets. See chapter 3 for details) 3mM sodium azide 50mM calcium acetate 25mM TRIS.HCl (pH 8.5) 1.0% β-OG 12.5% PEG 600
Reservoir constitution:	3mM sodium azide 100mM calcium acetate 50mM TRIS.HCl (pH 8.5) 25% PEG 600

This trial produced sheet like structures (fig 5.14) so further studies were undertaken based on the conditions in half-strength screen #20. The conditions were altered by changing the PEG concentration in the reservoir from 12.5% (half strength #20) to 22%. Amphiphiles were also added to separate trials. These were 2.5% (w/v) and 3.5% (w/v) of both heptane-triol and benzamidine hydrochloride. These new trials were allowed to incubate against the above reservoir solution at 14°C. Changing the PEG concentration gradient caused crystals to appear later where there was a smaller gradient. The addition of amphiphiles may have caused slightly better crystal formation as observed by the eye (i.e. they looked slightly better). However when 3.5% (w/v) benzamide hydrochloride was added red orthorhombic crystals formed. These structures were considered to be amphiphiles crystals with trapped protein inside. The use of 3.5% Benzamide caused the formation of feather or fern like pigmented structures to occur. X-ray analysis carried out by Mr. G. McDermott

(Chemistry Dept. University of Glasgow) indicated that the crystals were of poor quality. They diffracted only to 9-11Å.

### 5.6 *R. rubrum* strain S1:

The crystallisation conditions obtained by Dawkins, (1988) and Ferguson (unpublished) were used for crystallisation of the RC-LHI conjugate from *R. rubrum* strain S1. Varying the protein pH (5.0-9.0), salt ( $MgCl_2$ ) concentrations and PEG2000 concentrations from the observations by Ferguson (unpublished) probable crystals of LM-RC-LHI were produced. The best conditions were considered to be;

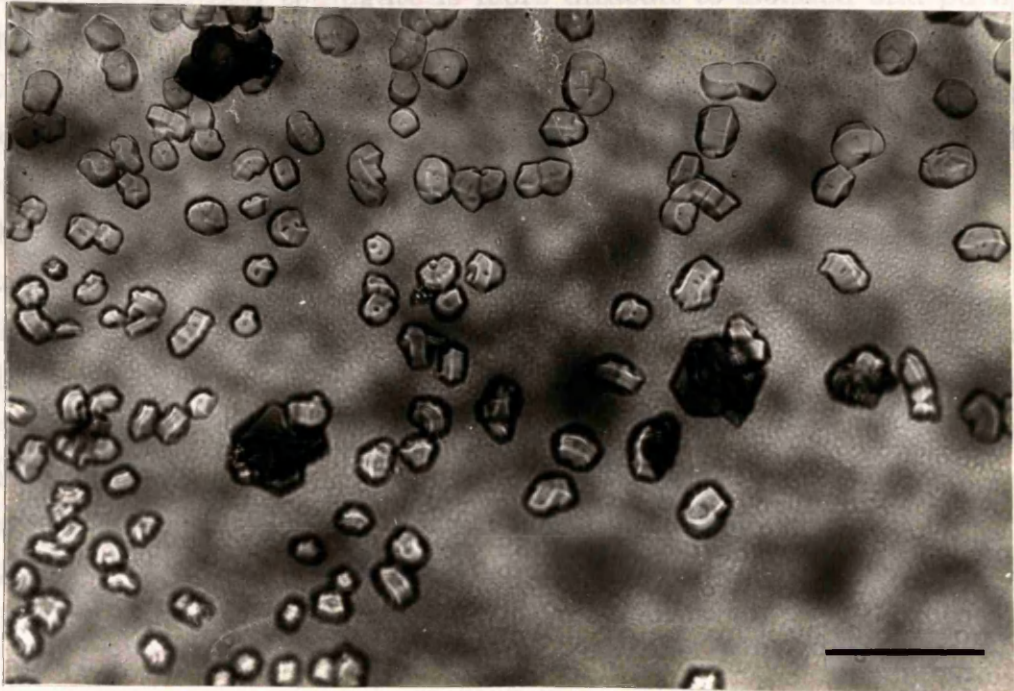
Droplet constitution:     *R. rubrum* strain S1 in 1%LM (w/v) at  $5mg.ml^{-1}$   
                                   20mM TRIS.HCl, pH7.5  
                                   100mM magnesium chloride  
                                   1.0%(w/v) LM  
                                   6.26% PEG 2000

Reservoir constitution:   100mM magnesium chloride  
                                   20mM TRIS.HCl, pH 8.0  
                                   12.5% PEG 2000

Figure 5.15 shows the typical results of sitting drop trials using the large vapour diffusion dishes (see Figure 5.2). The photograph shows the dark (red) objects (RC-LHI) in a sea of clear particulate material. The clear particulate material is PEG. As with the crystal-like structures of *Rp. palustris* strain 2.6.1 the RC-LHI appears to grow in a hexagonal manner. The trials from this species however produced a greater diversity of 'crystal' structure in the trial chambers. This may be due to the different crystallographic regimes or to specimen stability outwith the native membrane. Only continued crystallographic trials will establish whether this RC-LHI is suitable for structural determination.

## 5.7 Summary of Three Dimensional Crystallography

The membrane associated pigment-protein complexes from the Rhodospirillum rubrum can produce crystals. Of the two classes of proteins (RC-LHI and LHI) the RC-LHI component is more difficult to isolate and purify in a stable form.



Recently it has been shown that the resolution of x-ray diffraction patterns is directly related to the intensity and duration of protein isolation (Michel *et al.*, 1989). This suggests that an enhancement of the crystallographic data may occur if the isolation techniques are further improved.

**Figure 5.15:** Crystal-like structures of *R. rubrum* strain S1 RC-LHI. Small pigmented structures were formed in PEG incubations. The photograph illustrates that the pigmented structures (dark objects) have regular edges. They appear to have a hexagonal structure (centre right) similar to those observed previously for *Rp. palustris* 2.6.1. They are however less regular in shape. Bar: 0.1mm.

## 5.7 Summary of Three Dimensional Crystallography.

The membrane associated pigment-protein complexes from the Rhodospirillaceae can produce crystals. Of the two classes of proteins (RC-LHI and LHII) the RC-LHI conjugate is more difficult to isolate and purify in a stable state. This is mirrored in the results for the 3D crystallographic trials.

In general the creation of 3D crystals from these membrane proteins was difficult and the possibility of producing ordered 2D crystals, as described in Chapter Four, suggests that x-ray crystallography may not be the most suitable approach for structural determination of these supra-complexes.

As large 3D crystals of *Rb. sphaeroides* were produced (section 5.5.2) the addition of amphiphiles are not a prerequisite for crystal growth. It should be noted however that these were not examined by x-ray analysis. Of the species investigated low light grown cells of *Rp. palustris* strain 2.6.1 may prove to be the most useful source of protein suitable for further crystallographic screenings for both the RC-LHI and LHII pigment-protein complexes.

Since the majority RC-LHI conjugates are less than completely stable *in vitro* further screening from a greater range of core complexes may provide a new, and more suitable, source of material for 3D crystallographic trials. Recently it has been shown that the resolution of x-ray diffraction reflections is directly related to the number and duration of protein isolation methods (Michel *et al.*, 1993). This suggests that an enhancement in the crystallographic data may occur if the isolation techniques are further improved.

## 6.1 Discussion:

In 1979 Agard and Siström first postulated that the RC-LHI conjugate consisted of a RC and LH-BChl *a* in a fixed stoichiometry. Previous TEM reports indicated that in some species regular arrays could be observed on their photosynthetic membranes. Solubilising, using detergents, these membranes resulted that small disc-like particles were observed that were ~1000 in diameter (Garcia *et al.*, 1966; Garcia *et al.*, 1968; Halsey & Syce, 1975). More recent STEM and TEM data has shown that (a) naturally producing RC-LHI arrays from *R. rubrum* and *S. halobacteris* (which also contain the extra, but colourless,  $\gamma$ -polypeptide) have been shown to be that the RC-LHI contains a central RC which is surrounded by a ring of 24 LH molecules (Zuber, 1986; Zuber *et al.*, 1986; Engelhard *et al.*, 1987).

Using the LHI model proposed by Zuber, (1986), the LH ring placed surrounding the RC must contain a maximum of 24 light-harvesting BChl *a* since the model assumes that each  $\alpha/\beta$ -heterodimer contains two BChl *a*. The RC contains four BChl *a* (Deisenhofer *et al.*, 1984; Deisenhofer *et al.*, 1985; Allen *et al.*, 1987). Consequently the theoretical RC:BChl ratio for the RC-LHI conjugate is 1:24 (24+4). This ratio is constant throughout a range of species that naturally must have similar RC-LHI conjugates (proposed by Agard and Siström). A previous biochemical report of the RC-LHI conjugate that a RC:BChl *a* fixed stoichiometry may occur of approximately 1:24 (Dawkins, 1982).

## Chapter Six:

## Discussion

EM analysis over the range of bacterial species investigated here suggests that the purified RC-LHI consists of uniform disc-like particles of about 1000 in diameter (Figures 5.4 and 5.5). The biochemistry of the bacteria these come from (see Figure 3.32) further substantiates the suggestion that the different RC-LHI described have similar RC:BChl ratios of 1:24. The photochemical  $\alpha$  peaks from different species also appear to have a similar value for their photochemically derived BChl *a* extinction coefficient of around 100-120  $\text{cm}^2 \text{mol}^{-1}$ . There are however variations in the biochemistry of the RC-LHI ratio. These are partly due to the errors in the detecting system of the specific extinction coefficients, but are also due to variable RC loss during purification.

Crude purified pigment-protein complexes (RC-LHI and LHI) were obtained they were used as the solute in crystallisation trials. Two types of crystallisation techniques were used; 2D (which relies on detergent/liquid removal) and 3D (which relies on a non-equilibrated supersaturated solution). Crystallising membrane proteins as protein-detergent micelles is a hostile

## 6.1 Discussion:

In 1972 Aagard and Sistrom first postulated that the RC-LHI conjugate consisted of a RC and LH-BChl *a* in a fixed stoichiometry. Previous TEM reports indicated that in some species regular arrays could be observed on their photosynthetic membranes. Solubilising, using detergents, these membranes revealed that small disc-like particles were observed that were ~120Å in diameter (Garcia *et al.*, 1966; Garcia *et al.*, 1968; Halsey and Byers, 1975). More recent STEM and TEM data has shown that the naturally producing RC-LHI arrays from *R. viridis* and *E. halochloris* (which also contain the extra, but colourless,  $\gamma$ -polypeptide) have lead to the hypothesis that the RC-LHI contains a central RC which is surrounded by a ring of six LHI complexes (Stark, 1984; Stark *et al.*, 1986, Engelhardt, *et al.*, 1986).

Using the LHI model proposed by Zuber, (1986), the LHI complexes surrounding the RC must contain a maximum of 24 light-harvesting BChls since the model assumes that each  $\alpha/\beta$ -heterodimer contains two BChls. The RC contains four BChls (Deisenhofer *et al.*, 1984; Deisenhofer *et al.*, 1985; Allen *et al.*, 1987a). Consequently the theoretical RC:BChl ratio for the RC-LHI conjugate is 1:28 (24+4). If this ratio is constant throughout a range of species then they all must have similar RC-LHI conjugates envisaged by Aggard and Sistrom. A previous biochemical report of the RC-LHI indicates that a RC:BChl *a* fixed stoichiometry may occur of approximately 1:30 (Dawkins, 1988).

EM analysis from the range of bacterial species investigated here also suggests that the purified RC-LHI consists of uniform disk like structure of about 100-130Å in diameter (Figures 5.4 and 5.5). The biochemical data in this thesis (summarised in Figure 3.32) further substantiates the suggestion that the different RC-LHIs do indeed have similar RC:BChl stoichiometries (~1:30). The photosynthetic *cores* from different species also appear to have a similar value for the experimentally derived BChl *a* extinction coefficient at 880nm (100-120 mM<sup>-1</sup>cm<sup>-1</sup>). There are however variations in the biochemical RC:BChl ratios. These are partly due to the errors in the detecting system, species specific extinction coefficients, but are also due to variable RC loss from the *cores*.

Once purified pigment-protein complexes (RC-LHI and LHII) were obtained they were used as the solute in crystallisation trials. Two types of crystallisation techniques were used; 2D (which relies on detergent/lipid removal) and 3D (which relies on a non-equilibrated supersaturated solution). Crystallising membrane proteins as protein-detergent micelles is a hostile

environment for these complexes. For this reason it is difficult to grow well ordered membrane protein crystals, when compared to the 3D crystallisation of water soluble proteins. Since 2D arrays are formed by membrane associated proteins within a lipid bilayer the use of 2D crystallography may help to overcome the difficulty in forming suitable membrane protein crystals for structural analysis.

The 3D crystallographic trials of the RC-LHI and LHII generally produced negative results although small crystal-like structures were obtained, for RC-LHI from *Rp. palustris* and *R. rubrum*. LHII 3D crystallisation trials produced crystals from *Rb. sphaeroides* and *Rp. palustris*, the later diffracting to between 9-11Å. All the crystal-like structures mentioned above warrant further research, with more emphasis placed on screening the photosynthetic membrane proteins from *Rp. palustris*.

It was hoped that 2D crystallographic studies would have produced a greater number of RC-LHI crystals, but as with the 3D method mainly negative results occurred. 2D arrays of *Rp. palustris* and *Rp. acidophila* RC-LHI were produced including a preliminary reconstruction map of *Rp. acidophila* RC-LHI at a resolution of 19Å (Figure 4.20). The 2D reconstruction of the RC-LHI supra-complex from *Rp. acidophila* indicates that the rotationally averaged RC (~45Å in diameter) is surrounded by six LHIs in a hexagonal arrangement, with a centre-to-centre distance of  $115 \pm 5 \text{Å}$ . This is direct structural evidence that suggests that the RC-LHI constitutes of a RC with six LHIs surrounding it. The RC:BChl a data for *Rp. acidophila* RC-LHI indicates a ratio of  $1:30 \pm 4$  (or  $1:33 \pm 4$ , see Chapter Three),  $n=67$  which further integrates the biochemical and EM results.

The formation of 2D arrays from isolated BChl *a*-containing RC-LHI conjugates (*Rp. palustris* and *Rp. acidophila*) has now ruled out any direct structural rôle played by the  $\gamma$ -polypeptide in forming hexagonal arrays. The lack of any *in vivo* RC-LHI lattice in BChl *a*-containing species is more likely due to the presence of multiple types of light-harvesting complexes, as discussed by Zuber and Brunisholz, (1986) and not due to a lack of the  $\gamma$ -polypeptide. However BChl *a*-containing species such as *R. rubrum* which are 'core only' producing species do not produce *in vivo* arrays in the intracytoplasmic membrane. The presence of the  $\gamma$ -polypeptide may thus facilitate the close packing as seen in species such as *R. viridis*, or may simple be associated with the far red-shifted antenna that absorbs at 1020nm. Another explanation could simply be that only the flat lammellar species have suitable membrane structures which allow for natural array formation. This leaves a major question unanswered, why do only some 'core only' species form

arrays *in vivo*? If a non- $\gamma$ -polypeptide-containing, BChl *b*-containing species could be discovered or engineered it may lead to a fuller understanding of the structural differences between 'BChl *a*-' and 'BChl *b*-containing' species.

From all the 2D and 3D observations for the RC-LHI it was apparent that only the most stable *cores* were capable of producing any type of regular array. If RC-LHI arrays are formed from both approaches then, due to the presence of the phase information, an EM structure is generally easier to predict. A similar statement is also true for the LHII proteins that were studied. Ideally for the bacterial photosynthetic system a complete structure at atomic resolution from a single species is required. This means that all the pigment-proteins must be able to be isolated in a stable form suitable for structural analysis. An obvious candidate for such a scenario is *Rb. sphaeroides* since the RC structure has been solved (Allen *et al.*, 1987a/b). However *Rb. sphaeroides* RC-LHI conjugate is one of the most, if not the most unstable *core* that can be isolated and thus completely unsuitable for crystallisation studies. From the observations of this study *Rp. acidophila*, *Rp. cryptolactis* and *Rp. palustris* may prove to be the key species. *Rp. acidophila* does produce 2D arrays of RC-LHI and although LHII from *Rp. acidophila* was not investigated it may form 2D arrays (Simmons, A.E., personal communication). 2D and 3D crystals of *Rp. palustris* RC-LHI and 3D crystals of LHII were produced. It should be noted that the culture conditions may play a rôle in the eventual outcome of crystallisation trials. Only *Rp. palustris* low-light (LL) grown cells produced 3D crystals of LHII. The formation of arrays from only the LL form may be a coincidence, or a major factor. The obvious differences between LHII (LL) and LHII (HL) is the polypeptide composition, however, no such differences are observed between HL and LL RC-LHI. If further work is carried out and crystals from HL grown cells are never produced the question of lipid involvement must again be asked. It is also possible that the range of species and strains investigated here is too small, to provide a reliable window into pigment-protein stability *in vitro*. A further screening of other species, which may include the Chromatiaceae, may be required.

The rôle of lipids, especially the minor lipid species, in the purple bacteria have not been well characterised. There have been studies which suggest that there are variations in the lipid content, which have been linked to the growth conditions (Pucheu *et al.*, 1974; Kaufmann *et al.*, 1982). Slight differences in growth conditions may lead to significant lipid changes. Such potential variation in lipid composition may lead to a problem in the future if extensive, high resolution, 2D crystallographic studies are carried out. For example in the cases of Bacteriorhodopsin (Sternberg *et al.*, 1992) and LHCIIa/b

(Kühlbrandt and Wang, 1991) the lipid composition is critical for array formation. Lipid variation may account for the variation on 2D crystallisation results, however only further analysis will determine this. Consequently an in-depth probe into the lipids associated with the purified Rhodospirillineae photosynthetic pigment-proteins must be undertaken. Currently no such study is underway for the RC-LHI but there is a study into LHII lipid composition (Dahler *et al.*, 1992).

Although x-ray crystallography still regularly provides the highest structural resolutions the resolution now attainable by EM analysis can produce solved structures at atomic resolution. The latest example of this is the 3.5Å structure for the LHIIa/b complex (Kühlbrandt *et al.*, 1994). It is now possible to attain theoretical resolutions of between ~1-2Å using either liquid helium cooled microscopes (Fujiyoshi, J., personal communication) or the recent advances in maximum entropy techniques (Fryer, J., personal communication). These reasons alone warrant continued research using EM methods. In combination with the advantages over the conventional x-ray methods discussed in Chapter One make 2D crystallography a very powerful tool for the determination of the structure of the bacterial pigment-protein complexes. However, more detailed crystallographic experiments need to be carried out to increase the size of the 3D crystals of RC-LHI (Figure 5.10). As Figure 5.10 illustrates, the 2D crystals appear as hexagonal columns. Since the RC-LHI 2D array packing is a six-fold-like arrangement then it is possible the 3D crystals have a similar packing. This may indeed be the case since the six sides of the hexagonal columns are the same length and consequently the angles between the six sides are the same i.e. 120°. From this the 3D crystal packing may be of class 6, i.e. one of the space groups from  $p6_{1,6}$ .

Since some structural data is now available on the pigment-protein complexes of the Rhodospirillaceae it is appropriate for a basic model to be constructed. In Figure 6.1 the known structure of the RC (Deisenhofer *et al.*, 1984,1985; Yeates *et al.*, 1987a,b) and the structure of the light-harvesting antennae proposed by Papiz (see Cogdell and Hawthornthwaite, 1993) have been super-imposed onto a 2D reconstruction of the *Rp. acidophila* RC-LHI conjugate. The RC is an elliptical structure, having pseudo  $p2$  symmetry, with dimensions of 45Å by 54Å. The elliptical RC is the light grey elliptical shape in Figure 6.1. The RC, however, is thought to exist in any orientation within the membrane (Stark, 1984) consequently the RC has also been depicted as occupying the largest dimension (i.e. 54Å) in all orientations and is illustrated by the dark circular structure underneath the grey ellipse. As Figure 6.1

illustrates, the location and size of the 3D RC structure fits very well into the area of density in the 2D reconstruction, with little, or no overlap.

In the RC-LHI 2D reconstruction there is a reduced ring of density surrounding the RC. Beyond this is another adjacent a ring of increased density peaking at 45Å when measured from the centre of the RC. This ring of higher density has within it six peaks of density. It is proposed that these peaks are due to six LHI (6 x 2 x  $\alpha/\beta$  heterodimers) antennae.

The original model for LHI by Zuber, (1986) assumed that the polypeptides transverse through the membrane perpendicular to the membrane surface. More recent crystallographic evidence (Papiz *et al.*, 1989) has indicated that the polypeptides go through the membrane at an angle and are intertwined, like strands in a rope, thus reducing the confidence level of Zuber's model. The LHII model by Donnelly and Cogdell, (1993), although useful, only concentrates on the  $\alpha$ -helical region of the LHII complex. The model, based on 3D crystallographic evidence by Papiz (see Cogdell and Hawthornthwaite, 1993) is the best approximation, to date, of the proposed structure of the light-harvesting (2 x  $\alpha/\beta$  heterodimer) complex. The structure of LHI and LHII are generally regarded as being similar since their primary structures are so similar (see Figures 1.4 and 1.5; Zuber, 1986; Donnelly and Cogdell, 1993). By superimposing Papiz's model of the structure of LHII onto the 2D RC-LHI reconstruction the location and size of the LHI antennae may be revealed.

Placing Papiz's LHII model over the six rings of density in the 2D RC-LHI reconstruction reveal that they fit well (Figure 6.1, model "A"). If the six antennae are located directly next to the RC (Figure 6.1 model "B") the 2D and modelled 3D antennae densities do not overlap. As a result model "B" must be discounted. Translating the polypeptides in the light-harvesting antennae such that the 2 x  $\alpha/\beta$  heterodimer no longer looks like Papiz's model (see Figure 3.10) but requires a diamond-like shape produces model "C" in Figure 6.1. At the resolution of the 2D reconstruction it is unclear whether the "A" or "C" 3D model is a better superimposition onto the 2D reconstruction.

It is unlikely the LHI forms a ring of twelve  $\alpha/\beta$  heterodimers surrounding the RC since this would, most likely, produce twelve similar density peaks. As a result, based on the observations here, the native *in vivo* structure for the LHI complex consists of six sets of two  $\alpha$ - and two  $\beta$ -polypeptides. This agrees with the biochemical data obtained in Chapter Three.

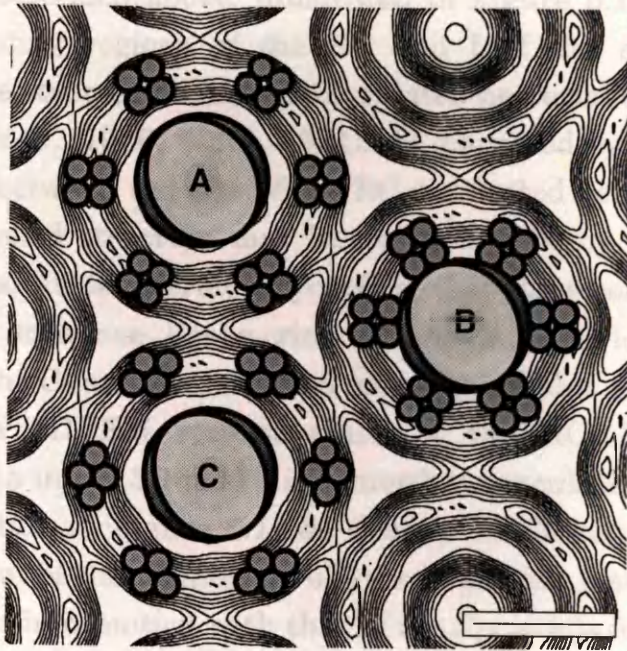


**Figure 6.1.** Comparison of the 2D and 3D structures for bacteriochlorophyll a-containing species. Bar: 50Å

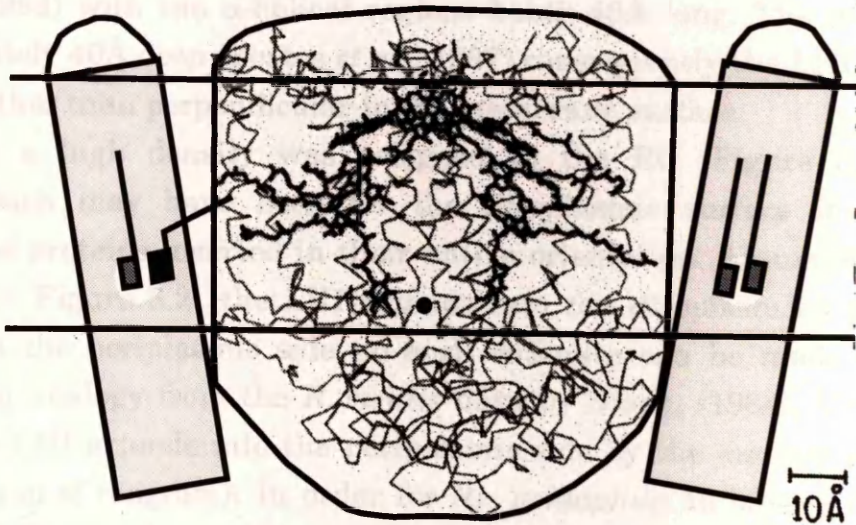


**Figure 6.2.** Model for the Rhodospirillaceae RC-LHI conjugate.

The models described above, illustrated in Figure 6.1, suggest that the membrane protruding regions of the RC and LHI are separated. This is consistent with the structural findings of related bacterial species (see Figure 1.14, Engelhardt *et al.*, 1986; Stark, 1984). As discussed by Roth *et al.*, (1991) the discrepancies between the size of the RC-associated detergent ( $\beta$ -OG) ring and the LHI modelled structure may be accounted for by the presence of *in vivo* phospholipids. It is therefore possible that between the RC and its surrounding LHI antennae lies a ring of lipids. The location and exact structural rôle of the C- and N- termini of the polypeptides are unknown.

Since only a 2D EM reconstruction of the RC-LHI was produced translating the data into a 3D model is somewhat speculative. However, using the 2D reconstruction in Figure 6.1 the density levels suggest that the LHI antennae extend out of the membrane bilayer to a point just below that of the RC. Combining this information with that of the *Rp. acidophila* LHII model by Donnelly and Cogdell, (1993) and that of the *Rb. sphaeroides* RC structure, (Yeates *et al.*, 1987) produces the model illustrated in Figure 6.2. In Figure 6.2, as in Figure 6.1, the objects are drawn to scale where possible. The molecular envelope of the RC is approximate; the *Rp. acidophila* RC is probably the same size since the size of the RC from *R. viridis* (Deisenhofer *et al.*, 1985) is similar.

The width of the LHI complex is approximately 20.1Å (Donnelly and Cogdell, 1993) with the  $\alpha$ -helical regions being 45Å long. The membrane is approximately 40Å deep (Yeates *et al.*, 1987) consequently the LHI must lie at an angle other than perpendicular to the membrane surface.

Since a high density was assigned to the RC (Figure 6.1) the 2D reconstruction may have been for the cytoplasmic surface if the arrays consisted of proteins inserted in their native orientation. Assuming this to be the case, in Figure 6.2 the LHI extends into the cytoplasm by the amount shown. On the periplasmic side no such estimate can be made other than drawing an analogy from the *R. viridis* data by Stark, (1984). Using Stark's model, the LHI extends into the periplasmic side by the amount shown (half circles on top of diagram). In order for *Rp. acidophila* to have a diameter of 115Å, the LHI must be angled as illustrated.

The estimate of the molecular shell have now been completed. However, the location of the BChl *as* has not been determined. Again using multiple sequence alignment Donnelly and Cogdell, (1993) concluded that the BChl *a* of each antenna polypeptide was located between 7-10Å from the cytoplasmic side. The actual orientation and configuration of these antennae pigments is of course unknown, however, their size can be estimated. There are two BChl *as* depicted in each of the LHI antennae drawn. It should be noted that it is

believed that four are present in every LHI complex (Zuber, 1991). If the carbon chain on the BChl *a* is bent (Figure 6.2, left-hand LHI complex) it may be possible for photons to pass directly to the RC pigments by the Dexter mechanism described by Frank and Cogdell, (1987). Further refinements of this model can only be made when more detailed crystallographic and biochemical data arises.

Once high resolution structures have been obtained for the RC-LHI and LHII complexes models for the kinetics of energy transfer can be studied in greater detail. The structures will also help to enhance some of the earlier EM work such as that for the spatial differentiation of *Rp. palustris* membranes done by Varga and Staehelin, (1983) as well as helping to understand the 'puddle' and 'lake' theories for the arrangement of the photosynthetic apparatus in the purple bacteria.

In summary a multi-disciplinary approach to obtain the structure of the bacterial photosynthetic membrane proteins should be undertaken. But prior to this further biochemical studies of the RC-LHI and a detailed investigation into rôle of lipids associated with the purified complexes must be undertaken. Once the detailed lipid composition is known a better understanding of the system will occur. It is hoped that the increased biochemical data will permit high resolution structures to be obtained, using either 2D or 3D, or both, crystallographic techniques.

**A.1: Bacterial Culture Solutions:**

*Rp. acidophila* grows on Pfannig's medium (appendix 1.1), *R. rubrum*, *Rb. sphaeroides*, *Bc. pasteurianus* and *Rp. palustris* grow on C-Saccharose medium (appendix 1.2). *Rp. cryophilus* grows on THERMED (appendix 1.3) while *R. costatum* grows on CENMED (appendix 1.4). All media were sterilized by autoclaving prior to use. Appendix 1.5 lists all the solutions required to make up the various bacterial growth media.

**A1.3: THERMED Medium:**

per L:	
200x potassium phosphate Buffer	5.0ml
10% ammonium sulphate solution	10.0ml
1M calcium DTPA	0.5ml
200x magnesium sulphate 100g/L	1.0ml
T.A.P.E.	1.0ml
7.5% calcium chloride 20g/100ml	1.0ml
Chelated iron solution	2.0ml
vitamin B12 100ppm solution	1.0ml
nicotinamide solution	1.0ml
P.A.H.A. 100ppm solution	1.0ml
10% potassium phosphate	5.0ml

**A1.1: Pfannig's Medium:**

per L:	
potassium dihydrogen orthophosphate	0.5g
magnesium sulphate 7-hydrate	0.5g
sodium chloride	0.4g
sodium sulphate	1.5g
ammonium chloride	0.5g
ammonium nitrate	0.5g
ferric chloride solution	5.0ml
Trace Element Solution	10.0ml
adjust pH to 5.2 then add 100ml of final volume	

**A1.2: C-Saccharose Medium:**

per L:	
Concentrate 100x	20.0ml
1M di potassium hydrogen orthophosphate	10.0ml
1M potassium dihydrogen orthophosphate	10.0ml
10% ammonium sulphate solution	5.0ml
1M sodium acetate, pH 5.5 solution	10.0ml
Growth Factors	1.0ml
Casamino Acids	1.0g
make upto 1L with deionised water.	

**A1.4: CENMED Medium:**

per L:	
potassium dihydrogen orthophosphate	0.5g
K <sub>2</sub> HPO <sub>4</sub>	0.5g
KH <sub>2</sub> PO <sub>4</sub>	1.5g
Na <sub>2</sub> CO <sub>3</sub>	0.5g
magnesium sulphate 7H <sub>2</sub> O	0.5g
Trace Element Solution	10.0ml
calcium chloride 20g/L	1.0ml
Chelated iron solution	2.0ml
vitamin B12	1.0ml
Buffer	5.0ml
adjust the solution to pH 5.5	
Adjust to pH 5.5 before use.	

**A1.5: Citrate Wash**

per L:	
nitric/acetic acid	5g
magnesium sulphate	4g
calcium chloride 20g/L	4.0ml
ammonium sulphate	2.5g
ferrous sulphate 10g/L	10.0ml

**Appendices:**

**A.1: Bacterial Culture Soln's:**

*Rp. acidophila* grows on Pfennig's medium (appendix 1.1). *R. rubrum*, *Rb. sphaeroides*, *Rc. gelatinosus* and *Rp. palustris* grow on C-Succinate medium (appendix 1.2). *Rp. cryptolactis* grows on THERMED (appendix 1.3) while *R. centenum* grows on CENMED (appendix 1.4). All media were sterilised by autoclaving prior to use. Appendix 1.5 lists all the solution required to make up the various bacterial growth media.

**A1.1: Pfennig's Medium:**

per 1L

potassium dihydrogen orthophosphate	1.0g
magnesium sulphate 7-hydrate	0.4g
sodium chloride	0.4g
sodium succinate	1.5g
calcium chloride 2-hydrate	0.05g
ammonium chloride	0.5g
ferric citrate solution	5.0ml
Trace Element Solution	10.0ml

adjust pH to 5.2 then adjust volume to final volume.

**A1.2: C-Succinate Medium:**

per 1L

Concentrate Base	20.0ml
1M di-potassium hydrogen orthophosphate	10.0ml
1M potassium di-hydrogen orthophosphate	10.0ml
10% ammonium sulphate solution	5.0ml
1M sodium succinate, pH 6.8 solution	10.0ml
Growth Factors	1.0ml
Casamino Acids	1.0g

make upto 1L with deionised water.

**A1.3: THERMED Medium:**

per 1L

0.64M potassium phosphate Buffer	5.0ml
10% ammonium chloride solution	10.0ml
1% disodium EDTA	0.5ml
20% magnesium sulphate.7H <sub>2</sub> O sol <sup>n</sup>	1.0ml
T.B.T.E.	1.0ml
7.5% calcium chloride 2-hydrate sol <sup>n</sup>	1.0ml
Chelated iron solution	2.0ml
vitamin B12 (20µg/ml) solution	1.0ml
niacin (10mg/ml) solution	1.0ml
P.A.B.A (3mg/ml) solution	1.0ml
sodium thiosulphate 5-hydrate	0.5g

**A1.4: CENMED Medium:**

per 1L

sodium pyruvate	2.2g
K <sub>2</sub> HPO <sub>4</sub>	0.9g
KH <sub>2</sub> PO <sub>4</sub>	0.6g
NH <sub>4</sub> Cl	1.0g
disodium EDTA	5.0mg
magnesium sulphate.7H <sub>2</sub> O	0.2g
Trace Element Solution	1.0ml
calcium chloride.2H <sub>2</sub> O	75.0mg
Chelated iron Solution	2.0ml
vitamin B12	20.0µg
Biotin	15.0µg
sodium thiosulphate.5H <sub>2</sub> O	0.5g

Adjust to pH 6.8 with NaOH.

**A1.5: Cluture Stock Solutions:****A1.5.1 Base Concentrate (Conc Base):**

per 1L

nitrilotriacetic acid	10.0g
magnesium sulphate	14.45g
calcium chloride.2H <sub>2</sub> O	3.4g
ammonium molybdate	9.25mg
ferrous sulphate.7H <sub>2</sub> O	99.0mg

## Appendix 1: Bacterial Culture Solutions

nicotinic acid	50.0mg	<b>A1.5.5. True Blue Trace Elements</b>
aneurine hydrochloride	25.0mg	<b>(T.B.T.E):</b>
Biotin	0.5µg	Per 250ml
Metos 44	50.0ml	To 200ml deionised water add:-
Add to 500ml of deionized water then pH to 6.8 with KOH.		disodium EDTA
		manganous chloride
		boric acid
		sodium molybdate
		zinc chloride
		nickel (II) chloride 7-hydrate
		cobalt (II) chloride 6-hydrate
		copper (II) chloride 2-hydrate
		sodium selenite
		sodium metavanadate
		Adjust volume to 250ml
<b>A1.5.2. Metos 44:</b>		
per 250ml		
disodium EDTA	2.5g	
zinc sulphate	10.95g	
manganous sulphate.4H <sub>2</sub> O	1.54g	
copper sulphate.5H <sub>2</sub> O	0.392g	
cobaltous nitrate.6H <sub>2</sub> O	0.248g	
ferrous sulphate.7H <sub>2</sub> O	5.0g	
di-sodium tetraborate.10H <sub>2</sub> O	0.177g	
conc H <sub>2</sub> SO <sub>4</sub>	20 drops	
		<b>A1.5.6. Chelated Iron Solution:</b>
		Per 1L
		To 900ml of deionised water add:-
		disodium EDTA
		iron (II) chloride 4-hydrate
		conc HCl
		then adjust volume to 1000ml.
<b>A1.5.3. Growth Factors:</b>		
per 100ml		
Biotin	0.002g	
sodium hydrogen carbonate	0.05g	
Add water and dissolve, then add;		
nicotinic acid	0.1g	
aneurine hydrochloride	0.05g	
4-aminobenzoic acid	0.1g	
then boil to dissolve.		
		<b>A1.5.7. Ferric Citrate Solution:</b>
		Per 100ml
		Add 100mg of ferric citrate to 100ml of boiling distilled water. Once dissolved store at 4°C.
<b>A1.5.4. 0.64M Potassium phosphate</b>		
<b>Buffer:</b>		
Per 1L		
To 900ml of deionised water add:-		
potassium dihydrogen orthophosphate	40.0g	
di-potassium hydrogen orthophosphate	60.0g	
pH to 6.8 and bring final volume to 1000ml with deionised water.		
		<b>A1.5.8. Trace Element Solution:</b>
		per 1L
		di-sodium EDTA
		ferrous sulphate.7H <sub>2</sub> O
		manganous chloride.4H <sub>2</sub> O
		boric acid
		cobalt chloride.2H <sub>2</sub> O
		calcium chloride.2H <sub>2</sub> O
		nickel chloride.6H <sub>2</sub> O



## A.2: Tannin Assay Solutions:

The Tannin assay is based on turbidity levels of proteins measured at an absorbance of 500nm (Mejbaum-Katenellenbogen and Dobryszczyka, 1959). The Tannin reagent is used to incubated the samples at 30°C then the reaction is terminated by fixation by Acacia solution. For the experimental procedure see section 2.7.1.

### Tannin Reagent:

per 200ml

196ml of 1M HCl

4g of phenol

20g of tannic acid

Heat 1M HCl to 80°C while adding the tannic acid. Add the phenol making sure it dissolves. Once dissolved the Tannin reagent is allowed to cool to room temperature, then filtered into a dark glass bottle. The reagent is filtered each time just before an assay is undertaken. The reagent is stored at 4°C until required.

### Acacia Solution:

A 0.2% Acacia (Gum Arabic) solution was prepared in distilled water and stored at 4°C prior to use.

### Bovine Serum Albumin (B.S.A.) Stock Solution:

A 1mg ml<sup>-1</sup> stock solution of B.S.A. (fraction V, Sigma Chemical Company) was serially diluted to concentrations ranging from 10 µg ml<sup>-1</sup> to 80 µg ml<sup>-1</sup> to provide a protein standard calibration curve.

**A3: PAGE Stock Solutions:**

Based on Schagger and von Jagow (1987).

**A3.1.1 49.5%T 6%C Acrylamide:** per 250ml

Acrylamide (BDH, Electran grade) 116.6g

Bis-acrylamide (BDH, Electran grade) 7.5g

**A3.1.2 49.5%T 3%C Acrylamide:** per 250ml

Acrylamide (BDH, Electran grade) 1120.0g

Bis-acrylamide (BDH, Electran grade) 3.75g

**A3.1.3 Gel Buffer:** per 250ml

Acrylamide (BDH, Electran grade) 1120.0g

Bis-acrylamide (BDH, Electran grade) 3.75g

**A3.1.4 Anode Buffer:** per 1000ml

TRIS 24.4g

Adjust pH with HCl to 8.45

**A3.1.5 Cathode Buffer:** per 1000ml

TRIS 3.0g

SDS 1.0g

glycine 14.56g

Adjust pH with HCl to 8.3

**A3.2: Sample Buffer:** per 10ml.

4% (w/v) SDS 0.4g

12% (v/v) glycerol 1.2ml

50mM TRIS.HCl 60.0mg

0.01% (w/v) Serva Blue G 1.0mg

2% (v/v) mercaptothanol 0.2ml

pH to 6.8 with HCl.

The above sample buffer is used for the non-reaction centre containing protein samples. When reaction centre containing samples are used the 2% mercaptothanol is replaced with 10mM DTT.

**Gel Casting:**

Gels were poured using the volumes listed below in the table. The separating gel was poured then immediately the spacer gel is layered on top. 50% (v/v) methanol is pipetted on top of the setting gel to prevent a meniscus forming. Once set the methanol/water is removed, the stacking gel is then prepared and poured. Abbreviations: Amp; 10%(w/v) ammonium persulphate; TEMED, N,N,N',N'-tetramethylthylenediamine (Aldrich Chemical Co. Ltd.).

Gel Casting						
Solution	6%C	3%C	Gel Buffer	H <sub>2</sub> O	Amp	TEMED
separating gel	10.02ml	-	10.02ml	6.0ml	150µl	15µl
	add 4.01ml of glycerol with the water.					
spacer gel	-	6.0ml	10.02ml	13.8ml	150µl	18µl
stacking gel	-	150µl	4.86ml	12.6ml	180µl	18µl

**A3.3: Stainer and Destainer:****A3.3.1 Stainer:** per 1L

distilled water	500 ml
methanol	500 ml
glacial acetic acid	200 ml
coomassie blue	1.2 g

**A3.3.2 Destainer:** per 1L

propan-2-ol	125 ml
glacial acetic acid	100 ml
distilled water	775 ml

**A4.1: Magic 46 Stock Solutions:**

The following stock solutions were prepared from *Analar*<sup>®</sup>, or equivalent, grade chemicals. To ensure consistency in PEG pH's sufficient quantities of PEG were bought to allow crystallographic studies from only one batch of PEG. All the solutions (except the PEG solutions) were prepared with *Analar*<sup>®</sup> water and filtered into virgin 50ml *Falcon*<sup>™</sup> tubes. Due to the viscosity of the PEG solutions they were only filtered when diluted to their working concentrations.

**Salts:**

2.0M ammonium acetate  
 3.5M ammonium sulphate  
 1.0M calcium acetate  
 2.0M calcium acetate  
 1.0M potassium phosphate, set to pH 6.42 with NaOH  
 2.0M potassium sodium tartrate  
 1.8M lithium sulphate  
 2.0M magnesium acetate  
 2.0M magnesium chloride  
 2.0M sodium acetate  
 1.0M sodium citrate  
 1.0M zinc acetate

**Buffers:**

1.0M sodium acetate, set to pH 4.28 with glacial acetic acid.  
 1.0M sodium cacodylate, set to pH 5.23 with HCl.  
 1.0M citrate (Citric acid), set to pH 4.13 with HCl.  
 1.0M HEPES, set to pH 7.50 with NaOH (free salt form).  
 1.0M imidazole, set to pH 7.50 with HCl.  
 1.0M TRIS, set to pH 8.50 with HCl.

**Precipitants:**

2.0M ammonium phosphate  
 3.5M ammonium sulphate  
 100% propan-2-ol  
 2.0M potassium Phosphate, set to pH 5.50 with NaOH.  
 2.0M potassium sodium tartrate  
 100% MPD (distilled)  
 100% PEG 400  
 50% (w/v) PEG 2000  
 50% (w/v) PEG 4000  
 50% (w/v) PEG 8000  
 4.0M sodium formate

**A4.2: FASTPEG Stock Solutions:**

The following stock solutions were prepared from *Analar*<sup>®</sup>, or equivalent, grade chemicals. To ensure consistency in PEG pH's sufficient quantities of PEG were bought to allow crystallogenesis studies from only one batch. All the solutions (except the PEG solutions) were prepared with *Analar*<sup>®</sup> water and filtered into virgin 50ml *Falcon*<sup>™</sup> tubes. Due to the viscosity of the PEG solutions they were only filtered when diluted to their working concentrations.

**Salts:**

2.0M ammonium acetate  
 3.5M ammonium sulphate  
 1.0M potassium phosphate  
 2.0M sodium citrate  
 2.0M sodium acetate  
 2.0M magnesium acetate  
 2.0M magnesium chloride  
 2.0M zinc acetate

**Buffers:**

1.0M MES, set to pH 6.00 with NaOH (free salt form)  
 1.0M MES, set to pH 6.50 with NaOH (free salt form)  
 1.0M HEPES, set to pH 7.00 with NaOH (free salt form)  
 1.0M HEPES, set to pH 7.50 with NaOH (free salt form)  
 1.0M TRIS, set to pH 8.0 with HCl (Trizma base<sup>™</sup>)  
 1.0M TRIS, set to pH 8.5 with HCl (Trizma base<sup>™</sup>)  
 1.0M CHES, set to pH 9.0 with NaOH  
 1.0M CHES, set to pH 9.5 with NaOH

**Precipitants:**

100% (v/v) PEG 200  
 100% (v/v) PEG 300  
 100% (v/v) PEG 400  
 100% (w/v) PEG 600  
 50% (w/v) PEG 1000  
 50% (w/v) PEG 2000  
 50% (w/v) PEG 4000  
 50% (w/v) PEG 6000  
 50% (w/v) PEG 8000

**References:**

- Aagard, J. and Sistrom, W.R. (1972). Control of Synthesis of Reaction Center Bacteriochlorophyll in Photosynthetic Bacteria. *Photochem. Photobiol.* **15**, 209-225.
- Agalides, I and Reiss-Husson, F. (1983). Several Properties of the LM Unit Extracted with Sodium Dodecyl Sulphate from *Rhodospseudomonas sphaeroides* Purified Reaction Centres. *Biochim. Biophys. Acta.* **724**, 340-351.
- Allen, J.P., Feher, G., Yeates, T.O., Komiya, H and Rees, D.C. (1987a). Structure of the Reaction Centre from *Rhodobacter sphaeroides*: The Cofactors. *Proc. Natl. Acad. Sci. USA.* **84**, 5730-5734.
- Allen, J.P., Feher, G., Yeates, T.O., Komiya, H and Rees, D.C. (1987b). Structure of the Reaction Centre from *Rhodobacter sphaeroides*: The Protein Subunits. *Proc. Natl. Acad. Sci. USA.* **84**, 6162-6166.
- Allen, J.P., Feher, G., Yeates, T.O., Komiya, H and Rees, D.C. (1988). In *The photosynthetic bacterial reaction centre* NATO ASI Series A: Life sciences (Breton, J. and Vermeiglio, A., eds) pp. 5-72 Plenum Press, New York.
- Allen, J.P., Theiler, R., and Feher, G. (1985a). Crystallization of an Antenna Pigment-Protein Complex from *Rhodospseudomonas sphaeroides*, *Biophys. J.* **47**, 4a.
- Allen, J.P., Theiler, R., and Feher, G. (1985b). *Crystallization and Linear Dichroism Measurements of the B800-850 Antenna Pigment-Protein Complex from Rhodobacter sphaeroides 2.4.1.* in *Antennas and Reaction Centres of Photosynthetic Bacteria, Structure, Interactions, and Dynamics.* (Ed. Michel-Beyerle, M.E.). Springer-Verlag, Berlin. pp82-84.
- Amesz, J. (1985). Photosynthesis: Structure of Membrane and Membrane Proteins. *Progress in Botany.* **47**, 87-104.
- Amos, L.A., Henderson, R., and Unwin, P.N.T. (1982). Three Dimensional Structure Determination by Electron Microscopy of Two-Dimensional Crystals. *Prog. Biophys. Molec. Biol.* **39**, 183-231.
- Baldwin, J.M., Henderson, R., Beckman, E., and Zemlin, F. (1988). Images Of Purple Membrane at 2.8 Å Resolution Obtained by Cryo-Electron Microscopy. *J. Mol. Biol.* **202**, 585-591.
- Bissig, I., Brunisholz, R.A., Suter, F., Cogdell, R.J., and Zuber, H. (1988). The Complete Amino Acid Sequences of the B800-850 Antenna Polypeptides from *Rhodospseudomonas acidophila* strain 7750. *Zeitschrift für Naturforschung* **43c**, 77-83.
- Bissig, I., Wagner-Huber, R.V., Brunisholz, R.A. and Zuber, H. (1990). Multiple Antenna Complexes in Various Purple Photosynthetic Bacteria. In *Molecular Biology of Membrane-bound Complexes in Phototrophic Bacteria* (Drews, G., and Dawes, E.A. eds) pp. 161-180. Plenum Press, New York.
- Bixon, M, Jortner, J., and Michel-Beyerle, M.E., and Ogrodnik, A. (1989). A Superexchange Mechanism for the Primary Charge Separation in Photosynthetic Reaction Centres. *Biochim. Biophys. Acta.* **977**, 273-286.
- Blundell, T.L. and Johnson, L.M. (1976). Crystallisation of proteins. In *Protein Crystallography* pp 59-82. Academic Press, London.

- Bolotina, I.A., Chekov, V.O., Lugauskas, V.Y., and Pisyn, O.B. (1981). Determination of the Secondary Structure of Proteins from Circular Dichroism Spectra. III. Protein Derived Reference Spectra for Antiparallel and Parallel  $\beta$  Structures. *J. Mol. Biol.* **15**, 130-137.
- Boonstra, A.F., Visschers, R.W., Calkoen, F., Van Grondelle, R., Vanbruggen, E.F.J, and Boekema, E.J. (1993). Structural Characterization of the B800-850 and B875 Light-harvesting Antenna Complexes from *Rhodobacter sphaeroides* by Electron Microscopy. *Biochim. Biophys. Acta.* **1142**, 181-188
- Boucher, F., van der Rest, M., and Gingras, G. (1977). Structure and Function of Carotenoids in the Photoreaction Center from *Rhodospirillum rubrum*. *Biochim Biophys. Acta.* **461**, 339-357.
- Bremer, A., Henn, C., Engel, A., Baumeister, W., and Aebi, U. (1992). Has Negative Staining Still a Place in Biomolecular Electron Microscopy? *Ultramicroscopy.* **46**, 85-111
- Breton, J. and Nabedryk, E. (1984). Transmembrane Orientation of  $\alpha$ -helices and Organisation of Chlorophyll in Photosynthetic Pigment-protein Complexes. *FEBS Lett.* **176**, 335-359.
- Breton, J., Martin J.L., Migus, A., Antonetti, A., and Orzag, A. (1986). Femtosecond Spectroscopy of Excitation Energy Transfer and Initial Charge Separation in the Reaction Centre of the Photosynthetic Bacterium *Rhodospseudomonas viridis*. *Proc. Natl. Acad. Sci. USA.* **83**, 5121-5125.
- Bril, C. (1958). Action of a Non-ionic Detergent on Chromatophores of *Rhodospseudomonas sphaeroides*. *Biochim. Biophys. Acta*, **29**, 458.
- Brogliè, R.M., Hunter, C.N., Delepelaire, P., Niederman, R.A., Chua, N.H., and Clayton, R.K. (1980). Isolation and Characterisation of the Pigment-Protein Complexes of *Rhodobacter sphaeroides* by Lithium Dodecyl Sulfate. *Proc. Natl. Acad. Sci. USA.* **77**, 87-91.
- Brunie, S., Bolin, J., Gewirth, D., and Sigler, P.B. (1985). The Refined Crystal Structure of Dimeric Phospholipase A<sub>2</sub> at 2.5Å. *J. Biol. Chem.* **260**, 9742-9749.
- Brunisholz, R.A., and Zuber, H. (1988). In Scheer, H and Schneider, S. (eds), *Photosynthetic Light Harvesting Systems, Organisation and Function*. De Gruyter, New York. pp 103-114.
- Brunisholz, R.A., Bissig, I., Niederer, E., Suter, F., and Zuber, H. (1987). *Structure Studies on the Light-harvesting Polypeptides of Rhodospseudomonas acidophila*. In 'Progress in Photosynthesis Research II' (Biggins, J., ed.) Martinus Nijhoff, The Netherlands.
- Brunisholz, R.A., Cuendet, P.A., Theiler, R. and Zuber, H. (1981a). The Complete Amino Acid Sequence of the Single Light-harvesting Protein from Chromatophores of *Rhodospirillum rubrum*. G9<sup>+</sup>. *FEBS lett.* **129**, 150-154.
- Brunisholz, R.A., Cuendet, P.A., Theiler, R. and Zuber, H. (1981b). The Light-Harvesting Polypeptides of *Rhodospirillum rubrum*. *Hoppe-Seyler's Z. Physiol. Chem.* **365**, 675-688.
- Brunisholz, R.A., Jay, A., Suter, F., and Zuber, H. (1982). Primary Sequence Analysis of the Light-Harvesting Polypeptides from Various Photosynthetic Bacteria. *Experientia.* **338**, 723.
- Brunisholz, R.A., Suter, F., and Zuber, H. (1984). The Light-Harvesting Polypeptides of *Rhodospirillum rubrum*. *Hoppe-Seyler's Z. Physiol. Chem.* **356**, 675-688.
- Brunisholz, R.A., Zuber, H., Valentine, J., Lindsay, J.G., Woolley, K.J. and Cogdell, R.J. (1986). The Membrane Location of the B890-complex from *Rhodospirillum rubrum* and the Effect of Carotenoid on the Conformation of its Two Proteins Exposed at the Cytoplasmic Surface. *Biochim. Biophys. Acta* **849**, 295-303.
- Butt, H.J., Wang, D.N., Hansma, P.K., Kühlbrandt, W. (1991). Effect of Surface Roughness of Carbon Support Films on High Resolution Electron Diffraction of 2-Dimensional Protein Crystals. *Ultramicroscopy.* **36**, 307-318.

## References:

- Bylina, E.J., Kirmaier, C., McDowell, L., Holten, D., and Youvan, D.C. (1988). Influence of an Amino Acid Residue on the Optical Properties and Electron Transfer Dynamics of a Photosynthetic Reaction Center Complex. *Nature*. **336**, 182-184.
- Carter, C.W., Jr and Carter, W.C. (1979). Protein Crystallization Using Incomplete Factorial Experiments. *J. Biol. Chem.* **254**, 12219-12223.
- Chang, C.H., Elkabbani, O., Tiede, D., Tang, J., Norris, J., and Schiffer, M. (1991). Structure of the Membrane Bound Protein Photosynthetic Reaction Centre from *Rhodobacter sphaeroides*. *Biochemistry* **30**, 5352-5360.
- Chang, C.H., Tiede, D., Tang, J., Smith, U., Norris, J., and Schiffer, M. (1986). Structure of the Reaction Centre from *Rhodobacter sphaeroides* R-26. *FEBS lett.* **205**, 82-86.
- Cherry, R.J., Müller, U., Henderson, R., and Heyn, M.P. (1978). Temperature-dependent Aggregation of Bacteriorhodopsin in Dipalmitoyl- and Dimyrstoylphosphatylcholine Vesicles. *J. Mol. Biol.* **121**, 283-298.
- Chiu, W. (1993). What Does Electron Microscopy Provide that x-ray Crystallography and NMR Spectroscopy Cannot? *Annu. Rev. Biophys. Biomol. Struct.* **22**, 233-255.
- Clarke, A.J., and Margulies, A.D. (1965). Isolation and Characterization of Recombination-deficient Mutants of *Escherichia coli* K12. *Proc. Natl. Acad. Sci.* **53**, 451-459.
- Clayton, R.K. (1971). Light and living Matter; A Guide to the Study of Photobiology. pp.2-66. McGraw-Hill Company, New York.
- Clayton, R.K. (1962). Primary Reactions in Bacterial Photosynthesis. I. Nature of Light-induced Absorption Changes in Chromatophores; Evidence for a Special Bacteriochlorophyll Component. *Photochem. Photobiol.* **1**, 201.
- Clayton, R.K. (1966). Spectroscopic Analysis of Bacteriochlorophylls *in vivo*. *Photochem. Photobiol.* **5**, 669-677.
- Clayton, R.K., (1978). Physicochemical Mechanisms in Reaction Centres of Photosynthetic Bacteria. In *The Photosynthetic Bacteria* (Clayton, R.K. and Sistrom, W.R. eds) pp. 387-396. Plenum Press, New York.
- Clayton, R.K., and Clayton, B.J. (1972). Relations Between Pigments and Proteins in the Photosynthetic Membranes of *Rhodobacter sphaeroides*. *Biochim. Biophys. Acta*, **283**, 492-504.
- Clayton, R.K., and Haselkorn, R. (1972). Protein Components of Bacterial Photosynthetic Membranes. *J. Mol. Biol.* **68**, 97-105.
- Clayton, R.K., and Sistrom, W.R. (1978). *The Photosynthetic Bacteria*. Plenum Press. New York.
- Clore, G.M., and Gronenborn, A.M. (1991). Two, Three-, and Four-Dimensional NMR Methods for Obtaining Larger and More Precise Three-Dimensional Structures of Proteins In Solution. *Annu. Rev. Biophys. Biophys. Chem.* **20**, 29-63.
- Cogdell, R.J., Hawthornthwaite, A.M., Ferguson, L.A., Evans, M.B., Li, M., Gardiner, A., Mackenzie, R.C., Thornber, J.P., Brunisholz, R.A., Zuber, H., van Grondelle, R., and van Mourik, F. (1990). The Structure and Function of Some Unusual Variable Antenna Complexes. In: *Molecular Biology of Membrane-bound Complexes in Phototrophic Bacteria*. (Eds Drews, G., and Dawes, E.A.) Plenum Press. New York.
- Cogdell, R.J. (1978). Carotenoids in Photobiology. *Phil. Trans. R. Soc. Lond.* **B284**, 569-579.
- Cogdell, R.J. and Frank, H. (1987). How carotenoids work in photosynthesis. *Biochim. Biophys. Acta.* **895**, 63-79.

\* References which were unavailable

- Cogdell, R.J., (1983). Light-harvesting Complexes in the Purple Photosynthetic Bacteria. In *Encyclopaedia of plant Physiology New Series*, Vol. 19, (Stalhelin, L.A. and Arntzen, C.J., eds) pp. 252.
- Cogdell, R.J., and Hawthornthwaite, A.M. (1993). Preparation, Purification and Crystallization of Purple Bacteria Antenna Complexes. In: *The Photosynthetic Reaction Center, Vol 1*. Deisenhofer, J., and Norris, J.R. (Eds.). pp 23-41. Academic Press, London.
- Cogdell, R.J., and Scheer, H. (1985). Circular Dichroism of Light-harvesting Complexes from Purple Photosynthetic Bacteria. *Photochem. Photobiol.* **42**, 669-689.
- Cogdell, R.J., and Thonber, J.P. (1980). Light-Harvesting Pigment-Protein Complexes of Purple Photosynthetic Bacteria. *F.E.B.S Letts.* **122**, 1-8.
- Cogdell, R.J., Andersson, P.O. and Gillbro, T. (1992). Carotenoid Singlet-States and their Involvement in Photosynthetic Light-Harvesting Pigments. *J. Photochem. Photobiol. B-Biol.* **15**, 105-112.
- Cogdell, R.J., Durant, I., Valentine, J., Lindsay, J.G., and Schimidt, K (1983). The Isolation and Partial Characterisation of the Light-harvesting Pigment-protein Complement from *Rhodospseudomonas acidophila* strain 10050. *Biochim. Biophys. Acta* **722**, 427-455.
- Cogdell, R.J., Lindsay, J.G., Valentine, J., and Durant, I. (1982). A Further Characterisation of the B890 Light-harvesting Pigment-protein Complexes from *Rhodospirillum rubrum* strain S1. *FEBS Lett.* **150**, 151-154.
- Cogdell, R.J., Monger, T.G. Parson, W.W. (1975). Carotenoid Triplet States in reaction centres from *Rhodospseudomonas sphaeroides* and *Rhodospirillum rubrum*. *Biochim. Biophys. Acta.* **408**, 189-199.
- Cogdell, R.J., Parson, W.W., and Kerr, M.A. (1976). The Type, Location and Energy Properties of the Carotenoid from *Rhodospseudomonas sphaeroides*. *Biochim. Biophys. Acta.* **430**, 89-93.
- Cogdell, R.J., Woolley, K.J., Dawkins, D.J. and Lindsay, J.G. (1986). In *Microbial Energy Transduction Current Communications in Molecular Biology* (Youvan, D.C. and Daldal, F., eds) pp. 47-51, Cold Spring Harbor Symposium, Cold-Spring Harbor, New York.
- Cogdell, R.J., Woolley, K.J., MacKenzie, R.C., Lindsay, J.G Michel, H., Dobler, J., and Zinth, W. (1985). Crystallisation of the B800-850 Complex from *Rhodospseudomonas acidophila* strain 7750. In *Springer Series in Chem. Phys.* **42**, 85-89.
- Cogell, R.J. and Crofts, A.R. (1978). Analysis of the Pigment Content of an Antenna Pigment-Protein Complex from Three Strains of *Rhodospseudomonas sphaeroides*. *Biochim Biophys. Acta.* **502**. 409-416.
- Cohen-Bazire, G. Sistrom, W.R., and Stanier, R.Y. (1957). Kinetic Studies of Pigment Synthesis by Non-sulphur Purple Bacteria. *J. Cell. Comp. Physiol.* **49**, 25-68.
- Cohen-Bazire, G. and Sistrom, W.R. (1966). In 'The Chlorophylls' (Eds. Veron, L.P. and Seely, G.R.) pp 313 Academic Press. New York.
- Cotton, T.M., Loach, P.A., Katz, J.J. and Ballsmiter, K. (1978). Studies of Chl-Chl and Chl-ligand Interactions by Visible Absorption and Infrared Spectroscopy at Low Temperatures. *Photochem. Photobiol.* **27**, 735-749.
- Crouse, J.B., Feldman, R.P., and Clayton, R.K. (1963). Accumulation of Polyene Precursors of Neurosporene in Mutant Strains of *Rhodospseudomonas sphaeroides*. *Nature.* **198**, 1227-1228.
- Davison, E and Cogdell, R.J. (1981). Reconstruction of Carotenoids into the Light-harvesting Pigment-protein Complexes from the Carotenoidless Mutant *Rhodobacter sphaeroides* R26. *Bochim biophys. Acta* **635**, 295-303.

- Dawkins, D.J., (1988). Isolation and Characterisation of Reaction Centre-antenna conjugates from a range of Bacteriochlorophyll *a*-containing species of Purple Bacteria. Phd Thesis. University of Glasgow.
- Debus, R.J., Feher, G., and Okamura, M.Y. (1985). LM Complex of Reaction Centers from *Rhodospseudomonas sphaeroides* R-26: Characterization and Reconstitution with the H-Subunit. *Biochem.* **24**, 2488-2500.
- Deinum, G., Otte, S.C.M., Gardiner, A.T., Aartsma, T.J., Cogdell, R.J. and Amesz, J. (1991). Antenna Organisation of *Rhodospseudomonas acidophila*: A Study of the Excitation Migration. *Biochim. Biophys. Acta* **1060**, 125-131.
- Deisenhofer, J. and Michel, H. (1989). The Photosynthetic Reaction Centre from the Purple Bacterium *Rhodospseudomonas viridis*. *EMBO J.* **8**, 2149-2170.
- Deisenhofer, J. and Michel, H. (1991a). Structures of the Bacterial Photosynthetic Reaction Center. *Ann. Rev. Cell.Biol.* **7**, 1-23.
- Deisenhofer, J. and Michel, H. (1991b). High-Resolution Structures of Photosynthetic Reaction Centre. *Ann. Rev. Biophysics and Biophysical Chemistry.* **20**, 247-266.
- Deisenhofer, J., Epp, O., Miki, K., Huber, R. and Michel, H. (1984). X-ray Structural Analysis of a Membrane Protein Complex. *J. Mol.Biol.* **180**, 385-398.
- Deisenhofer, J., Epp, O., Miki, K., Huber, R. and Michel, H. (1985). Structure of the Protein Subunits in the Photosynthetic Reaction Centre of *Rhodospseudomonas viridis* at 3Å resolution. *Nature* **318**, 618-624.
- Delarue, M., Poch, O., Tordo, N., Moras, D., and Argos, P. (1990). An Attempt to Unify the Structure of Polymerases. *Protein Eng.* **3**, 461-467.
- DeRosier, D.J. (1992). Enzyme Complexes - a Farewell to Arms. *Nature.* **357**, 196-197.
- Diamond, R. (1969). Profile Analysis in Single Crystal Diffractometry. *Acta Cryst.* **A25**, 43-55.
- DiMagno, T.J., and Norris, J.R. (1993). *Initial Electron Transfer Events in Photosynthetic Bacteria*. In; The Photosynthetic Reaction Centre, Vol II. Deisenhofer, J and Norris, R.J (Eds.). pp105-127. Academic Press, Ltd. London.
- Donnelly, D., and Cogdell, R.J. (1993). Predicting the Point at Which Transmembrane Helices Protrude From the Bilayer: a model of the Antenna Complexes From Photosynthetic bacteria. *Protein Eng.* **6**, 629-635.
- Donnelly, D., Overington, J.P., Ruffle, S.V., Nugent, J.H.A. and Blundell, T.L. (1993). Modeling Alpha-helical Transmembrane Domains - the calculation and Use of Substitution for Lipid-facing residues. *Protein Sci.*, **2**, 55-70.
- Donohue, T.J., Cain, B.D., Kaplan, S. (1982a). Purification And Characterization Of An N-Acylphosphatidylserine From *Rhodospseudomonas sphaeroides*. *Biochemistry.* **21**, 2765-2773.
- Donohue, T.J., Cain, B.D., Kaplan, S. (1982b). Alterations in the Phospholipid composition of *Rhodospseudomonas sphaeroides* and Other Bacteria Induced by Tris. *J. Bacteriol.* **152**, 595-606.
- Donohue, T.J., Hoger, J.H., Kaplan, S. (1986). Donohue, T.J., Hoger, J.H., Kaplan, S. (1986). Cloning and Expression of the *Rhodospseudomonas sphaeroides* Reaction Centre H gene. *J. Bacteriol.* **168**, 953-961.
- Dorset, D., Engel, A., Haner, M., Massalski, A., Rosenbusch, J.P. (1983). Two-Dimensional Crystal Packing of Matrix Porin. A Channel Forming Protein in *Escherichia coli* Outer Membranes. *J. Mol. Biol.* **165**, 701-710.

- Dressler, K., Umlauf, E., Schmidt, S., Hamm, P., Zinth, W., and Buchanan, S. (1991). Detailed Studies of the Subpicosecond Kinetics in the Primary Electron transfer of Reaction Centers of *Rhodospseudomonas viridis*. *Chem. Phys. Letts.* **183**, 270-276.
- Drews, G. (1985). Structure and functional organisation of the light-harvesting complexes and photochemical reaction centres in membranes of photosynthetic bacteria. *Microbiol. Rev.* **49**, 59-70.
- Dubochet, J., Adrian, M., Chang, J-J., Homo, J-C., Lepault, J., McDowell, A.W., and Schultz, P. (1988). Cryo-Electron Microscopy of Vitrified Specimens. *Q. Rev. Biophys.* **21**, 129-228.
- Dutton, P.L. (1986). Energy Transduction in Anoxygenic Photosynthesis. in "Photosynthesis III (Staelhelin L.A. and Arntzen, C.J. eds) Encyclopedia of plant Physiology" Vol. 19, Springer-Verlag.
- Egelman, E.H., (1993). What Do X-ray Crystallographic and Electron Microscopic Structural Studies of the RecA Protein Tell Us About Recombination? *Curr. Opin. Struct. Biol.* **3**, 189-197.
- Emerson, R and Arnold, W. (1932). Photochemical Reactions in Photosynthesis. *J. Gen. Physiol.* **16**, 191-205.
- Engel, A. (1982). Mass Determination by Electron Scattering.. *Micron.* **13**, 425-436.
- Engel, A., and Massalski, A. (1984). 3D Reconstruction from Electron Micrographs: its Potential and Practical Limitations. *Ultramicroscopy.* **13**, 71-84.
- Engel, A., Hoenger, A., Hefti, A., Henn, C., Ford, R.R., Kistler, J., and Zulauf, M. (1992). Assembly of 2-D Membrane Protein Crystals: Dynamics, Crystal Order, and Fidelity of Structure Analysis by Electron Microscopy. *J. Struct. Biol.* **109**, 219-234.
- Engelhardt, H., Baumeister, W., and Saxton, W.O. (1983). Electron Microscopy of Photosynthetic Membrane Containing Bacteriochlorophyll *b*. *Arch. Microbiol.* **135**, 169-175.
- Engelhardt, H., Engel, A., and Baumeister, W. (1986). Stoichiometric model of the photosynthetic unit of *Ectothiorhodospira halochloris*. *Proc. Natl. Acad. Sci. USA.* **83**, 8972-8976.
- Erickson, H.P., Voter, W.A., and Leonard, K. (1978). Image Reconstruction. *Methods in Enzymology* **XLIX**, 59-63.
- Evans, M.B. (1989). The Structure and Function of the Light-Harvesting Antenna Complexes from Purple Photosynthetic Bacteria. PhD Thesis, University of Glasgow.
- Feher, G., Allen, J.P., Okamura, M.Y., and Rees, D.C. (1989). Photosynthetic Reaction Centres. *Nature.* **339**, 111-116.
- Feher, G., and Okamura, M.Y. (1984). Structure and Function of the Reaction Center from *Rhodospseudomonas sphaeroides*. In *Advances in Photosynthesis Research. Volume II.* (Ed. Sybesma, C.). Nijhoff/Junk Publishers. The Hague. pp155-164.
- Feher, G., and Okamura. (1978). *Chemical Composition and Properties of Reaction Centres*. In *The Photosynthetic Bacteria* (Eds. Clayton, R.K., and Sistrom, W.R.). Plenum Press. pp349-386.
- Feher, J.P., and Okamura, M.Y. (1978) *Chemical Composition and Properties of Reaction Centres*. In *The Photosynthetic Bacteria*. (Eds. Clayton, R.K., and Sistrom, W.R.). Plenum Press, New York. pp349-386.
- Feick and Drews (1978). Isolation and Characterization of Light-harvesting Bacteriochlorophyll: Protein Complexes from *Rhodospseudomonas capsulata*. *Biochim Biophys. Acta.* **501**, 499-513.

## References:

- Fisrow, N.N., and Drews, G. (1977). Differentiation of the Intracitoplasmic Membrane of *Rhodospirillum rubrum* by Variation in Oxygen Partial Pressure of Light Intensity. *Arch. Microbiol.* **115**, 299-306.
- Foote, C.S., and Denny, R.W. (1968). *J. Am. Chem. Soc.* **90**, 6233. \*
- Foote, C.S., Chang, Y.C., and Denny, R.W. (1970). *J. Am. Chem. Soc.* **92**, 5216-5218. \*
- Fowler, G.J.S., Vischers, R.W., Grief, G.G., van Grondelle, R., and Hunter, C.N. (1992). Genetically Modified Photosynthetic Antenna Complexes With Blueshifted Absorbant Bands. *Nature.* **335**, 848-850.
- Frank, H and Cogdell, R.J. (1987). How Carotenoids Function In Photosynthetic Bacteria. *Biochim. Biophys. Acta.* **895**, 63-79.
- Fuglistaller, P.R., Rumbeli, R., Suter, F., and Zuber, H. (1984). The Light-harvesting Polypeptides of *Rhodospirillum rubrum*. I. The Amino Acid Sequence of the 2<sup>nd</sup> Light-harvesting Polypeptide B-880-beta (B-870-beta) of *Rhodospirillum rubrum* S1 and the Carotenoidless Mutant G9+ - Aspects of the Molecular Structures of the 2 Light-harvesting Polypeptides B-880-Alpha (B-870-alpha) and B-880-beta (B-870-beta) and of the Antenna Complex B-880 (B870) from *Rhodospirillum rubrum*. *Hoppe-seyler's Zeitschrift fur Physiol. Chem.* **365**, 675-688.
- Fukami, A., and Adachi, K. (1965). A New Method of Preparation of a Self-Perforated Micro Plastic Grid and its Application. *J. Electr. Microsc.* **14**, 112-118.
- Furcinitti, P.S., van Oostrum, J., and Burnett, R.M. (1989). Adenovirus polypeptide - IX Revealed as Capsid Cement by Difference Image From Electron Microscopy and Crystallography. *EMBO J.* **8**, 3563-3570.
- Ganong, W.F. (1908). *Laboratory Course in Plant Physiology*. Second Edition. Henry Holt and Company, New York.
- Garcia, A., Vernon, L.P., Ke, B., and Mollenhaur, H.M. (1966). Properties of *Chromatium* Subchromatophore Particles Obtained by Treatment with Triton X-100. *Biochemistry.* **5**, 2399-2407.
- Garcia, A., Vernon, L.P., Ke, B., and Mollenhaur, H.M. (1968). Some Structural and Photochemical Properties of *Rhodospseudomonas* NHTC 133 Subchromatophore Particles Obtained by Treatment with Triton X-100. *Biochemistry.* **7**, 326-332.
- Gardiner, A.T., Peripheral Antenna Complexes from *Rhodospseudomonas acidophila*: Structure, Function and Genetic Manipulation. Phd Thesis. University of Glasgow.
- Ghosh, R., Hoenger, A., Hardmeyer, A., Mitrailescu, Z.D., Bachofen, R., Engel, A., and Rosenbusch, J.P. (1993). Two-Dimensional Crystallisation of the Light-harvesting complex from *Rhodospirillum rubrum*. *J.Mol. Biol.* **231**, 501-504.
- Glazer, A.N., (1982). Phycobilisomes: Structure and Dynamics. *Ann. Rev. Microbiol.* **36**, 173-193.
- Glazer, A.N., Chan, C., and Williams, R.C. (1985). Kinetics of energy flow in the phycobilisome core. *Science.* **230**, 1051-1053.
- Goedheer, J.C. (1959). Energy Transfer Between Carotenoids and Bacteriochlorophyll in Chromatophores of Purple Bacteria. *Biochim Biophys. Acta.* **35**, 1-8.
- Green, D.W., Ingram, V.M., and Pertz, M.F. (1954). The Structure of Hemoglobin. *Proc. Roy. Soc.* **A225**, 287-295.
- Gregory, R.P.F. (1989). *Photosynthesis*. Blackie. Chapman and Hall, New York.

\* References which were unavailable

## References:

- Güner, S., Willie, A., Millett, F., Caffrey, M.S., Cusanovich, M.A., Robertson, D.A., and Knaff, D.B. (1993). The Interaction Between Cytochrome c<sub>2</sub> and the Cytochrome bc<sub>1</sub> Complex in the Photosynthetic Purple Bacteria *Rhodobacter capsulatus* and *Rhodospseudomonas viridis*. *Biochemistry*. **32**, 4793-4800.
- Guthrie, N., Macdermott, G., Cogdell, R.J., Freer, A.A., Isaacs, N.W., Hawthornthwaite, A.M., Halloren, E., Lindsay, J.G. (1992). Crystallization of the B800-820 Light-harvesting Complex from *Rhodospseudomonas acidophila* strain 7750. *J. Mol. Biol.* **224**, 527-528.
- Hall, J., Zha, X.H., Yu, L., Yu, C.A., and Millett, F. (1989). Role of Specific Lysine Residues in the Reaction of *Rhodobacter sphaeroides* Cytochrome c<sub>2</sub> with the Cytochrome bc<sub>1</sub> Complex. *Biochemistry*. **28**, 2568-2571.
- Halsey, Y.D., and Byers, B. (1975). A Large Photoreactive Particle from *Chromatium vinosum* Chromatophores. *Biochim. Biophys. Acta.* **387**, 349-367.
- Hayashi, H., Miyao, M., and Morita, S. (1982b). Absorption and Fluorescence Spectra of Light-harvesting Bacteriochlorophyll-protein Complexes from *Rhodospseudomonas palustris* in the near-infrared region. *J. Biochem.* **91**, 1017-1027.
- Hayashi, H., Nakano, M., and Morita, S. (1982a). Comparative Studies of Protein Properties and Bacteriochlorophyll Contents of Bacteriochlorophyll-Protein Complexes from Spectrally Different Types of *Rhodospseudomonas palustris*. *J. Biochem.* **92**, 1805-1811.
- Heinemeyer, E.A., and Schmidt, K. (1983). Changes in Carotenoid Biosynthesis Caused by Variations of Growth Conditions in Cultures of *Rps. acidophila* strain 7050. *Arch. Microbiol.* **134**, 217-221.
- Helenius, A., and Simons, K. (1975). Solubilisation of Membranes by Detergents. *Biochim. Biophys. Acta.* **415**, 29-79.
- Helenius, A., McCaslin, D.R., Fries, E., and Tanford, C. (1979). Properties of Detergents. *Meth. Enzymol.* **56**, 734-799.
- Henderson, R., Baldwin, J.M., Ceska, T.A., Zemlin, F., Beckmann, E., and Downing, K. (1990). Model for the Structure of Bacteriorhodopsin Based on High-resolution Electron Cryo-microscopy. *J. Mol. Biol.* **213**, 899-929.
- Henderson, W.A., and Wüthrich, K. eds. (1993). *Macromolecular Structures: Atomic Structures of Biological Macromolecules Reported During 1992*. Current Biology Ltd., London.
- Henderson, W.A., and Wüthrich, K. eds. (1991). *Macromolecular Structures: Atomic Structures of Biological Macromolecules Reported During 1990*. Current Biology Ltd., London.
- Henderson, W.A., and Wüthrich, K. eds. (1992). *Macromolecular Structures: Atomic Structures of Biological Macromolecules Reported During 1991*. Current Biology Ltd., London.
- Hovmöller, S., Slaughter, M., Berriman, J., Karlsson, B., Weiss, H., and Leonard, K. (1983). Structural Studies of Cytochrome Reductase. Improved Membrane Crystals of the Enzyme Complex and Crystallization of a Subcomplex. *J. Mol. Biol.* **165**, 401-406.
- Hunter, C.N., and R. van Grondelle. (1987). In: *Structure and Function in Photosynthetic light Harvesting Systems*. (Scheer, H., and Schneider, S., Eds) De Gruyter, Berlin.
- Imhoff, J.F., Kushner, D.J., Kushwaha, S.C., and Kates, M. (1982). Polar Lipids in Phototrophic Bacteria of the Rhodospirillaceae and Chromatiaceae Families. *J. Bacteriol.* **150**, 1192-1201.
- Imhoff, J.F., Trüper, H.G., and Pfennig, N. (1984). Rearrangement of the Species and Genera of the Phototrophic Purple Nonsulfur Bacteria. *Init. J. Syst. bacteriol.* **34**, 340-343.
- Isler, O., Guttman, G., and Solms (Eds.). (1971). *in The Carotenoids*, Birkhauser Verlag, Basel.
- IUPAC-IUB Joint Commission on Nomenclature. (1984). Nomenclature and Symbolism for Amino Acids and Peptides. *Eur. J. Biochem.* **138**, 9-37.

\* References which were unavailable

## References:

- Jap, B.K., Downing, K.H., and Walian, P.J. (1990). Structure of *Phoe* Porin in Projection at 3.5 Å Resolution. *J. Struct. Biol.* **103**, 57-63.
- Jap, B.K., Zulauf, M., Scheybani, T., Hefti, A., Baumeister, W., Aebi, U. (1992). 2D Crystallization: From Art to Science. *Ultramicroscopy.* **46**, 45-84.
- Jay, F., Lambillote, M., and Mühlethaler, K. (1983). Localization of *Rhodospseudomonas viridis* Reaction Center and Light-harvesting Proteins Using Ferritin-antibody Labelling. *Eur. J. Cell. Biol.* **30**, 1-8.
- Jay, F., Lambillote, M., Stark, E., and Mühlethaler, K. (1984). The Preparation and Characterization of Native Photoreceptor Units from the Thylakoids of *Rhodospseudomonas viridis*. *EMBO J.* **3**, 773-776.
- Jenney, F.R., Daldal, F. (1993). A Novel Membrane-associated c-type cytochrome, cyt *c*<sub>2</sub>, can Mediate the Photosynthetic Growth of *Rhodobacter capsulatus* and *Rhodobacter sphaeroides*. *EMBO J.* **12**, 1283-1292.
- Jolchine and Reiss-Husson (1974). Comparative Studies on the Two Reaction Centre Preparations from *Rps. sphaeroides* Y. *FEBS. Letts.* **40**, 5-8.
- Joliot, P., Verméglio, A., and Joliot, A. (1989). Evidence for Supercomplexes Between Reaction Centers, Cytochrome *c*<sub>2</sub> and Cytochrome *bc*<sub>1</sub> Complex in *Rhodobacter sphaeroides* Whole Cells. *Biochim Biophys. Acta.* **975**, 336-345.
- Kaptein, R. (1993). Protein-Nucleic Acid Interactions by NMR. *Current Opinion in Structural Biology.* **3**, 50-56.
- Kaufmann, N., Reidl, H.H., Golecki, J.R., Garcia, A.F., and Drews, G. (1982). Differentiation of the Membrane System in Cells of *Rhodospseudomonas capsulata* After Transition from the Chemotrophic to Phototrophic Growth Conditions. *Arch. Microbiol.* **131**, 313-322.
- Kellogg, E.C., Kolaczowski, S., Wasiewski, M.R., and Tiede, D.M. (1989). Measurement of the Extent of Electron Transfer to the Bacteriopheophytin in M-Subunit Reaction Centres of *Rhodospseudomonas viridis*. *Photosynth. Res.* **22**, 47-59.
- Kiley, P.J., and Kaplan, S. (1987). Cloning, DNA Sequence and Expression of the *Rhodobacter sphaeroides* light harvesting B800-850- $\alpha$  and B800-850- $\beta$  genes. *J. Bacteriol.* **169**, 3268-3275.
- Kiley, P.J., and Kaplan, S. (1988). Molecular Genetics of Photosynthetic Membrane Biosynthesis in *Rhodobacter sphaeroides*. *Microbiol. Revs.* **52**, 50-69.
- Kirmaier, C., and Holten, D. (1987) Primary Photochemistry of Reaction Centers from the Photosynthetic Purple Bacteria. *Photosynth. Res.* **13**, 225-260.
- Kirmaier, C., Holten, D., and Parson, W.W. (1985a). Picosecond-Photodichroism Studies of the Transient States in *Rhodospseudomonas sphaeroides* Reaction Centers at 5K - Effects of Electron Transfer on the 6 Bacteriochlorin Pigments. *Biochim. Biophys. Acta.* **810**, 49-61.
- Kirmaier, C., Holten, D., and Parson, W.W. (1985b). Temperature and Detection Wavelength Dependence of the Picosecond Electron Transfer Kinetics Measured in *Rhodospseudomonas sphaeroides* Reaction Centers - Resolution of New Spectral and Kinetic Components in the Primary Charge separation Process. *Biochim. Biophys. Acta.* **810**, 33-48.
- Kistler, J., and Kellenberger, J. (1977). *J. Ultrastruct. Res.* **59**, 76.\*
- Knacker, T., Harwood, J.L., Hunter, C.N., and Russell, N.J. (1985). Lipid Biosynthesis in Synchronized Cultures of the Photosynthetic Bacterium *Rhodospseudomonas sphaeroides*. *Biochem. J.* **229**, 701-710.
- Konstantinov, A.A., (1990). Vectorial Electron and Proton Transfer Steps in the Cytochrome *bc*<sub>1</sub> Complex. *Biochim. Biophys. Acta.* **1018**, 138-141.

\* References which were unavailable

- Kornberg, R.D., and Darst, S.A. (1991). Two-dimensional Crystals of Proteins on Lipid Monolayers. *Curr. Opin. Struct. Biol.* **1**, 642-646.
- Kramer, J.H.M., Grondelle, R. van, Hunter, C.N., (1984). Pigment Organization of the B800-850 Complex of *Rhodospseudomonas sphaeroides*. *Biochim. Biophys. Acta.* **765**, 156-165.
- Kühlbrandt, W. (1992). Two-dimensional Crystallization of Membrane Proteins. *Q. Rev. Biophys.* **25**, 1-49.
- Kühlbrandt, W., and Wang, D.N. (1991). Three Dimensional Structure of the Plant Light-harvesting Complex determined by Electron Crystallography. *Nature.* **350**, 130-134.
- Kühlbrandt, W., Wang, D.N., Fujiyoshi, Y. (1994). Atomic Model Of Plant Light-harvesting Complex By Electron Crystallography. *Nature.* **367**, 614-621.
- Laemmli, U.K. (1970). Cleavage of Structural Proteins During the Assembly of the Head of Bacteriophage T4. *Nature.* **227**, 680.
- Lake, J.A., Clark, M.W., Henderson, E., Fay, S.P., Oakes, M., Scheinman, A., Thornber, J.P., and Mah, R.A. (1985). Eubacteria, Halobacteria, and the Origin of Photosynthesis: The Photocytes. *Proc. Natl. Acad. Sci. U.S.A.* **82**, 3716-3720.
- Lampe, P.D., Kistler, J., Hefti, A., Bond, J., Muller, S., Johnson, R.G., and Engel, A. (1991). *In vitro* Assembly Of Gap-Junctions. *J. Struct. Biol.* **107**, 281-290.
- Lee, J.K., Kiley, P.J., and Kaplan, S. (1989). Post-translational Control of *puc* Operon Expression of B800-850 light-harvesting Complex Formation in *Rhodobacter sphaeroides*. *J. Bacteriol.* **171**, 3391-3405.
- Llopiz P., Neunlist, S., and Rohmer, M. (1992). Prokaryotic Tetrepenoids: O- $\alpha$ -D-Glucuronopyranosyl Bacteriohopanetetrol, a Novel Hopanoid from the Bacterium *Rhodospirillum rubrum*. *Biochem. J.* **287**, 15-161.
- Lyon, M.K., Marr, K.M., Furcinitti, P.S. (1993). Formation and Characterization of 2-Dimensional Crystals of Photosystem-II. *J. Struct. Biol.* **110**, 133-140.
- Mäntele, W., Steck, K., Becker, A., Wacker, T., Welte, W., Gad'on, N., and Drews, G. (1988). *Spectroscopic Studies of Crystallized Pigment-protein Complexes of R. palustris*. In: The Photosynthetic Reaction Centre (Eds. Breton, J., and Vermeiglio, A). Plenum Publishing Co. New York.
- Mäntele, W., Steck, K., Wacker, T., and Welte, W. (1985). *Antennas and Reaction Centers of Photosynthetic Bacteria*. in Spring Series in Chemical Physics **42**, (Ed. Michel-Beyerle, M.E.). Springer-Verlag, Berlin. pp88-94.
- McPherson, A. (1982). *The Preparation and Analysis of Protein Crystals*. John Wiley and Sons. New York.
- McPherson, A.Jr. (1976). Crystallization of Proteins from Polyethylene Glycol. *J. Biol. Chem.* **251**, 6300-6303.
- Meckenstock, R.U., Krusche, K., Brunisholz, R.A., and Zuber, H. (1992). The Light-harvesting Core-Complex and the B820-Subunit from *Rhodospseudomonas marina*. Part II. Electron Microscopic Characterisation. *FEBS. Letts.* **311**, 135-138.
- Meckenstock, R.U., Krusche, K., Staehelin, L.A., Cyrklaff, M., Brunisholz, R.A., and Zuber, H. (1993). The Sixfold Symmetry of the B880 Light-harvesting Membranes of *Rhodospseudomonas marina*. *Biol. Chem. Hoppe-Seyler.*, in press
- Mejbaum-Katzenellenbogen, S., and Drobyszzycka, W.J. (1959). New Method for Quantitative Determination of Serum Proteins Separated by Paper Electrophoresis. *Clin. Chim. Acta.* **4**, 515-522.

- Michel, H. (1982). Three Dimensional Crystals of a Membrane Protein Complex: The Photosynthetic Reaction Centre from *Rhodospseudomonas viridis*. *J. Mol. Biol.* **158**, 567-572.
- Michel, H. (1991). General and Practical Aspects of Membrane Protein Crystallisation. In: Crystallisation of Membrane Proteins. Michel, H. (Ed.). pp73-89. CRC Press. London.
- Michel, H., and Deisenhofer, J. (1986a). X-ray Diffraction Studies on a Crystalline Bacterial Photosynthetic Reaction Centre. In *Photosynthesis III: Photosynthetic Membranes and Light-Harvesting System Encyclopedia of Plant Physiology, New Series*, **19**. (Eds. Staehelin, L.A and Arntzen, C.J.) Springer-Verlag, Berlin.
- Michel, H., Weyer, K.A., Gruenberg, H., Dunger, I., Oesterhelt, D., and Lottspeich, F. (1986b). The Light and Heavy Subunits of the Photosynthetic Reaction Centre from *Rhodospseudomonas viridis* : Isolation of the Genes, Nucleotide and Amino-Acid Sequence. *EMBO. J.* **5**, 1149-1158.
- Michel, H., Weyer, K.A., Gruenberg, H., Lottspeich, F. (1985). The Heavy Subunit of the Photosynthetic Reaction Center from *Rhodospseudomonas viridis*: Isolation of the Gene Nucleotide and Amino-Acid Sequence. *EMBO. J.* **4**, 1667-1672.
- Michel-beyerle, M.E., Plato, M., Deisenhofer, J., Michel, H., Bixon, M., and Jortner, J. (1988). Unidirectionality of Charge Separation in Reaction Centers of Photosynthetic Bacteria. *Biochim. Biophys. Acta.* **932**, 52-70.
- Miller, K.R. (1979). Structure of a Bacterial Photosynthetic Membrane. *Proc. Natl. Acad. Sci. U.S.A.* **76**, 6415-6419.
- Miller, K.R. (1982). Three Dimensional Structure of a Photosynthetic Membrane. *Nature.* **300**, 53-55.
- Miller, K.R., and Jacob, J. (1983). Two Dimensional Crystals Formed from Photosynthetic Reaction Centers. *J. Cell. Biol.* **97**, 1266-1270.
- Mitchell, P. (1961). Coupling of Phosphorylation to Electron and Hydrogen Transfer by a chemi-osmotic Type of Mechanism. *Nature.* **191**, 144-148.
- Molisch, H. (1907). *Die Purpurbakterien nach neuen untersuchungen*. Fisher Verlag. Jena. 95.\*
- Neiderman, R.A., and Gibson, K.D., (1976). *Isolation and Physiochemical Properties of Membranes*. In: *The Photosynthetic Bacteria* (Clayton, R.K., and Sistrom, W.R., eds) Plenum Press, New York.
- Newman, R.H. (1991). 2 Dimensional Crystallization of Proteins on Lipid Monlayers. *Elect. Micro. Revs.* **4**, 197-203.
- Nicolls, D.G. (1982). *Bioenergetics: An Introduction to Chemiosmotic Theory*, Academic Press, New York.
- Nunn, R.S., Artymiuk, P.J., Baker, P.J., Rice, D.W., and Hunter, C.N. (1992). Purification and Crystallization of the Light Harvesting LH1 Complex from *Rhodobacter sphaeroides*. *J. Mol. Biol.* **228**, 259-1262.
- Okamura, M.Y., Feher, G., and Nelson, N. (1982). *Reaction Centers*. In *Photosynthesis Volume I: Energy Conservation by Plants and Bacteria*. (Ed. Govindjee). Academic Press. pp 195-272.
- Ourisson, G., Rohmer, M., and Poralla, K. (1987). Prokaryotic Hopanoids and Other Polyterpenoid Sterol Surrogates. *Ann. Rev. Microbiol.* **41**, 301-333.
- Papiz, M.Z., Hawthornthwaite, A.M., Cogdell, R.J., Woolley, K.J., Wightman, P.A., Ferguson, L.A., and Lindsay, J.G. (1989). Crystallisation and Characterisation of Two Crystal Forms of the B800-850 Light-Harvesting Complex from *Rhodospseudomonas acidophila* strain 10050. *J. Mol. Biol.* **209**, 833-835.

\* References which were unavailable

## References:

- Parkes-Loach, P., Sprinkle, J.R., and Loach, P.A. (1988). Reconstruction of the B873 Light-Harvesting Complex of *Rhodospirillum rubrum* from separated  $\alpha$ - and  $\beta$ - Polypeptides and Bacteriochlorophyll *a*. *Biochem. J.* **27**, 2718-2727.
- Parson, W.W. (1978) *Quinones as Secondary Electron Acceptors*. In: The Photosynthetic Bacteria. (Eds. Clayton, R.K., and Sistrom, W.R.) 445-470. Plenum Press, New York.
- Parson, W.W., and Holten, D. (1986). Primary Electron Transfer Reactions in Photosynthetic Bacteria: Energetics and Kinetics of Transient States. In: "Photosynthesis III: Photosynthetic Membranes and Light Harvesting Systems". Eds Staehelin, L.A., and Artzen, C.J.). Encyclopedia of Plant Physiology, **19**, Springer-Verlag.
- Paul, A., Engelhardt, U., Jakubowski, U., and Baumeister, W. (1992). 2-Dimensional Crystallization of a Bacterial Surface Protein on Lipid Vesicles Under Controlled Conditions. *Biophys. J.* **61**, 172-188.
- Pearl, R. (1927). The Growth of Populations. *Q. Rev. Biol.* **2**, 532-548.
- Pfennig, N (1967). Photosynthetic Bacteria. *Ann. Rev. Microbiol.* **21**, 285-324.
- Pfennig, N (1969). *Rps. acidophila*, sp. n., a new Species of the Budding Purple Nonsulphur Bacteria. *J. Bacteriol.* **99**, 597-602.
- Pfennig, N (1978). *General Physiology and Ecology of Photosynthetic Bacteria*. In 'The Photosynthetic Bacteria' (Eds. Clayton, R.K. and Sistrom, W.R.). pp 3-14. Plenum Press. New York. London.
- Pfennig, N and Truper, H. G. (1973). *The Rhodospirillales (Phototrophic or Photosynthetic Bacteria)*. IN: Handbook of Microbiology. Vol I Organismic Microbiology. Eds. Laskin, A.I. and Lechevalier, A. CRC Press. London
- Pfennig, N and Truper, H.G. (1974). *The Phototrophic Bacteria*. In 'Bergeys Manual of Determinative Bacteriology', 8<sup>th</sup> Edition. Eds. Buchan, R. E. and Gibbons, N. E., Williams and Williams Co. Baltimore.
- Pfennig, N and Truper, H.G. (1971). New nomenclature Combinations in the Phototrophic Sulphur Bacteria. *Int. J. Syst. Bacteriol.* **21**, 11-24.
- Phipps, B.M., Hoffmann, A., Stetter, K.O., and Baumeister, W. (1991). A Novel ATPase Complex Selectively Accumulated Upon Heat-Shock is a Major Cellular-Component of Thermophilic Archaeobacteria. *EMBO J.* **10**, 1711-1722.
- Popot, J.I., Gerchman, S.E., and Engelman, D.M. (1987). Refolding Of Bacteriorhodopsin In Lipid Bilayers - A Thermodynamically Controlled 2-Stage Process. *J. Mol. Biol.* **198** No.4 Pp.655-676
- Pucheu, N.L., Kerber, N.L., and Garcia, A.F. (1974). Comparative Studies on Membranes Isolated from *Rhodopseudomonas viridis* Grown in the Presence and in the Absence of Yeast Extract. *Arch. Microbiol.* **101**, 259-272.
- Reed, D., and Raveed, D. (1972). Some Properties of the ATPase from Chromatophores of *Rhodopseudomonas sphaeroides* and its Structural Relationship to the bacteriochlorophyll Proteins. *Biochim Biophys. Acta.* **283**, 79-91.
- Rees, D. C., Komiya, H., and Yeates, T. O. (1989) The Bacterial Reaction Center as a Model for Membrane Proteins. *Ann. Rev. Biochem.* **58**, 607-633.
- Reiss-Husson, R., Gaucher, J. F., Ducruix, A., and Arnoux, B. (1992). Structural Studies of Wild Type *Rhodobacter sphaeroides* Y Reaction Center. *Photosynthesis Research.* **34**, 85.
- Rhodes, G. (1993). Crystallography Made Clear. Academic Press, London.
- Rich, P.R., (1983). Electron and Proton Transfers Through Quinones and Cytochrome *bc* Complexes. *Biochim. Biophys. Acta.* **768**, 53-79.

\* References which were unavailable

## References:

- Robert, B., Andrainambinintsoa, S., and Lutz, M. (1985). Structural Characterization of High 800nm-absorbing Light-harvesting Complexes from Rhodospirillales from their Resonance Raman Spectra. *J. Biochem.* **98**, 349-354.
- Roberts, M.M., White, J.I., Grütter, M.G., and Burnett, R.M. (1986). Three-dimensional Structure Of The Adenovirus Major Coat Protein Hexon. *Science.* **232**, 1148-1151.
- Robertson, D.E., and Dutton, P.I. (1988). The Nature and Magnitude of the Charge Separation Reactions of Ubiquinol Cytochrome  $c_2$  Oxidoreductase *Biochim. Biophys. Acta.* **935**, 273-291.
- Roth, M., Arnoux, B., Ducruix, A., and Reiss-Husson, F. (1991). Structure of the Detergent Phase and Protein-Detergent Interactions in Crystals of the Wild-Type (Strain Y) *Rhodobacter sphaeroides* Photochemical Reaction Center. *Biochemistry.* **30**, 9403-9413.
- Roth, M., Lewit-Bentley, A., and Michel, H., (1989). Detergent Structure In Crystals of a Bacterial Reaction Centre. *Nature.* **340**, 659-662.
- Rowe, W.P., Huebner, R.J., Gilmore, L.K., Parrott, R.H., and Ward, T.G. (1953). Isolation of a Cytopathogenic Agent from Human Adenoids Undergoing Spontaneous Degeneration in Tissue Culture. *Proc. Soc. Exp. Biol.* **84**, 570-573.
- Russell, N.J., and Harwood, J.L. (1979). Changes in the Acyl Lipid Composition of Photosynthetic Bacteria Grown Under Photosynthetic and Non-photosynthetic Conditions. *Biochem. J.* **181**, 339-345.
- Sambrook, J., Fritsch, F.F., and Maniatis, T. (Eds)(1989). *Preparation of Dialysis Tubing.* In: Molecular Cloning. A laboratory Manual. 2<sup>nd</sup> Edition. pE39. Cold Harbor Laboratory Press.
- Sass, H.J., Beckmann, E., Zemlin, F., van Heel, M., Zeitler, E., Rosenbusch, J.P., Dorset, D.L., and Massalski, A. (1989). Densely Packed  $\beta$ -Structure at the Protein-lipid Interface of Porin Revealed by High-Resolution Cryo-electron Microscopy. *J.Mol.Biol.* **209**, 171-175.
- Sauer, K. and Austin, L.A. (1978). Bacteriochlorophyll-Protein Complexes from the Light-Harvesting Antenna of Photosynthetic Bacteria. *Biochemistry.* **17**, 2011-2019.
- Schägger, H and von Jagow, G. (1987). Tricine-Sodium Dodecyl Silfate-Polyacrylamide Gel Electrophoresis for the Serparation of Proteins in a Range from 1 to 100 kDa. *Ana. Biochem.* **166**, 368-379 .
- Schultz, P., Celia, H., Riva, M., Sentenac, A., and Oudet, P. (1993). 3-Dimensional Model of Yeast RNA Polymerase-I Determined by Electron-Microscopy of 2-Dimensional Crystals. *EMBO J.* **12**, 2601-2607.
- Semenov, A.Y. (1993). Electrogenic Steps During Electron Transfer *via* the Cytochrome  $bc_1$  Complex of *Rhodobacter sphaeroides* Chromatophores. *FEBS Letts.* **321**, 1.5.
- Sharp, K.A. (1991). The Hydrophobic Effect. *Curr. Opinion Struct. Biol.* **1**, 171-174.
- Shiozawa, J.A., Welte,W., Hodapp, N., and Drews, G. (1982). Studies on the Size and Composition of the Isolated Light-harvesting B800-850 Pigment-Protein Complex of *Rhodospseudomonas capsulatus*. *Arch. Biochem. Biophys.* **213**, 473-4885.
- Shreve, A.P., Cherepy, N.J., Franzen, S., Boxer, S.G., and Mathis, R.D. (1992). Rapid Flow Resonance Raman Spectroscopy of Bacterial Photostnthetic Reaction Centres. *FASEB Journal* **6**, Article #578.
- Singer, S.J., and Nicolson, G.L. (1972). The Fluid Mosaic Model of the Structure of Cell Membranes. *Science.* **175**, 720-731.
- Sistrom, W.R., Griffiths, M., and Stainer, R.Y. (1956). The Biology of a Photosynthetic Bacteria Which Lacks Colored Carotenoids. *J.Cell. Comp. Physiol.* **48**, 473.

\* References which were unavailable

- Spoehr, H.A. (1926). *Photosynthesis. American Chemical Society Monographic Series. The Chemical Catalog Company Inc., New York.*
- Stadtward-Demchick, R., Turner, F.R., and Gest, H. (1990). Physiological Properties of the Thermotolerant Photosynthetic Bacterium, *Rhodospirillum centenum*. *FEMS Microbiol. Letts.* **67**,139-144.
- Stadtward-Demchick, R., Turner, F.R., and Gest, H. (1990). *Rhodopseudomonas cryptolactis*, sp. nov., a New Thermotolerant Species of Buding Phototrophic Purple Bacteria. *FEMS Microbiol. Letts.* **71**,117-122.
- Staehelin, L.A., Golecki, J.R., and Drews, G. (1980). Supramolecular Organization of Chlorosomes (*Chlorobium* vesicles) and their Membrane Attachment Site in *Chlorobium limicola*. *Biochim. Biophys. Acta.* **589**, 30-45.
- Stainer, R.Y., Adelberg, E.A., and Ingraham, J.L. (Ed.) 1976. *The Photosynthetic Prokaryotes*. In 'General Microbiology; Fourth edition'. pp. 527-563. The MacMillan Press Ltd. London.
- Stark, W., Jay, F., and Mühlethaler, K. (1986). Localization of Reaction Center and Light-harvesting Complexes in the Photosynthetic Unit of *Rp. viridis*. *Arch. Microbiol.* **146**, 130-133.
- Stark, W. (1984). Isolierung und Charakterisierung der Thylakoidmembranen von *Rhodopseudomonas viridis*. PhD Thesis, Eidgenössischen Technischen Hochschule, Zürich.
- Sternberg, B., L'Hostis, C., Whiteway, C.A., and Watts, A. (1992). The Essential Role of Specific *Halobacterium halobium* Polar Lipids in 2D-array Formation of Bacteriorhodopsin. *Biochim. Biophys. Acta.* **1108**, 21-30.
- Stewart, P.L., Burnett, R.M., Cyrklaff, M., and Fuller, S.D., (1991). Image Reconstruction Reveals the Complex Molecular Organization of Adenovirus. *Cell.* **67**, 145-154..
- Stewart, P.L., Fuller, S.D., Burnett, R.M. (1993). Difference Imaging of Adenovirus - Bridging the Resolution Gap Between X-Ray Crystallography and Electron-Microscopy. *EMBO J.* **12**, 2589-2599.
- Stocker, J.W., Taguchi, A, K.W., Murchison, H.A., Woodbury, N.W., and Boxer, S.G. (1992). Spectroscopic and Redox Properties of sym1 and (M)F195H: *Rhodobacter capsulatus* Reaction Center Symmetry Mutants Which Affect the Initial Electron Donor. *Biochemistry.* **31**, 10356-10362.
- Story, R.M., and Steitz, T.A. (1992b). Structure of the Rec A Protein-ADP Complex: Implications for ATPase Coupling to DNA Binding. *Nature.* **355**, 374-376.
- Story, R.M., Weber, I.T., and Steitz, T.A. (1992a). The Structure of the *E. coli* RecA Protein Monomer and Polymer. *Nature* **355**, 318-325.
- Strak, W., Kühlbrandt, W., Wildhaber, J., Wehrli, E., and Mühlethaler, K. (1984). The Structure of the Photoreceptor Unit of *Rhodopseudomonas viridis*. *EMBO J.* **3**, 777-783.
- Straley, S.C., Parson, W.W., Mauzerall, D.C., Clayton, R.K. (1973). Pigment-content and Molar Extinction Coefficients of Photochemical Reaction Centres from *Rhodopseudomonas sphaeroides*. *Biochim. Biophys. Acta.* **305**, 597-609.
- Subramaniam, S., Gerstein, M., Oesterhelt, D., Henderson, R. (1993). Electron Analysis of Structural Changes in the Photocycle of Bacteriorhodopsin. *EMBO J.* **12**, 1-8.
- Tadros, M.H., Frank, R., and Drews, G. (1985). The Complete Amino Acid Sequence of the Small Bacteriochlorophyll-Binding Polypeptide B800-850 $\beta$  from Light-Harvesting Complex B800-850 of *Rhodopseudomonas capsulata*. *F.E.B.S. Lett.* **183**, 91-94.
- Tadros, M.H., Suter, F., Drews, G., and Zuber, H. (1983). The Complete Amino Acid Sequence of the Large Bacteriochlorophyll-Binding Polypeptide from Light-harvesting Complex II (B800-850) of *Rhodopseudomonas capsulata*. *Eur. J. Biochem.* **129**, 533-536.

- Tadros, M.H., Suter, F., Seydewitz, H.H., Witt, I., Zuber, H., and Drews, G. (1984). Isolation and Complete Amino Acid Sequence of the Small Bacteriochlorophyll-binding Polypeptide from Light-harvesting Complex I (B870) of *Rhodospseudomonas capsulata*. *Eur. J. Biochem.* **138**, 209-212.
- Taguchi, A, K.W., Stocker, J.W., Alden, R.G., Causgrove, T.P., Peloquin, J.M., Boxer, S.G., and Woodbury, N.W. (1992). Biochemical Characterization and Electron-Transfer Reactions of sym1, a *Rhodobacter capsulatus* Reaction Center Symmetry Mutant Which Affects the Initail Electron Donor. *Biochemistry.* **31**, 10345-10355.
- Tanford, C. (1980). *The Hydrophobic Effect*. John Wiley and Sons. Ltd. New York.
- Theiler, R., Suter, F., Wiemken, V., and Zuber, H. (1984a). The Light-harvesting Polypeptides of *Rhodospseudomonas sphaeroides* R-26.1. *Hoppe-Seylers Z. Physiol. Chem.* **365**, 689-701.
- Theiler, R., Suter, F., Zuber, H. and Cogdell, R.J. (1984b). A Comparison of the Primary Structure of the Two B800-850 Apoproteins from Wild-Type *Rhodospseudomonas sphaeroides* Strain 2.4.1. and a Carotenoidless Mutant Strain R-26.1. *F.E.B.S. Letts.* **175**, 231-237.
- Thorber, J.P, Cogdell, R.J., Pierson, K.B., and Seftor, R.E.B. (1983). Pigment-Protein Complexes of Purple photosynthetic Bacteria: An Overview. *J. Cell. Biochem.* **23**, 159-169.
- Trüper, H.G and Pfennig, N. (1978) *Taxonomy of the Rhodospirillales*. In 'The Phototropic Bacteria' (Eds. Clayton, R.K and Sistrom, W.R). pp 19-27. Plenum Press. New York. London
- Trüper, H.G. (1976). Higher Taxa of the Phototrophic Bacteria Chloroflexaceae Fam. nov. a Family for the Gliding Filamentous Phototrophic Bacteria. *Int. J. Syst. Bacteriol.* **26**, 74.
- Unwin, P.N.T., Henderson R., (1975) Molecular Structure Determination by Electron Microscopy of Unstained Crystalline Specimens. *J.Mol.Biol.* **94**, 425-440.
- Vagra, A.R., and Staehelin, L.A. (1983). Spatial Differentiation in Photosynthetic and Non-Photosynthetic Membranes of *Rhodospseudomonas palustris*. *J. Bacteriol.* **154**, 1414-1430.
- Vagra, A.R., and Staehelin, L.A. (1985). Pigment-Protein Complexes from *Rhodospseudomonas palustris*: Isolation, Characterization, and Reconstitution into Liposomes. *J. Bacteriol.* **161**, 921-927.
- Van Neil, C.B. (1941). The bacterial Photosynthesis and their Importance for General Problem of Photosynthesis. *Adv. Enzynol.* **1**. 263-328
- Vrendenberg, W.J. and Amez, J. (1967). Adsorption Characteristics of Bacteriochlorophyll Types in Purple Bacteria and Efficiency of Energy Transfer Between Them. In 'Brookhaven Symposia in Biology' **19**, 49-61.
- Wacker, T., Gad'on, N., Becker, A., Mäntele, W., Kreutz, W., Drews, G., and Welte, W. (1986). Crystallization and Spectroscopic Investigation With Polarised Light of the Reaction Centre B875 Light-Harvesting Complexes of *Rhodospseudomonas palustris*. *F.E.B.S. Letts.* **197**, 267-273.
- Wacker, T., Gad'on, N., Steck, K., Welte, W., and Drews, G. (1988). Isolation of Reaction Centre and Antenna Complexes from the Halophilic Purple Bacterium *Rs. salexigens*, crystallization and spectroscopic investigation of the B800-850 Complex. *Biochim. Biophys. Acta.* **933**, 299-305.
- Wagner, G., Hyberts, S.G., and Havel, T.F. (1992). NMR Determination In Solution: A Critique and Comparison with x-ray Crystallography. *Annu. Rev. Biophys. Biomol. Struct.* **21**, 167-198.

- Wagner-Huber, R., Brunisholz, R.A., Bissig, I., Frank, G., Suter, F., and Zuber, H. (1992). The Primary Structure of the Antenna Polypeptides of *Ectothiorhodospira halochloris* and *Ectothiorhodospira halophila*: Four Core-Type Antenna Polypeptides in *E. halochloris* and *E. halophila*. *Eur. J. Biochem.* **205**, 917-925.
- Wakabayashi, T., Senior, A.E., Hatase, O., Hayashi, H., and Green, D.E. (1972). *Bioenergetics.* **3**, 339-344.\*
- Wall, J.S., and Hainfeld, J.F. (1986). Mass Mapping with the Scanning Transmission Electron Microscope. *Ann. Rev. Biophys. Chem.* **15**, 355-376.
- Warburg, O., and Negelein, E. (1932). *Z. Physik. Chem.* **106**, 191.
- Weiss, M.S. Kreuzsch, A., Schiltz, E., Nestel, U., Welte, W., Weckesser, J., and Schulz, G.E. (1991). The Structure of Porin from *Rhodobacter capsulatus* at 1.8 Å Resolution. *F.E.B.S. Letts.* **2**, 379-382.
- Welte, W., Gadon, N., Becker, A., Mantele, W., Kreutz, W., Drews, G., and Welte, W. (1986). Crystallisation and Spectroscopic Investigation with Polarised Light of the Reaction Centre B875 Light-harvesting Complexes of *Rhodopseudomonas palustris*. *F.E.B.S. Letts.* **197**, 267-273.
- Welte, W., Wacker, T., Leis, M., Kreutz, W., Shiozawa, J., Gadon, N., and Drews, G. (1985). Crystallisation of the Photosynthetic Light-harvesting Pigment-Protein Complex B800-850 of *Rhodopseudomonas capsulata*. *F.E.B.S. Letts.* **182**, 260-264.
- Williams, J.C., Steiner, L.A., Feher, G., and Simon, M.I. (1984). Primary Structure of the L-Subunit of the Reaction Centre from *Rhodopsudomonas sphaeroides*. *Proc. Natl. Acad. Sci. U.S.A.* **81**, 7303-7307.
- Williams, J.C., Steiner, L.A., Ogden, R.C., Simon, M.I., and Feher, G. (1983). Primary Structure of the M-Subunit of the Reaction Center from *Rhodopseudomonas sphaeroides*. *Proc. Natl. Acad. Sci. U.S.A.* **80**, 6505-6509.
- Yeates, T.O., Korniya, H., Chirino, A., Rees, D.C., Allen, J.P., and Feher, G. (1988). Structure of the Reaction Centres from *Rhodobacter sphaeroides* R-26 and 2.4.1: Symmetry Relations and Sequence Comparisons Between Different Species. *Proc. Natl. Acad. Sci. U.S.A.* **85**, 9012-9025.
- Yeates, T.O., Korniya, H., Rees, D.C., Allen, J.P., and Feher, G. (1987). Structure of the Reaction Center from *Rhodobacter sphaeroides* R-26: Membrane-Protein Interactions. *Proc. Natl. Acad. Sci. U.S.A.* **84**, 6438-6442.
- Yildiz, F.H., Gest, H., and Bauer, C.E. (1991). Genetic Analysis of Photosynthesis in *Rhodospirillum centenum*. *J. bacteriol.* **173**, 4163-4170.
- Youvan, D.C., and Ismail, S. (1985). Light-harvesting II (B800-850 Complexes) Structural Genes from *Rhodopseudomonas capsulata*. *Proc. Natl. Acad. Sci. U.S.A.* **83**, 58-62.
- Youvan, D.C., Bylina, E.J., Alberti, M., Begusch, H., and Hearst, J.E. (1984). Nucleotide and Deduced Polypeptide Sequences of the Photosynthetic Reaction Center. B870-Antenna, and Flanking Polypeptide from *Rhodopseudomonas capsulata*. *Cell.* **37**, 949-957.
- Zinth, W., Kaiser, W., and Michel, H. (1983). Efficient Photochemical Activity and Strong Dichroism of Single Crystals of Reaction Centers from *Rhodopseudomonas viridis*. *Biochim. Biophys. Acta.* **723**, 128-131.
- Zinth, W., Knapp, E.W., Fischer, S.F., Kaiser, W., Deisenhofer, J., and Michel, H. (1985). Correlation of Structural and Spectroscopic Properties of a Photosynthetic Reaction Center. *Chem. Phys. Lett.* **119**, 1-4.
- Zuber, H. (1985). Yearly Review: Structure and Function of Light Harvesting Complexes and their Polypeptides. *Photochem. Photobiol.* **42**, 821-844.

\* References which were unavailable

## References:

- Zuber, H. (1986). Structure of Light-harvesting Antenna Complexes of Photosynthetic Bacteria, Cyanobacteria and Red Algae. *Trends. Biochem. Sci.* 11, 414-419.
- Zuber, H. (1990). *Considerations on the Structural Principles of the Antenna Complexes of Phototrophic Bacteria* in *Molecular Biology of Membrane-Bound Complexes in Phototrophic bacteria* (Drews, G., and Dawes, E.A. eds). Plenum Press, New York. p161-180.
- Zuber, H., and Brunisholz, R.A. (1986). Structure and Function of Antenna Polypeptides and Chlorophyll-Protein Complexes: Principles and Variability. In: *Chlorophylls*. (Scheer, H., Ed.) CRC Press. London.



\* References which were unavailable